

**MULTI-SCALE PETROGRAPHY AND FLUID DYNAMICS OF
CAPROCKS ASSOCIATED WITH GEOLOGIC CO₂ STORAGE**

by

Jason Elliott Heath

Submitted in Partial Fulfillment
of the Requirements for the

Doctorate of Philosophy in Earth and Environmental Science
with Dissertation in Hydrology

New Mexico Institute of Mining and Technology
Department of Earth and Environmental Science

Socorro, New Mexico

December 2010

ABSTRACT

Implementation of the underground storage of anthropogenic CO₂ in geologic media requires containment of the CO₂. The general concept for onshore, deep (> 800 m) geologic environments includes both a permeable reservoir and an overlying low permeability, high capillary-breakthrough-pressure “caprock”. Significant migration of the buoyant CO₂ from the reservoir may lead to inadequate performance in terms of storage goals and possibly impact underground sources of drinking water. Consequently, the sealing efficiency of a caprock is critical.

Carbon dioxide can migrate as a separate phase (e.g., supercritical or gaseous depending on pressure and temperature conditions) and as a dissolved aqueous species through caprock features that range in size. These features vary from the microscopic (e.g., pore networks with sub- μm pore sizes) to some appreciable fraction of the caprock thickness (e.g., mesoscopic fractures) and up to the full thickness of the caprock (e.g., faults, connected fracture networks, and large-scale sedimentary discontinuities). Caprocks must impede CO₂ migration at all these scales for effective storage. The larger-scale, high permeability “seal bypass systems” are a major concern due to the potential of relatively rapid, significant loss of CO₂. Thus, the evaluation of caprock for CO₂ storage is a multi-scale challenge. It requires determination of the spatial scale of the feature that dominates the overall response (i.e., both temporal and spatial) of the system.

The research objective of this study is to assess performance of caprocks from the pore-scale up to that of the entire thickness and the field-scale (i.e., projected areal extent of storage site). Methods of assessment combine novel, high resolution three-dimensional imaging techniques of pore networks of caprocks, fracture characterization, and collection of noble gases from the top and bottom of a caprock. Mudstones are the focus as they constitute a primary caprock type in sedimentary basins. Noble gases are especially key for elucidating dominant transport processes of a caprock, which indicate the impact of seal bypass features on fluid fluxes.

Sub- μm reconstructions of pore networks from continental to shallow to deeper marine mudstones indicate that primary depositional environmental and burial history strongly control sealing efficiency (i.e., capillary breakthrough pressures). The sealing efficiency generally increases from proximal to distal mudstone facies, which is indicated by differences in geometric pore structure, pore types, connectivity of pores, and mercury intrusion pressures. Burial history can influence organic materials through mobilization and filling of pores, resulting in higher breakthrough pressures. Therefore, in general, choice of a high quality caprock seal involves identification of caprocks with primary distal environments and that have undergone deep burial.

Examination of pore-lining solid phases indicates that capillary sealing is governed by pore shapes and phases that are not identifiable except through high resolution direct characterization of the pores. Pore-lining phases are not directly indicated by bulk X-ray diffraction data. Organics can line pores and such linings may be the remains of once-mobile organics that modified the wettability of an originally clay-lined pore system. For shallow formations (i.e., ~ 800 m depth or shallower) interfacial

tension and contact angles indicate that breakthrough pressures would be sufficient to fracture the rock—thus, sealing by capillarity is indicated. Deeper seals have poorer capillary sealing if mica-like wetting dominates the wettability. However, little information on wetting properties of the pore-lining phases observed in this study is available in the literature. The results of this study thus show that there is a high degree of uncertainty in prediction of capillary sealing behavior. The wettability properties of CO₂ and brine in contact with common caprock minerals (i.e., clays) and organics should be a major focus of future research.

Study of a proposed regional, overpressured caprock—the Kirtland Formation, San Juan Basin, USA—via multi-scale methods suggests that although pore network properties can contribute to very high capillary sealing capacity and low permeabilities, larger-scale high-permeability features may exist. Fracture mineralization and gas saturation within and directly above the caprock evidence multiple episodes of fluid flow. Interpretation of ⁴He concentrations, measured at the top and bottom of the caprock, suggests low fluid fluxes through the caprock: 1) Of the total ⁴He produced *in situ* (i.e., at the location of sampling) by U and Th decay since deposition of the Kirtland Formation, a large portion still resides in the pore fluids. 2) Simple advection-only and advection-diffusion models, using the measured ⁴He concentrations, estimate low permeability ($\sim 10^{-20}$ m² or lower) for the thickness of the Kirtland Formation. These findings, however, do not guarantee the lack of a large-scale bypass system. The measured data, located near the boundary conditions of the models (i.e., the overlying and underlying aquifers), limit our testing of conceptual models and the sensitivity of model parameterization. Thus, we suggest approaches for future studies to better assess the

presence or lack of a seal bypass system at this particular site and for other sites in general.

Results of this study provide insight into the multi-scale ability of caprocks to retain CO₂. A mechanistic understanding of caprock sealing behavior over the full range of scales can help scientists and engineers screen and evaluate caprock and better design effective CO₂ storage sites.

Keywords: caprock, seal, or mudstone; pore network; capillarity; multi-scale; noble gas; carbon dioxide or CO₂

ACKNOWLEDGMENTS

The U.S. Department of Energy provided financial support through the National Energy Technology Laboratory's Southwest Regional Partnership on Carbon Sequestration (SWP) and the Office of Basic Energy Sciences, Division of Chemical Sciences, Geosciences, and Biosciences (BES). I received the support as a research assistant at the Petroleum Recovery Research Center at New Mexico Tech (NMT) and as a student intern at Sandia National Laboratories (SNL).

I thank the following institutions or individuals for permission to reproduce and/or modify several figures that I use in this dissertation: Laura J. Pyrak-Nolte (Figure 1.1), Cambridge University Press (Figures 2.1 and 2.3), American Geophysical Union (Figure 2.2), Elsevier Science (Figure 2.2), Anthony Williams (Figure 2.2), Geological Society of London (Figure 2.4), the United States Geological Survey (Figures 3.1A, 5.1B,C,D; 5.2), James Fassett (Figures 3.1B, 5.1F, 5.2), Micropaleontology Press (Figure 3.1C), John Wiley & Sons (Figure 3.1D), The Salt Institute (Figure 3.1D), Thomas Chidsey Jr. (Figure 3.2J), SEPM (Society for Sedimentary Geology) (Figure 3.16), American Association of Petroleum Geologists (Figure 5.1B), New Mexico Bureau of Geology and Mineral Resources (Figure 5.1E), and Geological Society of America (Figure 5.11). Where requested, I give a complete citation noting permission for usage in the figure caption.

Collaboration between the SWP and ConocoPhillips (COP) enabled execution of a coring program in the San Juan Basin, New Mexico, that formed the foundation of this research. I thank Eddie Pippin, Ryan Frost, and Tom Cochrane of COP. The Southeast Regional Carbon Sequestration Partnership (SECARB), through Richard Esposito of the Southern Company and Robin Petrusak of Advanced Resources International, Inc., provided core samples from SECARB's saline reservoir CO₂ sequestration field test near Mississippi Power Company's Plant Daniel, located near Escatawpa, Mississippi. The Utah Geological Survey supplied core samples from the Gothic shale, which overlies an enhanced oil recovery site in southeastern Utah. TerraTek, a Schlumberger company, performed several important analyses on core. Poro-Technology conducted mercury intrusion porosimetry.

I thank my researcher advisor, Dr. Brian McPherson (University of Utah). He has helped me on a weekly basis for the past several years. He encouraged my appreciation of and interest in coupled processes in the earth sciences. He has guided me as I developed ideas about how I should study caprocks, the focus of this dissertation. I appreciate his friendship and kindness. He also helped me develop as a professional geoscientist through participation in the SWP, of which he is the PI. Dr. McPherson encouraged my interaction with several institutions, such as the Utah and Colorado Geologic Surveys, COP, Schlumberger, Resolute Natural Resources, Los Alamos National Laboratory, and EnTech Strategies (which leads the yearly Research Experience in Carbon Sequestration summer school).

Each member of my dissertation committee provided support with various aspects of the dissertation research. The committee included: Dr. John Wilson (academic

advisor), Dr. Fred Phillips, Dr. Peter Mozley, Dr. Manvendra Dubey (Los Alamos National Laboratory), Dr. Julianna Fessenden-Rahn (Los Alamos National Laboratory), and Dr. Thomas Dewers (Sandia National Laboratories (SNL)). Dr. Wilson acted as academic advisor. Through interaction with him, I have learned how to better express the key issues of a research problem. Dr. Phillips suggested the use of helium as a caprock assessment tool. Dr. Mozley taught me petrography of mudstones and sandstones. Dr. Dubey encouraged me to come to New Mexico for my Ph.D. Dr. Fessenden-Rahn provided assistance with planning fieldwork. Dr. Dewers was my mentor at SNL and contributed technically to every dissertation chapter. Since I have been at SNL for the past two years, I have consulted often with Dr. Dewers. I appreciate his time and technical guidance. Although not on my committee, I express appreciation for Dr. Robert Bowman (NMT), who died June 6, 2009. In the winter of 2008, Dr. Bowman encouraged me to take his class on intermolecular and surface forces, even though at the time I was not interested in taking more classes. I took the class, and it turned out that Dr. Bowman was a master teacher. I have benefited tremendously from that class. It has allowed me to think about wettability and supercritical CO₂ (a quadrupolar molecular system with unique properties) in ways that I could never have before.

Scott Cooper of Fracture Studies, formerly with Sandia National Laboratories, collaborated with me on the coring program. He introduced me to Dr. John Lorenz (also of Fracture Studies), who provided training on fracture characterization of core. Scott encouraged me to apply for a student internship at SNL, which has helped me tremendously as a researcher. Many individuals at SNL provided guidance for my research or moral support including the following: Dr. Greg Elbring (my manager in the

Geophysics Department), Dr. David Borns, Dr. Peter Kobos, James Brainard, Dr. James Krumhansl, Dr. Paul Kotula, and Dr. John Merson. I express special thanks to Dr. Borns, who shared many concepts of risk analysis with me.

I thank my friend Alex Rinehart, a Ph.D. candidate at NMT. He assisted with interpretation of mercury intrusion porosimetry data (Chapter 3) and noble gas data (Chapter 5) and, thus, will be a coauthor on the journal article versions of these chapters.

I thank Susan Delap Heath, my wife. She provided technical editing of the dissertation and drafting expertise for several figures in Chapter 3. She has patiently and lovingly supported me during the process of completing the Ph.D degree.

Jason Heath

TABLE OF CONTENTS

	Page
LIST OF FIGURES	x
LIST OF TABLES	xxii
PART I. INTRODUCTION AND OVERVIEW OF RESEARCH ON CAPROCKS.....	1
CHAPTER 1. INTRODUCTION	2
1.1 CO ₂ Storage and Multi-Scale Transport Processes of Caprock Seals ...	2
1.2 Science Questions	6
1.3 Organization of the Dissertation	7
1.4 References.....	9
CHAPTER 2. CAPROCKS: MUCH IS STILL UNKNOWN AND WHY THIS MATTERS FOR GEOLOGIC CO ₂ STORAGE	13
Abstract.....	13
2.1. Introduction.....	14
2.2 Caprocks and Their Properties and Processes: Historical Trends in Research	15
2.3 Caprocks and CO ₂ Storage: Current Research Trends	21
2.4 Research Needs for Caprock Evaluation	29
2.5 References.....	33
PART II. PORE-NETWORK PROPERTIES AND SEALING BEHAVIOR	40

CHAPTER 3. PORE NETWORKS IN CONTINENTAL AND MARINE MUDSTONES: CHARACTERISTICS AND CONTROLS ON SEALING BEHAVIOR.....	41
Abstract.....	41
3.1 Introduction.....	42
3.2 Geologic Settings.....	45
3.3 Materials and Methods.....	58
3.4 Results	62
3.5 Discussion: Pore Networks and Sealing Quality	99
3.6 Summary and Conclusions	104
Acknowledgments.....	106
References Cited.....	107
CHAPTER 4. PORE-LINING COMPOSITION AND CAPILLARY BREAKTHROUGH PRESSURE OF MUDSTONE CAPROCKS: SEALING EFFICIENCY OF GEOLOGIC CO ₂ STORAGE SITES.....	114
Abstract.....	114
4.1 Introduction.....	115
4.2 Breakthrough Pressure and Wettability	118
4.3 Methods and Materials.....	122
4.4 Results.....	130
4.5 Discussion.....	153
4.6 Conclusions.....	155
Acknowledgments.....	155
References.....	156

PART III. MULTI-SCALE EVALUATION OF SEALING BEHAVIOR USING NATURAL TRACERS	160
CHAPTER 5. THE HELIUM LEAK DETECTOR AND MULTI-SCALE ASSESSMENT OF CAPROCK SEALING BEHAVIOR	161
Abstract.....	161
Introduction.....	162
Site Location and Geologic and Hydrogeological Settings	166
Methods and Materials.....	175
Kirtland Pore-Scale Properties.....	181
Core-Scale Matrix Properties.....	184
Fracture Characteristics from FMI Logs and Core.....	192
Formation-Scale Noble Gas Results and Cross-Seal Transport	197
Discussion and Conclusions: Multi-Scale Evaluation of Seal Bypass Systems	221
Acknowledgments.....	223
References.....	225
PART IV. CONCLUSIONS AND RECOMMENDATIONS.....	232
CHAPTER 6. SUMMARY, CONCLUSIONS, AND RECOMMENDATIONS.....	233
6.1. Summary and Conclusions	233
6.2. Scientific and Engineering Contributions.....	237
6.3. Opportunities (Limitations), Recommendations, and Risk Analysis.....	239
6.4. References.....	269

APPENDICES	274
APPENDIX A. SUPPLEMENTAL VIDEO FILES FOR CHAPTER 3.....	275
APPENDIX B. SUPPLEMENTAL DATA FOR CHAPTER 5 AND DATA FROM THE CORE ANALYSIS PROGRAM OF THE PUMP CANYON SITE, NM.....	277
B.1 Field Core Handling Report	277
B.2 Core Handling and Data Collected by TerraTek, a Schlumberger Company	291
B.3 Mercury Intrusion Porosimetry Data Collected by Poro-Technology.....	359
B.4 Inventory of Thin Sections and Billets.....	393
B.5 Mud log of Well EPNG Com A Inj #1.....	400

LIST OF FIGURES

	Page
Figure 1.1. Features, processes, and measurement resolution for understanding and assessing caprock sealing behavior (adapted from Pyrak-Nolte (2007) in DOE, 2007) (Nelson, 2009).....	5
Figure 2.1. Trapping mechanisms and storage security for CO ₂ storage sites. (after IPCC, 2005, © 2005 by Intergovernmental Panel on Climate Change; reprinted with the permission of Cambridge University Press).	22
Figure 2.2. Schematic of the flow system at the Little Grand Wash Fault near Green River, Utah (after Heath et al., 2009; modified from Shipton et al., 2005, with permission from Elsevier). The flow system includes migration of CO ₂ from a deep, natural source into a shallower groundwater system, which then discharges CO ₂ -rich fluids at the surface.....	25
Figure 2.3. Potential leakage pathways envisioned by the IPCC (2005) neglect the effect of fracture networks. The determination of the relative role of CO ₂ leakage through wellbores versus fracture networks is a research need. (after IPCC, 2005, © 2005 by Intergovernmental Panel on Climate Change; reprinted with the permission of Cambridge University Press).....	27
Figure 2.4. Schematic view of a seal bypass system at a petroleum trap, in which small faults/fractures form a tortuous, connected leakage pathway through the entire caprock (after Ingram and Urai, 1999; reprinted with the permission of the Geological Society of London).....	29
Figure 3.1. (A) Map of regions covered by the U.S. Department of Energy’s Southwest and Southeast Regional Carbon Sequestration Partnerships, with locations of wells of core samples. (B) Depositional systems of the Kirtland Formation shown at a time when aggradation of the Fruitland Formation was occurring (adapted from Fassett and Hinds, 1971). Vertical exaggeration is approximately 60 times. The upper and lower Kirtland are more proximal than the swampy systems of the Fruitland. Kirtland can include a vast range of alluvial environments (see text). (C) Tuscaloosa Group depositional environments (adapted from Liu, 2005). The Lower Tuscaloosa was deposited as a transgressive systems tract. Marine Tuscaloosa deposition occurred during the maximum flooding event of the latest Cenomanian to early Turonian and represents the second Late	

Cretaceous Oceanic Anoxic Event. (D) Cross section showing the transgressive systems tract that deposited the Gothic shale (at the Aneth Unit) or “black shale” facies over shelfal carbonates (adapted from Goldhammer et al., 1994). Water depth was estimated at > 35 m.46

Figure 3.2. Scans of thin sections and photomicrographs of continental and marine mudstones. Thin sections (standard size of 24 mm × 46 mm) for a particular formation are located above corresponding photomicrographs. Images and petrographic descriptions for C, D, and J are from TerraTek (see Appendix B.2.1 and Chidsey et al., 2010). Fractures (i.e., magenta lines through the rock) are considered induced features due to desiccation of clays, pressure release during core collection, or other handling and sample preparation. (A) Thin section for upper Kirtland Formation from core depth of ~625.60 m. The upper two thirds is dominated by sand- and silt-sized grains. The lower third is a silt-bearing, argillaceous mudstone. Large opaque grain is pyrite. Younging direction is upward. (B) Plane light photomicrograph from the lower third of A. Diagonal parallel lines are an artifact from thin section polishing. The clay matrix has yellow birefringent colors in places and shows strong parallelism under crossed polarizers when the stage is rotated. The parallelism, however, is not across the entire area, but concentrated in a “zig-zag” pattern. Clasts include chert, volcanic rock fragments, quartz, feldspar, and sedimentary rock fragments. Opaque grains are pyrite and organics. (C) Thin section for lower Kirtland Formation from core depth of 820.60 m. The left half of the section was stained. White areas are a preparation artifact that removed rock. (D) Plane light photomicrograph of unstained area of overlying thin section. Silt and minor sand grains are quartz and feldspars. The cross hatched minerals are ferroan calcite. Clays are illite/smectite with kaolinite and chlorite and minor smectite. Scale bar is 0.5 mm. (E) Thin section for Lower Tuscaloosa Formation from core depth of 2615.05 m. Younging direction is to the left. Thin section shows abundant silt- and sand-sized grains. Bioturbation as burrows is visible at the thin section scale. (F) Plane light photomicrograph taken on E. Silt or fine sand layers with clay-rich layers above and below. Larger grains include angular quartz, probable feldspar, and micas. Authigenic minerals include pyrite. Many dark patches are visible in the thin section, which may be organics or pyrite. Pyrite framboids are visible at 40× magnification. Scale bar is 0.9 mm. (G) Thin section for Marine Tuscaloosa from core depth of 2416.27 m. The upper surface marked by the notch indicates the younging direction and is at a natural shear fracture that was visible in hand sample. The left side of the thin section may show deformation associated with the fracture. (H) Plane light photomicrograph from G. Sand- and silt-sized grains include quartz and micaceous flakes. Clay-rich areas do not show strong parallelism under crossed polarizers. Clay- and silt/sand-rich regions are abundant throughout the thin section and have non-planar boundaries. Scale bar is 0.9 mm. (I) Thin section for Gothic shale from core depth of 1642.6 m. Younging direction is to the left. (J) Plane light photomicrograph taken on a thin section from core depth of 1643.1 m. Sample is a phosphatic, argillaceous mudstone. Flattened, amalgamated pellets (lighter brown) are phosphatic in composition. Compacted siliceous forms (white) are composed of chert. The lighter brown matrix color and abundance of siliceous fossils, as well as phosphatic pellets, suggest a siliceous matrix cement component. Scale bar is 0.5 mm...51

Figure 3.3. Results of focused ion beam (FIB) milling and imaging of sample upper Kirtland 2047.9B and 3D pore network reconstruction. (A) Backscattered electron (BSE) image of FIB serial section. Horizontal field of view is 16.00 μm . Outlined box indicates cubic region of 3D pore network reconstruction, which has side lengths of 4.66 μm . (B) Segmentation of BSE image into pore (black) and non-pore (white). (C) 3D floodfill rendering of pores. Voxel size is 15.6 nm. (D) 3D plot of medial axis. (E) 3D plot of pore throat surfaces.65

Figure 3.4. Results of FIB milling and imaging of sample lower Kirtland 2692.9A and 3D pore network reconstruction. (A) BSE image of FIB serial section. Horizontal field of view is 16.00 μm . Outlined box indicates cubic region of 3D pore network reconstruction, which has side lengths of 4.66 μm . (B) Segmentation of BSE image into pore (black) and non-pore (white). (C) 3D floodfill rendering of pores. Voxel size is 15.6 nm. (D) 3D plot of medial axis. (E) 3D plot of pore throat surfaces.66

Figure 3.5. Results of FIB milling and imaging of sample Marine Tuscaloosa 7925.5 and 3D pore network and organic reconstruction of organic-rich region. (A) BSE image of FIB serial section. Horizontal field of view is 16.00 μm . Outlined box indicates cubic region of 3D pore network and organics reconstruction, which has side lengths of 4.66 μm . (B) Segmentation of BSE image into pore (black) and non-pore (white). (C) Segmentation of BSE image into organics (black) and non-organics (white). (D) 3D floodfill rendering of pores. Voxel size is 15.6 nm. (E) 3D plot of medial axis. (F) 3D plot of pore throat surfaces. (G) 3D flood fill rendering of organic phase.67

Figure 3.6. Results of FIB milling and imaging of sample Marine Tuscaloosa 7925.5 and 3D pore network reconstruction of organic-poor region. (A) BSE image of FIB serial section. Horizontal field of view is 16.00 μm . Outlined box indicates cubic region of 3D pore network reconstruction, which has side lengths of 4.66 μm . (B) Segmentation of BSE image into pore (black) and non-pore (white). (C) 3D floodfill rendering of pores. Voxel size is 15.6 nm. (D) 3D plot of medial axis. (E) 3D plot of pore throat surfaces. ...68

Figure 3.7. Results of FIB milling and imaging of sample Lower Tuscaloosa 8590 and 3D pore network reconstruction of region with polygonal pores (area 1). (A) BSE image of FIB serial section. Horizontal field of view is 16.00 μm . Outlined box indicates cubic region of 3D pore network reconstruction, which has side lengths of 4.66 μm . (B) Segmentation of BSE image into pore (black) and non-pore (white). (C) 3D floodfill rendering of connected (blue) and unconnected (red) pores. Voxel size is 15.6 nm. (D) 3D plot of medial axis. (E) 3D plot of pore throat surfaces.....69

Figure 3.8. Results of FIB milling and imaging of sample Lower Tuscaloosa 8590 and 3D pore network reconstruction of region with crescent-shaped pores (area 2). (A) BSE image of FIB serial section. Horizontal field of view is 16.00 μm . Outlined box indicates cubic region of 3D pore network reconstruction, which has side lengths of 4.66 μm . (B) Segmentation of BSE image into pore (black) and non-pore (white). (C) 3D floodfill

rendering of pores. Voxel size is 15.6 nm. (D) 3D plot of medial axis. (E) 3D plot of pore throat surfaces.70

Figure 3.9. Results of focused ion beam (FIB) milling and imaging of sample Gothic shale 5390.8A and 3D pore network and organic reconstruction. (A) BSE image of FIB serial section. Horizontal field of view is 16.00 μm . Outlined box indicates cubic region of 3D pore network and organics reconstruction, which has side lengths of 4.66 μm . White, circular region is a pyrite framboid. (B) Segmentation of BSE image into organics and pores (black) and non-pores/organics (white). (C) 3D flood fill rendering of both the organic phase and pores in red. Voxel size is 15.6 nm. (D) Segmentation of BSE image into pore (black) and non-pore (white). (E) 3D floodfill rendering of pores in cyan. (F) 3D plot of medial axis. (G) 3D plot of pore throat surfaces.71

Figure 3.10. Major pore types based on morphology, geometry (size), topology, and pore-lining material presented through focused ion beam backscattered electron micrograph and corresponding 3D floodfill images, which highlight particular pore types. Some pores are remnants of the primary depositional environment, whereas others are secondary or related to post-depositional processes.76

Figure 3.11. Montage of pore throat and body histograms from reconstructed 3D pore network models, arranged from proximal (left) to distal (right) depositional environments. The number of pore throats and bodies identified from the 3D geometric models varied from sample to sample. The square model volume of 101.5 μm^3 , however, was the same for each sample. The number of pore throats, bodies, or their ratio is given within each histogram (e.g., $n = 96$). Bin size was adjusted so that each figure contained ten bins. Ordinate and abscissa scales are the same along a row to facilitate comparison of the data, except for sample lower Kirtland 2692.9A. Variables are the following: t_a is pore-throat area; p_v is pore-body volume; r_t is pore-throat radius; and r_t/r_b is the pore-throat radius to pore-body radius ratio. Frequencies of variables were obtained from the output of the 3DMA-Rock software..82

Figure 3.12. A–D. Joint histograms of pore-body volume and coordination number, with marginal histograms for the Kirtland and Tuscaloosa. The series of joint histograms are presented in order from proximal to distal in terms of depositional environment. Binning for the coordination number is such that the number of bins is one plus the maximum number of coordination for a particular sample. This results in bins containing integer values. The first horizontal bin, starting from the bottom, is for the frequency of the value of zero. The second horizontal bin is for frequency of two, and so on. The last bin is for the frequency of the maximum coordination number. For example, UK 2049.7B had a maximum coordination number of seven, and thus it has eight bins. Plotting of values on the ordinate is such that the maximum value of the ordinate corresponds to the maximum coordination number, which is for the top, horizontal bin.....86

Figure 3.12. E–H. Joint with marginal histograms for the Tuscaloosa Group and Gothic shale.88

Figure 3.13. Cumulative mercury saturation versus intrusion pressure for all mudstone samples. Curves were corrected for closure pressure. “UK”, “LK”, “LT”, “MT”, and “GS” stand for upper Kirtland, lower Kirtland, Lower Tuscaloosa, Marine Tuscaloosa, and Gothic shale, respectively. Curve shapes indicate differences in pore structure and sealing properties.90

Figure 3.14. Mercury intrusion porosimetry (MIP) saturation curves and cumulative and incremental volumetric pore density distribution (VPD) curves, organized by formations and samples. (A–B, C–D, and E) Mercury saturation (S_{Hg}) versus injection pressure for the Kirtland Formation, Tuscaloosa Group, and the Gothic shale, respectively. Raw (before closure) and closure-pressure-corrected (after closure) data are given. (B, E, and H) Cumulative and incremental volumetric pore-density distributions, where r_t represents the radius from the “bundle of tubes” model. The ordinate of the cumulative VPD was plotted on a logarithmic scale for evaluation of power law distributions. The incremental VPD was plotted on a linear scale to emphasize the modal peaks.90

Figure 3.15. Sorted cumulative volumetric distributions (SVPD) based on MIP and FIB pore network models. The green and blue lines represent MIP data, whereas red lines represent FIB data. The equations used for the SVPDs are plotted by the ordinates. For mercury, the volumes of mercury intruded per pressure step (ΔV_{Hg}) were sorted from largest to small, and then summed incrementally from largest to smallest. $V_{Hg-total}$ is the total volume of mercury intruded at the end of a MIP test. The pore body volumes (p_v) as determined from FIB-based 3D pore network models were similarly sorted from largest to smallest, and then summed starting with the largest pore-body. $P_{v-total}$ is the total volume of all the pore body volumes for a single sample. (A) lower and upper Kirtland data. (B) Tuscaloosa Group data. (C) Gothic shale data.....97

Figure 3.16. Shale succession facies distributions (modified from Schieber, 1999) and schematic placement of mudstone types studied in this paper with breakthrough pressures from mercury intrusion porosimetry (see Table 3.3). The Schieber (1999) microfacies are: RM are red-gray coastal plain mudstones (Kirtland Formation); SM are sandy near-shore mudstones; BM are bioturbated offshore mudstones; GM refers to moderately bioturbated gray mudstones (probably equivalent to the Lower Tuscaloosa); LM are laminated organic rich mudstones (Marine Tuscaloosa); and CM are carbonaceous mudstones or so-called black shales (the Gothic shale is an example of this). The black and gray bars represent the two samples from approximately the same depth of a particular facies that were used for mercury intrusion porosimetry. The two samples give an indication of precision.....102

Figure 4.1. Interfacial tension (IFT) measurements of the CO₂ and water/brine fluid pair as function of pressure and temperature (Chiquet et al., 2007b; Bachu and Bennion, 2009; Chalbaud et al., 2009) with blue line to indicate pressure and temperature ranges that corresponds to depth in the subsurface for typical conditions (i.e., 25°C/km geothermal gradient; hydrostatic pressure for pure water). The line is placed on the pressure-

temperature plane and marked in intervals that correspond to depths from 0 to 3 km. (a) Three dimensional view that shows IFT steeply decreases as a function of pressure for a given temperature. The highest IFT values for a given pressure and temperature correspond to higher salinities. (b) Top down view which shows that much data has been collected in the depth range of 1 km.120

Figure 4.2. Map showing locations of wells from where core mudstone samples were obtained by the Southeast and Southwest Regional Carbon Sequestration Partnerships (SECARB and SWP).122

Figure 4.3. Results of scanning transmission electron microscopy (STEM) imaging combined with energy-dispersive X-ray spectroscopy for Kirtland Formation samples, along with the last focused ion beam (FIB) images from sets of serial sections. (a) through (e) correspond to sample upper Kirtland 2049.7B. (f) through (j) are associated with sample lower Kirtland 2692.9A. (a and f) Spectral shapes of chemical phases determined by the multivariate statistical analysis (MSA) of X-ray spectral images. Normalization of the y axis is such that, for a particular chemical phase, the product of the normalized counts and the intensity of the corresponding component image results in counts equivalent to the original X-ray counts. In the legend, elements with relatively low counts still above background noise are given in parentheses. (b and g) The last backscattered electron images for a set of FIB serial sections (see Chapter 3). Scale bar is 2 μm . (c and h) Total X-ray output images with hotter colors corresponding to higher output. Horizontal field of view for both images is 3000 nm and (c) and (h) have 20 and 10 nm/pixel resolution, respectively. (d and i) High-contrast component images that display spatial rendering of the MSA chemical phases. Colors correspond with those of the spectral shapes. (e and j) High-angle annular dark-field STEM images taken $\leq 3 \mu\text{m}$ from the location of the corresponding set of FIB serials. Red boxes delineate regions of the X-ray spectral images. Scale bars are 2 μm . The brightest spot on (j) in the upper left-hand side of the image is a piece of gold-palladium-coated material (i.e., an artifact). ...131

Figure 4.4. Results of scanning transmission electron microscopy (STEM) imaging combined with energy-dispersive X-ray spectroscopy for Lower and Marine Tuscaloosa Group samples, along with the last focused ion beam (FIB) images from sets of serial sections. (a) through (e) correspond to sample Lower Tuscaloosa 8590.0. (f) through (j) are associated with sample Marine Tuscaloosa 7925.5. (a and f) Spectral shapes of chemical phases determined by the multivariate statistical analysis (MSA) of X-ray spectral images. Normalization of the y axis is such that, for a particular chemical phase, the product of the normalized counts and the intensity of the corresponding component image results in counts equivalent to the original X-ray counts. In the legend, elements with relatively low counts still above background noise are given in parentheses. (b and g) The last backscattered electron images for a set of FIB serial sections (see Chapter 3). Scale bar is 2 μm . (c and h) Total X-ray output images with hotter colors corresponding to higher output. Horizontal field of view for both images is 3000 nm and (c) and (h) have 10 and 20 nm/pixel resolution, respectively. (d and i) High-contrast component images that display spatial rendering of the MSA chemical phases. Colors correspond

with those of the spectral shapes. (e and j) High-angle annular dark-field STEM images taken $\leq 3 \mu\text{m}$ from the location of the corresponding set of FIB serials. Red boxes delineate regions of the X-ray spectral images. Scale bars are $2 \mu\text{m}$133

Figure 4.5. Results of scanning transmission electron microscopy (STEM) imaging combined with energy-dispersive X-ray spectroscopy for Marine Tuscaloosa Group samples, along with the last focused ion beam (FIB) images from sets of serial sections. (a) through (e) correspond to sample Marine Tuscaloosa 7925.5, but at a different location than in Figure 4.4. (f) through (j) are associated with sample Marine Tuscaloosa 7931.9. (a and f) Spectral shapes of chemical phases determined by the multivariate statistical analysis (MSA) of X-ray spectral images. Normalization of the y axis is such that, for a particular chemical phase, the product of the normalized counts and the intensity of the corresponding component image results in counts equivalent to the original X-ray counts. In the legend, elements with relatively low counts still above background noise are given in parentheses. (b and g) The last backscattered electron images for a set of FIB serial sections (see Chapter 3). Scale bar is $2 \mu\text{m}$. (c and h) Total X-ray output images with hotter colors corresponding to higher output. Horizontal field of view for both images is 3000 nm and (c) and (h) both have 10 nm/pixel resolution. (d and i) High-contrast component images that display spatial rendering of the MSA chemical phases. Colors correspond with those of the spectral shapes. (e and j) High-angle annular dark-field STEM images taken $\leq 3 \mu\text{m}$ from the location of the corresponding set of FIB serials. Red boxes delineate regions of the X-ray spectral images. Scale bars are $2 \mu\text{m}$135

Figure 4.6. Results of scanning transmission electron microscopy (STEM) imaging combined with energy-dispersive X-ray spectroscopy for Marine Tuscaloosa Group and Gothic shale samples, along with the last focused ion beam (FIB) images from sets of serial sections. (a) through (e) correspond to sample Marine Tuscaloosa 7931.9, but at a different location than in Figure 4.5. (f) through (j) are associated with sample Gothic shale 5390.8A. (a and f) Spectral shapes of chemical phases determined by the multivariate statistical analysis (MSA) of X-ray spectral images. Normalization of the y axis is such that, for a particular chemical phase, the product of the normalized counts and the intensity of the corresponding component image results in counts equivalent to the original X-ray counts. In the legend, elements with relatively low counts still above background noise are given in parentheses. (b and g) The last backscattered electron images for a set of FIB serial sections (see Chapter 3). Scale bar is $2 \mu\text{m}$. (c and h) Total X-ray output images with hotter colors corresponding to higher output. Horizontal field of view for both images is 3000 nm and (c) and (h) both have 10 nm/pixel resolution. (d and i) High-contrast component images that display spatial rendering of the MSA chemical phases. Colors correspond with those of the spectral shapes. (e and j) High-angle annular dark-field STEM images taken $\leq 3 \mu\text{m}$ from the location of the corresponding set of FIB serials. Red boxes delineate regions of the X-ray spectral images. Scale bars are $2 \mu\text{m}$137

Figure 4.7. Results of scanning transmission electron microscopy (STEM) imaging combined with energy-dispersive X-ray spectroscopy for Gothic shale samples, along with the last focused ion beam (FIB) images from sets of serial sections. (a) through (e)

correspond to sample Gothic shale 5390.8B. (f) through (j) are associated with sample Gothic shale 5390.8B at a different location. (a and f) Spectral shapes of chemical phases determined by the multivariate statistical analysis (MSA) of X-ray spectral images. Normalization of the y axis is such that, for a particular chemical phase, the product of the normalized counts and the intensity of the corresponding component image results in counts equivalent to the original X-ray counts. In the legend, elements with relatively low counts still above background noise are given in parentheses. (b and g) The last backscattered electron images for a set of FIB serial sections (see Chapter 3). Scale bar is 2 μm . (c and h) Total X-ray output images with hotter colors corresponding to higher output. Horizontal field of view for both images is 3000 nm and (c) and (h) have 20 and 10 nm/pixel resolution, respectively. (d and i) High-contrast component images that display spatial rendering of the MSA chemical phases. Colors correspond with those of the spectral shapes. (e and j) High-angle annular dark-field STEM images taken $\leq 3 \mu\text{m}$ from the location of the corresponding set of FIB serials. Red boxes delineate regions of the X-ray spectral images. Scale bars are 2 μm139

Figure 4.8. Results of scanning transmission electron microscopy (STEM) imaging combined with energy-dispersive X-ray spectroscopy for a Gothic shale sample, along with the last focused ion beam (FIB) images from sets of serial sections. (a) through (e) correspond to sample Gothic shale 5390.8B, but at a different location than in Figure 4.7. (a) Spectral shapes of chemical phases determined by the multivariate statistical analysis (MSA) of the X-ray spectral image. Normalization of the y axis is such that, for a particular chemical phase, the product of the normalized counts and the intensity of the corresponding component image results in counts equivalent to the original X-ray counts. In the legend, elements with relatively low counts still above background noise are given in parentheses. (b) The last backscattered electron image for a set of FIB serial sections (see Chapter 3). Scale bar is 2 μm . (c) Total X-ray output image with hotter colors corresponding to higher output. Horizontal field of view is 3000 nm and has 20 nm/pixel resolution. (d) High-contrast component image that displays spatial rendering of the MSA chemical phases. Colors correspond with those of the spectral shapes. (e) High-angle annular dark-field STEM image taken $\leq 3 \mu\text{m}$ from the location of the corresponding set of FIB serials. Red box delineate regions of the X-ray spectral images. Scale bars are 2 μm141

Figure 4.9. Cumulative (a) and incremental (b) mercury (Hg) intrusion saturation curves for the upper and lower shale members of the Kirtland Formation, the Lower and Marine Tuscaloosa Groups, and the Gothic shale. Samples that were examined by scanning transmission electron microscopy are given as dashed red lines. For sample depths from the subsurface core, see Table 4.1.148

Figure 4.10. CO₂ pressures needed to cause breakthrough versus depth for the suite of five mudstones. Straight lines represent lithostatic and hydrostatic pressure gradients. Annotation on the figure gives the mass of rock and water columns used to generate the pressure gradients.....152

Figure 5.1. Maps of the San Juan Basin with geologic and hydrologic features. (a) Position of basin within Colorado and New Mexico. (b) Locations of the CO₂ injection well, the outcrop of the combined Fruitland and Kirtland Formations (after Kernodle et al., 1990), the Fruitland Fairway, the structural hingeline, and the area of artesian overpressure in the Fruitland Formation (after Scott et al., 1994). (c) Depth to top of Kirtland Formation (after Kernodle et al., 1990). (d) Thickness of the combined Kirtland and Fruitland Formations (after Kernodle et al., 1990). (e) Potentiometric surface map of the Fruitland Formation based on equivalent fresh water head (after Kaiser et al., 1994). (f) Regions where members of the Kirtland Formation and the Fruitland Formation are absent in the subsurface (after Fassett and Hinds, 1971).167

Figure 5.2. North-south cross section through the San Juan Basin with vertical lines that represent wells (adapted from Fassett and Hinds, 1971). The star indicates CO₂ injection well. Numbers on the inset map correspond with the numbers on the cross section.....169

Figure 5.3. Selected wireline logs, lithologic interpretation, and rose diagram fracture orientations from fullbore formation microimager (FMI) logs for well EPNG Com A Inj 1. The lower logging section, starting at a depth of ~696.2 m (2284 ft), was logged on a different date than the upper section. The mismatch of logging data near that depth may be due to casing before the second logging run. The first circle outward from the middle of the rose diagrams corresponds to a fracture measurement of one in the direction of the radial class intervals. North is at the top of the rose diagrams.170

Figure 5.4. Results of focused ion beam/scanning electron microscopy and image analysis. (a) Backscattered electron image of a vertical surface of a trough milled in an upper Kirtland Formation sample. The horizontal field of view is 16 μm. Darkest areas are pore space. The inset box shows the location of the 3D pore model, show in part b. (b) 3D “flood-fill” rendering of pore space in red. Cyan pore was used in pore-scale modeling. (c) Image of pore used in pore-scale fluid modeling. The inlet location for flow modeling was at the bottom right hand-side of the model, and the outlet was at the upper left... ..183

Figure 5.5. Mercury intrusion porosimetry data. (a) Cumulative mercury saturation versus pressure. (b) Incremental (inc) mercury saturation versus pore aperture diameter, based on data from (a) and the Washburn equation. Capillary pressure data were corrected for closure pressure (i.e., mercury that had not intruded the pore network was not included in the saturation curves). Depths of samples are given in m in the legend. “PV” stands for pore volume.184

Figure 5.6. CO₂ column heights plotted by depth for the upper and lower Kirtland Formation. The two columns per depth (in different colors) correspond to the two values of contact angles given in Table 5.1.187

Figure 5.7. Upper Kirtland photomicrographs and pore size distribution from mercury intrusion porosimetry (MIP) measurements. (a) Optical plane-polarized light

photomicrograph of sandy argillaceous mudstone from the unstained portion of slide from depth 628.59 m (see Appendix B.2.2). The scale bar is 0.5 mm. Information from TerraTek states that “Sharp feldspar, quartz, and rounded chert-replaced volcanic clasts are supported by a mixed smectitic matrix. Induced fractures are pervasive, as represented by the magenta lines (stained epoxy). The fabric exhibits blocky ped structure, especially when viewed under cross-polarized light, and the aligned, curved illite material at upper right is likely a result of illuviation.” (b) LSCM image of 2.0 mm by 2.0 mm by 50 micron (left) and 200 by 200 by 15 micron (right) portions of an upper Kirtland sample, showing interconnected fractures and matrix porosity, likely induced from coring, unloading, and dehydration. (c) SEM image with a scale bar of 100 microns (see Appendix B.2.2). TerraTek’s information on this photomicrography is the following: “Medium magnification view of sandy argillaceous mudstone with poorly laminated and mottled, irregular texture. Angular to subangular quartz and feldspar sand are scattered throughout the clay matrix, showing approximately vertical microfractures filled with illuvium. Spot EDS analysis identifies the dark grains at upper right and center right edge as alkaline feldspars.” The boxed area denotes an illuviation (soil-forming) texture. (d) Pore aperture size distribution of matrix determined by MIP analysis.188

Figure 5.8. Lower Kirtland photomicrographs and pore size distribution from MICP measurements. (a) Optical plane-polarized light photomicrograph of an argillaceous mudstone from the unstained portion of slide from depth 820.60 m (see Appendix B.2.2). The scale bar is 0.5 mm. TerraTek’s information on this photomicrograph is the following: “Argillaceous mudstone at lower magnification exhibits scattered silt and sand in a mixed clay matrix, with expandable I/S and chlorite as the predominant clay species (XRD). The crystals with cross-hatched cleavage in the lower part of the image are ferroan calcite (unstained). The horizontal fracture (magenta) is interpreted as an induced, stress-release or dehydration feature.” (b) LSCM image of 2.0 mm by 2.0 mm by 50 micron (left) and 200 by 200 by 15 micron (right) portions of lower Kirtland sample, showing relative lack of interconnected fractures and matrix porosity seen in the upper Kirtland (compare Figure 5.7b). (c) SEM image of argillaceous mudstone with a scale bar of 50 microns that displays, according to TerraTek, “moderate lamination parallel to bedding, near vertical in this image. Scattered silt and sand are supported in a lumpy, clay-rich matrix. An example of a large pore is seen in the boxed area at upper right” (see Appendix B.2.2). (d) Pore aperture size distribution of matrix determined by mercury injection capillary pressure analysis.189

Figure 5.9. Lithologic and fracture data from core examination and formation microresistivity imaging (FMI) well log interpretation for the upper (the upper panel) and lower members of the Kirtland Formation (the lower panel). The first column from the left for each panel is the mud log and core-based lithology (see Appendix B.5 for the legend of the lithologic symbols). The second column shows locations of mineralized fractures identified in core. The third column shows the location of core collection. The last column indicates fractures from the FMI log. The FMI fractures are organized by type. The azimuthal dip direction of FMI fractures is given by the “tadpoles.” Dip magnitude for both core (column two) and FMI fractures (column four) is given by the

placement of the red circles or tadpoles from left to right. Far left is 0°. Far right is 90°. Fracture type labels are given to the right of the tadpoles (labels overlap when multiple fractures occur in close vicinity to each other).193

Figure 5.10. Montage of fractured-related images for rock samples from the upper and lower members of the Kirtland Formation. Images include the following: backscattered electron images (i.e., grayscale images), energy-dispersive X-ray spectroscopy elemental maps (i.e., color images with legends for mapped elements), and a hand sample photograph of slabbed core that shows a fracture with mineralization. The younging direction is towards the top of the photomicrographs. The photomicrograph in the upper right hand corner shows a clear cross-cutting relationship between a calcite/quartz-filled fracture and a barite/quartz-filled fracture.195

Figure 5.11. Burial history, annotated with paragenesis of fracture mineralization and tectonic and hydrologic information (modified from Law, 1992).196

Figure 5.12. Depth profiles of noble gas concentrations and water saturations. Laboratory analysis Runs 1 and 2 were performed in September 2008 and March 2009, respectively. “ccSTP” is cm³ of helium or neon at standard temperature and pressure. “ccPV” stands for pore volume in cm³. “ASW” is “air saturated water” and has units of ccSTP of ²⁰Ne or ⁴He per gram of groundwater. Water saturations include those from calculations of closed system partitioning and the laboratory measured values of TerraTek (see Appendix B.2.6). The closed system partitioning estimated water saturations needed to match the difference between measured and expected ASW ²⁰Ne concentrations. Error bars are based on uncertainty in pore volume and laboratory analysis, using error propagation methods.199

Figure 5.13. Depth profiles of noble gas ratio data. $R = \text{measured } ^3\text{He}/^4\text{He}$ and $R_a = \text{atmospheric } ^3\text{He}/^4\text{He}$ (1.384e-6; Kipfer et al., 2002). Error bars are based on uncertainty in laboratory analysis.200

Figure 5.14. Interpretation of well logs in terms of mineral phases and fluid phases (Schlumberger’s ELAN log) for the Ojo Alamo Sandstone and the upper member of the Kirtland Formation. Upper contacts of the geologic units are labeled. The ELAN log does not indicate gas saturations at the depths of the core plugs within the lower member of the Kirtland Formation (not shown).202

Figure 5.15. Measured ⁴He concentrations versus depth and the solution to the 1D advection-only model with *in situ* ⁴He production (blue line).212


Figure 5.16. Helium concentration versus depth profiles for measured and modeled data. a) Profiles with varying groundwater velocity V_z (given in legend) and a constant ⁴He production value of $g = 1.78 \times 10^{-11} \text{ cm}^3 \text{ STP } ^4\text{He cm}^{-3} \text{ H}_2\text{O yr}^{-1}$. b) Profiles with varying *in situ* helium production (in units of $\text{cm}^3 \text{ STP } ^4\text{He cm}^{-3} \text{ H}_2\text{O yr}^{-1}$; values given in legend) and constant $V_z = 2.5 \times 10^{-5} \text{ m yr}^{-1}$217

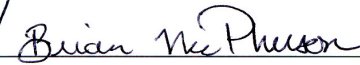
Figure 6.1. TOUGH2 simulation results comparing helium and CO₂ leakage through a caprock with and without a permeability perturbation (i.e., a vertical “fault” with 100× background caprock permeability; after Heath et al., 2009). The zero elevation on the figures corresponds to a depth below ground surface of ~1.5 km. (A and B) Profiles of dissolved ⁴He as mass fraction of aqueous solution (×10¹⁰) for “faulted” (A) and unfaulted (B) cases. Caprock is shown as grey horizon. (C and D) CO₂ gas saturation after one year of injection directly beneath the caprock. (E) Comparison of vertical profile in dissolved ⁴He both running through the fault zone (red line) and at an infinite distance from the fault (blue line) under steady state flow conditions (1 My). (F) Temperature profiles taken through the fault zone (red line) and at an infinite distance from the fault (blue line) under steady state flow conditions (1 My). (G) Vertical pressure profiles both through the fault (red line) and at an infinite distance from the fault (blue line), showing pressure dissipation through the fault (1 My).267

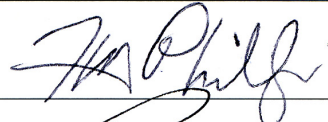
LIST OF TABLES

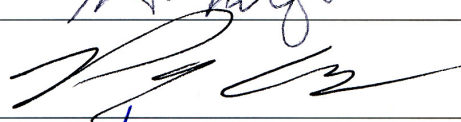
	Page
Table 3.1. Mudstone core sample identification and general information.....	48
Table 3.2. Closure and breakthrough pressures and pore radii	94
Table 3.3 Summary of petrophysical, burial history, facies types, and pore network properties for the suite of mudstones	101
Table 4.1. Summary of pore types and pore-lining phases from high resolution microanalysis with comparison to X-ray diffraction	127
Table 4.2. Breakthrough pressures estimated from mercury porosimetry for the suite of mudstone samples, along with supporting information	128
Table 4.3. High and low estimates of CO ₂ breakthrough pressure estimates based on uncertainty in interfacial tension and contact angles	129
Table 5.1. Information used for calculations of CO ₂ column heights.....	186
Table 5.2. Estimation of <i>in situ</i> ⁴ He production, parameters, and measured ⁴ He concentration from the core	210

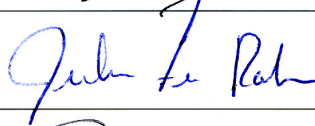
This dissertation is accepted on behalf of the
Faculty of the Institute by the following committee:

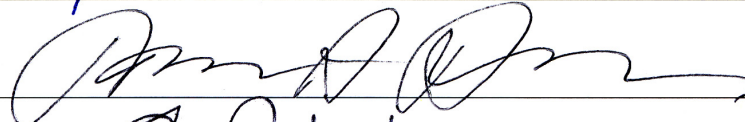



Advisor












Date

I release this document to the New Mexico Institute of Mining and Technology.



Student's Signature

30 Nov 2010

Date

**PART I. INTRODUCTION AND OVERVIEW OF
RESEARCH ON CAPROCKS**

CHAPTER 1. INTRODUCTION

1.1 CO₂ Storage and Multi-Scale Transport Processes of Caprock Seals

Geologic storage of CO₂ represents a promising option for reducing atmospheric emissions of this greenhouse gas. The general concept includes capture of CO₂ from fossil fuel combustion (i.e., power plants), pressurization, and underground injection into voluminous, permeable, and porous rocks at depths below ~800 to 1000 m (Haszeldine, 2009; Orr, 2009). These depths correspond to CO₂ densities that act to reduce both the volume occupied by the CO₂ and the buoyancy due to density differences between formation water and the CO₂ (IPCC, 2005; Orr, 2009). Retention of CO₂ constitutes the key metric for acceptable performance of storage sites in both global and local senses. Atmospheric emission scenarios that incorporate geologic CO₂ storage on a massive scale suggest that CO₂ leakage rates of 1% or less per thousand years are needed to avoid strong global warming (Shaffer, 2010). Locally, CO₂ leakage from a storage site poses risks such as reducing the quality of underground sources of drinking water (IPCC, 2005).

For achieving retention of CO₂, a critical component of storage sites is low permeability, high capillary-breakthrough-pressure rock units that overlie the target injection zone. Such rocks constitute a barrier to the upward movement of the still buoyant CO₂ that is also pressurized from injection (Rohmer and Bouc, 2010). These

rock units are termed “caprock seals”, “top seals”, or simply caprocks or seals, although seals can also apply to faults that inhibit fluid flow (Cartwright et al., 2007). Since upward leakage of CO₂ could cause inadequate performance of a site by returning the CO₂ to the atmosphere more rapidly than planned and could impact underground sources of drinking water (Wilson et al., 2007), knowledge of processes that lead to either acceptable storage or unacceptable CO₂ leakage are receiving much attention (Wollenweber et al., 2010).

Current research evaluates the ability of caprocks to impede significant CO₂ leakage, which in this context constitutes acceptable sealing behavior. Many studies have focused on the scale of core plugs or smaller to determine effective CO₂ diffusion coefficients, sorption capacity of caprock solid phases, wetting characteristics of caprock minerals (e.g., micas), breakthrough pressures (i.e., excess pressure within the non-wetting phase, namely CO₂, that causes flow of that phase through the pore network of a caprock), absolute and relative permeabilities, Darcy fluxes of formation water and CO₂, and precipitation or dissolution reactions (Hildenbrand et al., 2004; Busch et al., 2007; Chiquet et al., 2007; Bennion and Bachu, 2008; Wollenweber et al., 2010).

Much less research has addressed CO₂ migration from storage sites via natural larger-scale fractures or faults (Gherardi et al., 2007; Andreani et al., 2008; Nelson et al., 2009; Silin et al., 2009). However, “seal bypass systems” are recognized in the petroleum geosciences as natural features that cause significant loss of fluids (e.g., hydrocarbons) from a reservoir through a caprock (Cartwright et al., 2007). These systems allow fluids to circumvent the small (i.e., typically on the scale of nm’s) pores and pore throats of the caprocks that offer high resistance to transport via viscous and capillary forces. Natural

seal bypass systems can include, for example: fractures, faults, sandstone injectites or other intrusions, dissolution pipes, and sedimentary architecture. I expand Cartwright et al.'s (2007) definition of seal bypass systems to include man-made features such as leaky wellbores that penetrate the caprock and reservoir (Nordbotten et al., 2009). Bypass systems can also include features induced by CO₂ injection activities such as newly created fractures.

The major aim of recent studies is the conceptual and quantitative assessment of near and long term processes that control sealing behavior. The potential evolution of sealing quality through the various stages of a CO₂ storage site (e.g., initial CO₂ injection; continued injection and development of the CO₂ plume; cessation of injection; see IPCC, 2005) due to large-scale changes in stresses and potential geochemical reactions represent new challenges not addressed by traditional assessment of caprocks for hydrocarbon exploration and production. Furthermore, CO₂ storage requires multi-scale knowledge of both the small pore networks that govern high quality sealing and the larger bypass systems. Large-scale CO₂ storage may necessitate evaluation of sedimentary basins on the regional scale (IPCC, 2005; DOE, 2007).

Accordingly, key data are needed to provide sound conceptual and subsequent quantitative models of sealing behavior that would lessen characterization costs and support performance assessments. Because sealing behavior is a consequence of fluid/rock properties and processes that vary over the nm- to basin-scale and over geologic timescales (Figure 1.1), acquisition of key data is paramount. The state-of-the-art for CO₂ storage assessment, however, is still developing an understanding of the nature of the coupled hydrological, mechanical, and chemical processes that govern

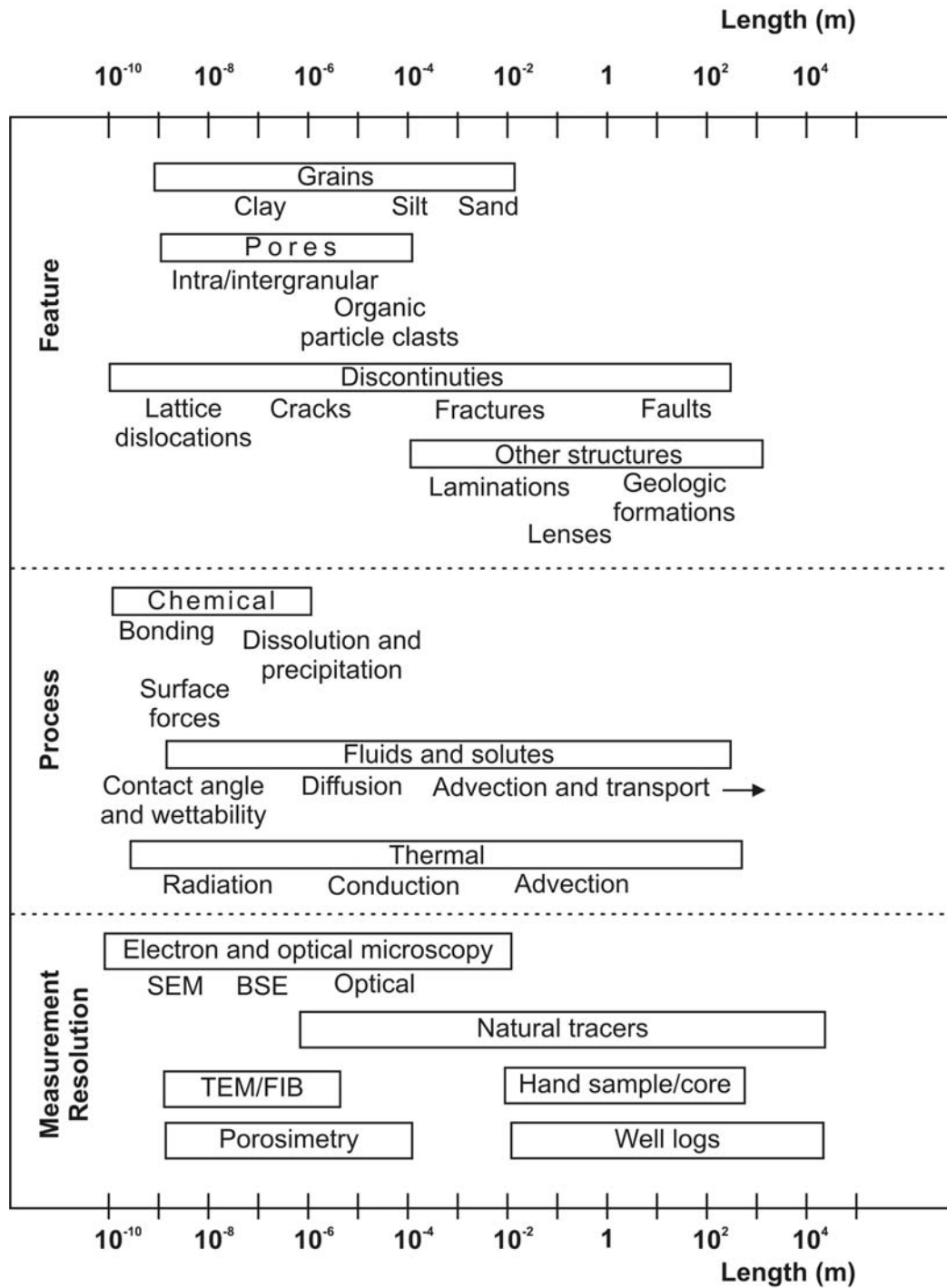


Figure 1.1. Features, processes, and measurement resolution for understanding and assessing caprock sealing behavior (adapted from Pyrak-Nolte (2007) in DOE, 2007) (Nelson, 2009).

sealing behavior (Gherardi et al., 2007; Rutqvist et al., 2007; LeNeveu, 2008; Oldenburg et al., 2009; Rohmer and Bouc, 2010). A formal definition of what constitutes key data is not yet determined since regulatory procedures and risk management practices for CO₂ storage are under development (IPCC, 2005; DOE, 2007; Wilson and Gerard, 2007; Oldenburg et al., 2009; Gaus, 2010).

In this research setting, taking an approach to address the challenges of multi-scale characterization and assessment, my dissertation investigates sealing behavior of caprock for CO₂ storage with a focus on both pore networks and the existence and impact of potential natural seal bypass systems. I do not focus on wellbores as a bypass system, which is a research challenge that is actively studied by the CO₂ research community (Carey et al., 2010).

1.2 Science Questions

CO₂ can migrate through caprock features with intrinsic scales that range from microscopic (i.e., the pore scale) to some appreciable fraction of the caprock thickness (i.e., small- to medium-scale fractures) up to the full thickness of the caprock. Caprock must resist CO₂ migration at all of these scales if it is to effectively seal off the injection CO₂ from migrating back towards Earth's surface. Thus, major science questions of this dissertation address pore-scale and larger features (e.g., seal bypass section, see Section 1.1) and processes that govern sealing quality. These questions include:

- 1) What geologic conditions contribute to the formation of pore networks capable of forming a high quality sealing caprock for CO₂ storage?

- 2) To what extent do pore network- and larger-scale natural seal bypass features and processes govern overall sealing behavior at specific storage sites, and how is this effectively determined?

Question 1 has not previously been addressed via direct observation of three-dimensional (3D) pore networks in caprocks, due to the small ($< \mu\text{m}$) sizes of the pores that result in high sealing behavior. I present novel 3D geometrical models obtained using state-of-the-art methods of high resolution serial sectioning and imaging of the pore networks. Geometrical and topological aspects are addressed along with the composition of solid phases that line pores and affect wettability.

Question 2 leads to research that focuses on the scale of the features and processes that govern overall sealing quality. Pore networks may have low-to-high quality sealing behavior. Seal bypass systems can lead to significant loss of fluids from a reservoir. Through study of a particular site, I demonstrate the combined use of petrological, petrophysical, and noble gas tracers to determine large-scale (i.e., the full thickness of the caprock) sealing quality. Attention is made to assess the importance of pore networks and/or seal bypass systems on the overall sealing quality.

1.3 Organization of the Dissertation

Four major theme-based parts comprise the dissertation. Part I provides an introduction (this chapter) and a viewpoint on caprock-related research (Chapter 2). Parts II and III specifically address the two major science questions of this dissertation (see Section 1.2). Part II (Chapters 3 and 4) focuses on pore-scale processes and caprock sealing behavior. Part III (Chapter 5) concerns multi-scale evaluation of caprock sealing

behavior. Part IV (Chapter 6) includes a summary of the dissertation research with an emphasis on scientific contributions, opportunities and limitations, recommendations, and risk analysis for caprocks. Details on specific chapters and the appendices follow below.

To set the stage for the rest of the dissertation, Chapter 2 addresses three topics: 1) a brief history of caprock research with a focus on past issues of importance; 2) the current research for geologic CO₂ storage; and 3) the additional research needs for large-scale implementation of CO₂ storage. Chapters 3 and 4 fall within Part II. Chapter 3 addresses the geologic controls of pore networks and their sealing behavior for several continental and marine caprock mudstones that lie above CO₂ storage demonstration projects of the U.S. Department of Energy's (DOE) Southeast and Southwest Regional Carbon Partnerships (Litynski et al., 2008). Investigation of these multiple caprocks is an important approach for answering Science Question 1 (see Section 1.2). Comparison of the different caprocks of varying sealing quality allows identification of the geologic attributes and processes that affect the sealing quality. Chapter 4 is a companion to Chapter 3. Chapter 4 specifically addresses sealing quality of the caprocks in terms of CO₂/brine/rock interfacial interactions, based on the knowledge of pore-lining compositions. Chapter 5 (Part III) presents a multi-scale examination of a field site in north-eastern New Mexico, the Pump Canyon site, where CO₂ was injected into deep unmineable coal seams. I examine a caprock at this site with pore- to formation-scale data to ascertain the importance of natural fractures as a potential seal bypass system. The investigation of pore networks and potential larger-scale bypass systems directly addresses Science Question 2 (see Section 1.2). Chapter 6 concludes the dissertation by discussing specific contributions and limitations of this work. I use "limitations" in the

sense of inherent challenges or opportunities in the study of mudstone caprocks that I faced, assumptions and approaches I employed, and uncertainty in the conclusions. The “limitations” represent opportunities for future research. Chapter 6 focuses on how well the multi-scale approach addresses the heterogeneous and uncertain nature of caprock systems. It suggests how the dissertation-specific “limitations” can be addressed in future work, while also recommending general research directions for the study of caprock.

Appendices include two sections: 1) a digital index with supplemental video files of the images used to generate the pore network models presented in Chapter 3 (CD in pocket at the back of dissertation); and 2) documentation and preservation of data collected for Chapter 5 and a core analysis program associated with that chapter. The video files do not include images at the full size used in the analysis of the pore networks. To facilitate reproduction of the pore network models (Chapter 3), a report with the full-size images will be made available through Sandia National Laboratories no later than one year after the completion of this dissertation.

Footnotes at the beginning of the chapters give the name of the scientific journals to which the chapters have been or will be submitted. Each chapter has been reformatted from the original journal style to conform to the New Mexico Tech dissertation style; however, chapters may contain their own abstracts, introductions, methods, and other sections as typical of scientific papers.

1.4 References

Andreani, M., Gouze, P., Luquot, L., and Jouanna, P., 2008, Changes in seal capacity of fractured claystone caprocks induced by dissolved and gaseous CO₂ seepage: *Geophysical Research Letters*, v. 35, no. 14, p. 6.

- Bennion, D. B., and Bachu, S., 2008, Drainage and imbibition relative permeability relationships for supercritical CO₂/brine and H₂S/brine systems in intergranular sandstone, carbonate, shale, and anhydrite rocks: *SPE Reservoir Evaluation & Engineering*, v. 11, no. 3, p. 487–496.
- Busch, A., Alles, S., Gensterblum, Y., Prinz, D., Dewhurst, D. N., Raven, M. D., Stanjek, H., and Krooss, B. M., 2007, Carbon dioxide storage potential of shales: *International Journal of Greenhouse Gas Control*, v. 2, p. 297–308.
- Carey, J.W., Svec, R., Grigg, R., Zhang, J.S., and Crow, W., 2010, Experimental investigation of wellbore integrity and CO₂-brine flow along the casing-cement microannulus: *International Journal of Greenhouse Gas Control*, v. 4, p. 272–282.
- Cartwright, J., Huuse, M., and Aplin, A., 2007, Seal bypass systems: *AAPG Bulletin*, v. 91, no. 8, p. 1141–1166.
- Chiquet, P., Broseta, D., and Thibeau, S., 2007, Wettability alteration of caprock minerals by carbon dioxide: *Geofluids*, v. 7, no. 2, p. 112–122.
- DOE, 2007, *Basic research needs for geosciences: Facilitating 21st century energy systems*, Report from the workshop held February 21–23: U.S. Department of Energy, Office of Basic Energy Sciences, available in PDF format at <http://www.sc.doe.gov/bes/reports/list.html>.
- Gaus, I., 2010, Role and impact of CO₂–rock interactions during CO₂ storage in sedimentary rocks: *International Journal of Greenhouse Gas Control*, v. 4, p. 73–89.
- Gherardi, F., Xu, T. F., and Pruess, K., 2007, Numerical modeling of self-limiting and self-enhancing caprock alteration induced by CO₂ storage in a depleted gas reservoir: *Chemical Geology*, v. 244, no. 1-2, p. 103–129.
- Haszeldine, R. S., 2009, Carbon capture and storage: How green can black be?: *Science*, v. 325, no. 5948, p. 1647–1652.
- Hildenbrand, A., Schlomer, S., Krooss, B. M., and Littke, R., 2004, Gas breakthrough experiments on pelitic rocks: comparative study with N₂, CO₂ and CH₄: *Geofluids*, v. 4, no. 1, p. 61–80.
- IPCC, 2005, *IPCC special report on carbon dioxide capture and storage*, prepared by Working Group III of the Intergovernmental Panel on Climate Change: Cambridge, United Kingdom and New York, NY, USA, Cambridge University Press, 442 p.

- LeNeveu, D. M., 2008, CQUESTRA, a risk and performance assessment code for geological sequestration of carbon dioxide: *Energy Conversion and Management*, v. 49, no. 1, p. 32–46.
- Litynski, J. T., Plasynski, S., McIlvried, H. G., Mahoney, C., and Srivastava, R. D., 2008, The United States Department of Energy’s regional carbon sequestration partnerships program validation phase: *Environment International*, v. 34, no. 1, p. 127–138.
- Nelson, P. H., 2009, Pore-throat sizes in sandstones, tight sandstones, and shales: *AAPG Bulletin*, v. 93, no. 3, p. 329–340.
- Nelson, S. T., Mayo, A. L., Gilfillan, S., Dutson, S. J., Harris, R. A., Shipton, Z. K., and Tingey, D. G., 2009, Enhanced fracture permeability and accompanying fluid flow in the footwall of a normal fault: The Hurricane Fault at Pah Tempe Hot Springs, Washington County, Utah: *Geological Society of America Bulletin*, v. 121, no. 1–2, p. 236–246.
- Nordbotten, J.M., Kavetski, D., Celia, M.A., and Bachu, S., 2009, Model for CO₂ leakage including multiple geological layers and multiple leaky wells: *Environmental Science & Technology*, v. 43, p. 743–749.
- Oldenburg, C. M., Bryant, S. L., and Nicot, J. P., 2009, Certification framework based on effective trapping for geologic carbon sequestration: *International Journal of Greenhouse Gas Control*, v. 3, no. 4, p. 444–457.
- Orr, F. M., 2009, Onshore Geologic Storage of CO₂: *Science*, v. 325, no. 5948, p. 1656–1658.
- Rohmer, J., and Bouc, O., 2010, A response surface methodology to address uncertainties in cap rock failure assessment for CO₂ geological storage in deep aquifers: *International Journal of Greenhouse Gas Control*, v. 4, no. 2, p. 198–208.
- Rutqvist, J., Birkholzer, J., Cappa, F., and Tsang, C. F., 2007, Estimating maximum sustainable injection pressure during geological sequestration of CO₂ using coupled fluid flow and geomechanical fault-slip analysis: *Energy Conversion and Management*, v. 48, no. 6, p. 1798–1807.
- Shaffer, G., 2010, Long-term effectiveness and consequences of carbon dioxide sequestration: *Nature Geoscience*, v. 3, p. 464–467.
- Silin, D., Patzek, T. W., and Benson, S. M., 2009, A one-dimensional model of vertical gas plume migration through a heterogeneous porous medium: *International Journal of Greenhouse Gas Control*, v. 3, no. 3, p. 300–310.

- Wilson, E. J., Friedmann, S. J., and Pollak, M. F., 2007, Research for deployment: Incorporating risk, regulation, and liability for carbon capture and sequestration: *Environmental Science & Technology*, v. 41, no. 17, p. 5945–5952.
- Wilson, E. J., and Gerard, D., 2007, Risk assessment and management for geologic sequestration of carbon dioxide, in Wilson, E. J., and Gerard, D., eds., *Carbon capture and sequestration: Integrating technology, monitoring and regulations*: Oxford, UK, Blackwell Publishing, p. 101–125.
- Wollenweber, J., Alles, S., Busch, A., Krooss, B. M., Stanjek, H., and Littke, R., 2010, Experimental investigation of the CO₂ sealing efficiency of caprocks: *International Journal of Greenhouse Gas Control*, v. 4, no. 2, p. 231–241.

CHAPTER 2. CAPROCKS: MUCH IS STILL UNKNOWN AND WHY THIS MATTERS FOR GEOLOGIC CO₂ STORAGE

Abstract

Caprocks impede fluid movement from subsurface reservoirs, and thus play a key role in hydrocarbon accumulation and in the underground storage of CO₂. Knowledge of caprocks historically originates from hydrocarbon exploration and production efforts. Conceptual and mathematical models detail the physics of caprock retention mechanisms in terms of multiphase fluid flow, which focus on capillarity and relative permeability. CO₂ storage poses abundant new challenges that currently spur research into areas addressing intermolecular and surface forces between supercritical CO₂, brine, and caprock solid phases (i.e., minerals, organics, and other amorphous/mineraloid phases). Such research enables predictions of fluxes of CO₂ through caprock pore networks of caprocks. Of critical importance are larger-scale “seal bypass systems”, which are features or events that lead to significant loss of fluids from a reservoir over relevant timescales. Bypass systems can include natural or man-made leakage pathways, such as fractures, faults, or wellbores. Risk assessment provides a potentially powerful integrative and iterative approach for determining what set of caprock and reservoir properties and processes will govern the successful performance of a CO₂ storage site.

2.1 Introduction

Caprock is the Cerberus of the subsurface, guarding the way to Earth's surface. The synonymous terms "caprocks", "sealing sequences", or "top seals" refer to rock units that play the key role of impeding upward fluid flow from a subsurface reservoir. Fluids of interest are typically buoyant, non-aqueous fluids such as hydrocarbons or supercritical CO₂. Caprocks have received considerable attention due to their strong impact on hydrocarbon exploration and production (Weber, 1997). The underground storage of CO₂, a way to reduce emissions of the greenhouse gas, targets locations below caprocks to ensure containment (Orr, 2009), which has accelerated the study of caprocks during the past decade.

This paper reviews the state of knowledge on caprocks, explains their importance, and discusses critical future work to adequately assess risks associated with subsurface CO₂ storage. While I focus on natural features and associated processes that affect caprock sealing behavior, I provide context on man-made features that constitute potential leakage pathways, such as wellbores or induced fractures due to injection activities. This first section presents conceptual models of important caprock properties and processes related to fluid retention as developed predominantly through the petroleum geosciences, which first extensively studied caprocks. Section 2.2 focuses on recent efforts to improve knowledge of the physico-chemical processes that affect CO₂ and brine transport through caprock at geologic CO₂ storage sites. Section 2.3 suggests directions for future research with a focus on risk assessment of caprocks for CO₂ storage.

The term “caprocks” is commonly used in the geologic CO₂ storage community, and I use it here. “Sealing sequences” or “top seals” (and “fault seals”) are more common in petroleum geoscience literature. (See Cartwright et al., 2007.)

2.2 Caprocks and Their Properties and Processes: Historical Trends in Research

Caprocks are lithofacies of generally low permeability and high capillary-breakthrough pressure (this term is defined below) that overlie reservoir rocks. They are most commonly fine-grained sedimentary rocks that consist mainly of siliciclastic or carbonate mud, or less commonly include evaporite minerals (i.e., gypsum/anhydrite), or cemented portions of coarser-grained rocks. Caprocks are traditionally referred to in the context of a trap system, in which the caprock serves to retain hydrocarbons within a porous and permeable reservoir (Halbouty, 1969). Permeabilities needed to retain fluids over geologic timescales range from $\sim 10^{-18}$ to 10^{-20} m² (Schlumberger, 2010). Traps are principally classified as structural or stratigraphic, in which the geometric relationship of the caprock to the underlying reservoir is affected by structural deformation (e.g., folding and faulting) or unconformities (e.g., erosional surfaces), pinch-outs, and reefs (Levorsen, 1966; Schlumberger, 2010). The nature of the contact between the caprock and the reservoir manifests in a variety of ways, including: gradational contacts from high quality reservoir rock (i.e., high permeabilities) to high quality caprock (i.e., low permeabilities and high capillary-breakthrough pressures) with a zone of intermediate quality (i.e., not high quality reservoir rock nor high quality caprock, typically deemed a “waste zone” by the petroleum industry); sharp contacts (i.e., large change in permeability and gas

breakthrough pressures over a short distance); contacts with cemented zones that are not present away from the contacts (Moraes and Surdam, 1993; Klein et al., 1999; Hall et al., 2004); and style of fracturing and connectivity of fractures across the caprock-reservoir interface.

The ability of caprocks to retain multiphase fluids arises from viscous and capillary forces associated with their small pores and pore throats (DOE, 2007). Mechanisms of capillarity are traditionally described by the Young-LaPlace or Washburn equations (Washburn, 1921; Berg, 1975), which express the relationship of the pressure difference between non-wetting and wetting fluids at which the non-wetting phase will penetrate into a pore body previously saturated with the wetting phase (i.e., the so-called capillary pressure):

$$P_c = P_{mw} - P_w = \gamma \left(\frac{1}{r_1} + \frac{1}{r_2} \right), \quad (1)$$

$$P_c = P_{mw} - P_w = \frac{2\gamma \cos \theta}{r}, \quad (2)$$

where γ is the interfacial tension between the two fluids, θ is the contact angle for the rock and multiphase fluid system, r_1 and r_2 are radii of curvature, and r is the radius of a right cylindrical tube. Equation 1 is the general formula for a non-spherical fluid-fluid interface where r_1 and r_2 represent the radii of curvature. Equation 2 presents the formula for a right cylindrical tube, which is commonly used when the caprock pore network is represented by a bundle of capillary tubes. The “wetting phase” refers to interfacial energy phenomena in which one fluid phase has a stronger adhesion force to a solid surface than another fluid and “wets” the solid surface. Contact angle expresses the

balance of the vector sum of the interfacial tensions of a fluid contacting a flat solid surface in the presence of another fluid, and thus contact angle represents the geometric relationship of the interface between the two fluids and the solid surface. Based on the models of Equations 1 and 2, prediction of the pressures needed for one fluid to displace another, such as a hydrocarbon fluid entering a caprock saturated with brine, requires knowledge of pore throat shapes and sizes, interfacial tensions, and contact angles or curvature of the fluid-fluid interface. Pore throats represent the constrictions or narrow places in the connected, three-dimensional (3D) system of bulges (pores) and constrictions (throats) that constitute the pore network (Wardlaw et al., 1987). Lindquist (1999) treats pore throats as the minimal surface area between pore bodies due to difficulties in geometrically defining where a pore body ends and a connecting channel begins (Lindquist et al, 2005).

Breakthrough pressure represents the capillary pressure at which the non-wetting phase establishes an interconnected pathway through a pore network of arbitrary size that was previously saturated with the wetting phase (Dullien, 1992). The pathway includes the largest connected pore throats through the system (Hildenbrand et al., 2002). It is not the “capillary-entry pressure” or “minimum capillary pressure”, which relates to the beginning of a non-wetting intrusion process that is controlled by the largest pore throats on the outside of a rock sample (Dullien, 1992; Almon et al., 2008). In general, it is breakthrough pressure that has received much attention historically to determine the quality of a caprock, and to facilitate comparison of different types of lithofacies considered to be caprocks. Breakthrough pressures are commonly converted to hydrocarbon (or non-wetting fluid phase) column heights, the “sealing capacity”, which

represent the maximum height a column of the non-wetting fluid that a caprock could retain by the balance of capillarity and buoyancy forces between the wetting and non-wetting phases.

Although the terms caprock and seal connote a barrier to fluid flow, they can still contain features of relatively high permeability (Cartwright et al., 2007). I adopt and broaden the terminology of Cartwright et al. (2007) and refer to features and events that lead to significant leakage of fluid(s) from a reservoir as “seal bypass systems”.

“Significant” may vary depending on site-specific details such as the size of the trap, the volume of the migrating fluids, and the timescale of interest. Cartwright et al.’s original seal bypass system applied to seismically-resolvable, natural features due to their use of seismic methods. Examples of features for hydrocarbon trap systems include fractures and connected fracture networks, faults, sedimentary facies changes, dissolution pipes, and injectites or other intrusions (Almon et al., 2004; Ingram et al., 1997; Pruess, 2008). Events can include formation of fractures due to engineered hydraulic processes. The concept here is that seal bypass systems allow fluids, especially hydrocarbons, to travel through preferential flowpaths rather than only through the pore networks of the caprock. “Seal bypass systems” typically do not refer to pore networks that have high permeability and low capillary-breakthrough pressures (Cartwright et al., 2007). Seal bypass systems facilitate leakage on short-to-very-long geologic timescales (Nelson et al., 1999).

Cartwright et al.’s (2007) concept of seal bypass system focuses on natural geologic features; however, the concept should encompass man-made features and events. Wellbores in oil and gas fields constitute a leakage risk (IPCC, 2005). Wellbores, if able to transmit fluids, can represent a leakage pathway for reservoir or other fluids

within formations that are intersected by the wellbores. The wellbore leakage risk is associated with detrimental effects to water quality of underground sources of drinking water, which is a concern of the Environment Project Agency's Underground Injection Control regulations (Wilson et al., 2007). Wellbores can also leak fluids to Earth's surface (Lewicki et al., 2007). Assessment of wellbore integrity, especially for CO₂ storage sites, constitutes a major challenge that many researchers actively investigate through field, laboratory, and modeling studies (Nordbotten et al., 2009; Carey et al., 2010; Crow et al., 2010). The major issues of concern are the following: 1) wellbores may provide a leakage pathway due to improper completion; and 2) wellbore materials might degrade with time and either enhance or create new leakage pathways. In addition to wellbores, geomechanical events represent another type of bypass system that is due to pressurization of a reservoir and caprock. Such events include possible creation of new fractures or the reactivation of pre-existing fractures or faults (Rohmer, 2010).

Conceptual models of the geologic characteristics necessary for high quality seals have been developed to enable prediction of caprock properties and improve hydrocarbon exploration and production efforts (Watts, 1987; Ingram et al., 1997; Ingram and Urai, 1999; Almon et al., 2005). These models also present information on lower quality caprocks or portions of caprocks, which are termed "waste zones" (Schowalter, 1979) due to their ability to contain hydrocarbons but their inability to transmit it economically. Mudstones, a common caprock lithology, have received much attention recently, with much of the work focused on determining the geologic controls on their sealing capacity so that prediction of the variation and heterogeneity of caprocks can be made. Studies on mudstones investigate relationships between sequence stratigraphy, depositional and

burial history, diagenesis, gamma ray signature (and other well logs), and sealing capacity (Almon et al., 2005). In general, however, mudstones are difficult to characterize in terms of sealing capacity on the field/reservoir scale due to their large-scale heterogeneity and control of sealing capacity by μm to sub- μm pore networks (MacQuaker et al., 2007).

Since the 1950s, the petroleum geosciences and industry have focused much effort on developing quantitative methods for characterizing and predicting the ability of caprocks to keep hydrocarbons from migrating out of reservoir rock over geologic timescales (Weber, 1997). A key goal has been to quantify the sealing capacity and to predict variations of sealing capacity over the scale of entire reservoirs. Although faults and other bypass systems have received attention, quantification of their impact on fluid fluxes and distribution of fluids remains a challenge. Much less attention has been paid to the evolution (i.e., dynamic change) of the ability of pore networks and seal bypass systems to transmit fluids through geologic time or shorter time-scales (e.g., the time period during exploration and production activities). Sealing capacity estimates include those modified to address scenarios of hydrodynamic pressure gradient in addition to simple balances of capillarity and buoyancy (Underschultz, 2007).

Methods for characterizing caprocks for hydrocarbon exploration and production incorporate a variety of sophisticated techniques, including capillary pressure measurements, seismology, tiltmeters, core collection and analysis, and downhole geophysical tools. However, in comparison to reservoir rock, caprocks have received little attention. Researchers have presented useful summaries, usually in the form of a flow chart presenting conceptual models, of the variety of sealing mechanisms and

concomitant failure processes that lead to migration of hydrocarbons out of a caprock (Watts, 1987; Ingram et al., 1997; Weber, 1997). However, for site specific studies, acquiring the multi-scale data necessary for identifying caprock properties and seal bypass system (e.g., fracture networks or faults) and quantifying their impact on leakage processes is difficult, especially for studies on the reservoir scale (Cartwright et al., 2007).

Lithologies that typically constitute caprocks, especially mudstones, strongly influence fluid dynamics in sedimentary basins, and thus they are studied for other reasons than hydrocarbon production. A great deal of literature exists on hydrologic properties of mudstones and their small-to-large scale impact on patterns of groundwater flow, contaminant transport, and effect on coupled processes such as fluid flow and solute transport, precipitation/dissolution, and geomechanical deformation (Aplin et al., 1999).

2.3 Caprocks and CO₂ Storage: Current Research Trends

Sequestration or storage of carbon dioxide into deep saline formations (i.e., not formations of underground sources of drinking water) or depleted hydrocarbon reservoirs is recognized as a potentially essential strategy for climate change mitigation (IPCC, 2005; Bachu, 2008), and central to this is the retention of CO₂ underground for relevant timescales. Retention is the key metric of both the global and local performance of CO₂ storage sites, which can be expressed as the total amount of CO₂ stored and the leakage rate from the intended reservoir. A recent study of atmospheric emission scenarios and global climate change that incorporates geologic CO₂ storage on a massive scale suggests

that CO₂ leakage rates (of CO₂ leaking back to the atmosphere) of 1% or less per thousand years are needed to avoid strong global warming (Shaffer, 2010). Locally, leaking CO₂ poses risks to the quality of underground sources of drinking water (Oldenburg et al., 2009). The key leakage metric will guide regulators to develop criteria of proper caprock performance if geologic CO₂ storage is implemented on a large, commercial scale.

Structural and/or stratigraphic trapping of supercritical CO₂ as a separate phase is arguably the most important trapping mechanism on a 10-to-100-year time scale (IPCC, 2005; see Figure 2.1), and this requires both a suitably porous reservoir for storage capacity and an overlying barrier to buoyant flow of CO₂. Leakage of CO₂ through the barrier/caprock could undermine the goal of reducing atmospheric emissions of the greenhouse gas and poses impacts to environmental health and safety (Price and Oldenburg, 2009).

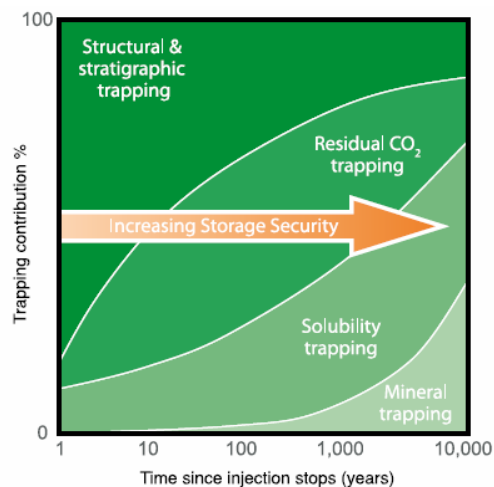


Figure 2.1. Trapping mechanisms and storage security for CO₂ storage sites (after IPCC, 2005, © 2005 by Intergovernmental Panel on Climate Change; reprinted with the permission of Cambridge University Press).

CO₂ storage has intensified research on caprocks and raised many issues that have not been addressed previously during the studies of hydrocarbon traps. Sealing mechanisms for CO₂ storage may be in some ways analogous to hydrocarbon systems in that stratigraphic and/or structural traps are targeted (IPCC, 2005). However, CO₂ systems differ in many regards and require new approaches and knowledge as detailed below:

- 1) CO₂ has different wetting characteristics and typically lower interfacial tensions with water, which affects multiphase flow and capillary processes and the predictions thereof (Chiquet et al., 2007; Wollenweber et al., 2010). A consequence of different wetting characteristics is that caprocks may have lower breakthrough pressures for CO₂-brine systems than hydrocarbon-brine systems (Chiquet et al., 2007).
- 2) Estimates of capillary breakthrough pressures and relative permeabilities of multiphase CO₂-bearing systems are needed for storage design and to estimate amounts of volumetric flow through potential caprocks (Li et al., 2006; Wollenweber et al., 2010).
- 3) Diffusional aqueous CO₂ transport through caprock and potential impacts on chemical processes requires attention (Busch et al., 2007; Lu et al., 2009).
- 4) CO₂ has enhanced or at least different chemical reactivity (Gaus, 2010) as compared to hydrocarbon systems in terms of precipitation/dissolution and intermolecular forces (Raveendran et al., 2005). Such reactivity necessitates novel research on CO₂-caprock reactivity.

- 5) Dry-out/desiccation of portions of caprocks, especially near areas of flow of separate phase CO₂ (e.g., flow within fractures), is a concern due to injection of anhydrous CO₂ and potential transport of water away from clay minerals (Gaus, 2010). Dry-out may compromise seal quality.
- 6) Storage potential of CO₂ in caprocks, especially shales, is a concern since the caprocks may attenuate some migrating CO₂ (Busch et al., 2008). Storage capacity, thus, is not a reservoir-only phenomenon.
- 7) Due to difficulties in predicting CO₂ behavior at storage sites in terms of reactivity and potential migration over geologic timescales, researchers investigate trap systems with abundant naturally occurring CO₂ (Gilfillan et al., 2009; Heath et al., 2009, see Figure 2.2). So-called natural analogs allowing testing of trapping and leakage mechanisms, which are difficult to evaluate through laboratory or numerical modeling studies.
- 8) Mathematical modeling and/or experiments of water-caprock-CO₂ chemical interaction to determine trapping mechanisms and relevant reactions over field spatial and time scales are needed (Gaus et al., 2005; Johnson et al., 2005; Gherardi et al., 2007; Gaus et al., 2008; Pruess, 2008). This must address challenges of upscaling data from laboratory studies.
- 9) Potential of injection-induced geomechanical damage in terms of reactivation of pre-existing fractures/faults or creation of new fractures and quantification of concomitant fluid fluxes is a major concern due to proposed extremely large CO₂ injection volumes (Hawkes et al., 2004; Gherardi et al., 2007; Rutqvist et al., 2008; Nelson et al., 2009; Rohmer and Bouc, 2010).

- 10) CO₂ storage necessitates risk assessment tailored specifically to environmental health and safety concerns, and to the needed performance in terms of storage amount and acceptable leakage rates (IEAGHG, 2009; Oldenburg et al., 2009; Rohmer and Bouc, 2010).

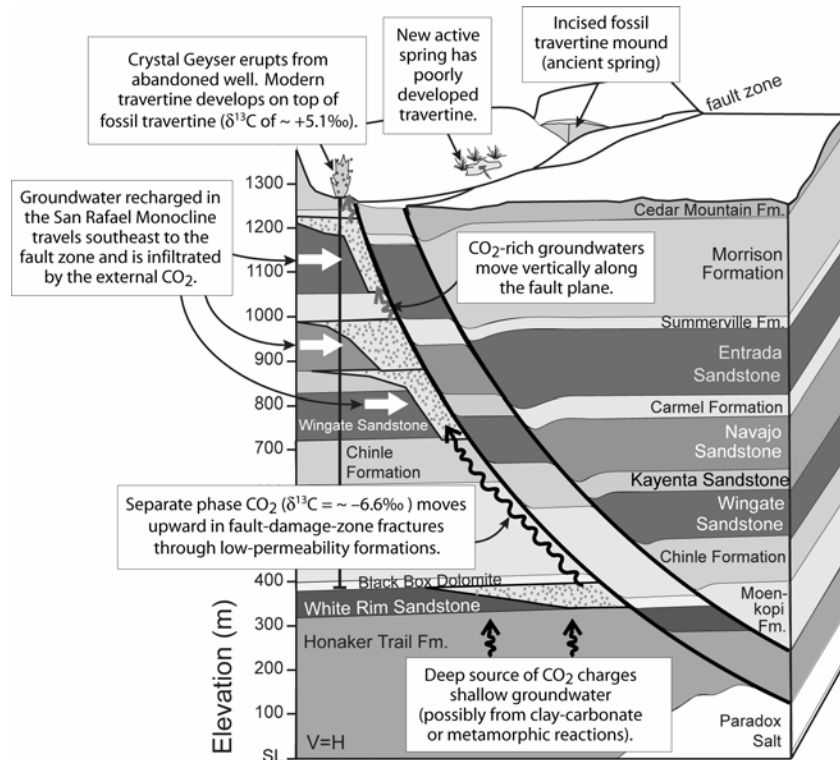


Figure 2.2. Schematic of the flow system at the Little Grand Wash Fault near Green River, Utah (after Heath et al., 2009; modified from Shipton et al., 2005, with permission from Elsevier). The flow system includes migration of CO₂ from a deep, natural source into a shallower groundwater system, which then discharges CO₂-rich fluids at the surface.

All of the processes listed above that affect the fate of CO₂ may impact the proper performance of a particular storage site; however, it is unclear which features, events, and processes (FEPs) will govern actual performance. Metrics for determining adequate and acceptable performance are still being developed. Such metrics are greatly needed to

allow researchers and scientists to assess the comparative importance and interdependence of the various FEPs. Risk assessment is not strictly scientific in nature, but also incorporates issues of policy and regulation. Identification of risk metrics and risk limits is the initial step of typical risk assessments (Rechard, 1999). CO₂-storage researchers (Wilson and Gerard, 2007; Oldenburg, 2008) and regulatory agencies are still developing criteria for what constitutes “significant” leakage, which incorporate the leakage potential through caprock. Until performance metrics are clearly identified and developed, knowledge of the dominant FEPs will be subjective. Risk assessment is needed to formally assess and rank FEPs, and to guide project management at identifying FEPs not already considered in the performance assessment (Rechard, 1999).

Sealing capacity of common caprocks is a critical ingredient in evolving methodologies for risk assessment (LeNeveu, 2008). This is especially relevant as the sealing capacity of most proposed caprocks have never been demonstrated in the sense of actual field-scale observation of retention of a non-aqueous phase fluid. Most CO₂ sites target locations that have had only groundwater/brine saturation. However, analogous lithofacies of target caprocks have probably been studied by the petroleum geosciences, but Issue 1 above should be taken into account. Fluid flow and pressure dissipation through the caprocks is also being considered as an important design criteria for a storage site in order to manage pressure build-up and avoid hydraulic fracturing, and to reduce impacts of brine and CO₂ migration into overlying aquifers (Cavanagh, 2010).

A potential high impact risk that may lead to failure of a storage site is the development and/or enhancement of seal bypass systems (see Section 2.2). The importance of micro- to meso-scale fractures in seal bypass processes is much more

recognized by the petroleum community than by the CO₂ community (Nelson, 1985; Apotria et al., 1994; Mallory, 1977; Narr et al., 2006; Andreani et al., 2008). For example, Figure 2.3 shows leakage scenarios for CO₂ that include large fault zones and abandoned wellbores, seen by the IPCC (2005) as important seal bypass systems, but the figure does not include ubiquitous networks of smaller fractures or sub-seismic faults.

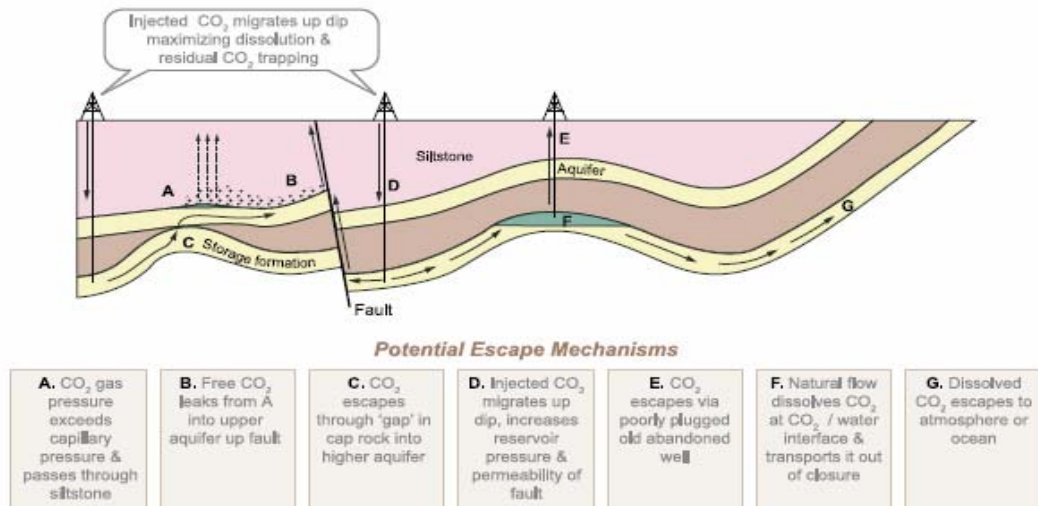


Figure 2.3. Potential leakage pathways envisioned by the IPCC (2005) neglect the effect of fracture networks. The determination of the relative role of CO₂ leakage through wellbores versus fracture networks is a research need. (after IPCC, 2005, © 2005 by Intergovernmental Panel on Climate Change; reprinted with the permission of Cambridge University Press).

The patterns and fluxes of potential brine and/or CO₂ leakage through natural fractures will probably be different from that of wellbores. The formation of natural fractures capable of transmitting fluids is related to the tendency of a caprock to dilate when deformed. The mechanical properties of a caprock, effective pressure, and shear zone geometry result in brittle/dilatant or ductile deformation (Ingram and Urai, 1998). Thus, the lithology, tectonic and burial histories, and fluid dynamics of a caprock will affect the pattern, connectivity, and openness of the fractures. Fracture diagenesis will

further modify the ability of fractures to transmit fluids. Wellbore leakage, in contrast, depends primarily upon the quality of the well completion and the degradation of wellbore materials (see Section 2.2). Thus, the style of penetration through reservoir/caprock systems and connectivity of the leakage pathway(s) is much different between those of natural fracture versus wellbore bypass systems.

Larger-scale faults, due to identification through seismic methods (Cartwright et al., 2007), may not be as much of a concern as smaller-scale fractures/faults. Smaller-scale fracture/fault systems can be significant hydraulic conductors or barriers, and in either case dominate fluid flow behavior in some rock types (NRC, 1996). A quantitative methodology for assessing the potential of complex fracture networks and/or sub-seismic fractures or faults (i.e., fractures or faults of length scales that are too small to be identified by standard seismic surveys) as seal bypass systems has not been attempted for CO₂ systems. Figure 2.4 portrays a fracture bypass system at a petroleum trap as a complex, tortuous, connected fracture network within a caprock, which constitutes an effective leakage pathway.

Petroleum geoscience researchers have presented useful summaries, usually in the form of flow charts presenting conceptual models, of the variety of sealing mechanisms and concomitant failure processes that lead to migration of hydrocarbons out of a seal (Watts, 1987; Ingram et al., 1997; Weber, 1997). Somewhat similar frameworks are being developed in the CO₂ research community for the purposes of risk assessment (LeNeveu, 2008; Lewicki et al., 2007; Oldenburg, 2008).

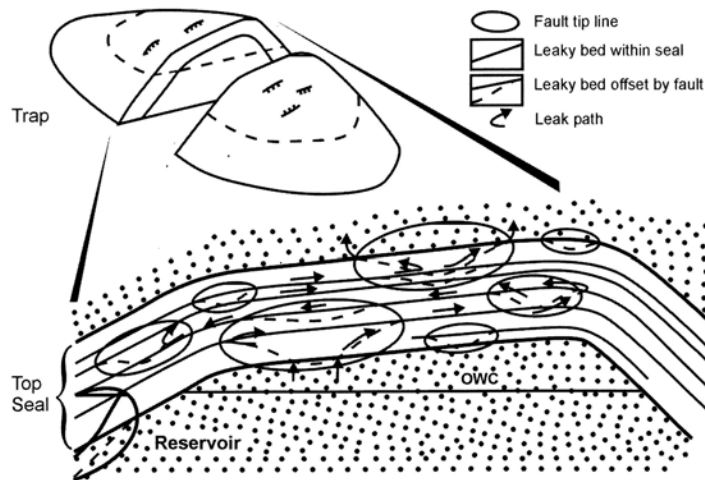


Figure 2.4. Schematic view of a seal bypass system at a petroleum trap, in which small faults/fractures form a tortuous, connected leakage pathway through the entire caprock (after Ingram and Urai, 1999; reprinted with permission from the Geological Society of London).

2.4 Research Needs for Caprock Evaluation

Based on Sections 2.2 and 2.3, important shortcomings in understanding caprocks for geologic CO₂ storage are discussed below. Seal bypass systems receive special focus due to their potential of significantly impacting CO₂ migration.

- 1) The rates of CO₂ leakage through (sub-seismic) fractures and fracture networks in caprocks are poorly known. Few studies have attempted quantification of the impact on sealing behavior due to reactive multiphase fluid flow in micro- to meso-scale (i.e. sub-seismic) fractures and fracture networks (Dewhurst et al., 1999; Gherardi et al., 2007). The need to examine potential leakage pathways in caprocks is great (IPCC, 2005; DOE, 2007; Silin et al., 2009). Leakage rate is the key metric for global and local performance of a caprock (see Section 2.3).

- 2) The relative role of CO₂ and associated brine leakage through natural fracture/fault versus wellbore bypass systems needs description and quantification (see Section 2.3).
- 3) The potential fluxes and patterns of CO₂ and associated brine flow that would negatively impact underground sources of drinking water are not well constrained or defined. In a local sense (i.e., for a particular storage site), clear metrics need to be developed and associated with leakage fluxes of CO₂ and/or brine that would lead to unwanted consequences in terms of environmental health or site performance (i.e., storage capacity goals). Such metrics may include net pH change, potential for release of metals due to changes in pH, mobilization of organic components from within the caprock or reservoir rocks, absolute magnitude of loss of CO₂ from the storage reservoir, etc.
- 4) Quantification of dynamic controls on the ability of fractures in caprocks to transmit fluids is needed (DOE, 2007). Effects due to CO₂ injection and the pressure perturbation on the dynamics of fluid movement especially need assessment. Work focused on fracture activation or creation has been performed (Rohmer and Bouc, 2010), but additional study is needed of associated fluid fluxes and their evolution during and after a storage project. Factors requiring investigation to determine their influence on fracture closing, opening, or “healing” due to mineralization include the following: pore pressure; variable fluid saturations and compositions; CO₂ sorption and diffusivity; chemical reactivity of both the CO₂ and aqueous phases; CO₂-

induced changes in clay-interparticle adhesive properties; the impact of pre-existing mineralization in fractures on reactive fluid flow; and geometrical/connectivity considerations.

- 5) Numerical models of sealing behavior are needed and necessary to make proper account of fracture-CO₂-brine interactions and the influence of fracture heterogeneity over a range of length and time scales. Such modeling needs to be not only theoretical, but related to observed experiments or evidence at the lab to field scale.
- 6) Dry-out processes are poorly understood. Injection of anhydrous CO₂ may transport water away from clay and other phases within caprocks, resulting in desiccation and shrinkage. Volume change poses significant risk for creation of new features or exacerbation of pre-existing discontinues.
- 7) Wettability experiments for common caprock solid phases in a brine/CO₂ fluid system are lacking (see Chapter 4). Caprock mineral phases with available data are limited to glass, quartz, calcite, and muscovite (Dickson et al., 2006; Chiquet et al., 2007; Chalbaud et al., 2009); these neglect common phases such as organics, iron-oxides, smectites, kaolinites, and illites. Thus, at the current time, prediction of breakthrough pressures using contact angles is limited.
- 8) Surface and intermolecular-related forces in general are not typically addressed in assessment of caprock. However, these processes can govern shrinkage/swelling, wettability, fines migration, solubilization or swelling of organics, and modification/aging of wettability.

The geologic CO₂ storage community should prioritize the study of these research needs as part of a formal risk assessment. Some of the features, events, and processes (FEPs) described by the research needs may pose greater risks than others. Since these needs require new research, the scientific and engineering community does not know *a priori*, especially quantitatively, the effect that the FEPs will have on the desired performance of a caprock/reservoir system. Risk assessment provides project management approaches to integratively and iteratively determine which processes have the greatest impact on the performance of the system (Rechard, 1999; Rohmer and Bouc, 2010). The risk assessment process requires clear identification of metrics for assessing and measuring performance. Such metrics must be based on both local, site-specific properties/processes (e.g., a particular lithology and tectonic history of site; see Point 2 of this section) and global requirements (e.g., overall quantities of CO₂ needed to meet CO₂ emission reduction targets).

Current approaches to determining what factors of the caprock system have the greatest effects on performance typically seek simple models, but not too simple (Oldenburg et al., 2009). The goal is to have models retain only the important behavior of the system so that they can be clearly and easily expressed, and evaluated both conceptually and mathematically. Sequential risk assessments (Rechard and Tierney, 2005) can facilitate further refinement of knowledge of a particular system if initial simple models do not capture the actual system behavior. Thus, risk assessments need to be iterative and to incorporate monitoring data of system performance. Currently, it is not known how simple (or complex) conceptual and mathematical models need to be.

Risk assessment can be a guiding tool to apply the expertise of researchers while seeking knowledge of the most important factors that govern performance. This approach could reduce individual researcher bias. If done through community-wide efforts, it could identify from the vast amounts of knowledge being generated by CO₂ researchers the most important caprock processes and properties.

2.5 References

- Almon, W. R., Dawson, W. C., Botero-Duque, F., Goggin, L. R., and Yun, J. W., 2008, Seal analysis workshop, printed materials, Chevron Energy Technology Company: held at the Joint Annual Meeting of the Geological Society of America, Soil Science Society of America, American Society of Agronomy, Crop Science Society of America, and the Gulf Coast Association of Geological Studies with the Gulf Coast Section of SEPM, October 5–9, Houston, Texas.
- Almon, W. R., Dawson, W. C., Ethridge, F. G., Rietsch, E., Sutton, S. J., and Castelblanco-Torres, B., 2005, Sedimentology and petrophysical character of Cretaceous Marine Shale sequences in foreland basins—potential seismic response issues, in Boulton, P., and Kaldi, J., eds., *Evaluating Fault and Cap Rock Seals: AAPG Hedberg Series*, no. 2, p. 215–235.
- Aplin, A. C., Fleet, A. J., and MacQuaker, J. H. S., 1999, Muds and mudstones: physical and fluid-flow properties, in Aplin, A. C., Fleet, A. J., and MacQuaker, J. H. S., eds., *Muds and mudstones: Physical and fluid-flow properties*: London, Geological Society [London] Special Publication 158, p. 1–8.
- Bachu, S., 2008, CO₂ storage in geological media: Role, means, status and barriers to deployment: *Progress in Energy and Combustion Science*, v. 34, no. 2, p. 254–273.
- Berg, R. R., 1975, Capillary pressures in stratigraphic traps: *AAPG Bulletin*, v. 59, no. 6, p. 939–956.
- Busch, A., Alles, S., Gensterblum, Y., Prinz, D., Dewhurst, D. N., Raven, M. D., Stanjek, H., and Krooss, B. M., 2007, Carbon dioxide storage potential of shales: *International Journal of Greenhouse Gas Control*, v. 2, p. 297–308.
- Carey, J. W., Svec, R., Grigg, R., Zhang, J. S., Crow, W., 2010. Experimental investigation of wellbore integrity and CO₂-brine flow along the casing-cement microannulus. *International Journal of Greenhouse Gas Control*, v. 4, 272–282.

- Cartwright, J., Huuse, M., and Aplin, A., 2007, Seal bypass systems: *AAPG Bulletin*, v. 91, no. 8, p. 1141–1166.
- Cavanagh, A., 2010, *Caprock integrity? Why the pressure is off when it comes to CO₂ storage, Caprocks and Seals for Geologic Carbon Sequestration*, Workshop by the Standord University Global Climate and Energy Project and the U.S. Geological Survey, January 12–15: Asilomar Conference Grounds, Pacific Grove, CA.
- Chalbaud, C., Robin, M., Lombard, J. M., Martin, F., Egermann, P., and Bertin, H., 2009, Interfacial tension measurements and wettability evaluation for geological CO₂ storage: *Advances in Water Resources*, v. 32, no. 1, p. 98–109.
- Chiquet, P., Broseta, D., and Thibeau, S., 2007, Wettability alteration of caprock minerals by carbon dioxide: *Geofluids*, v. 7, no. 2, p. 112–122.
- Couples, G.D., 2005, Seals: the role of geomechanics, in Boulton, P., and Kaldi, J., eds., *Evaluating Fault and Cap Rock Seals: AAPG Hedberg Series*, No. 2: Tulsa, Oklahoma, American Association of Petroleum Geologists, p. 87–108.
- Crow, W., Carey, J. W., Gasda, S., Williams, D. B., and Celia, M., 2010, Wellbore integrity analysis of a natural CO₂ producer: *International Journal of Greenhouse Gas Control*, v. 4, p. 186–197.
- Dewhurst, D. N., Yang, Y., and Aplin, A. C., 1999, Permeability and fluid flow in natural mudstones, in Aplin, A., Fleet, A. J., and Macquaker, J. H. S., eds., *Muds and Mudstone: Physical and Fluid Flow Properties*: London, Geological Society Special Publication 158, p. 23–43.
- Dickson, J. L., Gupta, G., Horozov, T. S., Binks, B. P., and Johnston, K. P., 2006, Wetting phenomena at the CO₂/water/glass interface: *Langmuir*, v. 22, no. 5, p. 2161–2170.
- DOE (Department of Energy), 2007, *Basic research needs for geosciences: Facilitating 21st century energy systems*, Report from the workshop held February 21–23: U.S. Department of Energy, Office of Basic Energy Sciences, available in PDF format at <http://www.sc.doe.gov/bes/reports/list.html>.
- Dullien, F. A. L., 1992, *Porous media—fluid transport and pore structure, Second Edition*: London, UK, Academic Press, Inc., 574 p.
- Gaus, I., 2010, Role and impact of CO₂–rock interactions during CO₂ storage in sedimentary rocks: *International Journal of Greenhouse Gas Control*, v. 4, p. 73–89.
- Gaus, I., Audigane, P., Andre, L., Lions, J., Jacquemet, N., Dutst, P., Czernichowski-Lauriol, I., and Azaroual, M., 2008, Geochemical and solute transport modelling

- for CO₂ storage, what to expect from it?: *International Journal of Greenhouse Gas Control*, v. 2, no. 4, p. 605–625.
- Gaus, I., Azaroual, M., and Czernichowski-Lauriol, I., 2005, Reactive transport modelling of the impact of CO₂ injection on the clayey cap rock at Sleipner (North Sea): *Chemical Geology*, v. 217, no. 3-4, p. 319–337.
- Gherardi, F., Xu, T. F., and Pruess, K., 2007, Numerical modeling of self-limiting and self-enhancing caprock alteration induced by CO₂ storage in a depleted gas reservoir: *Chemical Geology*, v. 244, no. 1–2, p. 103–129.
- Gilfillan, S. M. V., Lollar, B. S., Holland, G., Blagburn, D., Stevens, S., Schoell, M., Cassidy, M., Ding, Z. J., Zhou, Z., Lacrampe-Couloume, G., and Ballentine, C. J., 2009, Solubility trapping in formation water as dominant CO₂ sink in natural gas fields: *Nature*, v. 458, no. 7238, p. 614–618.
- Halbouty, M. T., 1969, Rationale for deliberate pursuit of stratigraphic, unconformity, and paleogeomorphic traps: *AAPG Bulletin*, v. 53, p. 3–29.
- Hall, J. S., Mozley, P., Davis, J. M., and Roy, N. D., 2004, Environments of formation and controls on spatial distribution of calcite cementation in Plio-Pleistocene fluvial deposits, New Mexico, USA: *Journal of Sedimentary Research*, v. 74, no. 5, p. 643–653.
- Hawkes, C. D., Bachu, S., and McLellan, P. J., 2004, Geomechanical factors affecting geological storage of CO₂ in depleted oil and gas reservoirs: *Journal of Canadian Petroleum Geology*, v. 44, no. 10, p. 52–61.
- Heath, J. E., Lachmar, T. E., Evans, J. P., Kolesar, P. T., and Williams, A. P., 2009, Hydrogeochemical characterization of leaking, carbon-dioxide-charged fault zones in east-central Utah, with implications for geologic carbon storage, in McPherson, B. J. O. L., and Sundquist, E. T., eds., *The Science and Technology of Carbon Sequestration, AGU Monograph Series*: Washington, D.C., American Geophysical Union.
- Heath, J. E., McPherson, B. J. O. L., Dewers, T. A., Petrusak, R., Chidsey, T. C., Jr., Kotula, P. G., and Mozley, P. S., in prep., Pore-lining composition and capillary breakthrough pressure of mudstone caprocks: sealing efficiency at CO₂ storage sites: *International Journal of Greenhouse Gas Control*.
- Hildenbrand, A., Schlomer, S., and Krooss, B. M., 2002, Gas breakthrough experiments on fine-grained sedimentary rocks: *Geofluids*, v. 2, no. 1, p. 3–23.
- IEAGHG, 2009, A review of the international state of the art in risk assessment guidelines and proposed terminology for use in CO₂ geological storage, *International Energy Agency Greenhouse Gas R&D Programme*.

- Ingram, G. M., and Urai, J. L., 1999, Top-seal leakage through faults and fractures: The role of mudrock properties, in Aplin, A., Fleet, A. J., and MacQuaker, J. H. S., eds., *Muds and Mudstones: Physical and Fluid Flow Properties, Special Publication 158*: London, Geological Society, p. 125–135.
- Ingram, G. M., Urai, J. L., and Naylor, M. A., 1997, Sealing processes and top seal assessment, in Moller-Pedersen, P., and Koestler, A. G., eds., *Hydrocarbon Seals: Importance for Exploration and Production: NPF Special Publication 7*: Singapore, p. 165–174.
- IPCC, 2005, *IPCC special report on carbon dioxide capture and storage*, prepared by Working Group III of the Intergovernmental Panel on Climate Change: Cambridge, United Kingdom and New York, NY, USA, Cambridge University Press, 442 p.
- Johnson, J. W., Nitao, J. J., and Morris, J. P., 2005, Reactive transport modeling of cap rock integrity during natural and engineered CO₂ storage, in Benson, S. M., ed., *Carbon Dioxide Capture for Storage in Deep Geologic Formations—Results from the CO₂ Capture Project, Vol. 2: Geologic Storage of Carbon Dioxide with Monitoring and Verification*: London, England, Elsevier, p. 787–814.
- Klein, J. S., Mozley, P., Campbell, A., and Cole, R., 1999, Spatial distribution of carbon and oxygen isotopes in laterally extensive carbonate-cemented layers: Implications for mode of growth and subsurface identification: *Journal of Sedimentary Research*, v. 69, no. 1, p. 184–201.
- LeNeveu, D. M., 2008, CQUESTRA, a risk and performance assessment code for geological sequestration of carbon dioxide: *Energy Conversion and Management*, v. 49, no. 1, p. 32–46.
- Levorsen, A. I., 1966, The obscure and subtle trap: *AAPG Bulletin*, v. 50, p. 2058–2067.
- Lewicki, J.L., Birkholzer, J., and Tsang, C.F., 2007, Natural and industrial analogues for leakage of CO₂ from storage reservoirs: identification of features, events, and processes and lessons learned: *Environmental Geology*, v. 52, p. 457–467.
- Lewis, H., and Couples, G.D., 1993, Production evidence for geological heterogeneities in the Anschutz Ranch East Field, western USA, in North, C.P., and Prosser, D.J., eds., *Characterization of Fluvial and Aeolian Reservoirs, Special Publication 73*, London, Geological Society, p. 321–338.
- Li, Z. W., Dong, M. Z., Li, S. L., and Huang, S., 2006, CO₂ sequestration in depleted oil and gas reservoirs - caprock characterization and storage capacity: *Energy Conversion and Management*, v. 47, no. 11–12, p. 1372–1382.
- Lindquist, W. B., 1999. *3DMA general users manual*. State University of New York at Stony Brook, pp. 47.

- Lindquist, W. B., Lee, S. M., Oh, W., Venkatarangan, A. B., Shin, H., Prodanovic, M., 2005. *3DMA-Rock: a software package for automated analysis of rock pore structure in 3-D computed microtomography images*: Department of Applied Mathematics and Statistics, State University of New York, Stony Brook, http://www.ams.sunysb.edu/~lindquis/3dma/3dma_rock/3dma_rock.html (March 2010)
- Lu, J. M., Wilkinson, M., Haszeldine, R. S., and Fallick, A. E., 2009, Long-term performance of a mudrock seal in natural CO₂ storage: *Geology*, v. 37, no. 1, p. 35–38.
- MacQuaker, J. H. S., Taylor, K. G., and Gawthorpe, R. L., 2007, High-resolution facies analyses of mudstones: Implications for paleoenvironmental and sequence stratigraphic interpretations of offshore ancient mud-dominated successions: *Journal of Sedimentary Research*, v. 77, no. 3–4, p. 324–339.
- Moraes, M. A. S., and Surdam, R. C., 1993, Diagenetic heterogeneity and reservoir quality - fluvial, deltaic, and turbiditic sandstone reservoirs, Potiguar and Reconcavo rift basins, Brazil: *AAPG Bulletin*, v. 77, no. 7, p. 1142–1158.
- Nelson, S. T., Mayo, A. L., Gilfillan, S., Dutson, S. J., Harris, R. A., Shipton, Z. K., and Tingey, D. G., 2009, Enhanced fracture permeability and accompanying fluid flow in the footwall of a normal fault: The Hurricane fault at Pah Tempe hot springs, Washington County, Utah: *Geological Society of America Bulletin*, v. 121, no. 1–2, p. 236–246.
- Nordbotten, J. M., Kavetski, D., Celia, M. A., and Bachu, S., 2009, Model for CO₂ leakage including multiple geological layers and multiple leaky wells: *Environmental Science & Technology*, v. 43, p. 743–749.
- NRC (National Research Council), 1996, *Rock Fractures and Fluid Flow*: Washington, D.C., National Academy Press.
- Oldenburg, C. M., 2008, Screening and ranking framework for geologic CO₂ storage site selection on the basis of health, safety, and environmental risk: *Environmental Geology*, v. 54, no. 8, p. 1687–1694.
- Oldenburg, C. M., Bryant, S. L., and Nicot, J. P., 2009, Certification framework based on effective trapping for geologic carbon sequestration: *International Journal of Greenhouse Gas Control*, v. 3, no. 4, p. 444–457.
- Orr, F. M., 2009, CO₂ capture and storage: Are we ready?: *Energy & Environmental Science*, v. 2, no. 5, p. 449–458.
- Price, P. N., and Oldenburg, C. M., 2009, The consequences of failure should be considered in siting geologic carbon sequestration projects: *International Journal of Greenhouse Gas Control*, v. 3, no. 5, p. 658–663.

- Pruess, K., 2008, Leakage of CO₂ from geologic storage: Role of secondary accumulation at shallow depth: *International Journal of Greenhouse Gas Control*, v. 2, no. 1, p. 37–46.
- Raveendran, P., Ikushima, Y., and Wallen, S. L., 2005, Polar attributes of supercritical carbon dioxide: *Accounts of Chemical Research*, v. 38, no. 6, p. 478–485.
- Rechard, R. P., 1999, Historical relationship between performance assessment for radioactive waste disposal and other types of risk assessment: *Risk Analysis*, v. 19, no. 5, p. 763–807.
- Rechard, R. P., and Tierney, M. S., 2005, Assignment of probability distributions for parameters in the 1996 performance assessment for the Waste Isolation Pilot Plant. Part 1: description of process: *Reliability Engineering & System Safety*, v. 88, no. 1, p. 1–32.
- Rohmer, J., and Bouc, O., 2010, A response surface methodology to address uncertainties in cap rock failure assessment for CO₂ geological storage in deep aquifers: *International Journal of Greenhouse Gas Control*, v. 4, no. 2, p. 198–208.
- Rutqvist, J., Birkholzer, J. T., and Tsang, C. F., 2008, Coupled reservoir-geomechanical analysis of the potential for tensile and shear failure associated with CO₂ injection in multilayered reservoir-caprock systems: *International Journal of Rock Mechanics and Mining Sciences*, v. 45, no. 2, p. 132–143.
- Schlumberger, 2010, *Oilfield glossary*, accessed July 10, 2010, <http://www.glossary.oilfield.slb.com/>.
- Schowalter, T. T., 1979, Mechanics of secondary hydrocarbon migration and entrapment: *AAPG Bulletin*, v. 63, no. 5, p. 723–760.
- Shaffer, G., 2010, Long-term effectiveness and consequences of carbon dioxide sequestration: *Nature Geoscience*, v. 3, p. 464–467.
- Shipton, Z. K., Evans, J. P., Dockrill, B., Heath, J., Williams, A., Kirchner, D., and Kolesar, P. T., 2005, Natural leaking CO₂-charged systems as analogs for failed geologic sequestration reservoirs, in Thomas, D., and Benson, S. M., eds., *Carbon Dioxide Capture for Storage in Deep Geologic Formations—Results from the CO₂ Capture Project, Vol. 2*: London, Elsevier Science, p. 699–712.
- Silin, D., Patzek, T. W., and Benson, S. M., 2009, A one-dimensional model of vertical gas plume migration through a heterogeneous porous medium: *International Journal of Greenhouse Gas Control*, v. 3, no. 3, p. 300–310.
- Underschultz, J., 2007, Hydrodynamics and membrane seal capacity: *Geofluids*, v. 7, no. 2, p. 148–158.

- Wardlaw, N. C., Li, Y., Forbes, D., 1987, Pore-throat size correlation from capillary-pressure curves: *Transp. Porous Media*, v. 2, p. 597–614.
- Washburn, E. W., 1921, The dynamics of capillary flow: *Physical Review*, v. 17, p. 273–283.
- Watts, N. L., 1987, Theoretical aspects of cap-rock and fault seals for single-phase and 2-phase hydrocarbon columns: *Marine and Petroleum Geology*, v. 4, no. 4, p. 274–307.
- Weber, K. J., 1997, A historical overview of the efforts to predict and quantify hydrocarbon trapping features in the exploration phase and in field development planning, in Moller-Pedersen, P., and Koestler, A. G., eds., *Hydrocarbon Seals: Importance for Exploration and Production: NPF Special Publication 7*: Singapore, Elsevier, p. 1–13.
- Wilson, E. J., Friedmann, S. J., and Pollak, M. F., 2007, Research for deployment: Incorporating risk, regulation, and liability for carbon capture and sequestration: *Environmental Science & Technology*, v. 41, p. 5945–5952.
- Wilson, E. J., and Gerard, D., 2007, *Carbon Capture and Sequestration: Integrating Technology, Monitoring and Regulation*: Ames, Iowa, Blackwell Publishing Ltd, p. 269.
- Wollenweber, J., Alles, S., Busch, A., Krooss, B. M., Stanjek, H., and Littke, R., 2010, Experimental investigation of the CO₂ sealing efficiency of caprocks: *International Journal of Greenhouse Gas Control*, v. 4, no. 2, p. 231–241.

**PART II. PORE-NETWORK PROPERTIES
AND SEALING BEHAVIOR**

CHAPTER 3. PORE NETWORKS IN CONTINENTAL AND MARINE MUDSTONES: CHARACTERISTICS AND CONTROLS ON SEALING BEHAVIOR¹

Abstract

Mudstones in sedimentary basins strongly affect the distribution of hydrocarbons and the containment of injected fluids, such as in the case of the underground storage of CO₂. Pore networks of these rocks are a primary control on hydraulic properties. This paper investigates the geologic conditions that contribute to the formation of pore networks that control the quality of “caprock” seals for the retention of hydrocarbons or other fluids. The intent is to enable better characterization of caprocks of different sealing quality. Novel sub- μm , three-dimensional (3D) quantitative and qualitative descriptions reveal seven dominant pore types distinguished by geometry, connectivity, and pore-lining material. Pore Type I, a sheet-like pore, occurs in all argillaceous mudstones and has coordination numbers (i.e., number of neighboring, connected pores) governed by the sheet-like geometry. This pore type contributes to high mercury capillary pressures due to small pore throats at the tips of the pores. The other six pore types may be categorized based on four fundamental characteristics, including: (1) authigenic (e.g., replacement or

¹ Heath, J.E., Dewers, T.A., McPherson, B.J.O.L., Petrusak, R., Chidsey, T.C. Jr., Rinehart, A.J., Mozley, P.S., Pore networks in marine and non-marine mudstones: characteristics and controls on sealing behavior: *Geosphere*, submitted May 29, 2010. This dissertation chapter contains some modification from the submitted journal manuscript.

pore-lining precipitation) clay and pyrite minerals, (2) pores in clays adjacent to larger, more competent grains, (3) pores in organics, and (4) stylolitic and microfracture-related pores. Originally distal (i.e., away from the continental and in deeper marine settings) environments that underwent deep burial generate pore types of high sealing quality. Prediction of sealing quality fits within depositional models of mudstone facies, which can aid in the choice of potential sites for engineered fluid storage.

3.1 Introduction

In most sedimentary basins, mudstones comprise the major portion (> 60%; MacQuaker and Gawthorpe, 1993) of sedimentary basin fill and thus play an integral role in many geologic processes and systems. These rocks dominate hydrodynamics of subsurface flow systems, affecting pore pressure distribution and local- to regional-scale patterns of groundwater and hydrocarbon transport (Aplin et al., 1999). Properties such as low permeability and high capillary-breakthrough pressure make these rocks ideal as barriers (seals or caprocks) to the movement of single or multiphase fluids (Potter et al., 2005). Hence, they are targets (primarily as bounding formations or caprocks) for hazardous waste storage (Marty et al., 2003; Davy et al., 2009) and caprocks for subsurface containment of anthropogenic CO₂ (IPCC, 2005). With respect to hydrocarbons, mudstones can act as source, migration pathway, and caprock for oil and gas, and even reservoir in the case of shale gas (Loucks et al., 2009).

Fundamentally, pore networks are a primary control on hydraulic properties, and thus greater understanding of the geometry, topology, and pore-lining material of pore networks in mudstones will yield insight into their predicted controls on transport and

storage of geologic and injected fluids (DOE, 2007). However, in spite of their societal and scientific importance, only limited work has achieved a detailed characterization of pore networks in mudstones due to constraints in measurement resolution and the heterogeneous nature of these rocks (Desbois et al., 2009).

Studies of pores in mudstones are hindered by the fact that they are composed of 50% or more material with grain sizes $< 63 \mu\text{m}$, and many are argillaceous with dominant components $< 4 \mu\text{m}$ (MacQuaker and Adams, 2003). Small component size results in small pore sizes. Such fine-grained material requires characterization by specialized, high-resolution techniques. In addition, at the nanometer (nm) to reservoir scale, many mudstones are extremely heterogeneous (MacQuaker et al., 2007; Loucks et al., 2009). Multi-scale characterization methods are appropriate to address the dual problems of macro-scale distribution of properties and nano- to micro-scale components and structure.

In this context, recent studies have demonstrated the utility and appropriateness of dual-beam focused ion beam/scanning electron microscopy (FIB/SEM) systems for imaging mudstone 3D pore structure and pore-lining material (Kotula et al., 2003; Kotula and Keenan, 2006; Tomutsa et al., 2007; De Winter et al., 2009; Desbois et al., 2009). FIB/SEM methods combine milling of smooth nm-scale surfaces via focused gallium ions (Ga^+) and high resolution imaging by field emission SEM (Yao, 2007). Successive milling and imaging yields a series of two-dimensional (2D) images, which are stacked and processed to construct a 3D pore network geometric model (Holzer et al., 2004; Tomutsa et al., 2007). SEM images taken in backscattered electron mode (BSE; De Winter et al., 2009) provide information on mineral and organic matter distributions by variation in mean atomic number (Z). Recent 3D pore network studies on low

permeability geologic samples have focused on defining and describing pore types and morphology, capillarity, fractal scaling, and fluids in pores using a cryogenic FIB/SEM system (Tomutsa et al., 2007; Desbois et al., 2008; De Winter et al., 2009; Desbois et al., 2009).

In this paper, we investigate the geologic conditions that contribute to the formation of pore networks capable of forming low-to-high quality sealing “caprocks” for the retention of hydrocarbons or other fluids. Of interest is the relative importance of primary depositional, deep burial, and diagenesis on controlling pore network properties. We examine mudstones from a variety of geologic settings (Section 3.2). We incorporate high-resolution 3D petrography of pore networks using FIB/SEM techniques (Sections 3.3.1–3.3.3 and 3.4.1) and compare pore types from different mudstone lithofacies (Section 3.4.2). We compile pore network statistics, including pore shape, connectivity, topology, and size distribution (Section 3.4.3). We use mercury intrusion porosimetry (Section 3.3.4) to determine pore-throat distributions and breakthrough pressures. We evaluate the porosimetry data in light of the 3D pore network information (Section 3.4.4). We interpret capillary sealing behavior of the studied mudstones, all of which have been proposed as caprocks for subsurface CO₂ storage, in light of pore network properties and mercury breakthrough pressures (Section 3.5). Results of this detailed analysis suggest a strong association between depositional environments, pore network properties, and sealing ability (Sections 3.5 and 3.6). This work is intended to provide a scientifically-sound characterization approach for mudstone (sealing) systems in order to optimize identification and location of potential sites for engineered fluid storage.

3.2 GEOLOGIC SETTINGS

Perhaps the most important influence on pore network properties is the geologic setting, especially lithofacies and associated depositional processes. We provide information on geologic settings and lithofacies of the rocks studied herein to facilitate evaluation of geologic controls on pore networks properties. Standard thin section petrographic descriptions in this section serve as a lead-in for the 3D FIB/SEM petrography and MIP data of the Results Section (Section 3.4). The Southeast Regional Carbon Sequestration Partnership (SECARB) and the Southwest Regional Carbon Sequestration Partnership (SECARB and SWP; Litynski et al., 2008) provided mudstone samples from cores through caprock “sealing sequences” at recently-deployed CO₂ sequestration demonstration sites (Figure 3.1A; see Litynski et al., 2008 for descriptions of the SECARB, SWP, and the U.S. Department of Energy’s Regional Carbon Sequestration Partnerships program in general). The mudstones cover a range of depositional environments from continental to marine shelf (Table 3.1; Figure 3.1B–D). Geologic units investigated include, from generally proximal to more distal or deeper water depositional environments: the Upper Cretaceous Kirtland Formation, the Upper Cretaceous Lower and Middle Tuscaloosa Group, and the Gothic shale of the Pennsylvanian Paradox Formation. The thin-section petrographic descriptions are summarized from reports by the SWP (see Appendix B) and unpublished descriptions by the lead author.

Figure 3.1. (A) Map of regions covered by the U.S. Department of Energy’s Southwest and Southeast Regional Carbon Sequestration Partnerships, with locations of wells of core samples. (B) Depositional systems of the Kirtland Formation shown at a time when aggradation of the Fruitland Formation was occurring (adapted from Fassett and Hinds, 1971). Vertical exaggeration is approximately 60 times. The upper and lower Kirtland are more proximal than the swampy systems of the Fruitland. Kirtland can include a vast range of alluvial environments (see text). (C) Tuscaloosa Group depositional environments (adapted from Liu, 2005). The Lower Tuscaloosa was deposited as a transgressive systems tract. Marine Tuscaloosa deposition occurred during the maximum flooding event of the latest Cenomanian to early Turonian and represents the second Late Cretaceous Oceanic Anoxic Event. (D) Cross section showing the transgressive systems tract that deposited the Gothic shale (at the Aneth Unit) or “black shale” facies over shelfal carbonates (adapted from Goldhammer et al., 1994). Water depth was estimated at > 35 m.

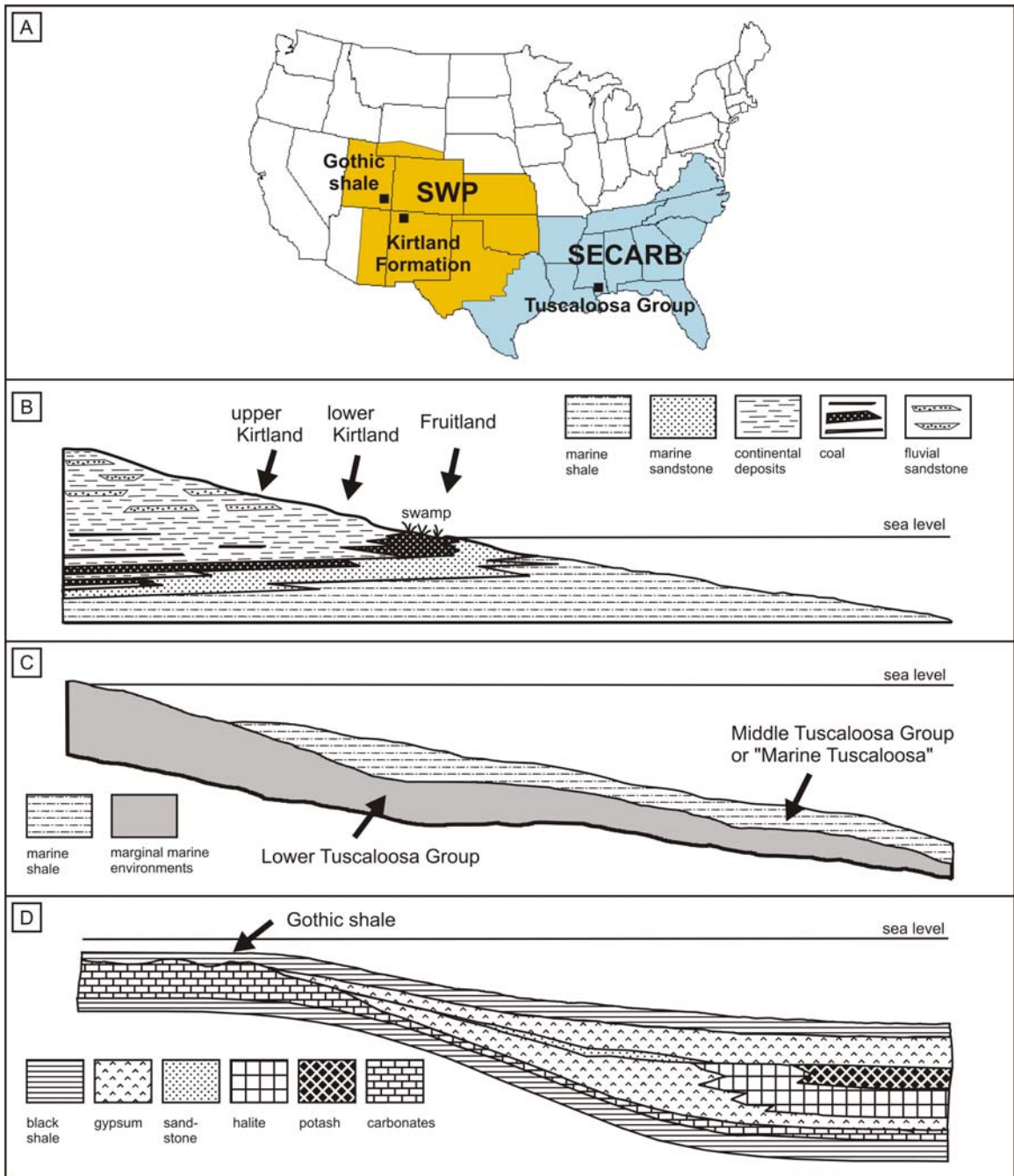


Figure 3.1. (Caption on preceding page.)

TABLE 3.1. MUDSTONE CORE SAMPLE IDENTIFICATION AND GENERAL INFORMATION

Sample ID	Depth (m)	Geologic Unit	Site of Interest	State	Depositional Environment and Dominant Rock Types
upper Kirtland 2049.7A	624.75	upper shale member of Kirtland Formation	Pump Canyon ECBM/CO ₂ *	NM	Multiple environments: floodplains, point-bar deposits, possible channel fills, reducing environments including swamps and oxbow lakes; sandy to silty argillaceous mudstones
upper Kirtland 2049.7B	624.75			NM	
lower Kirtland 2692.9A	820.80	lower shale member of Kirtland Formation	Pump Canyon ECBM/CO ₂ *	NM	Coastal-swamp, river, flood-plain, and lake deposits; silty to argillaceous mudstones
lower Kirtland 2692.9B	820.80			NM	
Marine Tuscaloosa 7925.5	2415.69	Middle Tuscaloosa Group or "Marine Tuscaloosa"	Plant Daniel CO ₂ injection [†]	MS	Represents maximum marine transgression during deposition of Tuscaloosa Group; inner shelf environments but deeper water than Lower Tuscaloosa; sandy to silty to argillaceous mudstones
Marine Tuscaloosa 7931.9	2417.64			MS	
Lower Tuscaloosa 8590	2618.23	Lower Tuscaloosa Group	Plant Daniel CO ₂ injection [†]	MS	Trangressive systems tract deposition; inner shelf but shallower water than Marine Tuscaloosa; sandstones with interbedded sandy to silty to argillaceous mudstones
Lower Tuscaloosa 8590.9	2618.51			MS	
Gothic shale 5390.8A	1643.12	Gothic shale	Aneth Unit EOR [§]	UT	Trangressive systems tract deposition; deeper subtidal in quiet, reducing bottom conditions; calcareous to phosphatic, silty to argillaceous mudstones
Gothic shale 5390.8B	1643.12			UT	

Note: Samples were obtained from core from the Southwest and Southeast Carbon Partnerships on Carbon Sequestration at Phase II CO₂ sequestration demonstration sites (Litynski et al., 2008).

*Pump Canyon Site is a project that involved enhanced coalbed methane recovery (ECBM) and CO₂ injection into unmineable coal seams.

[†]Plant Daniel Site was a CO₂ injection project into saline aquifers.

[§]The Aneth Unit is part of the Greater Aneth oil field in Utah, where CO₂ is injected underground for enhanced oil recovery (EOR).

3.2.1 Kirtland Formation of New Mexico and Colorado

The Upper Cretaceous Kirtland Formation is found in the San Juan Basin, New Mexico and Colorado (Figure 3.1A), and is a regional aquitard and reservoir seal (Ayers, 2003). It was deposited by streams flowing toward the retreating shoreline of the Western Interior Seaway in an alluvial plain with floodplain and channel depositional environments, which occurred landward of the swampy environments of the underlying Fruitland Formation (Figure 3.1B; Fassett and Hinds, 1971; Fassett, 2009). The Kirtland Formation is typically divided into upper and lower mudstone-rich members and a middle sandstone-rich member, the Farmington Sandstone (Bauer, 1916; Fassett and Hinds, 1971; Stone et al., 1983; Molenaar and Baird, 1992). Throughout most of the basin the Kirtland Formation conformably overlies the coal-bearing Fruitland Formation (Fassett and Hinds, 1971), which contains the world's most prolific coalbed methane play (Ayers, 2003).

Klute (1986) considered the upper shale member of the Kirtland Formation (or upper Kirtland) as similar to, although slightly sandier than, the muddy, fine-grained meandering river lithofacies classification of Jackson (1978). Through interpretation of a range of fine-grained and sandy lithofacies, Klute (1986) identified multiple depositional sub-environments of the upper Kirtland as follows: fine-grained material representing floodplains with deposition during overbank flow; fining-upward sandstone sequences interpreted as point-bars associated with meandering channels; cross-bedded sandstones indicating crevasse-splays with deposition of cross-bedded sandstones; massive sandstones representing possibly channel fill, levee, or floodplain environments;

coal, lignite, and carbonaceous siltstones interpreted as indicating reducing environments such as swamps, oxbow lakes, or abandoned chutes of point bars.

Fassett and Hinds (1971) considered the depositional environments of the lower shale member (or lower Kirtland) similar to those of the underlying and conformable Fruitland, which included coastal-swamp, river, flood-plain, and lake environments. However, the lower Kirtland is differentiated from the underlying Fruitland by a lack of carbonaceous mudstones or coal beds. The lower Kirtland's depositional environments were relatively well-drained and did not accumulate or preserve significant organic matter (Fassett and Hinds, 1971). Better drainage may indicate higher stream gradients. We did not find detailed lithofacies descriptions of the lower Kirtland in the literature.

Starting in May 2008, the SWP sponsored field operator ConocoPhillips to drill CO₂ injection well EPNG Com A Inj 1 (API No. 30-045-34305; Lat. 36.307735°N, Long. 107.251278°W; Figure 3.1A) with coring of the upper and lower shale members of the Kirtland Formation from depths of 624 to 631 m, and 820 to 822 m. The SWP injected CO₂ into unmineable coal seams at depths between ~889 m and 957 m for a 12 month period (i.e., from July 30, 2008, to August 12, 2009). Core samples studied for pore network characteristics herein were obtained from depths of 624.75 and 820.80 m, which represent the upper and lower shale members, respectively (Table 3.1).

Optical petrography complemented by standard SEM, X-ray diffraction (XRD), total organic carbon (TOC), porosity, and permeability analyses of several upper Kirtland samples are summarized here (see Chapter 5 and Appendices B.2.1 and B.2.2 for more details provided by TerraTek). Characterization of samples taken along the length of the core indicates sandy to silty argillaceous mudstones (Figures 3.2A and B), with abundant

Figure 3.2. Scans of thin sections and photomicrographs of continental and marine mudstones. Thin sections (standard size of 24 mm × 46 mm) for a particular formation are located above corresponding photomicrographs. Images and petrographic descriptions for C, D, and J are from TerraTek (see Appendix B.2.1 and Chidsey et al., 2010). Fractures (i.e., magenta lines through the rock) are considered induced features due to desiccation of clays, pressure release during core collection, or other handling and sample preparation. (A) Thin section for upper Kirtland Formation from core depth of ~625.60 m. The upper two thirds is dominated by sand- and silt-sized grains. The lower third is a silt-bearing, argillaceous mudstone. Large opaque grain is pyrite. Younging direction is upward. (B) Plane light photomicrograph from the lower third of A. Diagonal parallel lines are an artifact from thin section polishing. The clay matrix has yellow birefringent colors in places and shows strong parallelism under crossed polarizers when the stage is rotated. The parallelism, however, is not across the entire area, but concentrated in a “zig-zag” pattern. Clasts include chert, volcanic rock fragments, quartz, feldspar, and sedimentary rock fragments. Opaque grains are pyrite and organics. (C) Thin section for lower Kirtland Formation from core depth of 820.60 m. The left half of the section was stained. White areas are a preparation artifact that removed rock. (D) Plane light photomicrograph of unstained area of overlying thin section. Silt and minor sand grains are quartz and feldspars. The cross hatched minerals are ferroan calcite. Clays are illite/smectite with kaolinite and chlorite and minor smectite. Scale bar is 0.5 mm. (E) Thin section for Lower Tuscaloosa Formation from core depth of 2615.05 m. Younging direction is to the left. Thin section shows abundant silt- and sand-sized grains. Bioturbation as burrows is visible at the thin section scale. (F) Plane light photomicrograph taken on E. Silt or fine sand layers with clay-rich layers above and below. Larger grains include angular quartz, probable feldspar, and micas. Authigenic minerals include pyrite. Many dark patches are visible in the thin section, which may be organics or pyrite. Pyrite framboids are visible at 40× magnification. Scale bar is 0.9 mm. (G) Thin section for Marine Tuscaloosa from core depth of 2416.27 m. The upper surface marked by the notch indicates the younging direction and is at a natural shear fracture that was visible in hand sample. The left side of the thin section may show deformation associated with the fracture. (H) Plane light photomicrograph from G. Sand- and silt-sized grains include quartz and micaceous flakes. Clay-rich areas do not show strong parallelism under crossed polarizers. Clay- and silt/sand-rich regions are abundant throughout the thin section and have non-planar boundaries. Scale bar is 0.9 mm. (I) Thin section for Gothic shale from core depth of 1642.6 m. Younging direction is to the left. (J) Plane light photomicrograph taken on a thin section from core depth of 1643.1 m. Sample is a phosphatic, argillaceous mudstone. Flattened, amalgamated pellets (lighter brown) are phosphatic in composition. Compacted siliceous forms (white) are composed of chert. The lighter brown matrix color and abundance of siliceous fossils, as well as phosphatic pellets, suggest a siliceous matrix cement component. Scale bar is 0.5 mm.

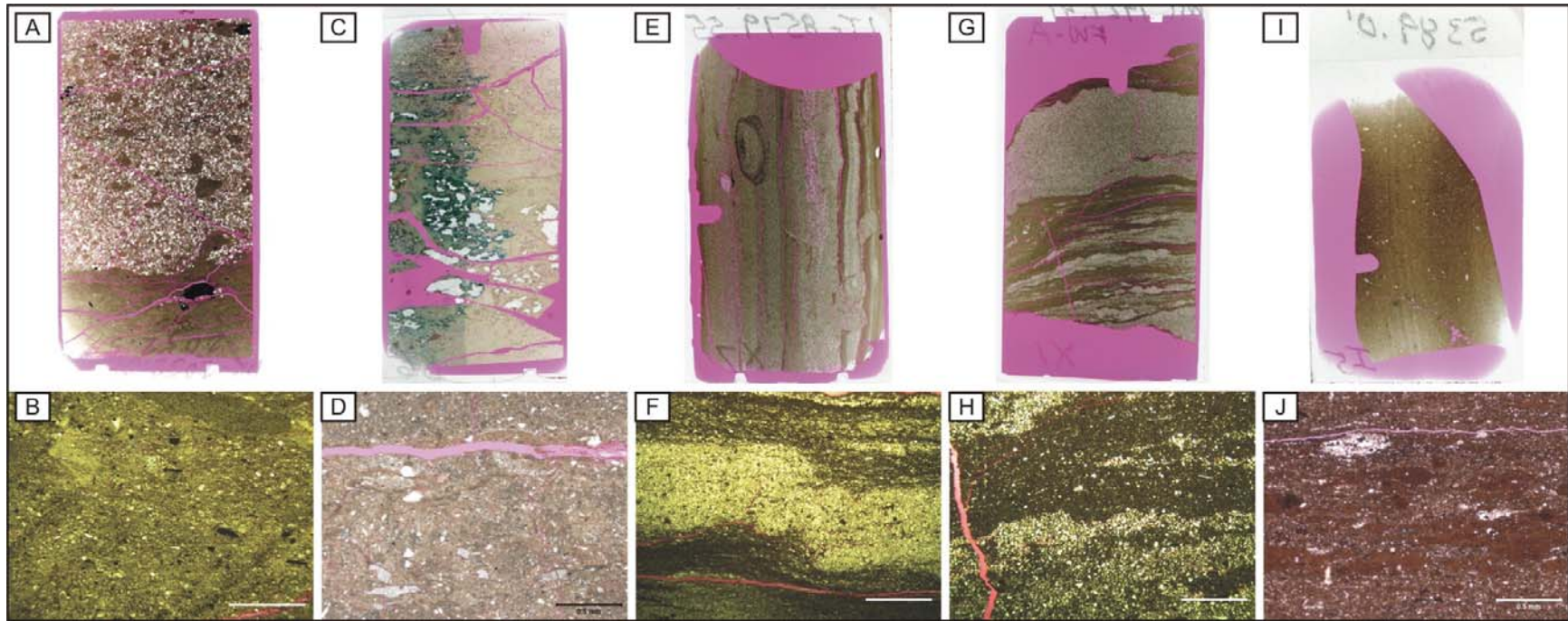


Figure 3.2. (Caption on preceding page.)

mottled, disorganized and poorly laminated textures. Pedogenic features include illuviation envelopes, which contain well-aligned clays transported into the sediments along root channels or desiccation cracks. Sand- and silt-sized grains include quartz, plagioclase feldspar, and volcanic and sedimentary rock fragments (e.g., chert replaced volcanic clasts and clay rip-up clasts). Some lithofacies can be dominated by sand-sized grains, whereas others by silt- and clay-sized material. Clay minerals include smectite, illite, mixed layer smectite/illite, chlorite, and minor kaolinite. Clay expandability ranges from 20 to 23% (see Appendix B.2.1 for more details). Authigenic minerals include minor carbonate cement (usually iron-rich) and pyrite.

Porosity types include:

- abundant induced porosity from coring (i.e., pressure release fractures), core handling, and dry-out (~5 to 20 μm in size), which is common for mudstones with high amounts of swelling clays;
- root and organic particle casts left by the decayed organic material (2 to 20 μm); and
- matrix-hosted pores between clay flakes and within cements (<5 μm).

Minor intragranular porosity within feldspar clasts also occurs. TOC ranges from 0.06 to 0.09 wt %. Porosity values vary from 6.5 to 9.9%. Low pressure decay permeabilities range from $\sim 7 \times 10^{-20}$ to $1 \times 10^{-19} \text{ m}^2$. (See TerraTek's report in Appendices B.2.1 and B.2.2 and Chapter 5 for raw data with discussion of analysis and results.)

3.2.2 Tuscaloosa Group of Alabama and Mississippi

The Upper Cretaceous Tuscaloosa Group contains predominately siliciclastic sediments and represents fluvial-deltaic and marginal marine to mid-shelf open marine depositional environments (Mancini et al., 1987; Rosen and Rosen, 2008). In the subsurface of Alabama and Mississippi, the Tuscaloosa Group is commonly divided into the Lower, Middle, and Upper Tuscaloosa Group, with the Middle Tuscaloosa Group informally called the “Tuscaloosa Marine Shale” or “Marine Tuscaloosa”.

The Marine Tuscaloosa is Cenomanian to Turonian in age and represents the maximum marine transgression during deposition of the Tuscaloosa Group (Liu, 2005). In the updip direction, the Tuscaloosa Group becomes predominately fluvial/continental; the Marine Tuscaloosa thins and transitions from a dark gray shale to a red-brown mudstone. In the downdip direction, the formation thickens and represents outer shelf, deeper water environments. Liu (2005) describes the Marine Tuscaloosa as dark gray to black, organic-rich, laminated shale in the northeastern portion of the basin. Across the northern Gulf of Mexico region where Lower Tuscaloosa Group sandstones occur at favorable depths for CO₂ storage, the overlying Marine Tuscaloosa shale is composed principally of gray, somewhat calcareous, siliciclastic mudstone. Thickness ranges from ~60 to > 180 m. Apparent organic and clay content is greatest in the lower part of the Marine Tuscaloosa, which has been interpreted as a condensed section that formed during the initial rapid rise in sea level (Mancini et al., 1987; Pashin et al., 2008). Thin siltstone and sandstone beds become thicker and more abundant upwards in the Marine Tuscaloosa, representing transgressive progradational infilling (Mancini and Puckett,

2005; Pashin et al., 2008). The Lower Tuscaloosa Group was deposited as a transgressive systems tract (TST) with deltaic and other marginal marine environments (Liu, 2005).

In 2009, SECARB conducted a CO₂ injection test (Litynski et al., 2008) in basal sandstones, the so-called “massive sand” unit, of the Lower Tuscaloosa Group at the Plant Daniel site in Jackson County, Mississippi (Figure 3.1C). The Marine Tuscaloosa and an interbedded fine-grained unit within the massive sand are considered sealing sequences for CO₂ storage associated with the injection test. Core samples for characterization of pore networks were obtained from Lower Tuscaloosa Group and Marine Tuscaloosa strata within the Mississippi Power Company No. 1 observation well (MPC #11-1; API No. 23-059-20023-00; Lat. 30.536902°N, Long. 88.558073°W).

Depth intervals cored include 2409.7 to 2418.3 m in the Marine Tuscaloosa and from 2600.2 to 2618.7 m in the Lower Tuscaloosa Group. The Lower Tuscaloosa Group core includes the bottom part of the upper massive sand unit from 2600 to 2612 m, interbedded and bioturbated sandstone and silt- and clay-rich or bearing mudstones from 2611.8 to 2615.8 m, and predominately clay-rich mudstone with silt-rich mudstone from 2615.8 to 2618.7 m. Pore network samples for this study were from depths 2415.7 m, 2417.6 m, 2618.2 m, and 2618.5 m. These sample depths correspond with the depths of the Marine Tuscaloosa and the interbedded mudstones in the Lower Tuscaloosa Group.

A thin section image and photomicrograph for the Lower Tuscaloosa Formation (Figures 3.2E and F) from core depth of 2615.05 m show an interbedded sand-, silt- and clay-rich mudstone, with individual layers that thin and pinch out. Some clay layers show similar extinction under cross-polarized light indicating particle alignment. Sand- and silt-sized grains include angular quartz, micas, and possible feldspar. Opaque regions are

authigenic pyrite and organics. Bioturbation (burrows) is visible at the thin section scale (Figure 3.2E). XRD from a similar depth (2613.6 m) indicates clays are chlorite, kaolinite, and illite, and non-clay minerals are predominately quartz with lesser amounts of plagioclase feldspar and minor K-feldspar (DOE, 2008).

A thin section scan and photomicrograph of the Marine Tuscaloosa (Figures 3.2G and H) from a core depth of 2416.27 m also show interbedding of sand-, silt-, and clay-rich layers. Clays do not show as strong of alignment under crossed polarizers as in the Lower Tuscaloosa thin section. Sand- and silt-sized grains include quartz and lesser amounts of micas and feldspars. X-ray diffraction (XRD) analysis of a sample from 2417.6 shows that clays are chlorite, kaolinite, and illite with about 5 wt % calcite (DOE, 2008).

A recent publication (DOE, 2008) reported some fundamental physical properties of the Tuscaloosa. Specifically, porosity (at 17 MPA) and Klinkenberg-corrected permeability for the Lower Tuscaloosa Group from a depth of 2618.2 m are 9.5% and $\sim 7 \times 10^{-17} \text{ m}^2$. TOC is 1.0 wt %. Marine Tuscaloosa porosity and permeability at 2415.7 m are 2.2% and $\sim 1 \times 10^{-19} \text{ m}^2$. Total organic carbon for depths of 2415.4 m and 2417.2 m are 0.65 and 0.73 wt %, respectively.

3.2.3 Gothic Shale of Utah and Colorado

The Pennsylvanian Gothic shale lies within the Blanding subbasin of the Paradox Basin in southeastern Utah and southwestern Colorado (Figure 3.1D), and overlies the Desert Creek hydrocarbon producing zone of the Greater Aneth oil field (Peterson, 1992). Goldhammer et al. (1994) describe Gothic shale lithology as sapropelic dolomite and

dolomitic shales to silty carbonate mudstones, deposited as a TST during fourth-order sea level rise.

The Gothic shale is the basal unit of the Ismay zone of the Paradox Formation. The Paradox contains cyclic shelfal carbonates and mudstones and corresponding cyclic basinal evaporites and mudstones (Figure 3.1D). Goldhammer et al. (1994) identified 29 cycles of basinal evaporite-shale. At the Aneth Unit, an unconformity (sequence boundary) separates the Gothic shale from the underlying mottled carbonates of a mound buildup complex, which shows evidence of erosion (Chidsey et al., 2010). The Gothic shale ranges from 1.5 to 8.2 m thick, averaging 3.6 m, and thins over the carbonate buildup compared to areas off the mound and more distal areas in the basin (Goldhammer et al., 1994; Chidsey et al., 2010). The Gothic shale is Goldhammer et al.'s (1994) "black laminated mudstone" (BLM) lithofacies that represents the TST. The BLM depositional environment is deeper subtidal zone (> 35 m water depths) in quiet, reducing bottom conditions.

The Gothic shale is the reservoir caprock at the Aneth Unit (Chidsey et al., 2010). As part of SWP evaluation of CO₂ injection into the Desert Creek zone for enhanced oil recovery, we sampled Gothic core from the Aneth Unit H-117 well (API No. 43-037-30153; Lat. 37.3093°N, Lon. 109.3035°W), which was drilled in 1974. The SWP performed a suite of tests on the core to evaluate sealing integrity (Chidsey et al., 2010). The cored interval examined for this study included a complete 5.09 m section of Gothic from depths 1638.5 to 1643.8 m. The core sample studied herein for pore network and petrographic properties came from the depth of 1643.1 m (Chidsey et al., 2010).

Figures 3.2I and J show a thin section image and photomicrograph of the Gothic shale. The Gothic shale is fine grained with faint lamination and well-developed fissility. Textural components include minor silt-sized quartz, calcite, dolomite, and mica in a dominant clay matrix, with common authigenic pyrite. Compacted siliceous forms (Figure 3.2J) are composed predominately of chert. Fossils include conodonts, brachiopods, and condalarids. Besides induced porosity, macro- and micro-porosity are difficult to identify. Thus, the Gothic appears less porous and more homogeneous than the other mudstone samples.

Porosity, pressure-decay permeability, and TOC measurements taken from four depths from the core range from 2.7 to 4.3%, 1.3×10^{-19} to 1.4×10^{-19} m², and 2.2 to 4.4 wt %, respectively (Chidsey et al., 2010).

3.3 MATERIALS AND METHODS

To facilitate interpretation of geologic controls on pore-network properties and capillarity, FIB/SEM techniques were used to image and chemically characterize pore-lining material and geologic structures. Representative samples from each core were characterized first by FIB/SEM and then with MIP. Mercury intrusion porosimetry was used to allow comparison of interpreted MIP pore-size distributions to the direct imaging of the pore networks, as well as to obtain breakthrough pressures in an assessment of sealing quality.

3.3.1 Sample Preparation

Ten mudstone samples, two from each of the study units, were prepared from plugs (2.5-cm diameter by < 1.5 cm long). Plug orientation was approximately parallel to the axis of the core, and roughly perpendicular to bedding. Prior to microanalysis, the top and bottom of the plugs were lightly sanded with fine-grit paper to achieve a nominally flat surface. Due to potential fluid sensitivity of these clay- and organic-rich samples, polishing using a saline solution or oil was not performed to avoid imbibition of fluids, deflocculation, contamination, or other alteration of pore structure, organics, and other solid phases. Plug cleaning was also not performed. Significant penetration of drilling fluids into the plugs was unlikely due to low permeability of the rocks and appearance of fresh surfaces.

3.3.2 FIB/SEM Microscopy

Samples were gold-palladium coated and painted with silver dag to provide a current path to ground and mitigate specimen charging. Samples were placed in mounts or vises and grounded. Serial sectioning and imaging by FIB/SEM was performed with FEI Company's Helios™ 600 Nanolab DualBeam™ instrument and semi-automated Slice and View™ software. To promote smooth, cross-sectioned faces and avoid “curtaining” artifacts (i.e., uneven vertical striations) during milling (Hayles et al., 2007), and to provide a fiducial reference for image alignment, a layer of Pt was deposited over the area of sample to be milled using the FIB's deposition system (Yao, 2007). During milling, the Ga⁺ ion beam was normal to the sample surface, and the electron beam was at an angle of 52° from the ion beam. Acceleration voltage for Ga⁺ was 30 kV, and the

beam current was 2.8 nA. A rough-cut trough was made to provide an area for deposition of milled material and to reveal the vertical cross section. Vertical cross-sectioned surfaces perpendicular to bedding and the upper surface of the sample were milled by the ion beam at 25 nm spacing. The Slice and View™ software facilitated cross-sectioning with automation for beam shifts and auto-focusing; however, manual adjustments were made during milling to ensure acquisition of high quality electron micrographs. Backscattered electron (BSE) imaging mode with a through-the-lens detector (TLD) was chosen for obtaining mineralogical information in terms of differences in mean atomic number, *Z*, which provided strong contrast in mineralogy and pores for most samples. The acceleration voltage and beam current were 1 kV and 1.4 nA, respectively. The BSE micrograph field of view was 16.00 μm × 13.81 μm.

3.3.3 Image Analysis

Digital reconstruction and quantification of 3D pore networks and organic distribution for selected samples required several steps. The computer program ImageJ 1.42q (Rasband, 1997–2010; Ferreira and Rasband, 2010) was employed to align, crop, and segment stacks of Slice and View™ images into regions of pore/non-pore or organics/non-organics. The TransformJ plugin program of ImageJ was used to interpolate between segmented images (Meijering, 2008), resulting in a cubic voxel length size of 15.6 nm. The cropped regions consisted of 299 × 299 × 299 voxels, with a total cubic data volume with side length sizes of 4.66 μm. TransformJ interpolation produced grayscale information, which necessitated further segmentation for proper delineation of pore/non-pore or organics/non-organics. 3D “floodfill” image rendering with calculation

of pore volume, organic volume, and porosity was performed using the computer program ScanIP™ by Simpleware, Ltd. Segmented images of pore/non-pore regions were evaluated using the 3DMA-Rock computer program (Lindquist, 1999) for further quantification of the pore networks.

Using 3DMA-Rock algorithms, the following steps were performed in sequence (Lindquist, 1999; Lindquist and Venkatarangan, 1999; Lindquist et al., 2005; Neethirajan et al., 2008; Udawatta et al., 2008): medial axis construction of pore pathways; throat finding and pore partitioning; throat and pore characterization including pore volume, coordination number, and throat area; and geometrical construction of the pore and throat network. The medial axis construction produces a centrally located skeletonization of the pore space, which preserves topology and geometry of the pore network. Voxel paths consisting of five voxels or less were excluded from the final medial axis construction. Throats are minimal cross-sectional surface areas located on the medial axis, and the throat surfaces may be non-planar. The coordination number of a pore gives the number of neighboring pores. This 3DMA analysis enabled compilation of pore statistics in the form of pore volume and pore throat radii frequency distributions and other topologic properties (Section 3.4.3).

The distribution of throat and pore body sizes, connectivity of the pore network, and surface area and shapes of pores have strong control on drainage and imbibition processes and fluid flow properties such as relative permeability (Neethirajan et al., 2008).

3.3.4 Mercury Intrusion Porosimetry

Mercury intrusion porosimetry (MIP) was performed on a Micromeritics AutoPore IV 9500 Series porosimeter. The inner diameter of the penetrometer bulb (Sigal, 2009) was 2.54 cm (1.0-in), which necessitated light sanding of the 2.54 cm plugs to a smaller size for placement into the bulb. Sanding removed the gold-palladium coating and silver dag previously applied to the samples. Prior to analysis, samples were dried at 100°C and photographed. To investigate capillary and transport properties in the direction perpendicular to bedding, some plugs were jacketed with epoxy for directional intrusion. Some plugs were too thin for proper jacketing and directional intrusion.

Breakthrough capillary pressure (also called bubbling pressure or sealing pressure) is the pressure at which a continuous filament of mercury extends across a MIP sample, or equivalently, the pressure when the non-wetting phase first appears on the outlet side of a sample plug (Katz and Thompson, 1987; Dullien, 1992; Dewhurst et al., 2002). For this study, it was estimated by identifying the point on the cumulative mercury saturation versus pressure curve with maximum inflection upwards (Dewhurst et al., 2002; Daniel and Kaldi, 2008). Closure pressure corrections (Sneider et al., 1997) followed a compressibility method that estimated the pressure when mercury first penetrated the pore network (Colombo and Carli, 1981; Almon et al., 2008).

3.4 RESULTS

3.4.1 FIB/SEM Imaging and 3D Image Analysis

3D pore network reconstructions of 101.5 μm^3 regions from each mudstone are presented in Figures 3.3 through 3.9, arranged in order from proximal to distal from

sediment source and deepening water depth of deposition. Shown for Kirtland Formation, Tuscaloosa Group, and Gothic shale samples are a single 1024×884 pixel 2D BSE image, usually taken from the back of an image stack, an extracted 299×299 segmented image to distinguish pores (in black), a 3D reconstruction of pores, and medial axis and pore throat 3D visualizations. Organic-rich samples have additional images to show 3D distributions of organic phases as layers and pore-filling entities. Medial axes, representing the skeletonization of pore networks, are shown using a rainbow color scale wherein red corresponds with low burn numbers, and blue/violet are higher burn numbers; burn numbers represent the max-norm distance in number of voxels from the medial axis to the grain boundary where a pore sharing a grain boundary has a number of one (Neethirajan et al., 2008). Voxel sizes for all 3D images are 15.6 nm.

To allow viewing of the FIB/SEM (in BSE mode) images used to construct 3D pore network models, video files were developed and are provided as a supplemental electronic index (see Appendix A for Supplemental Video Files 1 through 4). These videos present sets of serial sections for the upper Kirtland Formation², the Lower Tuscaloosa Group³, Marine Tuscaloosa⁴, and Gothic shale⁵, respectively. These present a

² **Supplemental Video File 1.** Video file of a set of 325 images of focused ion beam serial sections taken in backscattered electron mode at 25 nm spacing for sample upper Kirtland 2049.7B. The horizontal field of view is 16.00 μm . Up direction is not definitely known, but it is either towards the top or bottom of the images. Original TIFF images (1024×884 pixels) were compressed using JPEG algorithm at 100 quality when making the video file. Video files were further compressed by resampling images to 400×345 pixels and compressing using the Cinepak algorithm at 75 quality.

³ **Supplemental Video File 2.** Video file of a set of 278 images of focused ion beam serial sections taken in backscattered electron mode at 25 nm spacing for sample Lower Tuscaloosa 8590. The horizontal field of view is 16.00 μm . The large zone of charging (bright area) is probably at the location of organics. Original TIFF images (1024×884 pixels) were compressed using JPEG algorithm at 100 quality when making the video file. Video files were further compressed by resampling images to 400×345 pixels and compressing using the Cinepak algorithm at 75 quality.

variety of distinct 3D pore types for the different geologic environments. A pore type classification scheme is introduced in the next section and shown in Figure 3.10. Pore statistics, given in Section 3.4.2, for all analyzed digital samples are given in Figure 3.11.

Common artifacts visible in most of the FIB/SEM images are induced pores near the upper surface (i.e., top of micrographs) of samples, direct effects of mechanical cutting and rough polishing. Shapes of such induced pores can be different from and non-representative of those deeper in the cross section. Specimen charging, visible as bright white spots in the images, is also an occasional imaging artifact and was especially common on organics. It can be differentiated from high Z phases like pyrite by a dark halo around the margins of the bright areas.

Figure 3.3 presents the pore network of the upper Kirtland Formation, specific to a sample from 624.75 m (below ground surface, or bgs). The lack of lamination or planar clay fabric, and the more or less random distribution of pore and clay orientations in the BSE image (observable from the larger, higher Z clay packets that are likely chlorite) (Figure 3.3A) may reflect the compacted analogues of deposited clay packets or floccules, observed experimentally by Schieber and Southard (2009). The disorganized texture may reflect pedogenic processes of weathering and aggregation formation before

⁴ **Supplemental Video File 3.** Video file of a set of 340 images of focused ion beam serial sections taken in backscattered electron mode at 25 nm spacing for sample Marine Tuscaloosa 7925.5. The horizontal field of view is 16.00 μm . Original TIFF images (1024 \times 884 pixels) were compressed using JPEG algorithm at 100 quality when making the video file. Video files were further compressed by resampling images to 400 \times 345 pixels and compressing using the Cinepak algorithm at 75 quality.

⁵ **Supplemental Video File 4.** Video file of a set of 325 images of focused ion beam serial sections taken in backscattered electron mode at 25 nm spacing for sample Gothic shale 5390.8A. The horizontal field of view is 16.00 μm . The viewer should be careful in distinguishing pores from organics. Organics have a low grayscale value. Pores are discerned by the blackest grayscale values and careful observation of the grain/non-pore margins. Original TIFF images (1024 \times 884 pixels) were compressed using JPEG algorithm at 100 quality when making the video file. Video files were further compressed by resampling images to 400 \times 345 pixels and compressing using the Cinepak algorithm at 75 quality.

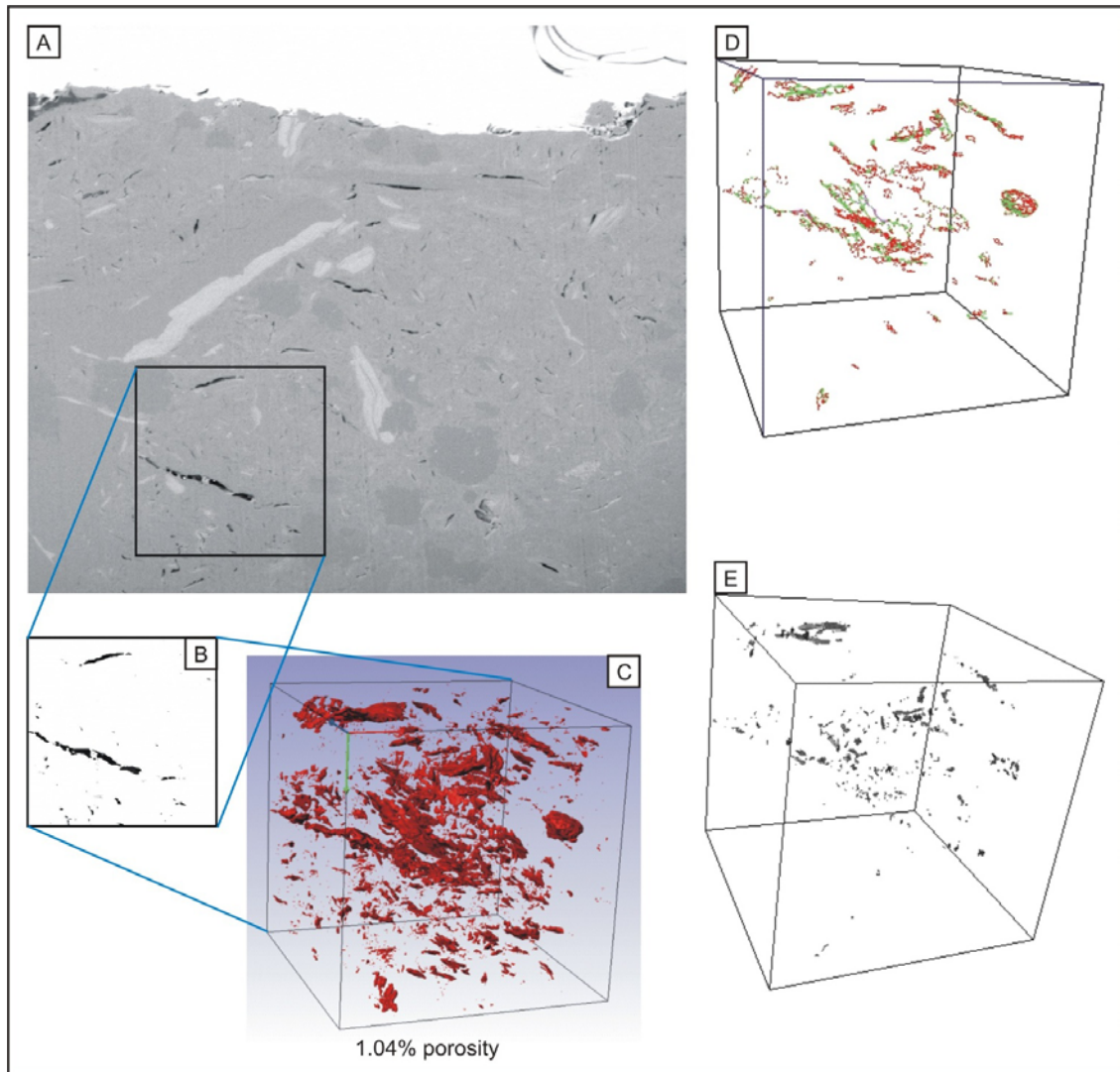


Figure 3.3. Results of focused ion beam (FIB) milling and imaging of sample upper Kirtland 2047.9B and 3D pore network reconstruction. (A) Backscattered electron (BSE) image of FIB serial section. Horizontal field of view is 16.00 μm . Outlined box indicates cubic region of 3D pore network reconstruction, which has side lengths of 4.66 μm . (B) Segmentation of BSE image into pore (black) and non-pore (white). (C) 3D floodfill rendering of pores. Voxel size is 15.6 nm. (D) 3D plot of medial axis. (E) 3D plot of pore throat surfaces.

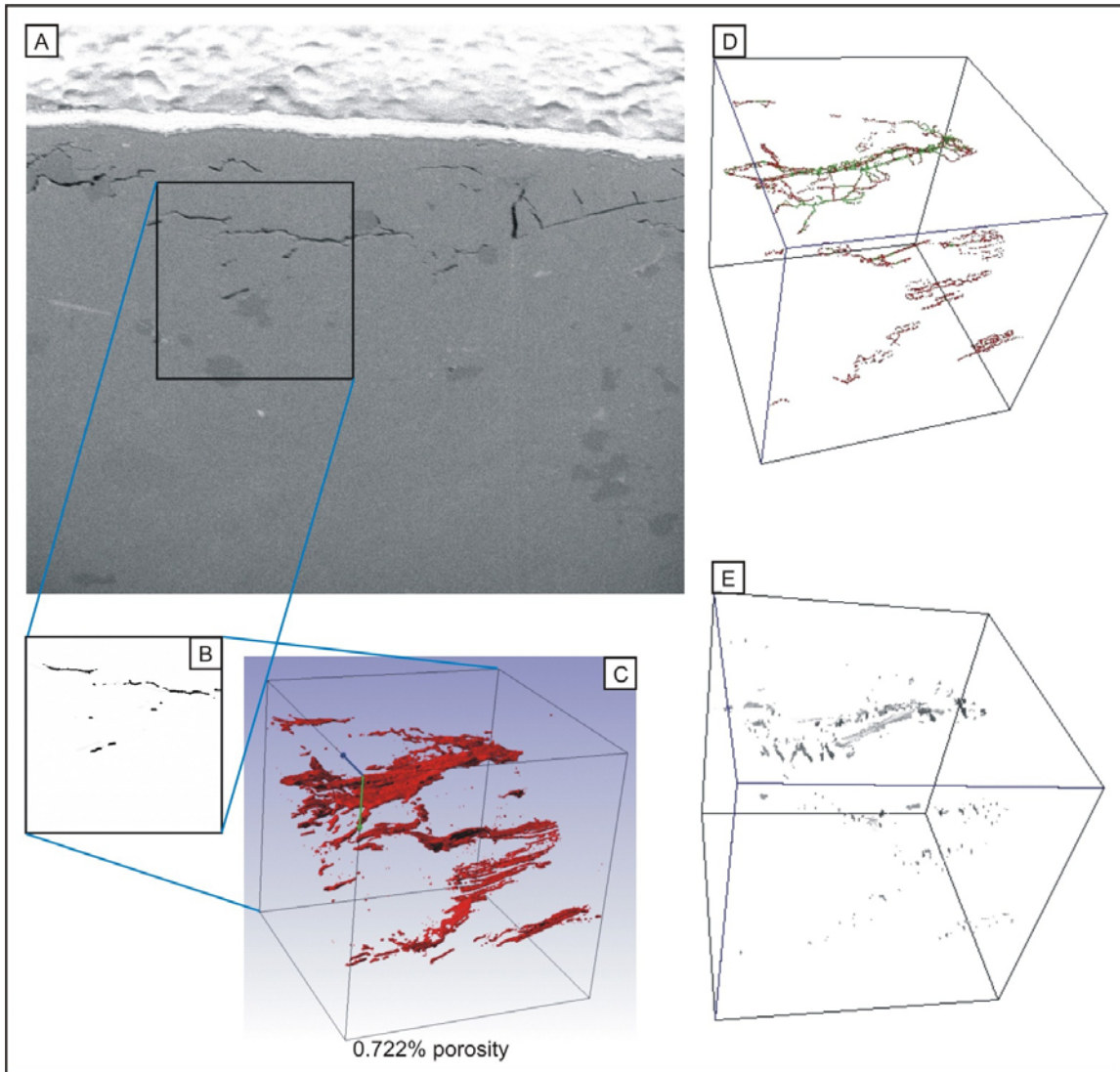


Figure 3.4. Results of FIB milling and imaging of sample lower Kirtland 2692.9A and 3D pore network reconstruction. (A) BSE image of FIB serial section. Horizontal field of view is 16.00 μm . Outlined box indicates cubic region of 3D pore network reconstruction, which has side lengths of 4.66 μm . (B) Segmentation of BSE image into pore (black) and non-pore (white). (C) 3D floodfill rendering of pores. Voxel size is 15.6 nm. (D) 3D plot of medial axis. (E) 3D plot of pore throat surfaces.

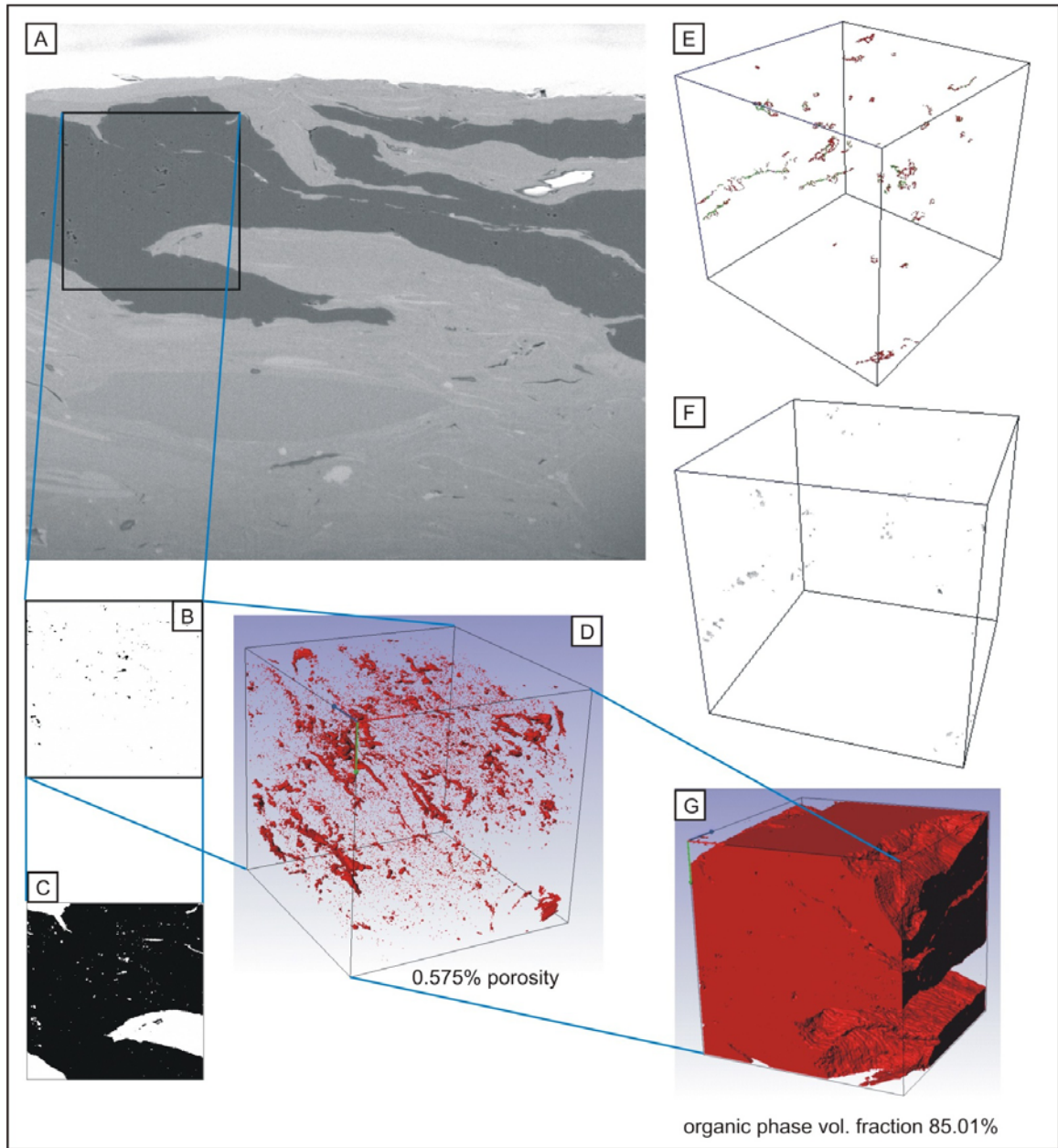


Figure 3.5. Results of FIB milling and imaging of sample Marine Tuscaloosa 7925.5 and 3D pore network and organic reconstruction of organic-rich region. (A) BSE image of FIB serial section. Horizontal field of view is 16.00 μm . Outlined box indicates cubic region of 3D pore network and organics reconstruction, which has side lengths of 4.66 μm . (B) Segmentation of BSE image into pore (black) and non-pore (white). (C) Segmentation of BSE image into organics (black) and non-organics (white). (D) 3D floodfill rendering of pores. Voxel size is 15.6 nm. (E) 3D plot of medial axis. (F) 3D plot of pore throat surfaces. (G) 3D flood fill rendering of organic phase.

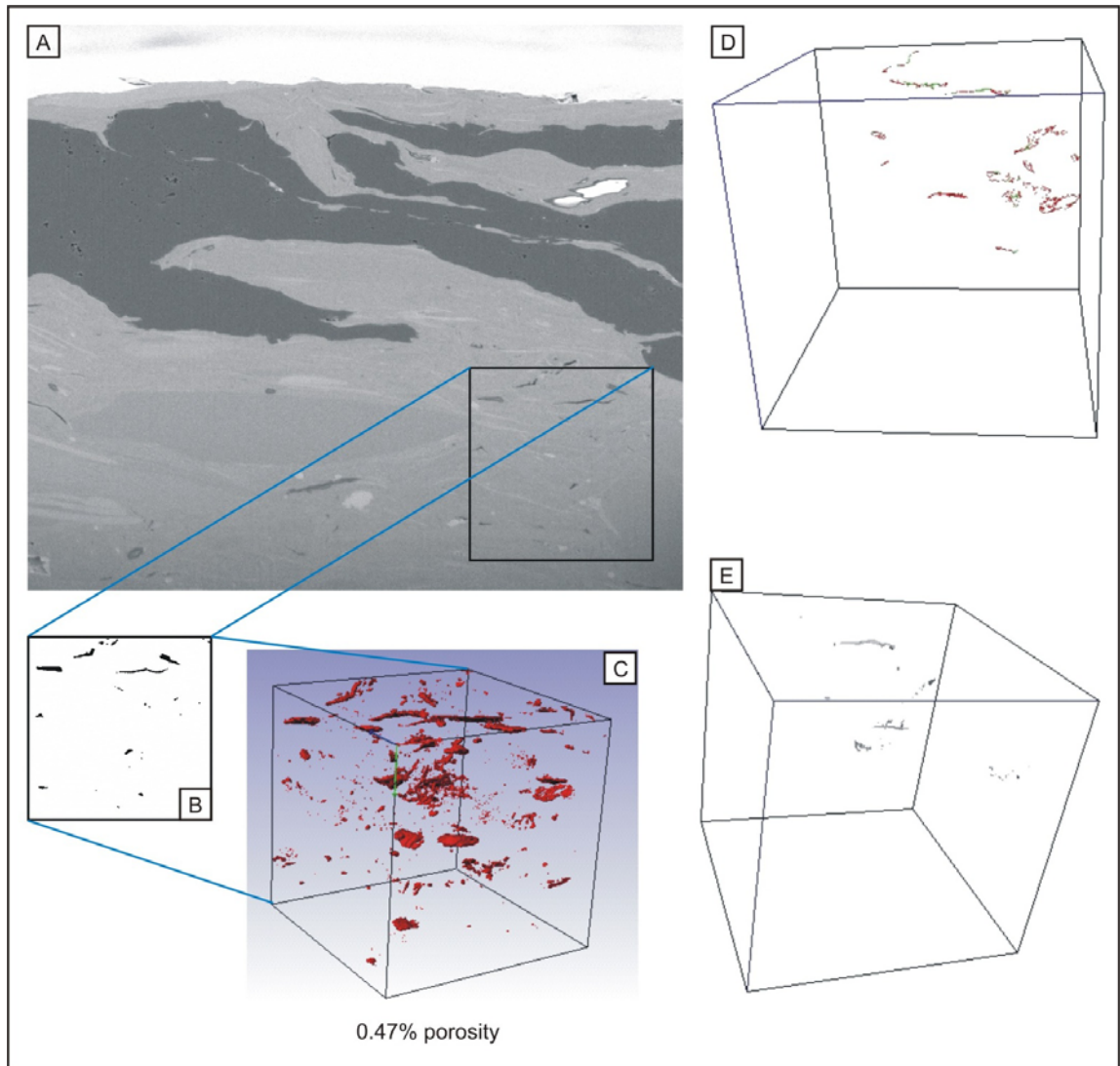


Figure 3.6. Results of FIB milling and imaging of sample Marine Tuscaloosa 7925.5 and 3D pore network reconstruction of organic-poor region. (A) BSE image of FIB serial section. Horizontal field of view is 16.00 μm . Outlined box indicates cubic region of 3D pore network reconstruction, which has side lengths of 4.66 μm . (B) Segmentation of BSE image into pore (black) and non-pore (white). (C) 3D floodfill rendering of pores. Voxel size is 15.6 nm. (D) 3D plot of medial axis. (E) 3D plot of pore throat surfaces.

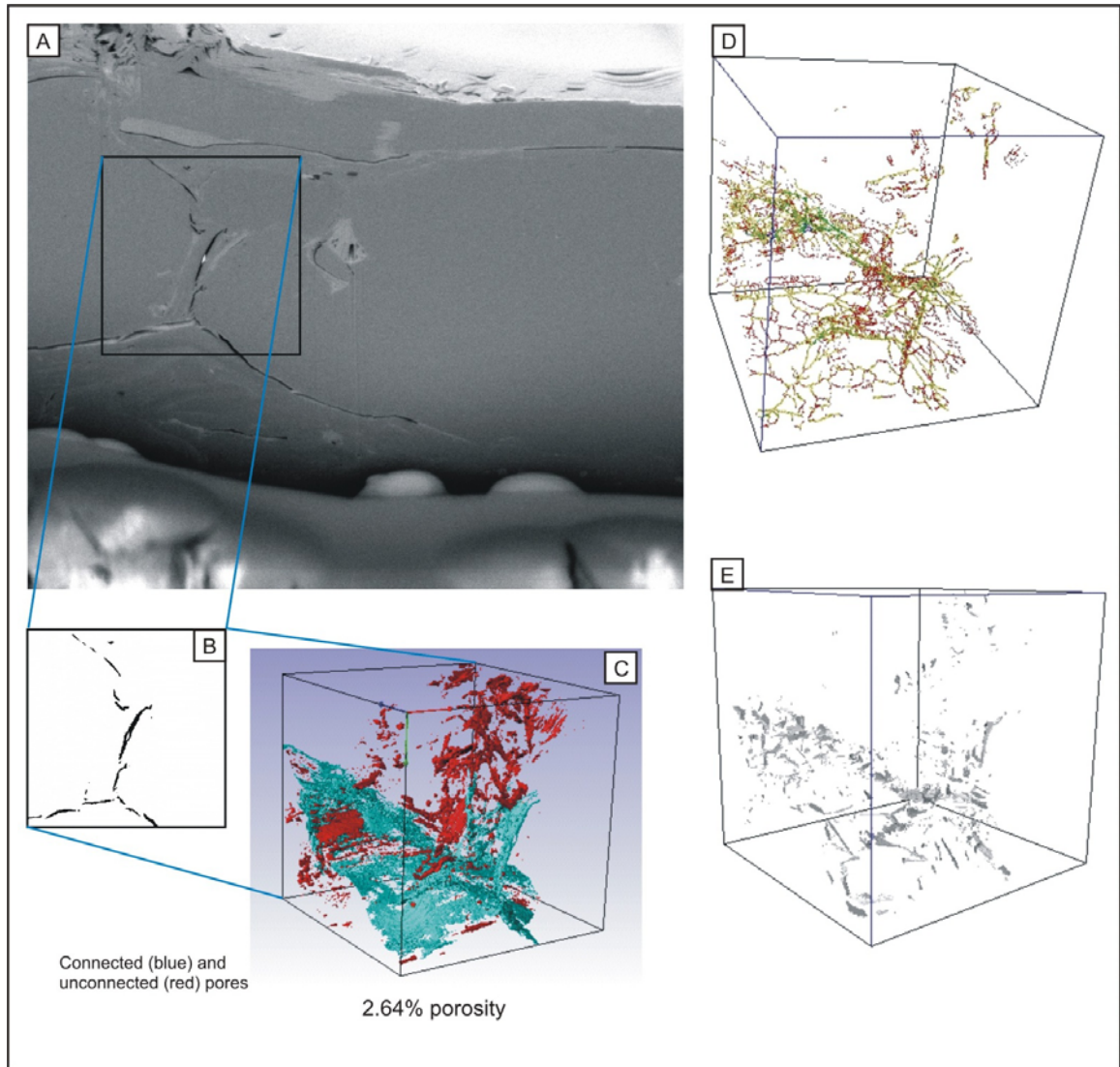


Figure 3.7. Results of FIB milling and imaging of sample Lower Tuscaloosa 8590 and 3D pore network reconstruction of region with polygonal pores (area 1). (A) BSE image of FIB serial section. Horizontal field of view is 16.00 μm . Outlined box indicates cubic region of 3D pore network reconstruction, which has side lengths of 4.66 μm . (B) Segmentation of BSE image into pore (black) and non-pore (white). (C) 3D floodfill rendering of connected (blue) and unconnected (red) pores. Voxel size is 15.6 nm. (D) 3D plot of medial axis. (E) 3D plot of pore throat surfaces.

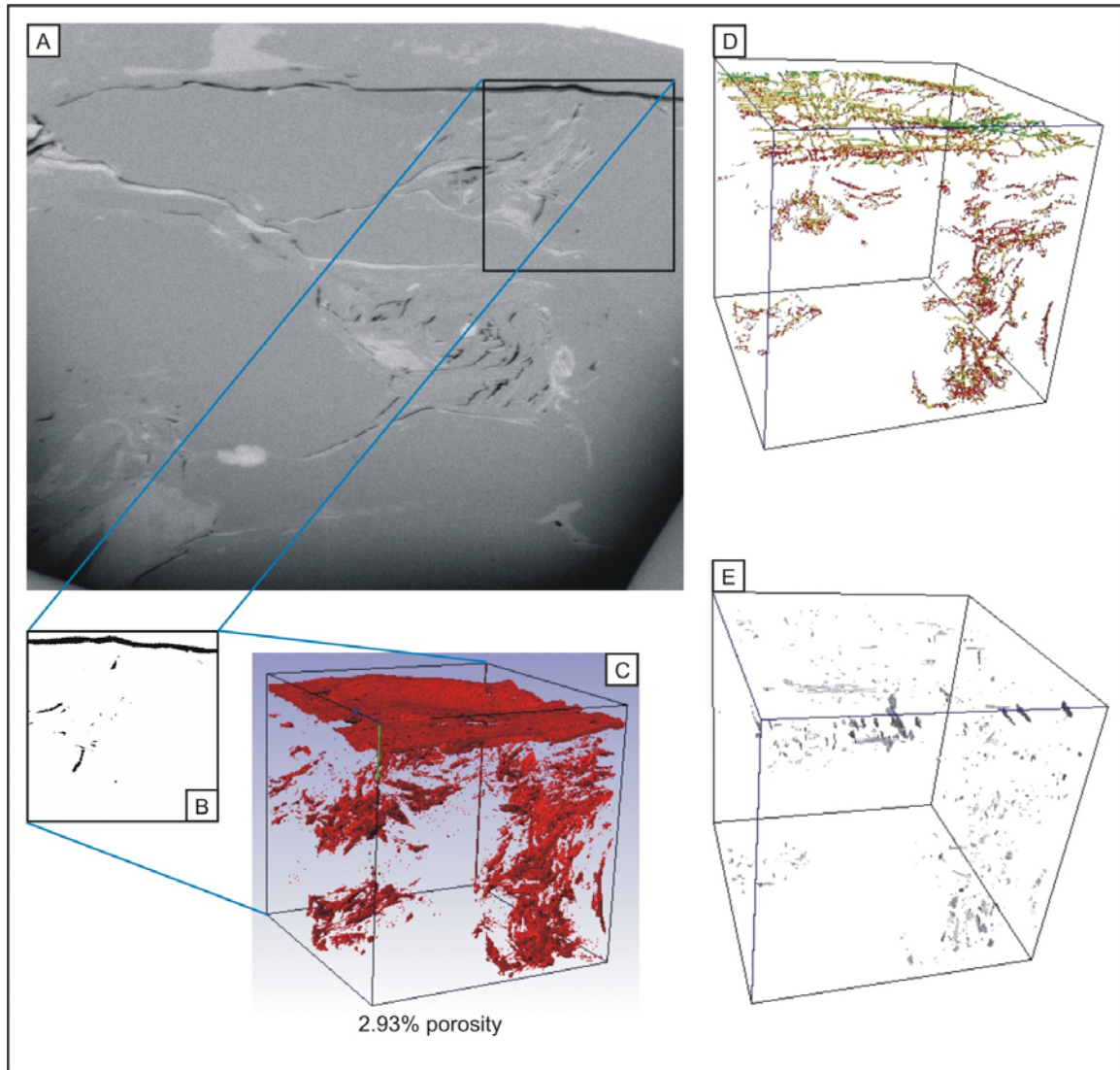


Figure 3.8. Results of FIB milling and imaging of sample Lower Tuscaloosa 8590 and 3D pore network reconstruction of region with crescent-shaped pores (area 2). (A) BSE image of FIB serial section. Horizontal field of view is $16.00\ \mu\text{m}$. Outlined box indicates cubic region of 3D pore network reconstruction, which has side lengths of $4.66\ \mu\text{m}$. (B) Segmentation of BSE image into pore (black) and non-pore (white). (C) 3D floodfill rendering of pores. Voxel size is $15.6\ \text{nm}$. (D) 3D plot of medial axis. (E) 3D plot of pore throat surfaces.

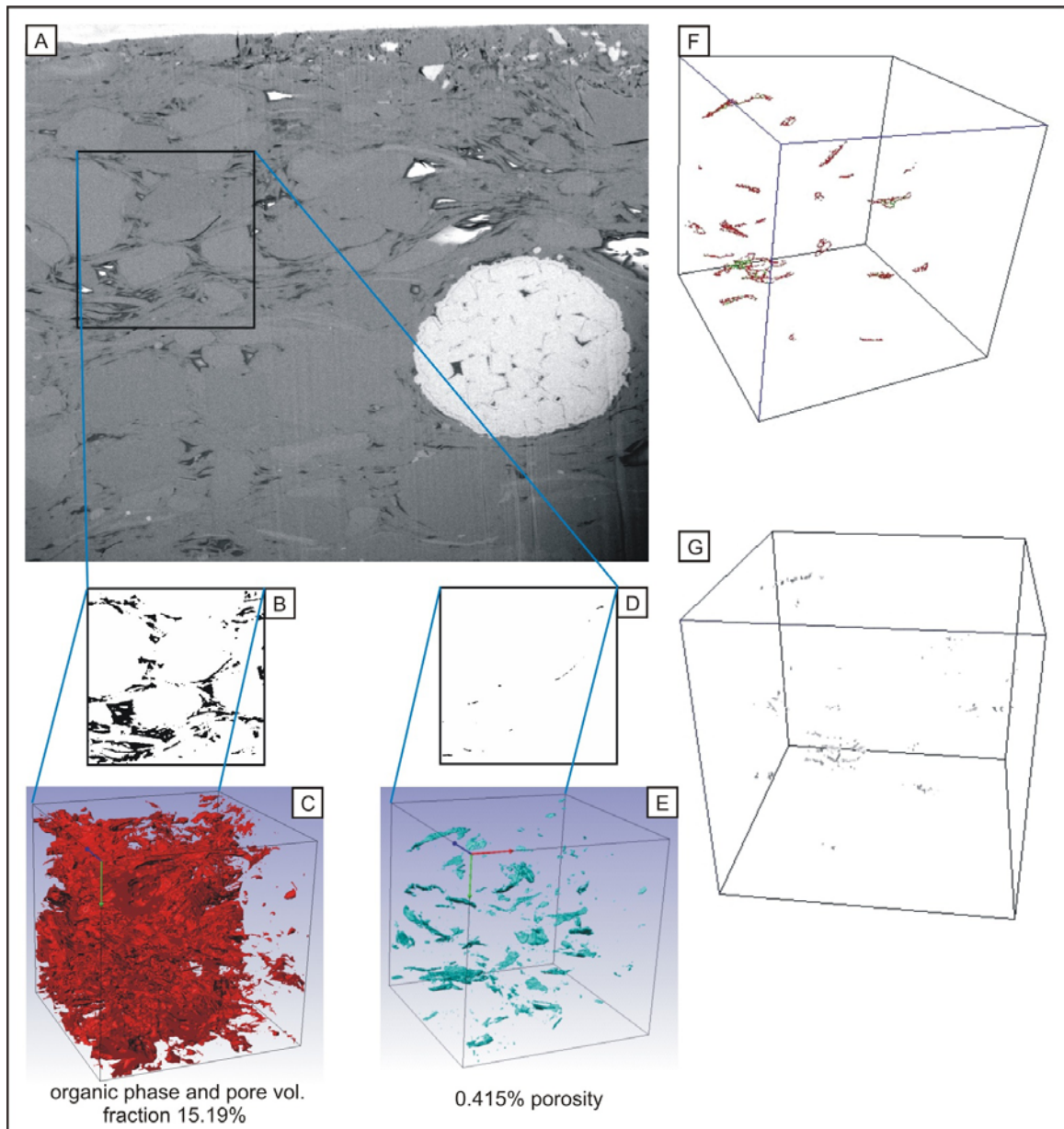


Figure 3.9. Results of focused ion beam (FIB) milling and imaging of sample Gothic shale 5390.8A and 3D pore network and organic reconstruction. (A) BSE image of FIB serial section. Horizontal field of view is 16.00 μm . Outlined box indicates cubic region of 3D pore network and organics reconstruction, which has side lengths of 4.66 μm . White, circular region is a pyrite framboid. (B) Segmentation of BSE image into organics and pores (black) and non-pores/organics (white). (C) 3D flood fill rendering of both the organic phase and pores in red. Voxel size is 15.6 nm. (D) Segmentation of BSE image into pore (black) and non-pore (white). (E) 3D floodfill rendering of pores in cyan. (F) 3D plot of medial axis. (G) 3D plot of pore throat surfaces.

deeper burial, such as by shrinking or swelling of clays. Pores are dominantly slit-shaped as shown by the image of the segmented pores (in black; Figure 3.3B). Larger pores are subparallel to surrounding clay fabric and are discernable by subtle changes in gray level perpendicular to the vertical axis. Voxel counts of the segmented 3D image (Figure 3.3C), with pores shown in red, indicate a porosity of 1.04%, and 3DMA-Rock analysis indicates that 34% of pores are connected. Figure 3.3D and E show representations of pore network medial axes (rainbow colored) and pore throat shapes (in gray). Even though some of the imaged pores appear quite large (Figure 3.3C), the pore throats themselves are quite small. Throat size has implications for interpretation of MIP data (presented in Sections 3.4.3 and 3.5).

An example from a carbonate-rich zone with quartz clasts (lower grayscale value) in the lower Kirtland Formation is shown in Figure 3.4A. Although there are a number of induced fractures in the upper portion of the image, the planar pores observed in the BSE image in Figure 3.4A may actually be associated with a microstylolitic structure. Such microstylolites were also interpreted from scanning transmission electron microscopy (STEM) and/or energy dispersive spectroscopy (EDS) analysis presented in Chapter 4. Interconnected porosity is observed in the 3D representation shown in Figures 3.4C and D, with larger pore throat radii than in the clay matrix of Figure 3.3 observable in Figure 3.4E. Total porosity by voxel count is 0.72%, with 28% as connected porosity.

Figure 3.5 shows interlamination between organics (lower Z and thus darker gray) and clay matrix (lighter gray) within an example from the Marine Tuscaloosa at 2415.7 m (bgs). Organic layer thickness can exceed 2 μm . The boundary between the clays and organics is wavy and convolute. Some clays appear isolated within the organics in the 2D

images. The organic phase was confirmed as dominantly carbon with chloride and sulfur by EDS analysis (see Chapter 4). Because the organics are located as an intact layer, they are likely syngenetic with surrounding clays. Tiny pores, barely discernable at the resolution of our method, are evident in the segmented image in Figure 3.5B. The 3D reconstruction (Figure 3.5C) shows that some of these are aligned to form contiguous tubes. Although representing very little porosity (0.58%), connectivity on the 3 μm scale is high at 62%, and these pathways may represent primary migration pathways for petroleum phases generated within them. Connectivity evaluated at longer length scales appears to be poorer, but this may be an artifact of our imaging resolution.

A clastic portion of the same image data set for the Marine Tuscaloosa is shown in Figure 3.6. Pores from this portion appear to have a similar “slit”-pore morphology to that in the upper Kirtland. Although the porosity is less (0.47%), a higher percentage is connected (52%). Elongate clays (higher Z and brighter grayscale) indicate possible muscovite, consistent with thin section observations. XRD data indicate clay phases may also include chlorite, illite, and kaolinite (DOE, 2008).

A polygonal crack pore structure is evident in an example from the Lower Tuscaloosa at 2618.2 m (bgs), shown in Figure 3.7. This may represent boundaries between depositional clay packets, but more likely represents a wetting/drying structure not unlike hexagonal fractures in mudcracks. A 3D floodfill image (shown in blue) shows a large degree of connectivity across the sampled region. This sample has 2.64% porosity with 74% connectivity, and this relatively large porosity value may be attributed to the polygonal structure of pores. However, these crack pores may be induced and not original *in situ* features.

A sample from the Lower Tuscaloosa (Figure 3.8) shows a nominally horizontal microfracture along with crescent-shaped pores aligned with a possible authigenic clay fabric. It is not known if the porosity was pre-existent to the clays, providing access to mineralizing fluids and concomitant authigenic precipitation, or if the porosity formed in response to a phase change, perhaps as more dense chlorite replaced a less dense clay. Crystal habit of the clay minerals appears to control the non-slit-like pore shapes. Chlorite rosettes, as seen in traditional SEM photomicrographs by other researchers (Welton, 1984), have similar triangular, trapezoidal, and rectangular pore shapes between the chlorite mineral plates. An example is visible in a video file provided in the digital appendix (see Appendix A, Supplemental Video File 2). Compaction is not the major control on these pore shapes.

Figure 3.9A shows a BSE image of the Gothic shale at 1643.1 m (bgs) with 3D representations of the distribution of organic matter at 15.19% by volume (Figures 3.9B and D), and porosity at 0.42% by volume (Figure 3.9C), occurring largely adjacent to clastic quartz and feldspar grains. All imaged porosity appears to be located within or adjacent to organic matter (see Appendix A, Supplemental Video File 4). Organic content is high, although not concentrated in layers as in the Marine Tuscaloosa sample. While some pores may be relatively large (shown in blue in Figure 3.9D), pore throats themselves, shown in Figure 3.9D, are small, and the pore bodies are not well connected (42%). Pore morphology in organics is slit/sheet like, as opposed to the circular/tubular pores of the Marine Tuscaloosa. The large bright circular structure to the lower right of Figure 3.9A is a pyrite framboid that contains pores. Note the orientation of clays and clasts around the framboid, indicating pyrite formation prior to significant compaction.

3.4.2 Summary of Pore Types

Distinct types of pores and 3D pore networks can be distinguished and placed into seven groups based on differences in a variety of characteristics (Figure 3.10). These characteristics include:

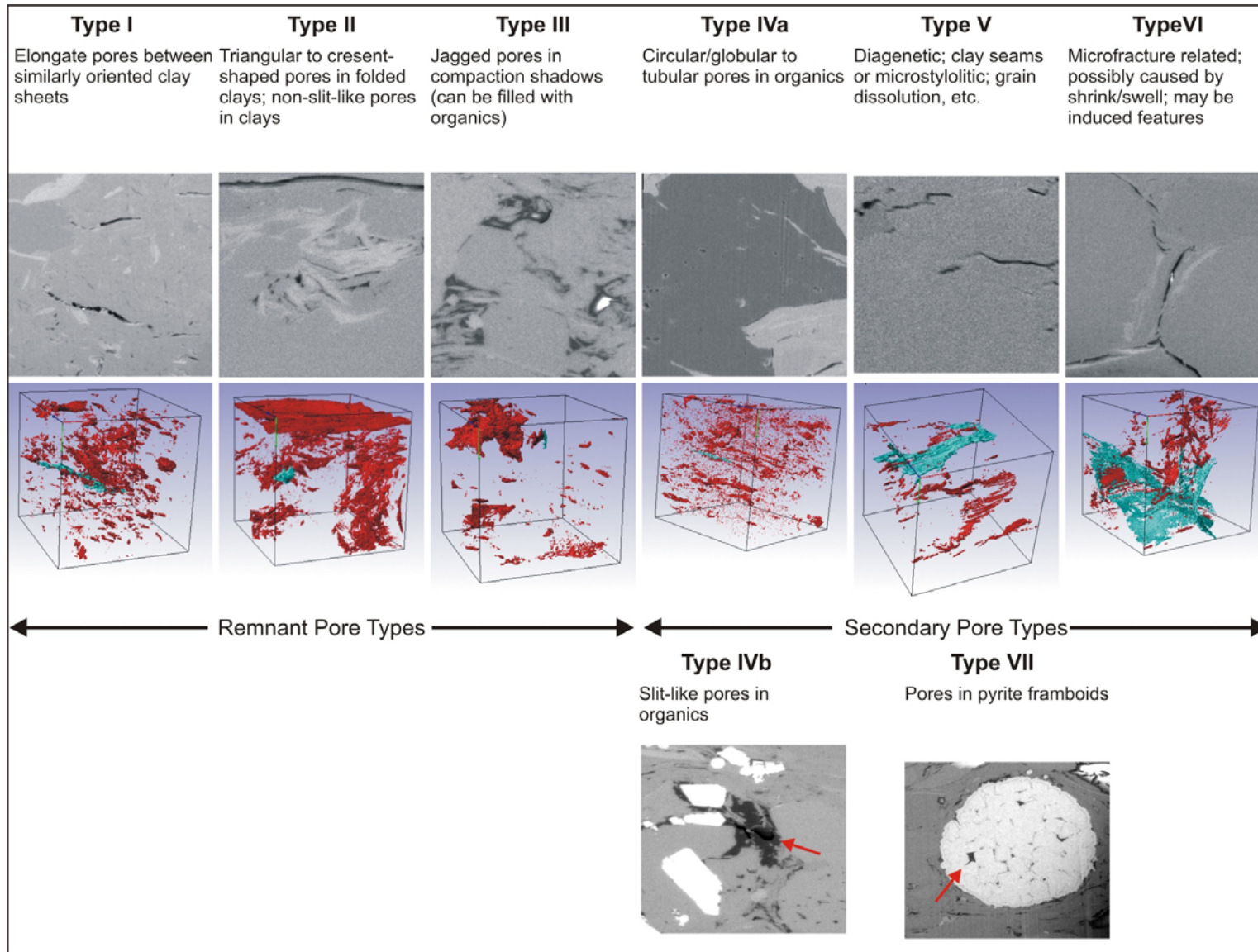
- morphology of pores; sizes and size distributions of pores;
- connectedness/topology of pores (e.g., coordination number and pattern of medial axis); size relationship of pore throats to pore bodies;
- roughness of pore body walls; geometrical relationships between the pores and surrounding grains; and
- the characteristic of being induced or present *in situ*.

This set of characteristics builds upon previous work on classifying pore types by focusing on both pores and their expression in 3D pore networks.

Based on 2D observations of a FIB serial section from a Boom clay sample, Desbois et al. (2009) identified three pore types using morphology and pore size. These authors' Type I pores encompass elongate pores in similarly oriented clay sheets and are < 100 nm. Type II includes crescent-shaped pores in folded clays and are 100 to 1000 nm in size. Type III pores are large, jagged pores associated with margins of larger, more competent grains and are typically > 1000 nm (Desbois et al., 2009).

Desbois et al.'s (2009) pore types apply to the mudstones studied herein. We use and extend their definitions to identify pore and pore network types while modifying their descriptors to encompass additional observations and by adding pore types IV through VII (see examples of all pore types in Figure 3.10). Type IV are pores in organics, which includes the two subtypes IVa and IVb. Type IVa is for the circular/tubular pores in

Figure 3.10. Major pore types based on morphology, geometry (size), topology, and pore-lining material presented through focused ion beam backscattered electron micrograph and corresponding 3D floodfill images, which highlight particular pore types. Some pores are remnants of the primary depositional environment, whereas others are secondary or related to post-depositional processes.



organics in the Marine Tuscaloosa (Figures 3.5 and 3.10; Appendix A, Supplemental Video File 3), whereas IVb is for the slit-like pores in organics in the Gothic shale (Figure 3.9 and 3.10; Appendix A, Supplemental Video File 4). Type V refers to microstylolitic or diagenetic-related pores, as based on lower Kirtland 2692.9A in Figures 3.4 and 3.10. The pores in Figure 3.4 have a jagged, dentate morphology that appears more natural than induced, and this is brought out more in STEM/EDS imaging (see Chapter 4). Type VI designates microfractures, which may or may not be induced (Figures 3.7 and 3.8). Type VII designates pores in pyrite framboids, illustrated by the Gothic shale in Figure 3.9.

Type I pores are abundant and dominant in the upper Kirtland. The lower Kirtland also exhibits this pore type, although our FIB/SEM sample from this rock type did not investigate a clay-rich zone. Some of the larger pores exceed 1000 nm (1 μm) in their axial directions and have a length perpendicular to their axis of $< \sim 130$ nm. A range of smaller sizes have similar shapes. The Tuscaloosa Group mudstone samples also show an abundance of Type I pores, although less commonly than the Kirtland. The Gothic shale has the most infrequent occurrence of Type I pores. Desbois et al. (2009) describes these pores' orientation as being similar to nearby clay sheets, which is verifiable as FIB/SEM in BSE mode distinguishes clay sheets based on differences in grayscale of parallel sheets (see Figures 3.3A–E). However, some FIB/SEM images show elongate pores where the clay fabric is not clearly visible. In addition, some elongate pores contain apparent bridging material inside the pores, not noted by Desbois et al., that is approximately perpendicular or slanted relative to the margins of the pores. Some pores have sharp tips whereas others have terminations that are curved, and thus the pores can appear as

narrow ellipses. In the Lower Tuscaloosa Group (Figure 3.8) many of these pores are curved and follow the undulate texture of the surrounding sheet clays (see Appendix A, Supplemental Video File 3).

Type I pores are interconnected through small pore throats due to the sharp tips, which contributes to high capillary pressures (see Section 3.4.4). Some Type I pores most likely are induced desiccation features due to desiccation of the swelling smectitic clays. If pores of this type are present *in situ*, they are geologically related to the geometry of the surrounding clay sheets, and the sheets are related to the original depositional setting and compaction. Compaction probably plays a major role on sheet orientation. Sub-horizontal Type I pores are probably stress sensitive. Thus, Type I pore apertures may be smaller when samples are subjected to *in situ* overburden stress.

Type II pores of Desbois et al. (2009) are crescent-shaped pores in folded clays. We extend their definition to include pores associated with clays that are in predominately non-parallel orientations, or packages of parallel clays that touch each other in non-parallel orientations and result in non-slit-like pores. Thus, Type II can include pores associated with authigenic pore-lining or pore-filling clay minerals, pores with recrystallized minerals, compacted detrital floccules (if preserved), or clays in non-horizontal orientations that have been deformed, resulting in non-slit-like pores. The Lower Tuscaloosa Group contains prime examples of this pore type (Figures 3.8 and 3.10; Appendix A, Supplemental Video File 2). The non-parallel orientations of groups of clay crystals probably indicate that they are authigenic and formed after primary deposition. Thus, the pores may be associated with chlorite precipitation that may be a

pore-filling or replacement feature. For example, replacement textures could entail conversion of less dense hydrous smectite to denser chlorite plus secondary pores.

Desbois et al. (2009) Type III represents pores associated with margins of clast grains. Our samples do not have clear examples of this pore type; however, the Gothic shale samples appear to have compaction shadows, or rather structures associated with deformation of relatively small material around larger clasts with possible pre-existing pores that are filled with organics (Figures 3.9 and 3.10; Appendix A, Supplemental Video File 4). The organics may have been squeezed into pores during compaction.

Type IVa pores in Marine Tuscaloosa organics are generally circular to bulbous to ellipsoidal in 2D (Figure 3.10), whereas Type IVb pores in organics in Gothic shale are slit-like (Figure 3.10). Networks of Type IVa pores can be arranged linearly and appear tubular, possibly due to original structure in the kerogen associated with hydrocarbon generation and migration. The generally circular pore cross sections indicate *in situ* formation that post-dates most compaction, probably due to interfacial tension and minimization of energy between gases and liquids during conversion of kerogen to hydrocarbons (Loucks et al., 2009). The slit-pores in organics in the Gothic shale (Figure 3.10) can be located near margins of organic particles while also cutting through the interior of the particles away from the margins. Formation of this pore type is unclear but may likely be related to maturation of the organic material within the Gothic shale.

Type V and VI represent sub-planar stylolitic and microfracture-related features. These can have generally planar, slit-like morphology and high connectivity across the 3D reconstructions (Figures 3.4, 3.8, and 3.10). These pore types may be induced due to

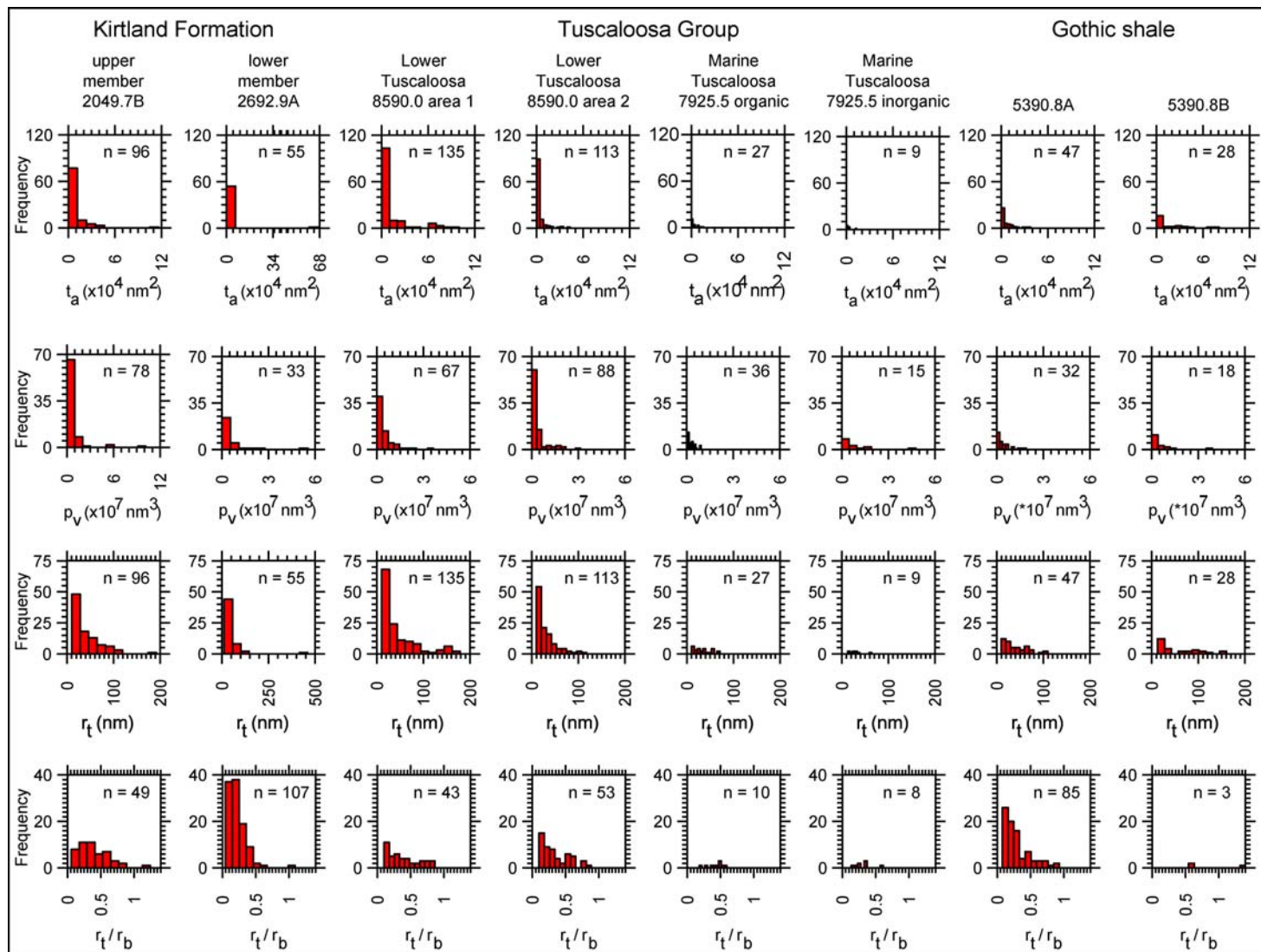
pressure release during coring and desiccation of swelling clays. Their large size could translate to significantly reduced capillary pressures if well-connected.

Type VII pores occur within pyrite framboids (Figure 3.9; Appendix A, Supplemental Video File 4). Framboids are generally isolated in both the Marine Tuscaloosa and Gothic shale; thus, this probably does not represent a dominant, connected pore type. Pores are irregular due to the packing of the individual pyrite crystals and precipitation around the crystals.

3.4.3 Pore Network Statistics

Figure 3.11 summarizes and presents frequencies of pore-throat areas (t_a) and equivalent circular radii (r_t) from the connected pore networks, pore body volumes (p_v), and ratios of pore throat to pore body equivalent circular radii (r_t/r_b), which were compiled from the 3DMA-Rock analysis. The figure presents histograms from left to right in order of proximal to more distal or deeper water depositional environments. Individual plots for most samples use the same x-axis and y-axis scales for a row and 10 bins. The same interrogation volume ($4.66 \mu\text{m} \times 4.66 \mu\text{m} \times 4.66 \mu\text{m}$) was used to construct the 3D geometric pore networks model. Thus, the frequencies on the y-axes reflect differences in pore throat areas or pore body volumes amongst the samples; in other words, the frequencies indicate differences in pore structure. Peak frequencies occur for the histogram bins of the smallest values for both pore-throat area and pore-body volume for all the samples. The equivalent pore-throat radii follow the same trend except for the Marine Tuscaloosa 7925.5 sample, which has three bins with the same highest frequency value. Thus, most of the connections in the pore networks (i.e., the

Figure 3.11. Montage of pore throat and body histograms from reconstructed 3D pore network models, arranged from proximal (left) to distal (right) depositional environments. The number of pore throats and bodies identified from the 3D geometric models varied from sample to sample. The square model volume of $101.5 \mu\text{m}^3$, however, was the same for each sample. The number of pore throats, bodies, or their ratio is given within each histogram (e.g., $n = 96$). Bin size was adjusted so that each figure contained ten bins. Ordinate and abscissa scales are the same along a row to facilitate comparison of the data, except for sample lower Kirtland 2692.9A. Variables are the following: t_a is pore-throat area; p_v is pore-body volume; r_t is pore-throat radius; and r_t/r_b is the pore-throat radius to pore-body radius ratio. Frequencies of variables were obtained from the output of the 3DMA-Rock software.



pore throats) are governed by the smallest pore throats. Even smaller throats may exist, but are not observable because they are below the resolution of the BSE images.

All samples have pore-throat-area frequencies that decrease with size following power law scaling (linear relationship in log-log space) over at least three and up to nine bins, except for the Marine Tuscaloosa inorganic FIB 3D model. Such scaling may indicate fractal structure, which may be consistent with the existence of slit/sheet-like pores over a range of length scales. The histograms for pore-throat area and pore-body volume have similar shapes, indicating possible scaling of pore throats with pore-body volume.

FIB histograms for pore-throat area and equivalent circular radii are generally unimodal for upper Kirtland 2049.7B, lower Kirtland 2692.9A, both Lower Tuscaloosa 8590 areas, with the first peak in the bin of the lowest values, and a second small peak of very low frequency in bins that lie from a half to a full order of magnitude larger in value along the abscissa (Figure 3.11). The large and very small peaks may indicate, respectively, pores within clays at the smallest values of pore-throat area (Type I pores) and possibly other pore types associated with larger pores (Type II–VI). Marine Tuscaloosa and Gothic shale histograms have the most distinct shapes from the other shapes, possibly due to lower counts of pores and the pore structure itself; these samples lack the numbers of slit/sheet pores in clays (Pore Type I) as compared to the other samples. Pore throat to body equivalent circular radii have peaks towards smaller ratio values, much below 0.5, indicating the departure of the pore structure from the cylindrical “bundle of tubes” model of the Washburn equation (Dullien, 1992).

We investigated the relationship between pore size and connectivity by constructing plots of joint and marginal frequency histograms of coordination number and pore-body volume (Figure 3.12). Joint histograms give the number of occurrences of different pore-body volumes associated with a particular coordination number. Each row in the joint can be thought of as the distribution of pore body volumes for a given coordination number. The frequency of occurrence of a given range of pore body volumes at a given coordination number is indicated by shading from light (low frequency) to dark (high frequency). The two marginal histograms are, respectively, the summation of the frequencies of the rows and columns in the joint histogram, which give the univariate histograms of pore-body volume and coordination number. In general, high frequencies of both small pore bodies and low coordination numbers are indicated by the cluster of high frequencies in the lower left hand quadrant of the joint histograms. This implies poor connectivity, impeded transport, and high capillary pressures.

For sample upper Kirtland 2047.9B, the most frequently occurring pores are small ($< 10^7 \text{ nm}^3$) and unconnected (coordination number = 0; 21 out of 69 pores; Figure 3.12A). Coordination numbers of one and two have the relatively high frequencies (i.e., 19 and 18), which also are associated with the smallest pore bodies. Larger bodies (of the second or higher bin for pore bodies) typically have coordination numbers of two or greater. Thus, pore network connectivity change with size of the pore bodies. The connectivity appears to be governed by the touching of tips of the elongate Type I pores that are similarly oriented (Figures 3.3C and D). Figures 3.12B and C have dominant fracture or stylolitic-like pores, Type V and VI, which have peak coordination numbers of 2 and 3 for the smallest pore bodies. These pore types seem to have relatively

Figure 3.12. A–D. Joint histograms of pore-body volume and coordination number, with marginal histograms for the Kirtland and Tuscaloosa. The series of joint histograms are presented in order from proximal to distal in terms of depositional environment. Binning for the coordination number is such that the number of bins is one plus the maximum number of coordination for a particular sample. This results in bins containing integer values. The first horizontal bin, starting from the bottom, is for the frequency of the value of zero. The second horizontal bin is for frequency of two, and so on. The last bin is for the frequency of the maximum coordination number. For example, UK 2049.7B had a maximum coordination number of seven, and thus it has eight bins. Plotting of values on the ordinate is such that the maximum value of the ordinate corresponds to the maximum coordination number, which is for the top, horizontal bin.

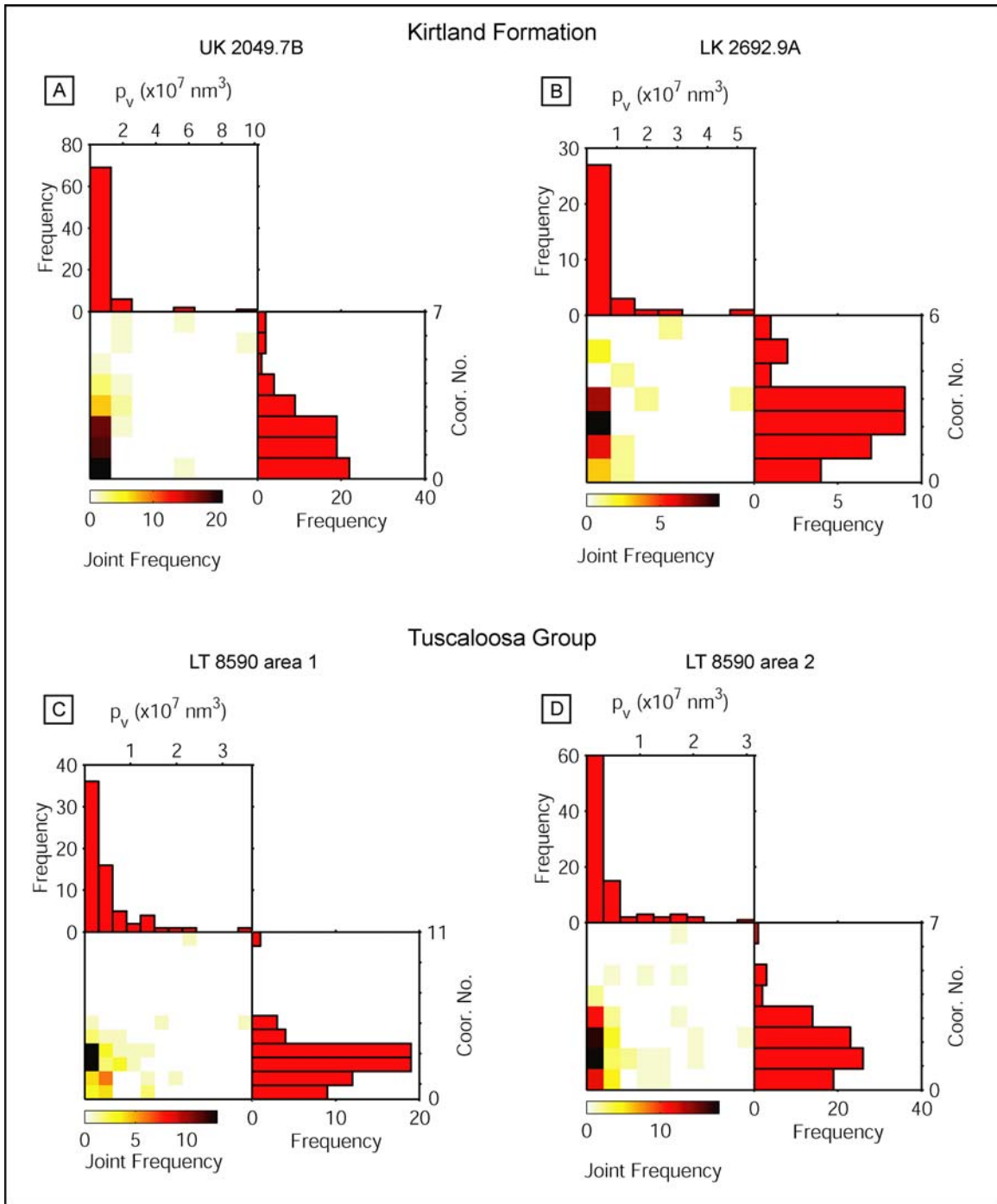


Figure 3.12. A–D. (Caption on preceding page.)

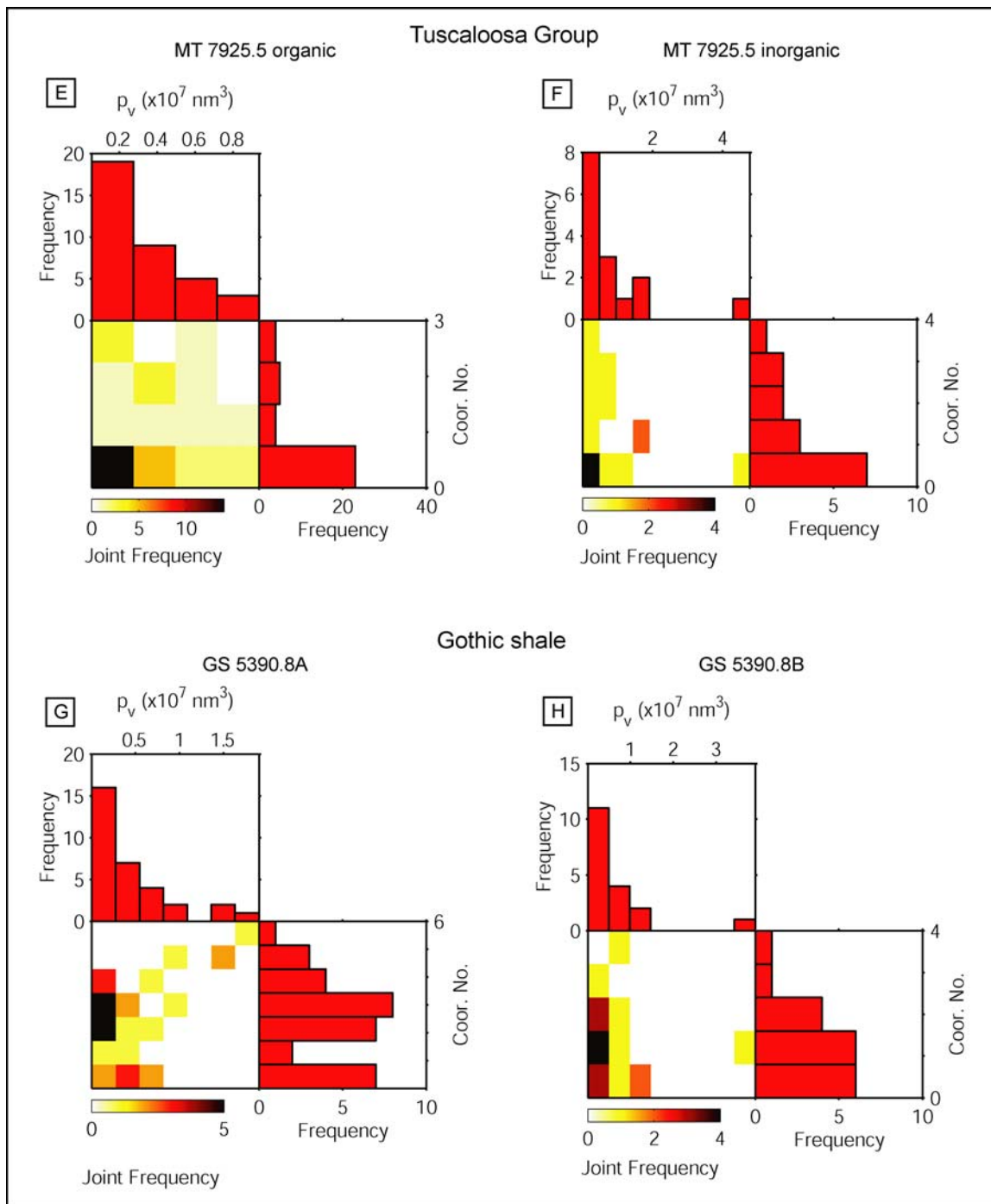


Figure 3.12. E–H. Joint with marginal histograms for the Tuscaloosa Group and Gothic shale.

fewer isolated pores than the bulk of the upper Kirtland example. The connections, for example, of the Type II non-slit-like pores in clays are dominated by one neighbor, with relatively high peaks for two and three. The pores in organics for the Marine Tuscaloosa 7925.5 sample (Figure 3.12E) are dominated by unconnected pores. The diagonal trend on the joint of the Gothic 5390.8A sample probably indicates a scaling relationship between connectivity and pore-body size.

3.4.4 Mercury Intrusion Porosimetry

Graphs of cumulative mercury saturation versus pressure or Washburn pore radii for the 10 samples, corrected for closure pressure (i.e., the pressure at which mercury first intrudes the pore network), have a range of shapes that cover approximately two orders of magnitude of pressure (Figures 3.13 and 3.14), reflecting a broad distribution of pore-throat sizes as based on the cylindrical “bundle of tubes” model (Diamond, 2000). However, Figure 3.11 shows that pore throat to body ratio indicates that pores are not cylindrical tubes (for most samples).

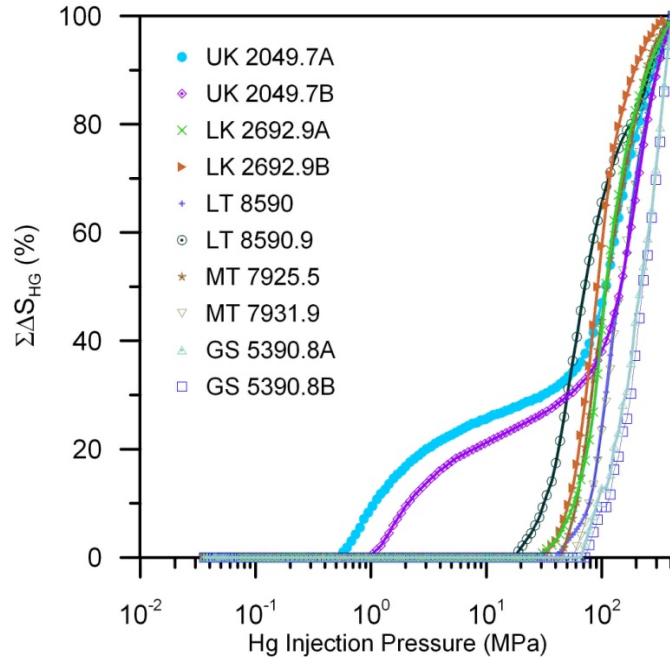


Figure 3.13. Cumulative mercury saturation versus intrusion pressure for all mudstone samples. Curves were corrected for closure pressure. “UK”, “LK”, “LT”, “MT”, and “GS” stand for upper Kirtland, lower Kirtland, Lower Tuscaloosa, Marine Tuscaloosa, and Gothic shale, respectively. Curve shapes indicate differences in pore structure and sealing properties.

Figure 3.14. (Next page) Mercury intrusion porosimetry (MIP) saturation curves and cumulative and incremental volumetric pore density distribution (VPD) curves, organized by formations and samples. (A–B, C–D, and E) Mercury saturation (S_{Hg}) versus injection pressure for the Kirtland Formation, Tuscaloosa Group, and the Gothic shale, respectively. Raw (before closure) and closure-pressure-corrected (after closure) data are given. (B, E, and H) Cumulative and incremental volumetric pore-density distributions, where r_t represents the radius from the “bundle of tubes” model. The ordinate of the cumulative VPD was plotted on a logarithmic scale for evaluation of power law distributions. The incremental VPD was plotted on a linear scale to emphasize the modal peaks.

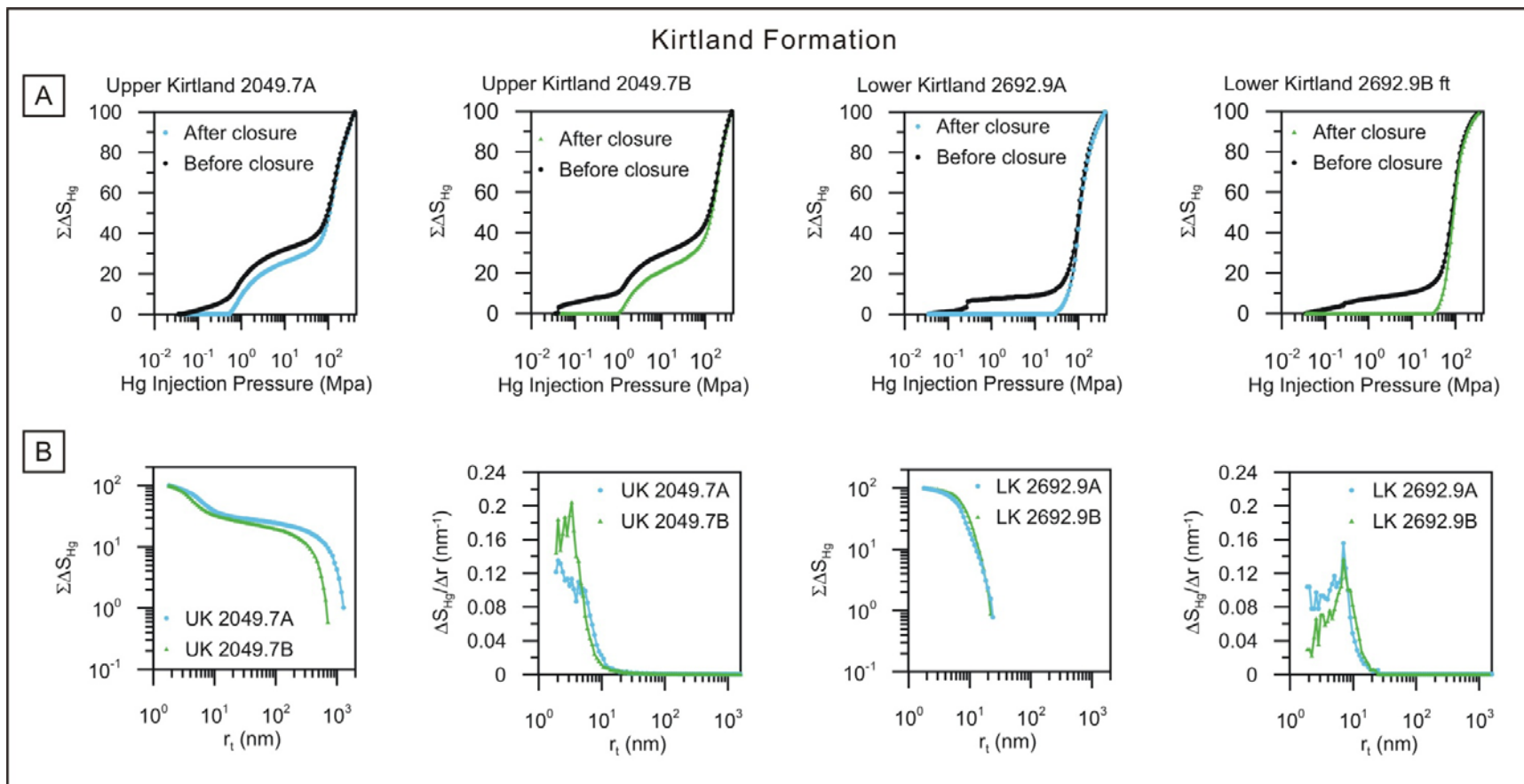


Figure 3.14. A–B. (Caption on preceding page.)

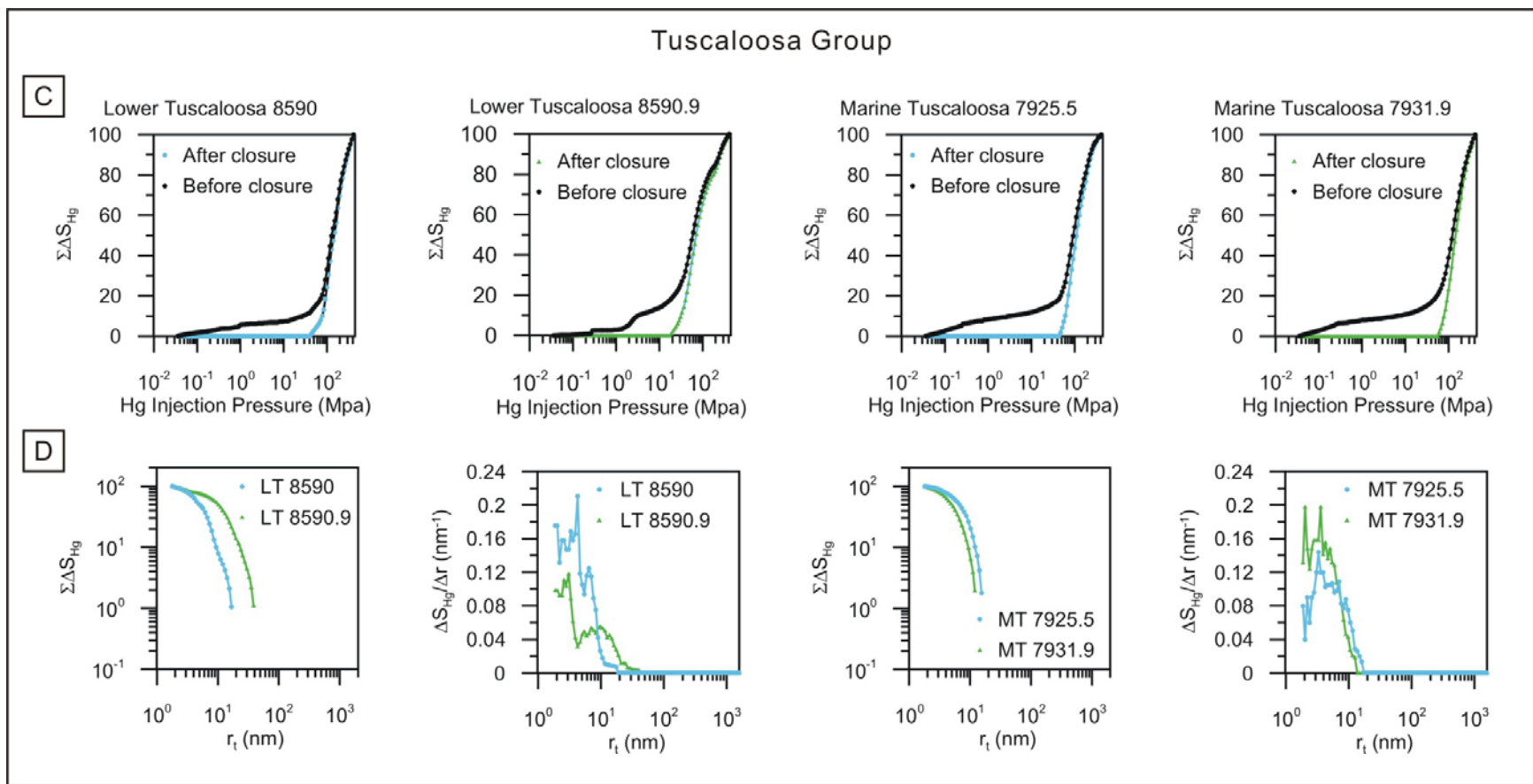


Figure 3.14. C–D. (Caption on page 90.)

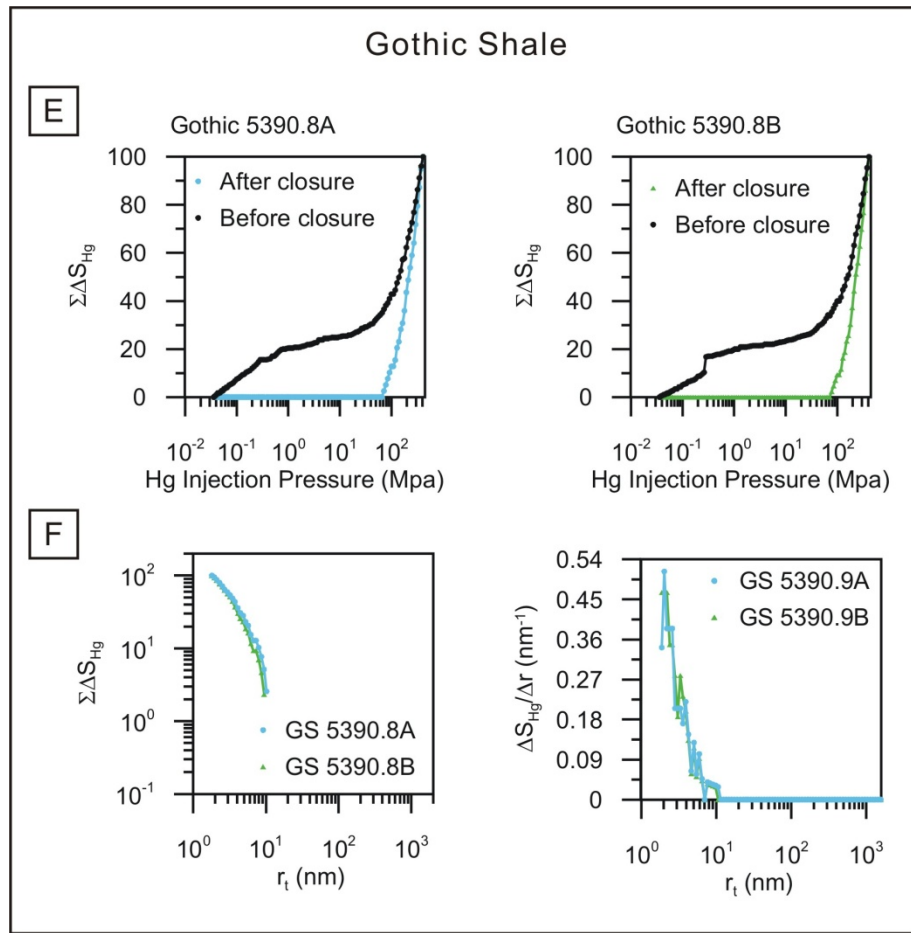


Figure 3.14. E–F. (Caption on page 90.)

Upper Kirtland Formation curves of Figures 3.13 and 3.14 differ the most from the other samples in terms of shape and range of pressure values. They have a broad shoulder of lower pressures possibly due to lacunar pores associated with silt- to sand-sized grains (see Figure 3.2; Fies, 1992). The Gothic shale curves have the highest pressure values for the corresponding mercury saturations and the highest breakthrough pressure (these are compiled for all samples in Table 3.2), whereas upper Kirtland samples have the lowest values. This is discussed further in Section 3.5.

TABLE 3.2. CLOSURE AND BREAKTHROUGH PRESSURES AND PORE RADII

Sample ID	Mercury intrusion porosimetry							Focused ion beam
	Directional intrusion	Closure pressure (MPa)	Closure pore-throat radius (μm)	Breakthrough pressure (MPa)	Breakthrough pore-throat radius (μm)	Second breakthrough pressure [§] (MPa)	Second breakthrough pore-throat radius [§] (μm)	Largest pore-throat radius in pore network (μm)
upper Kirtland 2049.7A		0.531	1.384	0.573	1.282	66.276	0.011	
upper Kirtland 2049.7B	x	0.959	0.767	1.221	0.602	92.450	0.008	0.1927
lower Kirtland 2692.9A	x	28.842	0.026	56.114	0.013			0.4616
lower Kirtland 2692.9B		30.571	0.024	47.494	0.016			
Lower Tuscaloosa 8590	x	40.224	0.018	66.269	0.011			0.1787
Lower Tuscaloosa 8590.9	x	17.492	0.042	28.843	0.026			
Marine Tuscaloosa 7931.9		56.107	0.013	66.272	0.011			
Marine Tuscaloosa 7925.5		43.728	0.017	56.124	0.013			0.0713*, 0.0645 [†]
Gothic shale 5390.8A		66.271	0.011	100.488	0.007			0.1099
Gothic shale 5390.8B		72.026	0.010	109.208	0.007			0.1607
*Organic area								
[†] Inorganic area								
[§] The bimodal pore structure of the upper Kirtland samples has an initial breakthrough into large pores (lacunar) and a secondary breakthrough into smaller pores.								

Figure 3.14 compiles MIP data for the suite of mudstone samples. Linear relationships in log-log space exist for portions of the curves (Figures 3.14A, D, and G), suggesting power-law scaling of pore-throat sizes, in agreement with relationships in the FIB histograms (Figure 3.11). Incremental volumetric pore density distribution curves (the slope of the cumulative mercury intrusion curves; Figures 3.14B, D, and F) are unimodal for the Kirtland, Gothic, and one Marine Tuscaloosa sample. The other Marine Tuscaloosa and both the Lower Tuscaloosa samples show bimodality. All modes occur at < 10 nm (Figures 3.14B, E, and H).

3.4.5 Comparison of MIP and FIB-SEM Pore Properties

As MIP and FIB data sample different numbers of pore bodies, a direct comparison of the two data sets in terms of pore volumes is not possible. MIP data do not give direct information on pore-body sizes (Meyer and Klobes, 1999). Thus, we present the two data sets in a manner more conducive to investigate scaling relationships, via new types of pore size distribution (PSD) plots. Figure 3.15 presents MIP data with ordinate and abscissa given by the following, respectively:

$$\frac{\sum_i \text{sorted } \Delta V_{Hg-i}}{V_{Hg-total}} \quad (1)$$

$$\text{sorted } \Delta V_{Hg-i} \quad (2)$$

where ΔV_{Hg-i} is the sorted i^{th} incremental mercury intrusion volume for a pressure step—the incremental volumes were sorted from largest to smallest volumes; $V_{Hg-total}$ is the total intruded mercury volume. The new PSD plots cumulative sorted incremental volumes per total volume, a non-standard form of saturation, by the corresponding incremental

volumes. Thus, only pore volume information is presented in the plot without explicit reference to entry throats. FIB data are plotted by similarly sorting the FIB-derived pore body volumes from largest to smallest, dividing by the total volume of all the FIB-derived pore bodies, and then plotting cumulative pore-body volumes versus the corresponding sorted pore-body volume. The y and x axes for the new FIB PSD are given by, respectively:

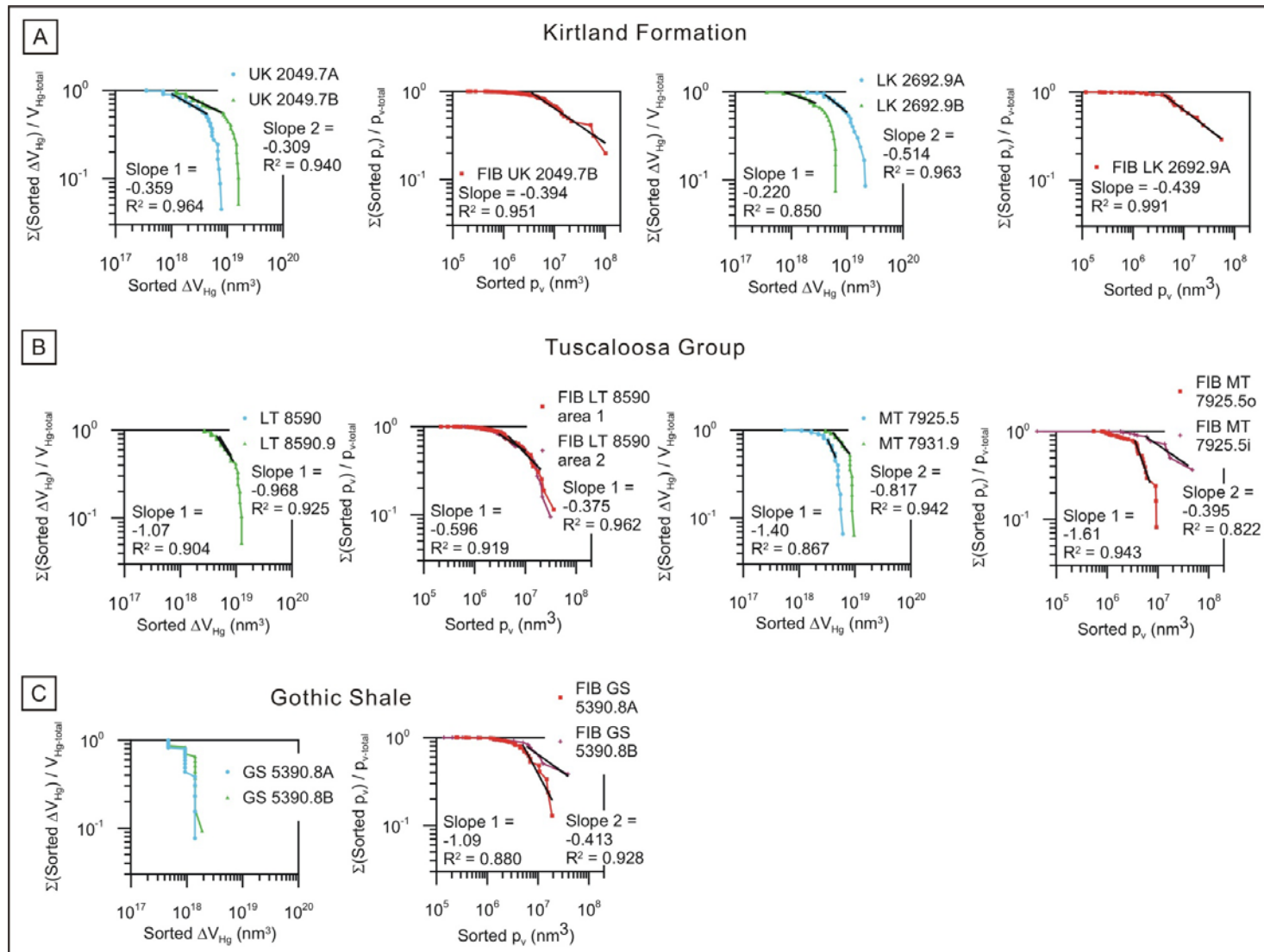
$$\frac{\sum_i \text{sorted } p_{v-i}}{P_{v-total}} \quad (3)$$

$$\text{sorted } p_{v-i} \quad (4)$$

where p_{v-i} is the i^{th} sorted pore body volume, and $P_{v-total}$ is the summation of all the pore-body volumes.

The slopes of the linear portions of the MIP and FIB PSD curves for sample upper Kirtland 2049.7B have similar slopes of -0.359 and -0.394 respectively. This suggests that the MIP and FIB sampled similar pore bodies, and that they both exhibit power law scaling. The scaling probably relates to the slit/sheet-like pores that dominate the FIB sample. The lower Kirtland 2692.9A has different slopes for the MIP and FIB data, suggesting that the FIB did not sample a representative pore type (Figure 3.15A). Correspondence between FIB and MIP slopes for the Tuscaloosa Group is low, probably due to the low number of pores sampled in the FIB data sets. The Gothic shale MIP PSDs have unique shapes, probably resulting from the extremely high capillary pressures, which may be due to pore structure alteration during the MIP test. In summary, the small volumes imaged by FIB/SEM were sufficient to capture representative pore statistics as seen by MIP analysis only in the case of the upper Kirtland.

Figure 3.15. Sorted cumulative volumetric distributions (SVPD) based on MIP and FIB pore network models. The green and blue lines represent MIP data, whereas red lines represent FIB data. The equations used for the SVPDs are plotted by the ordinates. For mercury, the volumes of mercury intruded per pressure step (ΔV_{Hg}) were sorted from largest to small, and then summed incrementally from largest to smallest. $V_{\text{Hg-total}}$ is the total volume of mercury intruded at the end of a MIP test. The pore body volumes (p_v) as determined from FIB-based 3D pore network models were similarly sorted from largest to smallest, and then summed starting with the largest pore-body. $P_{v\text{-total}}$ is the total volume of all the pore body volumes for a single sample. (A) lower and upper Kirtland data. (B) Tuscaloosa Group data. (C) Gothic shale data.



3.5 DISCUSSION: PORE NETWORKS AND SEALING QUALITY

Mudstone textural properties (pore and grain size, shape, connectivity, etc.) can be subdivided into four categories of influence: type of framework (i.e., framework-supported or matrix-supported); diagenetic maturity (e.g., pores are filled with cement, secondary, or created by dissolution); sorting (e.g., well-sorted or poorly-sorted); and compaction (e.g., pore volume loss through compaction processes) (Katsube and Williamson, 1994). Textural parameters that vary as a function of these categories are typically macroscopically measured (i.e., effective porosity, permeability, tortuosity, and specific surface area) (Katsube and Williamson, 1994). From our 3D imaging of a variety of mudstone types, it is evident these parameters are macroscopic manifestations of the collection of pore-body types described in Section 3.4.2 and the connecting pore throat radii such as imaged in Figures 3.3 through 3.9.

A full comparison of imaged pore types and macroscopic properties is beyond the scope of this paper, especially in consideration of the complexity of pore types and also the large degree of heterogeneity of the rocks at all scales. However, it is valuable to examine depositional controls (i.e., framework and sorting) and diagenetic controls (cementation, compaction, and dissolution) on the pore networks as well as MIP-estimated sealing efficiency. This information is directly applicable to subsurface CO₂ storage, as an understanding of the sealing processes could enable proper design of a CO₂ sequestration project with regard to performance of the mudstone seal. In addition, it is applicable to efforts in recovering hydrocarbons from tight reservoirs. For our purposes, we equate sealing efficiency with MIP breakthrough pressures discussed in Section 3.4.4;

or in other words, we assume that higher MIP breakthrough pressures correspond with better sealing quality in terms of capillary forces.

Framework and sorting correlate with depositional environment. Poorly sorted mudstones with a high framework-supporting silt content exist proximal to sediment sources and would be expected to have pore types and resulting macroscopic properties much different from more well-sorted clay-rich mudstones that are more distal to sediment sources. In Figure 3.16, we place our mudstone samples into the shale lithofacies depositional succession devised by Schieber (1999); the lithofacies designations, as well as those discussed by Almon et al. (2005), are given in Table 3.3. Dominant pore types as imaged by FIB-SEM are also summarized in Table 3.3.

The mudstone-rich portions of the Kirtland Formation, interpreted as a floodplain, overbank, and crevasse splay lithofacies, reflects deposition in shallow water depths (maybe 1–2 m) that is proximal to sediment source. With abundant mottled texture and pedogenic features, it is equivalent to the RM or red-gray mudstones of Schieber (1999). It represents the most proximal-to-source and most poorly sorted of the mudstones investigated. Note that some of the clay fabric is suggestive of compacted analogues of the clay floccule textures discussed by Schieber et al. (2007); consequently some caution is required when comparing depositional paleoenvironments of muddy sediments. The high silt content is likely responsible for the bimodal behavior of the MIP results (Figure 3.14B) where the lower breakthrough pressures (Tables 3.2 and 3.3) are likely due to possible lacunar pores occurring in silt-clay mixtures. The higher breakthrough pressures are likely due to the networks of Type I pores observable in Figure 3.3.

TABLE 3.3. SUMMARY OF PETROPHYSICAL, BURIAL HISTORY, FACIES TYPES, AND PORE NETWORK PROPERTIES FOR THE SUITE OF MUDSTONES.

Sample ID*	Core depth (m)	Maximum burial depth (m)	Water depth of deposition (m)	Facies designation [†]		Porosity (%)	Permeability ^{####} ($\times 10^{-20}$ m ²)	TOC (wt%)	Mercury breakthrough pressure (MPa)	Mercury breakthrough pore-throat radius (μ m)	Dominate FIB pore types	Highest frequency (non-zero) coordination number ^{*****}
				Almon et al. (2005)	Schieber (1999)							
UK 2049.7A	624.7	1633	1 or 2	5	RM	6.3–9.9 [§]	7–10 ^{§,†††}	0.06–0.13 [§]	1	1.282	N.A.	N.A.
UK 2049.7B									1	0.602	I	1 and 2
LK 2692.9A	820.8	1829	1 or 2	5 (or 4?)	RM or SM?	6.5–6.7 [#]	8 [#]	0.06–0.27 [#]	56	0.013	V	2 and 3
LK 2692.9B									47	0.016	N.A.	N.A.
LT 8590	2618.5	2618	10's	3	GM	8.5–9.0 ^{**}	0.004–0.5 ^{###} , 80–6810 ^{**}	1.06–1.23 ^{†††}	66	0.011	I, II, and IV	2 and 3; 1
LT 8590.9	2618.2	2619							29	0.026	N.A.	N.A.
MT 7925.5	2415.7	2416	10's	1 or 2	CM to LM	2.2–9.9 ^{††}	0.8–1 ^{***} , 10–380 ^{††}	0.56–0.73 ^{§§§}	56	0.013	I and IVa	2; 1
MT 7931.9	2417.6	2418							66	0.011	N.A.	N.A.
G 5390.8A	1643.1	3048	several 10's to 35??	1	CM	2.7–4.3 ^{§§}	13–14 ^{§§}	2.2–4.4 ^{§§}	100	0.007	IVb (and I, III, and IVb)	3
G 5390.8B									109	0.007	IVb (and I, III, and IVb)	1

Note: N.A. = not applicable.

*UK, LK, LT, MT, and G stand for upper and lower Kirtland, Lower and Marine Tuscaloosa Groups, and Gothic shale, respectively.

[†]Samples are matched to mudstone facies defined by Almon et al. (2005) and Schieber (1999).

[§]Measured on five UK core samples over the depth range of 624.3 to 630.3 m.

[#]Measured on two LK core samples from depths 820.6 and 822.1 m.

^{**}Measured on three LT samples over the depth range of 2616.5 to 2618.2 m.

^{††}Measured on six MT samples over the depth range of 2413.6 to 2418.4 m.

^{§§}Measured on four G samples over the depth range of 1639.6 to 1643.1 m.

^{###}Measured on three LT samples over the depth range of 2615.7 to 2617.7 m.

^{***}Measured on three MT samples over the depth range of 2412.2 to 2417.2 m.

^{†††}Measured on LT samples over the depth range of 2615.7 to 2617.7 m.

^{§§§}Measured on MT samples over the depth range of 2412.2 to 2417.2 m.

^{####}The first set of numbers for the LT and MT samples are Klinkenberg-corrected permeability. All other permeability measurements for all samples are pressure-decay permeabilities.

^{*****}If more than one focused ion beam (FIB) pore network model was constructed, peak coordination numbers for the two networks are separated by a semicolon.

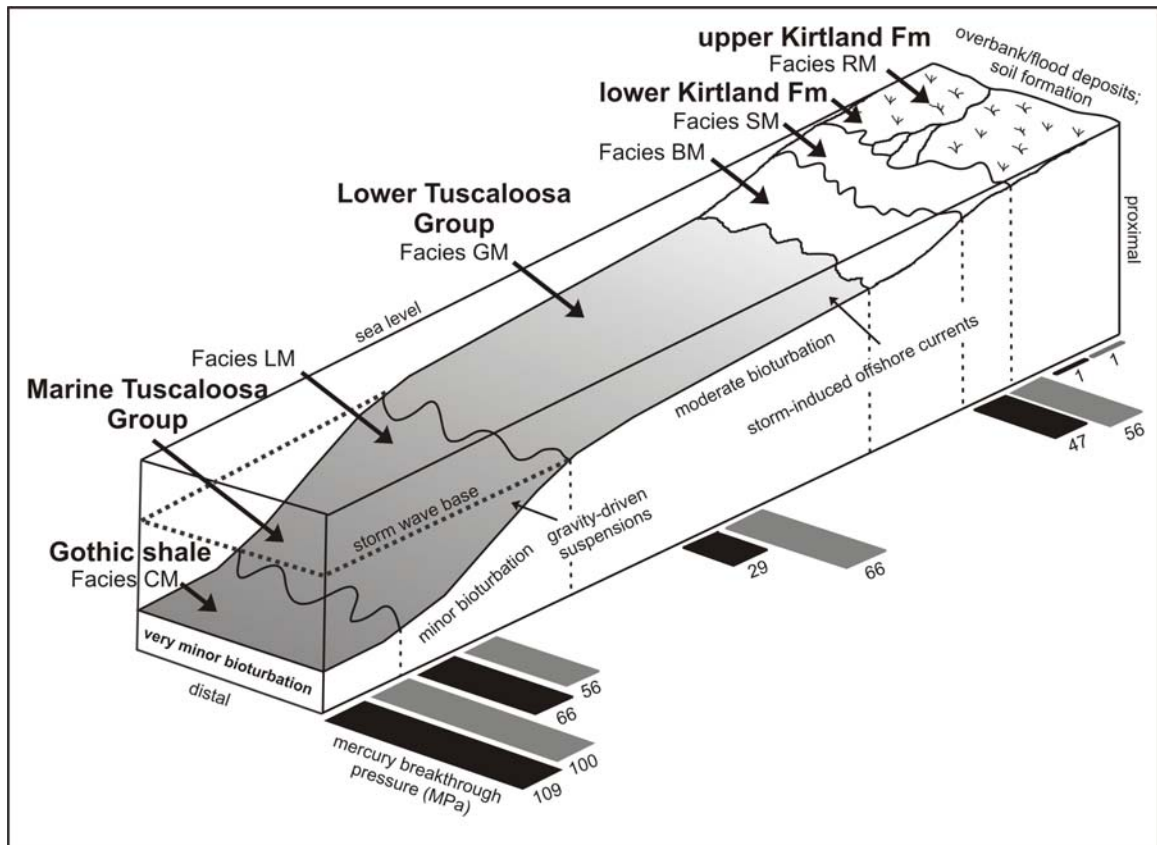


Figure 3.16. Shale succession facies distributions (modified from Schieber, 1999) and schematic placement of mudstone types studied in this paper with breakthrough pressures from mercury intrusion porosimetry (see Table 3.3). The Schieber (1999) microfacies are: RM are red-gray coastal plain mudstones (Kirtland Formation); SM are sandy near-shore mudstones; BM are bioturbated offshore mudstones; GM refers to moderately bioturbated gray mudstones (probably equivalent to the Lower Tuscaloosa); LM are laminated organic rich mudstones (Marine Tuscaloosa); and CM are carbonaceous mudstones or so-called black shales (the Gothic shale is an example of this). The black and gray bars represent the two samples from approximately the same depth of a particular facies that were used for mercury intrusion porosimetry. The two samples give an indication of precision.

The Lower Tuscaloosa Group, interpreted as a bioturbated shallow shelf deposit, represents deposition in roughly 10 meters of water (Billingsley, 1980). With abundant burrowed features and laminations, it is probably equivalent to the moderately bioturbated graded mudstone (GM) lithofacies of Schieber (1999). Breakthrough pressures for the Lower Tuscaloosa fall between the two breakthrough pressure values for

the Kirtland, reflecting connectivity via a network of Type I and Type IV pores. The existence of Type IV (microfracture) pore types probably enhances connectivity over the poorly connected network of Type I pores. The formation of some Type II pores (Figure 3.8A) may be due to the development of authigenic chlorite.

The more shelfal Marine Tuscaloosa Formation reflects a deeper water environment, being deposited during the TRK5 maximum regression during the Late Cretaceous (Mancini and Puckett, 2005). Being well-laminated and organic-rich, the Marine Tuscaloosa probably is equivalent to the LM (laminated mudstone) lithofacies of Schieber (1999) or microfacies 2 (organic laminated shales) of Almon et al. (2005). The relative lack of a connected network of Type I pores probably is responsible for the high breakthrough MIP pressures.

The Gothic shale is an open marine, euxinic, massive, black, organic-rich shale that was probably deposited below wave base in water at least tens of meters deep or more (Figure 3.16; Goldhammer et al., 1994). It contains the highest TOC of the mudstone types we examined. As such, it is the closest to belonging to the classic black shale lithofacies, equivalent to the CM (carbonaceous mudstone) lithofacies of Schieber (1999) or microfacies 1 (massive organic shale) of Almon et al. (2008). The dominant pore types are largely contained in organics (Type IVb), which are dominantly located in the compaction shadows between larger quartz and feldspar clasts (Figure 3.9). The small amount of porosity and very poor connectivity account for the highest breakthrough pressures of the studied mudstones (Table 3.3).

All of the mudstones have passed through the oil generation window, judging by the maximum depth of burial (Table 3.3), and this may be responsible for the generation

of secondary pore types in the organic phases in the high TOC mudstones (Type IVa in the Marine Tuscaloosa and Type IVb in the Gothic). These pore types undoubtedly factored in the generation and migration of petroleum in these rock types (Loucks et al., 2009). In terms of compaction and pore volume loss, the Gothic appears to have experienced the greatest amount of compactional pore volume loss. That, and the seeming lack of Type I pores, is responsible for the high breakthrough pressure values for the Gothic shale (Table 3.3).

In summary, Pore Type I and a lack of well-connected pore Types V and IV, result in high breakthrough pressures for lower Kirtland, Lower Tuscaloosa, and Marine Tuscaloosa samples. The Gothic shale's high breakthrough pressures are due to organics filling what otherwise might have been larger, connected pores. Pore Type II, based on the evidence of its localized nature in Lower Tuscaloosa samples, may be involved in the high breakthrough pressures as mercury intrudes from surrounding slit-pores in the clay fabric. Based on matrix pore types imaged herein, we suggest that more distal mudstones make better sealing lithologies (i.e., caprocks) as a result of their higher breakthrough pressures.

3.6 SUMMARY AND CONCLUSIONS

3D visualization and quantitative analysis of small ($101.5 \mu\text{m}^3$) samples of five mudstones from continental to deep marine depositional settings reveal seven distinct pore types. The most dominant pore type is a slit/sheet-like pore, designated Type I. It is elongate with sharp to curved tips and is co-located with parallel clay sheets. The associated coordination numbers of typically one to four are governed by the sheet-like

geometry. Small pore throat connections between these pores contribute to high (mercury) breakthrough pressures and concomitant high sealing capacity. The pores with slit/sheet-like geometries have length ranges over approximately an order of magnitude and may contribute to power law scaling of pores as illustrated by MIP and FIB data (Figure 3.15). Pore Type I is expected in all argillaceous mudstones and may be predominant in expandable clays, for example, smectites in the Kirtland Formation. The extent to which pore Type I is inherent versus induced by coring and the concomitant depressurizing and possible dehydration is unclear; however, these pores may indicate the possibility for pore formation if desiccation/dewatering in the sub-surface were to occur (i.e., injection of dry CO₂).

Other pore types, such as Types II (non-slit pores in clays) and III (non-slit pores within clays), are associated with authigenic clay minerals and deformation (compaction shadows). They probably contribute to increased mercury breakthrough pressure if they result in an overall reduction in pore-throat sizes (chlorite as a pore-filling mineral). In the case of the Gothic shale, organics appear to have been deformed, filling pores around clays in compaction shadows. Such interaction of organics and pores contributed to the Gothic having the highest mercury breakthrough pressures. Secondary (diagenetic) microfractures and stylolitic features (Pore Types V and VI) may not be present *in situ*; however, as imaged by the FIB and TEM (see Chapter 4), they may still reflect pre-existing features in the subsurface that may respond to changes in stress, as a perturbation due to CO₂ injection or as hydraulic fracturing for shale gas production is applied to the system. Type VII, the pores in pyrite framboids, did not have strong connectivity to other pore types outside of the framboids.

Depositional environment and burial history are both strong geologic controls on pore network properties that bear on the ability of mudstones to serve as sealing lithologies for subsurface CO₂ storage. More distal, organic-rich mudstone lithofacies may make the best seals, but this does not take into account CO₂-organic interactions. Understanding how the pore network topology and geometry varies as a function of depositional environment provides a “first-cut” approach to predicting the sealing behavior of mudstones. Sealing quality of mudstones is a relevant topic for future research, as performance of subsurface CO₂ reservoirs often require knowledge of mudstone caprock behavior in regions lacking in substantial subsurface data.

ACKNOWLEDGMENTS

FIB/SEM imaging and subsequent 3D image analysis was funded by the U.S. Department of Energy’s (DOE’s) Office of Basic Energy Sciences, Division of Chemical Sciences, Geosciences, and Biosciences. Rock samples were provided by the Southwest (SWP) and Southeast Regional Carbon Sequestration Partnerships, which are managed by the U.S. DOE’s National Energy Technology Laboratory. The SWP funded mercury intrusion porosimetry (MIP) analyses. Thanks also to the Southeast Regional Carbon Partnership and to Richard Esposito of the Southern Company for making the Tuscaloosa cores from the Mississippi Power Company #1 available for viewing and core description, as well as providing rock samples and access to core data.

We thank Joseph Michael and Michael Rye of the Materials Characterization Department at Sandia National Laboratories for performing FIB serial sectioning and image acquisition. John Neasham of Poro-Technology performed MIP measurements.

TerraTek—a Schlumberger company—aided in petrographic work on Kirtland Formation and Gothic shale thin sections. Brent Lindquist provided assistance with installation and use of the 3DMA-Rock software. We thank Susan Delap Heath for drafting expertise.

Sandia National Laboratories is a multi-program laboratory operated by Sandia Corporation, a wholly owned subsidiary of Lockheed Martin Company, for the U.S. Department of Energy's National Nuclear Security Administration under contract DE-AC04-94AL85000.

REFERENCES CITED

- Almon, W. R., Dawson, W. C., Botero-Duque, F., Goggin, L. R., and Yun, J. W., 2008, Seal analysis workshop, printed materials, Chevron Energy Technology Company: held at the Joint Annual Meeting of the Geological Society of America, Soil Science Society of America, American Society of Agronomy, Crop Science Society of America, and the Gulf Coast Association of Geological Studies with the Gulf Coast Section of SEPM, October 5–9, Houston, Texas.
- Almon, W. R., Dawson, W. C., Ethridge, F. G., Rietsch, E., Sutton, S. J., and Castelblanco-Torres, B., 2005, Sedimentology and petrophysical character of Cretaceous Marine Shale sequences in foreland basins—potential seismic response issues, in Boulton, P., and Kaldi, J., eds., *Evaluating Fault and Cap Rock Seals: AAPG Hedberg Series*, no. 2, p. 215–235.
- Aplin, A. C., Fleet, A. J., and MacQuaker, J. H. S., 1999, Muds and mudstones: Physical and fluid-flow properties, in Aplin, A. C., Fleet, A. J., and MacQuaker, J. H. S., eds., *Muds and mudstones: Physical and fluid-flow properties: Special Publication 158*, London, Geological Society, p. 1–8.
- Ayers, W. B. J., 2003, Coalbed methane in the Fruitland Formation, San Juan Basin, western United States: a giant unconventional gas play, in Halbouty, M. T., ed., *Giant oil and gas fields of the decade 1990-1999, AAPG Memoir 78*, p. 159–188.
- Bauer, C. M., 1916, Stratigraphy of a part of the Chaco River valley: *U.S. Geological Survey Professional Paper 98-P*, p. 271–278.
- Billingsley, A. L., 1980, *Unconventional energy resources in Tuscaloosa sediments of the "Tuscaloosa Trend", south Louisiana*: New Orleans, Louisiana, University of New Orleans, 63 p.

- Chidsey, T. C. Jr., Heath, J., and Dewers, T., 2010, *The Gothic shale in the Aneth Unit: seal for hydrocarbons and CO₂ geologic sequestration*: unpublished report by the Utah Geologic Survey for the Southwest Regional Partnership on Carbon Sequestration.
- Colombo, I., and Carli, F., 1981, Measurement of compressibility coefficient of nonporous polymer powders by mercury porosimetry: *Powder Technology*, v. 29, no. 2, p. 285–287.
- Daniel, R. F., and Kaldi, J. G., 2008, Evaluating seal capacity of caprocks and intraformational barriers for the geosequestration of CO₂, in *Proceedings, PESA Eastern Australia Basins Symposium III*: Sydney, Australia.
- Davy, C. A., Skoczylas, F., Lebon, P., and Dubois, T., 2009, Gas migration properties through a bentonite/argillite interface: *Applied Clay Science*, v. 42, no. 3–4, p. 639–648.
- De Winter, D. A. M., Schneijdenberg, C., Lebbink, M. N., Lich, B., Verkleij, A. J., Drury, M. R., and Humbel, B. M., 2009, Tomography of insulating biological and geological materials using focused ion beam (FIB) sectioning and low-kV BSE imaging: *Journal of Microscopy-Oxford*, v. 233, no. 3, p. 372–383.
- Desbois, G., Urai, J. L., Burkhardt, C., Drury, M. R., Hayles, M., and Humbel, B., 2008, Cryogenic vitrification and 3D serial sectioning using high resolution cryo-FIB SEM technology for brine-filled grain boundaries in halite: First results: *Geofluids*, v. 8, no. 1, p. 60–72.
- Desbois, G., Urai, J. L., and Kukla, P. A., 2009, Morphology of the pore space in claystones—evidence from BIB/FIB ion beam sectioning and cryo-SEM observations: *eEarth*, v. 4, p. 15–22.
- Dewhurst, D. N., Jones, R. M., and Raven, M. D., 2002, Microstructural and petrophysical characterization of Muderong Shale: Application to top seal risking: *Petroleum Geoscience*, v. 8, no. 4, p. 371–383.
- Diamond, S., 2000, Mercury porosimetry—an inappropriate method for the measurement of pore size distributions in cement-based materials: *Cement and Concrete Research*, v. 30, no. 10, p. 1517–1525.
- DOE, 2007, *Basic Research Needs for Geosciences: Facilitating 21st Century Energy Systems*, Report from the Workshop Held February 21–23: U.S. Department of Energy, Office of Basic Energy Sciences, available in pdf format at <http://www.sc.doe.gov/bes/reports/list.html>.
- , 2008, *Geologic characterization of the Lower Tuscaloosa Formation for the Phase II saline reservoir injection pilot test, Jackson County, Mississippi—volume II, appendices*, FY2008 annual report for geologic characterization task, Southeast

Regional Carbon Sequestration Partnership (SECARB): prepared by Advanced Resources International, Arlington, VA, for the Electric Power Research Institute and the Southern States Energy Board, three volumes.

Dullien, F. A. L., 1992, *Porous media—fluid transport and pore structure, Second Edition*: London, UK, Academic Press, Inc., 574 p.

Fassett, J. E., 2009, New geochronologic and stratigraphic evidence confirms the paleocene age of the dinosaur-bearing Ojo Alamo Sandstone and Animas Formation in the San Juan Basin, New Mexico and Colorado: *Palaeontologia Electronica*, v. 12, no. 1.

Fassett, J. E., and Hinds, J. S., 1971, Geology and fuel resources of the Fruitland Formation and Kirtland Shale of the San Juan Basin, New Mexico and Colorado. *U.S. Geological Survey Professional Paper 676*, p. 76.

Ferreira, T. A., and Rasband, W., 2010, *The ImageJ User Guide—Version 1.43*: <http://rsbweb.nih.gov/ij/docs/user-guide.pdf> (March 2010).

Fies, J. C., 1992, Analysis of soil textural porosity relative to skeleton particle size, using mercury porosimetry: *Soil Science Society of America Journal*, v. 56, no. 4, p. 1062–1067.

Goldhammer, R. K., Oswald, E. J., and Dunn, P. A., 1994, High-frequency, glacio-eustatic cyclicity in the Middle Pennsylvanian of the Paradox Basin: An evaluation of Milankovitch forcing, *in* de Boer, P. L., and Smith, D. G., eds., *Orbital forcing and cyclic sequences*: International Association of Sedimentologists, Special Publication 19, p. 243–283.

Hayles, M. F., Stokes, D. J., Phifer, D., and Findlay, K. C., 2007, A technique for improved focused ion beam milling of cryo-prepared life science specimens: *Journal of Microscopy-Oxford*, v. 226, no. 3, p. 263–269.

Holzer, L., Indutnyi, F., Gasser, P. H., Munch, B., and Wegmann, M., 2004, Three-dimensional analysis of porous BaTiO₃ ceramics using FIB nanotomography: *Journal of Microscopy-Oxford*, v. 216, p. 84–95.

IPCC, 2005, *IPCC special report on carbon dioxide capture and storage*, prepared by Working Group III of the Intergovernmental Panel on Climate Change: Cambridge, United Kingdom and New York, NY, USA, Cambridge University Press, 442 p.

Jackson, R. G., 1978, Preliminary evaluation of lithofacies models for meandering alluvial streams, *in* Miall, A. D., ed., *Fluvial Sedimentology*, Canadian Society of Petroleum Geologists Memoir 5, p. 543–576.

- Katsube, T. J., and Williamson, M. A., 1994, Effect of shale diagenesis on shale nanopore structure and implications for sealing capacity: *Clay Minerals*, v. 29, p. 451–461.
- Katz, A. J., and Thompson, A. H., 1987, Prediction of rock electrical conductivity from mercury injection measurements: *Journal of Geophysical Research-Solid Earth and Planets*, v. 92, no. B1, p. 599–607.
- Klute, M. A., 1986, Sedimentology and sandstone petrography of the Upper Kirtland Shale and Ojo Alamo Sandstone, Cretaceous-Tertiary Boundary, western and southern San Juan Basin, New Mexico: *American Journal of Science*, v. 286, no. 6, p. 463–488.
- Kotula, P. G., and Keenan, M. R., 2006, Application of multivariate statistical analysis to STEM X-ray spectral images: Interfacial analysis in microelectronics: *Microscopy and Microanalysis*, v. 12, p. 538–544.
- Kotula, P. G., Keenan, M. R., and Michael, J. R., 2003, Automated analysis of SEM X-ray spectral images: a powerful new microanalysis tool: *Microscopy and Microanalysis*, v. 9, no. 1, p. 1–17.
- Lindquist, W. B., 1999, *3DMA general users manual*, State University of New York at Stony Brook, 47 p.
- Lindquist, W. B., Lee, S. M., Oh, W., Venkatarangan, A. B., Shin, H., and Prodanovic, M., 2005, *3DMA-Rock: a software package for automated analysis of rock pore structure in 3-D computed microtomography images*: Department of Applied Mathematics and Statistics, State University of New York, Stony Brook, http://www.ams.sunysb.edu/~lindquis/3dma/3dma_rock/3dma_rock.html (March 2010)
- Lindquist, W. B., and Venkatarangan, A., 1999, Investigating 3D geometry of porous media from high resolution images: *Physics and Chemistry of the Earth Part a: Solid Earth and Geodesy*, v. 24, no. 7, p. 593–599.
- Litynski, J. T., Plasynski, S., McIlvried, H. G., Mahoney, C., and Srivastava, R. D., 2008, The United States Department of Energy's Regional Carbon Sequestration Partnerships Program Validation Phase: *Environment International*, v. 34, no. 1, p. 127–138.
- Liu, K., 2005, Upper Cretaceous sequence stratigraphy, sea-level fluctuations and oceanic anoxic events 2 and 3, northeastern Gulf of Mexico: *Stratigraphy*, v. 2, no. 2, p. 147–166.
- Loucks, R. G., Reed, R. M., Ruppel, S. C., and Jarvie, D. M., 2009, Morphology, genesis, and distribution of nanometer-scale pores in siliceous mudstones of the

- Mississippian Barnett Shale: *Journal of Sedimentary Research*, v. 79, no. 11-12, p. 848–861.
- MacQuaker, J. H. S., and Adams, A. E., 2003, Maximizing information from fine-grained sedimentary rocks: An inclusive nomenclature for mudstones: *Journal of Sedimentary Research*, v. 73, no. 5, p. 735–744.
- MacQuaker, J. H. S., and Gawthorpe, R. L., 1993, Mudstone lithofacies in the Kimmeridge Clay Formation, Wessex Basin, southern England—implications for the origin and controls of the distribution of mudstones: *Journal of Sedimentary Petrology*, v. 63, no. 6, p. 1129–1143.
- MacQuaker, J. H. S., Taylor, K. G., and Gawthorpe, R. L., 2007, High-resolution facies analyses of mudstones: implications for paleoenvironmental and sequence stratigraphic interpretations of offshore ancient mud-dominated successions: *Journal of Sedimentary Research*, v. 77, no. 3–4, p. 324–339.
- Mancini, E. A., Mink, R. M., Payton, J. W., and Bearden, B. L., 1987, Environments of deposition and petroleum geology of Tuscaloosa Group (Upper Cretaceous), south Carton and Pollard fields, southwestern Alabama: *AAPG Bulletin*, v. 71, no. 10, p. 1128–1142.
- Mancini, E. A., and Puckett, T. M., 2005, Jurassic and Cretaceous transgressive-regressive (T-R) cycles, northern Gulf of Mexico, USA: *Stratigraphy*, v. 2, no. 1, p. 31–48.
- Marty, B., Dewonck, S., and France-Lanord, C., 2003, Geochemical evidence for efficient aquifer isolation over geological timeframes: *Nature*, v. 425, no. 6953, p. 55–58.
- Meijering, E., 2008, *TransformJ—A Java package for geometrical image transformation*: <http://www.imagescience.org/meijering/software/transformj/> (March 2010).
- Meyer, K., and Klobes, P., 1999, Comparison between different presentations of pore size distribution in porous materials: *Fresenius Journal of Analytical Chemistry*, v. 363, no. 2, p. 174–178.
- Molenaar, C. M., and Baird, J. K., 1992, Regional stratigraphic cross sections of Upper Cretaceous rocks across the San Juan Basin, northwestern New Mexico and southwestern Colorado: *U.S. Geological Survey Open-File Report 92-257*, sheets 1–3.
- Neethirajan, S., Jayas, D. S., White, N. D. G., and Zhang, H., 2008, Investigation of 3D geometry of bulk wheat and pea pores using X-ray computed tomography images: *Computers and Electronics in Agriculture*, v. 63, no. 2, p. 104–111.

- Pashin, J. C., McIntyre, M. R., Grace, R. L. B., and Hills, D. J., 2008, *Geological Survey of Alabama Southeastern Regional Carbon Sequestration Partnership (SECARB) Phase III Report*, prepared for Advanced Resources International, Arlington, VA.
- Peterson, J. A., 1992, Aneth field - U.S.A. Paradox Basin, Utah, in Foster, N. H., and Beaumont, E. A., eds., *Stratigraphic traps III: American Association of Petroleum Geologists treatise of petroleum geology—atlas of oil and gas fields*, p. 41–82.
- Potter, P. E., Maynard, J. B., and Depetris, P. J., 2005, *Mud and mudstones—introduction and overview*: New York, Springer, 297 p.
- Rasband, W. S., 1997–2010, *ImageJ*: National Institutes of Health, Bethesda, Maryland, USA, <http://rsb.info.nih.gov/ij/> (March 2010).
- Rosen, R. N., and Rosen, N. C., 2008, Biostratigraphy and chronostratigraphy of the subsurface Cretaceous of the Gulf Coast Basin, emphasizing the Woodbine-Tuscaloosa, *Society of Economic Paleontologists and Mineralogists, Gulf Coast Section Special Publication No. 3*, CD.
- Schieber, J., 1999, Distribution and deposition of mudstone facies in the Upper Devonian Sonyea Group of New York: *Journal of Sedimentary Research*, v. 69, no. 4, p. 909–925.
- Schieber, J., Southard, J., and Thaisen, K., 2007, Accretion of mudstone beds from migrating floccule ripples: *Science*, v. 318, no. 5857, p. 1760–1763.
- Schieber, J., and Southard, J. B., 2009, Bedload transport of mud by floccule ripples—Direct observation of ripple migration processes and their implications: *Geology*, v. 37, no. 6, p. 483–486.
- Sigal, R. F., 2009, A methodology for blank and conformance corrections for high pressure mercury porosimetry: *Measurement Science & Technology*, v. 20, no. 4.
- Sneider, R. M., Sneider, J. S., Bolger, G. W., and Neasham, J. W., 1997, Comparison of seal capacity determinations: conventional cores vs. cuttings, in Surdam, R. C., ed., *Seals, Traps, and the Petroleum System: AAPG Memoir 67*, p. 1–12.
- Stone, W. J., Lyford, F. P., Frenzel, P. F., Nizell, N. H., and Padgett, E. T., 1983, Hydrogeology and water resources of San Juan Basin, New Mexico: *New Mexico Bureau of Mines and Mineral Resources Hydrologic Report 6*, p. 70, 7 sheets.
- Tomutsa, L., Silin, D., and Radmilovic, V., 2007, Analysis of chalk petrophysical properties by means of submicron-scale pore imaging and modeling: *SPE Reservoir Evaluation & Engineering*, v. 10, no. 3, p. 285–293.
- Udawatta, R. P., Gantzer, C. J., Anderson, S. H., and Garrett, H. E., 2008, Agroforestry and grass buffer effects on pore characteristics measured by high-resolution x-ray

computed tomography: *Soil Science Society of America Journal*, v. 72, no. 2, p. 295–304.

Welton, J. E., 1984, *SEM Petrology Atlas*: Tulsa, Oklahoma, American Association of Petroleum Geologists.

Yao, N., 2007, Introduction to the focused ion beam system, in Yao, N., ed., *Focused ion beam systems: basics and applications*: Cambridge, UK, Cambridge University Press, p. 1–29.

CHAPTER 4. PORE-LINING COMPOSITION AND CAPILLARY BREAKTHROUGH PRESSURE OF MUDSTONE CAPROCKS: SEALING EFFICIENCY OF GEOLOGIC CO₂ STORAGE SITES⁶

Abstract

Efficacy of the subsurface containment of CO₂ is predicated on effective caprock sealing. Many previous studies have relied on macroscopic measurements of capillary breakthrough pressure and other petrophysical properties without direct examination of the solid phases that line pore networks and directly contact fluids. However, the pore-lining phases strongly contribute to the sealing behavior through interfacial interactions among CO₂, brine, and the mineral or non-mineral phases. We examine continental and marine mudstones using high resolution (i.e., sub-micron) observations of pore-lining phases and X-ray diffraction (XRD). Our results indicate that sealing efficiency (i.e., breakthrough pressure) is governed by pore shapes and pore-lining phases that are not identifiable except through direct characterization of pores. The bulk X-ray diffraction data do not indicate which phases line the pores and may be especially lacking for mudstones with organic material. Organics can line pores and may represent once-mobile organics that modified the wettability of an originally clay-lined pore network. For shallow formations (i.e., < ~800 m depth), interfacial tension and contact angles result in

⁶Heath, J.E., McPherson, B.J.O.L., Dewers, T.A., Kotula, P.G., Mozley, P.S., Pore-lining composition and capillary breakthrough pressure of mudstone caprocks: sealing efficiency of geologic CO₂ storage, prepared for submission to the *International Journal of Greenhouse Gas Control*, not submitted as of this writing.

breakthrough pressures that may be as high as those needed to fracture the rock—thus, in the absence of fractures, capillary sealing efficiency is indicated. Deeper seals have poorer capillary sealing if mica-like wetting dominates the wettability.

Keywords: mudstone, caprock or seal, breakthrough pressure, composition, CO₂, pore network

4.1. Introduction

“Caprocks” or “seals” play a major role in the underground storage of CO₂ and other fluids. Caprock lithologies with low permeability and high capillary breakthrough pressure that lie above a target injection zone constitute a barrier that limits CO₂ and brine migration from the storage site (IPCC, 2005). Upward leakage of CO₂ and brine due to storage operations could cause inadequate performance of a site in terms of possible failed storage goals and possible damage to the quality of underground sources of drinking water or other resources (Wilson et al., 2007). Through evaluation of atmospheric emissions and massive application of underground CO₂ storage, recent work indicates the need for 99% or greater retention of injected CO₂ per thousand years to achieve low-CO₂-emission goals and mitigated climate change (Shaffer, 2010).

Micron to nanometer-sized pore sizes in caprocks present a technological challenge for identifying pore-lining phases and pore shapes, yet understanding such features is essential to predicting seal quality. Pore-lining phases strongly affect wettability, which in turn influence capillary breakthrough pressures. Pore size and shape influence the magnitudes of capillary breakthrough pressures and permeability. Lacking a means of obtaining a detailed understanding of pore structure, many previous studies

relied on macroscopic core-plug measurements for estimating breakthrough pressures and other petrophysical properties (Li et al., 2005; Andreani et al., 2008; Wollenweber et al., 2010). A goal of this study is to utilize chemical analysis of pore-lining phases and physical pore structure to facilitate not just estimates of the magnitudes of breakthrough pressures of caprocks, but also interpretation of factors that determine those magnitudes.

In this paper, we examine: 1) pore-lining phases (e.g., minerals and non-crystalline phases such as organics) of a suite of continental and marine mudstones; and 2) how knowledge of the pore-lining phases affects prediction of caprock sealing efficiency. Mercury intrusion porosimetry (MIP) data are interpreted using the pore-lining compositions to bound CO₂ capillary breakthrough pressures. Knowledge of the pore-lining phases informs the choice of contact angles when converting MIP breakthrough pressures to CO₂ breakthrough pressures. This work complements a companion study on the control of pore network characteristics on breakthrough pressures in the same mudstones using novel digital three-dimensional (3D) reconstructions of pore networks (Chapter 3). This current chapter extends the work of Chapter 3 by addressing the impact of pore-lining phases and making estimates of the capillary sealing behavior for the CO₂/brine/rock system.

The principal question driving this research is: What phases line pores in mudstones, and how do those phases affect CO₂ capillary breakthrough (seal efficacy) for different types of mudstones? To investigate the importance of this question, we also considered a related question: What is the benefit of a mechanistic understanding of capillary breakthrough for CO₂ storage when direct measurements of macro-scale (i.e., plug scale) breakthrough can be performed and are considered reliable indicators of

breakthrough processes (Li et al., 2005)? The possibility of direct macro-scale tests seem to circumvent the need for information on pore size, pore shape, interfacial tension, and contact angles in deriving breakthrough pressures. However, researchers evaluate CO₂ storage at many sites throughout the world with mudstone (or other) facies that have not previously been tested by direct breakthrough tests. The results of direct tests apply to specific rocks, and extending their values to systems of different pressure, temperature, and mineral and non-mineral (e.g., organics) phases may not be appropriate, especially when knowledge on how CO₂/brine/caprock wettability varies with different types of clay minerals is currently limited. Additionally, examination of pore-lining phases may identify potential weaknesses in a caprock. For example, portions of a caprock may include organics that would be susceptible to alteration by injection activities (e.g., deterioration of organic phases lining pores).

A mechanistic understanding may enable engineering activities that could modify wetting characteristics (e.g., adding surfactants or other molecular systems). A mechanistic understanding could lead to engineering of maximum efficiency of storage instead of simply characterizing breakthrough. Mercury intrusion porosimetry data have been collected for a very large number of mudstone and other rock types throughout the world due to oil and gas exploration efforts. Use of this data for prediction of the CO₂ breakthrough would be extremely valuable and lessen the need for direct breakthrough tests using CO₂. We present these concepts as motivation for the focus on determining what lines pores and how that knowledge could be used.

4.2. Breakthrough Pressure and Wettability

“Breakthrough pressure” refers to the excess pressure in the nonwetting phase at which that nonwetting phase penetrates a rock through its connected pore network, which is previously saturated with the wetting phase (Dullien, 1992). Breakthrough pressure is a macroscopic parameter that applies to core plugs or whole seal units, indicating that the percolation threshold is exceeded, and a nonwetting phase has migrated through connected paths across the system of interest. The paths include the largest connected pores through the system (Hildenbrand et al., 2002). This phenomenon differs from “capillary entry pressure” or “minimum capillary pressure”, which depend on the size of the largest pores on the outside of a rock sample given conditions of rock wettability and interfacial tension (IFT) (Dullien, 1992; Almon et al., 2008).

The Washburn equation describes the penetration of a nonwetting fluid into a capillary tube of radius r containing a wetting fluid (Washburn, 1921; Li et al., 2005):

$$P_c = P_{mw} - P_w = \frac{2\gamma \cos \theta}{r} \quad (1)$$

where P_c is the capillary pressure or difference between the pressures of the two immiscible fluids, γ is the IFT between the two fluids, and θ is the contact angle for the rock and fluid system. This equation can apply to penetration of single pores and illustrates the importance of pore size (and shape if a more generalized version of the Washburn equation is used; see Cook and Hover, 1993). With regard to breakthrough pressure, Equation 1 represents the smallest pore size along the flowpath in the connected pore network that forms the continuous network of the nonwetting phase through the system of interest.

Data pertaining to wettability of caprock minerals in CO₂-brine systems are very sparse in the literature. Chiquet et al. (2007a) present contact angle measurements for CO₂ by captive drop methods for mica and quartz. We find no other studies in the literature for the dominant clay phases that comprise typical caprock (i.e., mudstones) in sedimentary settings. Many recent studies cope with this lack of data by investigating breakthrough pressures without measurement of contact angles or IFT. These studies perform tests on small rock samples to measure the pressure when CO₂ penetrates across a previously brine-saturated sample (or equivalently the studies measure the capillary snap-off pressure after a drainage and imbibition cycle) (Hildenbrand et al., 2004; Wollenweber et al., 2010).

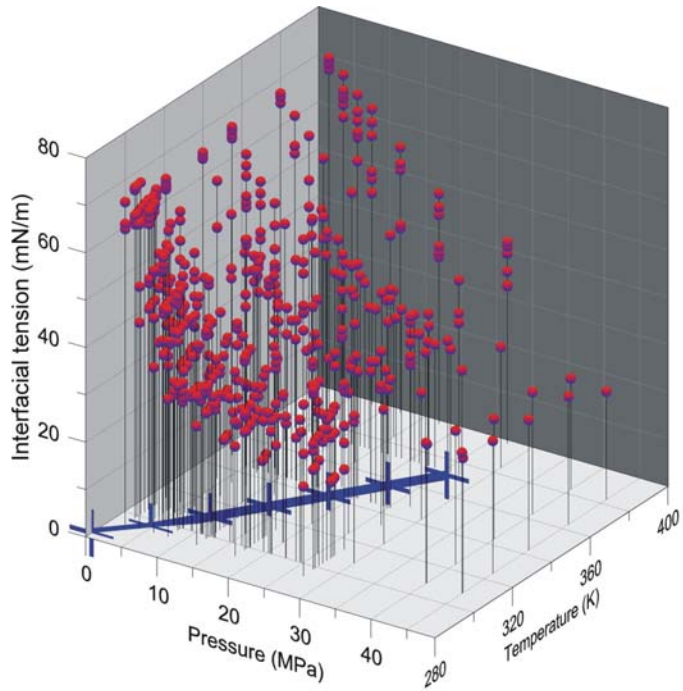
Recent papers present measurements of IFT between CO₂ and water over a range of low (0 mg/L) to high salinities (334,000 mg/L) (Chiquet et al., 2007b; Bachu and Bennion, 2009; Chalbaud et al., 2009). Considerable data are available for temperature, pressure, and salinity conditions pertaining to the depths of ~0.6 to 1.0 km, although large gaps exist for greater depths (Figure 4.1). Clear in the data, however, allow for estimation via empirical equations of the IFT for the conditions of CO₂ storage (Bachu and Bennion, 2009).

A method for estimating breakthrough pressure commonly used in the petroleum industry involves interpretation of mercury intrusion porosimetry (MIP) data (Sneider et al., 1997; Dewhurst and Hennig, 2003; Almon et al., 2005). Such interpretation provides a breakthrough pressure value that is converted from the mercury-air-rock system to other systems of interest. For example, the following equation expresses a conversion to the CO₂-brine-rock system (Berg, 1975; Dewhurst et al., 2002):

$$P_{b/CO_2} = P_{a/m} \frac{(\gamma_{b/CO_2} \cos \theta_{b/CO_2})}{(\gamma_{a/m} \cos \theta_{a/m})} \quad (2)$$

where P_{b/CO_2} is the capillary pressure for the brine-CO₂-rock system, $P_{a/m}$ is the mercury-air-rock capillary pressure, γ is interfacial tension, θ is the contact angle, and the subscripts indicate the CO₂-brine-rock or mercury-air-rock systems.

Figure 4.1. (Next page.) Interfacial tension (IFT) measurements of the CO₂ and water/brine fluid pair as function of pressure and temperature (Chiquet et al., 2007b; Bachu and Bennion, 2009; Chalbaud et al., 2009) with blue line to indicate pressure and temperature ranges that corresponds to depth in the subsurface for typical conditions (i.e., 25°C/km geothermal gradient; hydrostatic pressure for pure water). The line is placed on the pressure-temperature plane and marked in intervals that correspond to depths from 0 to 3 km. (a) Three dimensional view that shows IFT steeply decreases as a function of pressure for a given temperature. The highest IFT values for a given pressure and temperature correspond to higher salinities. (b) Top down view which shows that much data has been collected in the depth range of 1 km.



(b)

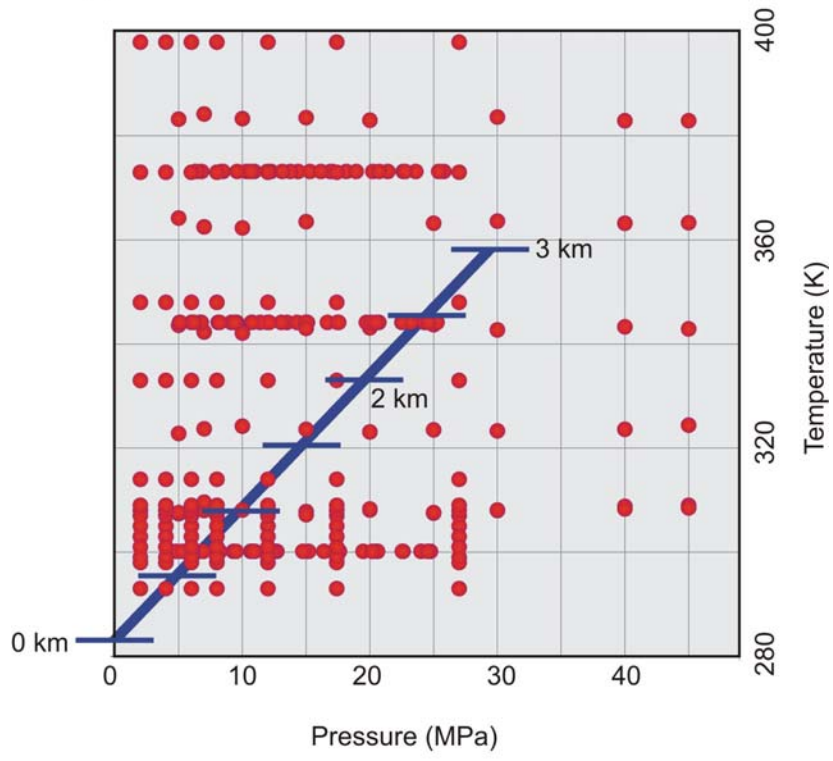


Figure 4.1. (Caption on preceding page.)

4.3. Methods and Materials

4.3.1 Geologic Samples

Previous studies (Schieber, 1999; Almon et al., 2005) provide a general framework for understanding key geologic controls, e.g., primary depositional setting, burial history, diagenesis, on the properties of mudstones. Chapter 3, a companion paper to this study, builds upon that framework by describing 3D pore network properties of several continental and marine mudstones. These mudstones represent seals at recently-deployed CO₂ storage demonstration projects of the Southeast Regional Carbon Sequestration Partnership (SECARB) and the Southwest Regional Carbon Sequestration Partnership (SECARB and SWP; Figure 4.2; Litynski et al., 2008), two research programs managed by the U.S. Department of Energy's National Energy Technology Laboratory. The same mudstone samples from Chapter 3 are used herein for investigating pore-lining properties. These samples were obtained from core collected by SECARB and SWP. We also present sample analyses for breakthrough pressure via MIP.

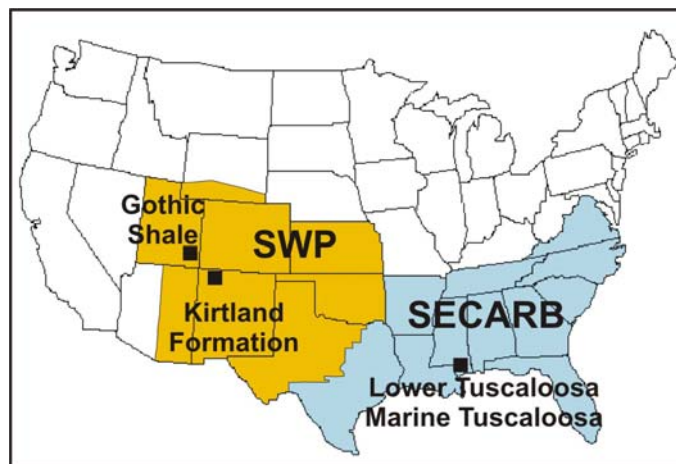


Figure 4.2. Map showing locations of wells from where core mudstone samples were obtained by the Southeast and Southwest Regional Carbon Sequestration Partnerships (SECARB and SWP).

The mudstones we selected are especially appropriate because they represent common continental and marine lithologies present in many candidate sequestration sites. The specific formations selected include: the upper and lower shale members of the Kirtland Formation, San Juan Basin, New Mexico; mudstone intervals within the Tuscaloosa Group, Gulf of Mexico Basin, Mississippi, from the Middle or “Marine” Tuscaloosa and Lower Tuscaloosa Groups; and the Gothic shale, Paradox Basin, Utah (Figure 4.2). See Chapter 3 for full descriptions of geologic settings of the mudstones and details of 3D pore network characterizations obtained by a dual-beam focused ion beam/scanning electron microscopy system (FIB/SEM) (Wirth, 2009). The Kirtland Formation includes continental mudstones deposited in floodplain environments. The Tuscaloosa Group includes shallow shelf to more shelfal depositional environments. The Gothic shale represents an open marine, organic-rich depositional setting.

4.3.2 Scanning Transmission Electron Microscopy and Elemental Analysis

We imaged sub- μm scale pore-lining material and interpreted associated compositional information using scanning transmission electron microscopy with energy dispersive X-ray spectroscopy (STEM/EDS). The analysis allows visualization of phases not detected by X-ray diffraction (XRD), including amorphous non-crystalline materials (e.g., volcanic glass and organics), minerals in insufficient amounts for XRD detection, and also pores.

We prepared STEM foils of ~ 100 nm thickness using the milling capabilities of FIB/SEM system (see Chapter 3 Section 3.3.2 for details on the FIB/SEM system). The FIB/SEM system milled the foils within a few μm of the locations of each of the last

serial cross sections of the 10 mudstone samples of Chapter 3. Thus, each 3D geometrical pore network model of Chapter 3 has corresponding high resolution imaging with compositional analysis by STEM/EDS.

The STEM foils were placed onto carbon-coated Cu-mesh grids and analyzed following methods similar to Kotula and Keenan (2006) on a FEI Company Tecnai F-30ST TEM/STEM equipped with a EDAX Super Ultra-Thin window energy-dispersive X-ray detector and Tecnai Imaging and Analysis software. The electron acceleration voltage and beam currents were 300 kV and 2 nA, which resulted in a probe of 2 nm full width tenth maximum. High-angle annular dark-field STEM images were obtained with a Fischione detector. Single-pass point-and-dwell spectral images were taken with 2048 energy channels over a 0-20-kV X-ray energy range from within regions where a dark-field image was acquired.

A spectral image consists of a complete X-ray spectrum from each point or pixel in a 2D array. The pixel spacing varied between ~4 to 20 nm/pixel. Details of data acquisition followed Kotula and Keenan (2006). Per-pixel dwell time and pulse-processor shaping time resulted in spectral images with ~100–300 counts per pixel for each sample. The primary advantage of acquiring spectral images is that the data can be retrospectively analyzed even for elements not expected prior to the data acquisition.

Once a spectral image has been acquired from a region of a STEM foil, analysis of the resulting data is difficult because of the high number of spectra, typically 10,000 or more. Furthermore, a goal is to analyze the data without *a priori* knowledge of what phases or combinations of elements may be present at different locations in the specimen down to the nm scale. Region-of-interest elemental “dot” maps could readily be extracted

from the spectral image, but then the analyst must ensure that the maps are representative of the elements of interest and not biased due to pathological overlaps of X-ray lines from other elements or continuum radiation. Therefore, multivariate statistical analysis (MSA) methods are utilized to quickly reduce the raw data into a small number of chemical phases.

We conducted a specific MSA approach that required the raw spectral image to first be normalized for Poisson statistics to down-weight the effect of noise in the subsequent factor analysis (Keenan and Kotula, 2004). An eigenanalysis is then performed on the normalized data to determine the number of linearly independent sources of non-noise information, which gives the number of factors that will be retained in the subsequent factor analysis. The normalized data are then factored into two matrices that describe the spatial distribution of the phases and their respective qualitative compositions (Kotula et al., 2003, 2006; Keenan, 2009). Because the goal was to image the spatial distribution of chemical phases, the analysis was performed so as to produce component images that are “high contrast” (Keenan, 2009). These high contrast images (along with their respective compositions) then describe the spatial distributions of the chemical phases in the sample. The last step in the data reduction process is to inversely normalize the data for the Poisson normalization to return the results to counts from scaled counts. Assumptions of the MSA include Poisson statistics, non-negative counts, and linear independence. The outcome of this MSA is the mineralogy in spatial relation to pores, organics, and other non-crystalline phases (which are identified as groups of constituent elements).

4.3.3 Mercury Intrusion Porosimetry and Breakthrough Pressure

Mercury intrusion porosimetry was performed by Poro-Technology, Sugar Land, Texas, on samples from the Kirtland Formation, Tuscaloosa Group, and Gothic shale using a Micromeritics AutoPore IV 9500 Series porosimeter. Some samples were cut perpendicular or horizontal to bedding and jacketed with epoxy for directional intrusion, whereas other samples were not jacketed and underwent omni-directional intrusion. Corrections for measured mercury intrusion that did not represent actual intrusion into the pore network, the so-called “closure pressure corrections”, were made using a compressibility method (Colombo and Carli, 1981; Almon et al., 2008). Closure pressure is the pressure at which mercury first enters the pore network during an MIP test. This compressibility closure correction applies to the Kirtland Formation and other samples labeled by the geologic unit name (either as the full name or as two-letter abbreviations) and depth (in ft) of the samples (in Tables 4.1–4.3). A subset of the samples was characterized by FIB/SEM (see Chapter 3) and TEM prior to the MIP. Additional results of Gothic shale analysis by MIP (Chidsey et al., 2010) include closure corrections by Poro-Technology, which may follow a different method than that given above. Additional MIP measurements, provided by SECARB, for Tuscaloosa Group samples were performed and corrected for closure pressure by OMNI Laboratories, Inc. These additional samples do not follow the naming scheme of the geologic unit name and depth (Tables 4.1–4.3).

Table 4.1. Summary of pore types and pore-lining phases from high resolution microanalysis with comparison to X-ray diffraction

STEM/EDS sample ID	STEM/EDS Sample depth (m)	Figures for STEM/EDS	Pore descriptions	Pore-lining phases	Depth of XRD sample	Bulk XRD mineralogy (wt%)
UK 2049.7B	624.7	3a-e	Predominately slit-like; some triangular shapes	Smectite (and possibly chlorite)	624.3	Quartz: 5; K-feldspar: 11; plagioclase: 18; calcite: 0; ankerite/fe-dolomite: 1; dolomite: 0; pyrite: 0; smectite: 23; illite/smectite: 4; illite+mica: 22; kaolinite: 7; chlorite: 19
LK 2692.9A	820.8	3f-j	Jagged, dentate; possibly stylolitic and diagenetic	Calcite and minor clays (possibly calcium smectite)	820.6	Quartz: 21; K-feldspar: 10; plagioclase: 13; calcite: 1; ankerite/fe-dolomite: 1; dolomite: 0; pyrite: 1; smectite: 3; illite/smectite: 28; illite+mica: 0; kaolinite: 9; chlorite: 12
LT 8590.0	2618.2	4a-e	Large, linear pore that is probably induced; pores not imaged are non-slit-like (see Heath et al., submitted)	Probably illite, kaolinite, and chlorite	2618.1	Quartz: 55; K-feldspar: 2; plagioclase: 10; calcite: 0; ankerite/fe-dolomite: 0; dolomite: 0; pyrite: 3; illite/smectite: 0; illite: 8; kaolinite: 8; chlorite: 14
MT 7925.5	2415.7	4f-j; 5a-e	Circular and located in organics; slit-like and located in clays	Organics; predominately illite	2417.6	Quartz: 50; K-feldspar: 2; plagioclase: 12; calcite: 0; ankerite/fe-dolomite: 0; dolomite: 0; pyrite: 2; illite/smectite: 0; illite: 5; kaolinite: 5; chlorite: 9
MT 7931.9	2417.6	5f-j; 6a-e	Slit-like	Illite with minor kaolinite		
GS 5390.8A	1643.1	6f-j	Crescent-shaped pore that may be lined with organics; the organics are surrounded by clay	Organics; predominately illite	5391	Quantitative XRD not performed; qualitative XRD indicates presence of: illite, chlorite, quartz, calcite, and dolomite
GS 5390.8B	1643.1	7a-j; 8a-e	Triangular to irregular shapes; organic near calcite and quartz clasts; can also contact clays	Quartz, calcite, organics, and probable illite		

Table 4.2. Breakthrough pressures estimated from mercury porosimetry for the suite of mudstone samples, along with supporting information.

Unit	Sample ID	Depth (m)	Depth (km)	Directional intrusion	TEM/EDS sample	Mercury breakthrough pressure (MPa)	Breakthrough pore-throat diameter (μm)	Saturation at breakthrough (%)
upper Kirtland Formation	UK 2047.9A	624.19992	0.6			0.6	2.565	1.0
	UK 2047.9B	624.19992	0.6	Vert.	x	1.2	1.205	2.2
	UK 2048.35	624.33708	0.6			0.7	1.981	1.3
	UK 2052.35	625.55628	0.6			56.1	0.026	6.0
	UK 2055.37	626.476776	0.6			43.7	0.034	6.6
	UK 2062.40	628.61952	0.6			37.0	0.040	5.6
	UK 2068.05	630.34164	0.6			43.7	0.034	13.6
lower Kirtland Formation	LK 2692.19	820.579512	0.8			66.3	0.022	7.1
	LK 2692.9A	820.79592	0.8	Vert.	x	51.6	0.029	7.4
	LK2692.9B	820.79592	0.8			47.5	0.031	7.1
Lower Tuscaloosa Group	3-41	2612.6	2.6			5.6	0.265	1.5
	3-44	2613.6	2.6			0.4	3.325	1.7
	3-51A	2615.7	2.6			82.0	0.018	4.8
	3-54A	2616.6	2.6			82.0	0.018	4.3
	3-58A	2617.7	2.6			75.1	0.020	3.8
	3-59	2618.1	2.6			47.9	0.031	5.6
	LT 8590.0	2618.2	2.6		x	66.3	0.022	6.3
	LT 8590.9	2618.1	2.6	Vert.		28.8	0.051	7.4
Marine Tuscaloosa Group	2-4	2410.8	2.4			33.4	0.044	2.0
	2-9A	2412.2	2.4			57.3	0.026	3.3
	2-19A	2415.4	2.4			68.6	0.021	3.9
	MT 7925.5	2415.7	2.4		x	47.5	0.031	1.8
	2-25A	2417.2	2.4			62.7	0.023	3.2
	2-25	2417.6	2.4			9.5	0.155	3.4
	MT 7931.9	2417.6	2.4		x	66.3	0.022	4.0
Gothic shale	Spl#1H 5378.0	1639.2	1.6	Horiz.		118.7	0.012	10.4
	GS 5390.8A	1643.1	1.6		x	100.5	0.015	9.3
	Gs 5390.8B	1643.1	1.6		x	109.2	0.014	12.8
	Spl#6V 5391.35	1643.3	1.6	Vert.		61.0	0.024	15.6

Note: "Vert." and "Horiz." stand for directional intrusion perpendicular or horizontal to bedding, respectively.

Table 4.3. High and low estimates of CO₂ breakthrough pressure estimates based on uncertainty in interfacial tension and contact angles

Unit	Sample ID	Depth (m)	Larger CO ₂ breakthrough pressure (MPa)	Smaller CO ₂ breakthrough pressure (MPa)	High γ_{b/CO_2} (N/m)	Low γ_{b/CO_2} (N/m)	High θ_{b/CO_2} for Mica	Low θ_{b/CO_2} for quartz	
upper Kirtland Formation	UK 2047.9A	624.1999	0.1	0.0	0.046	0.036	57	23	
	UK 2047.9B	624.1999	0.1	0.1	0.046	0.036	57	23	
	UK 2048.35	624.3371	0.1	0.0	0.046	0.036	57	23	
	UK 2052.35	625.5563	6.5	3.0	0.046	0.036	57	23	
	UK 2055.37	626.4768	5.1	2.3	0.046	0.036	57	23	
	UK 2062.40	628.6195	4.3	2.0	0.046	0.036	57	23	
lower Kirtland Formation	UK 2068.05	630.3416	5.1	2.3	0.046	0.036	57	23	
	LK 2692.19	820.5795	7.0	2.5	0.043	0.034	66	25	
	LK 2692.9A	820.7959	5.5	1.9	0.043	0.034	66	25	
	LK2692.9B	820.7959	5.0	1.8	0.043	0.034	66	25	
	Lower Tuscaloosa Group	3-41	2612.6	0.4	0.0	0.032	0.030	91	39
	3-44	2613.6	0.0	0.0	0.032	0.030	91	39	
	3-51A	2615.7	5.5	-0.1	0.032	0.030	91	39	
	3-54A	2616.6	5.5	-0.1	0.032	0.030	91	39	
	3-58A	2617.7	5.0	-0.1	0.032	0.030	91	39	
	3-59	2618.1	3.2	-0.1	0.032	0.030	91	39	
Marine Tuscaloosa Group	LT 8590.0	2618.2	4.4	-0.1	0.032	0.030	91	39	
	LT 8590.9	2618.1	1.9	0.0	0.032	0.030	91	39	
	2-4	2410.8	2.3	0.1	0.032	0.029	87	38	
	2-9A	2412.2	3.9	0.3	0.032	0.032	87	38	
	2-19A	2415.4	4.7	0.3	0.032	0.029	87	38	
	MT 7925.5	2415.7	3.3	0.2	0.032	0.029	87	38	
	2-25A	2417.2	4.3	0.3	0.032	0.029	87	38	
	2-25	2417.6	0.7	0.0	0.032	0.029	87	38	
	MT 7931.9	2417.6	4.5	0.3	0.032	0.029	87	38	
	Gothic shale	Spl#1H 5378.0	1639.2	7.5	2.4	0.027	0.023	72	31
Gothic shale	GS 5390.8A	1643.1	6.3	2.0	0.027	0.023	72	31	
	Gs 5390.8B	1643.1	6.9	2.2	0.027	0.023	72	31	
	Spl#6V 5391.35	1643.3	3.8	1.2	0.027	0.023	72	31	

Breakthrough pressures are estimated following Dewhurst et al. (2002) from incremental saturation curves (i.e., volume of mercury intruded per pressure). The point of maximum curvature as the curve approaches the first mode represents the breakthrough pressure. It indicates that a continuous filament of mercury has penetrated across the sample (Schowalter, 1979).

4.4. Results

4.4.1 Scanning Transmission Electron Microscopy and Elemental Analysis

General information applicable to most samples is presented first, followed by geologic unit-specific data. Figures 4.3 through 4.8 present the STEM/EDS results, along with backscattered electron images from Chapter 3, for 3D pore network models constructed from the FIB/SEM images taken in the vicinity of the STEM/EDS sample foils. The STEM/EDS results complement the backscattered electron images, which provide mineralogical information in terms of variation in mean atomic number Z . Spectral shapes (the “a” and “f” parts of the figures) give the combinations of elements that represent chemical phases of the MSA. Parts “b” and “g” of the figures consist of the last serial FIB/SEM image (taken in backscattered electron mode), and consequently is similar in composition to the STEM foils. Parts “c”, “d”, “h”, and “i” present total and interpreted X-ray output from the EDS analysis, which correspond to the colors of the spectral shapes. Parts “d” and “i” provide the spatial representation of the MSA chemical phases. Finally, “e” and “j” present the high-angle annular dark field STEM images with the location of the EDS analysis delineated by a red box. The variation in grayscale of the

Figure 4.3. Results of scanning transmission electron microscopy (STEM) imaging combined with energy-dispersive X-ray spectroscopy for Kirtland Formation samples, along with the last focused ion beam (FIB) images from sets of serial sections. (a) through (e) correspond to sample upper Kirtland 2049.7B. (f) through (j) are associated with sample lower Kirtland 2692.9A. (a and f) Spectral shapes of chemical phases determined by the multivariate statistical analysis (MSA) of X-ray spectral images. Normalization of the y axis is such that, for a particular chemical phase, the product of the normalized counts and the intensity of the corresponding component image results in counts equivalent to the original X-ray counts. In the legend, elements with relatively low counts still above background noise are given in parentheses. (b and g) The last backscattered electron images for a set of FIB serial sections (see Chapter 3). Scale bar is 2 μm . (c and h) Total X-ray output images with hotter colors corresponding to higher output. Horizontal field of view for both images is 3000 nm and (c) and (h) have 20 and 10 nm/pixel resolution, respectively. (d and i) High-contrast component images that display spatial rendering of the MSA chemical phases. Colors correspond with those of the spectral shapes. (e and j) High-angle annular dark-field STEM images taken $\leq 3 \mu\text{m}$ from the location of the corresponding set of FIB serials. Red boxes delineate regions of the X-ray spectral images. Scale bars are 2 μm . The brightest spot on (j) in the upper left-hand side of the image is a piece of gold-palladium-coated material (i.e., an artifact).

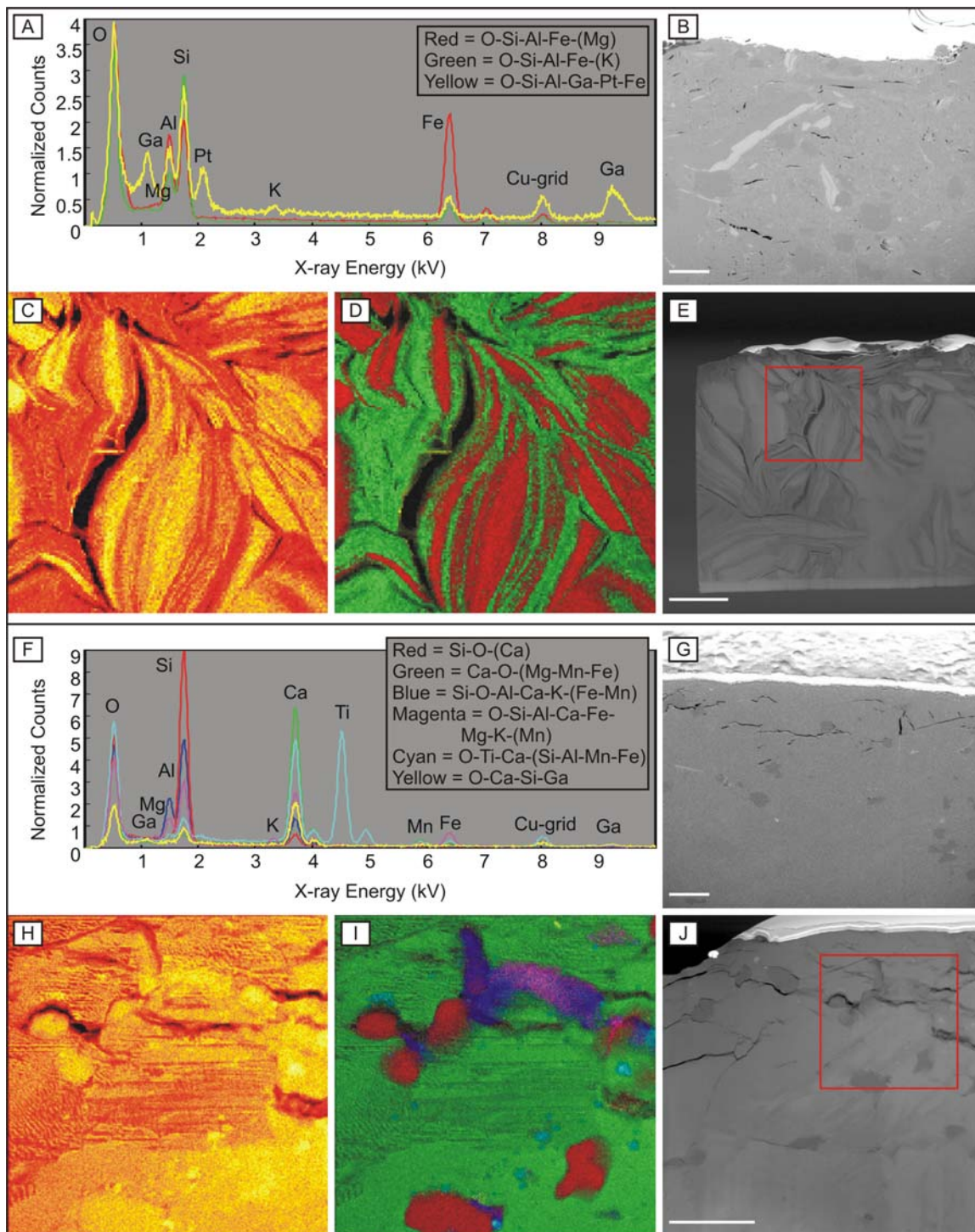


Figure 4.3. (Caption on preceding page.)

Figure 4.4. Results of scanning transmission electron microscopy (STEM) imaging combined with energy-dispersive X-ray spectroscopy for Lower and Marine Tuscaloosa Group samples, along with the last focused ion beam (FIB) images from sets of serial sections. (a) through (e) correspond to sample Lower Tuscaloosa 8590.0. (f) through (j) are associated with sample Marine Tuscaloosa 7925.5. (a and f) Spectral shapes of chemical phases determined by the multivariate statistical analysis (MSA) of X-ray spectral images. Normalization of the y axis is such that, for a particular chemical phase, the product of the normalized counts and the intensity of the corresponding component image results in counts equivalent to the original X-ray counts. In the legend, elements with relatively low counts still above background noise are given in parentheses. (b and g) The last backscattered electron images for a set of FIB serial sections (see Chapter 3). Scale bar is 2 μm . (c and h) Total X-ray output images with hotter colors corresponding to higher output. Horizontal field of view for both images is 3000 nm and (c) and (h) have 10 and 20 nm/pixel resolution, respectively. (d and i) High-contrast component images that display spatial rendering of the MSA chemical phases. Colors correspond with those of the spectral shapes. (e and j) High-angle annular dark-field STEM images taken $\leq 3 \mu\text{m}$ from the location of the corresponding set of FIB serials. Red boxes delineate regions of the X-ray spectral images. Scale bars are 2 μm .

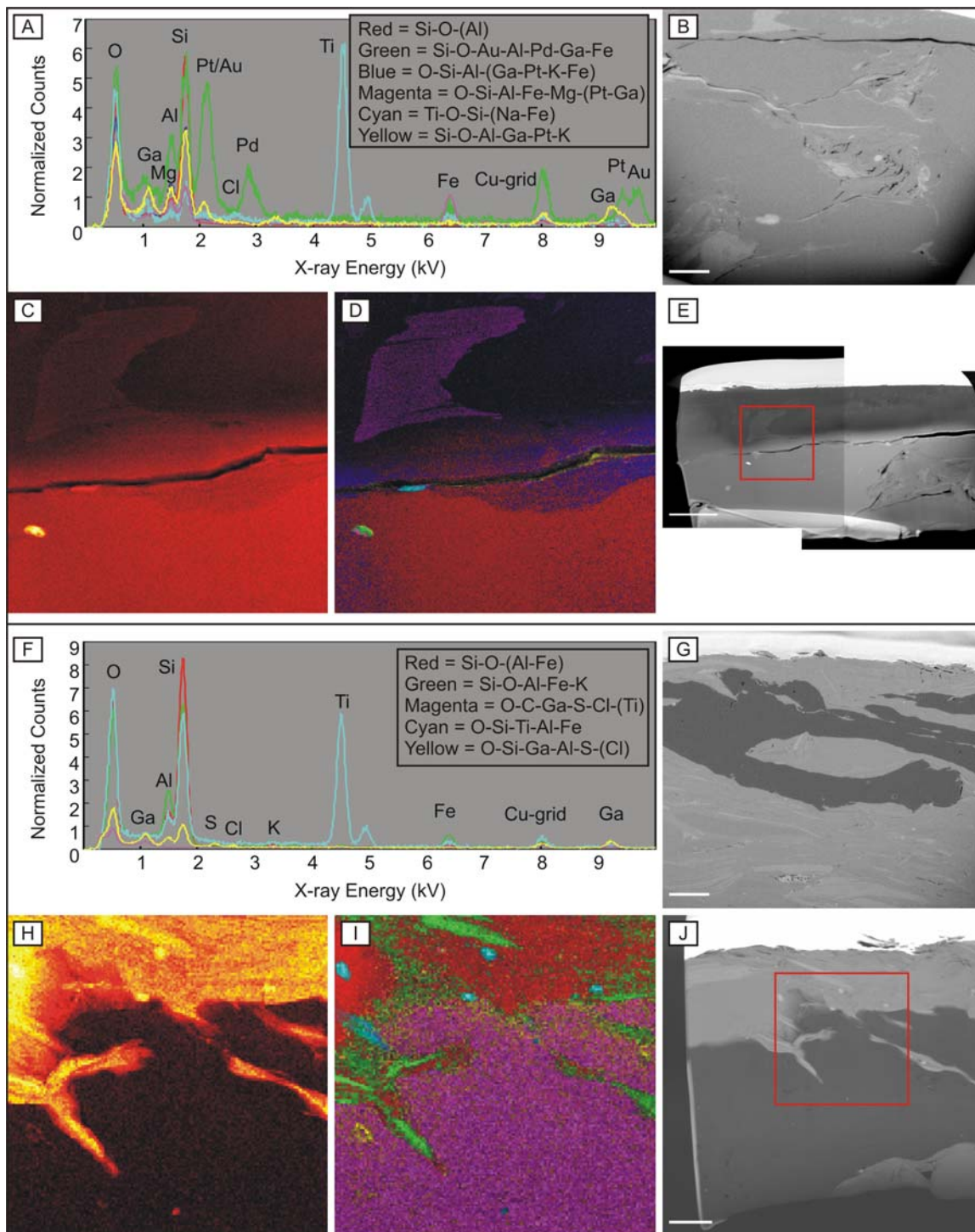


Figure 4.4. (Caption on preceding page.)

Figure 4.5. Results of scanning transmission electron microscopy (STEM) imaging combined with energy-dispersive X-ray spectroscopy for Marine Tuscaloosa Group samples, along with the last focused ion beam (FIB) images from sets of serial sections. (a) through (e) correspond to sample Marine Tuscaloosa 7925.5, but at a different location than in Figure 4.4. (f) through (j) are associated with sample Marine Tuscaloosa 7931.9. (a and f) Spectral shapes of chemical phases determined by the multivariate statistical analysis (MSA) of X-ray spectral images. Normalization of the y axis is such that, for a particular chemical phase, the product of the normalized counts and the intensity of the corresponding component image results in counts equivalent to the original X-ray counts. In the legend, elements with relatively low counts still above background noise are given in parentheses. (b and g) The last backscattered electron images for a set of FIB serial sections (see Chapter 3). Scale bar is 2 μm . (c and h) Total X-ray output images with hotter colors corresponding to higher output. Horizontal field of view for both images is 3000 nm and (c) and (h) both have 10 nm/pixel resolution. (d and i) High-contrast component images that display spatial rendering of the MSA chemical phases. Colors correspond with those of the spectral shapes. (e and j) High-angle annular dark-field STEM images taken $\leq 3 \mu\text{m}$ from the location of the corresponding set of FIB serials. Red boxes delineate regions of the X-ray spectral images. Scale bars are 2 μm .

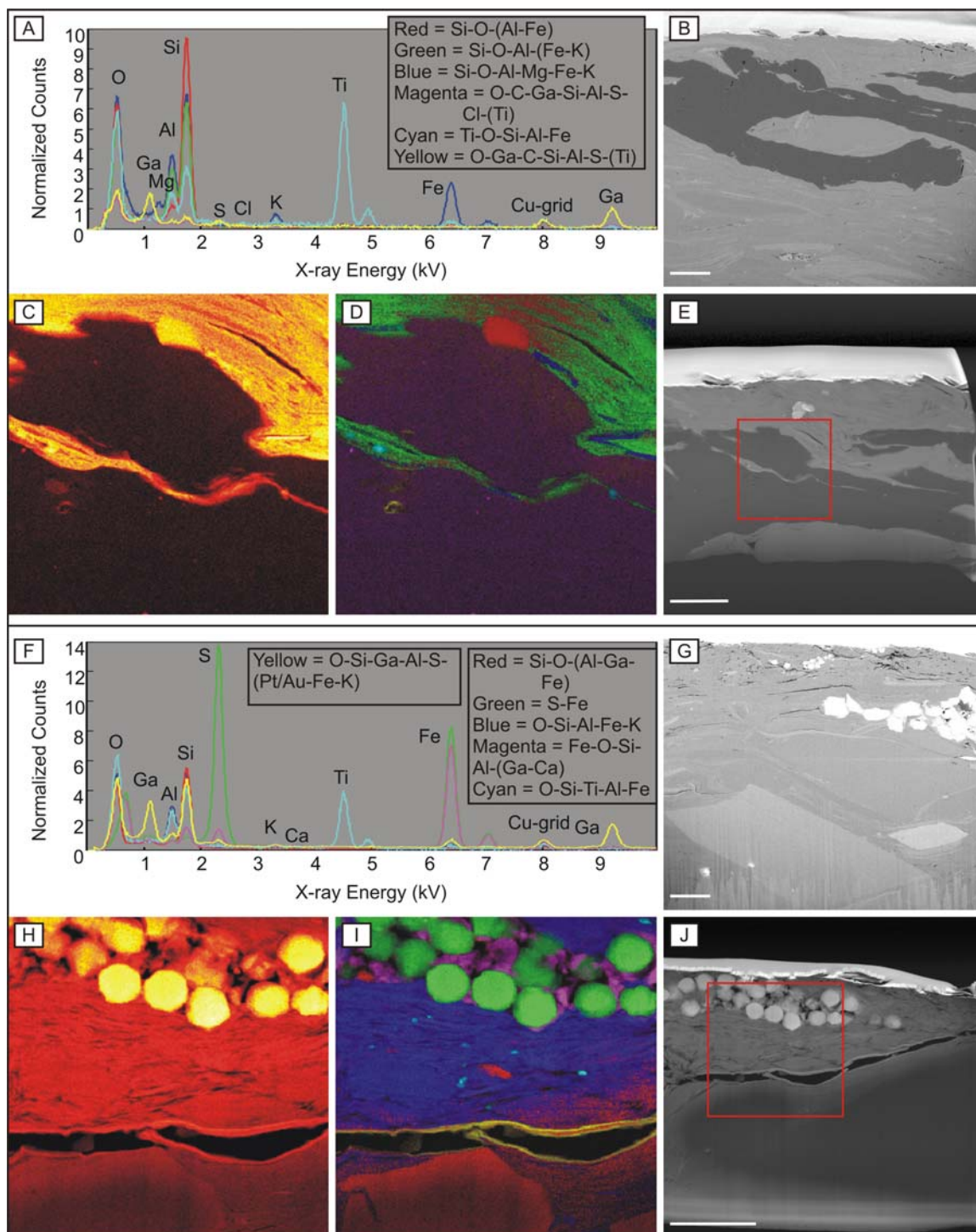


Figure 4.5. (Caption on preceding page.)

Figure 4.6. Results of scanning transmission electron microscopy (STEM) imaging combined with energy-dispersive X-ray spectroscopy for Marine Tuscaloosa Group and Gothic shale samples, along with the last focused ion beam (FIB) images from sets of serial sections. (a) through (e) correspond to sample Marine Tuscaloosa 7931.9, but at a different location than in Figure 4.5. (f) through (j) are associated with sample Gothic shale 5390.8A. (a and f) Spectral shapes of chemical phases determined by the multivariate statistical analysis (MSA) of X-ray spectral images. Normalization of the y axis is such that, for a particular chemical phase, the product of the normalized counts and the intensity of the corresponding component image results in counts equivalent to the original X-ray counts. In the legend, elements with relatively low counts still above background noise are given in parentheses. (b and g) The last backscattered electron images for a set of FIB serial sections (see Chapter 3). Scale bar is 2 μm . (c and h) Total X-ray output images with hotter colors corresponding to higher output. Horizontal field of view for both images is 3000 nm and (c) and (h) both have 10 nm/pixel resolution. (d and i) High-contrast component images that display spatial rendering of the MSA chemical phases. Colors correspond with those of the spectral shapes. (e and j) High-angle annular dark-field STEM images taken $\leq 3 \mu\text{m}$ from the location of the corresponding set of FIB serials. Red boxes delineate regions of the X-ray spectral images. Scale bars are 2 μm .

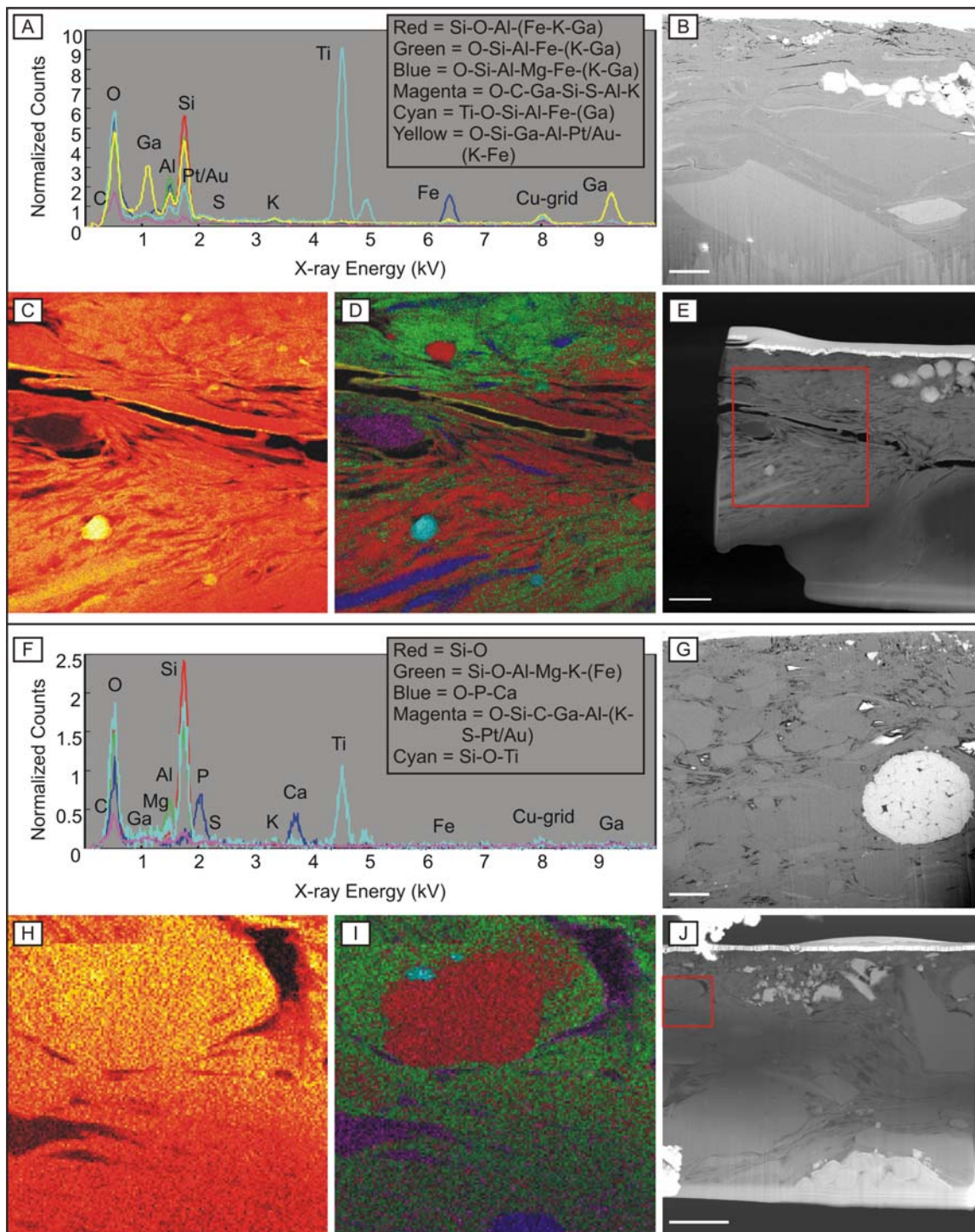


Figure 4.6. (Caption on preceding page.)

Figure 4.7. Results of scanning transmission electron microscopy (STEM) imaging combined with energy-dispersive X-ray spectroscopy for Gothic shale samples, along with the last focused ion beam (FIB) images from sets of serial sections. (a) through (e) correspond to sample Gothic shale 5390.8B. (f) through (j) are associated with sample Gothic shale 5390.8B at a different location. (a and f) Spectral shapes of chemical phases determined by the multivariate statistical analysis (MSA) of X-ray spectral images. Normalization of the y axis is such that, for a particular chemical phase, the product of the normalized counts and the intensity of the corresponding component image results in counts equivalent to the original X-ray counts. In the legend, elements with relatively low counts still above background noise are given in parentheses. (b and g) The last backscattered electron images for a set of FIB serial sections (see Chapter 3). Scale bar is 2 μm . (c and h) Total X-ray output images with hotter colors corresponding to higher output. Horizontal field of view for both images is 3000 nm and (c) and (h) have 20 and 10 nm/pixel resolution, respectively. (d and i) High-contrast component images that display spatial rendering of the MSA chemical phases. Colors correspond with those of the spectral shapes. (e and j) High-angle annular dark-field STEM images taken $\leq 3 \mu\text{m}$ from the location of the corresponding set of FIB serials. Red boxes delineate regions of the X-ray spectral images. Scale bars are 2 μm .

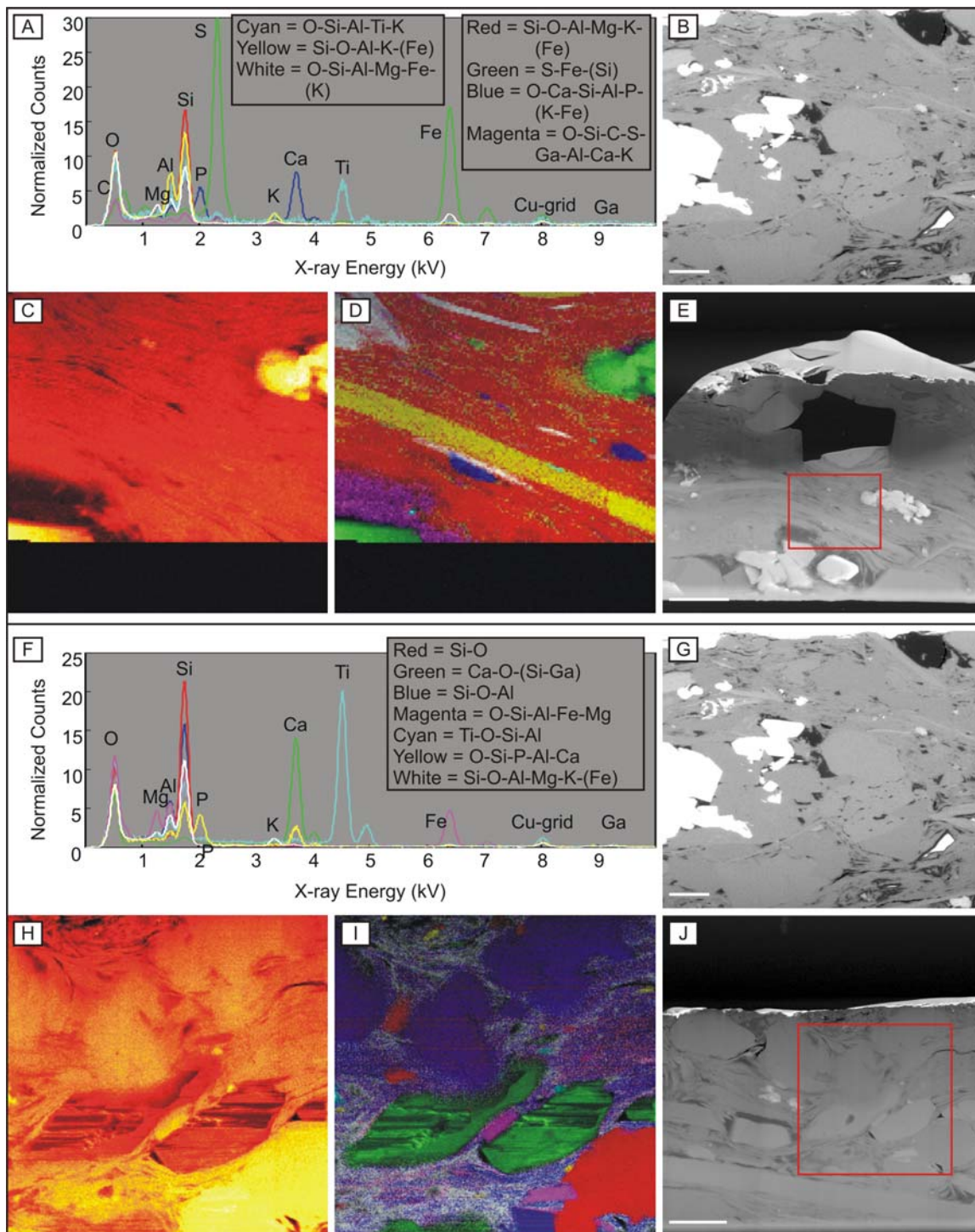


Figure 4.7. (Caption on preceding page.)

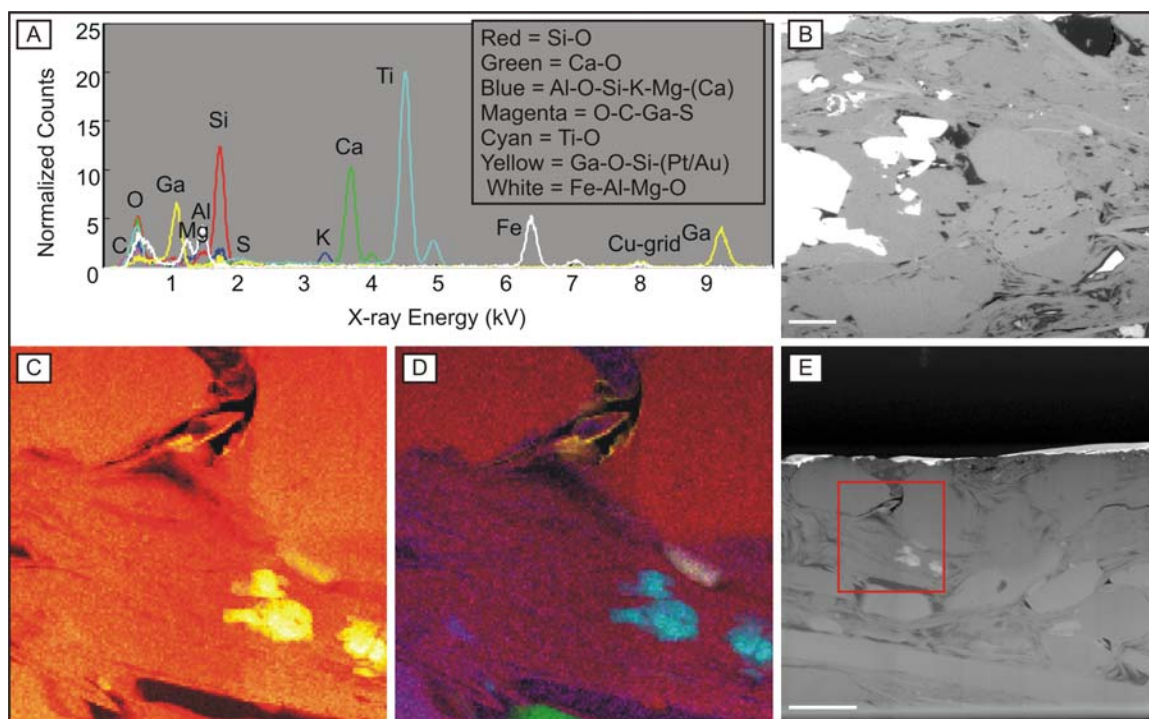


Figure 4.8. Results of scanning transmission electron microscopy (STEM) imaging combined with energy-dispersive X-ray spectroscopy for a Gothic shale sample, along with the last focused ion beam (FIB) images from sets of serial sections. (a) through (e) correspond to sample Gothic shale 5390.8B, but at a different location than in Figure 4.7. (a) Spectral shapes of chemical phases determined by the multivariate statistical analysis (MSA) of the X-ray spectral image. Normalization of the y axis is such that, for a particular chemical phase, the product of the normalized counts and the intensity of the corresponding component image results in counts equivalent to the original X-ray counts. In the legend, elements with relatively low counts still above background noise are given in parentheses. (b) The last backscattered electron image for a set of FIB serial sections (see Chapter 3). Scale bar is 2 μm . (c) Total X-ray output image with hotter colors corresponding to higher output. Horizontal field of view is 3000 nm and has 20 nm/pixel resolution. (d) High-contrast component image that displays spatial rendering of the MSA chemical phases. Colors correspond with those of the spectral shapes. (e) High-angle annular dark-field STEM image taken $\leq 3 \mu\text{m}$ from the location of the corresponding set of FIB serials. Red box delineate regions of the X-ray spectral images. Scale bars are 2 μm .

dark field images corresponds to mean Z, with higher Z associated with lighter grayscale values.

Artifacts revealed by STEM and MSA chemical component images include minor deposition of milled material or “resputter” on many STEM foils. Resputter accumulates predominantly in open voids. Its composition includes elements typically found in the mudstones along with Ga, Pt, Au, or Pd, which clearly indicate exogenous material from the gold-palladium coating or the Pt deposition at the top of the samples (which were used in the FIB/SEM study; see Chapter 3). Chemical phase and dark field images of the samples lower Kirtland 2692.9A and Lower Tuscaloosa 8590.9 (Figures 4.3j, 4d, and 4e) reveal pieces of gold-palladium material that moved from the outside of the sample to the STEM foil. Organic-rich chemical phases typically included a minor amount of Ga, which suggests the relatively long penetration range of the heavy milling ion in the low Z organics. Non-uniform sample thickness affects variation of grayscale in the dark field images, as well as the X-ray counts from oxygen. Beam damage of some carbonate phases occurred during STEM data collection (most clearly seen in Figure 4.7h and j), as indicated by parallel lines in X-ray output and chemical phase images. Finally, Figure 4.6j shows bright areas of charging that represent non-sample material on the STEM foils.

Data for mudstones are presented in order from proximal to distal or deeper water depositional settings of the samples (see Chapter 3 for more information on geologic settings). Dark-field and chemical phase images for sample upper Kirtland 2049.7B reveal an intermixed clay-rich region with two dominant phases that probably correspond with chlorite and smectite minerals (Figure 4.3a–e; green phase = smectite; red phase =

chlorite). The red phase of Figure 4.3d has higher mean Z due to the higher Fe content and thus a brighter grayscale value than the green phase in the dark-field images. The two phases appear to be interstratified smectite/chlorite, which may represent chloritization of an initial smectitic clay (cf. Salem et al., 2000; Hints et al., 2006). Packages of the phases can have curved outlines. Pores occur predominantly in the green/darker grayscale phase or at boundaries between the two phases (Figure 4.3d). A relatively large, sinuous pore may indicate an induced (i.e., not found at *in situ* conditions) pull-back structure due to desiccation of the probable smectite (Figure 4.3c–e). Pores tend to be generally planar when located between or near clay sheets. Triangular or less planar pores occur at the meeting of discrete packages of phases. Resputter occurred at the sinuous pore (Figure 3d). Correspondence between distinct features in the last FIB/SEM serial and the STEM foil were not identified.

The STEM and chemical images for Lower Kirtland 2692.9A indicate quartz, clay, and a minor Ti-rich phase within a larger region of carbonate. The Ti-phase is not ilmenite as it lacks a strong Fe peak in the spectral shape, nor is it titanite due to the relatively low Si peak (Figure 4.3f–j). Clays contain significant calcium and lesser iron, magnesium, manganese, and potassium peaks. The carbonate, probably calcite, may represent mineralization in a fracture or poikilotopic cementation. Thin section examination and XRD do not support calcite mineralization as a spatially dominant feature in the rock sample (see Chapter 3 for petrographic and XRD data). Thus, the STEM foil and FIB/SEM serials sampled a local, non-representative feature. The FIB/SEM serial (Figure 4.3g) has sub-horizontal, acicular/planar and jagged voids that are similar to those of the STEM image; although a one-to-one correspondence between

features does not occur (Figures 4.3g and 4.3j). The proximity of the pores to the upper sample surface may indicate that they were induced during sample preparation. However, pores in the STEM image appear stylolitic based on their jagged, dentate morphology. Thus, the pores may be diagenetic stylolitic features with surrounding pore-lining carbonate/calcite precipitation and residual clay material, which is likely calcium smectite (note the location of clays near the pores in Figure 4.3i).

For sample Lower Tuscaloosa 8590, a quartz grain (in red), clays, and a Ti-rich phase are indicated by the spectral shapes (Figure 4.4a–e). A piece of gold-palladium coating, an artifact, is also indicated (in green). Resputter is in yellow. Clays may include illite, chlorite, and kaolinite (Figure 4.4a). The brighter grayscale mineral in Figure 4.4b is probably chlorite. The large pore near the quartz and clay boundary may be an induced feature (i.e., not present *in situ*), as suggested by its large size in comparison to the rest of the sample. Pores visible in Figure 4.4b may be adjacent to chlorite (brighter grayscale) and other clay minerals.

The STEM and chemical phase images for sample Marine Tuscaloosa 7925.5 show clay- and organic-dominated regions (Figures 4.4f–j and 4.5a–e; magenta = organics). The organics have relatively low X-ray output compared to other phases (Figures 4.4h and 4.5c). The boundary between the clays and organics is wavy and convolute. Some clays appear isolated within the organics in the 2D images. Ga^+ penetrated into the low Z organics as evinced by spectral shape of the organics (Figure 4.4f; magenta = organics; the magenta phase includes O, C, Ga, S, and Cl as dominant elements). Vertical thickness of organics in the 2D FIB/SEM image (Figure 4.4g) can exceed two μm . Spectral shapes for clays and sheet-like morphology visible in STEM

images indicate possible muscovite (Figure 4i, green phase), which is consistent with thin section observations (see Chapter 3). The iron-rich chemical clay phases may be chlorite (Figure 4.4f). MSA phases also indicate possible kaolinite (red portions in Figure 4.4i). Resputter occurred into an open pore (yellow portions in Figures 4.4i and 4.5d). Pores within the organics are visible on the FIB/SEM (in backscatter electron mode) image (Figure 4.4g). Resputter accumulates in the pores as shown on Figure 4.4i in yellow. The pore shapes in the organic material are more circular than the slit/sheet-shaped pores in the surrounding clays (Figure 4.4g; also see Chapter 3). Figures 4.5d and e indicate possible illite as a pore-lining phase for slit-shaped pores.

Marine Tuscaloosa 7931.0 STEM samples (Figs. 4.5f–j and 6a–e) reveal pyrite framboids with intergranular pores with possible, surrounding siderite (Figure 4.5d; green = pyrite; magenta = siderite?). Clays are likely chlorite, illite, and kaolinite based on spectral shapes (Figs. 4.5f and 4.6a). Quartz is identified as the red phase in Figure 4.5i. A titanium-rich phase occurs as small grains. Resputter occurred (yellow phase) at the large horizontal separation in the images. The separation was induced due to sample preparation. Clay fabric is visible with small, slit-like pores surrounded by mainly illite (and minor kaolinite; Figure 4.5i, blue phase). An organic phase in Figure 4.6d (organic = magenta) is next to a pore that is also surrounded by what appears to be kaolinite.

Spectral shapes of Gothic shale samples indicate clay minerals that may include (degraded) mica (possibly biotite), smectite, chlorite, and illite (Figures 4.6f, 4.7a, 4.7f, and 4.8a). Other phases of probably detrital clasts include quartz, a titanium-rich phase, apatite, calcite (Figure 4.7i; green = calcite; red = quartz). Pyrite occurs as framboids and in other crystal habits (Figure 4.6g; Figure 4.7d, green = pyrite). Organics have a low X-

ray output (Figures 4.6h and 4.5i) and fill regions surrounding both clay minerals and detrital clasts, possibly indicating that the organics were once mobile and filled pre-existing porosity, or the organics were deformed around other grains, or both. Pores in Figures 4.7g–j and 4.8b–e have triangular to irregular shapes that differ from the slit-shaped pores within clays in other samples. These non-slit pores are lined by quartz, organics, calcite, and probable illite.

4.4.2 Summary of Pore-Lining Mineralogy Versus Bulk Mineralogy

Table 4.1 presents a summary of the pore types and pore-lining phases from the STEM/EDS analysis and includes XRD data. The XRD data are sourced from reports by or for SECARB and SWP (DOE, 2008; Chidsey et al., 2010; see Appendix B.2.1). Pore types include: slit-like (or sheet-like in 3D; see Chapter 3) pores in clays; possibly stylolitic pores associated with residual clays; non-slit-like pores in diagenetic clays (e.g., chlorite); non-slit-like pores associated with detrital clays; and circular to crescent shaped pores within or associated with organics. Major pore-lining phases include smectite, illite, organics, calcite, and quartz. Results of XRD analysis are consistent with these phases.

For the upper shale member of the Kirtland Formation, the high smectite in the XRD does correspond to the dominant STEM/EDS pore-lining phase. XRD for the lower shale member of the Kirtland Formation sample does not correspond to the major STEM/EDS, which is calcite. This is probably due to non-representative sampling of the STEM foil. For the Lower Tuscaloosa Group, the STEM/EDS phases and XRD mineralogies for the clay correspond to each other. For the Marine Tuscaloosa Group, no indication of the presence of the dominant pores in organics is given by the XRD data

because XRD applies to crystalline phases. Also, the illite chemical phase is dominant but does not have the highest XRD wt % of the clays. Chemical phases for the Gothic shale, except for the organics, are consistent with the XRD results. The possible coating of pores by once-mobile organic phases is not indicated by XRD analysis.

4.4.3 Mercury Intrusion Porosimetry

Figure 4.9 presents MIP results in terms of cumulative and incremental mercury intrusion saturations (see rows (a) and (b), respectively). Cumulative mercury saturation is the cumulative mercury intruded per pressure step divided by the total intruded mercury. Incremental mercury saturation represents the mercury intruded for each pressure step divided by the total intruded mercury. Samples that were first analyzed by FIB/SEM and STEM, and then by MIP are drawn as dashed red lines. The black solid lines represent data without STEM analysis. Incremental curve shapes include unimodal and bimodal distributions (row (b)), which indicate differences in pore structure between the samples. Samples analyzed by directional or omni-directional intrusion are listed in Table 4.2 as are the sample depths.

The samples with MIP curves for the upper shale member of the Kirtland Formation range represent a distance of ~6 m within the formation (see Table 4.1 for sample depths for MIP curves). Three samples of the shallowest depths (Table 4.1) exhibit bimodal distributions, which probably represent larger pores associated with sand- and silt-sized grains (so-called “lacunar” pores; Fies, 1992) and pores within clay fabric. This part of the Kirtland Formation does contain abundant sand and silt grains (see Chapter 3). The corresponding FIB/SEM study revealed that the pores with

Figure 4.9. Cumulative (a) and incremental (b) mercury (Hg) intrusion saturation curves for the upper and lower shale members of the Kirtland Formation, the Lower and Marine Tuscaloosa Groups, and the Gothic shale. Samples that were examined by scanning transmission electron microscopy are given as dashed red lines. For sample depths from the subsurface core, see Table 4.1.

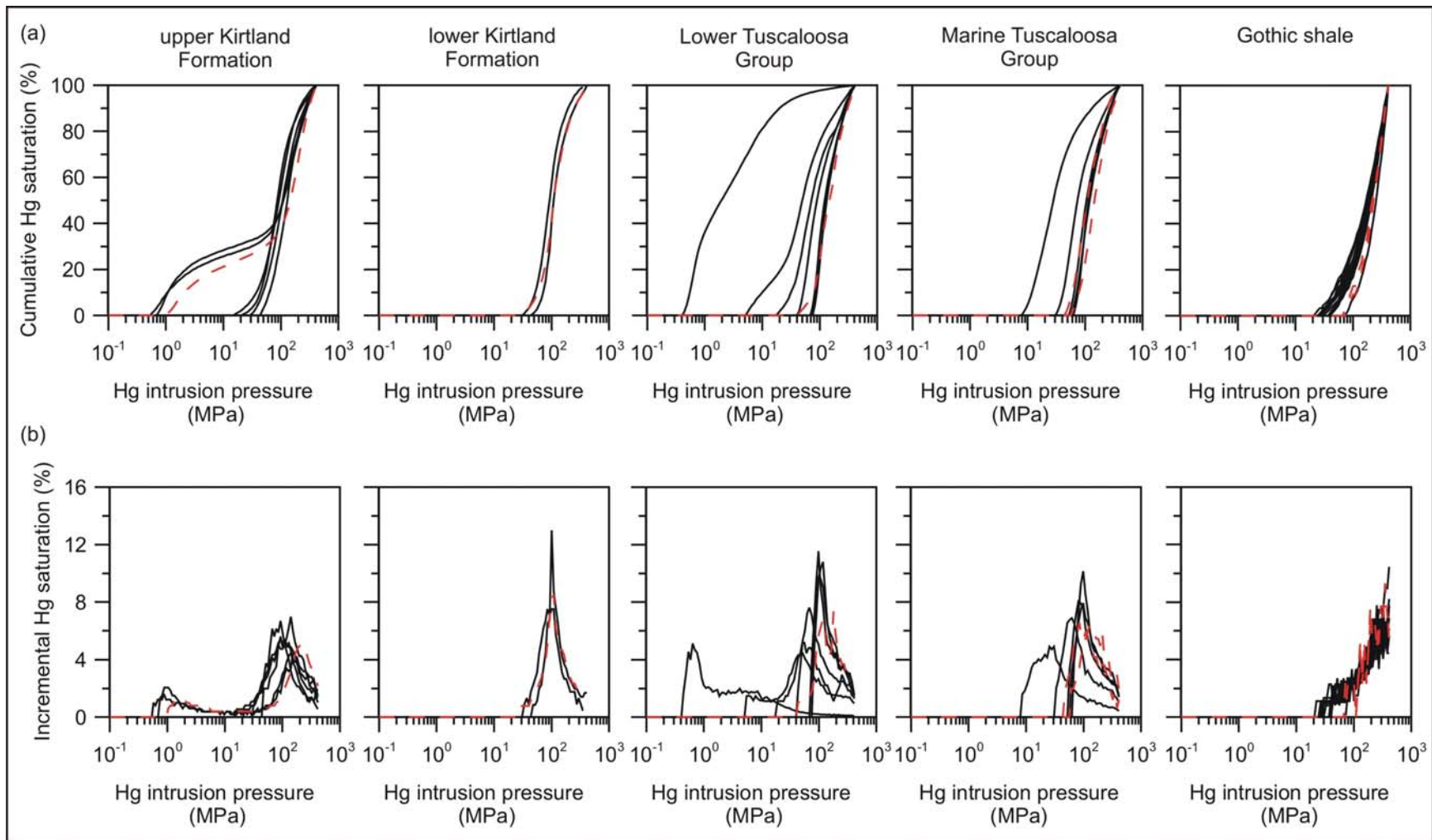


Figure 4.9. (Caption on preceding page.)

clays are slit/sheet-like in morphology (see Chapter 3). The Lower Tuscaloosa Group includes interbeds of sand-, silt-, and clay-rich layers on the scale of a thin section (see Chapter 3), and thus lacunar pores may cause the bimodality. Some samples from the Gothic shale and Lower Tuscaloosa Group have highest corresponding mercury intrusion saturations and pressures. The Tuscaloosa Group samples also show a range of curves shapes, indicating variations in lithology within the formations. The Gothic shale may have two slightly different types of pore structure, as indicated by the two groups of curves (Figure 4.9a) that range over different intrusion pressures.

4.4.4 Breakthrough Pressure

Table 4.2 presents breakthrough pressures estimated from the MIP curves of Figure 4.9. Some curves do not display distinct curvature for picking breakthrough (see Section 4.3.3); in this case, the point of breakthrough pressure is chosen where the rate of mercury intrusion increases rapidly before the first peak in incremental intrusion. We applied Equation 2 (see Section 4.2) to convert the breakthrough pressures to the CO₂/brine/rock systems (Table 4.3). Table 4.3 also gives ranges of IFT and contact angles used for the calculations for the CO₂/brine/rock system, based on the approximate depth and temperature of the geologic units. Interfacial tension and contact angles for mercury/air/rock, also needed for using Equation 2, are assumed to be 480 mN/m and 140°, respectively. Large variations occur in IFT and contact angles for the CO₂/brine/rock system, and thus calculations are made to obtain the largest and smallest CO₂ breakthrough pressure so that the uncertainty will be apparent. The salinity range for IFT for the calculations is from 0 to 144,300 mg/L, as based on Bachu and Bennion's

(2009) data. Contact angle measurements for quartz and mica are made for pressures below 10 MPa in Chiquet et al.'s (2007) study. Fitting straight lines to the higher and lower contact angle values for quartz (expressed as $\cos \theta$) from Chiquet et al.'s (2007) data yields predictions for the pressure conditions of the Tuscaloosa Group (~24 MPa) and the Gothic shale (~16 MPa). Quartz and mica are used here because other data on other caprock solid phases for the CO₂/brine system are lacking in the literature. The CO₂/brine/mica system shows complex behavior in terms of changes in contact angles with pressure (Chiquet et al., 2007a), which may result from changes in brine pH from dissolution of CO₂ into the brine that impacts surface charge of the mica and later wetting by the separate phase CO₂ bubble. Consequently, we fit a line to all the mica data, which shows a general decreasing trend of the $\cos \theta$ with increasing pressure. This fitted line predicts wetting of the minerals by CO₂ at the depths of the Tuscaloosa Group and thus loss of capillary sealing. The Kirtland Formation breakthrough pressure estimates are the least uncertain since the formation's pressure and temperature conditions fall within the ranges of data collected in the literature for IFT. However, the contact angle measurements may not be representative of *in situ* wetting of the dominant smectite clays surrounding pores. To capture the effect of the variation in contact angles, the CO₂ breakthrough estimates use the smallest quartz and largest mica contact angle values. Based on results from Section 4.4.2, quartz is not a dominant pore-lining phase in the clay-rich mudstones.

Figure 4.10 presents the range of pressures needed to induce capillary breakthrough of CO₂, as derived from the MIP curves, as a function of depth. The pressure values are plotted as bars that correspond to the larger and smaller CO₂

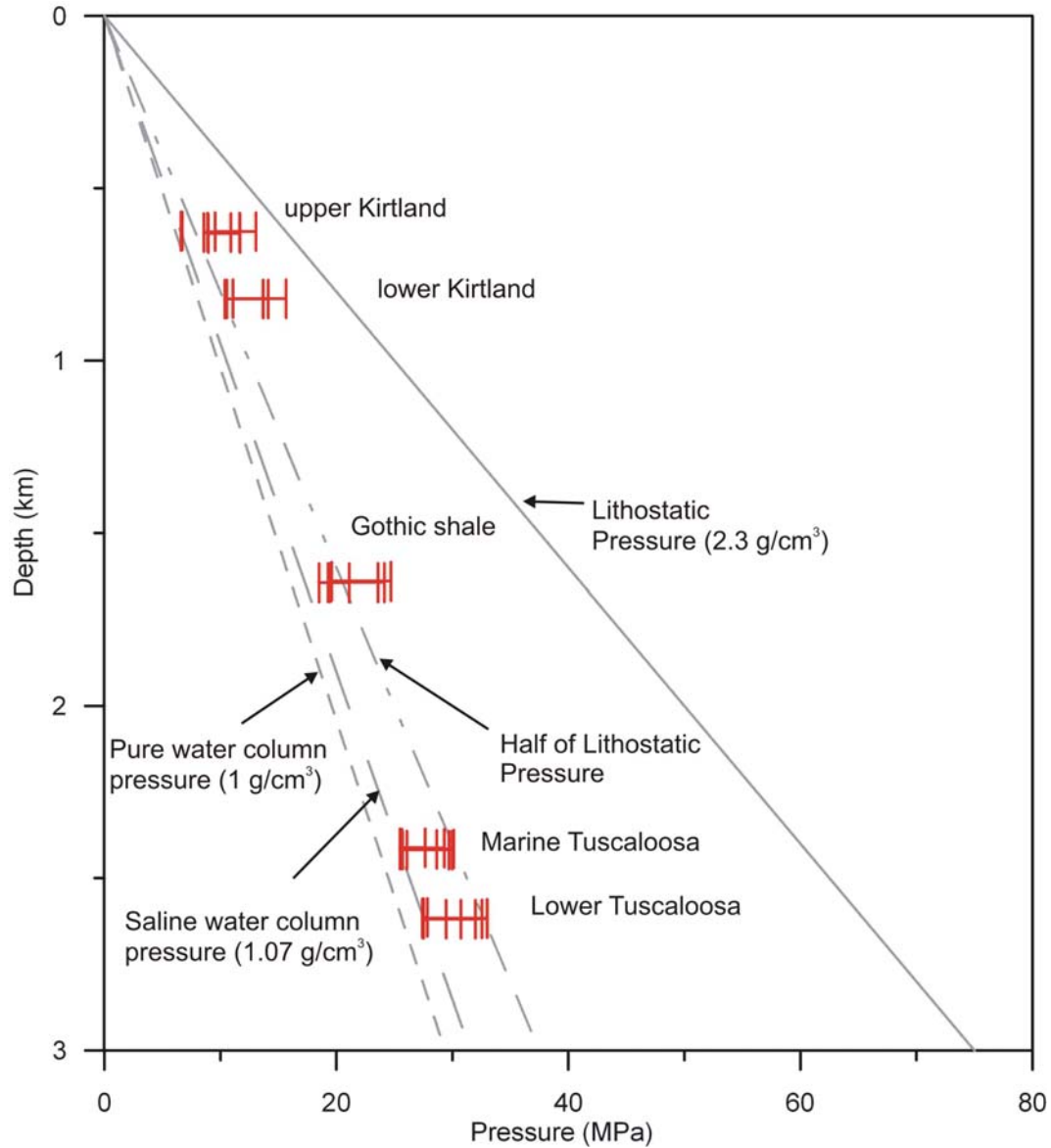


Figure 4.10. CO₂ pressures needed to cause breakthrough versus depth for the suite of five mudstones. Straight lines represent lithostatic and hydrostatic pressure gradients. Annotation on the figure gives the mass of rock and water columns used to generate the pressure gradients.

breakthrough pressures of Table 4.3, but the pressure due to a saline fluid column (water density of 1.07 g/cm³) at the appropriate depths is added to the breakthrough pressure to obtain the CO₂ pressure:

$$P_{CO_2} = P_{\text{capillary breakthrough}} + P_{\text{saline column}} = (P_{CO_2} - P_{\text{saline column}}) + P_{\text{saline column}} \quad (3)$$

Equation 3 is a modification of Equation 1 that isolates the pressure of the non-wetting phase only. Curves for the lithostatic pressure, half of lithostatic pressure, hydrostatic pressure, and a saline hydrostatic water column (Poston and Berg, 1997) are also presented. Assumptions for the lithostatic and saline water column curves are a column of saturated rock (uniform with depth) of 2.3 g/cm^3 and the mass of the saline water column (uniform with depth) of 1.07 g/cm^3 .

4.5. Discussion

As noted above, the bulk mineralogy of samples analyzed in this study does not always represent the phases that actually line pores. If a particular mudstone contains mixtures of clays, our results indicate that expandable smectites are more likely to line pores as opposed to less expandable clays (e.g., chlorite). Further study using cryo-FIB/SEM (Desbois et al., 2009) could characterize clays in their natural *in situ* state to investigate if the pores observed in our samples were induced by drying of the samples. Organics observed in the marine mudstones (i.e., Marine Tuscaloosa Group and Gothic shale) indicate pore types that have much different wetting characteristics than the siliciclastic minerals, and in some cases, the once-mobile organics may line pores that may have originally been lined by clay minerals. Thus, in some systems, organics may modify previously water-wetting pathways to being hydrophobic. Although our study did not focus on lacunar pores (Pore Type III, of Desbois et al., 2009) that are associated with relatively large silt or sand grains, pore-lining minerals on such grains may shield fluids from contacting the grains (often quartz or feldspar).

Using MIP breakthrough pressures to predict CO₂ breakthrough pressures is highly uncertain due to the lack of data on contact angles for the caprock phases identified in this study. In the contact angle study by Chiquet et al. (2007), muscovite displays complex wetting characteristics that may be due to evolving pH conditions (Chiquet et al., 2007). Other phyllosilicates with charged surface sites may have strong interactions with water or CO₂ due to the polar and quadrupolar nature (Raveendran et al., 2005), respectively, of the two molecules. A mechanistic study of these interactions, perhaps via molecular dynamics modeling, is needed to constrain and explain wetting characteristics. Our study relies on a simple linear fit to Chiquet et al.'s (2007a) data for mica, which might not be appropriate at high pressures (> 10 MPa). Wetting by CO₂ is suggested at the highest pressure and temperature conditions of the Lower Tuscaloosa Group for a mica (or rather mica-like) dominated caprock (Figure 4.10; left hand side of bars represents mica and right hand side represents quartz-dominated wetting).

The upper and lower Kirtland Formation samples (the red bars at the shallowest depths of Figure 4.10) show that most of the upper Kirtland Formation and the lower Kirtland formation will act as a capillary seal—the pressure to achieve breakthrough would have to reach that of 0.5 times the lithostatic, which would probably fracture the rock before causing CO₂ breakthrough. Half of lithostatic is used here as a “rule of thumb” to indicate pore pressures that would lead to failure/fracturing of the rocks (Ingebritsen et al., 2006). Only the samples at the very top of the upper Kirtland Formation would have CO₂ breakthrough with little change from hydrostatic conditions. The high sealing is indicated even for the “mica” wetting case and certainly for the “quartz” case. The Gothic shale and Tuscaloosa Group exhibits poor sealing if the system

were dominated with mica-like wetting and high sealing if dominated by quartz-like wetting. The presence of organic-coated pores may indicate an “oil-wet” pathway that may facilitate CO₂ transport. Further study on CO₂ interactions with solid organics in caprocks is needed for characterizing if CO₂ will wet the organics.

4.6. Conclusions

Based on this study, the shallower formations (< ~800 km) are better capillary seals for CO₂ as compared to the deeper formations. For these formations, the caprocks seal by capillarity, which may be a major concern when designing a sequestration project. For the deeper formations, capillary breakthrough may occur much more readily due to changes in water wetting with increased pressure and temperature, and thus an understanding of relative permeability may be more important than characterizing breakthrough pressure. In both cases, knowledge of interactions of CO₂ with organics and clays phases is needed to predict possible alteration of the pore network and changes in breakthrough and transport processes with time. Pore-lining mineral phases are not directly indicated by bulk XRD data for the mudstones, but rather by scanning transmission electron microscopy with energy dispersive X-ray spectroscopy.

Acknowledgments

The U.S. Department of Energy (DOE) funded TEM and MIP through the Southwest Regional Partnership on Carbon Sequestration and DOE’s Office of Basic Energy Sciences, Division of Chemical Sciences, Geosciences, and Biosciences. Robin Petrusak and Thomas Chidsey, Jr., respectively of the Southeast Regional Carbon

Sequestration Partnership (SECARB) and SWP, provided rock samples. We thank Fabian Duque-Botero of Chevron's Seal and Trap Team for helpful discussions of the interpretation of MIP. Jim Krumhansl of Sandia National Laboratories assisted in interpreting pore-lining phases. Sandia National Laboratories is a multi-program laboratory operated by Sandia Corporation, a wholly owned subsidiary of Lockheed Martin Company, for the U.S. Department of Energy's National Nuclear Security Administration under contract DE-AC04-94AL85000.

References

- Almon, W.R., Dawson, W.C., Botero-Duque, F., Goggin, L.R., Yun, J.W., 2008. Seal analysis workshop, printed materials, Chevron Energy Technology Company: held at the Joint Annual Meeting of the Geological Society of America, Soil Science Society of America, American Society of Agronomy, Crop Science Society of America, and the Gulf Coast Association of Geological Studies with the Gulf Coast Section of SEPM, October 5–9, Houston, Texas.
- Almon, W.R., Dawson, W.C., Ethridge, F.G., Rietsch, E., Sutton, S.J., Castelblanco-Torres, B., 2005. Sedimentology and petrophysical character of Cretaceous Marine Shale sequences in foreland basins—potential seismic response issues, *in*: Boulton, P., Kaldi, J. (Eds.), *Evaluating Fault and Cap Rock Seals*, pp. 215–235.
- Andreani, M., Gouze, P., Luquot, L., Jouanna, P., 2008. Changes in seal capacity of fractured claystone caprocks induced by dissolved and gaseous CO₂ seepage. *Geophys. Res. Lett.* 35, 6.
- Bachu, S., Bennion, D.B., 2009. Interfacial Tension between CO₂, Freshwater, and Brine in the Range of Pressure from (2 to 27) MPa, Temperature from (20 to 125) degrees C, and Water Salinity from (0 to 334 000) mg(·)L(-1). *J. Chem. Eng. Data* 54, 765–775.
- Berg, R.R., 1975. Capillary pressures in stratigraphic traps. *AAPG Bull.* 59, 939–956.
- Chalbaud, C., Robin, M., Lombard, J.M., Martin, F., Egermann, P., Bertin, H., 2009. Interfacial tension measurements and wettability evaluation for geological CO₂ storage. *Adv. Water Resour.* 32, 98–109.

- Chidsey, T.C.J., Heath, J., Dewers, T., 2010. The Gothic shale in the Aneth Unit: Seal for hydrocarbons and CO₂ geologic sequestration: *Report by the Utah Geological Survey for the Southwest Regional Partnership on Carbon Sequestration*, U.S. Department of Energy.
- Chiquet, P., Broseta, D., Thibeau, S., 2007a. Wettability alteration of caprock minerals by carbon dioxide. *Geofluids* 7, 112–122.
- Chiquet, P., Daridon, J.L., Broseta, D., Thibeau, S., 2007b. CO₂/water interfacial tensions under pressure and temperature conditions of CO₂ geological storage. *Energy Conversion and Management* 48, 736–744.
- Colombo, I., Carli, F., 1981. Measurement of compressibility coefficient of nonporous polymer powders by mercury porosimetry. *Powder Technology* 29, 285–287.
- Cook, R.A., Hover, K.C., 1993. Mercury porosimetry of cement-based materials and associated correction factors. *ACI Mater. J.* 90, 152–161.
- Desbois, G., Urai, J.L., Kukla, P.A., 2009. Morphology of the pore space in claystones -- evidence from BIB/FIB ion beam sectioning and cryo-SEM observations. *eEarth* 4, 15–22.
- Dewhurst, D.N., Hennig, A.L., 2003. Geomechanical properties related to top seal leakage in the Carnarvon Basin, Northwest Shelf, Australia. *Petroleum Geoscience* 9, 255–263.
- Dewhurst, D.N., Jones, R.M., Raven, M.D., 2002. Microstructural and petrophysical characterization of Muderong Shale: Application to top seal risking. *Petroleum Geoscience* 8, 371–383.
- DOE, 2008. *Geologic characterization of the Lower Tuscaloosa Formation for the Phase II saline reservoir injection pilot test, Jackson County, Mississippi—volume II, appendices*, FY2008 annual report for geologic characterization task, Southeast Regional Carbon Sequestration Partnership (SECARB): prepared by Advanced Resources International, Arlington, VA, for the Electric Power Research Institute and the Southern States Energy Board, three volumes.
- Dullien, F.A.L., 1992. *Porous media—fluid transport and pore structure, Second Edition*. Academic Press, Inc., London, UK.
- Fies, J.C., 1992. Analysis of soil textural porosity relative to skeleton particle size, using mercury porosimetry. *Soil Science Society of America Journal* 56, 1062–1067.
- Hildenbrand, A., Schlomer, S., Krooss, B.M., 2002. Gas breakthrough experiments on fine-grained sedimentary rocks. *Geofluids* 2, 3–23.

- Hildenbrand, A., Schlomer, S., Krooss, B.M., Littke, R., 2004. Gas breakthrough experiments on pelitic rocks: comparative study with N₂, CO₂ and CH₄. *Geofluids* 4, 61–80.
- Ingebritsen, S.E., Sanford, W.E., Neuzil, C.E., 2006. *Groundwater in Geologic Processes, second edition*. Cambridge University Press, Cambridge, United Kingdom.
- IPCC, 2005. *IPCC special report on carbon dioxide capture and storage*, prepared by Working Group III of the Intergovernmental Panel on Climate Change. Cambridge University Press, Cambridge, United Kingdom and New York, NY, USA.
- Keenan, M.R., 2009. Exploiting spatial-domain simplicity in spectral image analysis. *Surface and Interface Analysis* 41, 79–87.
- Keenan, M.R., Kotula, P.G., 2004. Accounting for Poisson noise in the multivariate analysis of ToF-SIMS spectrum images. *Surface and Interface Analysis* 36, 203–212.
- Kotula, P.G., Keenan, M.R., 2006. Application of multivariate statistical analysis to STEM X-ray spectral images: Interfacial analysis in microelectronics: *Microscopy and Microanalysis* 12, 538–544.
- Kotula, P.G., Keenan, M.R., Michael, J.R., 2003. Automated analysis of SEM X-ray spectral images: A powerful new microanalysis tool. *Microscopy and Microanalysis* 9, 1–17.
- Kotula, P.G., Keenan, M.R., Michael, J.R., 2006. Tomographic spectral imaging with focused ion beam/scanning electron microscopy/energy-dispersive spectroscopy and multivariate statistical analysis: Comprehensive three-dimensional microanalysis. *Scanning* 28, 63–63.
- Li, S., Dong, M., Li, Z., Huang, S., Qing, H., Nickel, E., 2005. Gas breakthrough pressure for hydrocarbon reservoir seal rocks: Implications for the security of long-term CO₂ storage in the Weyburn field. *Geofluids* 5, 326–334.
- Litynski, J.T., Plasynski, S., McIlvried, H.G., Mahoney, C., Srivastava, R.D., 2008. The United States Department of Energy's Regional Carbon Sequestration Partnerships Program Validation Phase. *Environment International* 34, 127–138.
- Poston, S.W., Berg, R.R., 1997. *Overpressured Gas Reservoirs*. Society of Petroleum Engineers, Inc., Richardson, TX.
- Raveendran, P., Ikushima, Y., Wallen, S.L., 2005. Polar attributes of supercritical carbon dioxide. *Accounts of Chemical Research* 38, 478–485.

- Schieber, J., 1999. Distribution and deposition of mudstone facies in the Upper Devonian Sonyea Group of New York. *Journal of Sedimentary Research* 69, 909–925.
- Schowalter, T.T., 1979. Mechanics of secondary hydrocarbon migration and entrapment. *AAPG Bull.* 63, 723–760.
- Shaffer, G., 2010. Long-term effectiveness and consequences of carbon dioxide sequestration. *Nature Geoscience* 3, 464–467.
- Sneider, R.M., Sneider, J.S., Bolger, G.W., Neasham, J.W., 1997. Comparison of seal capacity determinations: conventional cores vs. cuttings, *in*: Surdam, R.C. (Ed.), Seals, Traps, and the Petroleum System: *AAPG Memoir* 67, p. 1–12.
- Washburn, E.W., 1921. The dynamics of capillary flow. *Physical Review* 17, 273–283.
- Wilson, E.J., Friedmann, S.J., Pollak, M.F., 2007. Research for deployment: Incorporating risk, regulation, and liability for carbon capture and sequestration. *Environ. Sci. Technol.* 41, 5945–5952.
- Wirth, R., 2009. Focused ion beam (FIB) combined with SEM and TEM: Advanced analytical tools for studies of chemical composition, microstructure and crystal structure in geomaterials on a nanometre scale, pp. 217–229.
- Wollenweber, J., Alles, S., Busch, A., Krooss, B.M., Stanjek, H., Littke, R., 2010. Experimental investigation of the CO₂ sealing efficiency of caprocks. *International Journal of Greenhouse Gas Control* 4, 231–241.

**PART III. MULTI-SCALE EVALUATION OF SEALING BEHAVIOR
USING NATURAL TRACERS**

CHAPTER 5. THE HELIUM LEAK DETECTOR AND MULTI-SCALE ASSESSMENT OF CAPROCK SEALING BEHAVIOR⁷

ABSTRACT

The study of caprocks is a multi-scale endeavor. Caprocks impede movement of fluids by means of viscous and capillary forces, due to their small pores. However, larger-scale fractures, faults, or other “seal bypass systems” can circumvent the pore networks and lead to significant fluid migration through a caprock. Measurements of natural noble gas concentrations, especially helium-4 (⁴He), provide key insight into the ability of caprocks to retain fluids. Transport of noble gases can indicate the extent to which fractures or large-scale features bypass the small-scale pore networks that may contribute to high sealing capacity. Study of a regional caprock—the Kirtland Formation, San Juan Basin, USA—at the pore-network scale indicates high capillary sealing capacity and low permeabilities. Core and well-scale data, however, indicate a potential seal bypass system as evidenced by multiple mineralized fractures and methane gas saturations within the caprock. Our interpretation of ⁴He concentrations, measured at the top and bottom of the caprock, suggests low fluid fluxes through the caprock: 1) Of the total ⁴He produced *in situ* (i.e., at the locations of sampling) by U and Th decay since

⁷Heath, J.E., McPherson, B.J.O.L., Dewers, T.A., Phillips, F.M., Rinehart, A.J., The helium leak detector and multi-scale assessment of caprock sealing behavior, prepared for submission to the *AAPG Bulletin*, not submitted as of this writing.

deposition of the Kirtland Formation, a large portion still resides in the pore fluids. 2) Simple advection-only and advection-diffusion models, using the measured ^4He concentrations, indicate low permeability ($\sim 10^{-20} \text{ m}^2$ or lower) for the thickness of the Kirtland Formation. These findings, however, do not guarantee the lack of a large-scale bypass system. The measured data, located near the boundary conditions of the models (i.e., the overlying and underlying aquifers), limit our testing of conceptual models and the sensitivity of model parameterization. Thus, we suggest approaches for future studies to better assess the presence or lack of a seal bypass system at this particular site and for other sites in general.

INTRODUCTION

Processes acting over a large range of spatial and temporal scales affect the ability of “sealing sequences”, “seals”, or “caprocks” to retain hydrocarbons or other fluids within a reservoir. These terms in quotations refer to generally low permeability, high capillary-breakthrough pressure geologic units that overlie a reservoir, and “seal” can also apply to faults that impede fluid flow (Cartwright et al., 2007). Nanometer- to μm -scale pore networks contribute resistance to multiphase fluid transport by viscous and capillary forces (Hildenbrand et al., 2004). However, larger-scale, high-permeability “seal bypass systems” can cause significant fluid migration through a sealing sequence. Examples include fracture networks, faults, injectites, or sedimentary facies changes (Ingram et al., 1997; Cartwright et al., 2007). Seal bypass systems can evolve through time due to coupled hydrological, geochemical, or geomechanical processes (Eichhubl and Boles, 2000). Engineered activities, such as underground storage of CO_2 , require

prediction of the response of the seal/reservoir system to induced perturbations (Rohmer and Bouc, 2010).

The majority of research on sealing sequences has focused on two major scales—the plug scale or smaller and that of large faults. The scale in between, however, has received much less attention. Researchers use measurements on core plugs or smaller samples to determine capillary-breakthrough pressures and permeability of the matrix in order to estimate hydrocarbon or CO₂ column heights retained by capillarity, characterize capillary breakthrough, describe mechanisms of overpressure generation, and estimate potential fluxes of fluids through unfractured matrix (Berg, 1975; Schowalter, 1979; Aplin et al., 1999; Hildenbrand et al., 2004; Yang and Aplin, 2007). The scale of large faults or other high permeability features (e.g., dissolution pipes) typically includes those features that are resolvable by seismic surveys (Boult and Kaldi, 2005; Cartwright et al., 2007). Additionally, wellbores can constitute a significant risk as a man-made seal bypass system (Nordbotten et al., 2009).

Faults, fractures, or other potential seal bypass systems not resolvable by seismic surveys can be difficult to identify and characterize. Even when identified (e.g., via well logging by microresistivity methods), knowledge of their spatial dimensions, their connectivity through a sealing sequence, and their ability to transmit fluids is difficult to ascertain. Numerical modeling is typically used to predict reactivation and potential transport behavior (Chiaramonte et al., 2008).

CO₂ storage, in particular, poses challenges of predicting seal behavior under perturbed conditions. It may be implemented at the large scale in deep, “saline” aquifers/reservoirs below sealing sequences where few deep wells have been drilled

(IPCC, 2005; Orr, 2009). In such systems, the *a priori* ability of sealing sequences to contain buoyant, non-aqueous phases is not immediately apparent as hydrocarbons may never have been in these systems (IPCC, 2005). Recent research addresses possible migration of CO₂ through preferential flowpaths with a focus on geochemical, geomechanical, and multiphase flow effects (Johnson et al., 2005; Carey et al., 2007; Gherardi et al., 2007; Andreani et al., 2008; Chiaramonte et al., 2008; Pruess, 2008; Zhang et al., 2008; Heath et al., 2009; Nordbotten et al., 2009; Silin et al., 2009). However, little work has focused on formation-scale bypass systems that may be difficult to resolve with well logging or seismic survey methods. Evaluation of the extent to which pore network properties are bypassed by larger-scale features at field and basin scales, and how these features evolve in time, is a major research challenge (DOE, 2007).

Natural noble gases, especially helium isotopes (i.e., ³He and ⁴He), represent a potentially powerful tool to evaluate the presence (or lack) of seal bypass systems in hydrocarbon or CO₂ systems. Many studies demonstrate that, for aquitard/seal and aquifer/reservoir systems, noble gases facilitate qualitative and quantitative assessment of rates and patterns of groundwater flow, interaction between aquitards and aquifers (e.g., cross-formational flow) over local (e.g., well or field) to regional scales, the presence of preferential flowpaths and associated fluid flow (e.g., connected fractures), residence time distributions, the dominance of diffusion or advection, and interactions between groundwater and a separate fluid phase (e.g., oil, methane, or CO₂) (Castro et al., 1998; Bethke et al., 1999; Rubel et al., 2002; Lippmann et al., 2003; Ma et al., 2005; Bethke and Johnson, 2008; Gilfillan et al., 2008). Consequently, these tracers seem suited to addressing the challenge of characterizing the transmissive nature of seal bypass systems

that may exhibit slow leakage over local to regional scales (DOE, 2007). The application of natural noble gases to explicitly characterize potential seal bypass features at hydrocarbon traps or CO₂ storage sites has so far received little attention, according to our search of the literature (Lafortune et al., 2008).

In this study, we investigate the extent to which μm - to m-scale features and processes govern sealing behavior of the Kirtland Formation, San Juan Basin, USA. We restrict our study to the site of a CO₂ injection demonstration in deep (> 880 m) unmineable coal seams by the Southwest Regional Partnership on Carbon Sequestration (SWP), a project sponsored and managed by the National Energy Technology Laboratory (NETL) of the U.S. Department of Energy (DOE) (Litynski et al., 2008). Our data collection program facilitates investigation of both pore-scale phenomena and possible larger-scale discontinuities or other features that could act as seal bypass systems. These data, in turn, support a multi-scale assessment of the likelihood of CO₂ migration from the storage site.

After a review of the geologic and hydrogeologic setting and the Methods and Materials Section, we sequentially present data and interpretations of caprock transport properties at the pore network scale, the core scale (i.e., hand-sample identification of fractures) and well-log scale, and finally at the scale of the full thickness of the caprock based on noble gas data. Data for each particular scale of assessment is presented with discussion and conclusions on sealing behavior for that scale. We examine progressively larger scale data and the coherency of the data sets in terms of the sealing behavior.

A unique aspect of this work involves the use of natural noble gas data, namely helium and neon, collected from within the upper and lower portions of the Kirtland

Formation, to characterize transport properties and sealing behavior over geologic time scales. Our interpretation of the noble gas data, using models of fluid flow and helium transport through the Kirtland Formation, suggests low fluid fluxes through the caprock and does not invoke a seal bypass system to explain the data. However, our findings do not guarantee the lack of a bypass system due to limitations in the data and models. Thus, we suggest approaches for future studies to better assess the presence or lack of a seal bypass system at this particular site and for other sites in general.

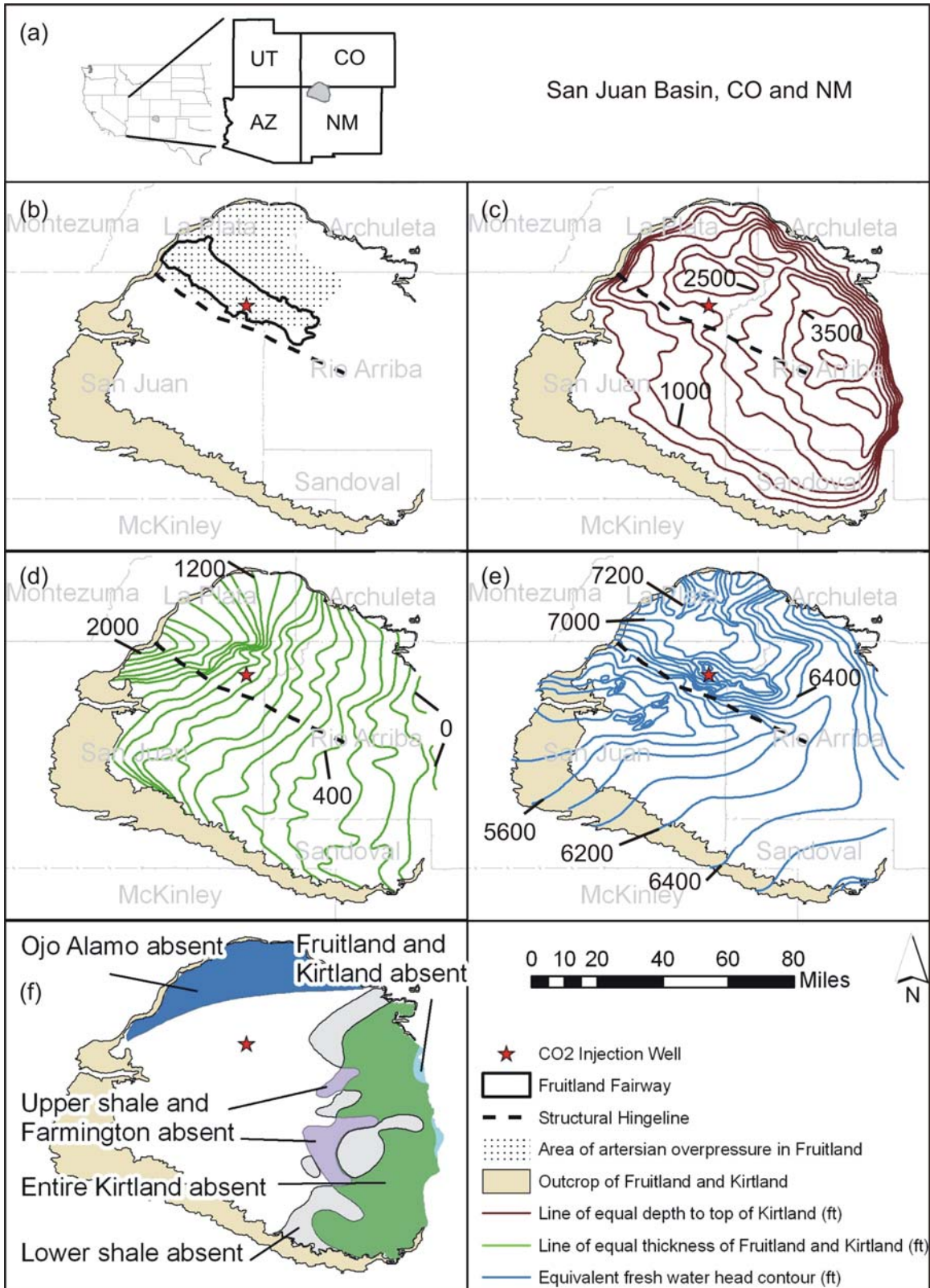
SITE LOCATION AND GEOLOGIC AND HYDROGEOLOGICAL SETTINGS

Location of Coring Program

The study location is the Pump Canyon Site in the north central portion of the San Juan Basin, New Mexico (Figure 5.1). The SWP oversaw drilling of a CO₂ injection well, EPNG Com A Inj 1, in May and June, 2008 (Figures 5.1 and 5.2). The injection site lies within the high permeability Fruitland Fairway, the world's largest and most prolific coalbed methane gas play (Ayers, 2003).

Information on San Juan Basin geology and hydrology follows to facilitate investigation of sealing behavior and transport of natural tracers through the Kirtland Formation. Formations above and below the Kirtland Formation can impact tracer transport and hence are described here.

Figure 5.1. Maps of the San Juan Basin with geologic and hydrologic features. (a) Position of basin within Colorado and New Mexico. (b) Locations of the CO₂ injection well, the outcrop of the combined Fruitland and Kirtland Formations (after Kernodle et al., 1990), the Fruitland Fairway, the structural hingeline, and the area of artesian overpressure in the Fruitland Formation (after Scott et al., 1994). (c) Depth to top of Kirtland Formation (after Kernodle et al., 1990). (d) Thickness of the combined Kirtland and Fruitland Formations (after Kernodle et al., 1990). (e) Potentiometric surface map of the Fruitland Formation based on equivalent fresh water head (after Kaiser et al., 1994). (f) Regions where members of the Kirtland Formation and the Fruitland Formation are absent in the subsurface (after Fassett and Hinds, 1971).



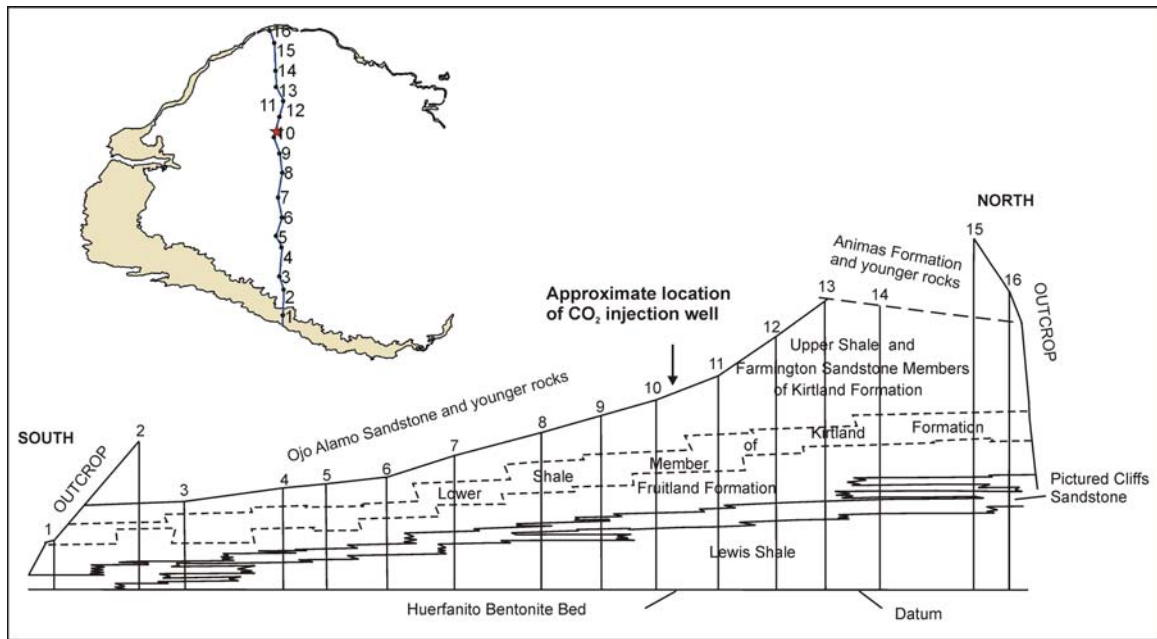


Figure 5.2. North-south cross section through the San Juan Basin with vertical lines that represent wells (adapted from Fassett and Hinds, 1971). The star indicates CO₂ injection well. Numbers on the inset map correspond with the numbers on the cross section.

San Juan Basin Geology

The Kirtland Formation includes a lower shale member, the Farmington Sandstone Member, and an upper shale member (Fassett and Hinds, 1971). Stone (1983) and Molenaar and Baird (1992) developed cross sections for the San Juan Basin using wireline logs, which illustrate a one-to-three member division of the Kirtland Formation depending on the location in the basin and the degree of difficulty in identifying the members due to heterogeneity.

Based on wireline logs, a mud log, and core at the Pump Canyon site, we designate an upper shale member as a unit consisting predominately of interbedded mudstone and sandstone. These data also help delineate the Farmington Sandstone Member, the lower shale member, and the Fruitland Formation (Figure 5.3). The depth of

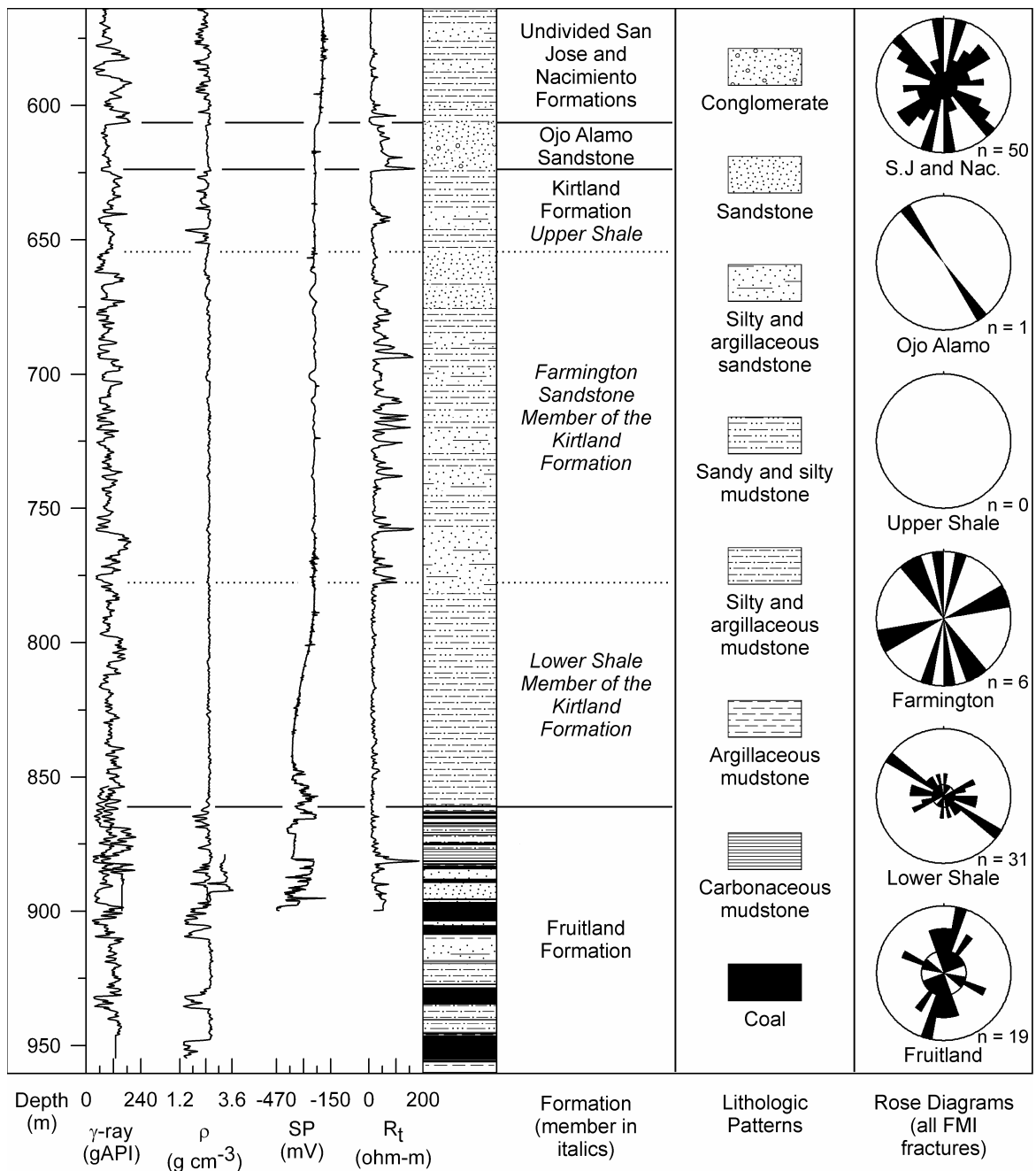


Figure 5.3. Selected wireline logs, lithologic interpretation, and rose diagram fracture orientations from fullbore formation microimager (FMI) logs for well EPNG Com A Inj 1. The lower logging section, starting at a depth of ~696.2 m (2284 ft), was logged on a different date than the upper section. The mismatch of logging data near that depth may be due to casing before the second logging run. The first circle outward from the middle of the rose diagrams corresponds to a fracture measurement of one in the direction of the radial class intervals. North is at the top of the rose diagrams.

the base of the Ojo Alamo Sandstone, which overlies the upper shale member of the Kirtland Formation, is at the location of a scour and disconformity. The top of the Farmington Sandstone Member divides a sequence of silt- and sand-bearing and sandy/silty argillaceous mudstones from a sequence of interbedded sandstones and mudstones. The top of the lower shale member of the Kirtland Formation is at the location of the overall downward-fining sequence, in which the sandstone lenses become less dominant with depth. The top of the Fruitland Formation is at the location of the last carbonaceous mudstone bed within the Fruitland Formation.

Kirtland Formation lithology includes interbedded mudstones (i.e., claystone/shale and siltstone) and sandstone. Existing data suggest it was deposited in the late Cretaceous in an alluvial plain with floodplain and channel environments, landward of the swampy environments of the underlying Fruitland Formation (Fassett and Hinds, 1971; Klute, 1986). The Kirtland Formation lies conformably on the Fruitland Formation throughout most of the basin except in the east where uplift and erosion occurred during the Miocene (Figure 5.1f). Thickness of the undivided Farmington Sandstone and upper shale members ranges from ~0–457 m (0–1500 ft). The lower shale member varies from ~0–137 m (0–450 ft) in thickness with an average of ~61–76 m (200–250 ft) (Fassett and Hinds, 1971). At Pump Canyon, thicknesses of the upper shale, Farmington Sandstone Member, and lower shale members are, respectively, 30.8 m (101 ft), 123 m (404 ft), 83.5 m (274 ft) (Figure 5.3).

The Fruitland Formation contains the primary coal reserves of the San Juan Basin (Ayers, 2003) and extensive sandstone beds that constitute a regional aquifer (Stone et al., 1983). The Fruitland Fairway (Figure 5.1a) is the world's most prolific coalbed

methane play (Ayers, 2003). The Fairway trends northwest in the direction of the structural hingeline of the basin (Figure 5.1a). Fruitland Formation thickness ranges from ~0–152 m (0–500 ft; variable contact makes this estimate uncertain) with an average of ~91–107 m (300–350 ft) (Fassett and Hinds, 1971). CO₂ injection by the SWP targeted coals at depths between ~889.2 m (2917 ft) and 956.5 m (3138 ft) (below ground surface; bgs).

The Tertiary Paleocene Ojo Alamo Sandstone disconformably overlies the Kirtland Formation throughout most of the basin except for the far northern portion of the basin where the Kirtland may be overlain by other Tertiary formations (Figures 5.1f, 5.2, and 5.3; Fassett and Hinds, 1971).

Hydrogeologic Setting and Properties

Although hydrogeologic investigations of Upper Cretaceous and Tertiary formations have focused on the Ojo Alamo Sandstone, Kirtland Formation, Fruitland Formation, and Pictured Cliffs Sandstone, the Fruitland Formation has received the greatest attention due to its coalbed methane plays (Stone et al., 1983; Phillips et al., 1989; Kaiser and Ayers, 1994; Castro et al., 2000; Snyder et al., 2003; Zhou and Ballentine, 2006). Based on potentiometric surface mapping, pressure data, and hydrochemical evaluations, the Fruitland Formation aquifer system is divided into three areas with distinct conditions: Area 1, a region of artesian overpressure north of the basin's structural hingeline in the northwestern area of the basin (Figure 5.1b); Area 2, the underpressured and regional discharge area south of the structural hingeline in the west-central part of the basin; and Area 3, the underpressured region in the south-central

and eastern portions of the basin (Ayers et al., 1994; Kaiser and Ayers, 1994). Some studies include the upper portion of the Pictured Cliffs Formation as a hydrostratigraphic unit with the Fruitland Formation due to similar head values between the two Formations (Kaiser and Ayers, 1994). Area 1 is described here in detail because it contains the Pump Canyon Site, and the hydrogeology is relevant to our sealing assessment.

Recharge of the groundwater system in Area 1 occurs in the northern outcrops of the Fruitland Formation as indicated by the potentiometric surface and outcrop locations (Figure 5.1e). Groundwater flow is generally southward towards the basin's structural hingeline (Figure 5.1e). Overpressure is attributed to natural artesian conditions, driven by topographic forcing, and does not reflect fossil geopressure (Ayers, 2003). The structural hingeline is a location of permeability reduction in the Fruitland Formation, which greatly impacts the regional flow system by causing a strong upward pressure gradient at the hingeline (Figure 5.1e) due to possible pinching out of aquifer coal seams, other sedimentary facies changes, or faulting associated with the hingeline (Kaiser et al., 1994). In the Sedro Canyon-Meridian 400 area, near to the CO₂ injection well, the vertical pressure gradient is ~0.018 MPa/m (0.79 psi/ft), which is greater than the hydrostatic gradient of 0.00979 MPa/m (0.433 psi/ft) and indicates an upward flow gradient (Kaiser and Ayers, 1994).

The artesian hydrodynamic conditions probably developed during the Middle Pliocene (Kaiser and Ayers, 1994) after Miocene uplift and erosion. Maximum heat flow occurred during the Oligocene when the San Juan Mountain volcanic field erupted (Law, 1992; Zhou et al., 2005). Pore waters in the Fruitland Formation north of the hingeline (Area 1) are meteoric as indicated by isotopes of water, chlorinity, potentiometric surface

maps, and estimates of groundwater residence time (Kaiser et al., 1994; Zhou et al., 2005).

Direct measurements of hydrologic properties of the Kirtland Formation are scarce. Farmington Sandstone Member hydraulic conductivity, measured from oil producing well El Paso Natural Gas Company No. 4 Riddle, 36.8651°N and 105.9902°W (sec. 4, T. 30 N., R. 9 W., NMPM), ranges from 6×10^{-9} to 9×10^{-8} m/s (0.002 to 0.03 ft/day; permeability is 6×10^{-16} to 9×10^{-15} m²) (Fassett and Thomaidis, 1978). Kernodle (1996) presents a calibrated three-dimensional (3D) groundwater model for a combined Ojo Alamo, Kirtland Formation, and Fruitland Formation with vertical hydraulic conductivities of 4×10^{-10} to 2×10^{-8} m/s (1×10^{-4} to 0.006 ft/day; permeability is 4×10^{-17} to 2×10^{-15} m²) and horizontal conductivity of 7×10^{-7} m/s (0.2 ft/day; permeability is 7×10^{-14} m²) near the Pump Canyon Site (Kernodle, 1996; his figures 40c and 41). Estimates of the hydrologic properties of the Kirtland Formation can be inferred from a 2D model of regional groundwater flow by Kaiser et al. (1994) for a northeast-southwest cross section through Area 1 and Area 2. Simulations that best fit measured hydraulic head data used horizontal permeability values of 10^{-17} m² (corresponding hydraulic conductivity is 1×10^{-10} m/s or 3×10^{-5} ft/day), 10^{-16} m² (hydraulic conductivity is 1×10^{-9} m/s or 3×10^{-4} ft/day), and 10^{-17} m² (corresponding hydraulic conductivity is 1×10^{-10} m/s or 3×10^{-5} ft/day) for the lower shale, the Farmington Sandstone Member, and upper shale, respectively, with an anisotropy ratio of $k_h/k_v = 100$. For comparison, Stone et al. (1983) reported transmissivity tests ranging from 6×10^{-7} to 1.40×10^{-4} m²/s (0.6 to 130 ft²/day) with a calculated hydraulic conductivity of 3.5×10^{-6} m/s (~1.0 ft/day; corresponding

permeability is $3.6 \times 10^{-13} \text{ m}^2$) for coal beds and associated sediments within the Fruitland Formation.

METHODS AND MATERIALS

Coring Program, Field Sample Preservation, and Well Logging

Fresh core from the lower and upper shale members (Figure 5.3) was obtained for noble gas isotopic determination and for petrographic and petrophysical examination. Two sections of 0.10-m (4.0-in) diameter conventional core were retrieved from the upper and lower members of the Kirtland Formation, beginning in the overlying Ojo Alamo Sandstone at a depth of 615.1 m (2018 ft) (bgs), including 9.04 m (29.7 ft) of Ojo Alamo Sandstone and 6.85 m of upper shale member of Kirtland Formation, respectively. Coring in the lower shale member targeted a clay-rich zone, began at a depth of 819.9 m (2690 ft), and retrieved only 2.53 m (8.3 ft). Difficulties in coring, such as the bit becoming “packed off” with clay, resulted in less core than the intended 18.29-m (60-ft) core barrels for each depth.

Core preservation for noble and other pore fluid gases followed procedures similar to Osenbrück (1998). Prior to field work for this study, specially designed canisters were built from high-vacuum service equipment to seal samples against atmospheric contamination or significant pore fluid degassing (see Appendix B.1). After sub-sampling of core, sample plugs were weighed and placed into the canisters. A purging and vacuum pumpdown process evacuated atmospheric noble gases from the canisters (see Appendix B.1).

Core preservation, in addition to the plugs for noble-gas samples, included transporting core in the aluminum barrels to TerraTek—a Schlumberger company, Salt Lake City—where the core was pieced together and wrapped in cellophane. Six pieces of whole core, each ~0.3 m (i.e., 1 ft) in length, were preserved in wax against drying before slabbing of the core. After slabbing, six thick (butt) sections were preserved against drying.

Schlumberger ran fullbore formation microimager (FMI) microresistivity logs from depths of 98.8 m (324 ft) to 897 m (2943 ft), covering 35.7 m (117 ft) of the interval of sandstone and mudstone within the Fruitland Formation above the significant coal seams (Figure 5.3). Schlumberger analysts compiled fracture orientation data from the FMI logs. A suite of other wireline tools were run, including a SonicScanner tool, that are further described by Wilson et al. (submitted). Fracture characterization data were extracted from the FMI results, and then presented and evaluated with true dip and dip direction. Dipset data were used in the study of the fractures.

Petrographic, Petrophysical, and Geologic Characterization

Mercury intrusion porosimetry (MIP) is used to estimate sealing capacity. For sake of convenience, we define the sealing capacity as the height of a hydrocarbon or CO₂ column that would be retained by a brine-saturated seal (Berg, 1975; Dewhurst et al., 2002). To obtain CO₂ column heights for the Kirtland Formation, omni-directional and directional MIP was performed by Poro-Technology, Sugar Land, Texas, using small pieces and plugs from the core, the plugs being ~0.02 m (0.8 in) long by ~0.02 m (0.8 in) in diameter. The MIP tests were run on a Micromeritics AutoPore IV 9500 Series

porosimeter. To investigate anisotropy, two plugs were cut perpendicular and parallel to bedding and jacketed with epoxy.

TerraTek performed X-ray diffraction (XRD) to determine whole rock mineralogy, including $< 4 \mu\text{m}$ grain-size (i.e., clay size fraction), as well as total organic carbon (TOC) analysis, standard petrographic analysis, and scanning electron microscopy (SEM) with energy dispersive X-ray spectroscopy (EDS). Routine core analysis was performed for porosity, gas permeability, and bulk and grain density on three plugs from the Ojo Alamo Sandstone. Seven samples of the Kirtland Formation were analyzed for (pressure-decay) permeability, porosity, bulk and grain density, and fluid saturations using TerraTek's suite of Tight Rock Analysis (TRA) methods.

Additional thin sections and fluorochrome-epoxied billets were made from samples containing natural, mineralized fractures made parallel with the dip direction or parallel with visible slickenlines. Thick sections or billets up to 1.8 cm thick were prepared from core pieces, also prepared with the fluorochrome epoxy, so that epoxy-filled pore bodies would fluoresce during laser scanning confocal microscopy.

Connected porosity and organic material was imaged using a Zeiss 510-Meta Laser Scanning Confocal Microscope (LSCM). Three-dimensional sections were measured at $5\times$ (voxel size of $1.8 \mu\text{m}$ in x and y and $1.0 \mu\text{m}$ in z) using a Zeiss $5x/0.13\text{NA}$ HD DIC EC Epiplan-Neofluar lens and at $50\times$ (voxel size of 0.36 or $0.18 \mu\text{m}$ in x and y and $1.0 \mu\text{m}$ in z) using a Zeiss $50x/0.55\text{NA}$ DIC LD EC Epiplan-Neofluar lens. Porosity and organic material (including that associated with pyrite nodules) were simultaneously imaged using 543 nm excitation from a HeNe laser and a 560-nm long-pass filter for emissions from the rhodamine-dyed epoxy occupying connected pore

spaces, and 477-nm excitation from an Ar laser and a 745–525 nm band-pass filter for emissions from organic material.

Geometry of submicron-scale 3D pore networks were obtained for Kirtland Formation samples using a FEI Company Helios™ 600 Nanolab DualBeam™ focused ion beam/scanning electron microscopy (FIB/SEM) system (Yao, 2007). The FIB creates serial sections, which are imaged in sequence with a field-emission SEM. Successive milling and imaging yields a series of 2D images that can be stacked and processed to reconstruct 3D pore networks. Additional backscattered electron imaging of fracture mineralization was performed on a JEOL JSM-59002V SEM with a JEOL Shadow Backscatter Detector with EDS mapping using a Zeiss SUPRA 55VP instrument equipped with a Bruker quad silicon drift detector.

Upper and lower member Kirtland Formation core was examined for the presence of natural and induced fractures and lithology. Since the core was extremely friable, especially upon drying, much of the core was reviewed while still wrapped in cellophane.

Noble Gas Analyses

Neon-20 (^{20}Ne), ^3He , and ^4He from pore fluids of preserved core plugs were analyzed at the University of Utah's Dissolved and Noble Gas Laboratory. As described above, core plugs were collected and sealed in vacuum-tight canisters on May 7 and 9, 2008, immediately after two sections of core were brought to ground surface. Due to low solubility of noble gases in water, the gases partitioned from the pore water into the surrounding canister volume (Osenbruck et al., 1998). After transfer of the gases into a purification line, analysis followed methods described by Hendry et al. (2005). Each

sample had high methane concentrations, which necessitated removal of all gases during purification except helium and neon. Thus, concentrations of other gases are unknown except for measurements made during mud logging (see Appendix B.5). Two analysis runs were completed, one in September 2008 and the other in October 2009. The second run was intended as a check on the quantitative release of the noble gases from the pore fluids. Helium and neon data from the two runs were combined to obtain the “total” quantitative release of these gases from the pore space. Due to high helium concentrations, splitting of the original gas samples into aliquots of 1% or 10% was necessary for all samples of the first run except the field blanks; whereas 50% splitting was necessary for two samples during the second run. Helium was diverted into a MAPL 215-50 sector-field linear mass spectrometer for determination of ^3He and ^4He . Neon-20 was analyzed on a quadrupole mass spectrometer. Non-linearity corrections were required for some samples. Analytical precision is approximately 1% for helium and 2% for neon, respectively.

The greatest uncertainty in the concentration of the noble gases is due to the field sampling procedure and estimation of pore volumes. Estimates of uncertainty of noble gas concentration from the core plug samples are based on uncertainties of pore volumes (estimated from the volume of sample material removed from the core and the porosity values) and laboratory analysis using error propagation methods (Harris, 2007). Uncertainty due to possible sampling-related degassing (e.g., due to pressure release during drilling and coring) and loss of noble gases prior to sealing of canisters is not explicitly estimated here. Previous work using similar core sample collection methods estimated noble gas loss prior to sample preservation in canisters to be < 20–30%

(Osenbruck et al., 1998; Sacchi et al., 2001). This previous work used estimates of atmospheric ^{20}Ne in groundwater samples to assess the degree of degassing (Osenbruck et al., 1998). However, this uncertainty estimate of noble gas loss may not be appropriate here because wireline well and mud logs (see Appendix B.5) indicate separate-phase gas (i.e., predominately methane) at various depths within the Kirtland Formation and the overlying Ojo Alamo Sandstone, which may be responsible for some loss of noble gases from the groundwater by degassing (i.e., partitioning of noble gases between the groundwater and the separate gas phase) *in situ*, not just during the time period after coring and before preservation of samples in the canisters. Osenbruck et al. (1998) studied a system that did not have the situation of *in situ* partitioning processes involving noble gases, groundwater, and a separate gas phase (e.g., methane). Furthermore, our system may contain aqueous or sorbed methane that degassed due to pressure release, which is an additional difference from Osenbruck et al.'s (1998) study. Thus, we use the measured concentrations of noble gases for interpretations while being cautious of possible *in situ* or sampling-related degassing.

Atmospheric solubility equilibrium concentrations, or “air saturated water (ASW)” concentrations, of dissolved noble gases in recharging groundwater are a starting reference for interpreting measured concentrations (Kipfer et al., 2002). Methods for estimating ASW concentrations require knowledge of pressure, temperature, and salinity conditions at the recharge area. Elevation is used to estimate pressure. The recharge area for groundwater in the Farmington Sandstone Member of the Kirtland Formation and the Fruitland Formation is most likely along the northern margin of the San Juan Basin (Figure 5.1e). The elevation and mean annual air temperature (from 1900 to 1909) vary,

respectively, from approximately 2,173 to 2,660 m and 5.0 to 6.2°C, for the recharge area (PRISM, 2009; USGS, 2009). Assuming that mean annual ground temperatures can be up to 2°C higher than air temperatures for this area, and that ground temperatures may have been up to 5.5°C cooler during recharge in the past than modern recharge (Stute et al., 1995), and assuming salinity is negligible, we assign a temperature range of 0.5 to 8.2°C and the above elevation range for calculating solubility equilibrium concentrations of ²⁰Ne and helium for ASW using equations by Weiss (1971), as implemented by Kipfer et al. (2002).

KIRTLAND PORE-SCALE PROPERTIES

Nano-Scale FIB/SEM Imaging and Pore-Scale Modeling

This section begins the presentation of data, starting at the nano or pore scale, with discussion and statements on sealing behavior for the scale in question before moving to a larger scale of characterization. A Ga⁺-ion-beam-milled image of upper Kirtland Formation mudstone pore and sedimentary structures from a depth of 624.75 m (2049.7 ft) is shown in Figure 5.4a. This image is one in a set of 319 serial images taken at 25 nm spacing. Backscattered electron imaging was used to image each section, which allows visualization of mineral phases that differ in mean atomic number. Pore bodies (near black gray level) are narrow and slit-shaped, some of which are correlated with mineral phases indicated by variations in grayscale.

Chapter 3 examines pore structures in the Kirtland Formation in detail, and compares mudstone pore types and pore network statistics and topology among several depositional facies. Results suggest that the dominant pore types in the Kirtland

Formation are slit-like pores that often parallel clay mineral planar fabric. Figure 5.4b shows a 3D pore network geometric model constructed from the sequence of images, of which Figure 5.4a is an example. To examine pore-scale hydraulic conductivity, we use this 3D pore network model (see Chapter 3 for more details on this particular example from the upper Kirtland Formation and a sample from the lower Kirtland Formation). The red portions render pores in a cubic $101.5 \mu\text{m}^3$ digital region at 15.6-nm voxel size (see Chapter 3). Shown in blue is a single connected pore network (Figure 5.4c), which is expanded to the right of the figure. Note that the connected pore network consists of large flattened pores several μm in size separated by a small pore throat.

To determine single phase hydraulic conductivity of this pore network subset, we ran a 3D computational fluid dynamics simulation at low Reynolds number for this pore network using the COMSOL Multiphysics software. A small (10^{-4} Pa) pressure gradient was imposed across the sample inlet and outlet, and hydraulic conductivity for the network was calculated by applying Darcy's law using the modeled pressure gradient and distance across the network. The calculated permeability for this pore network is approximately $1.0 \times 10^{-19} \text{ m}^2$. TerraTek's Tight Rock Analysis Klinkenberg-corrected value for the upper member of the Kirtland Formation is $7.2 \times 10^{-20} \text{ m}^2$, which suggests consistency among pore network and core conductivities.

We emphasize the limited nature of this conclusion as the modeling was very simple (e.g., ignoring the changing properties of water in the nm-sized pores) and does not account for heterogeneity beyond the few microns in the digital sample. Nonetheless, this result would support that core plug-scale matrix flow properties are representable by

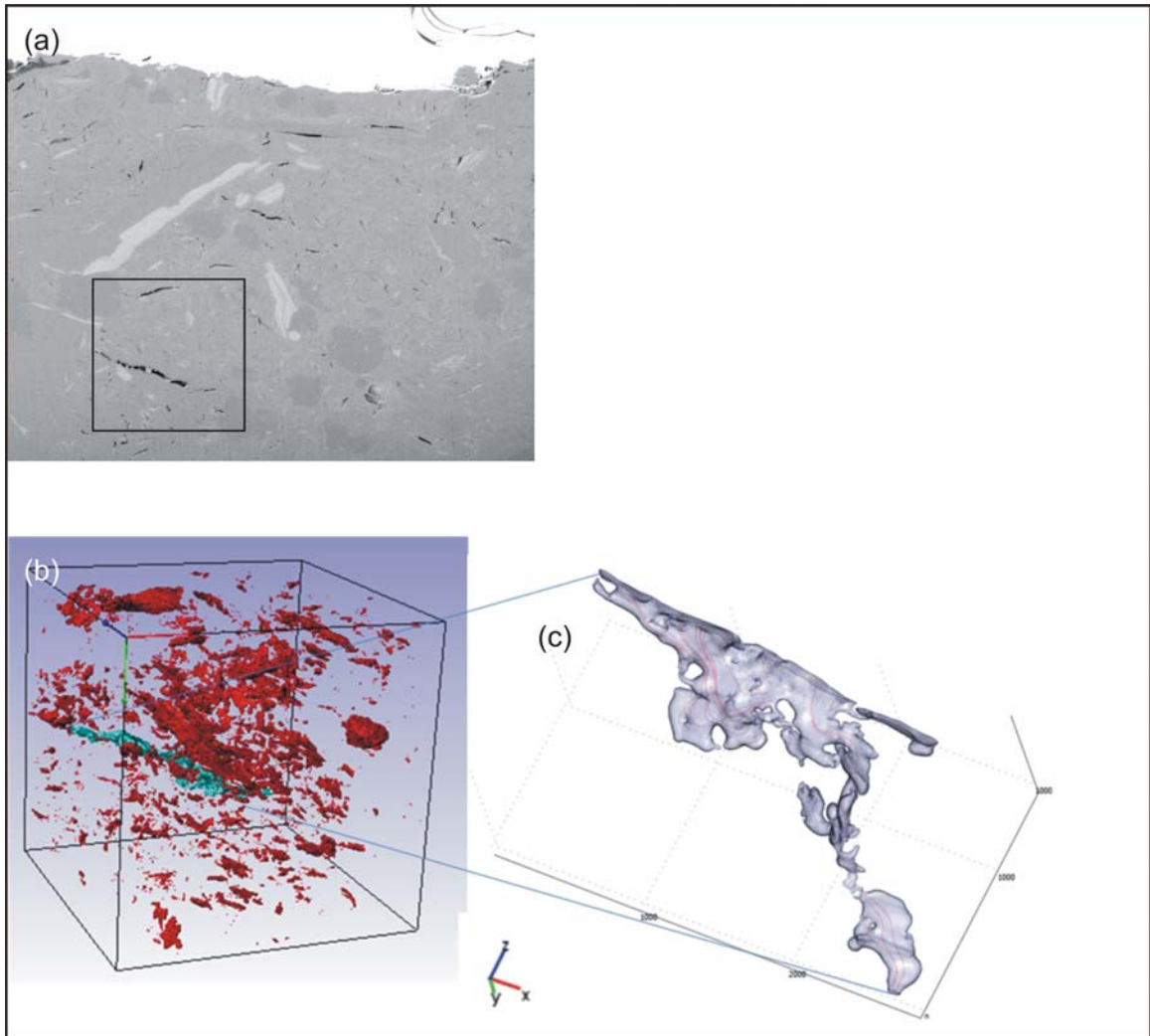


Figure 5.4. Results of focused ion beam/scanning electron microscopy and image analysis. (a) Backscattered electron image of a vertical surface of a trough milled in an upper Kirtland Formation sample. The horizontal field of view is 16 μm . Darkest areas are pore space. The inset box shows the location of the 3D pore model, shown in part b. (b) 3D “flood-fill” rendering of pore space in red. Cyan pore was used in pore-scale modeling. (c) Image of pore used in pore-scale fluid modeling. The inlet location for flow modeling was at the bottom right hand-side of the model, and the outlet was at the upper left.

types of pore networks imaged in Figure 5.4b. These pore-scale characterizations of very low permeabilities indicate lithologies that would constitute effective seals.

CORE-SCALE MATRIX PROPERTIES

Mercury Intrusion Porosimetry Results and Sealing Efficiency

Results of MIP measurements for eight samples, seven from the upper member of the Kirtland Formation and one from the lower member of the Kirtland Formation, are shown in Figure 5.5 as mercury saturation versus injection pressures. The sample for the lower Kirtland Formation (red curve) shows the highest injection pressures and thus has the potentially better sealing quality. The samples for the upper Kirtland Formation, including two directional core plugs, all show somewhat similar shapes and thus pore throat distributions except for the sample at 624.35 m (bgs) (green curve), which shows a bimodal distribution. Additional samples, which were taken from depths near to 624.35 m and analyzed for Chapters 3 and 4, also show similar bimodal distributions.

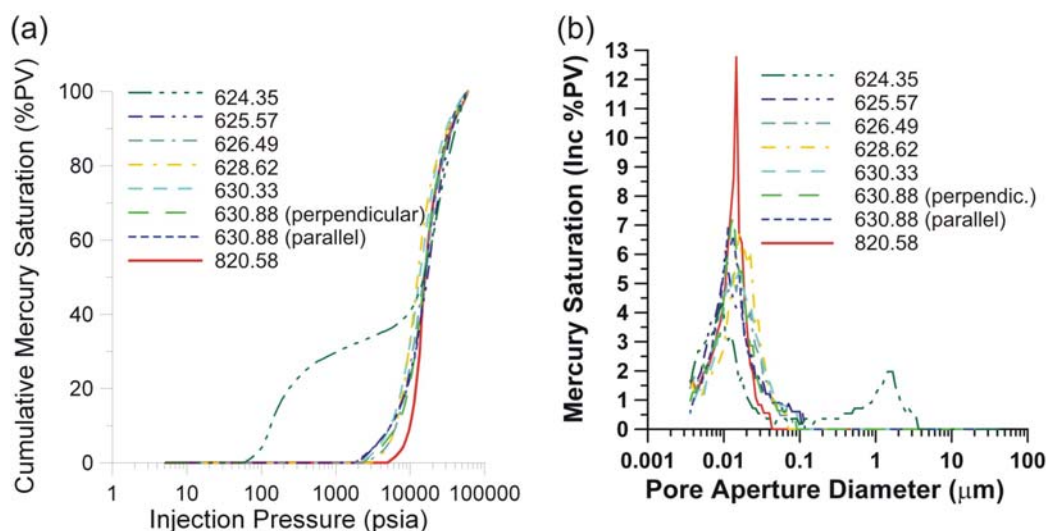


Figure 5.5. Mercury intrusion porosimetry data. (a) Cumulative mercury saturation versus pressure. (b) Incremental (inc) mercury saturation versus pore aperture diameter, based on data from (a) and the Washburn equation. Capillary pressure data were corrected for closure pressure (i.e., mercury that had not intruded the pore network was not included in the saturation curves). Depths of samples are given in m in the legend. “PV” stands for pore volume.

Sealing efficiencies in hydrocarbon systems are often cast as the column height of buoyant gas or oil that a sealing lithology can support prior to capillary intrusion.

Equations used to convert threshold pressures from a mercury-air-rock system to a CO₂-brine-rock system are detailed by Dewhurst et al. (2002). Carbon dioxide column heights are calculated using:

$$h_{CO_2} = \frac{P_{th}}{(\rho_b - \rho_{CO_2})g} \quad (1)$$

and

$$P_{b/CO_2} = P_{a/m} \frac{(\sigma_{b/CO_2} \cos \theta_{b/CO_2})}{(\sigma_{a/m} \cos \theta_{a/m})} \quad (2)$$

where h_{CO_2} is the CO₂ column height; P_{th} is the breakthrough pressure (i.e., the pressure at which the non-wetting phase forms a continuous filament across the sample; Chiquet et al., 2007a; Dewhurst et al., 2002); ρ_b and ρ_{CO_2} are the density of seal formation water or brine (formation water and brine are used synonymously here) and CO₂; g is the gravitational acceleration; P_{b/CO_2} and $P_{a/m}$ are capillary pressure for brine-CO₂-rock and air-mercury-rock systems, respectively; σ_{b/CO_2} is interfacial tension for the brine-CO₂ pair; and θ is the contact angle for the brine-CO₂-rock or air-mercury-rock systems, as indicated by the subscripts.

Table 5.1 gives values of the parameters of Equations 1 and 2 used in this study. Estimates of interfacial tension values for the brine-CO₂ system were obtained from Bachu and Bennion (2009) and Chiquet et al. (2007b) and assume hydrostatic pressure and a geothermal gradient of 25°C/km (Table 5.1). Air-mercury(-rock) interfacial tension and contact angle were obtained from Pittman (1992). A range of brine-CO₂ contact

angle values was chosen after reviewing wettability experiments using quartz and mica by Chiquet et al. (2007).

Table 5.1. Information used for calculations of CO₂ column heights

Air-mercury interfacial tension (N m ⁻¹)	0.481
CO ₂ -brine interfacial tension - upper Kirtland (N m ⁻¹)	0.040
CO ₂ -brine interfacial tension - lower Kirtland (N m ⁻¹)	0.031
Density of brine - upper Kirtland (kg m ⁻³)	1030
Density of brine - lower Kirtland (kg m ⁻³)	1030
Density of CO ₂ - upper Kirtland (kg m ⁻³)	176
Density of CO ₂ - lower Kirtland (kg m ⁻³)	338
Air-mercury-rock contact angle	140°
CO ₂ -brine-rock contact angle - low value	40°
CO ₂ -brine-rock contact angle - high value	60°
Temperature - upper Kirtland	27°C
Temperature - lower Kirtland	32°C

Note: Brine (i.e., formation water) density for the Kirtland Formation is unknown at this time and the value above was assumed.

CO₂ column heights that could be retained by the Kirtland Formation at various depths, calculated using Equations 1 and 2, the values from Table 5.1, and breakthrough pressure from the MIP data, range from a few tens of meters (for the upper Kirtland Formation sample at 624.35 m bgs) to a kilometer or more (for the lower Kirtland Formation sample at 820.6 m bgs), depending on the values of contact angle used (Figure 5.6). Thus, sealing capacity in terms of column heights is very high for the upper and lower Kirtland Formation.

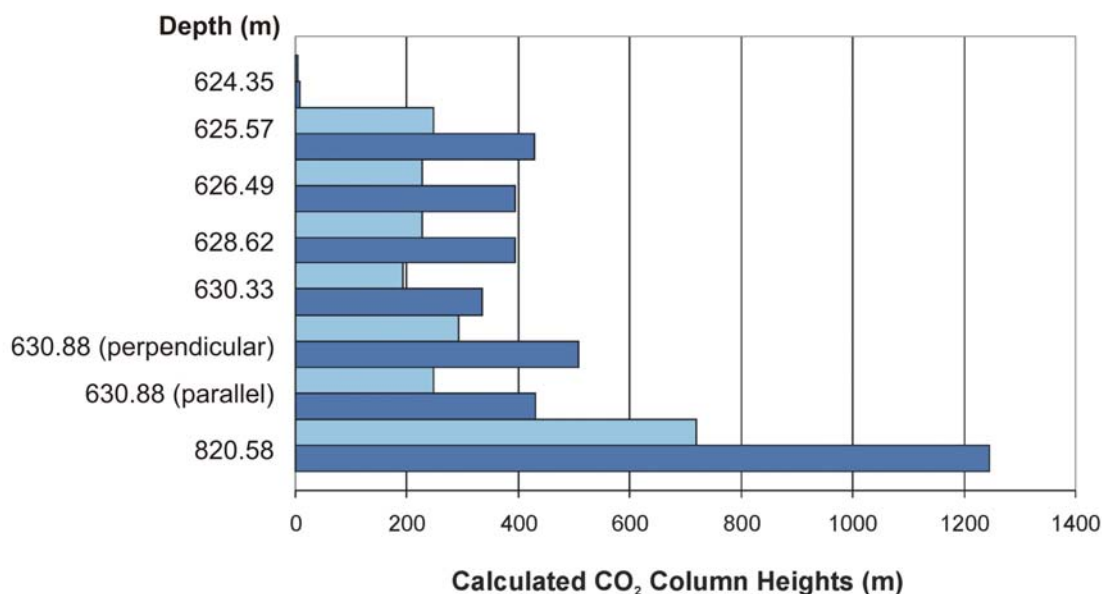


Figure 5.6. CO₂ column heights plotted by depth for the upper and lower Kirtland Formation. The two columns per depth (in different colors) correspond to the two values of contact angles given in Table 5.1.

Petrography, Petrophysical Properties, and Geologic Characterizations

Representative optical, LSCM, and SEM photomicrographs from upper and lower Kirtland Formation samples are summarized by Figures 5.7a–c and 5.8a–c. MIP pore aperture size distributions are given in Figures 5.7d and 5.8d. The optical photomicrographs show that upper Kirtland Formation samples are classified as argillaceous mudstones or sandy argillaceous mudstones based on the matrix-supported texture and matrix composition. Samples from the lower shale member of the Kirtland Formation were argillaceous or silty argillaceous mudstones based on the same criteria. In thin section, “mottled” colors along with apparent root material and illuviation structures suggest soil formation at several horizons as was seen in hand-sample descriptions of the core. Silt- to sand-sized grains are quartz, alkali feldspar, some

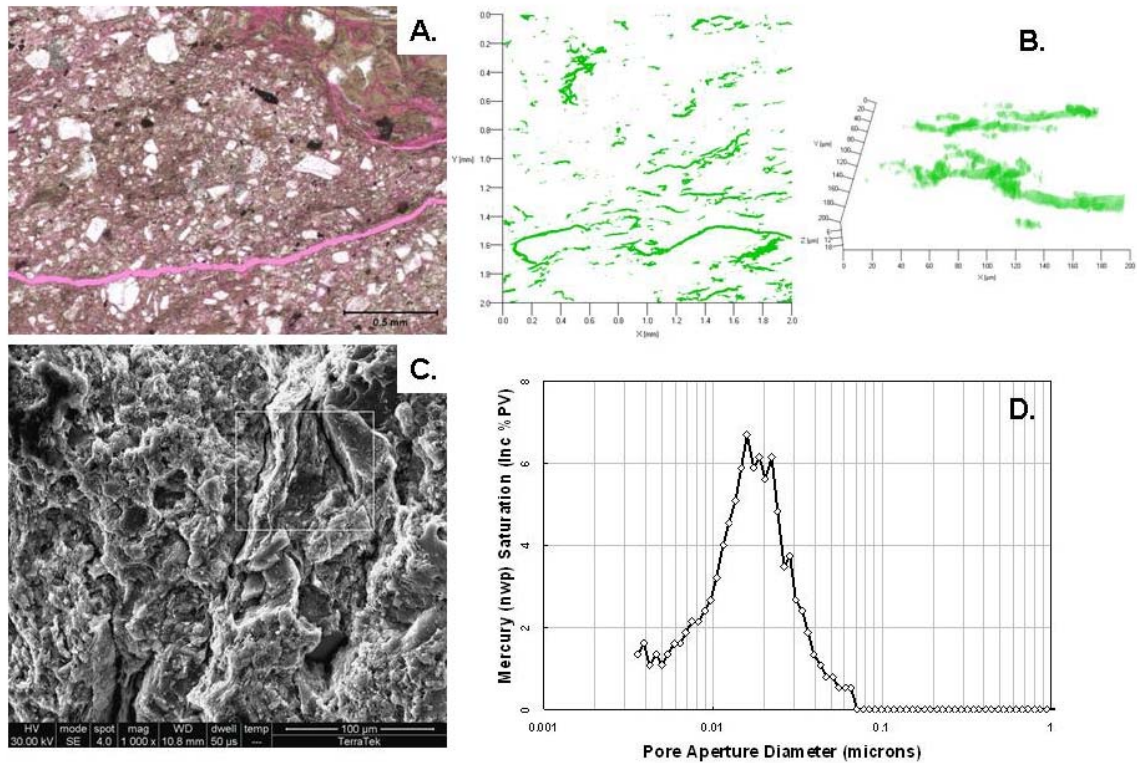


Figure 5.7. Upper Kirtland photomicrographs and pore size distribution from mercury intrusion porosimetry (MIP) measurements. (a) Optical plane-polarized light photomicrograph of sandy argillaceous mudstone from the unstained portion of slide from depth 628.59 m (see Appendix B.2.2). The scale bar is 0.5 mm. Information from TerraTek states that “Sharp feldspar, quartz, and rounded chert-replaced volcanic clasts are supported by a mixed smectitic matrix. Induced fractures are pervasive, as represented by the magenta lines (stained epoxy). The fabric exhibits blocky ped structure, especially when viewed under cross-polarized light, and the aligned, curved illite material at upper right is likely a result of illuviation.” (b) LSCM image of 2.0 mm by 2.0 mm by 50 micron (left) and 200 by 200 by 15 micron (right) portions of an upper Kirtland sample, showing interconnected fractures and matrix porosity, likely induced from coring, unloading, and dehydration. (c) SEM image with a scale bar of 100 microns (see Appendix B.2.2). TerraTek’s information on this photomicrography is the following: “Medium magnification view of sandy argillaceous mudstone with poorly laminated and mottled, irregular texture. Angular to subangular quartz and feldspar sand are scattered throughout the clay matrix, showing approximately vertical microfractures filled with illuvium. Spot EDS analysis identifies the dark grains at upper right and center right edge as alkaline feldspars.” The boxed area denotes an illuviation (soil-forming) texture. (d) Pore aperture size distribution of matrix determined by MIP analysis.

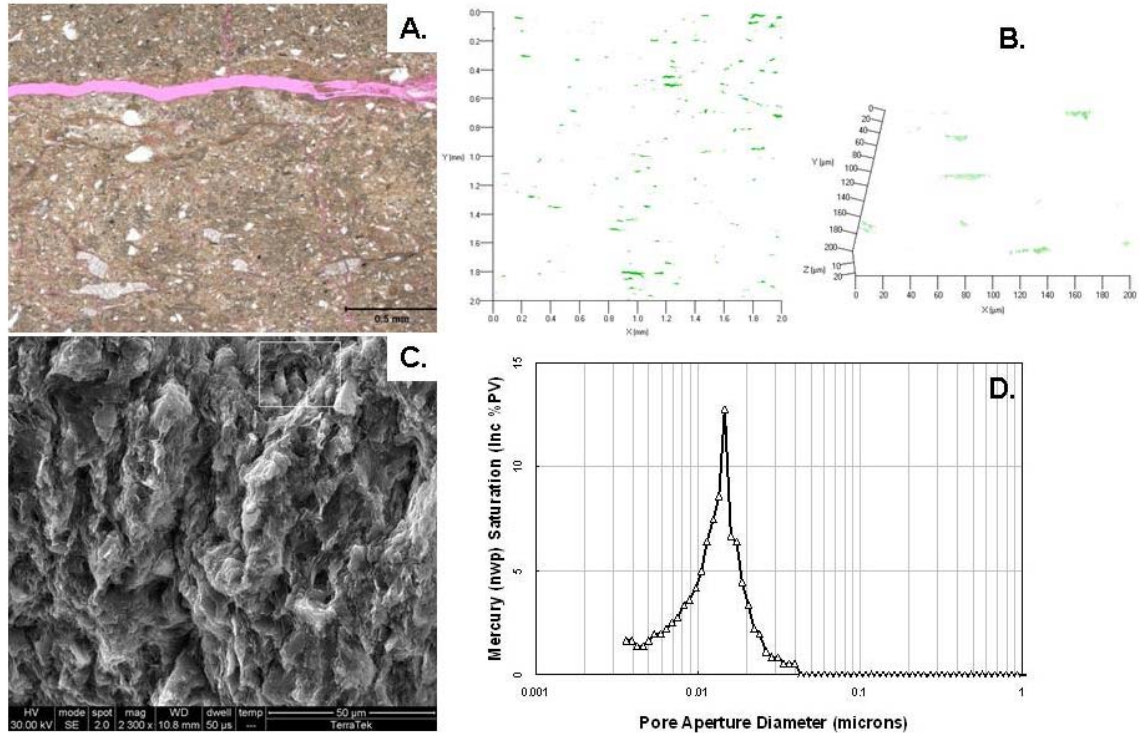


Figure 5.8. Lower Kirtland photomicrographs and pore size distribution from MICP measurements. (a) Optical plane-polarized light photomicrograph of an argillaceous mudstone from the unstained portion of slide from depth 820.60 m (see Appendix B.2.2). The scale bar is 0.5 mm. TerraTek’s information on this photomicrograph is the following: “Argillaceous mudstone at lower magnification exhibits scattered silt and sand in a mixed clay matrix, with expandable I/S and chlorite as the predominant clay species (XRD). The crystals with cross-hatched cleavage in the lower part of the image are ferroan calcite (unstained). The horizontal fracture (magenta) is interpreted as an induced, stress-release or dehydration feature.” (b) LSCM image of 2.0 mm by 2.0 mm by 50 micron (left) and 200 by 200 by 15 micron (right) portions of lower Kirtland sample, showing relative lack of interconnected fractures and matrix porosity seen in the upper Kirtland (compare Figure 5.7b). (c) SEM image of argillaceous mudstone with a scale bar of 50 microns that displays, according to TerraTek, “moderate lamination parallel to bedding, near vertical in this image. Scattered silt and sand are supported in a lumpy, clay-rich matrix. An example of a large pore is seen in the boxed area at upper right” (see Appendix B.2.2). (d) Pore aperture size distribution of matrix determined by mercury injection capillary pressure analysis.

plagioclase, and volcanic rock fragments. Some micas, including biotite, are seen as depositional flakes. Authigenic mineralogy observable in thin section is dominated by quartz cement and overgrowths, replacing portions of volcanic rock fragments and lithic

grains. Results of XRD analysis, although not shown, indicate that the Kirtland samples have very little carbonate cement ranging from 0 to 3% (by weight) at most, although what calcite and dolomite does exist is ferroan in composition. XRD clay mineral fractions in the upper Kirtland are dominated by smectite and illite or mica, while the lower Kirtland Formation is dominated by illite-smectite mixed-layered clays. The abundance of these clay types as matrix material induces a roughly 15–40% expandability to the mudstones. There is also significant iron-bearing chlorite in both upper and lower Kirtland samples. The SEM photomicrographs show pedogenic (soil forming) illuviation textures (Figure 5.7c) as well as expandable clay fabric with moderate lamination (Figure 5.8c).

LSCM imaging of pores impregnated with fluorescing epoxy are shown in Figures 5.7b and 5.8b. Porosity is shown in green. Figure 5.7c shows much more interconnected porosity in the upper versus lower shale member of Kirtland Formation in Figure 5.8c. All LSCM images show a planar pore fabric as well as microfractures oriented subparallel to bedding. (The “up” or younging direction in the LSCM images is towards the top of the page of the figures.) Much of this porosity is probably enhanced by unloading and/or clay mineral desiccation after coring. Such induced porosity is inferred from the lack of mineral fill, slickenlines, illuviated clays, or plume structures that would indicate natural fractures (as seen in hand sample). Illuviation textures may represent primary porosity. (An example of this is seen in the sub-vertical structure in upper left corner of Figure 5.7b, left panel.) The interconnectedness and spatial extent of these features likely do not represent much interconnected porosity on length scales larger than thin section.

Petrographic analysis reveals several pore types in the samples, with the most dramatic likely reflecting unloading and dehydration processes, as discussed above. Induced porosity (0.005 to 0.02 mm; 5 to 20 microns) is the most pervasive pore type in the samples and is typical of rocks with significant amounts of expandable clays. Induced pores are not present *in situ* and may introduce error in porosity and permeability measurements. A second pore type in the Kirtland Formation is due to decay of organic material associated with root and organic particle casts (0.002 to 0.02 mm; 2 to 20 microns), observed both in thin section and SEM results. This pore type is associated with well-aligned clays and probably does not contribute to interconnected effective porosity on length scales of interest for subsurface carbon storage. The third type is the matrix-hosted intercrystalline microporosity (< 0.005 mm) and is the *in situ* porosity in typical mudstones. This microporosity is found between clay particles and cements, as seen in Figure 5.4a. MIP analysis suggests that pore apertures associated with microporosity are log-normally distributed with modal size at approximately 0.015 μm . Some are visible at the highest resolution in LSCM. The pores are tiny and poorly connected. In the case of expandable clays, due to dehydration, the microporosity visible under SEM is a maximum size. At *in situ* conditions, the microporosity will probably be even smaller or absent. Chapter 3 discusses pore volume and pore throat size distributions in detail, and shows a power-law character to the matrix porosity as determined from MIP that closely matches the power law distribution of pore types determined by FIB/SEM and shown in Figure 5.5.

FRACTURE CHARACTERISTICS FROM FMI LOGS AND CORE

The presence of several mineralized and open fracture types, as described below, leads to the question of seal bypass associated with flow along potentially-connected fracture sets. While Kirtland Formation matrix properties indicate good sealing potential, as described above, the fracture sets may represent potential leakage pathways.

Fracture data from interpreted FMI logs and core examination are given in Figure 5.9a–b. The first column indicates lithology, the second column contains dip magnitude of fractures measured from core (left side of column is 0° and right side is 90°), the third column includes location of core collection, and the fourth column details fractures from FMI-log interpretations, including orientation information by “tadpoles”, which indicate dip azimuth (i.e., the direction of bearing that is perpendicular to the strike of a fracture or planar feature).

Open, healed, and partially-healed interpreted fractures were more dominant in the lower Kirtland Formation member than the upper member (Figure 5.9a–b). Petal or other induced fractures (Lorenz and Hill, 1992) that would provide information on *in situ* stress orientations were not identified. In both the upper and lower Kirtland Formation, pervasive induced fractures were prevalent as disc fractures (i.e., orientation was ~ perpendicular to core axis) and desiccation fractures—such fractures being common in core with abundant expandable clays.

In the upper member of the Kirtland Formation, several mineralized fractures were found in the core within the depth range of 625.8 m to 627 m (2053 to 2057 ft; depths from Kelly Bushing) (Figures 5.9 and 5.10). Fracture mineralization includes

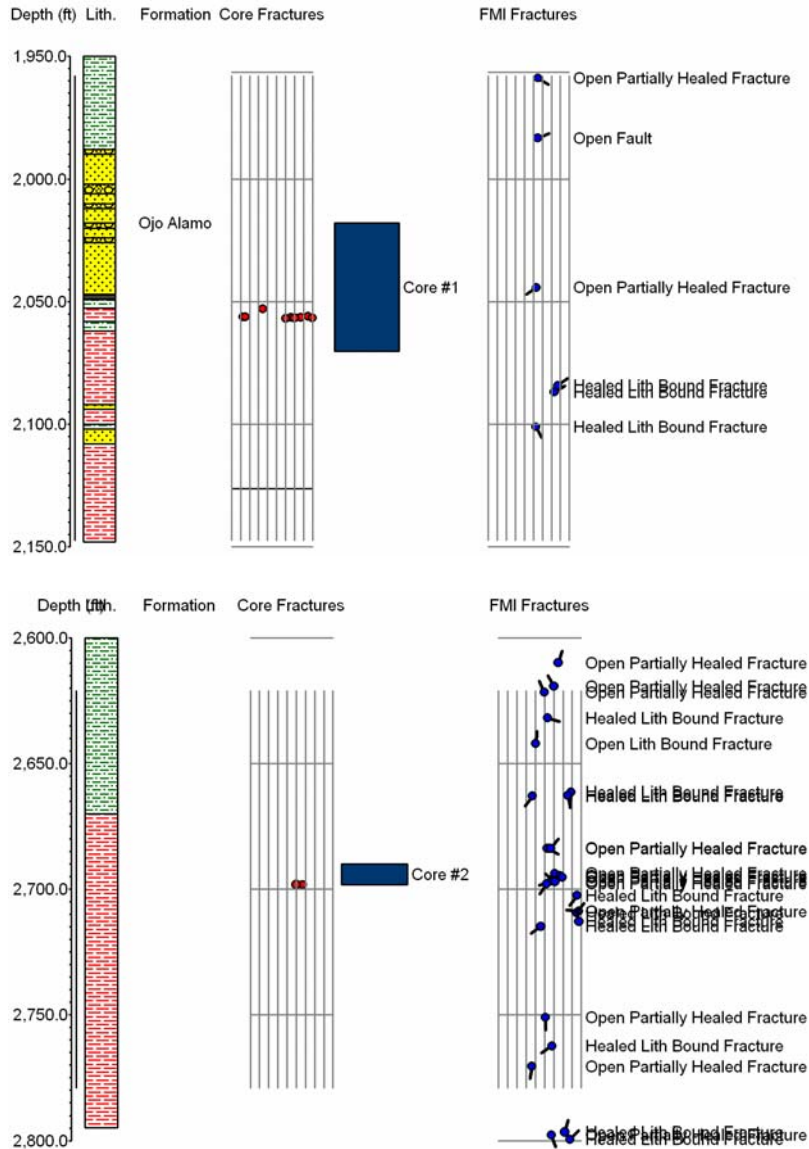


Figure 5.9. Lithologic and fracture data from core examination and formation microresistivity imaging (FMI) well log interpretation for the upper (the upper panel) and lower members of the Kirtland Formation (the lower panel). The first column from the left for each panel is the mud log and core-based lithology (see Appendix B.5 for the legend of the lithologic symbols). The second column shows locations of mineralized fractures identified in core. The third column shows the location of core collection. The last column indicates fractures from the FMI log. The FMI fractures are organized by type. The azimuthal dip direction of FMI fractures is given by the “tadpoles.” Dip magnitude for both core (column two) and FMI fractures (column four) is given by the placement of the red circles or tadpoles from left to right. Far left is 0°. Far right is 90°. Fracture type labels are given to the right of the tadpoles (labels overlap when multiple fractures occur in close vicinity to each other).

apatite, calcite, barite, and quartz, as identified via energy-dispersive X-ray spectroscopy (EDS) elemental mapping (Figure 5.10). Cross-cutting relationships seen in microscopic analysis of thin sections indicates that some calcite-filled fractures cut apatite-filled fractures. The apatite-filled fractures existed prior to the formation of the calcite-filled fractures. These calcite-filled fractures are cut by barite- and quartz-filled fractures (Figure 5.10). In EDS images (Figure 5.10), caries texture (i.e., “bite-like” or irregular curved boundaries) is at the interface between quartz (the guest mineral) and barite (the host mineral). Relics of barite and calcite occur within the quartz mineralization, which indicate that quartz has followed the calcite and barite, either during direct replacement or following prior dissolution of barite and calcite at the margins of the fractures. Thus, these fractures indicate multiple episodes of fluid flow by different types of fluids. The fluid flow and mineralization probably occurred at different depths of burial and, since the orientation of the fractures are not all the same, at different stress states. The lower member of the Kirtland Formation contains calcite-filled fractures that do not show quartz at the fracture margins. The history of fluid for the lower member of the Kirtland Formation is different than that of the upper member.

A burial curve reconstruction determined from the thermal modeling of Law (1992) is shown in Figure 5.11 for the boundary between the lower member of the Kirtland Formation and the Fruitland Formation. Annotation on this figure summarizes relevant hydrogeological, diagenetic, and tectonic events that have shaped fracture development and mineral infill. Fracture types observed in this study include: 1) those formed early in the history of the sediments by pedogenic (i.e., soil forming) processes; 2) compactional/dewatering fractures that can be related to soft-sediment deformation

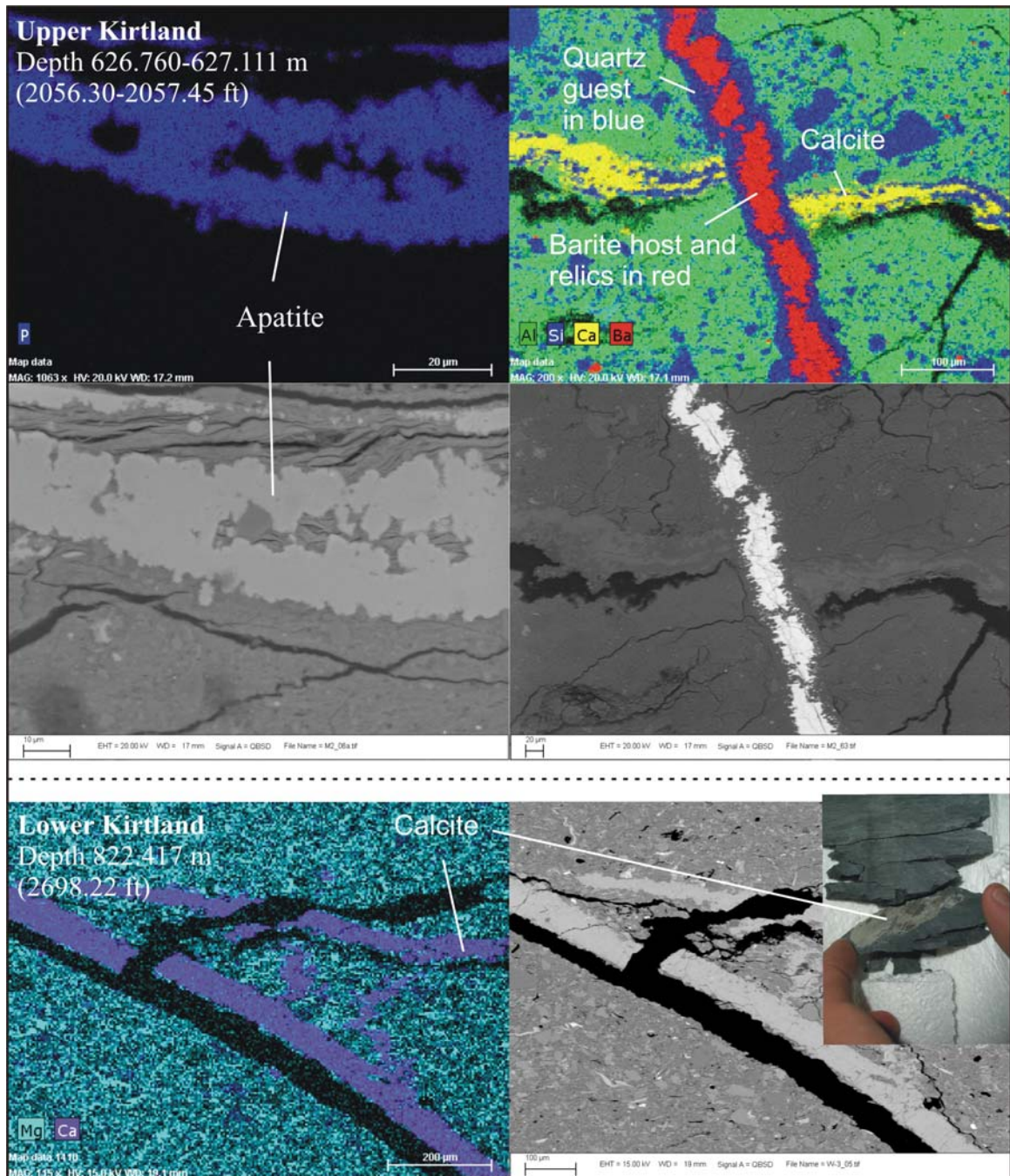


Figure 5.10. Montage of fractured-related images for rock samples from the upper and lower members of the Kirtland Formation. Images include the following: backscattered electron images (i.e., grayscale images), energy-dispersive X-ray spectroscopy elemental maps (i.e., color images with legends for mapped elements), and a hand sample photograph of slabbed core that shows a fracture with mineralization. The younging direction is towards the top of the photomicrographs. The photomicrograph in the upper right hand corner shows a clear cross-cutting relationship between a calcite/quartz-filled fracture and a barite/quartz-filled fracture.

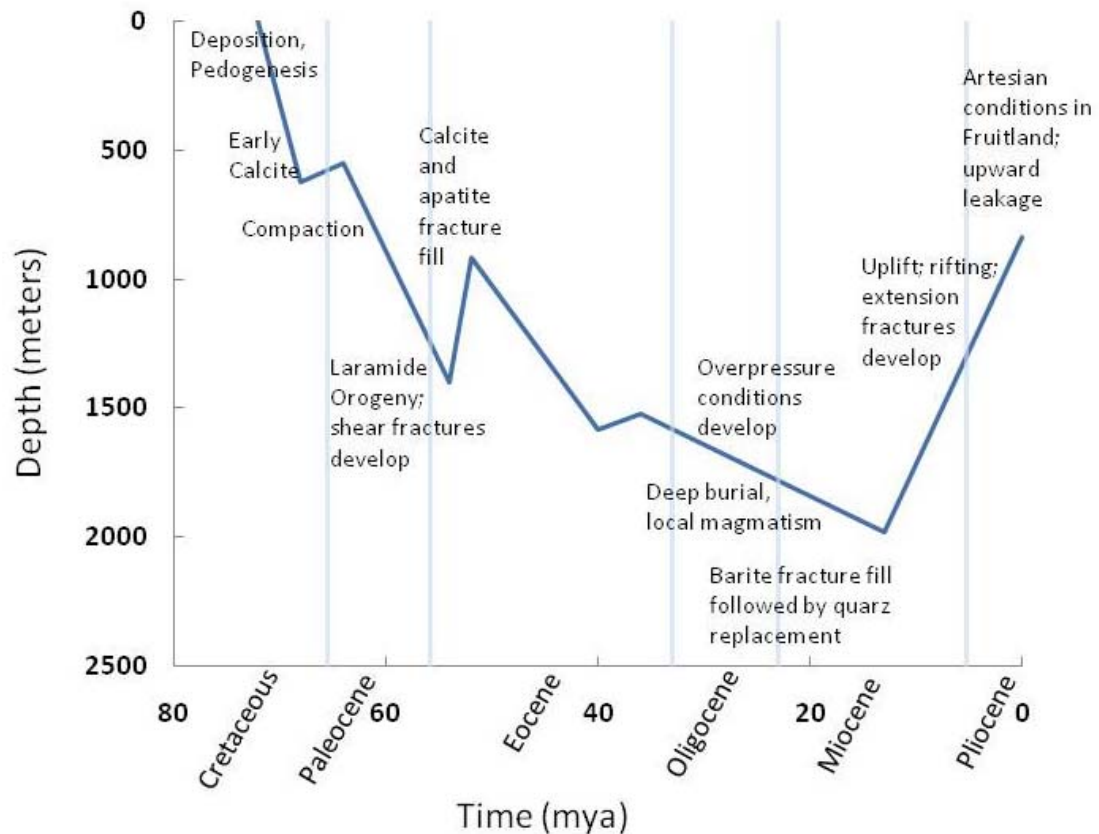


Figure 5.11. Burial history, annotated with paragenesis of fracture mineralization and tectonic and hydrologic information (modified from Law, 1992).

and are not typically greatly influenced (in terms of orientation) by tectonic stresses (these fractures can be prevalent in low-permeability sediments/rocks); and 3) fractures formed by tectonic processes. The latter include shear fractures with orientations consistent with Laramide stress states and a fracture-formation model discussed by Lorenz and Cooper (2003). These are mineralized by calcite and apatite and contain microstructures with shear-sense indicators. These also show later offset by barite and quartz mineralized fractures, which are largely mode I extensive fractures.

We hypothesize that quartz from barite mineralization in the upper member of the Kirtland Formation may indicate fluid flow from as deep as the Fruitland Formation through the entire seal, during the deepest portions of burial in the Oligocene, when thermal gradients were highest in the San Juan Basin (Law, 1992). This hypothesis could be tested by isotopic analysis of the barite and calcite fracture filling (i.e., sulfur, carbon, and oxygen isotopes) to determine if the fluids in the upper Kirtland were sourced from the Fruitland. Barite fracture-fills might have arisen from upward migration of reducing barium-sulfide fluids and subsequent oxidation and barite deposition.

The fracture mineralization indicates that fluid have been transmitted through parts of the Kirtland Formation in the past. However, these fracture descriptions are nonconclusive with regard to large-scale transport through the entire Kirtland Formation. To address the hypothesis that the observed fracture sets will act as seal bypass systems for subsurface CO₂ storage, we now turn to noble gas tracer analysis as a means to estimate large-scale conductivities.

FORMATION-SCALE NOBLE GAS RESULTS AND CROSS-SEAL TRANSPORT

Helium and Neon Concentration Profiles

Results from noble gas concentration analysis are presented first, followed by brief discussion of general observations. We discuss ²⁰Ne concentrations first because they indicate interaction between the groundwater and a separate phase (i.e., methane). We then present and discuss conceptual and quantitative models to evaluate ⁴He transport and the existence of a seal bypass system that may be present due to the fractures

observed in core and by the FMI logging (see Section Fracture Characteristics from FMI Logs and Core).

For the samples taken at different depths, Figures 5.12 and 5.13 present the measured ^{20}Ne , ^4He , and ^3He concentrations and the ratios of $^3\text{He}/^4\text{He}$, $^4\text{He}/^{20}\text{Ne}$, and $^3\text{He}/^{20}\text{Ne}$. These data are based on the combined amount of helium and neon from the two analysis runs. The concentrations are given as cm^3 of neon or helium at standard temperature and pressure (STP) per cm^3 of pore volume (i.e., the volume of the pore/void space). Because laboratory analysis on fresh core indicated gas saturations (see Appendix B.2.6), we present the concentrations using pore volume as opposed to typical methods of presenting concentrations per gram of groundwater for systems that are fully saturated by groundwater. We do not *a priori* assume that the samples were fully saturated with groundwater at depth. The figures also present the ratios of the two separate laboratory analysis runs of helium and neon.

Ratios of the two separate analysis runs (first columns in Figures 5.12 and 5.13) indicate that most samples degassed significantly into the preservation canisters after the second run (values closer to zero indicate greater degassing). However, two samples show incomplete degassing for helium (values $> 2\%$; Figure 5.12), and one shows incomplete degassing for neon (value $> 2\%$; Figure 5.12). Thus, in our interpretations below, we use the data that show incomplete degassing with caution. (Note that by “degassing” we mean the quantitative release of the helium and neon into the canisters prior to analysis. In the discussion below, we use “degassing” in the sense of a noble gas partitioning process due to interaction between groundwater and a separate fluid phase.)

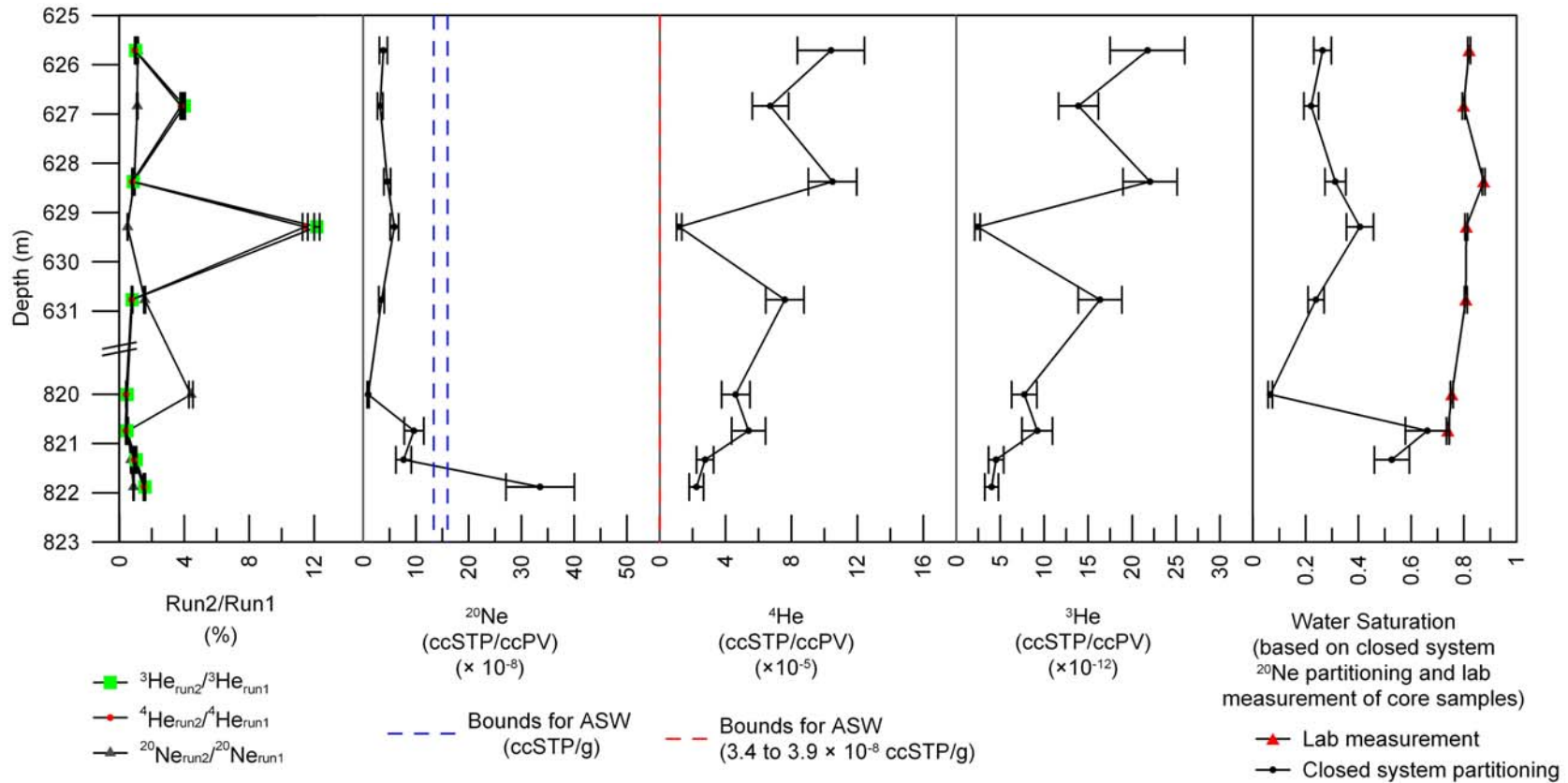


Figure 5.12. Depth profiles of noble gas concentrations and water saturations. Laboratory analysis Runs 1 and 2 were performed in September 2008 and March 2009, respectively. “ccSTP” is cm^3 of helium or neon at standard temperature and pressure. “ccPV” stands for pore volume in cm^3 . “ASW” is “air saturated water” and has units of ccSTP of ^{20}Ne or ^4He per gram of groundwater. Water saturations include those from calculations of closed system partitioning and the laboratory measured values of TerraTek (see Appendix B.2.6). The closed system partitioning estimated water saturations needed to match the difference between measured and expected ASW ^{20}Ne concentrations. Error bars are based on uncertainty in pore volume and laboratory analysis, using error propagation methods.

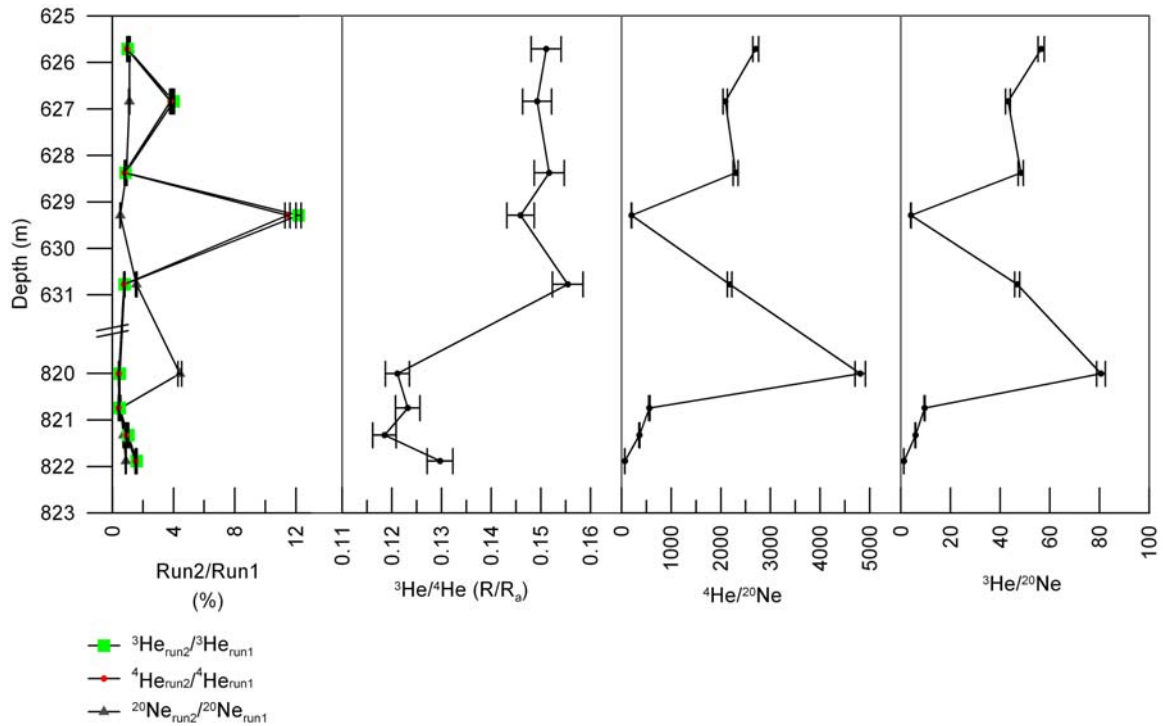


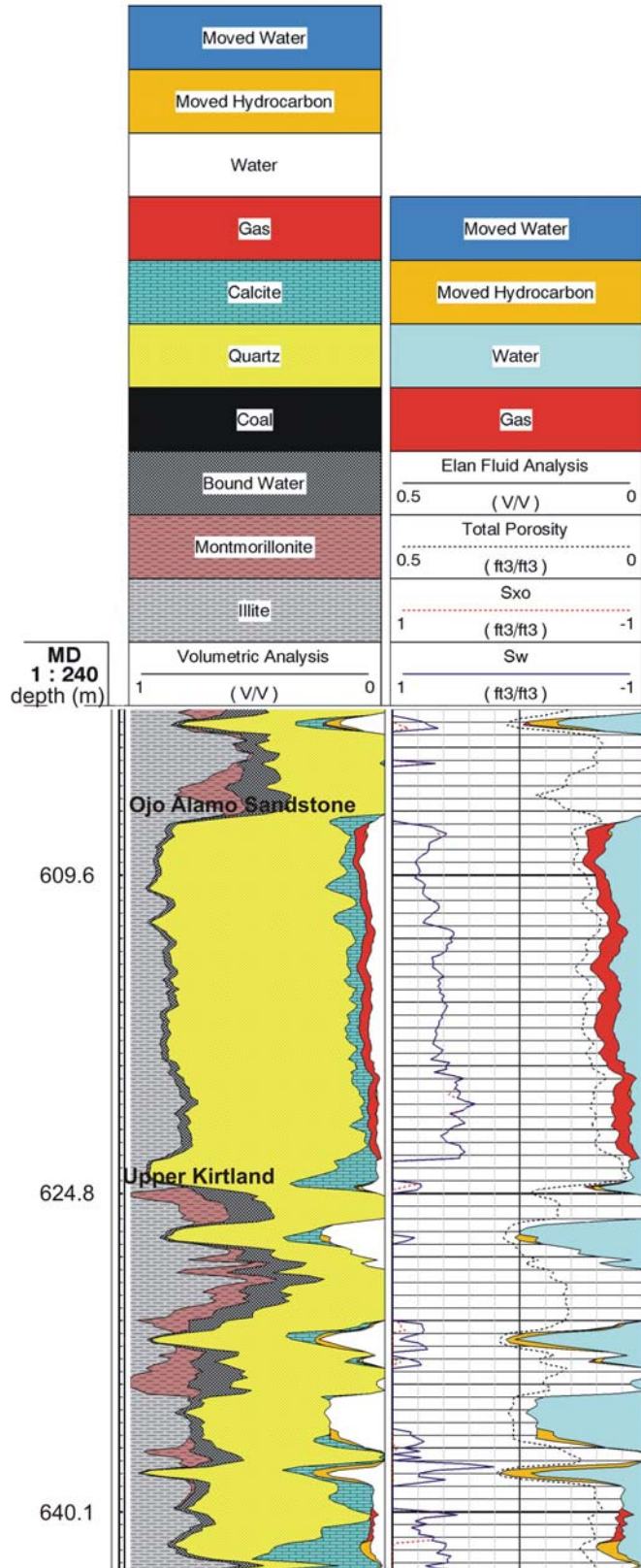
Figure 5.13. Depth profiles of noble gas ratio data. R = measured $^3\text{He}/^4\text{He}$. R_a = atmospheric $^3\text{He}/^4\text{He}$ (1.384×10^{-6} ; Kipfer et al., 2002). Error bars are based on uncertainty in laboratory analysis.

For all except one sample, the measured ^{20}Ne concentrations are lower than estimates of ASW concentrations, the atmospheric solubility equilibrium concentrations (indicated by blue lines on the second column of Figure 5.12). Typically, waters recharging a groundwater system have ^{20}Ne concentrations that reflect conditions at the recharge area (see Subsection Noble Gas Analyses in the Methods and Materials section), such as temperature, pressure, salinity, and the fluctuations in water table elevation that can trap and result in dissolution of air bubbles (i.e., the processes that produce “excess air”; Kipfer, 2002). Neon-20 typically does not have a source in the subsurface in sedimentary basins that would increase the ASW concentration from that imparted at the recharge area. The units of ^{20}Ne concentration of ASW are cm^3 STP per gram of

groundwater. These units are equivalent to those of the measured ^{20}Ne values, which are concentration per pore volume, if one assumes that the one gram of water equals 1 cm^3 . Thus, the comparison of measured ^{20}Ne and those of the ASW concentrations indicates a degassing/partitioning process that decreased the measured ^{20}Ne below their expected ASW concentrations.

Processes that may have decreased the measured ^{20}Ne from the ASW concentrations include both *in situ* and sampling-related possibilities. Noble gases will partition between groundwater and a separate fluid phase (or phases) that are in contact (Ballentine et al., 2002). *In situ* partitioning requires the presence of a separate phase (e.g., methane or oil) at depth. Sampling-related partitioning would require the development of a separate phase (e.g., methane) from the groundwater due to pressure release after drilling/coring and prior to sealing of the samples in the preservation canisters. Such a separate phase, if generated, may have been extracted during the purge-and-pumpdown procedure that removed gases from the canisters (see Appendix B.1). Analysis by TerraTek on fresh core (see Appendix B.2.6) indicates gas saturations (i.e., “saturation” here meaning that part of the pore space is filled with a separate phase in addition to groundwater) that range from ~11 to ~24%. In contrast, the ELAN well log (Schlumberger’s Elemental Analysis on wireline logs) (Figure 5.14) indicates no separate-phase gas saturations at the depths where core plugs were taken except for one plug (at the depth of ~626.8 m). Note that gas saturations are indicated (usually within quartz- and sandstone-rich interbeds) in the Ojo Alamo Sandstone and at various depths within the upper and lower members of the Kirtland Formation, the Farmington

Figure 5.14. Interpretation of well logs in terms of mineral phases and fluid phases (Schlumberger's ELAN log) for the Ojo Alamo Sandstone and the upper member of the Kirtland Formation. Upper contacts of the geologic units are labeled. The ELAN log does not indicate gas saturations at the depths of the core plugs within the lower member of the Kirtland Formation (not shown).



Sandstone Member, and the Fruitland Formation. The ELAN well log supports the assumption that all but one of the core plugs were fully saturated by groundwater. We suggest that the core, in general, may have degassed after sampling to produce the saturations measured by TerraTek (see Appendix B.2.6). The mud log (see Appendix B.5) indicates methane was present within the Kirtland Formation. Considering both the mud log and the ELAN log, some dissolved or sorbed methane is likely at the depth of the core plugs.

We are still left with the possibilities that: 1) desorbing or exsolving methane due to pressure release after drilling/coring may have produced a methane phase into which ^{20}Ne may have partitioned and then was lost during the purge-and-pumpdown process; 2) groundwater within the upper and lower members of the Kirtland Formation that is (or was in the past) in contact with methane within the Ojo Alamo Sandstone and Kirtland Formation caused *in situ* partitioning; and 3) some combination of the first two possibilities occurred. For the upper member of the Kirtland Formation, differences in the amount of plug material and in pore structure amongst the samples probably would have caused variation in the degassing/release of the methane and stripping of ^{20}Ne prior to sealing of the plugs in the canisters. However, the concentrations are similar to each other. Hence, we suggest that the uniformity of the measured ^{20}Ne concentrations support *in situ* degassing as the dominant degassing mechanism that affected the upper member of the Kirtland Formation core plugs.

The $^4\text{He}/^{20}\text{Ne}$ values of the upper member of the Kirtland Formation range from 2177, 202, 2300, 2087, to 2702, respectively, from the lowest to highest depths (note that the sample with the value of 202 had not fully degassed into the canister in the sense of

quantitative release measured by Run2/Run1; see Figure 5.13). The $^4\text{He}/^{20}\text{Ne}$ ratio calculated for ASW is ~ 0.25 (based on equations in Kipfer et al., 2002). Thus, the atmospheric contribution of ^4He to the upper Kirtland Formation samples is negligible.

The ^{20}Ne concentrations of the lower member of the Kirtland Formation (Figure 5.12) are not uniform and more difficult to assess. Possible explanations include little to no *in situ* or sampling-related degassing and/or some degree of atmospheric contamination in the preservation canisters. The ^{20}Ne values range from lower-than-ASW to higher-than-ASW concentrations (see depths of ~ 820 to 822 m on Figure 5.12). The $^4\text{He}/^{20}\text{Ne}$ values for the lower Kirtland Formation are approximately 12, 67, 359, 557, and 4807, respectively, from the lowest to the highest sample depth (see Figure 5.13; note that sample at depth 820 m has a relatively large Run2/Run1 ratio, indicating that a relatively large percentage of ^{20}Ne is still left in the sample). The trend of higher ^{20}Ne concentration with lower $^4\text{He}/^{20}\text{Ne}$ may indicate input of atmospheric ^{20}Ne due to contamination during the sample preservation procedure since ASW has a $^4\text{He}/^{20}\text{Ne}$ value of ~ 0.25 . The same purge-and-pumpdown procedure was used for upper and lower Kirtland Formation samples, but with different vacuum pumps (the pump used for the upper Kirtland Formation failed at the beginning of acquiring samples from the lower Kirtland Formation). Field measurements of pressure within the canisters during pumpdown were similar, however, for both vacuum pumps. Thus, we suggest atmospheric contamination as a reason of the relative increase in ^{20}Ne of lower Kirtland Formation samples or less *in situ* degassing than the upper Kirtland Formation samples. Other noble gas data (e.g., Ar, Kr, and Xn) not collected could have further constrained

possible sources of atmospheric contamination or *in situ* degassing processes (Lippmann et al., 2003).

In situ degassing can occur via multiple processes: 1) closed system equilibrium partitioning of the noble gases between groundwater and a separate phase (e.g., methane or oil) (Lippmann et al., 2003); 2) diffusive degassing in a non-equilibrium state (i.e., rapid degassing without reaching equilibrium); and 3) local equilibrium in an open system (Rayleigh degassing process).

To evaluate Process 1, closed system equilibrium partitioning, we use a simple mass-balance approach (after Ballentine et al., 2002) to estimate the volumes of liquid and separate phase gas needed to partition the expected ASW ^{20}Ne to match the measured ^{20}Ne concentration. Relevant assumptions for pressure and temperature conditions at depth were used to estimate Henry coefficients. Results shown in Figure 5.12 (last column) present the calculated volume of liquid-to-gas ratios, expressed as water saturations. These water saturations fall within the range of values seen on the ELAN well log for the Ojo Alamo Sandstone, which vary from 0.14 to 0.74 (as calculated from the ELAN data of total porosity and volumetric water content). Figure 5.12 also presents the water saturations measured by TerraTek (see Appendix B.2.6). The close system equilibrium calculations suggest that *in situ* equilibrium partitioning may have occurred for the upper member of the Kirtland Formation. The other two non-equilibrium or open system partitioning processes may be operative; however, they are difficult to assess without additional noble gas concentrations (e.g., Ar, Kr, and Xn; see Lippmann et al., 2003).

In summary, we suggest that degassing is less dominant for the lower member of the Kirtland Formation than the upper member. Possible atmospheric contamination occurred in the lower Kirtland Formation, although this is difficult to explain due to the similar purge-and-pumpdown procedures used for both upper and lower data sets. The upper member of the Kirtland Formation likely experienced *in situ* degassing. Estimating the relative degree-of-degassing loss of noble gases due to *in situ* or sampling-related processes is problematic. Previous studies demonstrate the use of elemental fractionation of a suite of noble gases (Ar, Kr, and Xn; see Lippmann et al., 2003, and Ballentine et al., 2002) for constraining *in situ* or sampling-related degassing. We are not able to apply this fractionation “finger-printing” due to the loss of these other noble gases during sample purification.

In the following discussion, we use the measured concentrations of ^4He to assess fluid transport processes within the Kirtland Formation, while being cautious of possible *in situ* degassing. The lower Kirtland Formation data, in terms of the helium values and possible atmospheric contamination, are probably more robust than the neon data since the atmospheric concentrations of helium are much lower than the measured values (see Figure 5.13; the ASW concentrations are orders of magnitude lower than the measured ^4He concentrations).

Testing Conceptual Models of Helium Transport

To understand the evolution of ^4He in Kirtland Formation pore waters and infer sealing behavior, discussion of helium sources and sinks is in order. In general, total pore

water ^4He can be derived from air or water table interactions, produced *in situ* by U and Th decay, or derived from external fluxes (Ballentine et al., 2002):

$$[^4\text{He}] = [^4\text{He}]_{ASW} + [^4\text{He}]_{ea} + [^4\text{He}]_{is} + [^4\text{He}]_{external\ flux} \quad (3)$$

where $[^4\text{He}]$ is the concentration in the groundwater, $[^4\text{He}]_{ASW}$ is the ASW concentration, $[^4\text{He}]_{ea}$ is the “excess air” contribution that can occur due to dissolution of air bubbles when fluctuations in the groundwater table occur at the recharge area, $[^4\text{He}]_{is}$ is radiogenically produced ^4He , and $[^4\text{He}]_{external\ flux}$ is the portion of the ^4He concentration that is derived from sources external to the location of measurement.

As a starting point of interpretation, we estimate the *in situ* production of ^4He for the important components of our systems: the Fruitland Formation, the lower and upper shale members of the Kirtland Formation, and the overlying Ojo Alamo Sandstone. We neglect $[^4\text{He}]_{ASW}$ and $[^4\text{He}]_{ea}$ as their concentrations are small compared to the measured values (10^{-8} vs. 10^{-5} ccSTP/g; see Figure 5.12). Helium-4 production is estimated via equations presented by Castro et al. (2000):

$$P(^4\text{He}) = 1.207 \times 10^{-13} [U] + 2.867 \times 10^{-14} [Th] \text{ cm}^3 \text{ STP g}_{rock}^{-1} \text{ yr}^{-1} \quad (4)$$

$$[P_{He}^4]_{H2O} = P(^4\text{He}) \times \rho_{rock} \times \Lambda \times \frac{1-\phi}{\phi} \text{ cm}^3 \text{ STP cm}_{H2O}^{-3} \text{ yr}^{-1} \quad (5)$$

$$[^4\text{He}]_{is} = [P_{He}^4]_{H2O} \times t \quad (6)$$

where $P(^4\text{He})$ is the *in situ* production rate of ^4He due to U and Th decay, $[U]$ and $[Th]$ are the U and Th concentrations (in ppm), $[P_{He}^4]_{H2O}$ is the accumulation rate of ^4He in the groundwater, ρ_{rock} is the mass density (in g cm^{-3}), Λ is the transfer efficiency of ^4He from the rock matrix to the groundwater (assumed equal to 1), ϕ is the porosity, and t is time (in years). Parameters of Equations 4 and 5 for this study are given in Table 5.2. The

measured [^4He], given in units of cm^3 STP (standard temperature and pressure) of gas of helium per pore volume, is approximately one order of magnitude or more lower than [^4He]_{is} (Table 5.2). These calculations indicate that after millions of years (~73 to ~74 Ma for the upper and lower shale members, respectively) up to ~10% of produced ^4He (Table 5.2, last column) is still within the pore fluids!

Conceptual explanations of the observed trends include:

- (1) variation in production of ^4He in the upper and lower Kirtland Formation;
- (2) diffusive transport driven by concentration gradients in both groundwater and a gas phase (e.g., methane) and possible free gas saturations in the overlying Ojo Alamo Sandstone (gas saturations in the Ojo Alamo Sandstone are indicated by mud log and other well logs; see Appendix B.5 and Figure 5.14);
- (3) advective transport of helium via groundwater or a separate gas phase or both through the system driven by the artesian hydrologic conditions; equilibrium or non-equilibrium partitioning of noble gases between groundwater and a separate gas phase (e.g., methane) within the caprock during the advective transport; and
- (4) impact on ^4He concentrations in the upper and lower Kirtland Formation by meteoric waters in the Fruitland and Ojo Alamo aquifer systems.

Next, we test conceptual models of noble gas transport to evaluate large-scale permeability of the Kirtland Formation.

Table 5.2. Estimation of *in situ* ^4He production, parameters, and measured ^4He concentration from the core

Formation	Depth (m)	ρ_{rock} (g cm ⁻³)	ϕ	[U] (ppm)	[Th] (ppm)	P(^4He) (cm ³ STP ρ_{rock}^{-1} yr ⁻¹)	[P ⁴ He] _{H2O} (cm ³ STP cm ⁻³ H ₂ O)	Age of deposition (Ma)	[^4He] _{is} (cm ³ STP cm ⁻³ H ₂ O)	Measured	Measured
										[^4He] (cm ³ STP cm ⁻³ PV)	[^4He] /[^4He] _{is} (%)
Ojo Alamo	616.34	2.66	0.12	0.836	6.482	2.87E-13	5.38E-12	65.04	3.50E-04		
	620.12	2.67	0.09	3.706	0.000	4.47E-13	1.15E-11	65.04	7.45E-04		
	623.96	2.73	0.02	2.408	6.003	4.63E-13	7.66E-11	65.04	4.98E-03		
Upper Kirtland	625.71	2.61	0.06	2.891	0.699	3.69E-13	1.42E-11	73.04	1.04E-03	1.04E-04	10.0
	626.84	2.65	0.08	4.906	8.321	8.31E-13	2.65E-11	73.04	1.94E-03	6.73E-05	3.5
	628.38	2.65	0.09	4.391	0.000	5.30E-13	1.35E-11	73.04	9.87E-04	1.05E-04	10.6
	629.29	2.65	0.09	4.619	4.658	6.91E-13	1.76E-11	73.04	1.29E-03	1.19E-05	0.9
	630.77	2.63	0.08	4.094	3.108	5.83E-13	1.72E-11	73.04	1.26E-03	7.60E-05	6.0
Lower Kirtland	820.00	2.68	0.07	0.653	9.585	3.54E-13	1.33E-11	74.44	9.90E-04	4.62E-05	4.7
	820.74	2.68	0.07	0.942	3.510	2.14E-13	8.06E-12	74.44	6.00E-04	5.40E-05	9.0
	821.33	2.68	0.07	3.994	5.301	6.34E-13	2.38E-11	74.44	1.77E-03	2.76E-05	1.6
	821.88	2.65	0.06	2.732	12.349	6.84E-13	2.62E-11	74.44	1.95E-03	2.24E-05	1.1
Fruitland*		1.79	0.15	1.5	4.6	3.13E-13	3.17E-12	74.56	2.37E-04		

*Values for the Fruitland Formation are taken from Zhou et al. (2006)

Steady-State ⁴He Advection, Diffusion, and In Situ Generation

As a base case, we first evaluate single-phase, fully-saturated-by-groundwater, steady-state, 1D-advection-only transport through the Kirtland Formation, with homogeneous material properties (e.g., uniform U and Th concentration, porosity, etc.) and a constant helium production source term. The hydrologic gradient just north of the structural hingeline has been thought by many workers to be essentially vertical (Kaiser and Ayers, 1994), and thus we suggest such a 1D approach is appropriate. This simple case allows an initial evaluation of the importance of upward advective transport through the system, which is the major concern of the assessment of the potential seal bypass system. A following model tested herein subsequently adds diffusion. These models form the foundation for a discussion of the ⁴He trends and sealing behavior. Due to the restricted nature of these models, we present our conclusions with the caveat that additional conceptual models (e.g., lateral flow in the Farmington Sandstone Member) are possible to explain these data. We discuss our conclusions in the context of these other conceptual models.

One-dimensional, advection-only transport is represented by the following equation:

$$V_z \frac{\partial c}{\partial z} = \frac{G^*}{\phi} \quad (7)$$

where V_z is the vertical groundwater velocity, c is the concentration of ⁴He, z is depth, G^* is the ⁴He release rate from solid rock grains, and ϕ is porosity. Letting G^*/ϕ be equal to g (i.e., the accumulation of ⁴He in cm³ STP per cm³ of pore water per year, which is calculated by Equation 5), the solution is the following:

$$V_z = g \frac{z_u - z_l}{c_u - c_l} \quad (8)$$

where z and c represent depths and corresponding concentrations in the upper (subscript “u”) and lower (subscript “l”) members of the Kirtland Formation. As molar concentration units are conserved, we conveniently use measured concentration values in cm^3 STP per cm^3 pore water volume. Using a g production rate of $1.78 \times 10^{-11} \text{ cm}^3$ STP $^4\text{He cm}^{-3} \text{H}_2\text{O yr}^{-1}$ (i.e., the average $[P^4_{\text{He}}]_{\text{H}_2\text{O}}$ for the upper and lower Kirtland Formation samples, based on Table 5.2), and upper and lower concentration values that correspond to the most robust measured data points (see the discussion in the immediately previous section), a value of $6.9 \times 10^{-5} \text{ m/yr}$ is obtained for V_z (Figure 5.15).

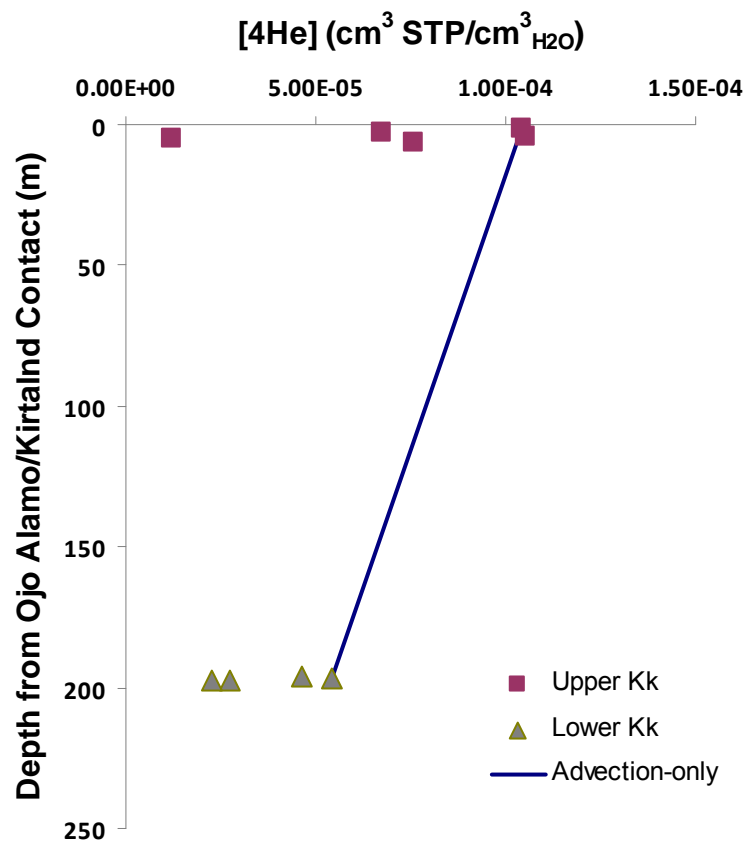


Figure 5.15. Measured ^4He concentrations versus depth and the solution to the 1D advection-only model with *in situ* ^4He production (blue line).

To obtain permeability from V_z , we estimate a hydraulic gradient, solve Darcy's Law for hydraulic conductivity (while multiplying V_z by the average porosity), and convert for permeability. Measurements of hydraulic head were not performed during the Pump Canyon project; however, Kaiser et al. (1994) listed a measured head in the Fruitland Formation from a well near the Pump Canyon site of 1170 m (3840 ft) above a datum of 933 m (3060 ft) above mean sea level. A 2D groundwater model by these authors, along a N-S cross section line running close to the Pump Canyon site, gives an upper head value (Kaiser et al., 1994) of 884 m (2900 ft) above datum (Kaiser et al., 1994, their Figure 8.24). Note that a 3D groundwater model by Kernodle (1996) includes the study area; however, Kernodle's model simulated the entire San Juan basin and grouped the Fruitland, Kirtland, and Ojo Alamo Formations as a single hydrogeologic unit. We also estimated the hydraulic head in the Ojo Alamo Formation using the potentiometric map of Thorn et al. (1990). With these data and using the Kirtland Formation thickness at Pump Canyon of 240 m, we constrain the vertical hydraulic gradient at the Pump Canyon site to be 0.6 to 1.2 (dimensionless). Given the estimated V_z , (using the average porosity value of 0.08), we obtain hydraulic conductivity and permeability estimates, respectively, of 4.6×10^{-6} to 9.3×10^{-6} m/yr, and approximately 1×10^{-20} to 3×10^{-20} m². These low values suggest that advection through the system is extremely low. For this particular conceptual model, the matrix properties, such as the TerraTek-measured permeability, seem to represent the formation-scale permeability. We reassess this conclusion in light of other conceptual models given below.

Next we add diffusion to the model. We also add boundary conditions as controlled by the overlying and underlying aquifers. The Kirtland Formation is bounded

by two aquifers, the Ojo Alamo Sandstone and the Fruitland Formation, both of which have been studied for their noble gas systematics. Zhou et al. (2005, 2006) have compiled an extensive data set of Fruitland Formation noble gases in produced methane in both the over-pressured (artesian) portion north of the structural hingeline, and in the under-pressured portion south of the line. Castro et al. (2000) examined ^4He in the Ojo Alamo Sandstone and the overlying formations. Both authors focus mostly on a portion of the San Juan Basin west and south of the Pump Canyon site of interest here, but spatial coherency in both data sets allow us to draw some general conclusions about ^4He in the Ojo Alamo Sandstone and Fruitland Formation.

The simple 1D advection-diffusion model for helium transport (Rubel et al., 2002; Sheldon et al., 2003) is given in Equation 9 for the fully groundwater saturated case. The 1D equation applicable in the vertical direction, z , for a homogeneous aquitard of thickness L bounded by two aquifers, is (e.g., Solomon et al., 1996)

$$V_z \frac{\partial c}{\partial z} - D \frac{\partial^2 c}{\partial z^2} = \frac{G^*}{\phi} \quad 0 < z < L \quad (9)$$

where V_z , c , D , G^* , and ϕ are the same as above. If ^4He generation and transport in the bounding aquifers are at steady state (Zhou et al., 2006, and Castro, 2000, suggest that this is the case for the Fruitland Formation and Ojo Alamo Sandstone, respectively), then we can apply the following boundary conditions:

$$\begin{aligned} c(z = 0) &= c_U \\ c(z = L) &= c_L \end{aligned} \quad (10)$$

where c_U and c_L are the steady-state concentrations of ^4He in the Ojo Alamo Sandstone and Fruitland Formation, respectively. As before, letting g denote the ratio G^*/ϕ , the solution to Equations 9 and 10 is:

$$c(z) = \left(c_L - \frac{gL}{V_z}\right) \frac{(1 - \exp(zV_z/D))}{(1 - \exp(LV_z/D))} + c_u \left(\frac{\exp(zV_z/D) - \exp(LV_z/D)}{1 - \exp(LV_z/D)} \right) + gz/V_z \quad (11)$$

If c_u is equal to zero, Equation 9 reverts to the solution presented by Solomon et al. (1996; Equation 4).

A range of values for groundwater helium concentration c_L can be estimated from the [^4He] measured in methane gas samples in the Fruitland Formation by Zhou et al. (2005). We do this assuming equilibrium partitioning of ^4He between methane and pore waters. We use Equation 2 in Ballentine et al. (2002) and their Figures 5 and 2, respectively, for the values of Henry's coefficient and the fugacity coefficient. Our estimates use an *in situ* temperature of 36°C and pore pressure of 8.2 MPa. As an example, the Stull100 well in Zhou et al. (2005) contains a [^4He] content in produced methane gas of 0.42 ppm, from which we calculate a [^4He] in pore water of $2.6 \times 10^{-6} \text{ cm}^3 \text{ } ^4\text{He STP/cm}^3 \text{ H}_2\text{O}$. In general the methane gas phase [^4He] values reported by Zhou et al. (2005) for the over-pressured Fruitland Formation are one to two orders of magnitude less than values reported for the under-pressured region, ranging from 0.0443 to 2.32 ppm. Zhou et al. (2005) suggested the lower values north of the hingeline are due to gas stripping during biogenic methane production that was initiated after artesian conditions developed in the Fruitland Formation during the Pliocene.

A value for pore water [^4He] in the Ojo Alamo Sandstone can be derived from the work of Castro et al. (2000), who suggested evolution of [^4He] as a function of recharge

distance (see their Figure 5.11). Upper bounding values from the base of the Ojo Alamo Sandstone from these authors' work range from 1.0 to $2.0 \times 10^{-5} \text{ cm}^3 \text{ } ^4\text{He STP/cm}^3 \text{ H}_2\text{O}$ for recharge distances of ~ 20 to 35 km. This is an order of magnitude larger than the value we determined from the Fruitland Formation; this may be a result of pore water ^4He being stripped by biogenic gas production. (It is unknown how much $[^4\text{He}]$ variation is caused by gas production, or whether this could affect our steady-state assumption.)

To calculate steady-state profiles of $[^4\text{He}]$, we need values for g , D , and V_z of Equation 9. The value for g is simply that calculated earlier for the Kirtland Formation, equal to $1.7 \times 10^{-11} \text{ cm}^3 \text{ } ^4\text{He STP cm}^{-3} \text{ H}_2\text{O yr}^{-1}$. The *in situ* apparent diffusion coefficient for ^4He , D , is estimated as $0.001 \text{ m}^2/\text{yr}$ (Rubel et al., 2002). To constrain V_z , we assume a Darcy vertical flux (divided by porosity) equal to the vertical hydraulic conductivity multiplied by the vertical hydraulic gradient (using the range from above of 0.6 to 1.2). Given a vertical velocity, we can then use Equation 11 to calculate vertical helium profiles. We use this steady state model and the measured $[^4\text{He}]$ concentrations to constrain V_z and bulk vertical permeability of the Kirtland Formation.

Figure 5.16a shows $[^4\text{He}]$ profiles as a function of depth for varying velocities of minus (indicating upward groundwater movement) 2.5×10^{-6} , 2.5×10^{-5} , 7.5×10^{-5} , 2.5×10^{-4} , and $2.5 \times 10^{-3} \text{ m/yr}$, corresponding to Peclet numbers (equal to LV_z/D) of 0.6 , 6 , 18 , 60 , and 600 , respectively, and a constant g value of $1.78 \times 10^{-11} \text{ cm}^3 \text{ STP } ^4\text{He cm}^{-3} \text{ H}_2\text{O yr}^{-1}$. Figure 5.16b shows profiles at a constant V_z of $-2.5 \times 10^{-5} \text{ m/yr}$ and a range of g values from 5.0×10^{-12} to 1.78×10^{-11} (the average value of production at the depths of the samples) to $5.0 \times 10^{-11} \text{ cm}^3 \text{ } ^4\text{He STP/cm}^3 \text{ H}_2\text{O yr}^{-1}$. The qualitative best fit model involves a

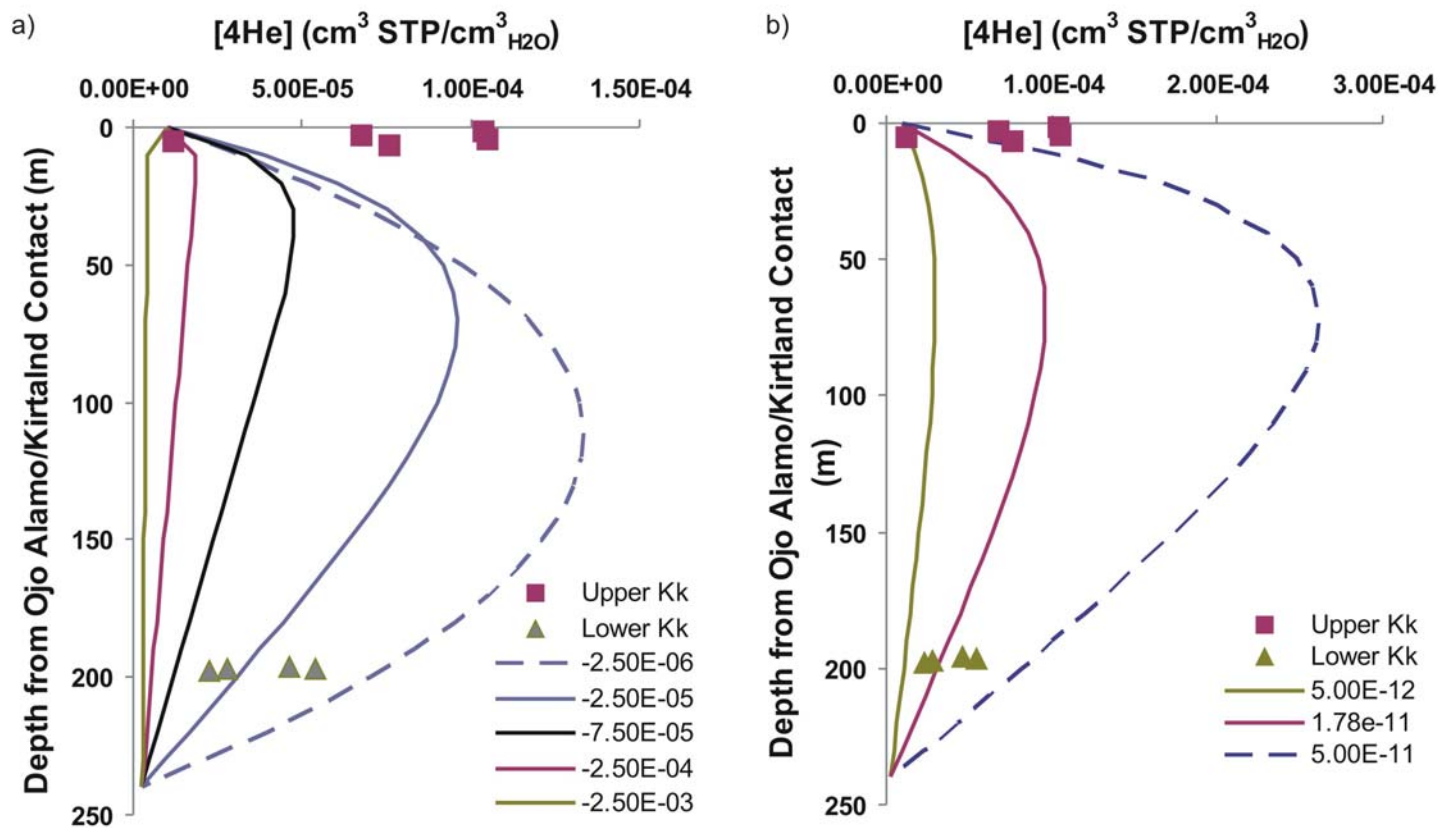


Figure 5.16. Helium concentration versus depth profiles for measured and modeled data. a) Profiles with varying groundwater velocity V_z (given in legend) and a constant ^4He production value of $g = 1.78 \times 10^{-11} \text{ cm}^3 \text{ STP } ^4\text{He cm}^{-3} \text{ H}_2\text{O yr}^{-1}$. b) Profiles with varying *in situ* helium production (in units of $\text{cm}^3 \text{ STP } ^4\text{He cm}^{-3} \text{ H}_2\text{O yr}^{-1}$; values given in legend) and constant $V_z = 2.5 \times 10^{-5} \text{ m yr}^{-1}$.

g value of $5.0 \times 10^{-11} \text{ cm}^3 \text{ STP } ^4\text{He cm}^{-3} \text{ H}_2\text{O yr}^{-1}$, about twice the calculated value in Table 5.2, and a velocity of $-2.5 \times 10^{-5} \text{ m/yr}$. This corresponds to a hydraulic conductivity of 1.7×10^{-6} to $3.3 \times 10^{-6} \text{ m/yr}$ or a vertical permeability of approximately 5×10^{-21} to $1 \times 10^{-20} \text{ m}^2$. These permeability values are lower, but comparable to those of the advection-only model. The scenarios of advection-dominated transport from Figure 5.16a do not fit the measured data very well due to the $[^4\text{He}]$ at the boundary conditions (note that the upper Kirtland Formation data point with the lowest $[^4\text{He}]$ is suspect due to incomplete gas release from the core plugs). The lowest velocity case ($V_z = -2.5 \times 10^{-6} \text{ m/yr}$) of Figure 5.16a covers the range of values seen in the measured data better than the higher velocity scenarios. A higher ^4He production term than that measured at the depths of the upper and lower Kirtland Formation samples improves the correspondence of the model and the measured data (Figure 5.16b). The higher production term of $5 \times 10^{-11} \text{ cm}^3 \text{ STP } ^4\text{He cm}^{-3} \text{ H}_2\text{O yr}^{-1}$, however, would require U and Th concentrations to be more than double their current value, which may not be realistic. In general, the scenarios of Figure 5.16 suggest that the diffusion-dominated cases, with higher ^4He production than what was estimated from measured U and Th concentrations, correspond better with the measured data than the advection-dominated cases.

An interesting finding is that both the advection-only and advection-diffusion models suggest permeability on the order of 10^{-20} m^2 or less for this system. We cannot say whether the system is advection- or diffusion-dominated. Being at an order of magnitude lower than the values based on core plug measurements values and the pore-scale model result ($\sim 10^{-19} \text{ m}^2$), these advection-only and advection-diffusion models suggest that the bulk Kirtland Formation permeability is even lower (at least one order of

magnitude) than the core-scale measured values. In summary, both core permeability and the ^4He data and analysis suggest that the fluid flux through the Kirtland Formation is low. We warn the reader, however, that other conceptual models are possible to explain the ^4He data.

Additional transport scenarios for the Kirtland Formation include the following:

1) lateral fluid flow in the Farmington Sandstone Member, which contains abundant sandstone interbeds that are probably permeable (see Appendix B.5 for mud log that shows the sandstone interbeds); 2) variation in production of ^4He throughout the system; and 3) a gas phase that is either stagnant or advecting relative to the groundwater. If the Farmington Sandstone Member is a significant aquifer and transmits fluids from the recharge area, then the helium concentrations would be lowered relative to the situation of the Farmington Sandstone Member not acting as an aquifer (i.e., if an aquifer, the Farmington Sandstone Member may contain significant, relatively young groundwater with relatively low ^4He concentrations). These scenarios are currently difficult to test due to little data on the Farmington Sandstone Member. The *in situ* ^4He production rate does not seem to be greatly different from the upper and lower members of the Kirtland Formation and probably does not have a strong impact on the difference in ^4He concentration here.

We find it difficult to evaluate transport models when the measured data are located near model boundary conditions. The location of the data limits our ability to test different model conceptualizations and parameterizations. Data points within the Farmington Sandstone Member would have allowed us to test if these 1D models are appropriate or if other conceptualizations (e.g., lateral flow in the Farmington Sandstone

Member or higher or lower ^4He production) would correspond better with the data. Furthermore, we have inferred the ^4He concentration in the Ojo Alamo Sandstone and the Fruitland Formation from previous work without direct measurement at the Pump Canyon site. When planning the coring program, the lead author's original conceptual model of helium transport focused on helium gradients across a caprock as an important metric of sealing quality, and thus core was collected in the upper and lower members of the Kirtland. Furthermore, the cost of drilling and coring restricted the number of separate lengths of core that could be collected. However, the Kirtland Formation may experience upward and downward (diffusional) transport of helium towards the Ojo Alamo Sandstone and the Fruitland Formation (and possibly transport upward or downward toward the Farmington Sandstone Member from the lower and upper shale members, respectively). This bi-directional diffusion within the Kirtland Formation was not properly anticipated when designing the coring program. The possible transport of ^4He by a separate gas phase adds to the complexity of assessing transport, which could have been evaluated with a suite of noble gases (Ne, Ar, Kr, and Xn) as done in previous studies (see Lippmann et al., 2003).

In spite of the nonconclusive findings (i.e., the body of evidence supports, but does not guarantee the lack of a bypass system), we emphasize the simple calculations of the large percentage (up to ~10%) of the *in situ* produced ^4He still remaining in the pore fluids after millions of years (Table 5.2, last column). Active, advective fluid flow has not flushed out the produced ^4He , which suggests low fluid fluxes occur in the system. With this finding and the indication of low fluid fluxes by the 1D advection-only and advection-diffusion models, we propose that the Kirtland Formation is controlled more

by the matrix-scale data than a larger-scale seal bypass system. We submit that what we inferred as potential seal bypass features (seismic and sub-seismic fractures and faults) in the FMI log likely do not create an appreciable cross-Kirtland Formation seal bypass. These statements are not guaranteed by our analysis, and further work is needed. We recommend additional sampling within the Farmington Sandstone Member and collection of other noble gases to assess multiphase partitioning and flow processes.

DISCUSSION AND CONCLUSIONS: MULTI-SCALE EVALUATION OF SEAL BYPASS SYSTEMS

This section addresses the multi-scale assessment of caprock sealing quality for the Kirtland Formation and other sites in general. Our Kirtland Formation-specific investigation involves data collected from the pore, core, well log, and formation scale (i.e., helium data collected at the top and bottom of the Kirtland Formation). Our multi-scale assessment is not based on upscaling a variety of data sets, but simply comparing different types of data collected at different scales to determine if the data are coherent.

Mercury intrusion porosimetry (MIP), permeability measured on core, FMI log-based fracture measurements, and other pore-, core-, and well log-scale data do not provide clear indication of the connectedness of transmissive features over the vertical scale of the entire Kirtland Formation. The MIP and core-scale permeability indicate high sealing capacity. However, the core and well log data indicate potentially transmissive fractures, such as open and mineralized fractures. The mineralization and methane gas saturations within the Kirtland Formation and the overlying Ojo Alamo Sandstone suggest possible large-scale connectivity. Thus, the natural tracer data—helium and

neon—are especially important since they are affected by actual transport through the seal. The goal is to determine if the tracer data indicate connectedness and relatively high permeability at the scale of the entire Kirtland Formation. If this is the case, then fractures or other features would have to be invoked as a seal bypass system to explain the data.

Our analysis of the noble gas data supports a low fluid flux through the Kirtland Formation. Key findings supporting this statement are: 1) a large percentage of the radiogenically produced ^4He is in the pore fluids of the Kirtland Formation, indicating low advective fluid flow from the surrounding aquifers; and 2) simple advection-only and advection-diffusion models estimate low permeability ($\sim 10^{-20} \text{ m}^2$ or lower) for the entire thickness of the Kirtland Formation. Thus, following our multi-scale approach, we propose that the formation-scale data are coherent with those of the pore-scale (e.g., permeability and MIP). However, our findings do not guarantee low fluid fluxes and the lack of a seal bypass system. Our models rely on restricted conceptualizations (e.g., 1D, fully groundwater saturated fluid flow with homogeneous formation properties). Furthermore, the measured data points are located near the boundary conditions of the models, which are the overlying and underlying aquifers. Tests of different conceptualizations (e.g., lateral flow in the Farmington Sandstone Member) and model parameterization are limited by the location of these data. *In situ* advective transport of a gas phase may also be possible, which we are not able to constrain with only neon and helium data.

The limitations of our analysis indicate the need for careful feasibility studies prior to coring and drilling programs to ensure that the collected natural tracer data will

support tests of different conceptualizations. Future studies should tailor data collection programs to the system of interest in terms of flow units, sampling locations, and the types of tracers. Analytical or numerical modeling should be used prior to data collection to optimize the sampling locations. We sought to use natural helium and other noble gases because they occur in all groundwater systems and reflect transport processes. However, in addition to these tracers, our investigation would have benefited from examining the methane in the system, which may have been an effective tracer at indicating the degree of large-scale transport. Other sites may have particular, local, natural tracers that would be valuable in addition to the noble gases.

Our study is part of the effort, encouraged by the CO₂ research community (DOE, 2007), to develop approaches for large-scale caprock assessment for CO₂ storage. Industrial-scale CO₂ storage may involve reservoir/caprock evaluation at the scale of entire sedimentary basins (Birkholzer and Zhou, 2009). Previous work using noble gases, especially helium, have assessed basin-scale aquifer transport in terms of large-scale permeability and groundwater residence times (Castro et al., 1998; Bethke et al., 1999; Bethke and Johnson, 2008). The goal, however, has not been the diagnosis of seal bypass systems. Future work can build on these studies and ours presented herein to assess basin-scale reservoir-aquifer/caprock systems with a focus on identifying and characterizing seal bypass systems.

ACKNOWLEDGMENTS

We gratefully acknowledge the U.S. Department of Energy's (DOE) National Energy Technology Laboratory (NETL) for sponsoring this project. DOE's Basic Energy

Science Office funded the dual-beam focused ion beam/scanning electron microscopy analysis, confocal microscopy, and pore-scale modeling.

We thank Dr. D. Kip Solomon for his review of this dissertation chapter in preparation for later journal publication. He and Alan Rigby performed the noble gas analysis at the Dissolved and Noble Gas Laboratory, University of Utah. We thank them for helpful discussions on noble gas geochemistry and sample collection. We also appreciate the assistance of Dr. Martin Stute, Lamont-Doherty Earth Observatory, with the design of the noble gas preservation canisters and guidance for field sampling.

Scott Cooper assisted with background geologic information and planning the coring program. We thank Ryan Frost, Eddie Pippin, and Tom Cochrane from ConocoPhillips for executing the coring program under the auspices of the Southwest Regional Partnership on Carbon Sequestration, a project supported by the DOE and managed by NETL. William Holub, Randy Everett, Lee Harris, and Dr. Reid Grigg helped with core handling and sample preservation in the field. We thank John Keller and Mary Milner of TerraTek—a Schlumberger company, Scott Wagner of Wagner Petrographic, and Dr. John Neasham of Poro-Technology for petrophysical and petrographic core analysis, thin section preparation, and mercury intrusion porosimetry, respectively. Dan McGinn of Softrock Geological Services, Inc., provided geologic characterization and assistance in choosing core points.

Sandia National Laboratories is a multi-program laboratory operated by Sandia Corporation, a wholly owned subsidiary of Lockheed Martin Company, for the U.S. Department of Energy's National Nuclear Security Administration under contract DE-AC04-94AL85000.

REFERENCES

- Andreani, M., P. Gouze, L. Luquot, and P. Jouanna, 2008, Changes in seal capacity of fractured claystone caprocks induced by dissolved and gaseous CO₂ seepage: *Geophysical Research Letters*, v. 35, p. 6.
- Andrews, J. N., 1985, The isotopic composition of radiogenic helium and its use to study groundwater movement in confined aquifers: *Chemical Geology*, v. 49, p. 339–351.
- Aplin, A. C., A. J. Fleet, and J. H. S. MacQuaker, 1999, Muds and mudstones: Physical and fluid-flow properties, in A. C. Aplin, A. J. Fleet, and J. H. S. Macquaker, eds., *Muds and mudstones: Physical and fluid-flow properties*, v. 158: London, Geological Society [London] Special Publication 158, p. 1–8.
- Ayers, Jr., W. B., 2003, Coalbed methane in the Fruitland Formation, San Juan Basin, western United States: A giant unconventional gas play, in M. T. Halbouty, ed., *Giant oil and gas fields of the decade 1990–1999, AAPG Memoir 78*, p. 159–188.
- Ayers, Jr., W. B., W. A. Ambrose, and J. S. Yeh, 1994, Coalbed methane in the Fruitland Formation, San Juan Basin: Depositional and structural controls on occurrence and resources: Coalbed Methane in the Upper Cretaceous Fruitland Formation, San Juan Basin, New Mexico and Colorado, *New Mexico Bureau of Mines and Mineral Resources Bulletin 146*, p. 13–40.
- Bachu, S., and D. B. Bennion, 2009, Interfacial Tension between CO₂, Freshwater, and Brine in the Range of Pressure from (2 to 27) MPa, Temperature from (20 to 125) degrees C, and Water Salinity from (0 to 334 000) mg(.)L(-1): *Journal of Chemical and Engineering Data*, v. 54, p. 765–775.
- Ballentine, C. J., R. Burgess, and B. Marty, 2002, Tracing fluid origin, transport and interaction in the crust, in D. Porcelli, C. J. Ballentine, and R. Wieler, eds., *Noble Gases in Geochemistry and Cosmochemistry: Reviews in Mineralogy and Geochemistry*, v. 47: Washington, DC, Mineralogical Society of America, p. 539–614.
- Berg, R. R., 1975, Capillary pressures in stratigraphic traps: *AAPG Bulletin*, v. 59, p. 939–956.
- Bethke, C. M., and T. M. Johnson, 2008, Groundwater age and groundwater age dating: *Annual Review of Earth and Planetary Sciences*, v. 36, p. 121–152.
- Bethke, C. M., X. Zhao, and T. Torgersen, 1999, Groundwater flow and the He-4 distribution in the Great Artesian Basin of Australia: *Journal of Geophysical Research-Solid Earth*, v. 104, p. 12999–13011.

- Birkholzer, J. T., and Q. L. Zhou, 2009, Basin-scale hydrogeologic impacts of CO₂ storage: Capacity and regulatory implications: *International Journal of Greenhouse Gas Control*, v. 3, p. 745–756.
- Boult, P., and J. Kaldi, eds., 2005, Evaluating Fault and Cap Rock Seals: *AAPG Hedberg Series, No. 2*: Tulsa, Oklahoma, American Association of Petroleum Geologists, 268 p.
- Carey, J. W., M. Wigand, S. J. Chipera, G. WoldeGabriel, R. Pawar, P. C. Lichtner, S. C. Wehner, M. A. Raines, and G. D. Guthrie, 2007, Analysis and performance of oil well cement with 30 years of CO₂ exposure from the SACROC Unit, West Texas, USA: *International Journal of Greenhouse Gas Control*, v. 1, p. 75–85.
- Cartwright, J., M. Huuse, and A. Aplin, 2007, Seal bypass systems: *AAPG Bulletin*, v. 91, p. 1141–1166.
- Castro, M. C., P. Goblet, E. Ledoux, S. Violette, and G. de Marsily, 1998, Noble gases as natural tracers of water circulation in the Paris Basin 2. Calibration of a groundwater flow model using noble gas isotope data: *Water Resources Research*, v. 34, p. 2467–2483.
- Castro, M. C., M. Stute, and P. Schlosser, 2000, Comparison of He-4 ages and C-14 ages in simple aquifer systems: implications for groundwater flow and chronologies: *Applied Geochemistry*, v. 15, p. 1137–1167.
- Chiaromonte, L., M. D. Zoback, J. Friedmann, and V. Stamp, 2008, Seal integrity and feasibility of CO₂ sequestration in the Teapot Dome EOR pilot: Geomechanical site characterization: *Environmental Geology*, v. 54, p. 1667–1675.
- Chiquet, P., D. Broseta, and S. Thibeau, 2007, Wettability alteration of caprock minerals by carbon dioxide: *Geofluids*, v. 7, p. 112–122.
- Dewhurst, D. N., R. M. Jones, and M. D. Raven, 2002, Microstructural and petrophysical characterization of Muderong Shale: Application to top seal risking: *Petroleum Geoscience*, v. 8, p. 371–383.
- DOE, 2007, Basic Research Needs for Geosciences: Facilitating 21st Century Energy Systems, Report from the Workshop Held February 21–23: U.S. Department of Energy, Office of Basic Energy Sciences, available in pdf format at <http://www.sc.doe.gov/bes/reports/list.html>.
- Eichhubl, P., and J. R. Boles, 2000, Rates of fluid flow in fault systems—Evidence for episodic rapid fluid flow in the Miocene Monterey Formation, coastal California: *American Journal of Science*, v. 300, p. 571–600.

- Fassett, J. E., and J. S. Hinds, 1971, Geology and fuel resources of the Fruitland Formation and Kirtland Shale of the San Juan Basin, New Mexico and Colorado, *U.S. Geological Survey Professional Paper 676*, p. 76.
- Fassett, J. E., and N. D. Thomaidis, 1978, *Oil and gas fields of the Four Corners area, Volumes I and II*, Four Corners Geological Society.
- Gherardi, F., T. F. Xu, and K. Pruess, 2007, Numerical modeling of self-limiting and self-enhancing caprock alteration induced by CO₂ storage in a depleted gas reservoir: *Chemical Geology*, v. 244, p. 103–129.
- Gilfillan, S. M., C. J. Ballentine, G. Holland, D. Blagburn, B. S. Lollar, S. Stevens, M. Schoell, and M. Cassidy, 2008, The noble gas geochemistry of natural CO₂ gas reservoirs from the Colorado Plateau and Rocky Mountain provinces, USA: *Geochimica et Cosmochimica Acta*, v. 72, p. 1174–1198.
- Harris, D. C., 2007, *Quantitative Chemical Analysis, Seventh Edition*: New York, New York, W. H. Freeman and Company, 44–49 p.
- Heath, J., B. McPherson, F. Phillips, S. Cooper, and T. Dewers, 2009, Natural helium as a screening tool for assessing caprock imperfections at geologic CO₂ storage sites, in J. Gale, H. Herzog, and J. Braitsch, eds., *Greenhouse Gas Control Technologies 9: Energy Procedia*, v. 1, p. 2903–2910.
- Hendry, M. J., T. G. Kotzer, and D. K. Solomon, 2005, Sources of radiogenic helium in a clay till aquitard and its use to evaluate the timing of geologic events: *Geochimica et Cosmochimica Acta*, v. 69, p. 475–483.
- Hildenbrand, A., S. Schlomer, B. M. Krooss, and R. Littke, 2004, Gas breakthrough experiments on pelitic rocks: comparative study with N₂, CO₂ and CH₄: *Geofluids*, v. 4, p. 61–80.
- Ingram, G. M., J. L. Urai, and M. A. Naylor, 1997, Sealing processes and top seal assessment, in P. Moller-Pedersen, and A. G. Koestler, eds., *Hydrocarbon Seals: Importance for Exploration and Production: NPF Special Publication 7*: Singapore, p. 165–174.
- IPCC, 2005, *IPCC special report on carbon dioxide capture and storage*, prepared by Working Group III of the Intergovernmental Panel on Climate Change: Cambridge, United Kingdom and New York, NY, USA, Cambridge University Press, 442 p.
- Johnson, J. W., J. J. Nitao, and J. P. Morris, 2005, Reactive transport modeling of cap rock integrity during natural and engineered CO₂ storage, in S. M. Benson, ed.,

Carbon Dioxide Capture for Storage in Deep Geologic Formations—Results from the CO₂ Capture Project, Vol. 2: *Geologic Storage of Carbon Dioxide with Monitoring and Verification*: London, England, Elsevier, p. 787–814.

- Kaiser, W. R., and W. B. Ayers, Jr., 1994, Coalbed methane production, Fruitland Formation, San Juan Basin: geologic and hydrologic controls, in W. B. Ayers, Jr., and W. R. Kaiser, eds., *Coalbed Methane in the Upper Cretaceous Fruitland Formation, San Juan Basin, New Mexico and Colorado*, *New Mexico Bureau of Mines and Mineral Resources Bulletin 146*, p. 187–207.
- Kaiser, W. R., T. E. Swartz, and G. J. Hawkins, 1994, Hydrologic framework of the Fruitland Formation, San Juan Basin, in W. B. Ayers, Jr., and W. R. Kaiser, eds., *Coalbed Methane in the Upper Cretaceous Fruitland Formation, San Juan Basin, New Mexico and Colorado*, *New Mexico Bureau of Mines and Mineral Resources Bulletin 146*, p. 133–163.
- Kernodle, J. M., 1996, Hydrogeology and steady-state simulation of ground-water flow in the San Juan Basin, New Mexico, Colorado, Arizona, and Utah: *U.S. Geological Survey Water-Resources Investigations Report 95-4187*.
- Kernodle, J. M., C. R. Thorn, G. W. Levings, S. D. Craigg, and W. L. Dam, 1990, Hydrogeology of the Kirtland Shale and Fruitland Formation in the San Juan Structural Basin, New Mexico, Colorado, Arizona, and Utah: *U.S. Geological Survey Hydrologic Investigations Atlas HA-720-C*, scale 1:1,000,000 and 1:2,000,000, 2 sheets.
- Kipfer, R., W. Aeschbach-Hertig, F. Peeters, and M. Stute, 2002, Noble gases in lakes and ground waters, in D. Porcelli, C. J. Ballentine, and R. Wieler, eds., *Noble Gases in Geochemistry and Cosmochemistry*, v. 47: Washington, D.C., Mineralogical Society of America, Geochemical Society, p. 615–700.
- Klute, M. A., 1986, Sedimentology and sandstone petrography of the Upper Kirtland Shale and Ojo Alamo Sandstone, Cretaceous-Tertiary Boundary, western and southern San Juan Basin, New Mexico: *American Journal of Science*, v. 286, p. 463–488.
- Lafortune, S., M. Moreira, P. Agrinier, H. Schneider, and H. Catalette, 2008, Noble gases as precursors of CO₂ deep storage leaks towards surface: *Geochimica et Cosmochimica Acta*, v. 72, p. A510.
- Law, B. E., 1992, Thermal maturity patterns of Cretaceous and Tertiary rocks, San Juan Basin, Colorado and New Mexico: *Geological Society of America Bulletin*, v. 104, p. 192–207.

- Lippmann, J., M. Stute, T. Torgersen, D. P. Moser, J. A. Hall, L. Lin, M. Borecik, R. E. S. Bellamy, and T. C. Onstott, 2003, Dating ultra-deep mine waters with noble gases and Cl-36, Witwatersrand Basin, South Africa: *Geochimica et Cosmochimica Acta*, v. 67, p. 4597–4619.
- Litynski, J. T., S. Plasynski, H. G. McIlvried, C. Mahoney, and R. D. Srivastava, 2008, The United States Department of Energy's Regional Carbon Sequestration Partnerships Program Validation Phase: *Environment International*, v. 34, p. 127–138.
- Lorenz, J. C., and S. P. Cooper 2003, Tectonic setting and characteristics of natural fractures in Mesaverde and Dakota reservoirs of the San Juan Basin: *New Mexico Geology*, v. 25, p. 3–14.
- Lorenz, J. C., and R. E. Hill, 1992, Measurement and analysis of fractures in core, in J. W. Schmoker, E. B. Coalson, and C. A. Brown, eds., *Geologic Studies Relevant to Horizontal Drilling: Examples from Western North America*, Rocky Mountain Association of Geologists, p. 47–59.
- Ma, L., M. C. Castro, C. M. Hall, and L. M. Walter, 2005, Cross-formational flow and salinity sources inferred from a combined study of helium concentrations, isotopic ratios, and major elements in the Marshall aquifer, southern Michigan: *Geochemistry Geophysics Geosystems*, v. 6, p. 21.
- Molenaar, C. M., and J. K. Baird, 1992, Regional stratigraphic cross sections of Upper Cretaceous rocks across the San Juan Basin, northwestern New Mexico and southwestern Colorado, *U.S. Geological Survey Open-File Report 92-257*, sheets 1-3.
- Nordbotten, J. M., D. Kavetski, M. A. Celia, and S. Bachu, 2009, Model for CO₂ Leakage Including Multiple Geological Layers and Multiple Leaky Wells: *Environmental Science & Technology*, v. 43, p. 743–749.
- Orr, F. M., 2009, CO₂ capture and storage: Are we ready?: *Energy & Environmental Science*, v. 2, p. 449–458.
- Osenbruck, K., J. Lippmann, and C. Sonntag, 1998, Dating very old pore waters in impermeable rocks by noble gas isotopes: *Geochimica et Cosmochimica Acta*, v. 62, p. 3041–3045.
- Phillips, F. M., M. K. Tansey, L. A. Peeters, S. L. Cheng, and A. Long, 1989, An isotopic investigation of groundwater in the central San Juan Basin, New Mexico: Carbon 14 dating as a basis for numerical flow modeling: *Water Resources Research*, v. 25, p. 2259–2273.

- Pittman, E. D., 1992, Relationship of porosity and permeability to various parameters derived from mercury injection-capillary pressure curves for sandstones: *AAPG Bulletin*, v. 76, p. 191-198.
- PRISM Climate Group, 2009, 103-Year High-Resolution Temperature Climate Data Set for the Conterminous United States, PRISM Climate Group, Oregon State University, Spatial Climate Analysis Service, Oregon, accessed November 12, 2009, <http://www.prism.oregonstate.edu/>.
- Pruess, K., 2008, On CO₂ fluid flow and heat transfer behavior in the subsurface, following leakage from a geologic storage reservoir: *Environmental Geology*, v. 54, p. 1677–1686.
- Rohmer, J., and O. Bouc, 2010, A response surface methodology to address uncertainties in cap rock failure assessment for CO₂ geological storage in deep aquifers: *International Journal of Greenhouse Gas Control*, v. 4, p. 198–208.
- Rubel, A. P., C. Sonntag, J. Lippmann, F. J. Pearson, and A. A. Gautschi, 2002, Solute transport in formations of very low permeability: Profiles of stable isotope and dissolved noble gas contents of pore water in the Opalinus Clay, Mont Terri, Switzerland: *Geochimica et Cosmochimica Acta*, v. 66, p. 1311–1321.
- Sacchi, E., J. L. Michelot, H. Pitsch, P. Lalieux, and J. F. Aranyossy, 2001, Extraction of water and solutes from argillaceous rocks for geochemical characterisation: Methods, processes, and current understanding: *Hydrogeology Journal*, v. 9, p. 17–33.
- Schowalter, T. T., 1979, Mechanics of secondary hydrocarbon migration and entrapment: *AAPG Bulletin*, v. 63, p. 723–760.
- Scott, A. R., W. R. Kaiser, and W. B. Ayers, 1994, Thermogenic and secondary biogenic gases, San Juan Basin, Colorado and New Mexico-Implications for coalbed gas producibility: *AAPG Bulletin*, v. 78, p. 1186–1209.
- Sheldon, A. L., D. K. Solomon, R. J. Poreda, and A. Hunt, 2003, Radiogenic helium in shallow groundwater within a clay till, southwestern Ontario: *Water Resources Research*, v. 39, p. 12.
- Silin, D., T. W. Patzek, and S. M. Benson, 2009, A one-dimensional model of vertical gas plume migration through a heterogeneous porous medium: *International Journal of Greenhouse Gas Control*, v. 3, p. 300–310.
- Snyder, G. T., W. C. Riese, S. Franks, U. Fehn, W. L. Pelzmann, A. W. Gorody, and J. E. Moran, 2003, Origin and history of waters associated with coalbed methane: I-

- 129, Cl-36, and stable isotope results from the Fruitland Formation, CO and NM: *Geochimica et Cosmochimica Acta*, v. 67, p. 4529–4544.
- Stone, W. J., F. P. Lyford, P. F. Frenzel, N. H. Nizell, and E. T. Padgett, 1983, Hydrogeology and water resources of San Juan Basin, New Mexico: *New Mexico Bureau of Mines and Mineral Resources Hydrologic Report 6*, p. 70, 7 sheets.
- Stute, M., J. F. Clark, P. Schlosser, W. S. Broecker, and G. Bonani, 1995, A 30,000-yr continental paleotemperature record derived from noble gases dissolved in groundwater from the San Juan Basin, New Mexico: *Quaternary Research*, v. 43, p. 209–220.
- USGS, 2009, National Elevation Dataset (NED) 1 Arc Second, U.S. Geological Survey, accessed November 12, 2009, <http://seamless.usgs.gov/products/1arc.php>.
- Weiss, R.F., 1971, Solubility of helium and neon in water and seawater: *Journal of Chemical and Engineering Data*, v. 16, p. 235–241.
- Wilson, T., A. Wells, D. Peters, A. Mioduchowski, G. Martinez, J. Heath, and G. Koperna, submitted, Fracture evaluation of the Southwest Regional Partnership's San Juan Basin Fruitland coal carbon sequestration pilot site, New Mexico: *AAPG Bulletin*.
- Yang, Y. L., and A. C. Aplin, 2007, Permeability and petrophysical properties of 30 natural mudstones: *Journal of Geophysical Research-Solid Earth*, v. 112, p. 14.
- Yao, N., 2007, Introduction to the focused ion beam system, in N. Yao, ed., *Focused ion beam systems: Basics and applications*: Cambridge, UK, Cambridge University Press, p. 1–29.
- Zhang, Y., C. M. Oldenburg, S. Finsterle, P. Jordan, and K. Zhang, 2008, Probability estimation of CO₂ leakage through faults at geologic carbon sequestration sites, *9th International Conference on Greenhouse Gas Control Technologies*, November 16–20, Washington D.C.
- Zhou, Z., and C. J. Ballentine, 2006, He-4 dating of groundwater associated with hydrocarbon reservoirs: *Chemical Geology*, v. 226, p. 309–327.
- Zhou, Z., C. J. Ballentine, R. Kipfer, M. Schoell, and S. Thibodeaux, 2005, Noble gas tracing of groundwater/coalbed methane interaction in the San Juan Basin, USA: *Geochimica et Cosmochimica Acta*, v. 69, p. 5413–5428.

PART IV. CONCLUSIONS AND RECOMMENDATIONS

CHAPTER 6. SUMMARY, CONCLUSIONS, AND RECOMMENDATIONS

6.1 Summary and Conclusions

This dissertation addresses the assessment of caprock performance for underground storage of CO₂. In this context, performance constitutes the ability of caprocks to impede CO₂ migration from a reservoir, over relevant timescales, to achieve reductions in emissions of this greenhouse gas and to not harm underground sources of drinking water. Specifically, the research objective is the multi-scale evaluation of the dominate mechanisms and features that govern the caprock sealing behavior. Viscous and capillary forces of the sub- μm pore networks can contribute to the sealing quality of caprocks. Larger-scale features such as fracture networks and faults can result in significant loss of CO₂ from a reservoir. Furthermore, industrial-scale injection of CO₂ necessitates assessment of large regions of sedimentary basins in terms of fluid pressurization and potential migration of formation brines and CO₂ (Birkholzer and Zhou, 2009; DOE, 2007). Consequently, caprock assessment is a multi-scale challenge.

This dissertation addresses and tests hypotheses of the geologic processes that create high quality caprocks in terms of pore network properties (Part II). In addition, at a field site with natural fractures and methane gas within the caprock, noble gases are used

to evaluate a potential large-scale seal bypass system by quantifying the large-scale transport properties of the caprock (Part III).

Part II of the dissertation addresses properties of pore networks and their sealing behavior through investigation of a suite of mudstones. Mudstones constitute the primary caprock type for CO₂ storage due to their abundance in sedimentary basins. Previous work has correlated several textural mudstone properties within a sequence stratigraphic framework. Following this approach, Chapter 3 describes the suite of continental and marine mudstones, caprocks at CO₂ sequestration demonstration sites in the southeast and southwest United States, with the facies models of Scheiber (1999) and Almon et al. (2005). The examination of the mudstones incorporates novel, high resolution 3D geometrical and topological models of the pore networks and complementary mercury intrusion porosimetry (MIP), placed within a micro- to nano-scale petrographic framework. Interpretation of the pore network models indicates that primary depositional environment and burial history strongly control sealing efficiency (in terms of breakthrough pressures) of the pore networks. The sealing efficiency generally increases from proximal to distal mudstone facies, which is indicated by difference in geometric pore structure (i.e., pore sizes and shapes), pore types, connectivity of pores, and MIP pressures. Deep burial of organic matter probably affected pore networks by causing the organics to mobilize and fill pores. Such pore-filling may have resulted in the highest measured breakthrough pressures of the Gothic Shale (see Chapter 3 Sections 3.4.1–3.4.4 and 3.5). It follows that choice of a high quality seal involves identification of caprocks with primary distal environments that were deeply buried.

Mechanistic understanding of capillary sealing can improve screening of caprocks for CO₂ storage and possibly enable better engineered underground storage sites. Examination of geometric and chemical composition of pore-lining solid phases of the suite of mudstones indicates that capillary sealing is governed by pore shapes and phases that are not identifiable except through high resolution direct characterization of the pores. Pore-lining phases are not directly indicated by bulk X-ray diffraction (XRD) data. The amount (in wt%) of a phase from XRD does not directly correlate with what lines the pores (see Table 4.1). In particular, organics can line or surround pores and may represent once-mobile organics that modified the wettability of an originally clay-lined pore system. For shallower formations (i.e., ~800 m depth or shallower) interfacial tension and contact angles result in breakthrough pressures that are as high as those needed to fracture the rock—thus, sealing by capillarity is indicated. Deeper seals have poorer capillary sealing if mica-like wetting dominates the wettability. The literature contains little information on wetting properties of the pore-lining phases observed in this study. Theory on how clay molecular systems and their functional groups interact with the supercritical (or gaseous or liquid) CO₂ quadrupolar molecular system (Raveendran et al., 2005) is lacking and limits prediction of wettability and associated surface forces (e.g., shrink/swell). Thus, this study indicates the high degree of uncertainty in current prediction of capillary sealing behavior and the need for future research on wettability with regard to CO₂, brine, clay, and organics.

Part III addresses the difficult challenge of diagnosing seal bypass systems at the scale of the entire thickness of a caprock. Many characterization techniques based on core examination and well logging can identify fractures and faults within caprocks. However,

their impact on flow processes can still be difficult to infer. Through study of a regional, overpressured caprock—the Kirtland Formation, San Juan Basin, USA—I demonstrate caprock evaluation using noble gases collected from within the caprock at its top and bottom boundaries. I incorporate data acquired across a range of scales, starting with the pore-network-scale data and up to that of core fractures and well logs to compare with the noble gas data. Examination of the data suggests that, although pore network properties can contribute to very high capillary-sealing efficiency and low permeabilities, larger-scale potential high-permeability features exist. Fracture mineralization and gas saturation within and directly above the seal evidence multiple episodes of past fluid flow. However, the mineralization may have healed fractures and the large-scale transport needs assessment.

Interpretation of helium concentration data indicates low fluid fluxes through the caprock. Two major findings include the following: 1) of the total ^4He produced since deposition of the Kirtland Formation, a large portion still resides in the pore fluids; and 2) simple advection-only and advection-diffusion models, using the measured ^4He concentrations, estimate low permeability ($\sim 10^{-20}$ m² or lower) for the thickness of the Kirtland Formation. These findings, however, do not guarantee the lack of a large-scale bypass system. The measured data were located near the boundary conditions of the models (i.e., the overlying and underlying aquifers), which limits my ability to test conceptual models and the sensitivity of model parameterization. Thus, in Chapter 5, I recommend approaches for future studies to further assess the presence or lack of a seal bypass system at this particular site and for other sites in general.

6.2 Scientific and Engineering Contributions

This dissertation contributes to the knowledge of multi-scale features and processes that affect the ability of caprocks to retain multiphase fluids. The contribution consists of:

- 1) an extension of sequence stratigraphic conceptual models on the controls of primary depositional environments and other geologic factors on the sealing behavior of mudstones through direct sub- μm 3D petrography of pore networks;
- 2) a description of the solid chemical phases that line the pore networks, with a description of the potential impact of those phases on capillary sealing processes;
- 3) demonstration of evaluation of caprock sealing behavior from the pore-scale up to that of the entire thickness of the caprock using noble gases as an indicator of the “effective” presence and impact of a seal bypass system; and
- 4) a foundation for comparing and ranking caprocks for CO₂ storage (or other activities).

These contributions matter because spatial prediction of mudstone-sealing properties is greatly needed for site ranking and characterization for CO₂ storage, and for hydrocarbon exploration and production efforts. Chapter 3 is one of the first studies to obtain several 3D geometric models of mudstone pore networks and place them within a facies model framework. The technical approach developed by this dissertation (see Chapter 3) and the conclusions on sealing behavior is an advance in the knowledge of how geologic conditions govern mudstone pore network characteristics and corresponding multiphase flow properties.

Knowledge of pore-lining phases facilitates a mechanistic understanding of capillary-sealing processes that are key to predicting the ability of caprocks to impede CO₂ movement. Chapter 4 represents an advance in the characterization of solid phases that line the pores of mudstones caprocks, a difficult problem due to the small pore sizes. The application of the demonstrated techniques and knowledge of the pore-lining phases can support many aspects of CO₂ storage research, such as modeling of reactive transport (e.g., precipitation/dissolution of minerals and organics and/or sorption of chemical species during flow and transport) and prediction of capillary sealing behavior. Chapter 4 also supports future research efforts by clearly indicating a major research gap in terms of wettability measurements for the clay, organic matter, and other phases that line pore networks.

Part III (Chapter 5) addresses the characterization of the transmissive nature of seal bypass systems, which is a major research challenge for the petroleum geosciences and CO₂ sequestration communities. Previous work has classified major types of seismically resolvable seal bypass systems (e.g., fault related, intrusion related, and pipe related) and their general characteristics in terms of fluid fluxes and spatial dimensions (Cartwright et al., 2007); however, additional work is needed to identify sub-seismic (i.e., below the resolution of typical seismic surveys) to seismic seal bypass systems and to quantify their ability to transmit fluids. The work of Part III represents an advance in the investigation of the “effective” presence or absence of seal bypass systems. “Effective” is used here to indicate that seal bypass features such as fractures may be mineralized and thus not actually conductive although they may be identified by well logging, or the fracture networks may not be connected through the entire thickness of the seal. Chapter

5 uses ^4He data to support the conclusion of a lack of an “effective” bypass system at the Pump Canyon field site, NM, although fractures are seen in the core and FMI logs. This conclusion, however, is not guaranteed due to uncertainty of the analysis. Chapter 5 suggests other natural tracers and sampling strategies to further test the conclusion. The Future Work Section (6.3.2), with a preliminary modeling study (see Section 6.3.4), addresses needed research to further develop the identification, characterization, and risking of seal bypass features using natural tracers to infer past and potential groundwater and CO_2 fluid fluxes (i.e., leakage rates) in response to engineered activities.

6.3 Opportunities (Limitations), Recommendations, and Risk Analysis

This section first discusses dissertation-specific limitations (Section 6.3.1) and recommendations for future studies (Section 6.3.2). I use the word “limitations” in the sense of inherent challenges and opportunities in the study of mudstone caprocks that I faced, assumptions and approaches I employed, and uncertainty in the conclusions. I do not present these “limitations” to detract from the positive contributions of this dissertation (see Section 6.2). My work represents a major advance in the understanding of 3D pore networks in the context of geologic conditions (e.g., depositional setting and pore-lining composition), and how those pore networks affect capillary sealing behavior. Furthermore, characterization of seal bypass systems at depth for CO_2 storage and hydrocarbon systems is a major research challenge that few others have attempted to address using natural tracers. Thus, the reader should think of the limitations as examples of the challenges and opportunities of studying the multi-scale sealing behavior of

mudstone caprocks, which are made apparent through my work. Others will also face these opportunities in future studies.

I list several “limitations” to inspire and support future work by the CO₂ storage and petroleum geoscience communities. The Future Work Section (6.3.2) also includes general suggestions for scientific investigations of caprock processes for geologic CO₂ storage. The limitations form the basis for discussion of future work.

Because risk analysis is not strictly a scientific endeavor, but rather one of policy analysis (Rechard, 1999), it is addressed in the last sections of this dissertation (6.3.3 and 6.3.4). Risk analysis in general incorporates current scientific and technological knowledge and methodologies to enable implementation of activities that have risks. Thus, I provide links between my work and risk analysis to make my results accessible for the decision-making processes that require knowledge of caprocks.

6.3.1 Opportunities (Limitations)

In this section, I list and describe the limitations of my research. I focus on specific samples, data, interpretations, and conclusions. These limitations represent opportunities as described in the introduction of Section 6.3. I then reiterate the major findings (i.e., what I know now) and what remains uncertain. The following section (6.3.2) then provides recommendations for future studies to address what remains uncertain in terms of the dissertation and in general.

The major limitations or opportunities of the studies on pore-network properties and sealing behavior of caprocks (Part II, Chapters 3 and 4) of this dissertation include the following:

- 1) the mudstone samples of Chapter 3 and 4 have different burial, diagenetic, and tectonic histories, which obscure the impact of each of these variables on the properties of the pore networks; thus, my conclusions are limited and would be improved by future work, for example, on samples that share similar characteristics except for one particular variable of interest;
- 2) funding restricted the number of mudstone samples that I could analyze from different facies; thus, my conclusions are based on a limited number of facies and are used to infer conclusions about pore types for particular mudstones and not for mudstones in general;
- 3) samples from the Kirtland Formation contained abundant expandable clay minerals (e.g., smectite) that probably caused many induced pores upon drying; these induced pores are difficult to separate from those pores that would represent “real” *in situ* pores; future work may require cryo-FIB/SEM or other techniques to minimize the formation of induced pores and fractures;
- 4) pores created by pressure-release during drilling/coring are similarly difficult to explicitly identify and separate from what would be natural *in situ* pores;
- 5) the pore-type classification scheme of Chapter 3 (see Figure 3.10) is descriptive and applies specifically to the mudstones studied and is not applicable as a universal mudstone pore-type classification scheme (however, note that it was not meant to be a universal scheme, but such a scheme would be helpful);

- 6) the identification of the seven pore-types is not based on statistically sound or taxonomic methods, but again, was descriptive and focused to meet the goals of Chapter 3 for understanding sealing behavior;
- 7) a “pore-throat” classification scheme, as opposed to a general pore-type scheme, may be more appropriate for providing insight into the controls on breakthrough processes and sealing behavior;
- 8) the FIB/SEM and MIP data sampled different numbers of pores, thus obscuring the comparison and integration of the two data sets; e.g., the porosity estimates from the analysis of 3D pore network models and the porosity measured in the laboratory (e.g., compare porosity values from Figures 3.4 through 3.9 with those of Table 3.3) are much different, suggesting that issues of “representative elementary volume” should be considered when obtaining porosity measurements;
- 9) the joint histograms of Chapter 3 (see Figure 3.12) do not provide the most useful information for the analysis of capillary-breakthrough processes; future joint histograms should incorporate pore-throat sizes instead of only pore body volume because the throats are the constrictions in the pore network that affect breakthrough processes;
- 10) Figure 4.10 is an advance in understanding how pore-lining phases impact capillary sealing processes due to the effects of temperature, pressure, salinity, and interfacial tension; however, this type of analysis requires more explicit investigation of salinity on IFT and heterogeneity of lithofacies on the overall sealing behavior of samples from different sites; lack of available

experimental data for caprock phases (both minerals and organics) limited my study in terms of contact angles;

11) due to funding restraints and facilities I had access to, Chapter 4 lacks a direct study of the interactions between CO₂, brine, and solid phases (e.g., organics) within caprocks;

12) Chapters 3 and 4 would have benefited from physical modeling of important processes using the pore-network models, such as: intrusion of mercury or CO₂ into the pore networks; and stress-sensitive permeability due to changing apertures of pores and pore throats under different *in situ* stress conditions; and

13) the link between the pore-scale studies and the transport of noble gas tracers could have been strengthened by investigation of mudstone tortuosity using the pore-network models.

Chapters 3 and 4 focused on particular samples from caprocks of CO₂ storage sites. Therefore, I did not develop approaches for creating a universal pore network classification scheme that incorporates breakthrough pressures, which would be extremely helpful for identifying and selecting CO₂ storage sites. After finishing these Chapters, I realize that CO₂ storage efforts can benefit from future studies that choose samples and develop techniques for analyzing and classifying pore types that involve statistically sound methods. In Chapter 3, only a small number of 3D pore network models (i.e., seven) were created from a limited number of rock samples. Limited by time and funding, I did not complete a careful analysis of whether those rock samples are the most common, dominant, and reoccurring mudstone facies within the formations in

question (however, I suggest that the mudstone samples represent facies that do occur in muddy environments as based on the similarity to facies identified in previous studies; see Section 3.5). Pondering ways to obtain statistically sound data to develop better understanding of mudstone pore networks in general, I ask these questions: “How sensitive is the development of pore classification types and breakthrough pressures on the number of samples studied?” “Would the results (e.g., the number of pore types identified) and conclusions change had I worked with 20, 100, or 1000 pore network models?” Thus, statistical approaches are needed to provide an assessment of the representativeness of the samples and the associated results and conclusions.

The pore network models and pore-lining phases of Chapters 3 and 4 provide information at extremely small scales; however, I make conclusions about sealing behavior for entire facies in terms of pore types and typical pore-lining phases. These conclusions are uncertain because information at the sub- μm scale is applied to facies of much larger scale and for unsampled locations—the conclusions about the facies extends beyond the available data. Such uncertainty is a manifestation of the common problem that scientific arguments are ampliative in nature, meaning that the informational content of the conclusions is greater and applies beyond that of the premises of an argument (Wheeler, 2001). In this case, the data at the pore scale can be taken as a form of premises, from which conclusions are made about the sealing behavior. These “premises” apply to specific locations and geologic conditions. Conditions at other locations may change, especially for mudstones that tend to be heterogeneous (MacQuaker et al., 2007). In general, gathering data to understand how the conditions and associated pore-network properties vary is limited by funding and time necessary for the study.

Direct study of sealing behavior requires knowledge of not just the geometries, topology, and pore-lining phases of pore networks, but of the interactions between the fluids of interest (CO₂ and brine) and the solid surfaces. Such interactions include those of interfacial energy, surface forces, and chemical alterations through precipitation and dissolution. These interactions depend on several factors and can occur over different time scales. The literature provides little support for predicting capillary-sealing behavior due to lack of a focus on specific caprock phases and interfacial tension (i.e., typically in terms of contact angles and wettability; see Chapter 4). Results of wettability experiments for caprock solid phases, CO₂, and brine are limited to amorphous silica, quartz, and muscovite (Dickson et al., 2006; Chiquet et al., 2007). Study of the different types of active sites or functional groups of caprock phases (e.g., clay minerals and amorphous phases such as organics) and their interactions with CO₂ and brine is greatly needed. Previous work on active sites of clays has already been done (Johnston, 1996) and could form the foundation for future work.

Surface forces can be important for caprocks that have inherent flaws such as those due to pedogenic processes (see Chapter 5) or deformation (e.g., tectonic fractures). Such flaws may increase (or decrease) in aperture if CO₂ can affect directly or indirectly the attractive forces between clay mineral particles and capillary forces. Electric double layers may be modified due to pH and other changes to aqueous conditions due to the presence of CO₂ in the system and thus modify the particles' attractive forces. Dehydration/dessication of clay minerals and concomitant cracking/fracturing due to water extraction from clays into the CO₂ phase is also a concern that this study did not address (Gaus, 2010). Precipitation and dissolution of caprock phases could potentially

greatly impact the performance of a caprock's sealing behavior. This study reveals pore geometries and pore-lining phases, but does not provide an assessment of how precipitation/dissolution would occur in these pore networks and in turn impact CO₂ transport and storage.

The link between the pore-scale studies and the transport of noble gas tracers could have been strengthened by investigation of mudstone tortuosity using pore-network models. Such tortuosity estimates could support or test estimates of diffusional transport of noble gases through the mudstones.

After this discussion of limitations or opportunities, I remind the reader that the goal of Chapters 3 and 4 was to answer Science Question 1 of the dissertation (see Section 1.2), which inquires about the geologic conditions of pore networks that are capable of forming high quality sealing caprock for CO₂ storage. Chapters 3 and 4 were not meant to be a characterization of all mudstones and all sealing-related processes, but an assessment of key geologic controls on sealing behavior. My analysis of the Gothic shale (the highest quality seal in terms of breakthrough pressures; see Figure 3.16) as compared to the other mudstone formations indicates that distal environments and deep burial are important controls on high quality sealing behavior. Organic matter is probably also an important factor. Chapters 3 and 4 represent one of the first studies to create and analyze 3D reconstructions of pores in mudstones with knowledge of pore-lining composition, and to place those reconstructions in a micro-petrographic context. Future studies should respond to Limitations/Opportunities 1 through 13 as they build and interpret a larger data set on mudstones porosity and breakthrough processes.

Limitations and challenges of the multi-scale evaluation of caprock sealing behavior (Chapter 5) include the following:

- 14) my intent was to develop methods using noble gases, especially ^4He , to characterizing sealing behavior since noble gases occur at all CO_2 storage sites; I now know focusing on other potentially already-present gas phases is very important: I did not design the data collection and laboratory analysis to accommodate the already-present methane within the caprock samples; the laboratory analysis did not collect a suite of noble gases (Ar, Kr, and Xn in addition to Ne and He) that were needed to assess partitioning/degassing processes due to the laboratory method used to remove the abundant (unanticipated) methane in the sample containers;
- 15) funding limited the collection of more noble gas samples from locations such as the Farmington Sandstone Member, the Ojo Alamo Sandstone, and the Fruitland Formation, which would have supported investigation of lateral flow in the Kirtland Formation and testing of model parameterization;
- 16) funding and time constraints restricted the collection of isotopic data from fracture mineralization and separate-phase gases within the Kirtland Formation caprock that could constrain the source of the mineralizing fluids and gases to indicate if once-connected flow paths from the Fruitland Formation up to the upper Kirtland Formation were once active;
- 17) this dissertation does not provide a direct link between noble gas concentration patterns, seal bypass systems or seal quality, and engineered

activities that incorporates changing physics (i.e., coupled geomechanical, geochemical, and fluid-flow processes); and

18) the multi-scale approach of the dissertation does not address all the scales of importance for CO₂ storage; the locations between wells were largely neglected and, in general, the regional or basin scale was not evaluated.

Obtaining representative noble gas samples from caprock is challenging. The purge-and-pumpdown process (see Appendix B.1 and Chapter 5 subsection Coring Program, Field Sample Preservation, and Well Logging) used to evacuate atmospheric gases from the preservation canisters may have removed natural separate-phase gas from the core plugs. The laboratory purification line extracted all noble gases (and other gases) except helium and neon. Thus, the field sampling and laboratory procedures caused a loss of information. Other studies have used a suite of noble gases to investigate and quantify gas partitioning processes. Additional noble gases would have constrained the degree of partitioning due to sampling and to *in situ* conditions at depth through use of degassing models (Lippmann, 2003; Ballentine et al., 2002).

The Kirtland Formation is not a homogeneous, low-permeability, high-breakthrough-pressure geologic unit for all of its thickness (and horizontal extent). Sampling was limited to the upper and lower portions of the formations, essentially giving two ⁴He data points due to the similarity of the data within those portions. Furthermore, these data points are located near model boundary conditions of prescribed “value.” Additional data within the overlying and underlying formations, and from within the middle portions of the Kirtland Formation, would provide data that could constrain or expand the conceptual and mathematical models of Chapter 5. Two-dimensional flow is

likely in the Farmington Sandstone Member, which is currently difficult to test due to the location of the data at the model boundary conditions.

The barite- and calcite-filled fractures could provide information on the source of the mineralizing fluids if sulfur and carbon isotopes were analyzed for the fractures and for the potential source of the fluids (i.e., fluids within the Fruitland Formation). Similarly, carbon isotopic signatures of gases within the Kirtland Formation may help constrain if those gases originated *in situ* within the Kirtland Formation or if they were sourced from the Fruitland Formation.

A major limitation of the approach of using noble gases to identify and characterize seal bypass systems or the lack thereof is the difficulty of predicting the response of the system to changing physics during engineered activities. Natural tracers from undisturbed states may not directly relate to the future possible events. Injecting CO₂ will induce geomechanical and geochemical changes with concomitant fluid flow that will perturb its state. Possible events include enhancement or healing of fractures due to precipitation/dissolution with CO₂ and brine flow through the fractures (Gherardi et al., 2007).

The multi-scale approach of the dissertation focuses predominately on the pore network scale and the upper and lower portions of the caprock. Modeling of the tracer transport allows inferences to be made about larger scale connectivity (see Chapter 5); however, while my analysis indicate low fluid fluxes through the caprock and high quality sealing behavior, the inferences are not conclusive because the middle portion of the caprock was not sampled, nor were the overlying and underlying reservoirs. Lateral flow may be important within caprocks that contain interbedded permeable units. Thus,

sampling at other wells and depths is needed. Finally, the basin-scale was largely neglected except for presentation of thickness and other maps of the caprock (see Figure 5.1). Larger basin-scale sampling, coupled with large-scale modeling, is needed to expand the tracer caprock assessment to the basin scale (see Section 6.3.3).

6.3.2 Future Work

Future work suggested herein continues the dissertation theme of examination of both the pore networks that can contribute to high quality sealing behavior and larger-scale features that can lead to fluids bypassing the pore networks. Future studies could address many of the limitations, opportunities, and challenges of the pore scale chapters (Chapters 3 and 4; see Section 6.3.1) by applying statistically sound methodologies. These methodologies are needed to create a universal pore-type classification with associated breakthrough pressures that could be used in site identification and selection for CO₂ storage. The number of rock samples should attempt to capture the variability in mudstone facies. The pore network models should sample a large enough volume to obtain statistically significant numbers of pores. The identification of pore types should follow stricter methodologies to reduce subjectivity. For example, pore type classification could be determined by topological and geometrical differences in pores (e.g., number of connected neighbors, departure from sphericity of pore body shape, size of pore body, size of pore throats, etc.) in a quantitative manner, implemented on a computer. Future work could attempt to classify each individual pore and then generate data on the relative fraction of pore types. This would be useful to improve understanding of the occurrence and representativeness of certain pore types for different samples. If representative pores

are identified, then these could be better associated with the mercury intrusion porosimetry data, perhaps through physical modeling of mercury pressure and volume relationships that then could be compared to the experimental data.

The 3D pore network characterization of mudstones (see Chapter 3) and corresponding knowledge of the chemical composition of pore-lining phases (see Chapter 4) are novel and could be used to investigate the ability of the particular pore types to conduct multiphase fluids. Particularly for mudstones, the lack of high resolution, 3D geometric and topological characterization has limited pore network modeling using realistic pore structure. Future modeling using 3D geometrical models based on FIB/SEM data, with knowledge of pore-lining phases, could examine processes related to dynamic breakthrough pressure, mixed wettability and capillarity, and geochemical and geomechanical impacts on fluid flow. Numerical modeling with the realistic pore network models could provide a stronger link between the experimental mercury intrusion porosimetry (MIP) measurements and breakthrough pressures. Since the MIP curves do not provide direct information on pore types and pore frequencies, the curves can be difficult to interpret in general (Diamond, 2000). The curve interpretation can be especially difficult for mudstones since knowledge of 3D pore geometry has been lacking. The modeling could investigate the relative importance of pore shape, pore size, pore-lining phases, and pore connectivity on breakthrough processes. Modeling of the intrusion process could provide a foundation for better use of MIP data.

Different types of mudstones examined in this dissertation display abundant drying/desiccation fractures at the thin-section scale. These fractures are not present *in situ*. They developed after collection of the rock cores. However, they may indicate

potential creation of fractures *in situ* if separate or dissolved phase CO₂ can affect surface forces of clay particles and their expanded versus collapsed texture (Andreani et al., 2008). One such mechanism for changing the clay texture is dry-out. Gaus (2010) points out the possible problem of caprock dry-out under *in situ* conditions due to injection of anhydrous CO₂. Injected CO₂ is likely to be initially anhydrous to avoid corrosion in the transportation system that delivers CO₂ to the subsurface (Gaus, 2010). Shrinkage due to dry-out can occur in rocks that are generally not well indurated and have high clay contents; thus, most mudstones are susceptible to dry-out if a gas phase (or supercritical phase) is able to transport water away from the clay minerals (Horseman and McEwen, 1996). Gaus (2010) suggests that dry-out may not be important for large portions of a caprock, but for local regions close to fractures where advection in the fractures may occur. The Kirtland Formation core and microresistivity well log display several types of fractures, some of which are pedogenic and associated with illuviation structures. Mudstones in general can have pedogenic (for continental rocks), dewatering, compaction/accommodation, and tectonic related fractures (for both continental and marine mudstones); thus, many types of discontinuities may be present. Were dry-out to occur, many discontinuities may be enlarged due to shrinkage of the surrounding clays, and creation of new discontinuities may occur. The reactivity of expandable clays in terms of surface forces (i.e., the effect of CO₂ on double-layer forces), their impact on apertures of existing discontinuities, and the potential for shrinkage needs investigation.

Dry-out processes could be studied using specialized techniques for laser scanning confocal microscopy, XRD, or neutron scattering that can include a pressurized vessel to characterize multiphase fluids and pore and fracture structures within a rock

sample at *in situ* pressure and temperature conditions at the sub- μm and larger resolutions. Such studies would need to focus on the sizes and connectivity of the desiccation cracks to quantify and estimate impacts on fluid flow. Fundamental understanding of the dry-out processes would require investigation of the change in attractive forces between clay particles as water is transported away and double-layer forces are affected.

Shrinkage may also be induced by dissolved aqueous CO_2 . If dissolved CO_2 and associated carbonate speciation results in pH decrease (Gaus, 2010), such decrease may impact surface charge of clay minerals and the electric double layer by introducing protons (hydrogen ions) to the system and possible divalent or other cations. Cations may be added to the system via dissolution of carbonates. Protons can modify surface charge and so can divalent cations, which could lead to collapse of the double layer and an increase in the attractive forces between the clay particles (Israelachvili, 1991).

Other pore-scale phenomena in need of study include CO_2 interactions with organics and other solid phases within caprocks. It is currently unclear how CO_2 can interact with various common kerogen types in caprocks. Interaction may include solubilization of organics or swelling of the organics, both of which can alter pore sizes, wetting conditions, capillary pressures, and fluid flow. Little research on organics and CO_2 (Okamoto et al., 2002) interactions has been conducted. Based on the organics identified in Chapters 3 and 4, further research on the impact of these organics on CO_2 and brine movement is suggested. Research within the chemical industry discusses clearly the mechanisms by which CO_2 interacts on a molecular level with other molecular systems by the quadrupole of the CO_2 molecule, which is manifested through Lewis

acid/Lewis base interactions and conventional and non-conventional hydrogen bonding (Raveendran et al., 2005). A systematic study of interactions of the CO₂ quadrupole and the functional groups of organics and other solid phases within caprocks could improve the understanding of which functional groups would lead to particular wetting conditions, solvation by CO₂, and shrink/swell phenomena.

Moving beyond the pore network or smaller scales: prior to drilling and coring, my Kirtland Formation study would have benefited from a feasibility study on the optimal locations of core to test various conceptual models of fluid flow within the formation. Future studies should gather data for the Farmington Sandstone Member to evaluate lateral transport. As mentioned in Section 6.3.1, isotopic studies of methane and fracture mineralization should be performed to constrain if mineralizing fluids or the gas were sourced from the Fruitland Formation, thus testing large scale connectivity. Future work should reassess the purge-and-pumpdown process since it can remove an exsolving or already present separate phase in the core.

Magnitudes and rates of potential (or actual) CO₂ migration through sub-seismic fractures and fracture networks to large faults in argillaceous caprock are poorly known. This severely limits assessment of caprocks for storage CO₂. Few studies have attempted quantification of the impact on sealing behavior due to reactive multiphase fluid flow in fractures, fracture networks, and faults (Gherardi et al., 2007; Nelson et al., 2009; Silin et al., 2009). The need for additional studies to address these issues has been emphasized by the scientific community (DOE, 2007). Basic knowledge on fracture characteristics in terms of apertures, amount and degree of mineralization, and orientations of fractures with respect to *in situ* stress regimes are needed to facilitate prediction of how the

fractures will respond under CO₂ injection conditions, and such data has been limited for most CO₂ storage projects.

Identification and characterization of the impact of fractures on single and multiphase transport of fluids through caprocks using noble gases seems promising based on the findings of this research; however, more work is needed to develop knowledge of paleohydrodynamics of seal bypass systems and how those systems evolve under the perturbations induced by CO₂ injection (see Section 6.3.4). Additional forward numerical modeling studies can incorporate fracture and fault zone architecture and different patterns of connectivity along with the noble gas systematics for helium (see Section 6.3.4). The goal would be to investigate patterns of helium isotopic and concentration distributions for different fracture/fault systems within representative pressure gradients for the deep saline reservoir conditions. Noble gases are well suited to examining interactions between groundwater and separate phases (e.g., oil or gas) in terms of partitioning (Ballentine et al., 2002; Zhou et al., 2005; Zhou and Ballentine, 2006). Noble gases partition between separate phases. Thus, the modeling could be used to elucidate the magnitude of gas and groundwater flow through the fracture/matrix system. Numerical-modeling studies could support sampling design for investigating caprocks that already have seen multiphase transport (i.e., groundwater and methane), like the Kirtland Formation (see Chapter 5). The Kirtland Formation exhibits fracture or fault zones, observable with seismic methods, that could serve as candidate sites for further investigation of noble-gas transport via multiphase fluids in a caprock. This study could provide insight into the connectivity of the fractures/faults through the caprock and

timescales of transport. This insight is needed to improve understanding of multiphase transport of CO₂ sequestration and other subsurface systems (see Section 6.3.4).

Future work at specific CO₂ storage sites should quantify potential diffusional and advective fluxes of CO₂ and brine through the variety of pore network and bypass systems for large-scale CO₂ storage sites. Comparison should be made between the fluxes and global (i.e., percentage leaked per time needed to mitigate climate change) and local performance metrics (i.e., total CO₂ amount that would cause detrimental impacts to an underground source of drinking water) to determine the suitability of the sites for proper storage.

6.3.3 Risk Analysis and Caprocks

Formal risk analysis of caprock is beyond the scope of this dissertation. Such analysis, however, is greatly needed for the implementation of geologic CO₂ storage. Typical designs for storage in sedimentary basins require a caprock as a key component of the system to keep the buoyant CO₂ from leaving the storage reservoir (Orr, 2009). The community of scientists and engineers focused on CO₂ storage are still developing and deciding upon common terminology and approaches for risk analysis (IEAGHG, 2009; Oldenburg et al., 2009). This last section provides comments on current trends in risk analysis that incorporate (or generate) knowledge of caprocks in terms of processes (conceptual and mathematical models), properties, and consequences. Implications for risk analysis from this dissertation are addressed.

General definitions are in order, which are taken from Rechar's (1999) paper on the history of risk analysis. Risk analysis is the most general "risk" related term that

describes all topics related to risk, such as risk assessment and risk management. “Risk” typically refers to some measure that combines both the degree of harm and the probability of the event leading to harm. Risk assessments are the activities that generate a measure of risk. Risk management refers to the activities through which an agent (e.g., a person, a corporation, or society in general) determines if a particular activity is safe, and then determines the risks associated with the activity, how to reduce the risks, and how to prioritize and select from different options. Additional terminology addresses uncertainty involved in risk assessment and what is focused upon during the assessment. Probabilistic risk assessment (PRA) incorporates direct examination of uncertainty. Performance assessment (PA) refers to evaluation of a particular system in which the performance of a system is the focus. In the United States, PA and PRA are synonymous.

Historically, integral steps for a risk assessment include, as quoted from Rechar (1999):

(0) identify appropriate measures of risk and corresponding risk limits; (1) define and characterize the system and agents acting on the system; (2) identify sources of hazards and, if desired, form scenarios; (3) quantify uncertainty of factors or parameters and evaluate probability of scenarios (if formed); (4) evaluate the consequences by determining the response to exposure and, possibly, the pathway to exposure; (5) combine the evaluated consequences and probabilities and compare them with risk limits; and (6) evaluate sensitivity of results to changes in parameters to gain further understanding (p. 764–766).

These seven steps provide the foundation for describing hazards and how they can occur, the probability of occurrence of the hazards, and the consequences of the hazards (Rechar, 1999). In addition, iteration can be part of the risk assessment approach. It can be implemented in different ways including sequential PAs, in which initial PAs draw on

preliminary data and are simple, but are followed by PAs that incorporate more details and more complicated (i.e., realistic) models (Rechard, 1999).

Two approaches for risk assessment of geologic CO₂ storage are developing. One approach adapts standard risk assessment concepts to focus predominately on site selection, which requires knowledge pertaining to both the reservoir, its caprock, and the injection design (Oldenburg, 2008; Oldenburg et al., 2009). The approach focuses on screening and ranking of sites. Its purpose is to provide relatively easily implemented assessments of properties and processes related to health and safety of the environment that will not require extensive scenario analysis or modeling (Oldenburg, 2008). The second approach views risk assessment as an iterative and integrative approach to project management (Rohmer and Bouc, 2010). Its purpose is to guide data collection and analysis to focus on the most important parameters that govern the behavior of the system that then will support decision-making for implementation or mitigation or other policy-related activities. The guidance is aided by clearly defined metrics (objective functions) that express the needed behavior of the system (e.g., leakage rate). Iteration comes into play as information is gained, which can in turn guide and influence the direction of the risk assessment. Thus, the second approach uses risk assessment to guide how data are collected and used to evaluate the performance of the system in question. Both approaches allow for site rejection or acceptance.

The site selection and ranking approach is very important for choosing locations of CO₂ injection and to define concepts of what constitutes a “good site” and a “high quality” caprock in a comparative sense. Oldenburg (2008) encourages current approaches to be qualitative and to use expert knowledge due to perceived difficulties in

detailed scenario analysis (e.g., feature, event, and processes analysis) at the screening stage (Oldenburg, 2008). Oldenburg's approach does not require modeling and probabilities are not assigned. Such ranking can help identify locations of interest that could be further investigated if a site's comparative ranked score is high from a group of proposed sites.

Speaking directly about caprocks, however, knowledge of the interdependence of caprock properties and processes on the needed performance of the caprock is still developing. Thus, picking a suite of features and processes to rank the caprock performance in a qualitative sense should be performed with caution. The relative impact of various caprock processes or features on CO₂ or formation brine leakage is poorly known. These caprock features and processes include: lithology; thickness; depositional environment; burial history; tectonic and hydrologic/diagenetic history; amount of original or mobile organic matter and the types of organic matter; pore-network characteristics; composition and heterogeneity of pore-lining phases; connectivity of fractures throughout the caprock; degree/amount and composition of fracture mineralization; presence of a pre-existing gas phase (e.g., methane) within the caprock; stress orientation with respect to fracture orientation; and susceptibility of caprock solid phases to shrinkage/swelling phenomena (e.g., dry-out) due to intermolecular and surface forces. Given the limited present-day knowledge, screening based on these features and processes would be subjective. Such subjective knowledge (i.e., the ranked values for a suite of caprocks) is useful, but should be accepted with caution.

The second approach to risk assessment has the potential to generate the knowledge needed about caprocks for the implementation of CO₂ storage. Many papers

on the topic of caprock performance do not explicitly tie themselves to key metrics that define the needed performance of the system, such as the acceptable leakage rate. However, some studies (see Shaffer, 2010) suggest particular global leakage rates for the massive application of geologic CO₂ storage (e.g., 1% leakage of CO₂ per thousand years) that should not be exceeded if climate change is to be adequately mitigated. Future work on caprocks needs to determine if globally all caprocks used for storage will adequately retain the CO₂.

This first step (Step 0 of Rechar, 1999, given above) needs much greater attention so that the processes and properties of caprocks that impact the needed performance can be properly assessed. In addition to issues of global retention of CO₂, for local systems the absolute amount of leaked CO₂ and its impact on underground sources of drinking water for specific sites or sites in general could serve as an additional constraint in determining what would be acceptable fluxes.

Rohmer and Bouc (2010) provide a good example of assessing parameters in a mathematical model of a certain type of caprock failure (i.e., fracture reactivation and genesis) in a way suited to determine which parameters have the greatest impact, and thus which parameters should receive the greatest attention. Similar studies for the variety of processes and features listed above are needed to determine the smallest set of key parameters that govern the performance of a caprock for CO₂ storage. Until such work is done, choosing a “simple” or small set of parameters that are thought to govern caprock performance will be greatly affected by subjectivity. I believe that primary depositional environment (e.g., proximal versus distal), seal bypass systems, and various intermolecular-forces-related processes (e.g., wettability and dry-out) need much

attention during caprock performance assessment. These may indeed be important; however, an integrative version of risk assessment would assess, in addition to what I think is important, other processes and features in a formal way to reduce my bias and to investigate the actual controls on sealing behavior. I have made advances (see Section 6.2) in the characterization of caprock sealing quality for CO₂ storage and the evaluation of natural, non-wellbore-related bypass systems, such as fracture networks (which have received less attention in the literature than wellbores); however, a full, combined assessment of the natural and induced bypass systems is needed. Risk assessment that reduces researcher bias and involves knowledge being gained by the whole CO₂ community is needed to ensure successful implementation of CO₂ storage.

6.3.4 A critical need for geologic CO₂ storage to move forward: quantification of potential CO₂ leakage rates and impacts

Risk assessment has a fundamental step of defining metrics of risks and risk limits. Leakage of CO₂ has been studied previously by others (Oldenburg, 2008), but much more work is needed to define what constitutes “high” or “unacceptable” leakage rates that pose unacceptable impacts. Some studies attempt to understand the physico-chemical processes associated with leaking CO₂ (Gherardi et al., 2007; Silin et al., 2009), but it seems clear that more focus on risk metrics is needed. Measures of risk limits have not yet been defined, at least not definitively, by the CO₂ research community.

Here I discuss my initial efforts to define needed measures of the leakage risk and its limits (see Heath et al., 2009, for a version of this preliminary modeling study). I developed some preliminary conceptual and numerical models of generalized fluid

dynamics of a reservoir/caprock system in an attempt to provide a basis for estimating CO₂ leakage rates and associated risks. The modeling also initially investigates the ability to screen caprocks for CO₂ storage using patterns of helium concentration and temperature.

As shown by Chapter 5, natural helium data can reveal important aspects of a field site, such as the presence of a pre-existing gas phase and the impact (or lack thereof) of fractures as a seal bypass system. Knowledge of diffusion and advective fluxes can inform modeling studies on potential CO₂ transport across a caprock via diffusion and advection (as an aqueous or separate phase). Thus, investigation of patterns of natural helium below, within, and above a caprock prior to CO₂ injection may reveal the presence of a seal bypass system and the potential impact of CO₂ leakage through preferential flowpaths. Or, if a seal bypass system is non-existent at a site, helium patterns may indicate the dominance of diffusion on transport through the caprock, which could support calculation of effective diffusion coefficients to predict estimates of aqueous-phase leakage of CO₂.

My preliminary modeling approach uses two general situations: 1) transport of ³He, ⁴He, and heat in the subsurface under scenarios of pre-CO₂ injection (“natural” conditions); and 2) injection of CO₂ under the same conditions of the pre-injection models (“engineered” conditions). These models are intended to determine if helium and temperature can indicate the presence of preferential flowpaths through a caprock that may lead to unacceptable amounts of leakage. In this capacity, such models may be used to screen caprock suitability for CO₂ storage (i.e., models become a “screening tool”). To simulate helium tracer transport and potential leakage of CO₂ through a caprock, I

develop models using the TOUGH2 family of software (Pruess et al., 1999). I utilize the ECO2N equation-of-state module for the two-phase CO₂ fluid injection simulations and the EOSN equation-of-state module (Shan and Pruess, 2004) for ³He and ⁴He generation and transport simulations.

For this simplified analysis, I assumed a measure of sealing integrity (for the modeled scenarios) based on the percentage of injected CO₂ that migrates through the top of the caprock over the time period of the simulations. Such a criterion is an intensive quantity because it expresses a percentage of the total injected CO₂. However, with additional consideration, I realize that an additional risk criterion for future work is the total amount leaked (extensive quantity) over a period of time. If the total amount of injected CO₂ is small, then even the total migration through the caprock may not constitute a risk to underground sources of drinking water or other systems of local concern. Future modeling work should balance global caprock performance measures of leakage rate (such as 1% per thousand years for all combined storage sites; see Shaffer, 2010) and local performance measures (e.g., total amount injected does not induce detrimental pH changes or other unacceptable effects within an overlying underground source of drinking water.)

For the analysis below, I follow the literature that deals with leakage rates in terms of percentages of injected CO₂, and these studies typically focus on impacts of leakage risks associated with economics and climate (Wilson and Gerard, 2007b). For my preliminary scenarios, rates of 0.0% yr⁻¹, 0.1% yr⁻¹, 1.0% yr⁻¹, and 7% yr⁻¹ of the injected CO₂ are examined. From the literature mentioned above (Wilson and Gerard, 2007a), I consider leakage over 0.1 % yr⁻¹ unacceptable. However, future work must focus on the

total amount that can cause unacceptable impacts to underground sources of drinking water sources in addition to economic and climate-associated risks. Thus, I am not able at this time to express the (extensive) amounts of leaked CO₂ that would constitute CO₂ leakage risk, but the approach can be re-evaluated from that viewpoint.

To demonstrate numerically the use of helium and temperature as CO₂ caprock screening tools, the following modeling scenarios are utilized: 1) a basin model with hydrological conditions loosely modeled after the San Juan Basin in Northern New Mexico, run to steady state flow conditions (~1 My); 2) a sub-basin model with boundary and initial conditions taken to represent a sub domain from the basin model results; and 3) a sub-basin model identical to case 2 except for a single zone of higher permeability representing a seal bypass system. Following the hydrostratigraphy used for the basin model, the simulation domain includes a target storage reservoir 200 m in thickness, a 50-m-thick caprock, and an overlying aquifer 250 m in thickness.

The modeling scenarios are designed to establish equilibrium helium and temperature distributions before injection, and then to evaluate the amount of CO₂ leakage under the same conditions. Leakage of CO₂ is evaluated by invoking a CO₂ source in a single cell just beneath the caprock, to mimic injection at an arbitrary rate of approximately 25 tonnes/d (which facilitated convergence of these initial simulations). Helium systematics for the models are represented by following typical procedures in the literature (Zhao et al., 1998), which include a basal flux of helium (³He and ⁴He) that corresponds to the helium sourced from the underlying rocks at the base of the domain, *in situ* production of ⁴He from uranium (U) and thorium (Th) decay, and groundwaters at recharge areas in equilibrium with atmospheric helium. To approximate basin-scale

boundary conditions, the sub-basin models were run with basal cell volumes of effectively infinite extent. This enabled constant sources of overpressure, helium generation, and heat generation. Basal heat production was assigned 50 mW m^{-2} , representative of typical continental heat flow. Basal helium fluxes were set at $1.0 \times 10^{-23} \text{ kg m}^{-2} \text{ s}^{-1}$ for ^3He and $1.7 \times 10^{-16} \text{ kg m}^{-2} \text{ s}^{-1}$ for ^4He , from Mahara and Igarashi (2003). For simplicity, the left- and right-hand vertical boundaries were taken to have no-flux conditions, and values of pressure, temperature, and ^3He and ^4He aqueous mass fractions at the top of the sub-domains were held constant at values dictated by the basin model.

In all models, reservoir and aquifer porosities were taken to be 0.15, with a value of 0.07 used for the caprock. Absolute permeability tensors were taken to be isotropic with 10^{-14} m^2 used for the reservoir and aquifer layers and 10^{-18} m^2 used for the caprock. These values were suggested by values for regional aquifers and aquitards in the San Juan Basin in the calibrated groundwater model of Kernodle (1996). Capillary pressure and relative permeability relationships used the Van Genuchten-Mualem model in TOUGH2 (Pruess et al., 1999) for liquid relative permeability and capillary pressure function (Van Genuchten, 1980) and the Corey (1954) model for gas relative permeability (parameters used in the multiphase flow runs were as follows: $\lambda = 0.4$, $S_{lr} = 0.2$, $S_{ls} = 0.99$ for all three rock types, $1/P_o = 1.60 \times 10^{-7} \text{ Pa}^{-1}$ for caprock and $2.79 \times 10^{-4} \text{ Pa}^{-1}$ for reservoir and aquifer, and $P_{max} = 1.0 \times 10^8 \text{ Pa}$ for caprock and $1.0 \times 10^7 \text{ Pa}$ for reservoir and aquifer).

Preliminary simulations indicated that a perturbed permeability for the fault flow pathway of $1\times$, $10\times$, and $100\times$ gave CO_2 leakage rates of 0.0, 1.0, and 7.0% yr^{-1} , and thus these values were used in both CO_2 injection and steady-state heat and helium transport simulations to examine sensitivity to permeability perturbation magnitude. Here I show

examples for only the 0.0 and 7.0% yr⁻¹ leakage rate examples because helium and temperature spatial profiles for the 1.0% yr⁻¹ rate case were very similar to the 7.0% yr⁻¹ case. Figures 6.1A and 6.1B compare steady-state ⁴He profiles for cases of 7% yr⁻¹ (100x fault zone permeability) and 0.0% yr⁻¹ (1x fault permeability; ³He profiles are similar in shape but differ in magnitude). In both cases, ⁴He profiles are steeper through the caprock, suggesting that helium tracer vertical profiles through caprock, relative to surrounding aquifers, might be used to infer caprock sealing capacities. In the case of a 100x fault permeability, significant elevations in ⁴He are observed above the fault zone compared to the no-fault case. It may be possible to discern the presence of such a flow pathway from the presence of the helium “mounding” above a target caprock. A vertical depth profile of ⁴He through the caprock is convex upward as compared to the linear-with-depth profile of the no-fault case (Figure 6.1E).

Responses to CO₂ injection after one year for both permeability scenarios are shown in Figure 6.1C (100x fault permeability above background) and Figure 6.1D (1.0x above background). Significant CO₂ leakage is observed for the former case, while no leakage is observed in the latter case. The steady-state vertical profiles of ⁴He, temperature, and pressure are shown in Figures 6.1E–6.1G for the 7% yr⁻¹ leakage case through the more permeable fault zone (red line) and at an effectively infinite distance (blue line). The ⁴He profiles (Figure 6.1E) demonstrate that a helium perturbation may be used to infer the presence of the leaky caprock. Capability to measure an actual perturbation would depend on uncertainty in data quality due to sampling methodology, the sensitivity and precision of the laboratory analysis, and the location of sampling relative to the leakage pathway. Typical groundwaters have a ⁴He concentration of

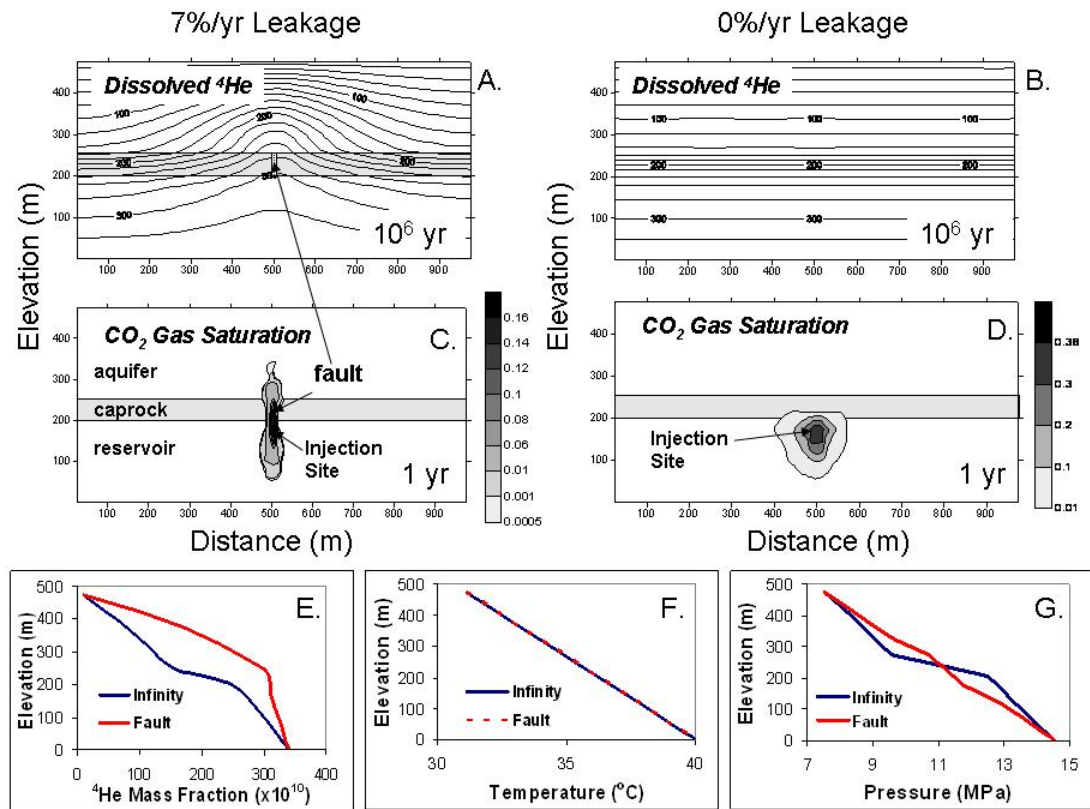


Figure 6.1. TOUGH2 simulation results comparing helium and CO_2 leakage through a caprock with and without a permeability perturbation (i.e., a vertical “fault” with $100\times$ background caprock permeability; after Heath et al., 2009). The zero elevation on the figures corresponds to a depth below ground surface of ~ 1.5 km. (A and B) Profiles of dissolved ^4He as mass fraction of aqueous solution ($\times 10^{10}$) for “faulted” (A) and unfaulted (B) cases. Caprock is shown as grey horizon. (C and D) CO_2 gas saturation after one year of injection directly beneath the caprock. (E) Comparison of vertical profile in dissolved ^4He both running through the fault zone (red line) and at an infinite distance from the fault (blue line) under steady state flow conditions (1 My). (F) Temperature profiles taken through the fault zone (red line) and at an infinite distance from the fault (blue line) under steady state flow conditions (1 My). (G) Vertical pressure profiles both through the fault (red line) and at an infinite distance from the fault (blue line), showing pressure dissipation through the fault (1 My).

$\sim 4.8 \times 10^{-5} \text{ cm}^3$ at standard temperature and pressure (STP) per kg water (Solomon, 2000). The value of $4.8 \times 10^{-5} \text{ cm}^3 \text{ STP kg}^{-1}$ corresponds to water equilibrated with atmosphere at 10°C . Precision of laboratory analysis for such waters is $\sim \pm 1\%$ (Castro et al., 2000). If the helium perturbation of Figure 6.1E is considered to represent a real system, the perturbation could be easily measured by laboratory analysis (1.0×10^{-8} mass fraction of ^4He corresponds to $5.6 \times 10^{-2} \text{ cm}^3 \text{ STP kg}^{-1}$). The corresponding temperature perturbation is relatively very small at $< 0.0001\%$, which would be very difficult or impossible to measure using temperature logging (Hurter et al., 2007). In this case, helium measurements could be much more effective than temperature in verifying the presence of a seal bypass system. The pressure profile through the leaky seal could be interpreted as being hydrostatic, and thus nothing could be inferred from the pressure profile by itself with regard to sealing capacity of the caprock.

These models do not account for changes in the effective diffusion coefficient and thermal conductivities, heterogeneity, horizontal groundwater flow, and other properties that may affect the distribution of helium and temperature observed in actual field sites. However, while these models are simplistic, they provide insight to unacceptable leakage rates and the potential usefulness of natural helium and temperature measurements revealing seal bypass systems. These models (Figure 6.1) suggest that patterns of natural helium may reveal the presence of seal bypass systems where temperature measurements may not be sensitive enough. They also indicate that monitoring above the caprock may better reveal the presence of the seal bypass system as opposed to investigating the patterns within the caprock itself. Additional modeling could investigate the hydrological conditions above the caprock that would redistribute helium (and heat), which then could

be accounted for in the design of monitoring strategies aimed at seal bypass systems. The additional models need to be tied to the total amount of CO₂ leakage into an overlying aquifer that would have negative impacts (e.g., in terms of pH and mobilization of metals).

Future work could use knowledge of fault zone and fracture networks through caprocks to inform the nature and representation of the simulated seal bypass systems. Such work is needed to estimate the impact of leakage rates due to seal bypass systems with various characteristics (e.g., uniform fracture set, fracture swarm, or sandstone injectite). The models could then estimate the helium concentration due to groundwater transport out from the top of the caprock and the associated potential CO₂ leakage rate, thus estimating leakage rates based on realistic geological scenarios. This modeling could be incorporated into iterative risk assessment to enable better simulations as data from a field site are collected

6.4 References

- Almon, W. R., Dawson, W. C., Ethridge, F. G., Rietsch, E., Sutton, S. J., and Castelblanco-Torres, B., 2005, Sedimentology and petrophysical character of Cretaceous Marine Shale sequences in foreland basins—potential seismic response issues, in Boulton, P., and Kaldi, J., eds., *Evaluating Fault and Cap Rock Seals: AAPG Hedberg Series*, no. 2, p. 215–235.
- Andreani, M., Gouze, P., Luquot, L., and Jouanna, P., 2008, Changes in seal capacity of fractured claystone caprocks induced by dissolved and gaseous CO₂ seepage: *Geophysical Research Letters*, v. 35, no. 14, p. 6.
- Ballentine, C. J., Burgess, R., and Marty, B., 2002, Tracing fluid origin, transport and interaction in the crust, in Porcelli, D., Ballentine, C. J., and Wieler, R., eds., *Noble Gases in Geochemistry and Cosmochemistry: Reviews in Mineralogy and Geochemistry*: Washington, DC, Mineralogical Society of America, p. 539–614.

- Birkholzer, J. T., and Zhou, Q. L., 2009, Basin-scale hydrogeologic impacts of CO₂ storage: Capacity and regulatory implications: *International Journal of Greenhouse Gas Control*, v. 3, no. 6, p. 745–756.
- Cartwright, J., Huuse, M., and Aplin, A., 2007, Seal bypass systems: *AAPG Bulletin*, v. 91, no. 8, p. 1141–1166.
- Castro, M. C., Stute, M., and Schlosser, P., 2000, Comparison of He-4 ages and C-14 ages in simple aquifer systems: Implications for groundwater flow and chronologies: *Applied Geochemistry*, v. 15, no. 8, p. 1137–1167.
- Chiquet, P., Broseta, D., and Thibeau, S., 2007, Wettability alteration of caprock minerals by carbon dioxide: *Geofluids*, v. 7, no. 2, p. 112–122.
- Corey, A. T., 1954, The interrelation between gas and oil relative permeabilities: *Producers Monthly*, v. 19, p. 38–41.
- Diamond, S., 2000, Mercury porosimetry—an inappropriate method for the measurement of pore size distributions in cement-based materials: *Cement and Concrete Research*, v. 30, no. 10, p. 1517–1525.
- Dickson, J. L., Gupta, G., Horozov, T. S., Binks, B. P., and Johnston, K. P., 2006, Wetting phenomena at the CO₂/water/glass interface: *Langmuir*, v. 22, no. 5, p. 2161–2170.
- DOE, 2007, *Basic Research Needs for Geosciences: Facilitating 21st Century Energy Systems*, Report from the Workshop Held February 21–23: U.S. Department of Energy, Office of Basic Energy Sciences, available in pdf format at <http://www.sc.doe.gov/bes/reports/list.html>.
- Gaus, I., 2010, Role and impact of CO₂–rock interactions during CO₂ storage in sedimentary rocks: *International Journal of Greenhouse Gas Control*, v. 4, p. 73–89.
- Gherardi, F., Xu, T. F., and Pruess, K., 2007, Numerical modeling of self-limiting and self-enhancing caprock alteration induced by CO₂ storage in a depleted gas reservoir: *Chemical Geology*, v. 244, no. 1–2, p. 103–129.
- Heath, J., McPherson, B., Phillips, F., Cooper, S., and Dewers, T., 2009, Natural helium as a screening tool for assessing caprock imperfections at geologic CO₂ storage sites, in Gale, J., Herzog, H., and Braitsch, J., eds., *Greenhouse Gas Control Technologies 9: Energy Procedia*, p. 2903–2910.
- Horseman, S. T., and McEwen, T. J., 1996, Thermal constraints on disposal of heat-emitting waste in argillaceous rocks: *Engineering Geology*, v. 41, no. 1–4, p. 5–16.

- Hurter, S., Garnett, A., Bielinski, A., and Kopp, A., 2007, *Thermal signature of free-phase CO₂ in porous rocks: Detectability of CO₂ by temperature logging, Offshore Europe: Aberdeen, Scotland, U.K.*, Society of Petroleum Engineers, p. 12.
- IEAGHG, 2009, A review of the international state of the art in risk assessment guidelines and proposed terminology for use in CO₂ geological storage, *International Energy Agency Greenhouse Gas R&D Programme*.
- Israelachvili, J., 1991, *Intermolecular and Surface Forces, Second Edition*: London, UK, Elsevier Academic Press, 450 p.
- Johnston, C. T., 1996, Sorption of organic compounds on clay minerals: A surface functional group approach, in Sawhney, B. L., ed., *Organic Pollutants in the Environment: Cms Workshop Lectures*, p. 1–44.
- Kernodle, J. M., 1996, Hydrogeology and steady-state simulation of ground-water flow in the San Juan Basin, New Mexico, Colorado, Arizona, and Utah: *U.S. Geological Survey Water-Resources Investigations Report 95-4187*.
- MacQuaker, J. H. S., Taylor, K. G., and Gawthorpe, R. L., 2007, High-resolution facies analyses of mudstones: Implications for paleoenvironmental and sequence stratigraphic interpretations of offshore ancient mud-dominated successions: *Journal of Sedimentary Research*, v. 77, no. 3–4, p. 324–339.
- Mahara, Y., and Igarashi, T., 2003, Changes in isotope ratio and content of dissolved helium through groundwater evolution: *Applied Geochemistry*, v. 18, no. 5, p. 719–738.
- Nelson, S. T., Mayo, A. L., Gilfillan, S., Dutson, S. J., Harris, R. A., Shipton, Z. K., and Tingey, D. G., 2009, Enhanced fracture permeability and accompanying fluid flow in the footwall of a normal fault: The Hurricane Fault at Pah Tempe Hot Springs, Washington County, Utah: *Geological Society of America Bulletin*, v. 121, no. 1–2, p. 236–246.
- Okamoto, I., Li, X. C., and Ohsumi, T., 2002, Effect of supercritical CO₂ as the organic solvent on cap rock sealing performance for underground storage: *Energy*, v. 30, no. 11–12, p. 2344–2351.
- Oldenburg, C. M., 2008, Screening and ranking framework for geologic CO₂ storage site selection on the basis of health, safety, and environmental risk: *Environmental Geology*, v. 54, no. 8, p. 1687–1694.
- Oldenburg, C. M., Bryant, S. L., and Nicot, J. P., 2009, Certification framework based on effective trapping for geologic carbon sequestration: *International Journal of Greenhouse Gas Control*, v. 3, no. 4, p. 444–457.

- Orr, F. M., 2009, Onshore Geologic Storage of CO₂: *Science*, v. 325, no. 5948, p. 1656–1658.
- Pruess, K., Oldenburg, C., and Moridis, G., 1999, *TOUGH2 User's Guide, Version 2.0*, Lawrence Berkeley National Laboratory, LBNL-43134, 198 p.
- Raveendran, P., Ikushima, Y., and Wallen, S. L., 2005, Polar attributes of supercritical carbon dioxide: *Accounts of Chemical Research*, v. 38, no. 6, p. 478–485.
- Rechard, R. P., 1999, Historical relationship between performance assessment for radioactive waste disposal and other types of risk assessment: *Risk Analysis*, v. 19, no. 5, p. 763–807.
- Rohmer, J., and Bouc, O., 2010, A response surface methodology to address uncertainties in cap rock failure assessment for CO₂ geological storage in deep aquifers: *International Journal of Greenhouse Gas Control*, v. 4, no. 2, p. 198–208.
- Schieber, J., 1999, Distribution and deposition of mudstone facies in the Upper Devonian Sonyea Group of New York: *Journal of Sedimentary Research*, v. 69, no. 4, p. 909–925.
- Shaffer, G., 2010, Long-term effectiveness and consequences of carbon dioxide sequestration: *Nature Geoscience*, v. 3, p. 464–467.
- Shan, C., and Pruess, K., 2004, EOSN—a new TOUGH2 module for simulating transport of noble gases in the subsurface: *Geothermics*, v. 33, no. 4, p. 521–529.
- Silin, D., Patzek, T. W., and Benson, S. M., 2009, A one-dimensional model of vertical gas plume migration through a heterogeneous porous medium: *International Journal of Greenhouse Gas Control*, v. 3, no. 3, p. 300–310.
- Solomon, D. K., 2000, ⁴He in groundwater, in Cook, P. G., and Herczeg, A. L., eds., *Environmental Tracers in Subsurface Hydrology*: Dordrecht, Kluwer Academic Publishers, p. 425–439.
- Van Genuchten, M. T., 1980, A closed form equation for predicting the hydraulic conductivity of unsaturated soils: *Soil Science Society of America Journal*, v. 44, p. 892–898.
- Wheeler, M., 2001, Historical background, in Kyburg, H. E. J., and Teng, C. M., eds., *Uncertain Inference*: Cambridge, UK, Cambridge University Press, p. 1–20.
- Wilson, E. J., and Gerard, D., 2007a, Risk assessment and management for geologic sequestration of carbon dioxide, in Wilson, E. J., and Gerard, D., eds., *Carbon Capture and Sequestration: Integrating Technology, Monitoring and Regulation*: Oxford, UK, Blackwell Publishing, p. 101–125.

- , 2007b, Risk assessment and management for geologic sequestration of carbon dioxide, in Wilson, E. J., and Gerard, D., eds., *Carbon Capture and Sequestration: Integrating Technology, Monitoring and Regulation*: Oxford, UK, Blackwell Publishing, p. 101–125.
- Zhao, X., Fritzel, T. L. B., Quinodoz, H. A. M., Bethke, C. M., and Torgersen, T., 1998, Controls on the distribution and isotopic composition of helium in deep groundwater flows: *Geology*, v. 26, no. 4, p. 291–294.
- Zhou, Z., and Ballentine, C. J., 2006, He-4 dating of groundwater associated with hydrocarbon reservoirs: *Chemical Geology*, v. 226, no. 3-4, p. 309–327.
- Zhou, Z., Ballentine, C. J., Kipfer, R., Schoell, M., and Thibodeaux, S., 2005, Noble gas tracing of groundwater/coalbed methane interaction in the San Juan Basin, USA: *Geochimica et Cosmochimica Acta*, v. 69, no. 23, p. 5413–5428.

APPENDICES

APPENDIX A. SUPPLEMENTAL VIDEO FILES FOR CHAPTER 3

This digital appendix on CD-ROM contains four supplemental video files for Chapter 3. Their captions, given as footnotes in the main text, are repeated here:

Supplemental Video File 1. Video file of a set of 325 images of focused ion beam serial sections taken in backscattered electron mode at 25 nm spacing for sample upper Kirtland 2049.7B. The horizontal field of view is 16.00 μm . Up direction is not definitely known, but it is either towards the top or bottom of the images. Original TIFF images (1024 \times 884 pixels) were compressed using JPEG algorithm at 100 quality when making the video file. Video files were further compressed by resampling images to 400 \times 345 pixels and compressing using the Cinepak algorithm at 75 quality.

Supplemental Video File 2. Video file of a set of 278 images of focused ion beam serial sections taken in backscattered electron mode at 25 nm spacing for sample Lower Tuscaloosa 8590. The horizontal field of view is 16.00 μm . The large zone of charging (bright area) is probably at the location of organics. Original TIFF images (1024 \times 884 pixels) were compressed using JPEG algorithm at 100 quality when making the video file. Video files were further compressed by resampling images to 400 \times 345 pixels and compressing using the Cinepak algorithm at 75 quality.

Supplemental Video File 3. Video file of a set of 340 images of focused ion beam serial sections taken in backscattered electron mode at 25 nm spacing for sample Marine Tuscaloosa 7925.5. The horizontal field of view is 16.00 μm . Original TIFF images (1024 \times 884 pixels) were compressed using JPEG algorithm at 100 quality when making the video file. Video files were further compressed by resampling images to 400 \times 345 pixels and compressing using the Cinepak algorithm at 75 quality.

Supplemental Video File 4. Video file of a set of 325 images of focused ion beam serial sections taken in backscattered electron mode at 25 nm spacing for sample Gothic shale 5390.8A. The horizontal field of view is 16.00 μm . The viewer should be careful in distinguishing pores from organics. Organics have a low grayscale value. Pores are discerned by the blackest grayscale values and careful observation of the grain/non-pore margins. Original TIFF images (1024 \times 884 pixels) were compressed using JPEG algorithm at 100 quality when making the video file. Video files were further compressed by resampling images to 400 \times 345 pixels and compressing using the Cinepak algorithm at 75 quality.

APPENDIX B. SUPPLEMENTAL DATA FOR CHAPTER 5 AND DATA FROM THE CORE ANALYSIS PROGRAM OF THE PUMP CANYON SITE, NM

Appendix B documents and preserves data and reports generated in conjunction with Chapter 5 of this dissertation and, additionally, the core analysis program of the Pump Canyon Site, NM. The Southwest Partnership on Carbon Sequestration (SWP) oversaw the core analysis program, which supported the writing of Chapter 5. However, some tasks and data collection activities of the core analysis program are not explicitly detailed in Chapter 5; and thus they are described here because all of the core analysis activities are intended to support study of the Kirtland Formation and its sealing behavior.

B.1 Field Core Handling Report

Appendix B.1 presents the original core handling report that was developed prior to the execution of the coring program in May 2008. The report was required by ConocoPhillips (the field site operator), Sandia National Laboratories, and the SWP to ensure clear planning of the field activities and to identify potential safety hazards of the field work.



Southwestern Regional Partnership for Carbon Sequestration (Phase 2)

Procedures for Core Handling at the Pump Canyon CO₂- ECBM/Sequestration Demonstration, San Juan Basin, New Mexico

Prepared by:

***Jason Heath and Lee Harris
New Mexico Institute of Mining and Technology***

***Scott Cooper
Sandia National Laboratories***

April 21, 2008

1. Introduction

This report details plans for handling core from the new CO₂ injection well that ConocoPhillips will drill as part of the Phase 2 activities of the Southwest Regional Partnership on Carbon Sequestration. The core will be used in studies to further understanding of cap rock sealing behavior with respect to CO₂.

The well site is located in Sec. 32, T31N, R8W, which lies east of Aztec, NM (Fig. 1). A total of 120 ft of conventional vertical core will be collected, with approximately 60 ft at both the top and bottom of the Kirtland Shale (Fig. 2).

Subsamples of the core will be preserved in the field for the laboratory analysis of helium concentration and isotopic signatures. We will use the helium data to characterize the transport properties of the shale and infer sealing behavior. The majority of the core will be delivered to TerraTek, Inc., in Salt Lake City, Utah, for petrophysical and petrological analyses, including measurements of gas breakthrough pressure and wettability.

Drilling and coring will most likely begin on April 26th.

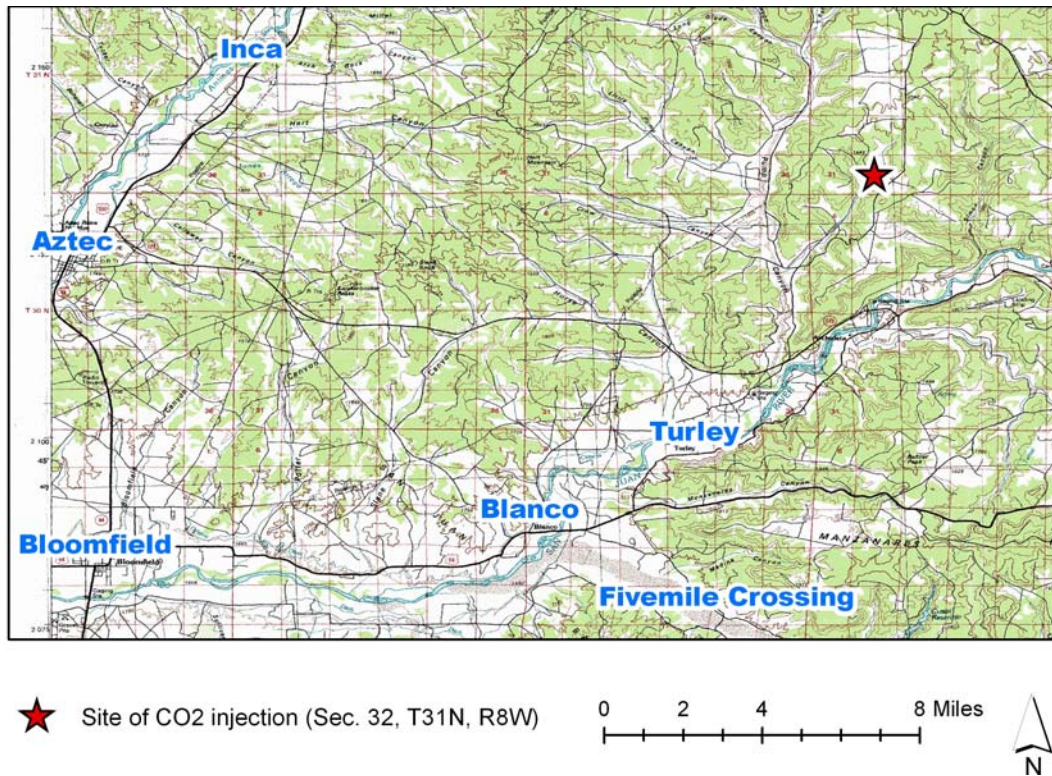


Fig. 1. Map showing the location of the new CO₂ injection well.

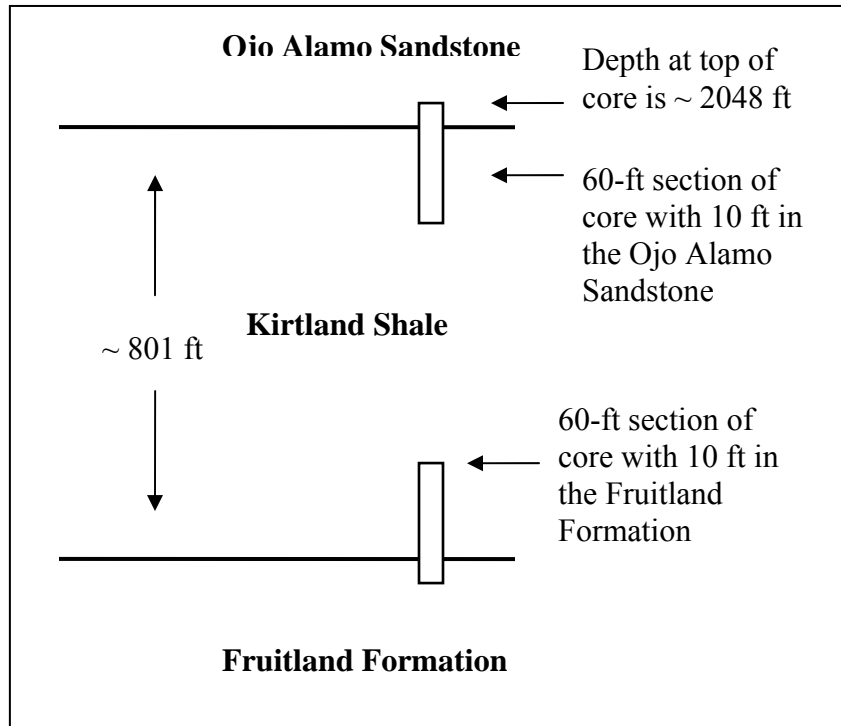


Fig.2. Schematic of the locations of vertical coring.

2. Description of Core Handling Activities

2.1 Team Members and List of Activities

The core handling team includes, respectively, three members from New Mexico Tech (NMT) and three from Sandia National Laboratories (SNL):

1. Jason Heath
2. Lee Harris
3. Reid Grigg
4. Scott Cooper
5. Randy Everett
6. Bill Holub

Five members of the team will be assigned to specific core handling activities (Table 1), whereas the remaining person, Dr. Grigg, will be available as the “gopher” to help with any unforeseen problems.

The core handling activities are listed in Table 1. ConocoPhillips has contracted Coring Services, Inc., to collect the 4-in diameter vertical core. Coring Services has requested that one member of the core-handling team help mark depths on the aluminum core barrels so that it can be cut into 3-ft sections (see Activity 1 on Table 1).

Table 1. Major core handling activities associated with team members.

Activity	Team members
1. Mark depths on core barrels, cut core into 3-ft sections, and place rubber end caps on core barrels.	Coring Services and Bill Holub
2. Push core out of barrels at specific depth intervals and choose locations of core subsamples.	Scott Cooper and Jason Heath
3. Use the drill press to cut 1-in diameter by 3-in long subsamples of core.	Lee Harris
4. Seal subsamples in ultra-tight, high vacuum canisters.	Jason Heath and Randy Everett
5. Load 3-ft core barrels into the trailer.	Everyone
6. Transport core to TerraTek and deliver preservation canisters to Noble Gas Laboratory at University of Utah.	Lee Harris and Jason Heath

Activities 2 through 4 relate to the major goal of properly preserving 12 subsamples of core for the laboratory analysis of helium concentration and isotopic signatures in the pore fluids. To prevent loss of helium, 1-in diameter by 3-in long subsamples of core will be placed into canisters with an extremely low leak rate. The canisters have been constructed from parts typically used for vacuum service. The subsamples will be cut using a drill press with cooling fluid that may be tap water, a dilute KCl solution, or mineral spirits. The cooling fluid chosen will depend on whether the core samples will disintegrate when exposed to tap water. All fluids will be collected and not allowed to drain onto the ground. We are developing quality control and assurance protocols for drilling the subsamples and sealing them in the preservation canisters.

2.2 Instructions for Activity 1

The following is a list of activities, important issues or concerns, and instructions for Activity 1 of Table 1:

1. Pay attention from the dog house to the coring activities on the drill rig. This includes watching for any core that falls out of top or bottom of the core barrels onto the rig floor. Pay close attention to the orientation of any pieces of core that are dropped.
2. Assist Coring Services, if needed, to remove core from the core catcher. Use a hammer or a wrench as necessary.
3. For convenience, use a tape measure labeled in tenths of a foot to mark depths on the aluminum core barrels.

4. Ask the rig operator and mud logger for the depth at which coring began. Sometimes rig operators and loggers may not report the same depth. Ask anyone else involved with the drilling who might know the depth at which coring began.
5. Core will most likely be placed on the catwalk. This is where the core will be marked and cut, using an “island cut”, into 3-ft sections.
6. Use the start-of-coring depth to begin marking depths every foot on the outside of the aluminum core barrel.
7. Assume that any loss of core was at the bottom of the length of the core, not at the top.
8. If the core (i.e., the rock itself) does not lie flush with the top of the core barrel, measure the distance from the core to the top of the core barrel (Fig. 3). Using that measurement, mark a line on the top of the core barrel with the start-of-coring depth. This line will be the datum from which all subsequent marked depths will be based.

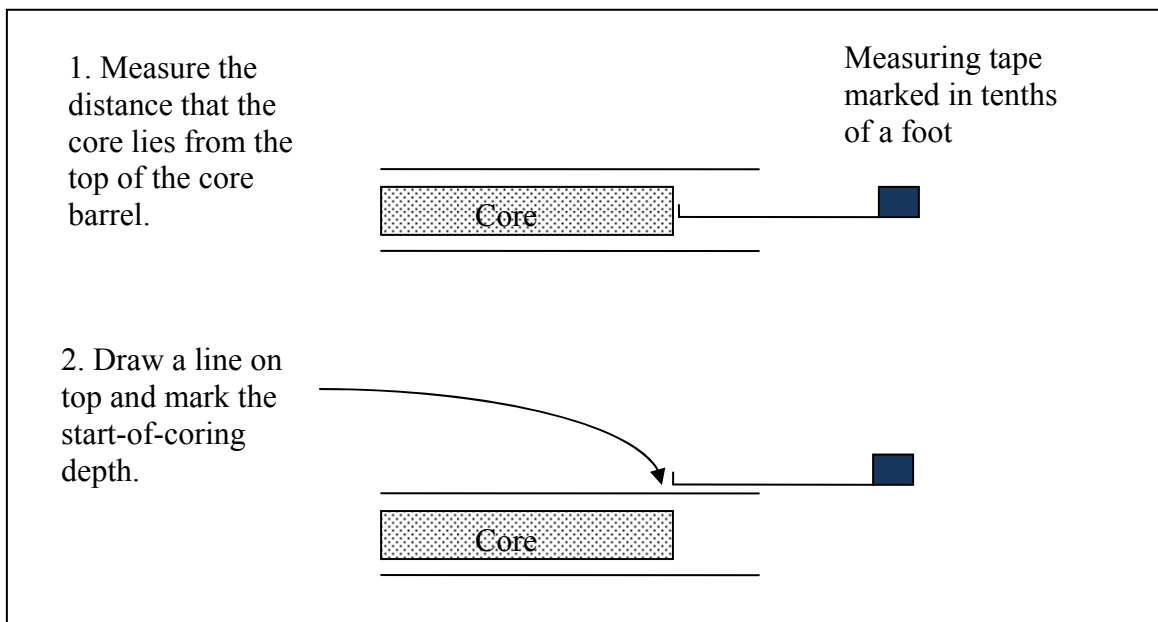


Fig 3. Schematic cross-section of core barrel with instructions for marking start-of-coring depth line, if core does not lie flush with the top of the core barrel

9. If core extends out the top of the core barrel, use the measurement of the distance of extension and the start-of-coring depth to mark a line with the depth to the nearest foot as close as possible to the top of the core barrel (Fig. 4).

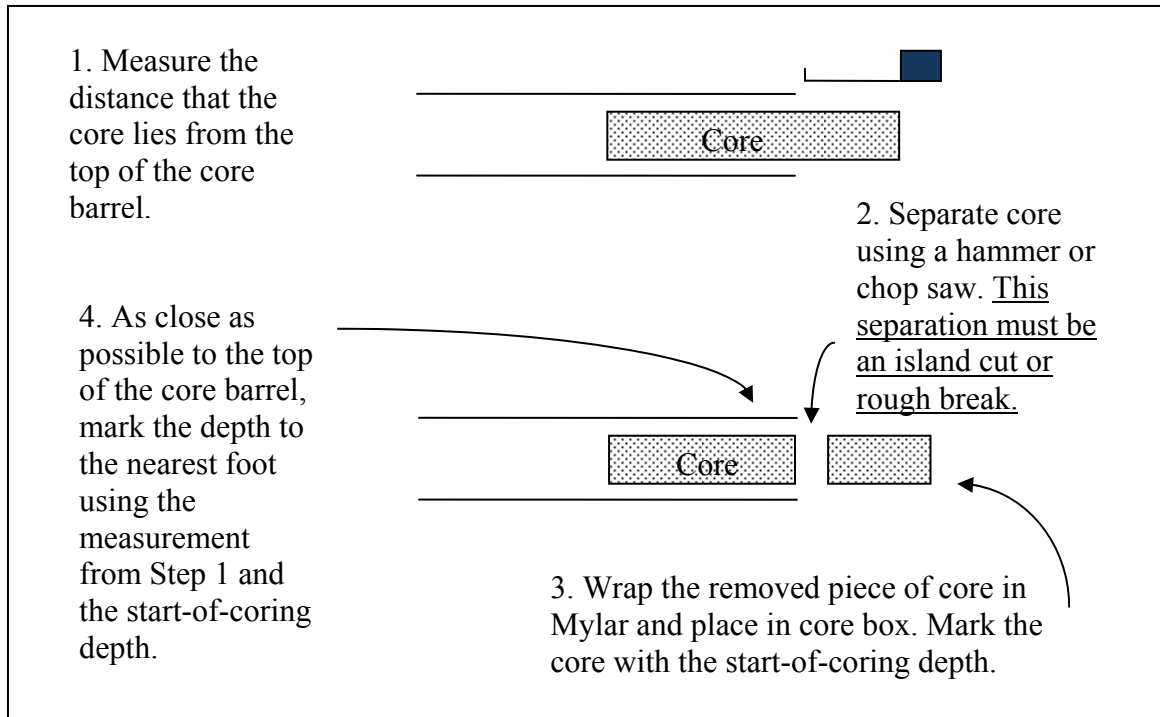


Fig. 4. Schematic cross-section of core barrel with instructions for marking the depth near top of core barrel, if core extends out the top of the barrel

10. Use indelible paint pens for writing on aluminum core barrels.
11. Mark the orientation of the core using black and red paint pens. This is done by placing two stripes of black and red, next to each other, along the entire length of the core. The lines should be such that if a person were to be at the bottom of the barrel looking towards the top (i.e., the bottom of the hole looking up), the red line would be on the right (Fig. 5).

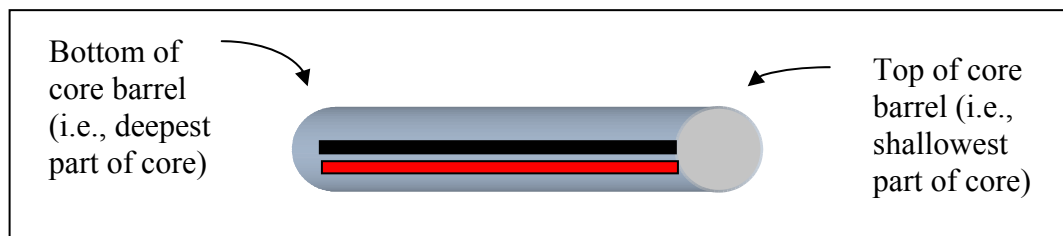


Fig. 5. Schematic of core barrel with red and black lines, which indicate orientation of the core.

12. Depths should be marked every foot along the length of the core barrel.
13. With the assistance of Coring Services, cut through the aluminum core barrel and the core with a chop saw every three feet. Cut on the depth mark. Do not cut straight through with a planar cut; instead, use an island cut. The island cut is made by cutting towards the middle of the core, then rotating the core and cutting

towards the middle again. This is done until a small neck of rock remains. The neck of rock can then be broken so that the core on either side can be fit together again. Without island cuts, the core can rotate, making it difficult to impossible to properly place the core back together. Improper placement may preclude the interpretation of fractures and other features.

14. The top and bottom of the 3-ft core-barrel tubes should be labeled (e.g., T1, T2, T3, etc.).
15. The 3-ft core-barrel tubes should be sealed with rubber end caps from Coring Services. Attach the caps with duct tape and/or hose clamps. Clamps are preferable because the tubes will need to be reopened to obtain subsamples of core for preservation for the helium analysis.
16. Coordinate with the rig supervisor on the time needed to properly label and handle the core.
17. Acquire a copy of the core report, which will have information such as weight on bit, core barrel parameters, starting depth, time for cutting, rate of penetration, etc.
18. Any loose pieces of core not in the aluminum barrels should be wrapped in Mylar and placed in core boxes with proper labels.
19. If questions arise while in the field, John Keller at TerraTek can be contacted to give guidance. His office number is: 801-584-2467.

2.3 Instructions for Activity 2

The following is a list of activities, important issues or concerns, and instructions for Activity 2:

1. The goal is to determine the locations along the core for 12 subsamples of core for the preservation of helium and other noble gases in the pore fluids.
2. In general, the subsamples should be evenly spaced across the 120 ft of core (i.e., one sample every 10 ft). However, the exact location will depend on factors discussed below.
3. Using a cart or wheel barrow, carry the labeled 3-ft barrels of core over to the location of the drill press.
4. Using a pole attached to a round piece of wood (or plastic) less than 4-in in diameter, push the core onto a tray made from a 6-in diameter PVC pipe. Remove any jagged metal, if needed, from the ends of the core barrels using a deburring tool.
5. Inspect the core and note lithology, fractures, fissility, etc.
6. For samples within the Kirtland, choose the location for subcoring based on regions with relatively high clay content. Subcoring locations with high clay content adjacent to fractures are preferable.
7. One or two samples will be collected from the Ojo Alamo Sandstone. Regions with relatively low permeabilities, based on clay and silt content opposed to sand, should be chosen.
8. Mark locations for subcoring by placing a thin section of Mylar on top of core.

9. Carefully transfer the core to those in charge of using the drill press.
10. Core should only be examined immediately prior to the using the drill press to minimized disturbance to core before subcoring. Disturbance of core may facilitate loss of helium along microfractures or stress-release fractures.

2.4 Instructions for Activity 3

The following is a list of activities, important issues or concerns, and instructions for Activity 3:

1. The core will be subsampled with the drill press in the direction perpendicular to the long axis of the core.
2. Place the core onto the wooden tray designed to hold the core below the drill.
3. Use a 1-in drill bit. Use the 1.5-in if the smaller bit does not work. Extra bits will be available.
4. The cooling fluid should be tap water at first. If the core disintegrates, use a dilute KCl solution or mineral spirits. The cooling fluids will be held in a bucket attached to a tripod. Tubing will allow the fluid to flow to the cutting area.
5. Coring should be started slowly.
6. Use a trim saw to cut off the part of the subsamples that was the original outside surface of the core. The length of the subsample should be approximately 3 in.
7. After subcoring, immediately weigh the subsample and then place it into a preservation canister. Hand the canister over to the person who will seal it.
8. Minimize agitation of the core during subcoring.
9. Use gloves when handling the core.
10. Subcoring should occur immediately prior to placement in the preservation canisters. Subsamples of core should not be left to degas helium into the atmosphere.
11. Subcoring will be done within or over a catch basin. No fluids will contact the ground. We will contact ConocoPhillips for instructions on disposal of fluids.
12. Place the core back into the core barrels and reseal using the rubber end caps and duct tape or hose clamps.

2.5 Instructions for Activity 4

The following is a list of activities, important issues or concerns, and instructions for Activity 4:

1. The subsamples of core will be sealed in high-vacuum, low leak-rate canisters (Fig. 6).
2. Receive the canisters with core subsamples from those operating the drill press.
3. Place the large copper gasket onto the canister.

4. Immediately placed the lid onto the canister and the copper gasket. Seal the canister by finger tightening ten bolts with washers.
5. Tighten the bolts in pairs in a cross-hatch pattern as shown on Fig. 7. Go through the pattern tightening the bolts three times until the torque on each bolt is 190 in-lb. Tightening must be done carefully to ensure that the lid closes evenly onto the canister.
6. Connect the valve on the lid into the vacuum line system. Use proper gaskets for the VCR fittings. The fittings should be finger tightened and then tightened to a quarter of a full turn.
7. Place the canister under vacuum and purge using ultra-high purity nitrogen, which should be connected to the vacuum line. The pump down and purging process should follow this process (Shala, pers. com., 2007):
 - a. pump for 30 seconds;
 - b. flush with 5-10 psig nitrogen;
 - c. pump for 30 seconds;
 - d. flush with 5-10 psi nitrogen;
 - e. pump for 45 seconds; and
 - f. close the valve at top of canister and remove canister from vacuum line.
8. Repeat the closing and sealing process in the same manner for all subsamples. Perform the procedure on an empty canister after sealing all other canisters. The empty canister will serve as a blank.
9. For quality assurance, a sheet listing the steps of the closing and sealing process will be taken to the field. As each step is finished properly, check marks on the sheet besides the steps will be made.
10. The canisters will be delivered to the Noble Gas Laboratory of the University of Utah for analysis of helium and other noble gases.



Fig. 6. Photographs of canisters built from high vacuum equipment to preserve noble gases that will degas from pore fluids in core samples.

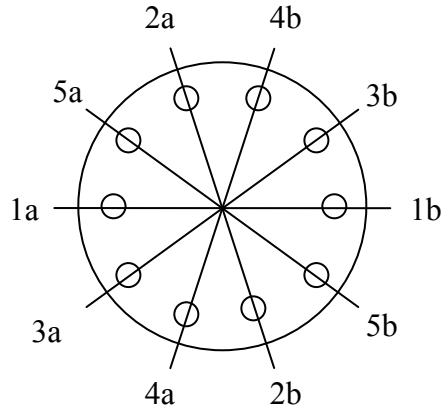


Fig. 7. Plan view schematic of lid of preservation canisters with lines indicating tightening pattern. “1a” stands for the bolt chosen to be tightened first. “1b” is the corresponding bolt in the pair that lies in line with 1a. “2a” and “2b” comprise the second pair that should be tightened and so on.

2.6 Instructions for Activities 5 and 6

The following is a list of activities, important issues or concerns, and instructions for Activity 5:

1. A trailer capable of transporting ~ 3,000 lbs will be driven to the site.
2. Load the 3-ft core barrels into the trailers. Use two people, if needed, to avoid straining when picking up the core.
3. Secure the core on the trailer using rope.
4. Two members of the coring team will transport the core to TerraTek in Salt Lake City, Utah. Transport should occur immediately following coring activities.

3. Equipment needed for Core Handling

The majority of the equipment in Table 2 has been obtained by New Mexico Tech. Sandia National Laboratories will supply the following:

1. generator;
2. first-aid kit;
3. 305-gallon water tank; and
4. backup drill press.

To be allowed on site by ConocoPhillips, the personal protection equipment of Category 1 in Table 2 has been included.

The list of equipment will be provided to ConocoPhillips prior to coring to make sure that these items can be brought to or near the well site. Items or activities of special concern include:

1. using a U-Haul truck for shelter in which the subsamples of core will be drilled and preserved;
2. using water, KCl solutions, or mineral spirits as cooling fluids for the drill press;
3. using electrical equipment such as the vacuum pump and workshop lights;
4. tank of a nitrogen gas.

We do not know what cooling fluid will be best when we drill of subsamples of core. We will most likely use tap water or KCl solution. We will obtain KCl solution from the drillers, if possible. We will dispose of cooling fluids ourselves.

4. National Environmental Policy Act (NEPA)

The Department of Energy approved the environmental questionnaires that were completed for this project. The NEPA requirements have been met. We have copies of the NEPA paperwork. These will be made available, if needed.

Table 2. List of equipment for coring handling activities.

Equipment Category	Item #	Description
1. Personal protection equipment	1	Steel-toed boots
	2	Hard hats
	3	Safety glasses
	4	Gloves
	5	Fire-retardant overalls
	6	Fire extinguisher
	7	Fire-aid kit
2. Handling aluminum core barrels and preparing core for transport	8	Diagraph GP-X paint markers in black, red, and white
	9	25' tape measures, engineer's scale (marked in tenths)
	10	Ratchet straps and rope
	11	Core packing boxes (for loose pieces of core)
	12	Utility knife or carpet-hook knife for removing burrs from the core barrel
	13	Duct tape
	14	Chop saw with cutting blades (provided by Coring Services)
	15	Hammer (or wrench) for removing core from the core catcher
	16	Rags for wiping mud from core
	17	1 gallon Ziploc bags
	18	Roll of mylar (like what the butcher uses) for wrapping core
19	Rubber end caps (provided by Coring Services)	
3. Cutting subsamples of core	20	Pole with round piece of wood on end for pushing core out of barrel
	21	Scale for weighing subsamples of core
	22	Drill press with 15 amp, 120 V coring motor and drill bits
	23	Trim saw
	24	6" PVC pipe cut in half for holding sections of core
	25	Wooden frame for holding core during drilling
	26	Tripod for holding cooling fluid
	27	305 gallon water container; water used as cooling fluid for drill press
	28	Water-catcher oil pan or rubber maid container
	29	Mineral spirits, cooling fluid (in case water disintegrates samples)

Table 2 (continued). List of equipment for coring handling activities

Equipment Category	Item #	Description
4. Preserving subsamples of core	30	13 preservation canisters (see Fig.)
	31	Torque wrench for bolting shut the canisters
	32	Anti-seize for bolts on preservations canisters
	33	99.999% purity nitrogen tank with regulator
	34	Rotary vane vacuum pump with 115 V, 60 Hz supply voltage
	35	Vacuum gauge with 115 V power supply
	36	Assembly support for attaching canisters to nitrogen tank and vacuum gauge
	37	¼" Copper, roll – refrigerator grade soft copper
	38	Flaring tool
5. Working conditions and miscellaneous items	39	Silicon
	40	Workshop lights
	41	Generator
	42	Trailer to transport core to TerraTek in Salt Lake City. UT
	43	Field notebook
	44	All weather writing pens and pencils
	45	Plastic gloves
	46	Cold weather clothing
	47	Uhaul truck as our shelter to work in
	48	Cart
49	Tables	
6. Transportation of core	50	Large trailer hitched to truck for transporting core

B.2 Core Handling and Data Collected by TerraTek, a Schlumberger Company

TerraTek performed petrologic and petrophysical measurements on fresh core samples from the EPNG Com A Inj 1 well, which are given herein. The company also performed handling and preservation procedures, which included wrapping core in Mylar plastic film, aluminum foil, and dipping some core samples in sealant to prevent drying.

B.2.1 Petrologic Evaluation of Kirtland Shale Core – San Juan BU EPNG Com A Inj #1 Well, TR08-502488 Report

TerraTek performed petrologic evaluation of several Kirtland Formation core samples, the locations of which were first identified by Jason Heath and Scott Cooper (formerly of Sandia National Laboratories) during a preliminary examination of the core in May 2008. The depth locations were chosen to characterize major lithostratigraphic units of the Kirtland Formation core and to obtain petrologic data near to locations of plugs for noble gas analysis. TerraTek's petrologic report follows:

***Petrologic Evaluation of Kirtland Shale Core
– San Juan BU EPNG Com A Inj #1 Well –***

Prepared for:

**ConocoPhillips
3401 E. 30th Street
Farmington, NM
87402**

Attention:

**Mr. Ryan Frost
Mr. Jason Heath**



1935 S. Fremont Drive • Salt Lake City, Utah 84104
Telephone (801) 584-2400
FAX (801) 584-2406

**TR08-502488
October 2008**

Table of Contents

EXECUTIVE SUMMARY	1
PETROLOGIC ANALYSIS	1
1 Introduction and Procedures.....	1
1.1 Thin Section Preparation.....	2
1.2 Semi-quantitative X-ray Diffraction (XRD) Procedures	2
2 Petrographic Analysis.....	3
2.1 Argillaceous mudstone and sandy/silty argillaceous mudstone	3
3 Porosity	3
4 Clay Mineralogy and Fluid Sensitivity	4
5 Petrographic/SEM Summary	4
6 XRD Results.....	7

EXECUTIVE SUMMARY

Core samples of Kirtland Shale recovered from EPNG's Com A Inj #1 Well in the San Juan Basin consist of poorly laminated to mottled argillaceous mudstones with variable silt and sand content. Both core and petrologic examination reveal evidence of soil-forming processes. Total organic content is negligible, and matrix clays include significant amounts of smectite and highly expandable mixed layer illite-smectite. The rocks are not potential reservoir.

The *risk of fresh water sensitivity is high* due to large amounts of expandable clays. Smectite and mixed layer illite/smectite with 15-40% expandability are the predominant clay species. Total expandable clays of 11-23% are determined by XRD analysis. Expected *sensitivity to acid-based fluids is also high*, due to the presence of significant amounts of iron-bearing chlorite in most of the samples (0-13%).

PETROLOGIC ANALYSIS

1 Introduction and Procedures

At the request of Mr. Ryan Frost of ConocoPhillips, petrologic evaluation was conducted on selected core samples from EPNG's Com A Inj #1 Well in the San Juan Basin. The following report includes a discussion of composition, texture, cements and porosity based on general thin section examination and scanning electron microscopy (SEM) of 7 samples. Whole-rock X-ray diffraction (XRD) analysis was also performed to better constrain mineralogy and potential reservoir sensitivity issues. Descriptions are complimented by digital, annotated photomicrographs presented in the accompanying CD. XRD results are included at the end of this report.

All selected petrographic samples, associated depths, and lithotypes are listed in Table P1. Generalized lithotypes are based on the dominant texture and composition observed in thin section.

Table P1. Petrologic Testing Matrix

Sample No.	Sample Depth (ft)	Lithotype	TS	SEM	XRD
CP-1	2048.25	sandy argillaceous mudstone	✓	✓	✓
CP-2	2052.06	sandy argillaceous mudstone	✓	✓	✓
CP-3	2055.20	argillaceous mudstone	✓	✓	
CP-4	2062.30	sandy argillaceous mudstone	✓	✓	✓
CP-5	2067.98	sandy argillaceous mudstone	✓	✓	✓
CP-6	2692.25	argillaceous mudstone	✓	✓	✓
CP-7	2697.15	silty argillaceous mudstone	✓	✓	✓
Total			7	7	7

1.1 Thin Section Preparation

Core pieces were initially impregnated with a low-viscosity fluorescent red-dye epoxy resin under high vacuum to highlight porosity types. The impregnated samples were surfaced, mounted to standard (24 mm × 46 mm) thin section slides, and ground to a thickness of approximately 30 microns. The thin sections were then stained with a mixture of potassium ferricyanide and Alizarin Red 'S' to aid in identification of carbonate minerals. The prepared sections were examined and digitally imaged at various magnifications under plane-polarized, cross-polarized, and reflected UV light using a Nikon polarizing binocular microscope equipped with a Spot Insight digital camera, reflected light source, and various UV filters. At least two images (one at lower magnification, one at higher magnification) were collected for each sample.

1.2 Semi-quantitative X-ray Diffraction (XRD) Procedures

Bulk Analysis - Representative splits of the selected bulk samples are ground using a McCrone micronizing mill and loaded into aluminum sample holders. The powdered samples are analyzed with a Rigaku Ultima III X-ray diffractometer from 2 to 66 degrees two-theta (2θ) using Cu K-alpha radiation and various slit and filter geometries. The raw data is interpreted using JADE software, which identifies the mineralogy based on peak profile fitting and whole pattern fitting methods. This analysis yields semi-quantitative analysis of the whole rock and best characterizes overall mineralogy and amount of clay in the bulk sample.

The percent expandability is the total amount of swelling clay in the whole rock sample and is determined by adding the amounts of discrete smectite and interlayered smectite in mixed-layer clays in the whole rock sample. For example, a bulk sample with 25 percent mixed-layer illite-smectite that is composed of 20 percent interlayered smectite is approximately 5 percent expandable.

Clay Analysis - Bulk samples are crushed and disaggregated to obtain a sample less than 4 microns, decanted and centrifuged. Resulting slurries are sedimented on glass slides, and scanned after air-drying and vapor glycolation treatments. Clay minerals are identified and their approximate weight percentages are determined by comparison with mixtures of standard clay minerals in known percentages. XRD analysis of the clay size fraction yields the relative abundance of the clay minerals and determines the amount of expandability (amount of swelling clay) in the mixed-layer clays. The amount of interlayered smectite (swelling clay) in mixed-layer illite/smectite is used to determine the percent expandability of whole rock samples.

2 Petrographic Analysis

The seven core samples in the studied interval are classified as *argillaceous mudstone*, *sandy argillaceous mudstone*, or *silty argillaceous mudstone*. Lithotype nomenclature is based on grain-supported vs. matrix-supported texture, and dominant composition of the matrix. The lithotypes are described in the following section.

2.1 Argillaceous mudstone and sandy/silty argillaceous mudstone

Samples from the cored interval comprise mudstones with poor lamination or mottled texture. The rocks are entirely matrix-supported, with variable amounts of dispersed detrital silt and sand. The matrix composition is argillaceous, and XRD determines a mixed composition including predominantly mixed layer illite-smectite and smectite, with subordinate amounts of chlorite and locally abundant kaolinite. Mottled color, along with apparent root material, root casts, and illuviation structures observed in thin section and SEM are evidence of soil-forming processes. Total organic content is negligible in the samples, with measured values less than 0.20% by weight.

Silt to medium sand-sized grains in the samples are composed of quartz, alkaline feldspar, plagioclase, and volcanic rock fragments of both argillaceous and chert-replaced types. A few micas are visible as accessories, particularly chlorite and biotite. No faunal grains are observed.

The most common secondary mineral noted in these mudstones is authigenic quartz, occurring as replacements in volcanic and lithic grains. Small amounts of calcite, ferroan calcite, dolomite, ferroan dolomite and pyrite are also present as crystals within the matrix, or associated with root structures.

3 Porosity

Several porosity types are present in the selected samples, the most prominent of which are induced microfractures. Intergranular/intercrystalline micropores and pores associated with decayed organic material are interpreted as natural. Pore types are described below:

- Induced porosity [0.005 to 0.02 mm; 5 to 20 microns] is pervasive in the suite, and is typical of rocks with significant amounts of expandable clays. Induced pores tend to form lenses between elongate clay ridges, or pock-like cavities in the matrix (SEM

Images 20, 26 and 32). Laminae or parting surfaces are interpreted as induced in some samples (SEM Images 2 and 21). Induced pores are not present *in-situ*, and may introduce error in porosity and permeability measurements.

- Root and organic particle casts [0.002 to 0.02 mm; 2 to 20 microns] are observed in both thin section and SEM (SEM Images 4 and 28). These voids are left by organic material which has decayed. Pores tend to be enclosed in envelopes of well-aligned clays (SEM Images 16 and 19), and contribute little to effective porosity.
- Matrix-hosted intercrystalline microporosity [<0.005 mm; up to 5 microns] is the typical porosity type in most mudstones. It comprises tiny voids between clay flakes and cements, and within porous carbonaceous patches. The pores are tiny and poorly connected. In the case of expandable clays, pores visible under SEM represent a maximum size and dehydrated condition, and therefore are assumed to be smaller or absent *in situ*.

4 Clay Mineralogy and Fluid Sensitivity

The clay fractions of argillaceous sandy mudstones, sandy argillaceous mudstones, and silty argillaceous mudstones in this suite consist of mixtures of predominantly expandable clays, of which smectite and illite-smectite are the most abundant. Illite-smectite ranges from 5% to 40% expandable interlayers. Chlorite is present in amounts from 0% to 13%.

Overall matrix expandability is high in the suite (total expandable clays 11-23%). *Reservoir sensitivity related to the water-sensitive clays is considered high.*

Iron-bearing minerals in the mudstones include chlorite, minor ferroan calcite and dolomite, and minor pyrite. Reaction of these iron-bearing constituents with acid-based completion fluids could produce ferric iron hydroxide gels, which may act to clog pores and reduce permeability. *Reservoir sensitivity to acid based completion fluids should be considered.*

5 Petrographic/SEM Summary

Tables P2 and P3 below summarize the petrographic characteristics of the selected core sample from the studied well. These tables are also presented in electronic format on the accompanying CD.

Table P2. Summary of Petrographic/SEM Results (Samples 1-4)

Sample Number and Depth	CP-1 2048.25 ft	CP-2 2052.06 ft	CP-3 2055.20 ft	CP-4 2062.30 ft
Lithology	sandy argillaceous mudstone	sandy argillaceous mudstone	argillaceous mudstone	sandy argillaceous mudstone
Maximum Grain Size	fine to medium sand	fine to medium sand	coarse silt to medium sand	coarse silt to medium sand
Detrital Grain Types	quartz, feldspar, vrfis	quartz, feldspar, chert, vrfis	quartz, feldspar, chert	quartz, feldspar, chert
Dominant Matrix Composition	argillaceous	argillaceous	argillaceous	argillaceous
Detrital Clay Minerals	smectite, illite, CHL, (KAOL)	smectite, CHL, I/S	smectite, CHL, (KOAL)	smectite, IL, I/S
Biotic Grains	none observed	none observed	none observed	none observed
Organic components	scattered discrete flecks	flecks, blebs	flecks, blebs	flecks, blebs
Accessory Grains	chlorite/biotite	chlorite/biotite, rare heavies, pyroxene	illitic intraclasts representing illuviation features	chlorite/biotite, illitic intraclasts
Authigenic Minerals	quartz, pyrite	quartz, pyrite	quartz, pyrite, Fe-cal	quartz, pyrite, Fe-cal
Pore Types	matrix intercrystalline; induced	matrix intercrystalline; induced	matrix intercrystalline; induced	matrix intercrystalline; induced
Petrographic and SEM Comments	well-laminated; pervasive induced microfractures; swelling clays; chert-replaced vrfis common	nearly grain-supported; plag and vrfis > quartz; smectitic matrix; similar to previous	unsorted, dispersed detrital grains; illuviation features; minor ferroan calcite cement	mottled texture; induced fractures pervasive; minor carbonate cement replaces grains

Abbreviations: arg = argillaceous, cal = calcite, carb = carbonaceous, CHL = chlorite, dol = dolomite, Fe-cal = ferroan calcite, Fe-dol = ferroan dolomite, fx = fractures, IL = illite, I/S = mixed-layer illite-smectite, KAOL = kaolinite, plag = plagioclase, qtz = quartz, sil = siliceous, TOC = total organic carbon, vrfis = volcanic rock fragments

Table P3. Summary of Petrographic/SEM Results (Samples 5-7)

Sample Number and Depth	CP-5 2067.98 ft	CP-6 2692.25 ft	CP-7 2697.15 ft
Lithology	sandy argillaceous mudstone	argillaceous mudstone	silty argillaceous mudstone
Maximum Grain Size	coarse silt to medium sand	coarse silt to medium sand	very fine to fine sand
Detrital Grain Types	quartz, feldspar, vrf's	quartz, feldspar, vrf's	quartz, feldspar, vrf's
Dominant Matrix Composition	argillaceous	argillaceous	argillaceous
Detrital Clay Minerals	I/S, IL, smectite	I/S, CHL, KAOL	I/S, IL, CHL, (KAOL)
Biotic Grains	rare silicified spore	none observed	none observed
Organic components	streaks, flecks	flecks, blebs	streaks, flecks
Accessory Grains	chlorite/biotite, illitic intraclasts	chlorite, biotite, illitic intraclasts	chlorite/biotite, illitic intraclasts
Authigenic Minerals	quartz, pyrite	quartz, pyrite, Fe-cal, Fe-dol	Fe-dol, silica, calcite, Fe-cal
Pore Types	matrix intercrystalline; induced	matrix intercrystalline; induced	matrix intercrystalline; induced
Petrographic Comments	mottled texture; induced fractures; illuviation features; root casts with associated plant debris	Fe-cal replaces grains and fills fractures; tiny clusters of chlorite throughout matrix; root cast	vertical to sinuous clay-filled fx; carb streaks; mixed clay matrix; root casts

Abbreviations: arg = argillaceous, cal = calcite, carb = carbonaceous, CHL = chlorite, dol = dolomite, Fe-cal = ferroan calcite, Fe-dol = ferroan dolomite, fx = fractures, IL = illite, I/S = mixed-layer illite-smectite, KAOL = kaolinite, plag = plagioclase, qtz = quartz, sil = siliceous, TOC = total organic carbon, vrf's = volcanic rock fragments

6 XRD Results

Table P4 presents results of semi-quantitative X-ray diffraction analysis for seven Kirtland Shale core samples. The upper portion of each table lists the whole rock or bulk mineralogy, and relative proportions of the clay minerals in the bulk samples, and the lower portions list the clay mineralogy of the < 4 micron size fraction. All percentages represent relative abundances of the crystalline phases by weight.

A few additional comments follow:

- ✓ Carbonaceous material cannot be accurately detected by XRD because of typically poor crystallinity.
- ✓ Ferroan composition of calcite and dolomite is confirmed through thin section analyses.
- ✓ Micromicas are recognized by X-ray diffraction as illite and chlorite. Glauconite has an illite crystal structure.
- ✓ Total expandable clay is the sum of the smectite mineral % and the expandable fraction of the illite/smectite %.
- ✓ Whole rock (bulk) XRD data provides the best representation of reservoir mineralogy.

Table P6. Whole Rock and Clay X-Ray Diffraction Data

**WHOLE ROCK
 MINERALOGY**

SAMPLE ID	1	2	3	4	5	6	7
DEPTH (FT)	2048.25	2052.06	2055.20	2062.30	2067.98	2692.25	2697.15
QUARTZ	5	11	37	23	12	21	21
K-FELDSPAR	11	15	15	9	10	10	6
PLAGIOCLASE	18	26	2	14	12	13	22
CALCITE	0	1	2	0	1	1	0
ANKERITE/FE-DOLOMITE	1	3	0	1	1	1	1
DOLOMITE	0	0	0	0	0	0	0
PYRITE	0	0	2	1	1	1	0
TOTAL NON-CLAY	35	56	58	48	38	48	50
SMECTITE	23	22	21	19	5	3	4
ILLITE/SMECTITE (I/S)	4	9	2	11	43	28	20
ILLITE+MICA	22	0	0	13	14	0	11
KAOLINITE	5	3	5	1	0	9	5
CHLORITE	12	10	13	7	0	12	10
TOTAL CLAY	65	43	42	52	62	52	49
GRAND TOTAL	100	100	100	100	100	100	100

**RELATIVE CLAY ABUNDANCE IN BULK
 SAMPLE**

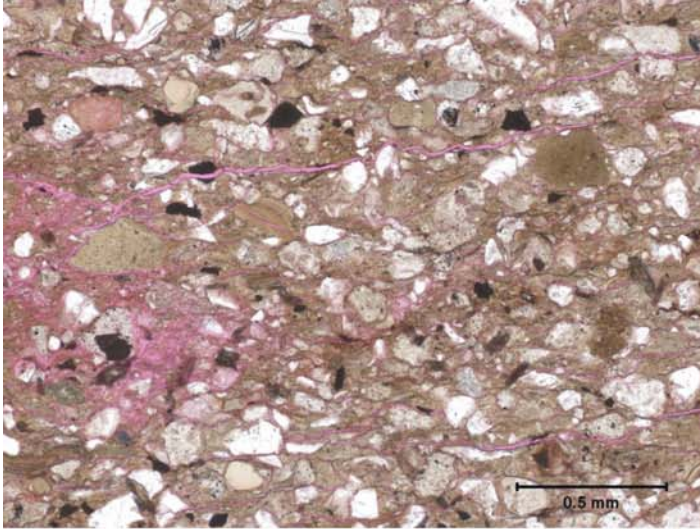
% I/S Expandability	15	20	5	15	35	40	35
SMECTITE	35	50	51	38	8	6	8
ILLITE/SMECTITE (I/S)	6	20	5	22	69	54	40
ILLITE+MICA	34	0	0	26	23	0	22
KAOLINITE	7	6	12	1	0	17	10
CHLORITE	19	24	32	14	0	23	20
TOTAL	100	100	100	100	100	100	100
TOTAL EXPANDABLE CLAY	23	23	21	21	20	14	11

CLAY MINERALOGY **RELATIVE CLAY ABUNDANCE (LESS THAN 4 MICRON SIZE
 FRACTION)**

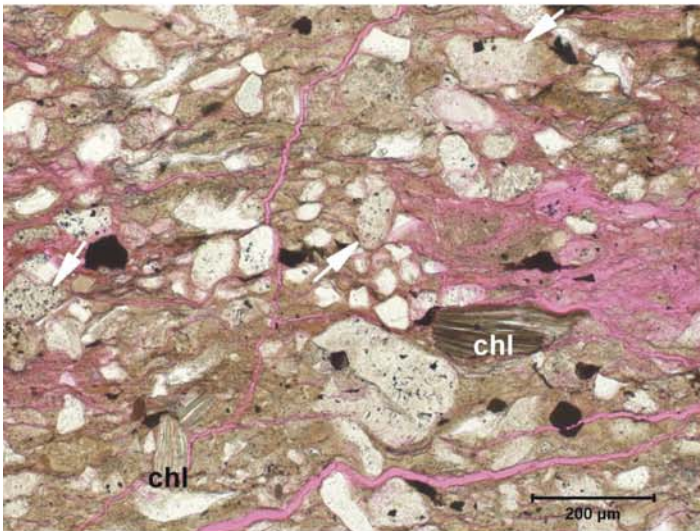
SAMPLE ID	1	2	3	4	5	6	7
DEPTH (FT)	2048.25	2052.06	2055.20	2062.30	2067.98	2692.25	2697.15
% I/S Expandability	15	20	5	15	35	40	35
SMECTITE	58	38	37	48	9	4	9
ILLITE/SMECTITE (I/S)	9	15	3	28	75	37	48
ILLITE	5	4	4	10	13	7	8
KAOLINITE	14	11	11	7	1	8	6
CHLORITE	14	32	45	7	2	44	29
TOTAL	100	100	100	100	100	100	100

B.2.2 Photomicrographs from Petrographic and SEM Analysis

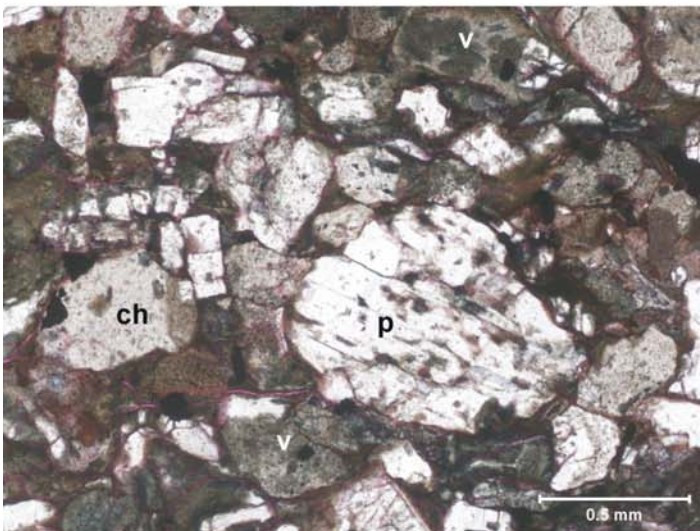
Thin sections and scanning electron microscope (SEM) images taken by TerraTek that are associated with the report of Appendix B.2.1 are presented here. Methods of image acquisition and interpretation are also given in Appendix B.2.1. The first line of description of each photo follows this format: name of original jpeg image file, identification number of core sample, depth of core sample, and TS or SEM abbreviation for petrographic thin section image or secondary electron microscope image.



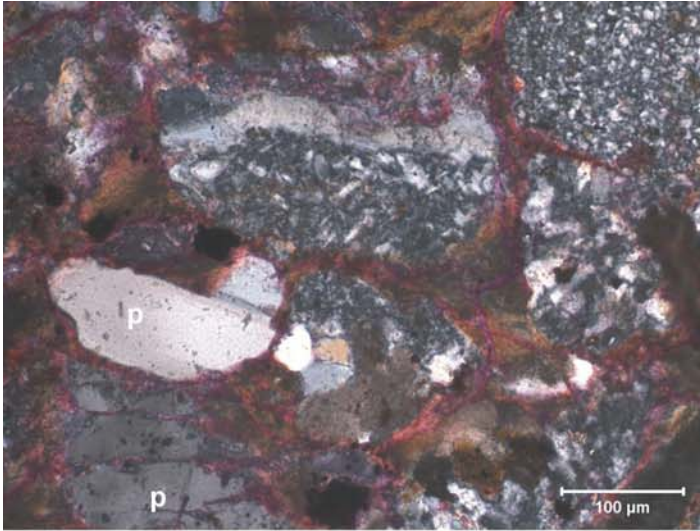
TS_1.jpg, CP-1, 2048.25 ft, TS. Sandy argillaceous mudstone. The clay matrix is a mixture of illite, smectite, and chlorite, with small amounts of kaolinite and mixed layer illite-smectite (XRD). Detrital grains are sand sized quartz, feldspars and volcanic clasts. Numerous horizontal fissures in this view (stained magenta by dyed epoxy) represent dehydration and pressure-release fractures. (Plane-polarized light. Scale bar = 0.5 mm)



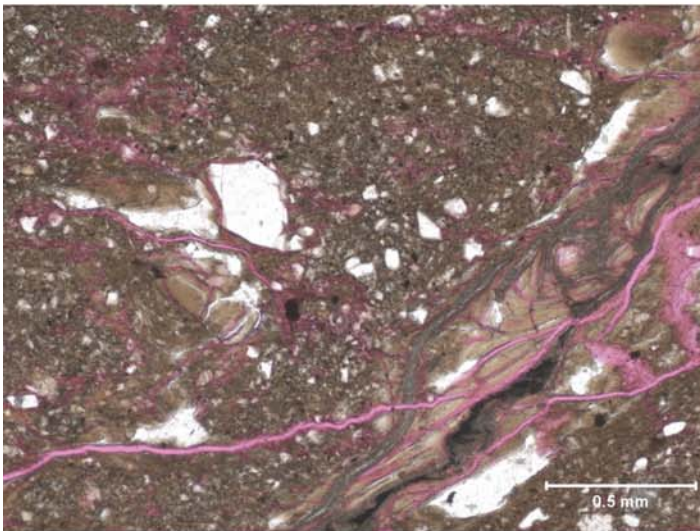
TS_2.jpg, CP-1, 2048.25 ft, TS. Clay minerals in the matrix form layers separated by fractures or wavy planes. A portion of the chlorite noted in XRD (12%) is present as detrital kernels (chl). Speckled, rounded grains (arrows) are chert and volcanic fragments; white clasts are quartz and feldspar. Black dots are authigenic pyrite. (Plane-polarized light. Scale bar = 200 microns)



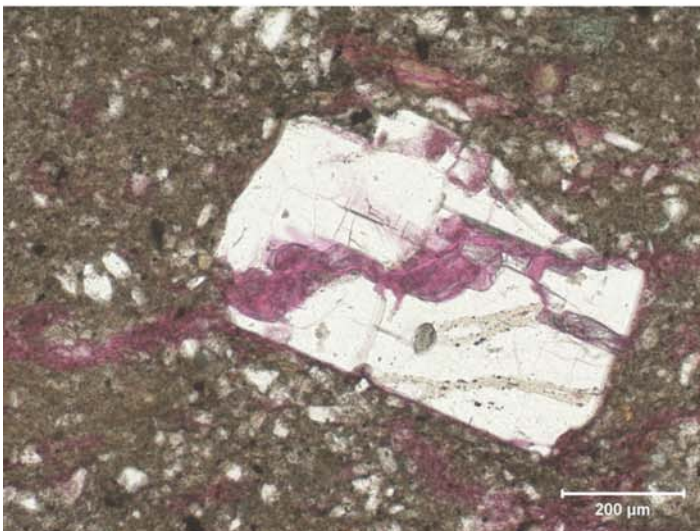
TS_3.jpg, CP-2, 2052.06 ft, TS. Sandy argillaceous mudstone with smectitic and chloritic matrix. The dark matrix color is due to the response of iron-rich smectite to dual carbonate stain, a reaction commonly noted in smectites. Poorly sorted grains from fine to upper medium sand size comprise plagioclase (p), volcanic quartz, fine-grained volcanic fragments (v), and chert (ch). (Plane-polarized light. Scale bar = 0.5 mm)



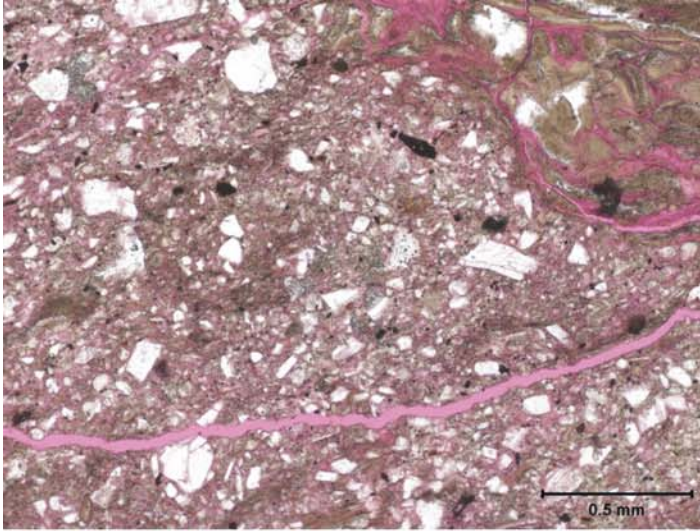
TS_4.jpg, CP-2, 2052.06 ft, TS. Crossed Nichols view of sandy argillaceous mudstone at higher magnification showing chert-replaced volcanic clasts (top right and center), and plagioclase grains (p). Lighter brown material is clay matrix. (Cross-polarized light. Scale bar = 100 microns)



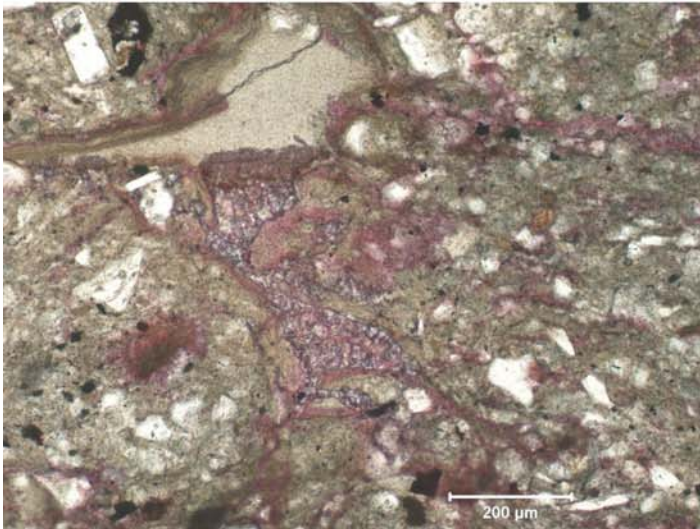
TS_5.jpg, CP-3, 2055.20 ft, TS. Mudstone composed of smectite and chlorite matrix. Poorly sorted detrital grains include medium sand to coarse silt sized material (mainly quartz and feldspar) dispersed in the matrix. The smooth, lighter brown streak at right is interpreted as illuvial clay material resulting as remobilized illite infiltrates soil along root channels and desiccation cracks. (Plane-polarized light. Scale bar = 0.5 mm)



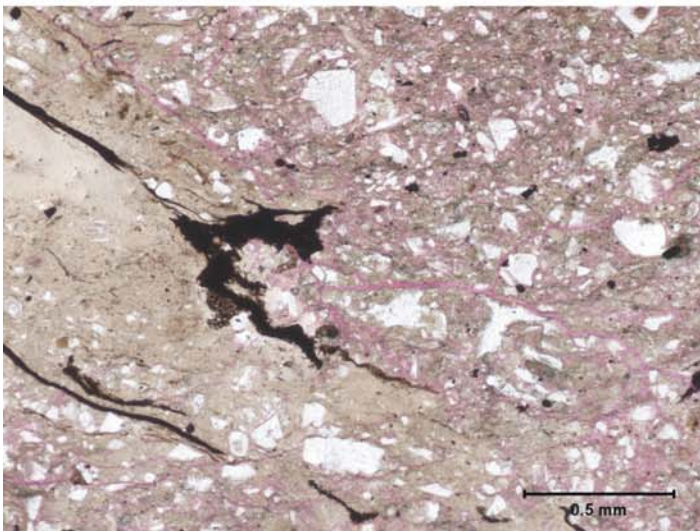
TS_6.jpg, CP-3, 2055.20 ft, TS. Feldspar grain fractured diagonally; clay along the fracture suggests movement late in the rock's history. (Plane-polarized light. Scale bar = 200 microns)



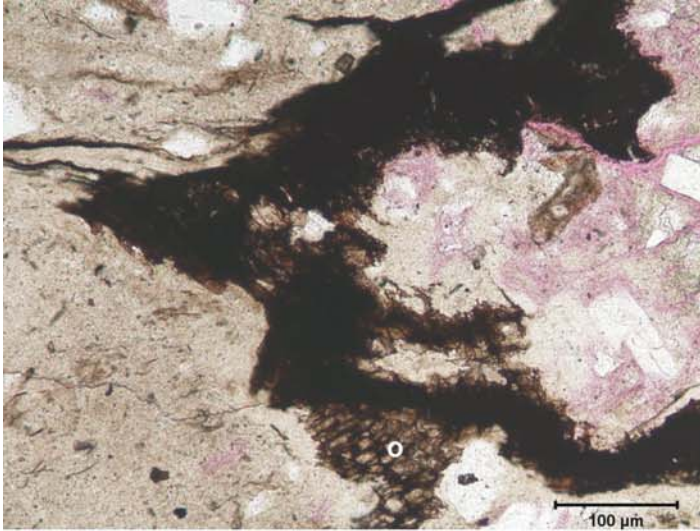
TS_7.jpg, CP-4, 2062.30 ft, TS. Sandy argillaceous mudstone, unstained portion of slide. Sharp feldspar and quartz, and rounded chert-replaced volcanic clasts are supported by a mixed smectitic matrix. Induced fractures are pervasive, as represented by the magenta lines (stained epoxy). The fabric exhibits blocky ped structure, especially when viewed under cross-polarized light, and the aligned, curved illite material at upper right is likely a result of illuviation. (Plane-polarized light. Scale bar = 0.5 microns)



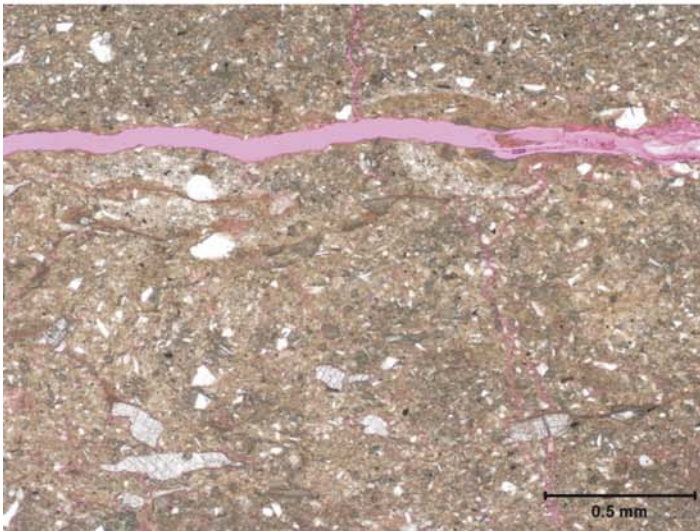
TS_8.jpg, CP-4, 2062.30 ft, TS. Detail of mudstone texture showing a fine-grained possible biotic clast at upper left, with associated authigenic ferroan calcite (center; stained purple with dual carbonate stain). Also note lath-shaped plagioclase crystal at upper left. The mottled, disorganized texture evident here is a typical pedogenic feature, along with disruption by roots. (Plane-polarized light. Scale bar = 200 microns)



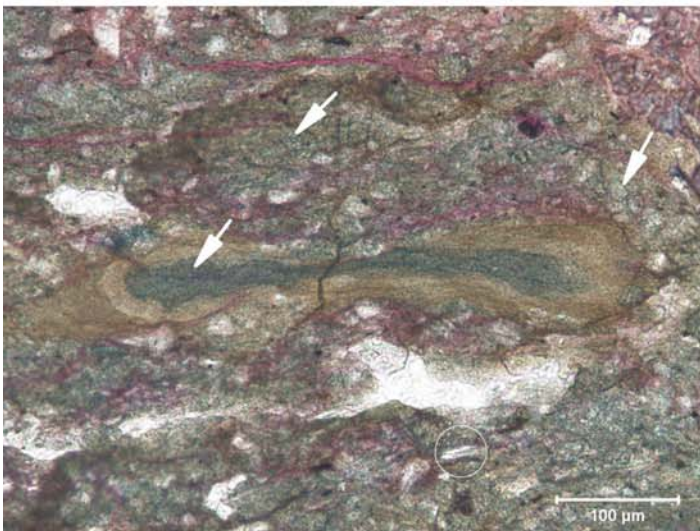
TS_9.jpg, CP-5, 2067.98 ft, TS. Sandy argillaceous mudstone displaying mottled and blocky ped structure, better visible under cross-polarized light. Dispersed coarse silt to medium sand grains are composed of quartz, feldspar, and subordinate lithic clasts. The tan streak at left cutting the image diagonally consists of well-aligned illite crystals (visible under crossed Nichols) and represents an illuviation layer associated with roots. The stringy black material is an organic remnant of these roots. (Plane-polarized light. Scale bar = 0.5 mm)



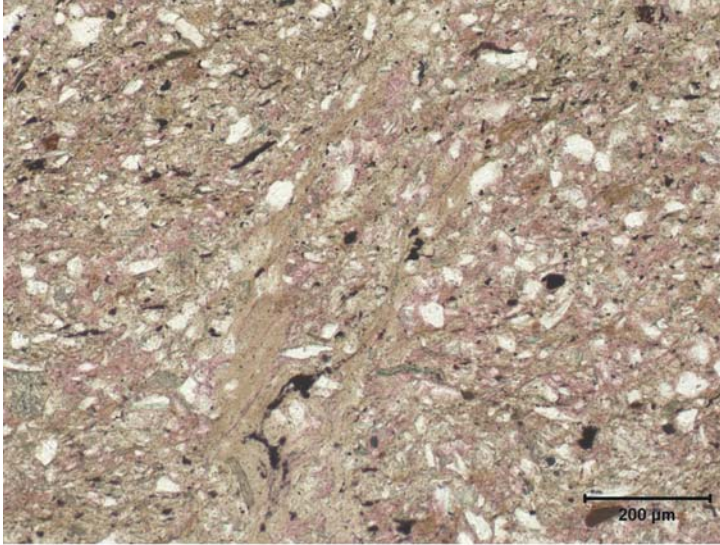
TS_10.jpg, CP-5, 2067.98 ft, TS. Detail of aligned illite and associated carbonaceous material shown in the previous image. The rectilinear, cellular morphology of the dark, carbonaceous particle (o) indicates plant tissues. Feldspars in this sample typically exhibit sharp grain shapes. Subtle pink areas in the clay matrix indicate epoxy-filled microporosity which may be due in part to dehydration of swelling clays. (Plane-polarized light. Scale bar = 100 microns)



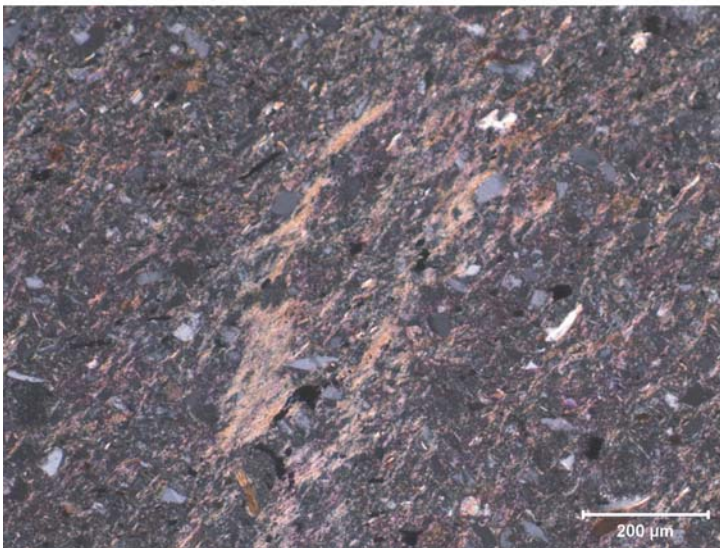
TS_11.jpg, CP-6, 2692.25 ft, TS. Argillaceous mudstone at lower magnification exhibits scattered silt and sand in a mixed clay matrix, with expandable I/S and chlorite as the predominant clay species (XRD). The crystals with cross-hatched cleavage in the lower part of the image are ferroan calcite (unstained). The horizontal fracture (magenta) is interpreted as an induced, stress-release or dehydration feature. (Plane-polarized light. Scale bar = 0.5 mm)



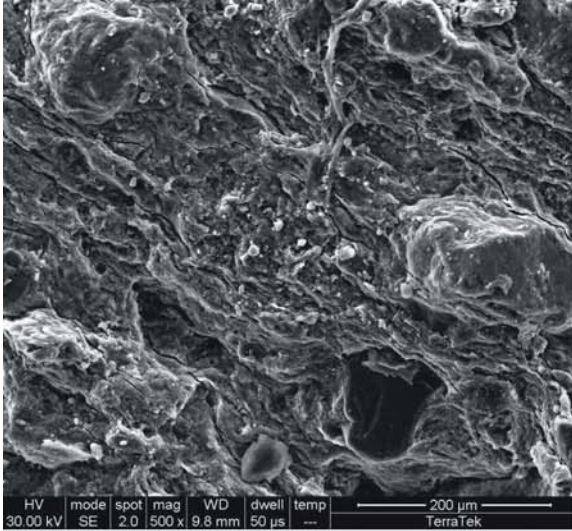
TS_12.jpg, CP-6, 2692.25 ft, TS. Detail showing chlorite in rounded and scallop-shaped clusters (arrows; pale green) and detrital kernels (circled). The tapered, flattened form at center, possibly representing a compacted biotic particle, root, or envelope around degraded organic material, contains minor replacive ferroan dolomite (stained blue), and an outer rind of illuviated clays. The clay matrix is stained blue in this high magnification view, reflecting ankerite and/or iron-rich expandable I/S. (Plane-polarized light. Scale bar = 100 microns)



TS_13.jpg, CP-7, 2697.15 ft, TS. Silty argillaceous mudstone, medium magnification, in the unstained part of the slide. The vertical clay feature at center is likely associated with root formation. The structure shows illuviation along this root cast, typical of soil layers. Clays are mainly I/S, illite and chlorite, with minor smectite and kaolinite. Pink areas reflect dyed epoxy in micropores, which are inferred to be induced dehydration features. (Plane-polarized light. Scale bar = 200 microns)



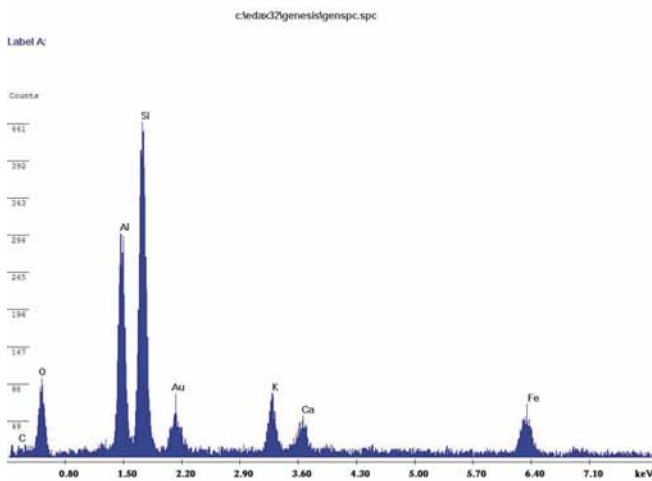
TS_14.jpg, CP-7, 2697.15 ft, TS. Same view as in the previous image except under cross-polarized light. Well-aligned illite streaks appear as brightly birefringent streaks around root casts. The black dots and wisps represent carbonaceous flakes and remnants of root material, and associated replacive pyrite. (Cross-polarized light. Scale bar = 200 microns)



SEM_1.jpg, CP-1, 2048.25 ft, SEM.
Sandy argillaceous mudstone, low magnification view. Mottled and disturbed clay-rich matrix hosts quartz and feldspar sand grains. Thin microfractures in the matrix are lined with illite, identified by spot EDX analysis. (Scale bar = 200 microns)



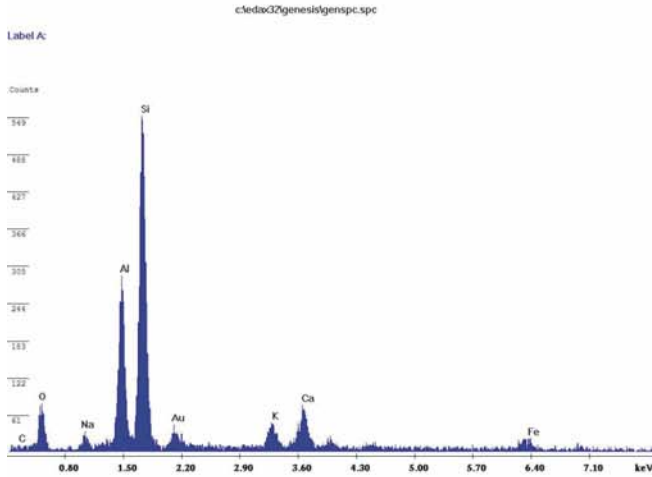
SEM_2.jpg, CP-1, 2048.25 ft, SEM.
Detail of microtexture emphasizing the network of illite-lined microfractures. Features visible in thin section are enlarged here. The clay flake visible as a ridge at top left (+) produces the EDX spectrum shown in the next image. (Scale bar = 50 microns)



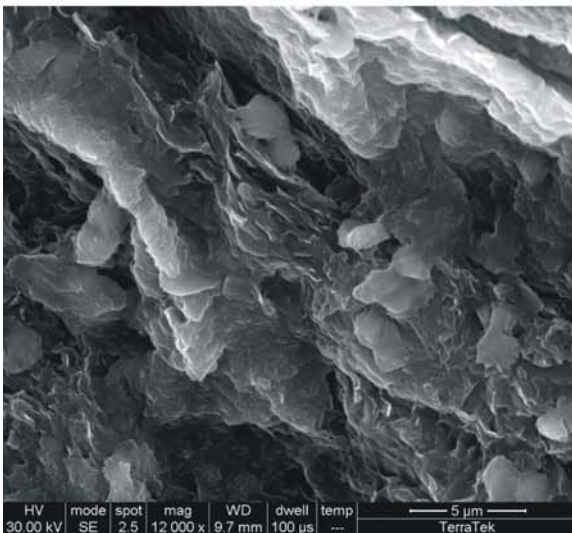
SEM_3.jpg, CP-1, 2048.25 ft, SEM.
Elemental spectrum for the clay flake in the previous image (+). Si, Al, O, K, and Fe are consistent with iron-rich smectite. Ca may reflect the swelling I/S portion of clays. The gold peak reflects sample coating.



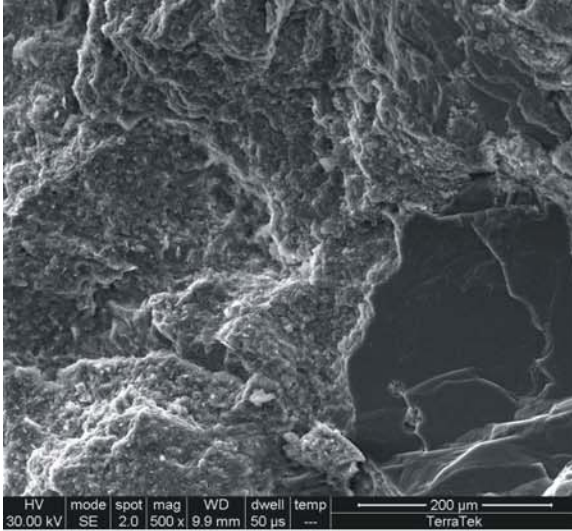
SEM_4.jpg, CP-1, 2048.25 ft, SEM.
 Detailed view of a possible root cast (center). The adjoining fracture features are lined with delicate illuviated clays identified by spot EDX as mixed layer illite-smectite or smectite. Spot EDX results for the clay ridge at bottom (+) are presented in the next image. (Scale bar = 20 microns)



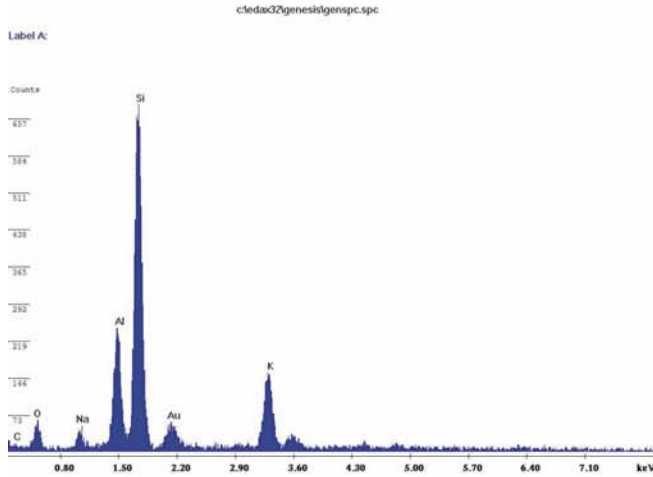
SEM_5.jpg, CP-1, 2048.25 ft, SEM.
 Elemental spectrum corresponding to the white ridge of clay at center bottom in the previous image (+). Si, Al, and O peaks are common to clays, whereas the array of cations (K, Fe, Na, and Ca) point to a smectitic or mixed composition.



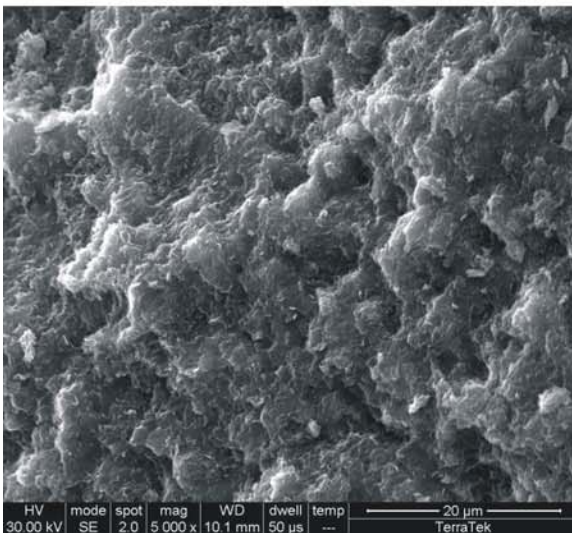
SEM_6.jpg, CP-1, 2048.25 ft, SEM.
 High magnification view of matrix highlighting expanded, porous texture of the clays. Flakey illite and web-like smectite expand and contract to leave induced fractures. Whole view EDX shows large Ca and Fe peaks, suggesting secondary ferroan calcite cement. (Scale bar = 10 microns)



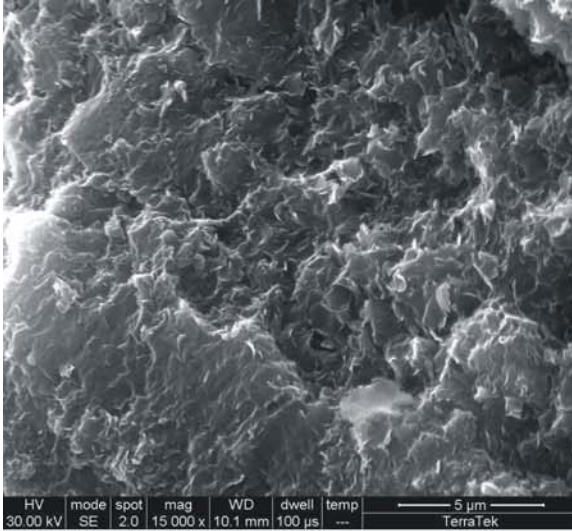
SEM_7.jpg, CP-2, 2052.06 ft, SEM.
Sandy argillaceous mudstone at low magnification. The sand grains are supported by disorganized clay matrix. Matrix clays form tiny clumps or granules. The dark grain at lower right has a feldspathic composition. (Scale bar = 200 microns)



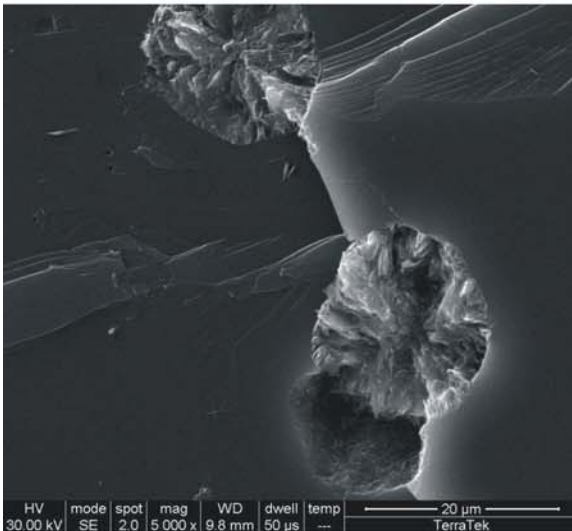
SEM_8.jpg, CP-2, 2052.06 ft, SEM.
The sand grain in the previous image produces this spot EDX spectrum. Dominant Si, O, and Al peaks, along with peaks for K and Na indicate an alkaline feldspar composition. The gold peak reflects sample coating.



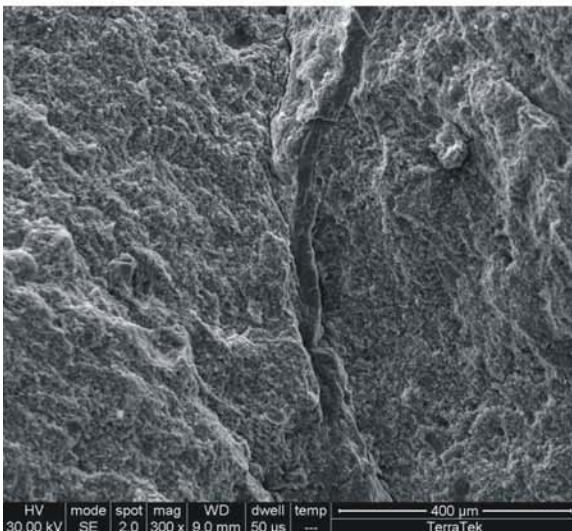
SEM_9.jpg, CP-2, 2052.06 ft, SEM.
Closer view of the mixed composition clay matrix. XRD analysis determines smectite as the dominant clay species, mixed with I/S and chlorite in approximately 2:1:1 ratio. A small amount of kaolinite is also found by XRD, although discretely not recognizable in SEM. No lamination is evident, and webby to granular clay microcrystals form masses. (Scale bar = 20 microns)



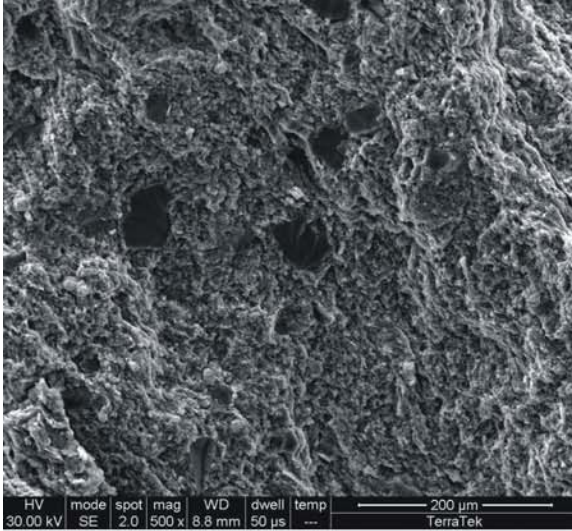
SEM_10.jpg, CP-2, 2052.06 ft, SEM.
 At high magnification the matrix is seen to be composed of tiny crenulated clay flakes a fraction of a micron in size. The crenulated morphology of flakes supports XRD determination of smectite or expandable I/S composition. (Scale bar = 5 microns)



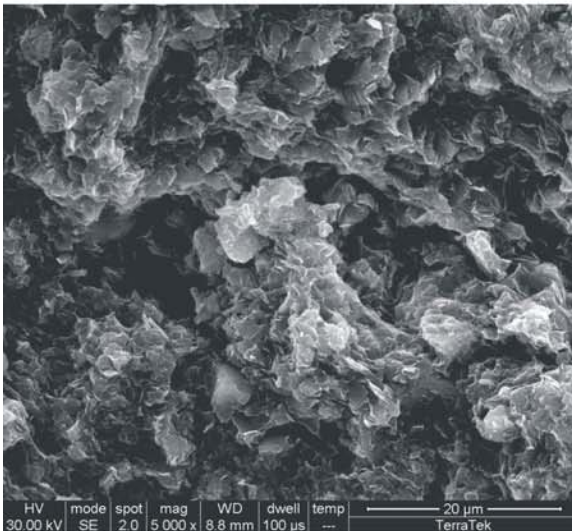
SEM_11.jpg, CP-2, 2048.25 ft, SEM.
 Enlarged view of the feldspar grain shown in SEM Image 7. Tiny round voids in the grain host radially arranged clay crystals; spot EDX shows an iron-rich chlorite composition. (Scale bar = 20 microns)



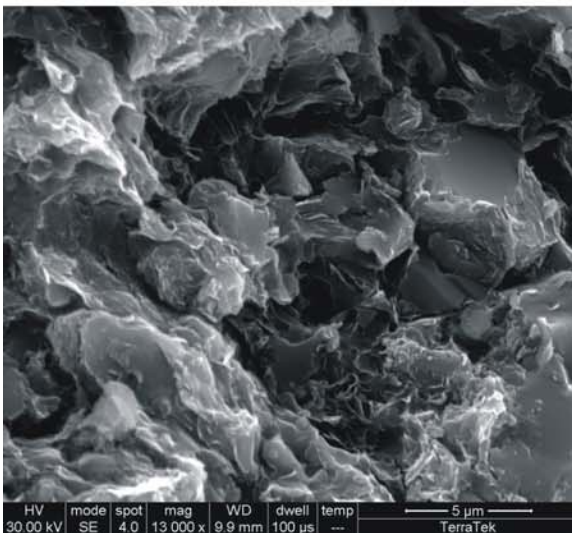
SEM_12.jpg, CP-3, 2055.20 ft, SEM.
 Overview of argillaceous mudstone showing a calcite-filled root cavity. Whole view EDX shows an elemental spectrum consistent with variable clay composition and calcite. Spot EDX on the central vertical feature reveals calcite. (Scale bar = 400 microns)



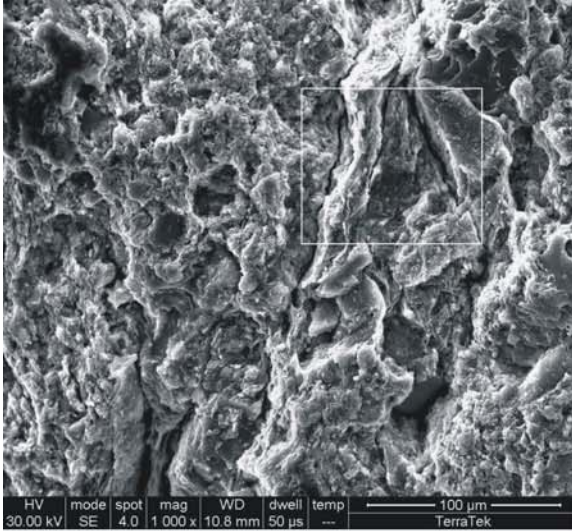
SEM_13.jpg, CP-3, 2055.20 ft, SEM.
 Similar overview in another, siltier portion of the sample. The disarranged, lumpy fabric is composed of granules or clumps of mainly expandable smectite (21% by weight smectite; XRD). (Scale bar = 200 microns)



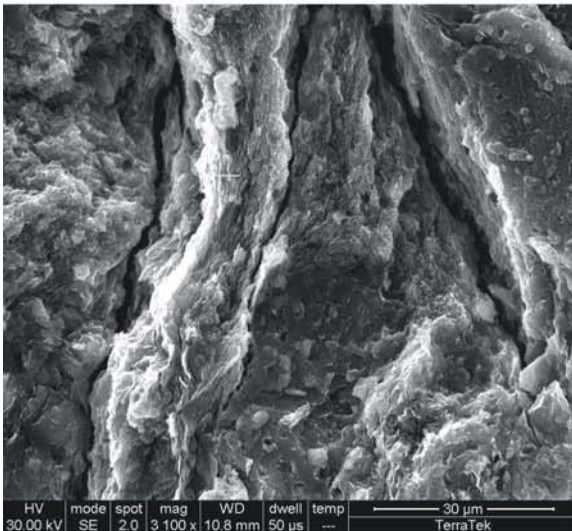
SEM_14.jpg, CP-3, 2055.20 ft, SEM.
 Clay granules in the previous image, when viewed at higher magnification, appear as cabbage-shapes and expanded ridges around induced pores, a texture typical of swelling clays. Spot EDX results for the light clump at center contains Si, Al, and O peaks accompanied by smaller Fe, K, Ca, and Mg peaks, consistent with expandable clays of variable composition. (Scale bar = 20 microns)



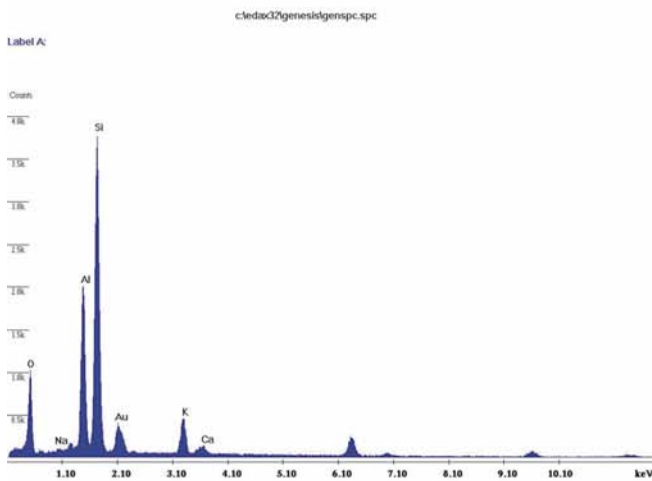
SEM_15.jpg, CP-3, 2055.20 ft, SEM.
 High magnification highlights clays with crenulated to webby flake morphology, most likely smectite. Clays adhere to admixed carbonaceous material as well as chlorite, and authigenic cement crystals. (Scale bar = 5 microns)



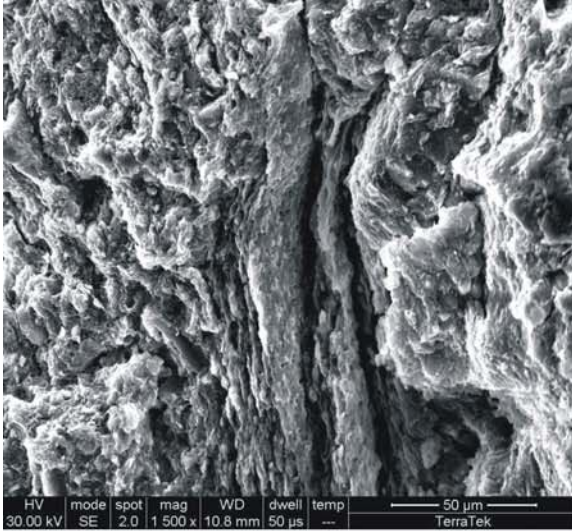
SEM_16.jpg, CP-4, 2062.30 ft, SEM. Medium magnification view of sandy argillaceous mudstone with poorly laminated and mottled, irregular texture (see slab images). Angular to subangular quartz and feldspar sand are scattered throughout the clay matrix, showing approximately vertical microfractures filled with illuvium (see TS Image 7). Spot EDX analysis identifies the dark grains at upper right and center right edge as alkaline feldspars. The boxed area is enlarged in the next image. (Scale bar = 100 microns)



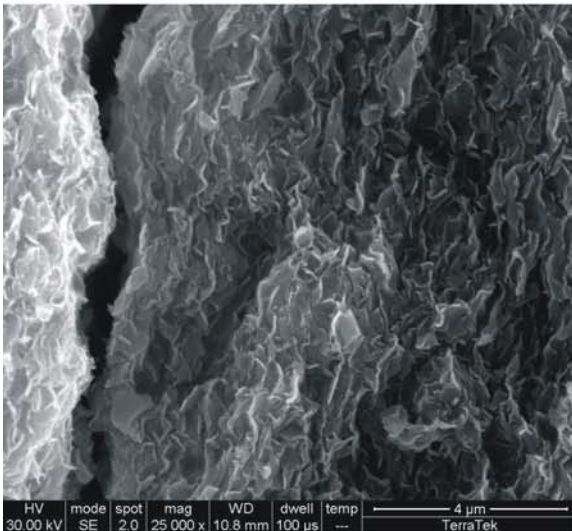
SEM_17.jpg, CP-4, 2062.30 ft, SEM. Closer view of illuviation envelope shown in the rectangle in the previous image. Clays exhibit web-like morphology, with flake stacks collapsed into thin ridges around inferred root material or cast. (Scale bar = 30 microns)



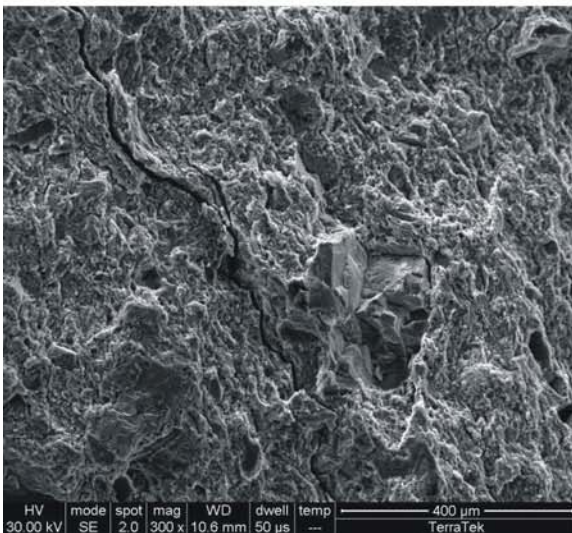
SEM_18.jpg, CP-4, 2062.30 ft, SEM. Elemental spectrum associated with the clay ridge in the previous image (+). Peaks for Si, Al, O are common to clays; diverse smaller peaks (K, Ca, Na, and unlabeled Fe at 6.2 keV) are indicative of mixed layer I/S and smectite.



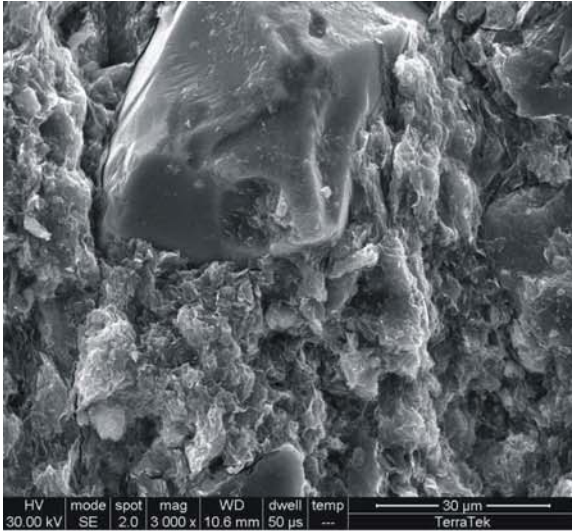
SEM_19.jpg, CP-4, 2062.30 ft, SEM.
 Detail of possible root cast or illuviation envelope. Note the vertical clay ridges with distinctly aligned crystals compared to disorganized surrounding clay aggregates. (Scale bar = 50 microns)



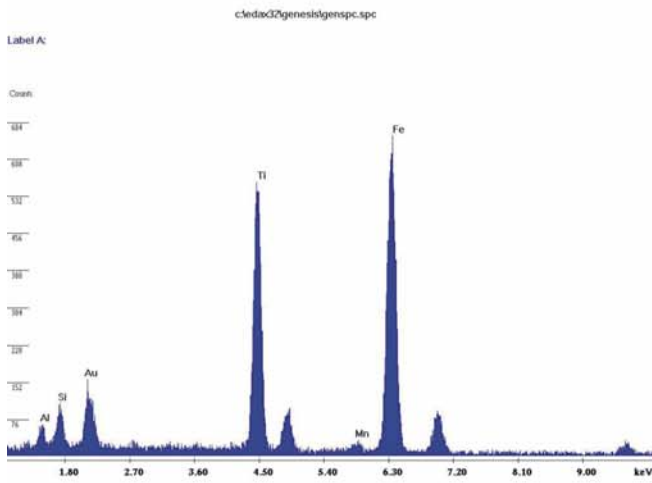
SEM_20.jpg, CP-4, 2062.30 ft, SEM.
 High magnification reveals collapsed networks of swelling clays from the previous image. The tiny flakes are arranged in parallel webs which expand when wet and collapse when dry. The fissure at the left of the screen is interpreted as a dehydration feature. (Scale bar = 4 microns)



SEM_21.jpg, CP-5, 2067.98 ft, SEM.
 Textural overview of sandy argillaceous mudstone exhibiting moderate clay orientation and wavy, parted lamination planes, diagonal in this image. Sand grains consisting of detrital quartz and feldspar are widely dispersed in the clay matrix. The diagonal fissure is an induced dehydration fracture. XRD finds 52% total clay by weight. Clays are predominantly expandable I/S and illite, with a lesser amount (8%) of smectite. (Scale bar = 400 microns)



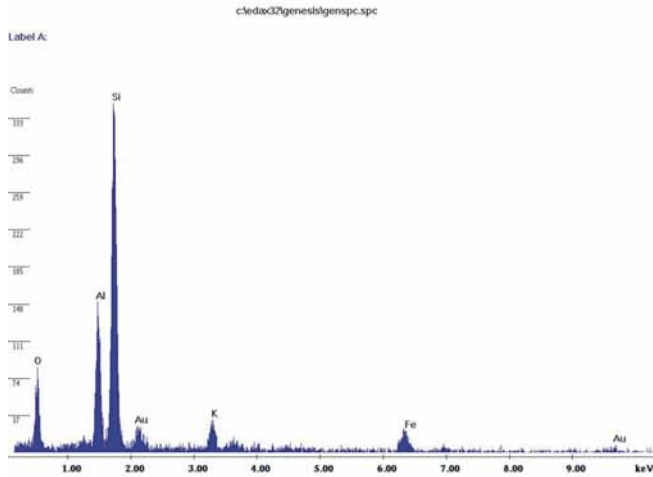
SEM_22.jpg, CP-5, 2067.98 ft, SEM.
 Detrital coarse silt-sized ilmenite grain with smooth, abraded edges indicating transport and recycling. The surrounding matrix is mixed expandable clays showing characteristic crumpled clump morphology. (Scale bar = 30 microns)



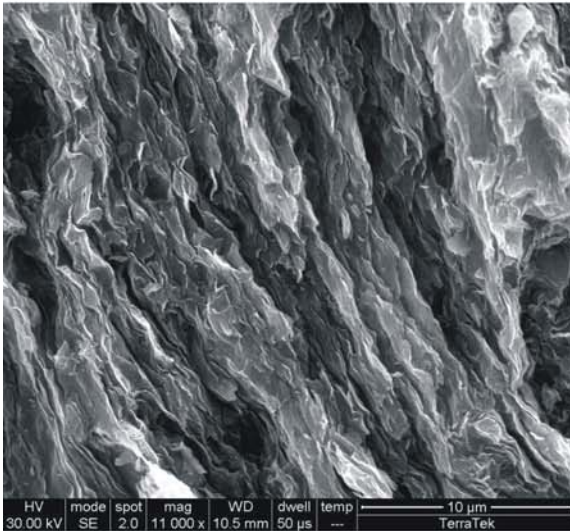
SEM_23.jpg, CP-5, 2067.98 ft, SEM.
 Spot EDX spectrum corresponding to the smooth grain in the previous image. Fe, Ti, and O peaks are characteristic of the iron oxide, ilmenite, a relatively common detrital accessory in sands.



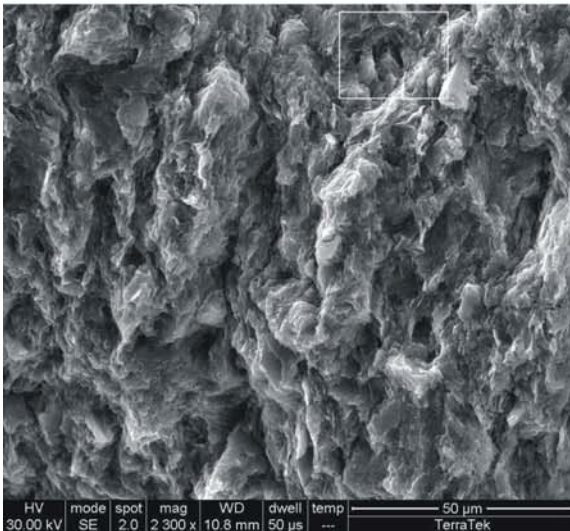
SEM_24.jpg, CP-5, 2067.98 ft, SEM.
 Enlarged view of a degraded plagioclase feldspar grain. Spot EDX shows an intermediate composition between albite and anorthite. The left side of the grain shows a reaction front with a skin of authigenic clay. (Scale bar = 20 microns)



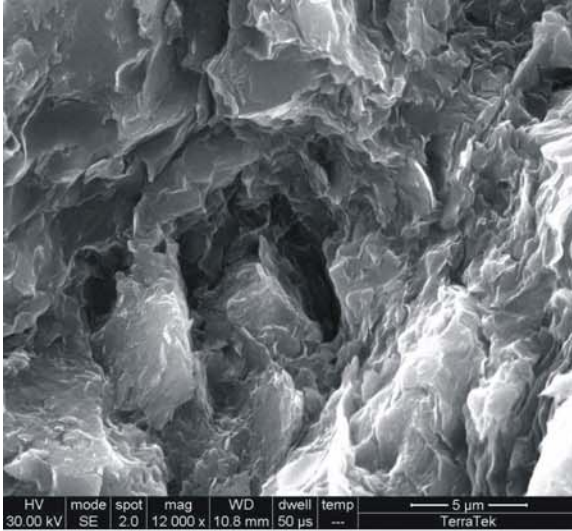
SEM_25.jpg, CP-5, 2067.98 ft, SEM.
Elemental spectrum corresponding to the wrinkly packet of clay flakes in the previous image (+). Si, Al, and O peaks with associated K, Fe, and minor Ca (unlabeled, approx 3.6 keV) denote an iron-rich mixed clay composition. Gold reflects sample coating.



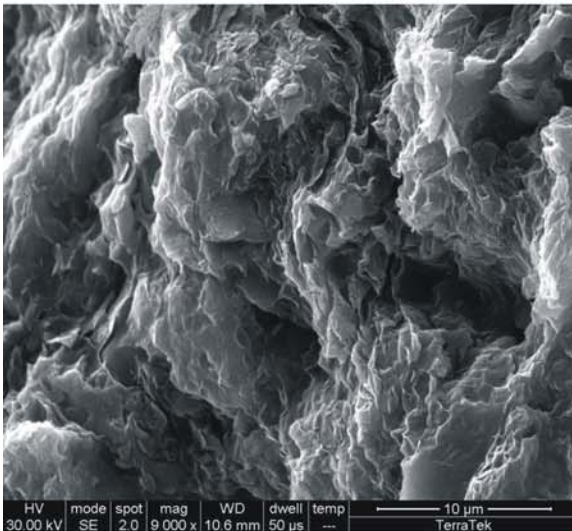
SEM_26.jpg, CP-5, 2067.98 ft, SEM.
High magnification detail of well-aligned clays in an illuviation envelope. According to whole view EDX results for the area in the image, the clay composition is a mixture, with the dominant peaks for Fe, K, and Ca in addition to the Si, Al, and O peaks common to clay minerals. (Scale bar = 10 microns)



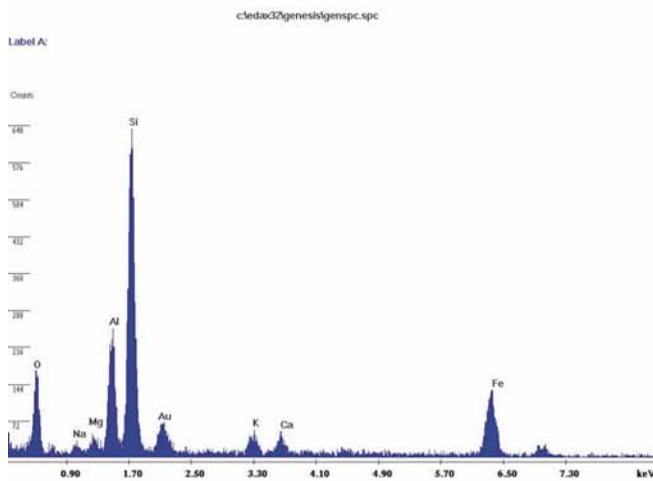
SEM_27.jpg, CP-6, 2692.25 ft, SEM.
Argillaceous mudstone displaying moderate lamination, near vertical in this image. Scattered silt and sand are supported in a lumpy, clay-rich matrix. Some of the pores may be real in this sample, as illustrated in the next image, an enlargement of the boxed area at upper right. (Scale bar = 50 microns)



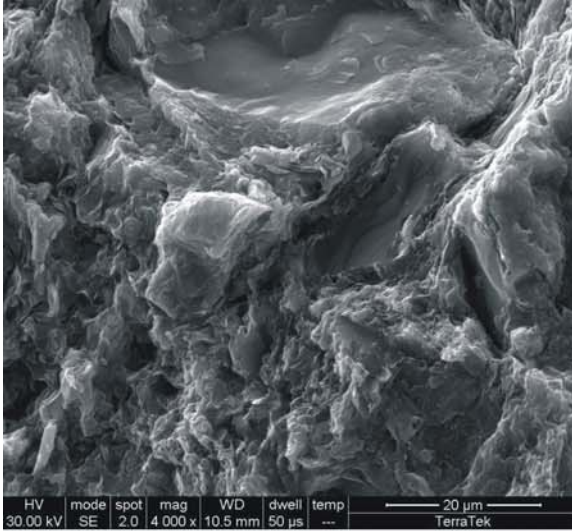
SEM_28.jpg, CP-6, 2692.25 ft, SEM.
Detail of a possible natural pore, center of the image. The irregular, elongate shape and baffled interior suggest a possible root cast. Mixed clays form clumps around the pore. (Scale bar = 5 microns)



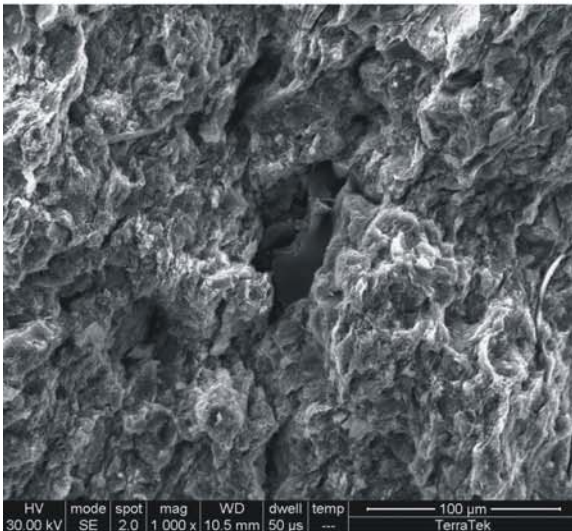
SEM_29.jpg, CP-6, 2692.25 ft, SEM.
Medium magnification view of argillaceous mudstone highlighting webby expandable clay aggregates. The dark pores 5-10 microns across may represent fluid pathways or voids associated with oxidized carbonaceous material. Larger elongate ridges are interpreted as artifacts of swelling clay response to hydration and dehydration. Thin section and core photo evidence suggests features of a paleosol. Whole view EDX results are shown in the next image. (Scale bar = 10 microns)



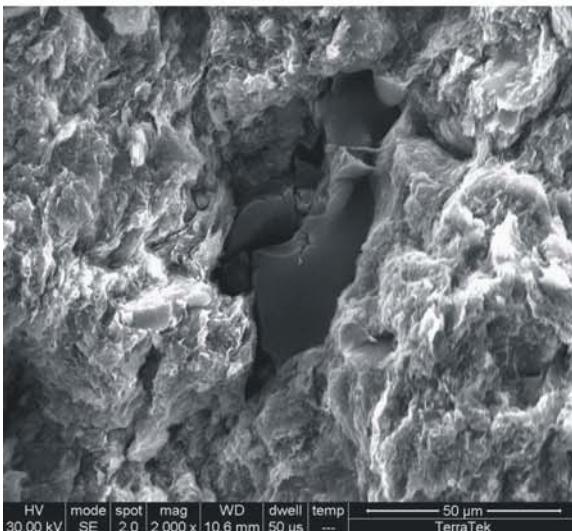
SEM_30.jpg, CP-6, 2692.25 ft, SEM.
Whole view EDX spectrum for the area in the previous image. Peaks for Si, Al, O and a smaller array including Fe > K = Ca = Mg > Na support the mixed suite of mixed layer I/S, chlorite, kaolinite, and smectite determined by XRD analysis.



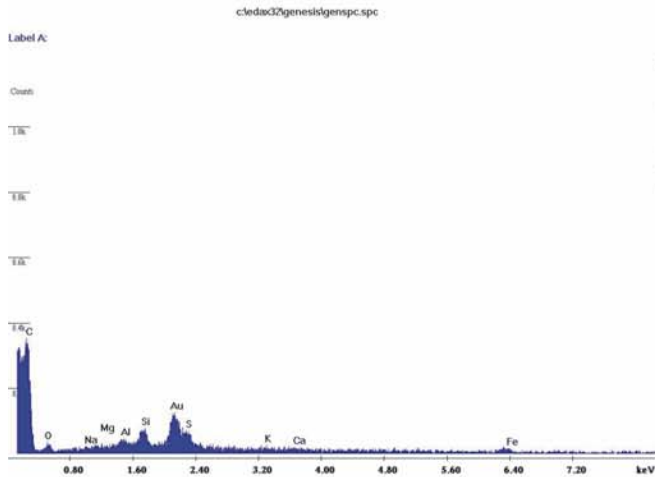
SEM_31.jpg, CP-6, 2692.25 ft, SEM.
 Medium magnification view showing compaction textures and ped-like structures in clay aggregates. Clumps are bounded by seams or surfaces sometimes hosting disc-shaped or flattened pores. (Scale bar = 20 microns)



SEM_32.jpg, CP-7, 2697.15 ft, SEM.
 Overview of silty argillaceous mudstone with moderate lamination, near vertical in this image. Scattered silt and sand are supported by a mixture of expandable and non-expandable clays. Crenulated clays are arranged in ridges separated by induced/natural parting surfaces. At center, a carbonaceous particle is visible along one such parting. (Scale bar = 100 microns)



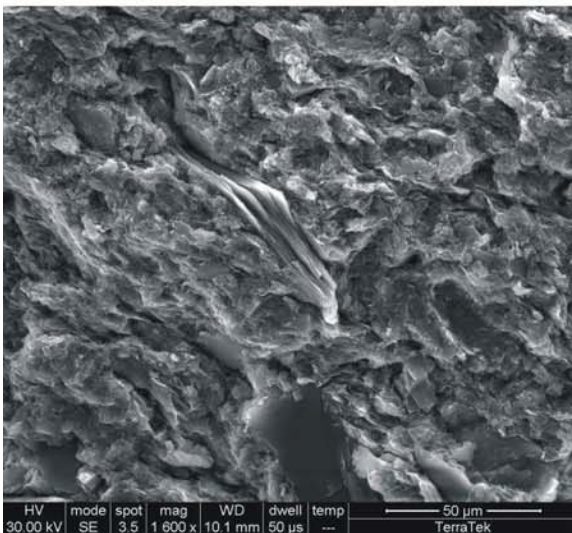
SEM_33.jpg, CP-7, 2697.15 ft, SEM.
 Enlarged view of the particle in the previous image. Note the smooth surface and slightly degraded edges of the particle. (Scale bar = 50 microns)



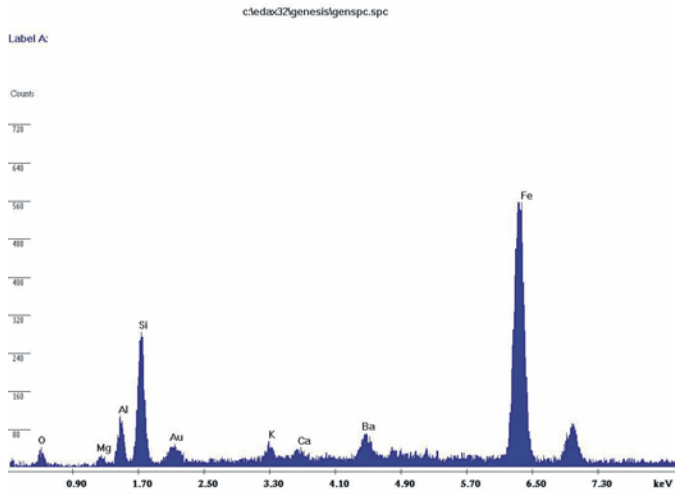
SEM_34.jpg, CP-7, 2697.15 ft, SEM.
 Spot EDX spectrum produced by the particle in the previous image. Overall low EDX response, and a spectrum dominated by a large C peak and gold (sample coating) characterize the spectra of organic particles and residue.



SEM_35.jpg, CP-7, 2697.15 ft, SEM.
 A probable detrital chlorite flake at center is surrounded by compacted, crenulated clays including illite, I/S, and kaolinite. Spot EDX results show prominent peaks for Fe and Mg, in addition to Si, Al, and O. (Scale bar = 20 microns)



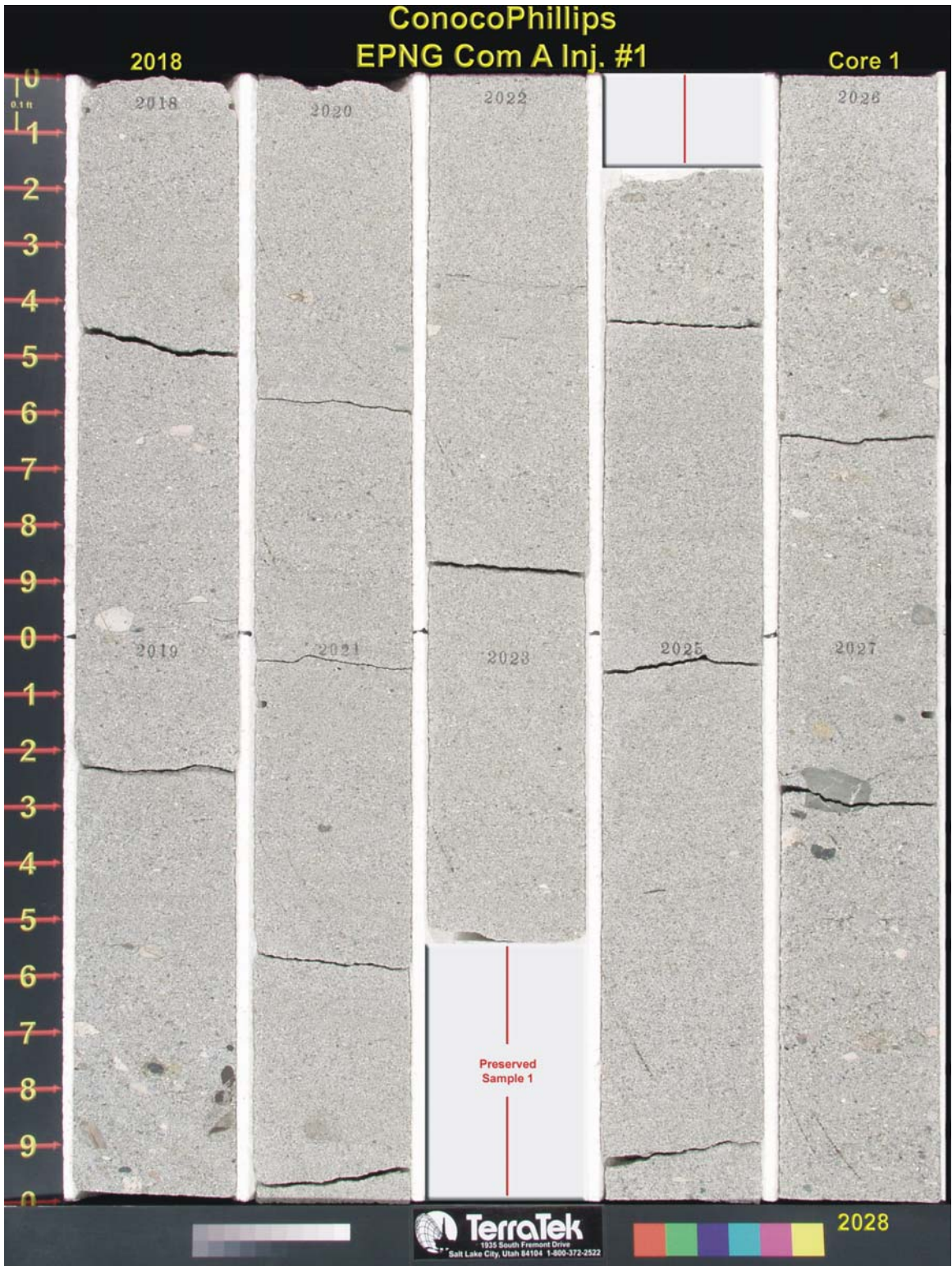
SEM_36.jpg, CP-7, 2697.15 ft, SEM.
 Medium magnification view showing wavy clay packets and slightly granular texture. The flake at center is biotite; the dark grain at the bottom of the image is potassium feldspar. (Scale bar = 50 microns)



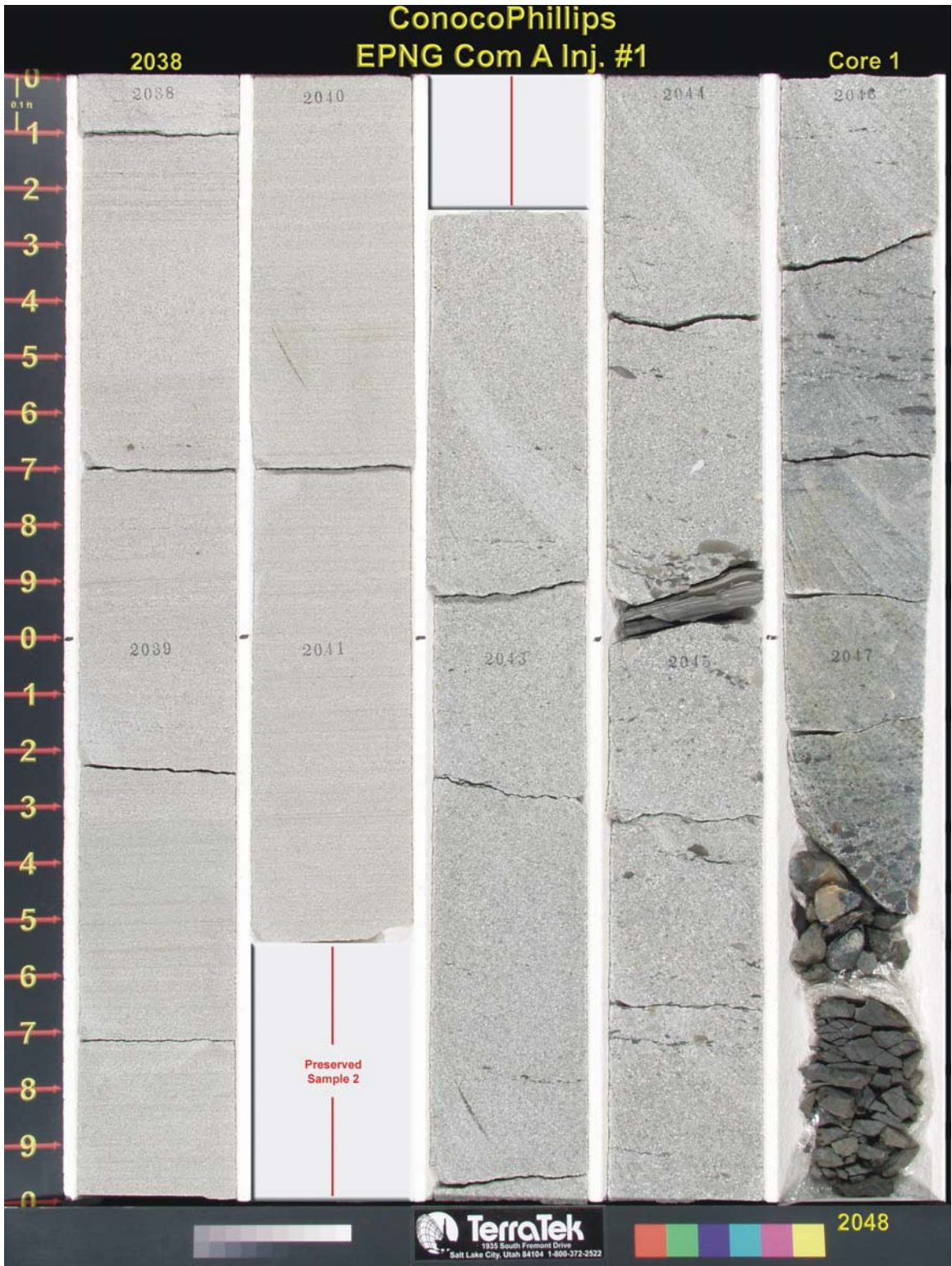
SEM_37.jpg, CP-7, 2697.15 ft, SEM.
Spot EDX results for the flake in the previous image. The iron peak, accompanied by Si, Al, and O peaks, in combination with the rigid layered morphology indicate the mica biotite. A portion of the chlorite recognized by XRD analysis is likely degraded detrital biotite.

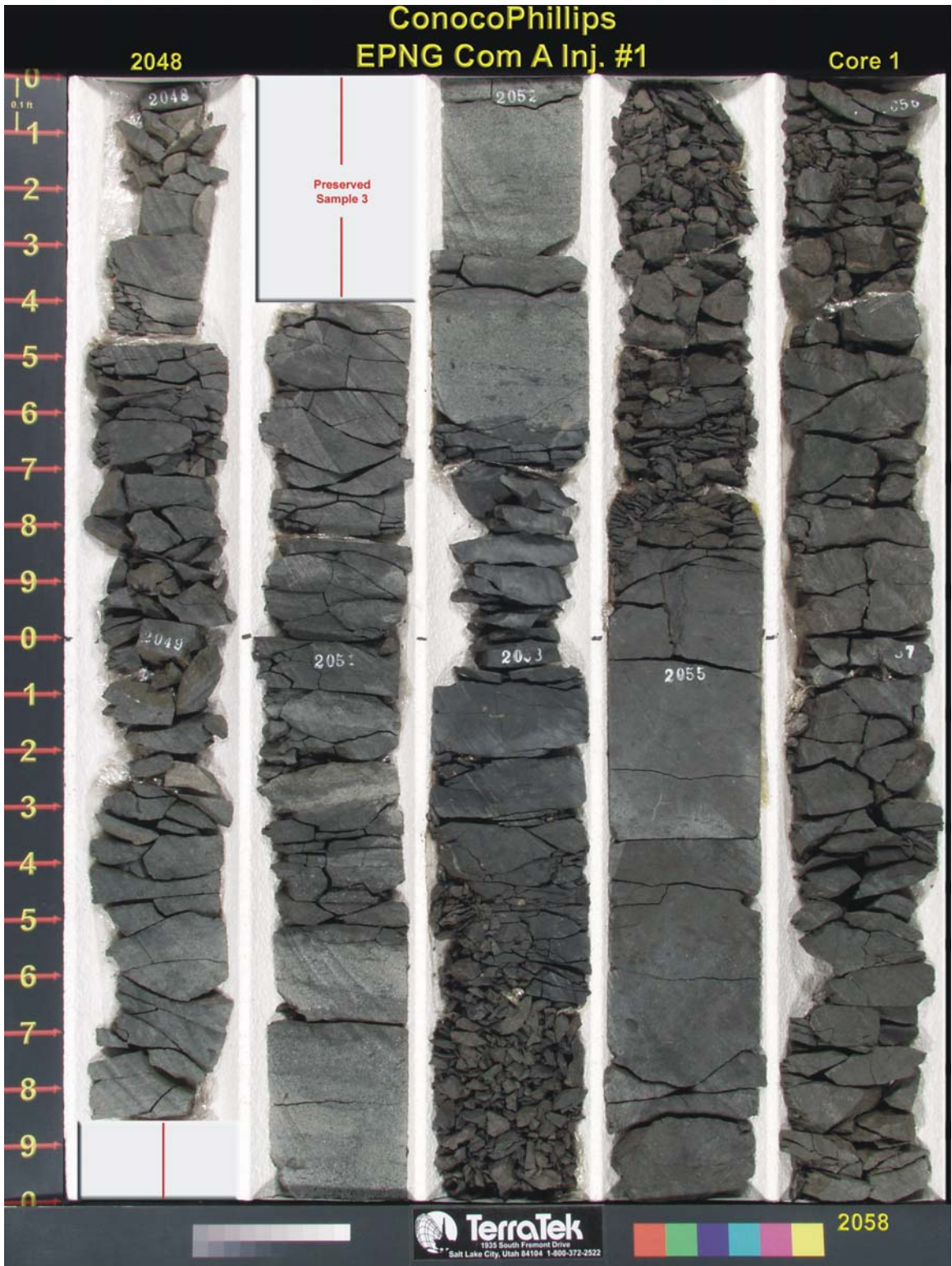
B.2.3 Photo Log of Slabbed Core

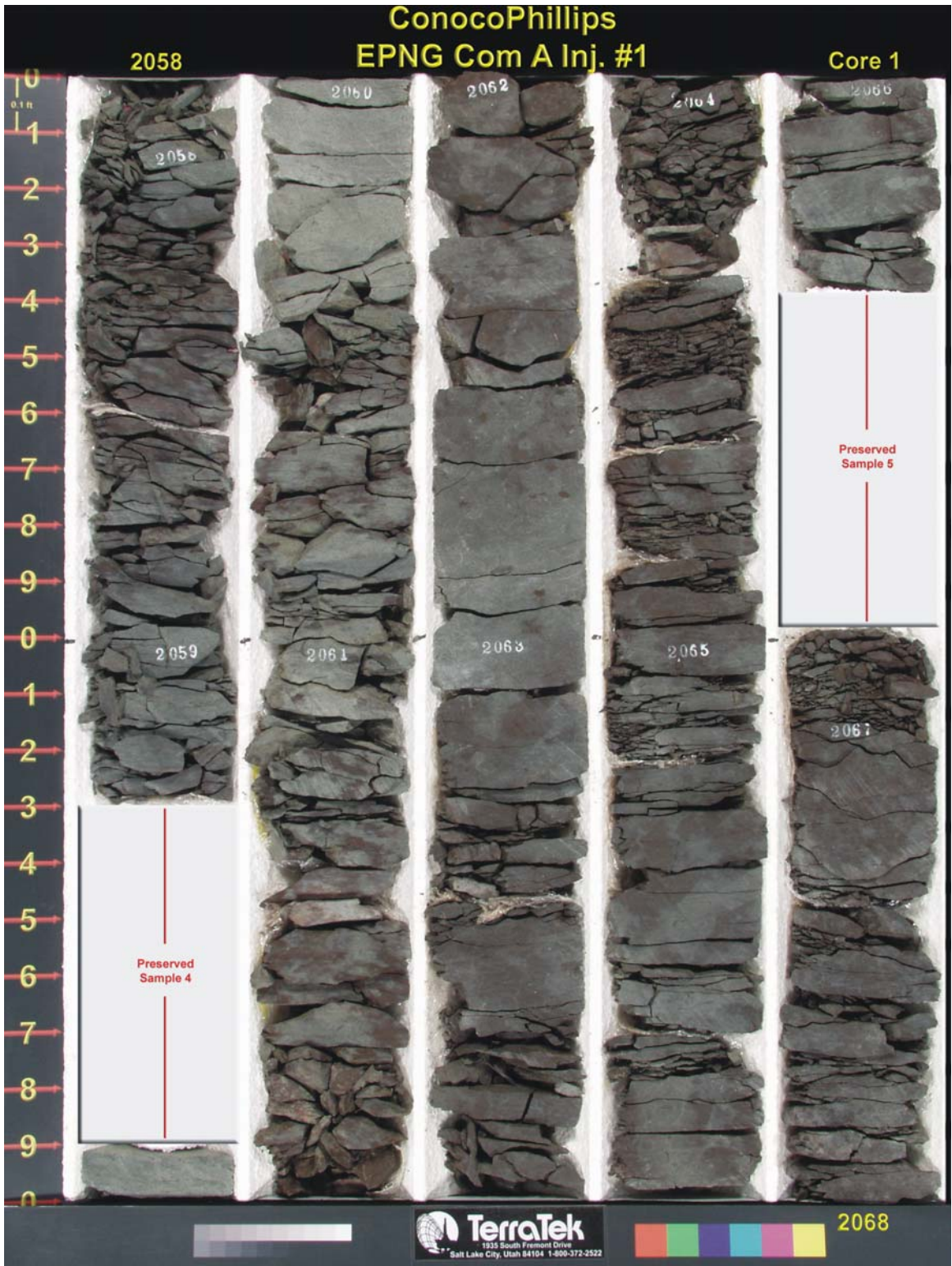
After the core was pieced together, preliminary reviewed, and samples chosen and preserved against drying, the core was slabbed and photographed by TerraTek. Slabbing damaged the mudstone sections of the core by inducing fractures.



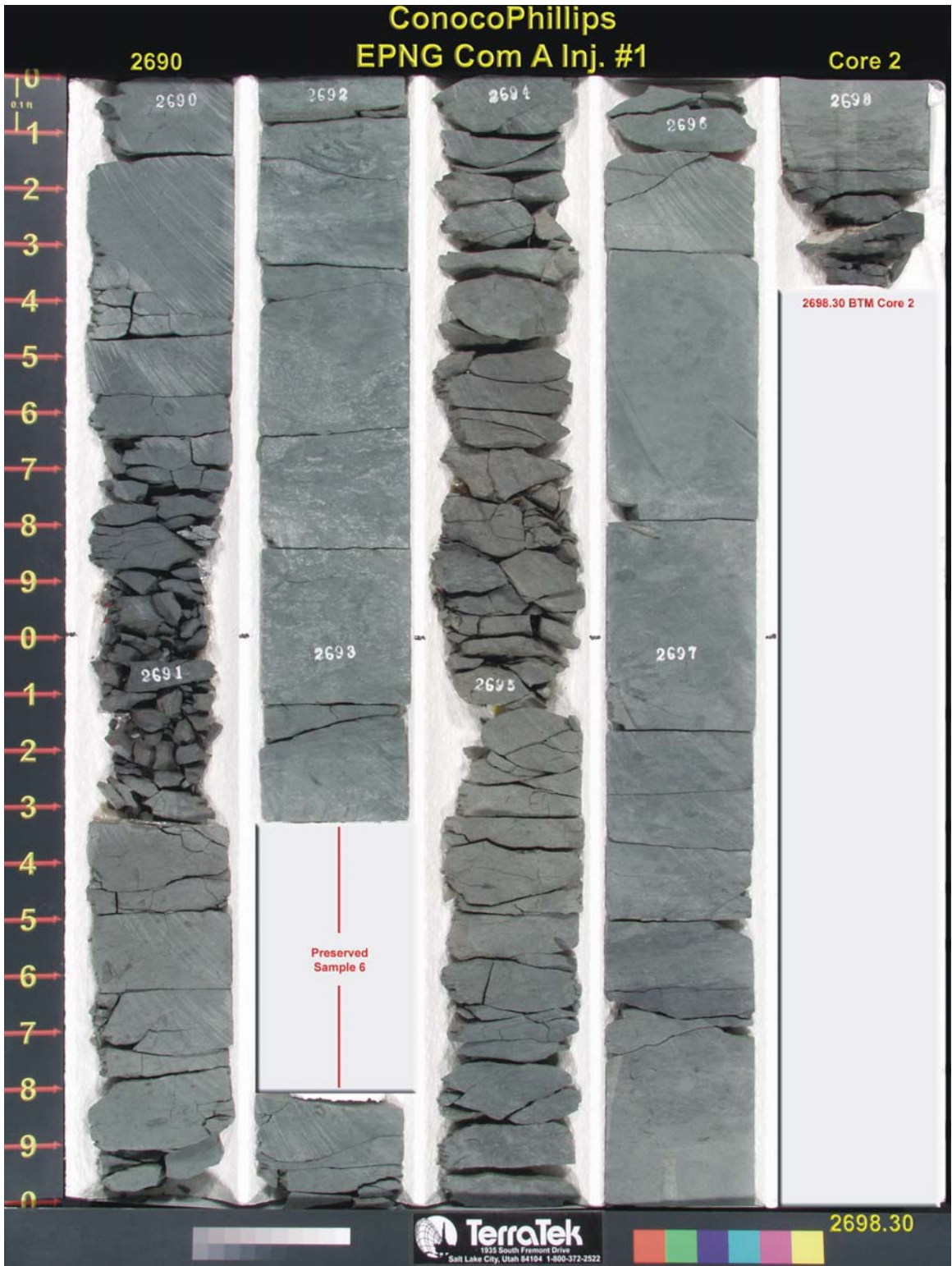












B.2.4 Gas Breakthrough Experiment Data

TerraTek performed gas breakthrough pressure measurements on core plugs following guidance from Jason Heath, Brian McPherson, and Thomas Dewers, as described in the following memo of Appendix B.2.4.1. The results of the measurements are given in Appendix B.2.4.2.

B.2.4.1 Instructions to TerraTek for Gas Breakthrough Pressure Measurements

Memo

To: John Keller, TerraTek

From: Jason Heath, Sandia National Laboratories

Date: July 29, 2009

Re: Recommendations for Gas breakthrough Testing

This memo provides information for the performance of gas breakthrough experiments on preserved core from the Kirtland Formation. Similarly to previous work on Kirtland core, the invoice for these tests should be sent to ConocoPhillips. The total remaining funds for the budget with ConocoPhillips is \$1896.20. If additional funds are needed for the new tests, please let me know so we could discuss a possible contract with Sandia.

Sample Descriptions

1. Three “seal peel” samples were sent to TerraTek in the Spring, samples 2A, 3A, and 6A from depths 2042.25-2043.25 ft, 2049.00-2049.89, and 2692.30-2693.30 ft, respectively. Sample 6A is the most valuable since it is from the deeper section of core in the lower Kirtland. Sample 3A is from the upper Kirtland, and 2A is from the Ojo Alamo.

I recommend using 3A first for the gas breakthrough tests to evaluate procedures before using sample 6A. Sample 2A will not be tested at this time.

Two Sets of Tests Based on Saturation

2. Based on analyses of fresh core, the preserved Kirtland Formation core is not fully saturated with groundwater. Thus, I recommend that two sets of tests be performed. The first should be on preserved samples of core and should not include any further saturation with brine. The second set should be on samples that are fully saturated with brine (information on brine salinity will be given below). At least one measurement at initial conditions of “in situ” saturation and one measurement at the fully saturated conditions are desired. More measurements would be desirable to determine the precision of the experimental methods, but we leave that to you since the budget is limited.
3. Li et al. (2005; page 328) provides guidance for saturating samples.

Sample Evaluation to Avoid Induced Fractures

4. The effect of induced micro-fractures on the pore structure is a major concern. If costs are not prohibitive, I recommend taking X-ray CT images of the samples prior to removing them from the preservation material. Such imaging could help avoid taking plugs at locations of induced fractures. Please let me know if “healed” natural fractures are found.
5. I recommend measurements of absolute permeability prior to the brine-saturated gas breakthrough tests. The measurement of permeability should be in the range of 10^{-8} to 10^{-9} d to correspond with previous measurements made in the summer 2008. For the first set of tests without saturating the samples, permeability measurements after the tests could be performed to check for the possible effects of fractures – again, if costs are not prohibitive.

Drilling of Plugs

6. Since the samples contain abundant swelling clays, I advise caution in drilling plugs. As the plugs are drilled, please take notes on the methods used, which could include drilling with or without fluid and whether the fluid was aqueous or non-aqueous.
7. Vertical plugs are requested for evaluation of vertical transport properties of the samples.
8. I will not recommend an exact diameter and length for the plugs. Please use what seems best for the size of the flow cells and for optimizing the quality of the results while minimizing the time of the tests. Previous studies by Hildenbrand (2004) used plugs 28.5 mm in diameter by 30 mm in length. Perhaps ~1 inch diameter plus by slightly less than 1 inch long would be suitable for the tests.

Additional Small Plugs for Poro-Technology/MICP

9. When taking plugs, please core such that a portion of rock, taken as a plug at the same location of the plugs for the breakthrough tests, could be sent off for mercury injection capillary pressure measurements (MICP). Thus, a small disc with dimensions up to approximately 0.85 inch long by 0.90 inch diameter. The drill bit used previously to core the Gothic Shale samples from the UGS worked well for the diameter of Poro-Technology’s MICP penetrometer cup, which could possibly be used again for these experiments. Thus, MICP data could be compared to the breakthrough results for approximately the same depth and lithology.
10. These additional samples should be shipped to:
Jason Heath
Sandia National Laboratories
1515 Eubank SE
Bldg 823 Rm 2241 Org 6314
Albuquerque, NM 87123-0750

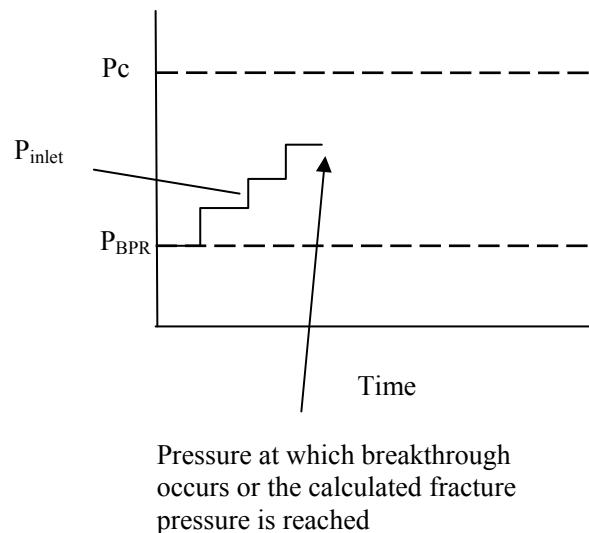
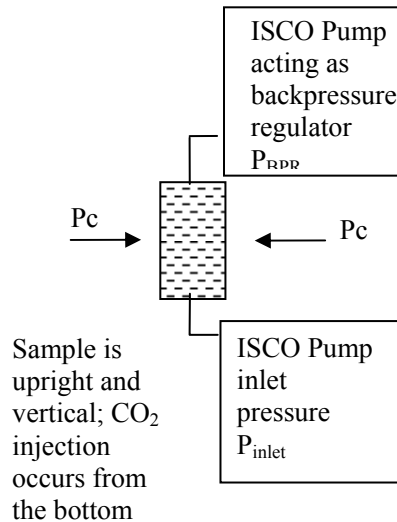
Hydrostatic Flow Vessel and P&T Conditions

11. During the gas breakthrough pressure test, the sample and vessel should be oriented vertically to simulate the vertical transport of CO₂ through the Kirtland.
12. We want the initial stress conditions of the test to be similar to the field conditions. The confining pressure will be based on estimated *in situ* field conditions, which will be different for samples 3A and 6A – the confining pressure will correspond to stress condition at the depths of the two samples. These estimates are based on the “rule-of-thumb” lithostatic pressure gradient of 25 MPa/km and a hydrostatic gradient of 10 MPa/km.

The initial confining, pore, and effective ($P_e = P_c - P_f$) pressures and temperatures for samples 3A and 6A should be as follows in the table below. The pressure and temperature conditions will result in gaseous and supercritical CO₂ for the two samples – both sets of conditions are very near to the critical point of CO₂. The critical point is 31.1°C and 7.38 MPa. Thus, for sample 3A, the CO₂ should be a vapor with a density of ~ 184 kg/m³. The CO₂ density for the initial conditions of sample 6A should be ~ 383 kg/m³.

Sample	Depth (ft)	Confining Pressure (MPa)	Confining Pressure (psi)	Pore Pressure (MPa)	Pore Pressure (psi)	Effective Pressure (MPa)	Effective Pressure (psi)	Temp (°C)
3A	2049.5	15.6	2265.0	6.2	906.0	9.4	1359.0	30
6A	2692.8	20.5	2976.0	8.2	1190.4	12.3	1785.6	37

13. The general setup is given below. The inlet pressure should vary from the initial back pressure regulator (BRP; or ISCO pump) value up to some fraction of the confining pressure (see below) – for these tests, go up to 0.5 times the confining pressure.



14. The brine used in the ISCO pumps should have a salinity of approximately 16,000 mg/L NaCl solution. This salinity/ionic strength should avoid shrinkage or swelling of the clays.
15. To check if the NaCl solution results in significant cation exchange, I recommend doing an XRD test on the samples (or simply review the results from Mary Milner's previous work on the Kirtland core). I then recommend soaking a ground-up sample in the brine solution and then comparing the peaks of the XRD data to see if basal spacing changed.
16. The time for each pressure step should be related to monitoring fluid movement from the sample at the outlet. Once fluid has halted moving for at least 2 hours, proceed to increase the pressure step.
17. Each pressure step should be 0.5 to 1 MPa.
18. The following website has a convenient calculator for determining CO₂ densities at various P&T conditions: <http://sequestration.mit.edu/tools/index.html>
19. If breakthrough is not reached for the P_c and P_{BPR} conditions, then these parameters could be adjusted to higher values while keeping P_c minus P_{BPR} constant. The test could then be continued with higher pore pressure values without major damage to the pore structure.

Please contact me with any questions. These instructions are recommendations – please implement the test as seems best suited to the quality of the samples, the apparatus available, and the cost.

Thanks!

Jason

Office: 505-845-1375

Cell: 801-815-5209

References

- Hildenbrand, A., Schlomer, S., Krooss, B.M., and Littke, R., 2004, Gas breakthrough experiments on pelitic rocks: comparative study with N₂, CO₂ and CH₄: *Geofluids*, v. 4, p. 61-80.
- Li, S., Dong, M., Li, Z., Huang, S., Qing, H., and Nickel, E., 2005, Gas breakthrough pressure for hydrocarbon reservoir seal rocks: implications for the security of long-term CO₂ storage in the Weyburn field: *Geofluids*, v. 5, p. 326-334.

B.2.4.2 Description of Gas Breakthrough Pressure Measurement Data

A “seal peel” sample from the upper Kirtland, from the depth interval 2049.00 to 2049.89 ft, was opened and cored for the breakthrough pressure measurement. The first test was performed at the water and gas saturations of the preserved plug. Thus, the test was run without fully saturating the plug with brine (Figure B.2.4.2.1). The second test included full brine saturation (Figure B.2.4.2.2). Breakthrough was only seen for the first test. The second test reached the maximum pressure allowable for the experimental system (Figure B.2.4.2.2). The lower Kirtland gas breakthrough test did not achieve breakthrough before the end of the test for a brine saturated sample (Figure B.2.4.2.3).

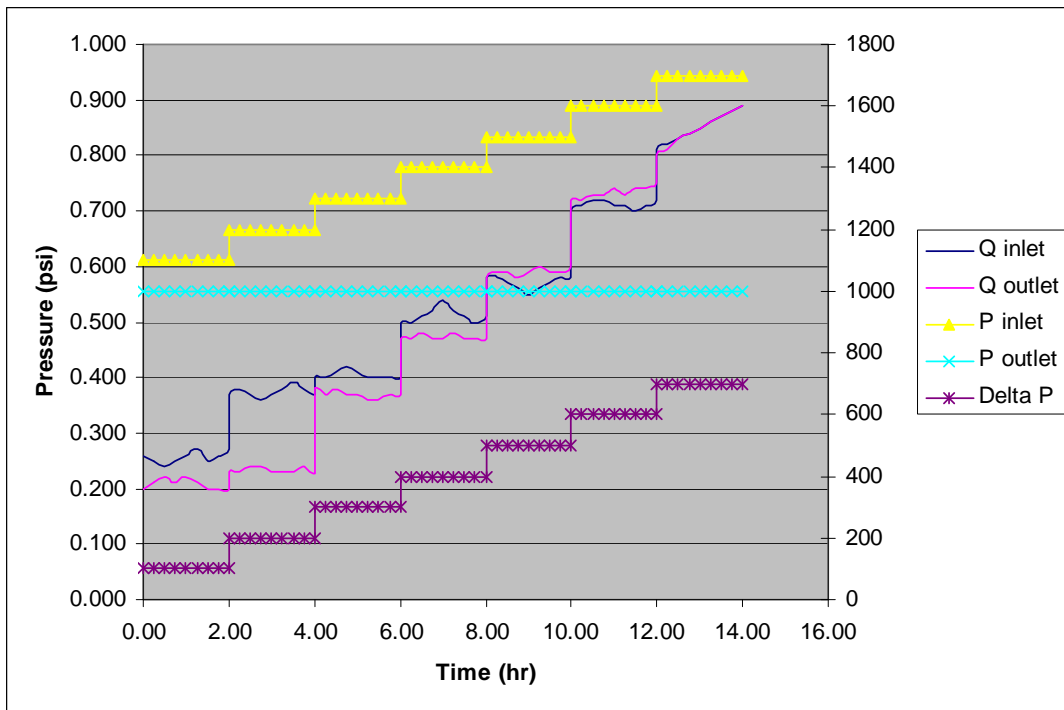


Figure B.2.4.2.1. Unsaturated, upper Kirtland gas breakthrough pressure test results.

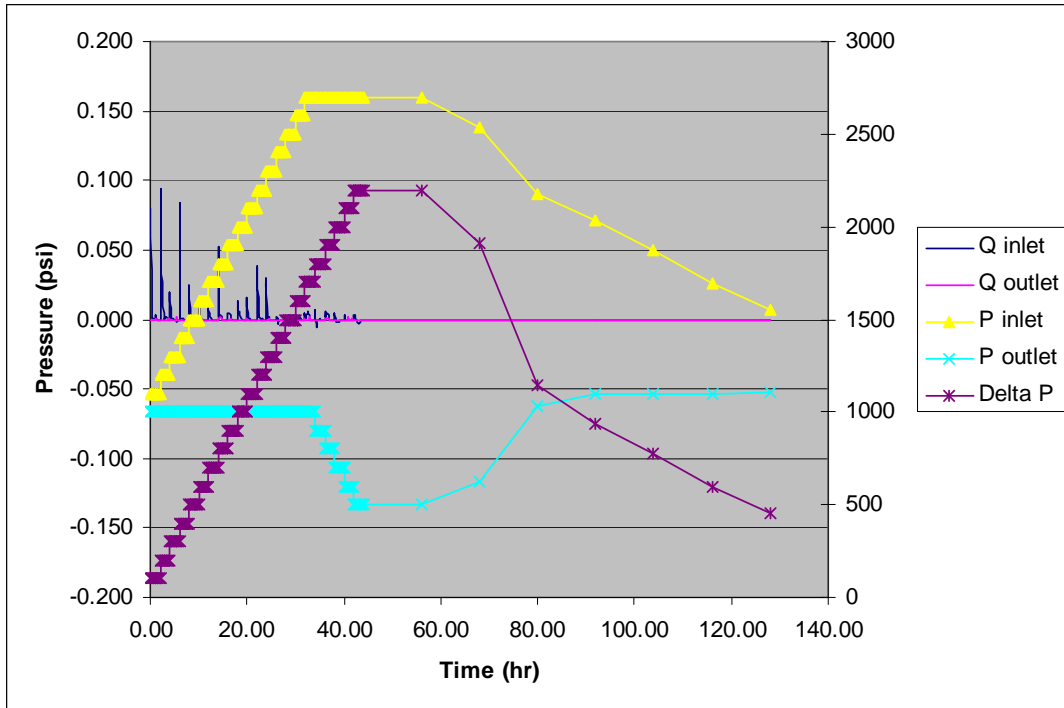


Figure B.2.4.2.2. Brine saturated, upper Kirtland gas breakthrough pressure test results.

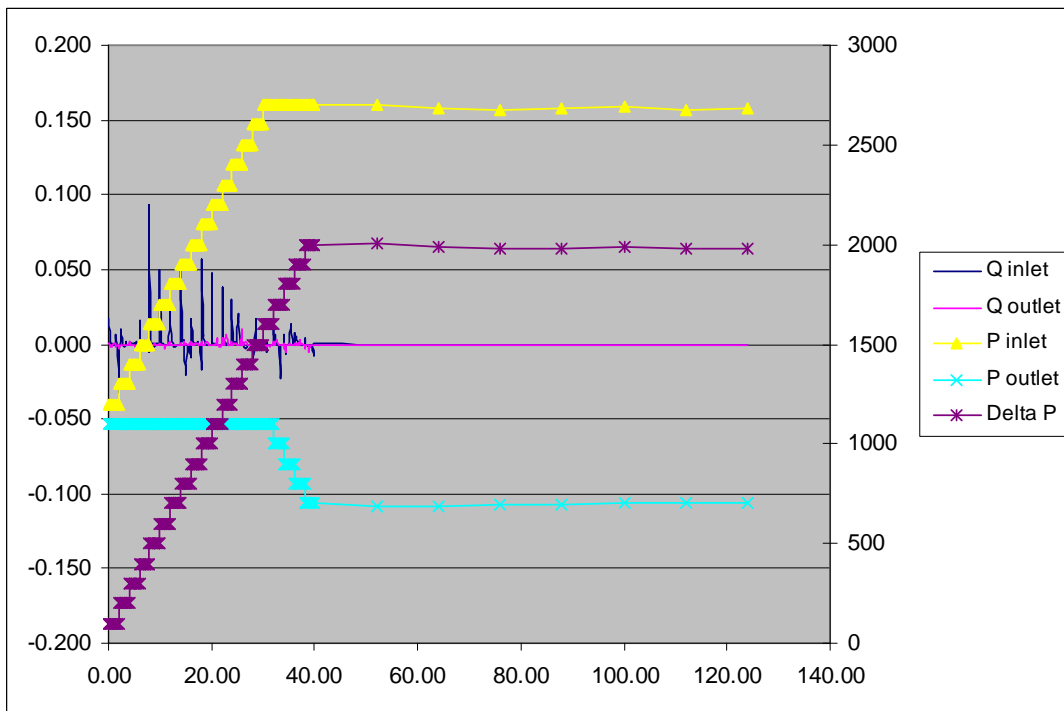


Figure B.2.4.2.3. Brine saturated lower Kirtland gas breakthrough pressure test results.

B.2.4.3 Tables of Gas Breakthrough Pressure Measurement Data

Table B.2.4.3.1. Gas breakthrough pressure measurement results for upper Kirtland, brine saturated sample

Project:	502488
Depth (ft):	2049.75
Length (in):	0.454
Diameter (in):	1.005
Temp (degC)	30

Brine Saturated Sample

Time (hours)	Q inlet (cc/min)	P inlet (psi)	P outlet (psi)	Q outlet (cc/min)	Delta P (psi)	P confining (psi)
(initial)	0	1000	1000	0	0	2265
0.00	0.080	1100	1000	0.000	100	2265
0.25	0.002	1100	1000	0.000	100	2265
0.50	0.001	1100	1000	0.000	100	2265
0.75	0.001	1100	1000	0.000	100	2265
1.00	0.001	1100	1000	0.000	100	2265
1.25	0.003	1100	1000	0.001	100	2265
1.50	-0.001	1100	1000	0.000	100	2265
1.75	0.000	1100	1000	0.000	100	2265
2.00	0.000	1100	1000	0.000	100	2265
2.00	0.091	1200	1000	0.000	200	2265
2.25	0.061	1200	1000	0.000	200	2265
2.50	0.010	1200	1000	0.000	200	2265
2.75	0.002	1200	1000	-0.001	200	2265
3.00	0.000	1200	1000	0.000	200	2265
3.25	0.002	1200	1000	0.000	200	2265
3.50	0.000	1200	1000	0.000	200	2265
3.75	0.000	1200	1000	0.000	200	2265
4.00	0.000	1200	1000	0.001	200	2265
4.00	0.020	1300	1000	0.000	300	2265
4.25	0.005	1300	1000	0.000	300	2265
4.50	0.001	1300	1000	0.000	300	2265
4.75	0.001	1300	1000	0.000	300	2265
5.00	0.000	1300	1000	0.000	300	2265
5.25	0.000	1300	1000	0.000	300	2265
5.50	-0.002	1300	1000	0.002	300	2265
5.75	0.000	1300	1000	0.000	300	2265
6.00	0.000	1300	1000	0.000	300	2265
6.00	0.084	1400	1000	0.000	400	2265
6.25	0.001	1400	1000	0.000	400	2265
6.50	0.001	1400	1000	0.000	400	2265
6.75	0.000	1400	1000	0.000	400	2265
7.00	0.000	1400	1000	0.000	400	2265
7.25	0.000	1400	1000	0.000	400	2265

Time (hours)	Q inlet (cc/min)	P inlet (psi)	P outlet (psi)	Q outlet (cc/min)	Delta P (psi)	P confining (psi)
7.50	0.000	1400	1000	0.000	400	2265
7.75	0.000	1400	1000	0.000	400	2265
8.00	0.000	1400	1000	-0.001	400	2265
8.00	0.025	1500	1000	0.000	500	2265
8.25	0.003	1500	1000	0.000	500	2265
8.50	0.001	1500	1000	0.000	500	2265
8.75	0.000	1500	1000	0.000	500	2265
9.00	0.000	1500	1000	0.000	500	2265
9.25	0.000	1500	1000	0.000	500	2265
9.50	0.000	1500	1000	0.000	500	2265
9.75	0.000	1500	1000	0.000	500	2265
10.00	0.000	1500	1000	0.000	500	2265
10.00	0.009	1600	1000	0.001	600	2265
10.25	0.002	1600	1000	0.000	600	2265
10.50	0.001	1600	1000	0.000	600	2265
10.75	0.000	1600	1000	0.000	600	2265
11.00	0.000	1600	1000	0.000	600	2265
11.25	0.000	1600	1000	0.000	600	2265
11.50	0.000	1600	1000	0.000	600	2265
11.75	-0.001	1600	1000	0.000	600	2265
12.00	0.000	1600	1000	0.000	600	2265
12.00	0.010	1700	1000	0.000	700	2265
12.25	0.002	1700	1000	0.000	700	2265
12.50	0.000	1700	1000	0.000	700	2265
12.75	0.000	1700	1000	0.000	700	2265
13.00	0.000	1700	1000	0.000	700	2265
13.25	0.000	1700	1000	0.000	700	2265
13.50	0.000	1700	1000	-0.001	700	2265
13.75	0.000	1700	1000	0.000	700	2265
14.00	0.000	1700	1000	0.000	700	2265
14.00	0.052	1800	1000	0.000	800	2265
14.25	0.002	1800	1000	0.000	800	2265
14.50	0.003	1800	1000	0.002	800	2265
14.75	0.001	1800	1000	0.000	800	2265
15.00	0.000	1800	1000	0.000	800	2265
15.25	-0.001	1800	1000	0.000	800	2265
15.50	-0.001	1800	1000	0.000	800	2265
15.75	0.000	1800	1000	0.000	800	2265
16.00	0.000	1800	1000	0.000	800	2265
16.00	0.004	1900	1000	0.000	900	2365
16.25	0.005	1900	1000	0.000	900	2365
16.50	0.002	1900	1000	0.001	900	2365
16.75	0.001	1900	1000	0.000	900	2365
17.00	0.000	1900	1000	0.000	900	2365
17.25	0.000	1900	1000	0.000	900	2365
17.50	0.000	1900	1000	0.000	900	2365
17.75	0.000	1900	1000	0.000	900	2365

Time (hours)	Q inlet (cc/min)	P inlet (psi)	P outlet (psi)	Q outlet (cc/min)	Delta P (psi)	P confining (psi)
18.00	0.000	1900	1000	0.000	900	2365
18.00	0.013	2000	1000	0.000	1000	2465
18.25	0.005	2000	1000	0.000	1000	2465
18.50	0.006	2000	1000	0.000	1000	2465
18.75	0.001	2000	1000	0.000	1000	2465
19.00	0.000	2000	1000	0.000	1000	2465
19.25	0.000	2000	1000	0.000	1000	2465
19.50	0.000	2000	1000	0.000	1000	2465
19.75	0.000	2000	1000	0.000	1000	2465
20.00	0.000	2000	1000	0.001	1000	2465
20.00	0.016	2100	1000	0.000	1100	2565
20.25	0.001	2100	1000	0.000	1100	2565
20.50	0.001	2100	1000	0.000	1100	2565
20.75	-0.001	2100	1000	0.000	1100	2565
21.00	0.000	2100	1000	0.000	1100	2565
21.25	0.000	2100	1000	0.000	1100	2565
21.50	0.000	2100	1000	0.000	1100	2565
21.75	0.000	2100	1000	0.000	1100	2565
22.00	0.000	2100	1000	0.000	1100	2565
22.00	0.038	2200	1000	0.000	1200	2665
22.25	0.002	2200	1000	0.000	1200	2665
22.50	0.003	2200	1000	0.000	1200	2665
22.75	0.000	2200	1000	0.000	1200	2665
23.00	0.001	2200	1000	0.000	1200	2665
23.25	0.000	2200	1000	0.000	1200	2665
23.50	0.000	2200	1000	-0.001	1200	2665
23.75	0.000	2200	1000	0.000	1200	2665
24.00	0.000	2200	1000	0.000	1200	2665
24.00	0.030	2300	1000	0.000	1300	2765
24.25	0.001	2300	1000	0.000	1300	2765
24.50	0.002	2300	1000	0.001	1300	2765
24.75	0.000	2300	1000	0.000	1300	2765
25.00	0.000	2300	1000	0.000	1300	2765
25.25	0.000	2300	1000	0.000	1300	2765
25.50	0.000	2300	1000	0.000	1300	2765
25.75	0.000	2300	1000	0.000	1300	2765
26.00	0.000	2300	1000	0.000	1300	2765
26.00	0.002	2400	1000	0.000	1400	2865
26.25	0.001	2400	1000	0.000	1400	2865
26.50	-0.003	2400	1000	0.000	1400	2865
26.75	0.000	2400	1000	0.000	1400	2865
27.00	0.000	2400	1000	0.000	1400	2865
27.25	0.000	2400	1000	0.000	1400	2865
27.50	0.000	2400	1000	0.000	1400	2865
27.75	0.000	2400	1000	0.002	1400	2865
28.00	0.000	2400	1000	0.000	1400	2865
28.00	0.002	2500	1000	0.000	1500	2965

Time (hours)	Q inlet (cc/min)	P inlet (psi)	P outlet (psi)	Q outlet (cc/min)	Delta P (psi)	P confining (psi)
28.25	0.000	2500	1000	0.000	1500	2965
28.50	0.000	2500	1000	0.000	1500	2965
28.75	0.000	2500	1000	0.000	1500	2965
29.00	0.000	2500	1000	0.000	1500	2965
29.25	0.000	2500	1000	0.000	1500	2965
29.50	0.000	2500	1000	-0.001	1500	2965
29.75	0.000	2500	1000	0.000	1500	2965
30.00	0.000	2500	1000	0.000	1500	2965
30.00	0.003	2600	1000	0.000	1600	3065
30.25	0.001	2600	1000	0.000	1600	3065
30.50	-0.005	2600	1000	0.000	1600	3065
30.75	0.002	2600	1000	0.000	1600	3065
31.00	0.000	2600	1000	0.000	1600	3065
31.25	0.000	2600	1000	0.000	1600	3065
31.50	0.000	2600	1000	0.000	1600	3065
31.75	0.000	2600	1000	0.000	1600	3065
32.00	0.000	2600	1000	0.001	1600	3065
32.00	0.005	2700	1000	0.000	1700	3165
32.25	0.001	2700	1000	0.000	1700	3165
32.50	0.006	2700	1000	0.000	1700	3165
32.75	0.000	2700	1000	0.002	1700	3165
33.00	0.000	2700	1000	0.000	1700	3165
33.25	0.000	2700	1000	0.000	1700	3165
33.50	0.000	2700	1000	0.000	1700	3165
33.75	0.000	2700	1000	0.000	1700	3165
34.00	0.000	2700	1000	0.000	1700	3165
34.00	0.007	2700	900	0.000	1800	3165
34.25	-0.006	2700	900	0.000	1800	3165
34.50	0.000	2700	900	0.000	1800	3165
34.75	0.000	2700	900	0.000	1800	3165
35.00	0.001	2700	900	0.000	1800	3165
35.25	0.000	2700	900	0.000	1800	3165
35.50	0.000	2700	900	0.000	1800	3165
35.75	0.000	2700	900	0.000	1800	3165
36.00	0.000	2700	900	0.000	1800	3165
36.00	0.006	2700	800	0.000	1900	3165
36.25	0.002	2700	800	0.000	1900	3165
36.50	0.005	2700	800	0.001	1900	3165
36.75	0.001	2700	800	0.000	1900	3165
37.00	0.000	2700	800	0.000	1900	3165
37.25	0.000	2700	800	0.000	1900	3165
37.50	0.000	2700	800	-0.001	1900	3165
37.75	0.000	2700	800	0.000	1900	3165
38.00	0.000	2700	800	0.000	1900	3165
38.00	0.004	2700	700	0.000	2000	3165
38.25	0.001	2700	700	0.000	2000	3165
38.50	0.000	2700	700	0.000	2000	3165

Time (hours)	Q inlet (cc/min)	P inlet (psi)	P outlet (psi)	Q outlet (cc/min)	Delta P (psi)	P confining (psi)
38.75	-0.002	2700	700	0.000	2000	3165
39.00	0.000	2700	700	0.000	2000	3165
39.25	0.000	2700	700	0.000	2000	3165
39.50	0.000	2700	700	0.000	2000	3165
39.75	0.000	2700	700	0.000	2000	3165
40.00	0.000	2700	700	0.000	2000	3165
40.00	0.003	2700	600	0.000	2100	3165
40.25	0.000	2700	600	0.000	2100	3165
40.50	0.000	2700	600	0.000	2100	3165
40.75	0.000	2700	600	0.000	2100	3165
41.00	-0.001	2700	600	0.002	2100	3165
41.25	0.000	2700	600	0.000	2100	3165
41.50	0.000	2700	600	0.001	2100	3165
41.75	0.000	2700	600	0.000	2100	3165
42.00	0.000	2700	600	0.000	2100	3165
42.00	0.002	2700	500	-0.001	2200	3165
42.25	0.003	2700	500	0.000	2200	3165
42.50	0.001	2700	500	0.000	2200	3165
42.75	0.000	2700	500	0.000	2200	3165
43.00	-0.003	2700	500	0.000	2200	3165
43.25	0.000	2700	500	0.000	2200	3165
43.50	0.000	2700	500	0.000	2200	3165
43.75	0.000	2700	500	0.000	2200	3165
**Stop Constant Pressure Pump Mode						
44.00	0.000	2700	500	0.000	2200	3165
56.00	0.000	2700	500	0.000	2200	3165
68.00	0.000	2534	625	0.000	1909	3165
80.00	0.000	2172	1027	0.000	1145	3165
92.00	0.000	2030	1095	0.000	935	3165
104.00	0.000	1872	1099	0.000	773	3165
116.00	0.000	1698	1102	0.000	596	3165
128.00	0.000	1555	1104	0.000	451	3165

Table B.2.4.3.2. Gas breakthrough pressure measurement results for upper Kirtland, non-saturated sample

Project:	502488
Depth (ft):	2049.75
Length (in):	0.454
Diameter (in):	1.005
Temp (degC)	30

Non-Saturated Sample

Time (hours)	Q inlet (cc/min)	P inlet (psi)	P outlet (psi)	Q outlet (cc/min)	Delta P (psi)	P confining (psi)
(initial)	0	1000	1000	0	0	2265
0.00	0.260	1100	1000	0.200	100	2265
0.25	0.250	1100	1000	0.210	100	2265
0.50	0.240	1100	1000	0.220	100	2265
0.75	0.250	1100	1000	0.210	100	2265
1.00	0.260	1100	1000	0.220	100	2265
1.25	0.270	1100	1000	0.210	100	2265
1.50	0.250	1100	1000	0.200	100	2265
1.75	0.260	1100	1000	0.200	100	2265
2.00	0.270	1100	1000	0.200	100	2265
2.00	0.370	1200	1000	0.230	200	2265
2.25	0.380	1200	1000	0.230	200	2265
2.50	0.370	1200	1000	0.240	200	2265
2.75	0.360	1200	1000	0.240	200	2265
3.00	0.370	1200	1000	0.230	200	2265
3.25	0.380	1200	1000	0.230	200	2265
3.50	0.390	1200	1000	0.230	200	2265
3.75	0.380	1200	1000	0.240	200	2265
4.00	0.370	1200	1000	0.230	200	2265
4.00	0.400	1300	1000	0.380	300	2265
4.25	0.400	1300	1000	0.370	300	2265
4.50	0.410	1300	1000	0.380	300	2265
4.75	0.420	1300	1000	0.370	300	2265
5.00	0.410	1300	1000	0.370	300	2265
5.25	0.400	1300	1000	0.360	300	2265
5.50	0.400	1300	1000	0.360	300	2265
5.75	0.400	1300	1000	0.370	300	2265
6.00	0.400	1300	1000	0.370	300	2265
6.00	0.500	1400	1000	0.470	400	2265
6.25	0.500	1400	1000	0.470	400	2265
6.50	0.510	1400	1000	0.480	400	2265
6.75	0.520	1400	1000	0.470	400	2265
7.00	0.540	1400	1000	0.470	400	2265
7.25	0.520	1400	1000	0.480	400	2265
7.50	0.510	1400	1000	0.470	400	2265
7.75	0.500	1400	1000	0.470	400	2265
8.00	0.510	1400	1000	0.470	400	2265

Time (hours)	Q inlet (cc/min)	P inlet (psi)	P outlet (psi)	Q outlet (cc/min)	Delta P (psi)	P confining (psi)
8.00	0.580	1500	1000	0.580	500	2265
8.25	0.580	1500	1000	0.590	500	2265
8.50	0.570	1500	1000	0.590	500	2265
8.75	0.560	1500	1000	0.580	500	2265
9.00	0.550	1500	1000	0.590	500	2265
9.25	0.560	1500	1000	0.600	500	2265
9.50	0.570	1500	1000	0.590	500	2265
9.75	0.580	1500	1000	0.590	500	2265
10.00	0.580	1500	1000	0.600	500	2265
10.00	0.700	1600	1000	0.720	600	2265
10.25	0.710	1600	1000	0.720	600	2265
10.50	0.720	1600	1000	0.730	600	2265
10.75	0.720	1600	1000	0.730	600	2265
11.00	0.710	1600	1000	0.740	600	2265
11.25	0.710	1600	1000	0.730	600	2265
11.50	0.700	1600	1000	0.740	600	2265
11.75	0.710	1600	1000	0.740	600	2265
12.00	0.720	1600	1000	0.750	600	2265
12.00	0.810	1700	1000	0.800	700	2265
12.25	0.820	1700	1000	0.810	700	2265
12.50	0.830	1700	1000	0.830	700	2265
12.75	0.840	1700	1000	0.840	700	2265
13.00	0.850	1700	1000	0.850	700	2265
13.25	0.860	1700	1000	0.860	700	2265
13.50	0.870	1700	1000	0.870	700	2265
13.75	0.880	1700	1000	0.880	700	2265
14.00	0.890	1700	1000	0.890	700	2265

Table B.2.4.3.3. Gas breakthrough pressure measurement results for lower Kirtland, brine saturated sample

Project: 502488
 Depth (ft): 2692.98
 Length (in): 0.699
 Diameter (in): 0.999
 Temp (degC) 30

Brine Saturated Sample

Time (hours)	Q inlet (cc/min)	P inlet (psi)	P outlet (psi)	Q outlet (cc/min)	Delta P (psi)	P confining (psi)
(initial)	0	1100	1100	0	0	2976
0.00	0.017	1200	1100	0.000	100	2976
0.25	0.002	1200	1100	0.000	100	2976
0.50	0.001	1200	1100	0.000	100	2976
0.75	0.001	1200	1100	-0.002	100	2976
1.00	0.000	1200	1100	0.001	100	2976
1.25	0.001	1200	1100	0.001	100	2976
1.50	0.006	1200	1100	-0.001	100	2976
1.75	0.000	1200	1100	0.000	100	2976
2.00	-0.033	1200	1100	-0.001	100	2976
2.00	-0.013	1300	1100	-0.003	200	2976
2.25	0.005	1300	1100	0.000	200	2976
2.50	0.010	1300	1100	0.000	200	2976
2.75	0.002	1300	1100	-0.001	200	2976
3.00	-0.001	1300	1100	-0.001	200	2976
3.25	0.002	1300	1100	0.000	200	2976
3.50	0.000	1300	1100	0.000	200	2976
3.75	0.000	1300	1100	0.000	200	2976
4.00	0.001	1300	1100	0.002	200	2976
4.00	0.001	1400	1100	0.002	300	2976
4.25	0.002	1400	1100	0.000	300	2976
4.50	0.001	1400	1100	0.000	300	2976
4.75	0.001	1400	1100	0.000	300	2976
5.00	0.000	1400	1100	0.000	300	2976
5.25	0.000	1400	1100	0.000	300	2976
5.50	0.001	1400	1100	-0.002	300	2976
5.75	0.000	1400	1100	0.000	300	2976
6.00	0.003	1400	1100	-0.003	300	2976
6.00	0.015	1500	1100	-0.002	400	2976
6.25	-0.001	1500	1100	0.000	400	2976
6.50	0.001	1500	1100	0.000	400	2976
6.75	-0.003	1500	1100	0.000	400	2976
7.00	0.003	1500	1100	0.003	400	2976
7.25	0.000	1500	1100	0.000	400	2976
7.50	0.000	1500	1100	0.000	400	2976
7.75	0.000	1500	1100	0.000	400	2976
8.00	-0.005	1500	1100	-0.002	400	2976

Time (hours)	Q inlet (cc/min)	P inlet (psi)	P outlet (psi)	Q outlet (cc/min)	Delta P (psi)	P confining (psi)
8.00	0.093	1600	1100	-0.001	500	2976
8.25	-0.003	1600	1100	0.000	500	2976
8.50	0.001	1600	1100	0.000	500	2976
8.75	0.000	1600	1100	0.000	500	2976
9.00	-0.001	1600	1100	0.001	500	2976
9.25	0.000	1600	1100	0.000	500	2976
9.50	0.001	1600	1100	0.000	500	2976
9.75	0.000	1600	1100	0.000	500	2976
10.00	0.003	1600	1100	0.001	500	2976
10.00	0.050	1700	1100	0.000	600	2976
10.25	0.002	1700	1100	0.000	600	2976
10.50	0.001	1700	1100	0.000	600	2976
10.75	0.000	1700	1100	0.000	600	2976
11.00	0.000	1700	1100	-0.003	600	2976
11.25	0.000	1700	1100	0.000	600	2976
11.50	0.000	1700	1100	0.000	600	2976
11.75	-0.001	1700	1100	0.000	600	2976
12.00	0.014	1700	1100	0.001	600	2976
12.00	0.024	1800	1100	0.000	700	2976
12.25	0.002	1800	1100	0.000	700	2976
12.50	0.000	1800	1100	0.000	700	2976
12.75	0.000	1800	1100	0.000	700	2976
13.00	-0.001	1800	1100	0.000	700	2976
13.25	0.000	1800	1100	0.000	700	2976
13.50	0.000	1800	1100	-0.001	700	2976
13.75	0.000	1800	1100	0.000	700	2976
14.00	0.000	1800	1100	0.000	700	2976
14.00	0.052	1900	1100	0.001	800	2976
14.25	0.002	1900	1100	0.000	800	2976
14.50	0.003	1900	1100	0.002	800	2976
14.75	0.001	1900	1100	0.000	800	2976
15.00	-0.021	1900	1100	0.000	800	2976
15.25	-0.001	1900	1100	0.000	800	2976
15.50	-0.001	1900	1100	0.000	800	2976
15.75	0.000	1900	1100	0.000	800	2976
16.00	-0.008	1900	1100	0.002	800	2976
16.00	0.017	2000	1100	0.000	900	2976
16.25	0.005	2000	1100	0.000	900	2976
16.50	0.002	2000	1100	0.001	900	2976
16.75	0.001	2000	1100	0.000	900	2976
17.00	0.000	2000	1100	0.001	900	2976
17.25	0.002	2000	1100	0.000	900	2976
17.50	0.000	2000	1100	0.000	900	2976
17.75	0.000	2000	1100	0.000	900	2976
18.00	-0.015	2000	1100	0.002	900	2976
18.00	0.057	2100	1100	-0.001	1000	2976
18.25	0.005	2100	1100	0.000	1000	2976

Time (hours)	Q inlet (cc/min)	P inlet (psi)	P outlet (psi)	Q outlet (cc/min)	Delta P (psi)	P confining (psi)
18.50	0.006	2100	1100	0.000	1000	2976
18.75	0.001	2100	1100	0.000	1000	2976
19.00	0.000	2100	1100	0.002	1000	2976
19.25	0.000	2100	1100	0.000	1000	2976
19.50	0.000	2100	1100	-0.001	1000	2976
19.75	0.000	2100	1100	0.000	1000	2976
20.00	-0.001	2100	1100	-0.001	1000	2976
20.00	0.048	2200	1100	-0.001	1100	2976
20.25	0.001	2200	1100	0.000	1100	2976
20.50	0.001	2200	1100	0.000	1100	2976
20.75	-0.001	2200	1100	0.000	1100	2976
21.00	0.000	2200	1100	0.004	1100	2976
21.25	0.000	2200	1100	0.000	1100	2976
21.50	0.000	2200	1100	0.000	1100	2976
21.75	0.000	2200	1100	-0.002	1100	2976
22.00	-0.001	2200	1100	0.004	1100	2976
22.00	0.038	2300	1100	0.000	1200	2976
22.25	0.002	2300	1100	0.000	1200	2976
22.50	0.003	2300	1100	0.000	1200	2976
22.75	0.000	2300	1100	0.006	1200	2976
23.00	0.001	2300	1100	0.000	1200	2976
23.25	0.000	2300	1100	0.000	1200	2976
23.50	0.000	2300	1100	-0.001	1200	2976
23.75	0.000	2300	1100	0.000	1200	2976
24.00	-0.001	2300	1100	0.002	1200	2976
24.00	0.030	2400	1100	0.000	1300	2976
24.25	0.001	2400	1100	0.000	1300	2976
24.50	0.002	2400	1100	0.001	1300	2976
24.75	0.000	2400	1100	0.000	1300	2976
25.00	0.000	2400	1100	0.000	1300	2976
25.25	0.021	2400	1100	0.000	1300	2976
25.50	0.000	2400	1100	0.000	1300	2976
25.75	0.000	2400	1100	0.010	1300	2976
26.00	-0.001	2400	1100	0.000	1300	2976
26.00	0.002	2500	1100	0.000	1400	2976
26.25	0.001	2500	1100	0.000	1400	2976
26.50	-0.003	2500	1100	0.002	1400	2976
26.75	0.000	2500	1100	-0.001	1400	2976
27.00	0.000	2500	1100	0.000	1400	2976
27.25	0.000	2500	1100	0.000	1400	2976
27.50	0.000	2500	1100	0.000	1400	2976
27.75	-0.002	2500	1100	0.002	1400	2976
28.00	0.000	2500	1100	0.001	1400	2976
28.00	-0.015	2600	1100	-0.001	1500	2976
28.25	0.000	2600	1100	0.000	1500	2976
28.50	0.017	2600	1100	0.000	1500	2976
28.75	0.000	2600	1100	0.003	1500	2976

Time (hours)	Q inlet (cc/min)	P inlet (psi)	P outlet (psi)	Q outlet (cc/min)	Delta P (psi)	P confining (psi)
29.00	0.000	2600	1100	0.001	1500	2976
29.25	0.000	2600	1100	0.000	1500	2976
29.50	0.000	2600	1100	-0.001	1500	2976
29.75	0.002	2600	1100	0.000	1500	2976
30.00	0.000	2600	1100	-0.002	1500	2976
30.00	0.003	2700	1100	0.000	1600	2976
30.25	0.001	2700	1100	0.000	1600	2976
30.50	-0.005	2700	1100	-0.002	1600	2976
30.75	0.002	2700	1100	0.000	1600	2976
31.00	0.000	2700	1100	0.000	1600	2976
31.25	0.000	2700	1100	-0.002	1600	2976
31.50	0.000	2700	1100	0.000	1600	2976
31.75	0.000	2700	1100	0.000	1600	2976
32.00	0.000	2700	1100	0.002	1600	2976
32.00	0.013	2700	1000	0.000	1700	2976
32.25	0.001	2700	1000	0.000	1700	2976
32.50	0.006	2700	1000	0.000	1700	2976
32.75	0.000	2700	1000	0.003	1700	2976
33.00	0.000	2700	1000	0.000	1700	2976
33.25	-0.023	2700	1000	0.000	1700	2976
33.50	0.000	2700	1000	0.000	1700	2976
33.75	0.000	2700	1000	0.000	1700	2976
34.00	0.000	2700	1000	0.001	1700	2976
34.00	0.007	2700	900	0.000	1800	2976
34.25	-0.006	2700	900	-0.005	1800	2976
34.50	0.000	2700	900	0.000	1800	2976
34.75	0.000	2700	900	0.000	1800	2976
35.00	0.001	2700	900	0.000	1800	2976
35.25	0.000	2700	900	0.001	1800	2976
35.50	0.014	2700	900	0.000	1800	2976
35.75	0.000	2700	900	0.000	1800	2976
36.00	0.000	2700	900	0.000	1800	2976
36.00	0.008	2700	800	0.000	1900	2976
36.25	0.002	2700	800	0.000	1900	2976
36.50	0.005	2700	800	0.001	1900	2976
36.75	0.001	2700	800	0.000	1900	2976
37.00	0.000	2700	800	0.003	1900	2976
37.25	0.000	2700	800	0.000	1900	2976
37.50	0.000	2700	800	0.001	1900	2976
37.75	0.000	2700	800	0.000	1900	2976
38.00	0.000	2700	800	0.000	1900	2976
38.00	0.004	2700	700	-0.003	2000	2976
38.25	0.001	2700	700	0.000	2000	2976
38.50	0.000	2700	700	0.000	2000	2976
38.75	-0.002	2700	700	0.000	2000	2976
39.00	0.000	2700	700	-0.005	2000	2976
39.25	0.000	2700	700	0.000	2000	2976

Time (hours)	Q inlet (cc/min)	P inlet (psi)	P outlet (psi)	Q outlet (cc/min)	Delta P (psi)	P confining (psi)
39.50	0.000	2700	700	0.000	2000	2976
39.75	-0.008	2700	700	0.000	2000	2976
40.00	0.001	2700	700	0.000	2000	2976
**Stop Constant Pressure Pump Mode						
52.00	0.000	2700	690	0.000	2010	2976
64.00	0.000	2680	688	0.000	1992	2976
76.00	0.000	2672	694	0.000	1978	2976
88.00	0.000	2679	699	0.000	1980	2976
100.00	0.000	2689	705	0.000	1984	2976
112.00	0.000	2678	700	0.000	1978	2976
124.00	0.000	2684	702	0.000	1982	2976

B.2.5 Routine Core Analysis

TerraTek performed “routine core analysis” on three, fresh core samples from the Ojo Alamo Sandstone. The analysis was suited to non-mudstone lithologies and thus chosen for the Ojo Alamo Sandstone.

**Conoco/Phillips
EPNG Com A Inj. #1
Routine Core Analysis Test Results
Project No: 502488
June 18, 2008**



Sample Number	Sample Depth (ft)	Sample Length (in)	Sample Diameter (in)	Ambient Porosity (%)	Dry Bulk Density (g/cc)	Grain Density (g/cc)	Gas Permeability (md)	Saturation	
								Water (%)	Oil (%)
1	2022.10	2.290	1.473	12.41	2.329	2.659	5.182	54.59	N/A
2	2034.50	2.271	1.475	9.44	2.418	2.670	0.058	61.10	N/A
3	2047.10	2.527	1.474	1.62	2.683	2.727	0.001	44.87	N/A

		+/-0.0005 (in)	+/-0.0005 (in)	+/-0.5 (%)	+/-0.005 (g/cc)	+/-0.005 (g/cc)	+/-0.1 (md)	+/- 0.5 (%of PV)	+/- 0.5 (%of PV)
% = Percent									
g/cc = Grams per cubic centimeter									
md = Millidarcy									
ft = Feet									

B.2.6 Tight Rock Analysis Results

TerraTek performed analysis of upper and lower Kirtland Formation samples using their “Tight Rock Analysis” methods, which are suited for mudstone lithologies. The methods are designed to measure matrix properties and not the effect of pressure-release due to drilling, coring, and core handling activities.

Conoco/Phillips
EPNG Com A Inj. #1
Tight Rock Analysis
Project No: 502488
June 18, 2008



Sample ID	Depth (ft)	As Received Bulk Density (g/cc)	As Received Grain Density (g/cc)	Dry Grain Density (g/cc)	Porosity (% of BV)	Water Saturation (% of PV)	Gas Saturation (% of PV)	Mobile Oil Saturation (% of PV)	Gas Filled Porosity (% of BV)	Bound Hydrocarbon Saturation (% of BV)	Bound Clay Water (% of BV)	Pressure-Decay Permeability (md)
1	2048.25	2.353	2.394	2.521	9.88	81.99	17.22	0.79	1.70	0.51	20.71	0.000073
2	2052.06	2.493	2.523	2.607	6.33	79.95	18.74	1.31	1.19	0.24	13.70	0.000097
3	2055.20	2.515	2.537	2.651	7.66	87.56	11.35	1.09	0.87	0.49	14.75	0.000069
4	2062.30	2.474	2.515	2.645	9.40	80.95	17.30	1.75	1.63	0.18	13.08	0.000090
5	2067.98	2.482	2.516	2.629	8.17	80.80	16.39	2.81	1.34	0.33	14.79	0.000093
6	2692.25	2.550	2.590	2.677	6.65	75.39	23.34	1.27	1.55	0.22	14.76	0.000080
7	2697.15	2.526	2.565	2.649	6.46	73.89	23.53	2.58	1.52	0.14	13.35	0.000085
Error		+/- 0.005 (g/cc)	+/- 0.005 (g/cc)	+/- 0.005 (g/cc)	+/- 0.02 (% of BV)	+/- 0.5 (% of PV)	+/- 0.5 (% of PV)	+/- 0.5 (% of PV)	+/- 0.02 (% of BV)	+/- 0.5 (% of BV)	+/- 0.5 (% of BV)	+/- 0.000010
% of PV = Percent of Pore Volume												
% of BV = Percent of Bulk Volume												
g/cc = grams per cubic centimeter												
md = millidarcy												
ft = feet												

B.2.7 Gamma Ray on Core

TerraTek ran a component core gamma ray log to facilitate correlation between the core and the field well logs and to obtain information on U, Th, and K content. The U and Th concentrations were needed for assessing *in situ* production of helium. Herein is presented graphs of the data, plotted by TerraTek, and the raw data as given in a “.las” file. Note that from depths 2072.45 to 2690.45 ft, “no data” entries were removed for presentation here.



TerraTek
 A Schlumberger company
 Pioneer Business Park
 1935 S. Fremont Dr.
 Salt Lake City, UT 84104
 (801) 584-2400

Total Counts		
0.0	GR CPM	1,500.0

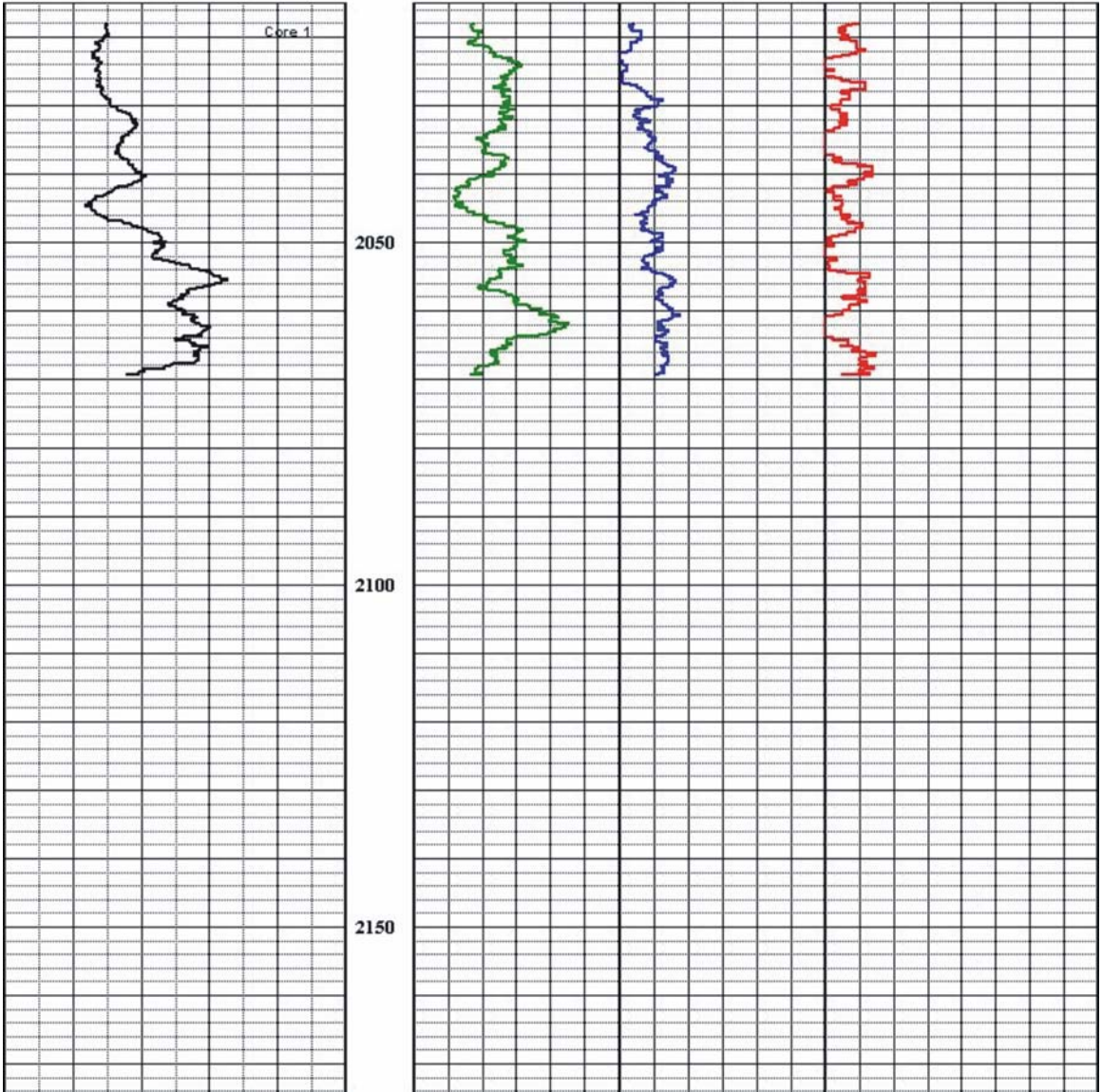
Component Core Gamma Log

Conoco/Phillips
 San Juan
 NM
 San Juan
 May 13, 2007

TerraTek No: TBD

Potassium	Uranium	Thorium
0.0 % 3.0	0.0 ppm 24.0	0.0 ppm 56.0

Depth





TerraTek
A Schlumberger company
Pioneer Business Park
1935 S. Fremont Dr.
Salt Lake City, UT 84104
(801) 584-2400

Total Counts		
0.0	GR CPM	1,500.0

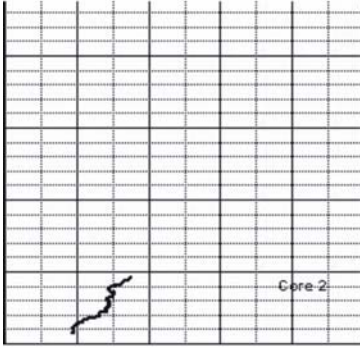
Component Core Gamma Log

Conoco/Phillips
San Juan
NM
San Juan
May 13, 2007

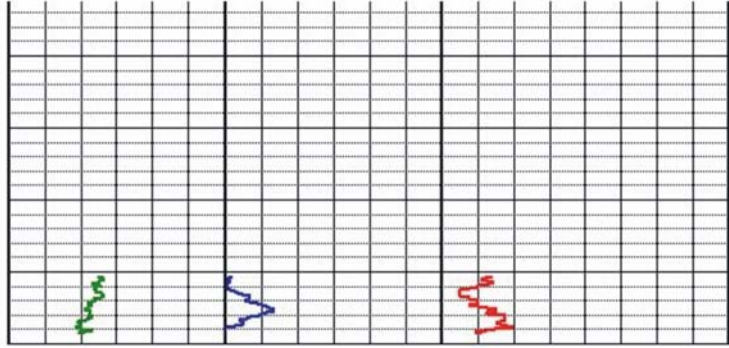
TerraTek No: TBD

Potassium		Uranium		Thorium	
0.0	%	3.0	0.0	ppm	24.0
0.0			0.0	ppm	56.0

Depth



2700



```
#Do NOT edit this file. Doing so will render it un-usable
~VERSION INFORMATION
VERS.      2.0                      :LOG ASCII STANDARD - VERSION 2.0
WRAP.      NO                       :One line per Depth Step
~WELL INFORMATION
STRT.FT    -2018                    :START DEPTH
STOP.FT    -2698.5                  :STOP DEPTH
STEP.FT    3                        :STEP
COMP.      EPNG                     :COMPANY
WELL.      San Juan                 :WELL
LOC.       NM                       :LOCATION
DATE.      May 13 2008              :DATE
~CURVE INFORMATION
DEPT.FT    MD                       :DEPTH IN FEET
GAMMA.CPM  :TOTAL GAMMA
K.%        :POTASSIUM
UR.PPM     :URANIUM
TH.PPM     :THORIUM
~PARAMETER INFORMATION
DREF.      :Depth Reference
EREF.FT    :ELEVATION OF DEPTH REFERENCE
DEX.       :DELTA EPISON X
DEY.       :DELTA EPISON Y
CALM.TEQ1  :CALIBRATION METHOD

~ASCII
#  DEPT      GAMMA      K      UR      TH
-2018      453.5389    0.8902  1.6696  6.6282
-2018.18   447.6420    0.8353  1.3360  5.2999
-2018.36   437.4973    0.8394  1.0630  4.2132
```

#	DEPT	GAMMA	K	UR	TH
-2018.54		445.6633	0.8356	1.4515	3.3076
-2018.73		447.1208	0.8595	1.2116	2.5413
-2018.91		450.8464	0.8584	1.5549	4.0759
-2019.1		454.4920	0.9668	1.3402	3.3605
-2019.27		454.5112	0.9830	2.5502	2.7346
-2019.46		447.7435	0.9461	2.3022	3.8729
-2019.64		455.9683	0.9372	2.5021	3.2091
-2019.83		438.4922	0.9134	2.5021	4.8058
-2020		439.7567	0.9373	2.5021	3.1664
-2020.18		431.2189	0.8897	2.5021	3.0559
-2020.37		432.9244	0.8991	2.0828	4.9516
-2020.55		416.2133	0.7918	2.0828	6.5761
-2020.73		402.7250	0.8079	1.6396	6.5761
-2020.91		396.9161	0.7856	1.2362	6.5761
-2021.1		405.5178	0.8605	1.2594	6.5761
-2021.28		421.1161	1.0214	1.2594	6.5761
-2021.46		421.2767	1.0892	1.2594	6.5761
-2021.65		415.8050	1.1132	1.2629	6.5761
-2021.83		410.1717	1.1381	1.2629	8.1867
-2022.01		393.8528	1.1360	0.8360	6.4823
-2022.19		387.3661	1.0852	0.8360	6.4823
-2022.37		381.4312	1.1555	0.0000	6.4823
-2022.55		393.6156	1.2037	0.0000	4.8857
-2022.73		388.0584	1.1545	0.0000	3.2073
-2022.91		385.2784	1.2698	0.0000	1.5874
-2023.09		415.8423	1.4282	0.0000	0.0000
-2023.27		403.3401	1.3585	0.0000	0.0000
-2023.45		408.1184	1.4552	0.3976	0.0000
-2023.63		412.1517	1.4210	0.3976	0.0000
-2023.81		429.5728	1.5381	0.3976	0.0000
-2024		416.0905	1.5542	0.3976	0.0000
-2024.19		416.5373	1.5805	0.8367	0.0000
-2024.37		410.9506	1.5058	0.8146	0.0000
-2024.55		404.1151	1.4422	0.8146	0.0000
-2024.74		403.8485	1.4931	0.8146	1.6347
-2024.92		401.6757	1.4679	0.4004	1.6347
-2025.1		411.2741	1.3779	0.4004	0.0241
-2025.28		422.3474	1.4227	0.4004	0.0241
-2025.46		413.6256	1.3792	0.4004	0.0241
-2025.64		417.3501	1.3126	0.4004	0.0241
-2025.82		413.6584	1.2652	0.4004	1.6487
-2026		418.6418	1.3633	0.4004	3.3429
-2026.19		421.5573	1.3173	0.4004	3.3429
-2026.36		402.8195	1.2960	0.0005	4.9535
-2026.54		419.5234	1.2967	0.0005	4.9535
-2026.72		420.8719	1.2717	0.4062	8.2415
-2026.9		411.4785	1.3422	1.2322	8.2415
-2027.08		400.7419	1.2480	2.0437	8.2415
-2027.26		428.0113	1.1588	2.0437	8.2415
-2027.44		431.2485	1.2949	2.4258	8.1282
-2027.62		424.3318	1.3602	2.4144	4.9070
-2027.81		420.8934	1.4058	2.4144	4.9070
-2027.99		424.8951	1.2597	2.8311	3.2026
-2028.17		425.6768	1.3074	3.2417	3.2026

#	DEPT	GAMMA	K	UR	TH
-2028.35		426.9017	1.3308	3.2417	4.8810
-2028.53		429.9540	1.2836	3.2417	4.8810
-2028.71		444.6174	1.4029	3.6585	4.8810
-2028.9		443.9297	1.3774	3.6585	4.8810
-2029.08		458.7842	1.4040	3.6585	4.9655
-2029.27		466.5531	1.4032	4.9237	3.2714
-2029.46		456.7220	1.3352	4.5168	3.2714
-2029.64		466.7559	1.2926	4.5168	3.3141
-2029.82		458.7414	1.4088	4.5168	3.3141
-2030		461.6747	1.3829	4.2885	1.2140
-2030.18		487.9113	1.2661	3.4625	1.2140
-2030.36		496.3463	1.3801	2.6510	1.2140
-2030.54		488.6615	1.4711	2.6510	2.8199
-2030.72		498.7843	1.3788	1.8299	2.8292
-2030.9		515.3527	1.3642	1.8634	2.8292
-2031.07		532.7571	1.2456	2.2692	2.8292
-2031.25		552.0450	1.3170	1.8525	4.5030
-2031.43		551.7089	1.2911	1.4418	4.5030
-2031.61		559.5573	1.4570	1.8611	2.8246
-2031.8		555.8455	1.4128	2.2804	4.4983
-2031.99		561.3271	1.2472	2.2694	4.4983
-2032.17		575.6298	1.2698	3.1054	4.4983
-2032.35		566.4392	1.2672	3.5184	2.7893
-2032.53		566.9399	1.2896	2.2531	2.7893
-2032.71		580.6287	1.2903	2.2531	4.4779
-2032.9		573.4364	1.3362	2.6650	2.8246
-2033.08		574.2908	1.2422	2.6650	2.8246
-2033.26		566.8992	1.2456	2.0696	1.6366
-2033.45		559.8309	1.3382	2.4791	1.6366
-2033.62		560.6504	1.2468	2.8813	1.6366
-2033.8		558.2331	1.1578	3.2955	0.0307
-2033.98		539.9496	1.0873	3.7024	0.0000
-2034.17		548.5712	1.0605	3.2769	0.0000
-2034.34		526.9417	1.0382	3.2829	0.0260
-2034.52		512.3726	1.0393	3.7059	0.0000
-2034.7		519.5070	1.0673	4.1238	0.0204
-2034.88		509.5059	0.8995	3.7045	0.0204
-2035.06		518.7166	0.9692	4.1112	0.0000
-2035.25		522.8309	0.9932	3.7055	0.0000
-2035.43		508.5228	1.0363	3.6810	0.0000
-2035.62		506.7083	1.0834	3.2680	0.0000
-2035.8		495.7854	1.0337	3.2680	0.0000
-2035.98		496.9371	1.0320	3.2680	0.0000
-2036.16		494.2183	1.0063	2.8562	0.0000
-2036.34		503.2339	1.0078	3.2780	0.0000
-2036.52		501.6884	1.0563	3.2780	0.0000
-2036.7		488.0295	0.9873	4.1224	0.0000
-2036.89		485.5551	1.0356	4.5486	0.0000
-2037.07		499.4030	1.1293	4.1345	0.0000
-2037.25		510.2296	1.3141	4.1357	1.6245
-2037.43		509.0176	1.3383	4.9642	1.6245
-2037.61		516.6536	1.3767	4.5524	1.4787
-2037.79		523.2643	1.3352	4.1294	3.3178
-2037.98		539.1810	1.3301	4.5114	1.6496

#	DEPT	GAMMA	K	UR	TH
-2038.16		547.7493	1.3308	4.9209	1.6496
-2038.34		548.8965	1.2608	4.9235	3.3029
-2038.52		548.2005	1.3528	5.3330	6.5715
-2038.69		566.2472	1.3292	5.7317	8.1821
-2038.87		562.9915	1.3111	5.7317	6.5288
-2039.06		560.6189	1.2611	6.1196	9.6246
-2039.24		562.3329	1.2593	6.5116	9.6246
-2039.43		575.5484	1.1709	6.5116	9.6246
-2039.61		574.2205	1.1467	6.0898	9.6246
-2039.79		596.0833	1.0757	6.0898	7.9406
-2039.97		597.4772	1.1689	5.2490	7.9406
-2040.15		620.5876	1.1449	4.4204	9.5800
-2040.34		605.1882	1.0990	5.2564	9.5800
-2040.52		611.4570	0.9387	5.6868	7.9508
-2040.7		599.2042	0.8924	5.2776	7.9508
-2040.88		599.7491	0.8075	6.1061	6.4526
-2041.07		582.9744	0.7759	6.1061	4.6135
-2041.25		567.3932	0.7752	5.3062	4.6135
-2041.43		559.0471	0.8261	5.7557	6.3281
-2041.6		539.7858	0.8027	5.7680	4.6748
-2041.79		517.4091	0.6637	5.3585	3.0456
-2041.96		497.3207	0.6668	4.1482	1.4350
-2042.14		484.3097	0.6141	4.1482	1.4350
-2042.33		479.4154	0.5953	4.5912	0.0000
-2042.5		470.4894	0.6227	4.1992	0.0279
-2042.68		458.2826	0.6675	5.0277	1.6812
-2042.87		444.4453	0.6433	5.0277	1.6812
-2043.05		432.3806	0.6415	5.4384	1.6812
-2043.23		429.4219	0.5947	5.0254	3.3299
-2043.41		398.1645	0.5716	5.4372	1.6905
-2043.59		399.9677	0.5920	4.6012	1.6905
-2043.77		390.8270	0.6155	4.1806	1.6905
-2043.95		384.5677	0.6174	3.7613	3.4320
-2044.13		363.7439	0.6835	3.7127	3.4320
-2044.31		380.3012	0.7079	4.1305	3.4320
-2044.49		363.5308	0.5954	4.1305	3.4320
-2044.67		354.4054	0.5911	3.6822	3.3568
-2044.85		374.1671	0.6608	3.2520	3.3568
-2045.04		381.4588	0.7808	3.2520	1.7174
-2045.21		381.6866	0.7787	3.2520	3.3419
-2045.4		395.3537	0.7806	3.2520	3.3419
-2045.58		401.6437	0.8725	2.4211	3.3419
-2045.76		402.2969	0.8704	2.4211	3.2927
-2045.94		407.6779	0.9658	1.5926	3.3076
-2046.12		419.8190	1.0344	2.8102	4.9275
-2046.3		432.1762	1.0595	2.8213	4.9275
-2046.48		447.5256	1.0366	3.2380	3.2788
-2046.66		448.7969	1.0676	2.8262	4.3739
-2046.84		515.3680	1.0668	2.8262	4.3739
-2047.02		518.2400	1.2037	2.4083	6.0030
-2047.2		525.4089	1.2704	3.2294	4.2615
-2047.38		552.1250	1.3254	2.4495	7.6805
-2047.56		558.0013	1.3241	2.8527	7.6805
-2047.74		581.7773	1.4906	2.8527	7.6805

#	DEPT	GAMMA	K	UR	TH
-2047.92		608.6892	1.5163	2.4421	6.0411
-2048.1		619.8871	1.6032	2.4270	6.0411
-2048.29		625.6306	1.5533	3.2529	6.0411
-2048.47		647.9110	1.5104	3.6785	4.4166
-2048.65		655.3312	1.5098	4.0989	4.4166
-2048.83		674.7864	1.4901	4.9423	4.4166
-2049.01		679.5886	1.4914	4.9423	2.7772
-2049.19		687.1996	1.3703	4.9423	1.1090
-2049.37		687.5148	1.4465	4.5733	0.0000
-2049.54		684.8156	1.5399	4.1515	1.1527
-2049.73		683.6081	1.6293	3.7348	1.1527
-2049.91		711.8680	1.6227	3.7348	0.0576
-2050.1		654.6975	1.5079	4.9523	0.0576
-2050.27		681.4427	1.4859	4.9523	0.0678
-2050.45		704.3325	1.5116	4.9672	1.7360
-2050.63		698.4019	1.4382	4.9672	0.0000
-2050.81		687.0825	1.4857	4.1461	0.0000
-2050.99		679.6749	1.4155	4.5717	0.0000
-2051.17		658.9297	1.3437	4.9847	0.0000
-2051.35		657.0495	1.3078	4.5891	0.0000
-2051.54		672.4167	1.3320	4.1799	0.0000
-2051.72		650.2903	1.3307	3.7543	0.0000
-2051.9		653.3832	1.4237	3.3339	0.0000
-2052.08		648.7036	1.4005	2.9149	0.0000
-2052.26		651.0208	1.4482	2.9149	2.3620
-2052.44		692.9926	1.4878	2.9149	2.3620
-2052.62		701.0612	1.3813	2.4288	2.3620
-2052.8		722.7109	1.3732	2.8911	0.6985
-2052.98		749.5504	1.3941	2.8911	0.6985
-2053.15		774.3099	1.4938	3.3220	0.6985
-2053.33		810.2995	1.5870	2.9256	0.6985
-2053.51		813.3060	1.4966	3.3474	0.7431
-2053.69		812.9657	1.3548	2.5114	0.7143
-2053.87		844.1541	1.3304	3.3351	0.7143
-2054.06		853.0087	1.2345	3.7113	0.7143
-2054.24		884.2496	1.2378	3.7262	2.4725
-2054.42		901.4202	1.2606	4.1319	4.1073
-2054.6		912.3737	1.2804	4.9605	9.0682
-2054.78		917.3485	1.2333	5.3772	9.0682
-2054.97		947.1970	1.2788	5.7890	9.0682
-2055.15		946.0690	1.2021	6.1652	7.4149
-2055.33		965.3429	1.1853	5.7408	7.4149
-2055.51		979.2005	1.0901	6.1538	6.6718
-2055.69		954.4527	1.1020	6.5768	6.6718
-2055.87		946.9809	1.0639	6.2143	8.3205
-2056.06		921.5555	1.0463	5.7520	8.3205
-2056.24		905.9114	1.0725	6.1578	8.3205
-2056.42		873.1680	0.9491	5.7269	8.3205
-2056.6		840.3845	0.9502	4.9058	8.3205
-2056.78		832.0525	0.9913	4.4839	8.2425
-2056.96		810.9922	1.0604	4.8909	6.6031
-2057.14		796.5521	1.2537	4.4928	6.6031
-2057.32		812.2765	1.3449	4.5142	8.1904
-2057.5		797.5820	1.3465	4.9686	8.2183

#	DEPT	GAMMA	K	UR	TH
-2057.68		773.7548	1.4210	4.5135	6.5836
-2057.87		782.4388	1.4543	4.5631	3.3754
-2058.05		781.5855	1.4989	4.1354	3.3754
-2058.23		767.4739	1.5214	4.5424	6.6439
-2058.41		758.9332	1.5268	4.5742	6.6439
-2058.6		741.4080	1.4476	5.0037	8.3586
-2058.78		734.2765	1.5205	5.0163	6.7099
-2058.96		715.1532	1.4678	4.9877	6.7099
-2059.13		720.4978	1.6638	5.4186	5.0612
-2059.31		747.1593	1.6894	5.4186	5.0612
-2059.5		753.9423	1.6894	5.8243	5.0612
-2059.69		769.0876	1.7807	5.8243	5.0612
-2059.87		780.2352	1.8593	6.2089	5.0612
-2060.06		789.6714	1.8454	6.2089	3.4553
-2060.24		800.1749	1.9370	6.2078	3.4553
-2060.41		779.1146	1.8229	6.0845	3.4553
-2060.59		835.0430	2.0629	6.9332	1.8679
-2060.77		824.0360	2.1023	6.0384	0.0817
-2060.95		850.4163	2.1219	6.0877	0.0817
-2061.13		831.6702	2.0171	6.0237	0.0000
-2061.31		816.5699	2.0213	5.6180	0.0000
-2061.5		824.5855	1.9781	4.7992	0.0000
-2061.69		837.1484	2.1020	4.3911	0.0000
-2061.87		854.1081	2.2710	4.8155	0.0000
-2062.05		858.6085	2.1986	4.3900	0.0000
-2062.24		888.0695	2.2254	4.8241	0.0000
-2062.42		902.4262	2.2079	4.3932	0.0000
-2062.6		894.4653	2.1608	5.2266	0.0000
-2062.78		884.1129	2.0253	4.4151	0.0000
-2062.96		870.8342	2.0726	5.6468	0.0000
-2063.14		868.7309	1.9694	5.2622	0.0000
-2063.32		857.1571	1.9417	5.2622	0.0000
-2063.49		846.4167	1.8286	4.8565	0.0000
-2063.67		863.2578	1.7712	4.9542	0.0000
-2063.85		785.0356	1.4856	4.1021	0.0000
-2064.03		778.1111	1.4388	4.1021	1.5623
-2064.21		746.2249	1.3375	4.2399	1.5623
-2064.39		818.1511	1.3562	4.2013	4.6581
-2064.57		818.3455	1.3548	4.6191	4.6581
-2064.75		831.9626	1.4276	5.4705	4.6581
-2064.93		838.3898	1.3523	5.4705	4.6581
-2065.11		821.0625	1.2862	4.9200	2.9537
-2065.29		893.9827	1.3700	5.5545	5.4866
-2065.48		860.4132	1.3416	4.7259	7.0220
-2065.66		858.7804	1.2121	5.1529	5.4383
-2065.85		848.2830	1.1176	5.1454	5.4383
-2066.04		831.1580	1.2258	5.4909	8.1970
-2066.22		850.8238	1.1274	4.7743	10.2534
-2066.4		836.7422	1.1238	5.1675	10.2534
-2066.57		835.1267	1.1721	5.1675	10.2534
-2066.75		853.8489	1.2205	5.5919	8.5750
-2066.94		851.6719	1.2217	5.6026	6.9783
-2067.12		850.7708	1.1789	5.6338	6.9783
-2067.3		842.1172	1.2030	5.6338	6.9886

#	DEPT	GAMMA	K	UR	TH
-2067.49		834.5017	1.2280	5.4686	8.5276
-2067.67		740.6371	1.1640	5.5340	7.1102
-2067.85		730.3950	1.0826	5.1161	7.1102
-2068.04		711.8704	0.9949	4.6137	7.9199
-2068.22		701.8721	0.9532	5.0062	8.8308
-2068.4		703.1427	0.9238	5.0870	9.8631
-2068.58		606.5993	0.8842	4.7537	7.7863
-2068.76		614.0841	0.8973	5.2476	6.7712
-2068.93		593.0690	0.9017	5.1833	7.8900
-2069.11		583.2756	0.9873	4.4545	9.2122
-2069.3		588.0187	0.8506	4.4447	5.8333
-2069.45		532.9548	0.8214	4.0935	3.1079
-2690.6		524.9428	1.2420	0.6533	9.5845
-2690.8		519.3751	1.2981	0.3909	8.5086
-2690.99		515.6177	1.3124	0.1688	7.5981
-2691.19		494.1300	1.2638	0.4972	8.8885
-2691.39		488.0267	1.2510	0.2976	10.0414
-2691.58		481.2869	1.1613	0.1230	9.2059
-2691.79		455.9489	1.2636	0.1158	6.9836
-2691.98		440.2959	1.2893	0.0000	6.9836
-2692.18		440.7412	1.1860	0.0697	6.9079
-2692.38		428.9995	1.1675	0.0919	5.2458
-2692.58		435.5718	1.2177	0.5292	3.5100
-2692.78		441.8771	1.1902	0.9418	3.5100
-2692.98		456.3618	1.2868	1.3678	3.5100
-2693.17		454.4783	1.3006	1.7750	3.5100
-2693.38		452.6400	1.3273	2.6471	3.5454
-2693.57		431.9500	1.2808	2.6471	5.2911
-2693.77		422.9018	1.1799	2.6471	5.2911
-2693.97		432.5882	1.2048	2.2211	7.0062
-2694.17		436.5871	1.1306	2.6559	7.0062
-2694.36		427.4000	1.0818	3.5253	7.0062
-2694.56		437.7859	1.1613	3.9939	5.3009
-2694.76		432.7335	1.1112	4.4198	6.9659
-2694.97		422.0265	1.0867	4.8598	8.7224
-2695.17		415.6429	1.0448	5.3092	10.5163
-2695.37		426.6976	1.1351	5.3092	10.5163
-2695.56		392.4376	1.1383	4.4622	8.8257
-2695.76		394.1476	1.1398	4.0237	8.8257
-2695.96		392.5641	1.1164	3.5864	12.3485
-2696.16		377.8194	1.1643	2.7244	12.3485
-2696.36		360.1911	1.0933	2.7321	12.3485
-2696.56		342.7811	1.1218	2.3248	12.3485
-2696.75		325.6335	1.0700	1.4527	12.2885
-2696.95		328.2143	0.9645	1.6995	11.4097
-2697.15		308.7833	0.9587	1.9792	10.4483
-2697.34		293.2599	0.9804	1.7709	11.4322
-2697.54		291.6376	1.0056	0.9623	12.5675
-2697.74		283.3283	0.9240	0.0000	13.8921
-2697.93		280.2954	0.9881	0.0000	10.2016
-2698.13		288.5079	1.1470	0.0000	8.5685
-2698.33		288.9621	1.0531	0.0000	6.5018
-2698.5		274.9149	0.9595	0.0000	7.7304

B.3 Mercury Intrusion Porosimetry Data Collected by Poro-Technology

Poro-Technology, Sugar Land, Texas, performed directional and omni-directional mercury capillary pressure measurements as described in Section 2.4.1. Data was provided in Microsoft Excel spreadsheet format and as a hard copy, which is reproduced here.

Poro-Technology

MERCURY INJECTION CAPILLARY PRESSURE (MICP) DATA REPORT

Company: Sandia Labs

**Samples/Well: 8 Kirtland Shale Core Samples;
(2048.35 – 2692.19ft)**

Job Ref. No.: SANDIA004

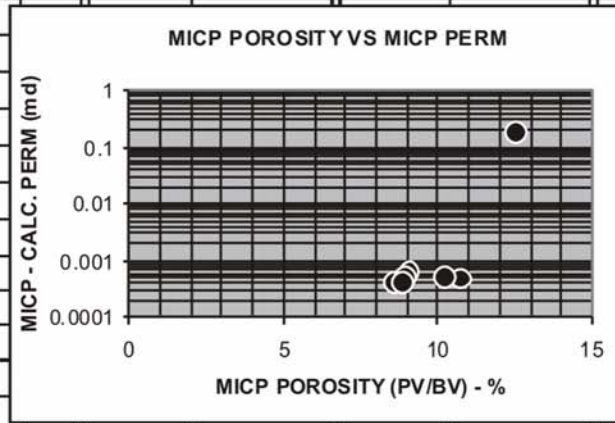
Date: October 20, 2008

**Provided By: John W. Neasham PhD
104 Industrial Blvd., Ste G
Sugar Land, Texas 77478 USA
281/240-3600 jnporotek@aol.com**

POROTECHNOLOGY: 10/2008

SPL ID: Kirtland Shale Core Samples

Sample\Depth	Tab No.	Sample Porosity(%)	Spl MICP Porosity(%)	Sample Air Perm(md)	Calc MICP Perm(md)	MICP Bulk Den(g/cc)	MICP Gr. Den (g/cc)
Plug parallel to bedding*	1	N/A	8.78	N/A	0.00043	2.433	2.667
Plug perpendicular to bed**	2		8.52		0.00043	2.435	2.661
Spl @ 2048.35ft	3		12.5		0.199	2.24	2.56
@ 2052.35ft	4		10.7		0.00051	2.342	2.623
@ 2055.37ft	5		10.2		0.00054	2.397	2.669
@ 2062.40ft	6		9.02		0.00065	2.412	2.652
@ 2068.05ft	7		8.89		0.00054	2.416	2.652
@ 2692.19ft	8		8.84		0.00045	2.455	2.694



NOTE 1: All samples were dried at ~100C prior to MICP testing. Additionally, selected samples may have been subsampled and/or examined under a binocular microscope for proper MICP analysis. * Denotes spls jacketed with epoxy.

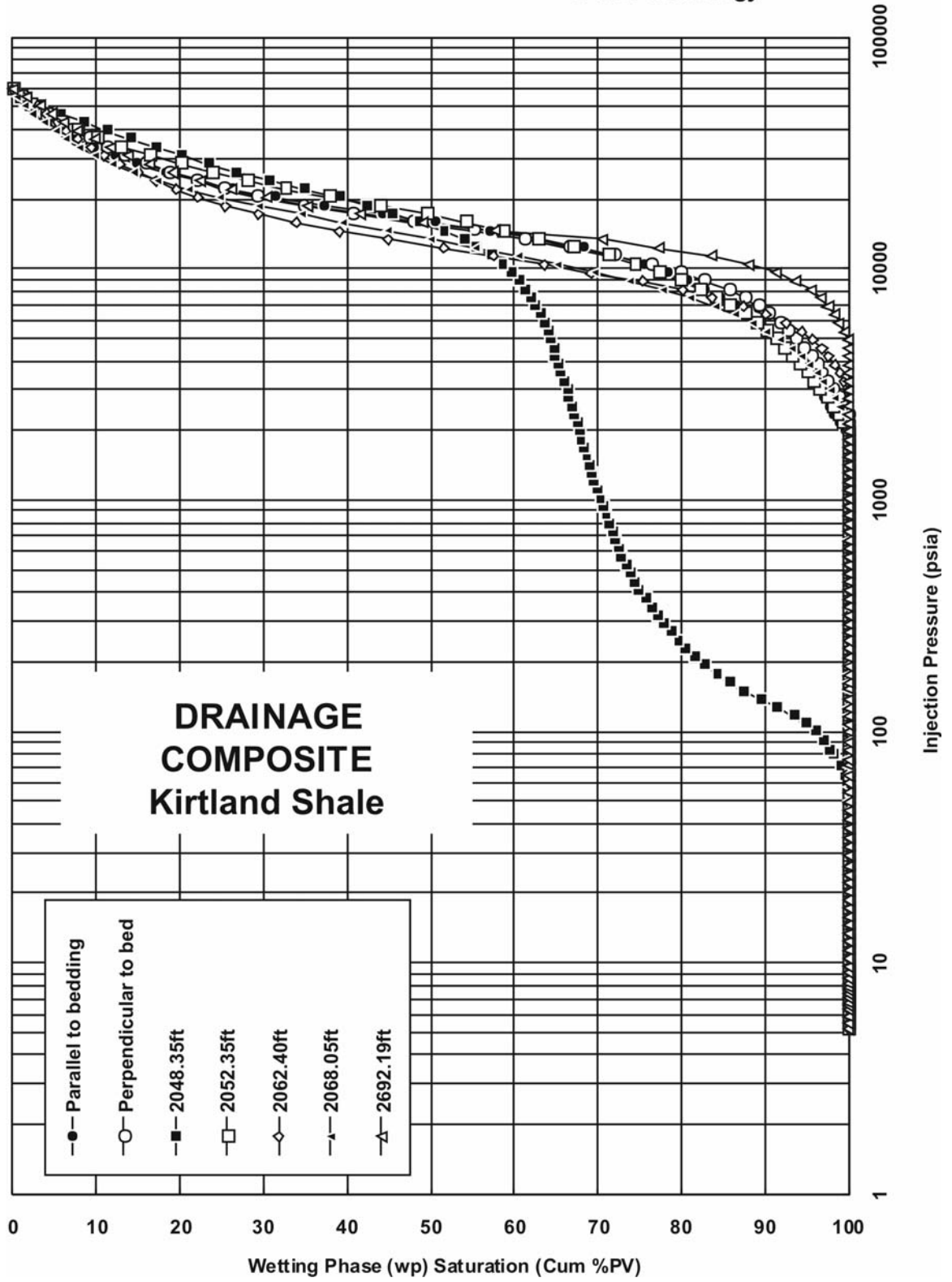
OTHER Pc SYSTEMS

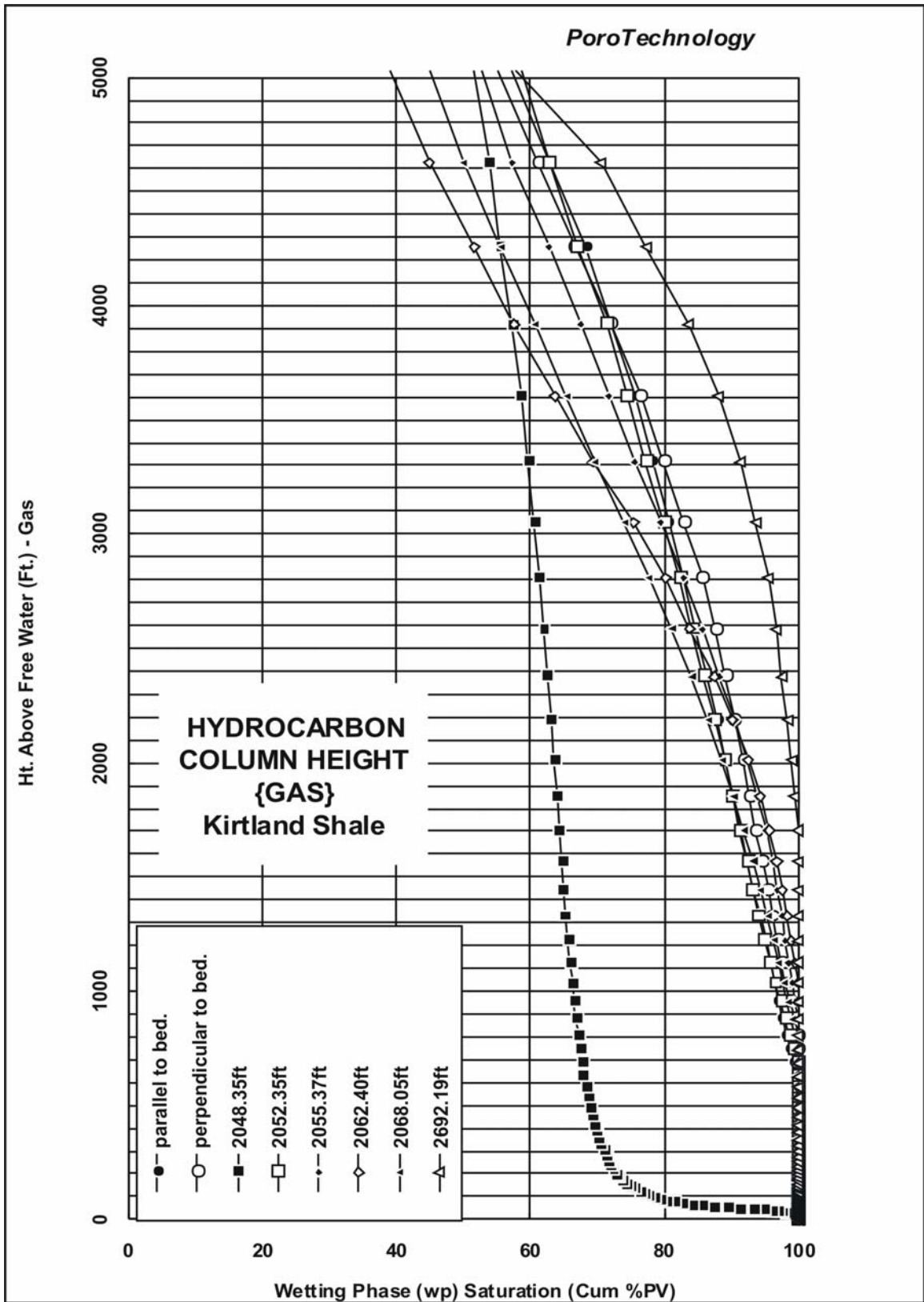
Pc gas/brine =	0.1	$[(50/480)X(1.766) X Pc air/Hg]$
Pc gas/oil =	0.1	$[(24/480)X(1.766) X Pc air/Hg]$
Pc oil/brine =	0.1	$[(30/480)X(1.766) X Pc air/Hg]$

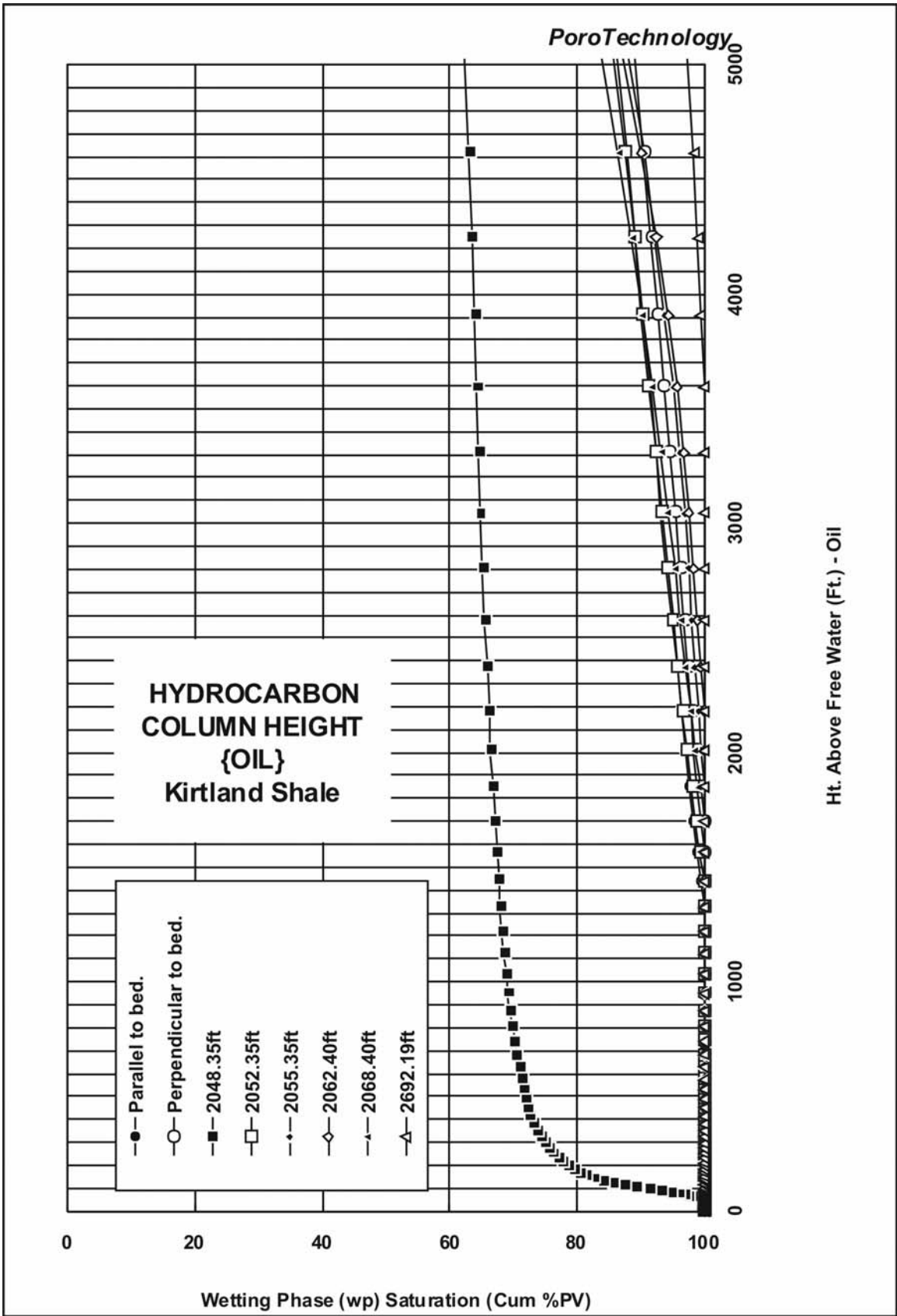
HEIGHT ABOVE FREE WATER(FT)		Brine Density = 1.11g/cc
Height(gas/brine)=	0.3	(X Pc air/Hg) Gas Density = 0.20g/cc
Height(oil/brine) =	0.7	(X Pc air/Hg) Oil Density = 0.85g/cc

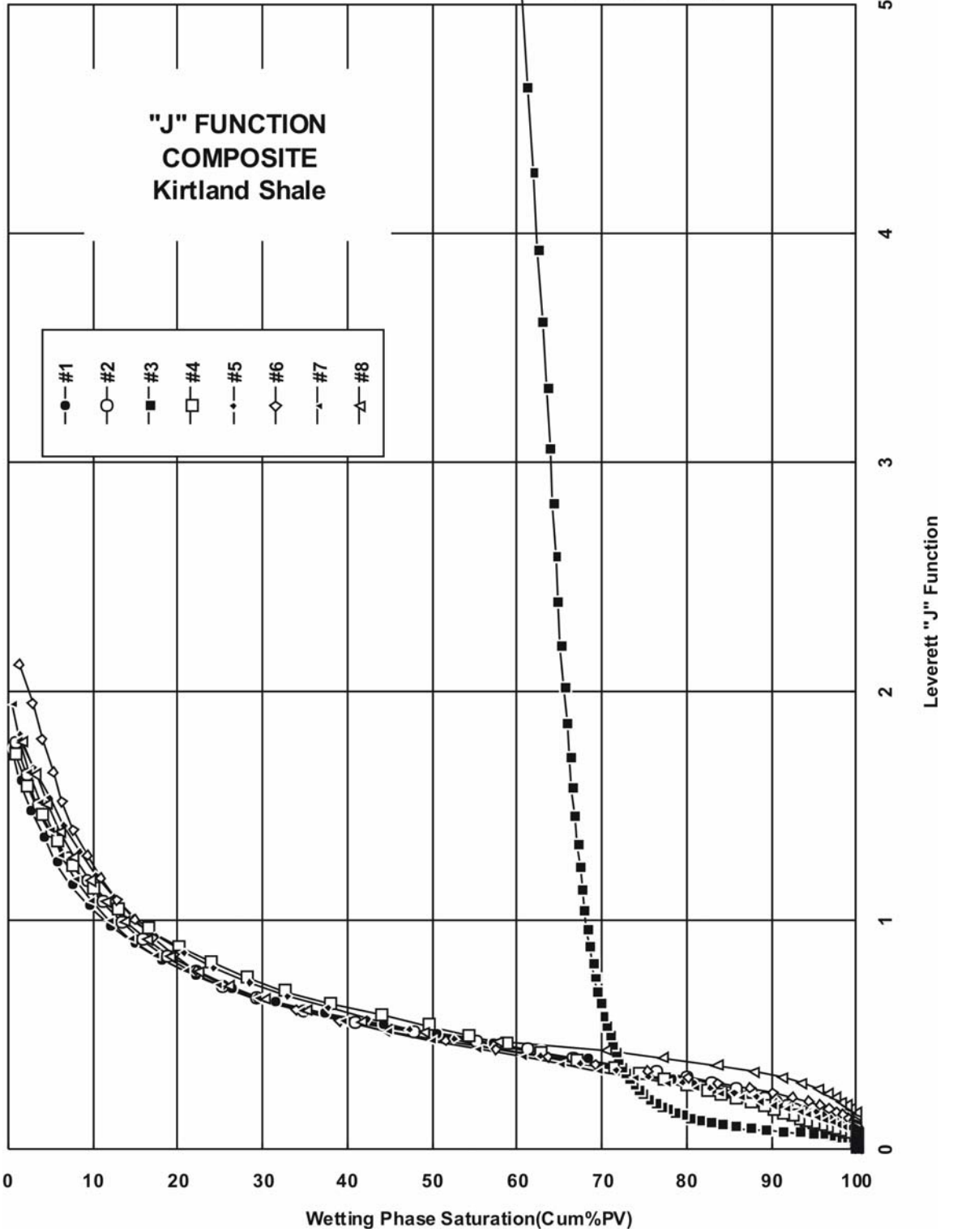
NOTE: SPL PERM(CALC) = Air Perm(md) = Max value of (Sb/Pc); To 1.691 power; Multiply by 39 (After SWANSON, SPE 8234, 1978)

NOTE: Leverett "J" Function = $[(k/por.) X 0.5 exp.] X Pc(PSIA) X 0.2166] / 480$
 {The "k" value used for J-Funct. calculations on the "RPTx" tables is that provided by client (ie, client's PPGD data). If such data not provided, then "MICP-Calculated" k value used. Th "por."(porosity) value used is the "MICP" porosity measured @ 60000psia.









AIR|MERCURY CAPILLARY PRESSURE DATA : BY PoroTechnology

Jacketed Plug Parallel to Bedding

MICP Closure(psia) = 1820.

MICP Porosity = 8.78%

MICP Gr. Den.(gm\cc) = 2.667

Spl Bulk Density = 2.433 gm/cc

MICP-Calc. Air Perm = 0.00043 md

Median Pore Aperture Dia.(microns) = 0.0134

Injection Pressure (psia)	Pore Diameter (microns)	Hg (nwp) Saturation cum%PV	100-Hg(wp) Saturation cum%PV	Leverett "J" Function	Gas/Brine Pc (psia)	Gas/Oil Pc (psia)	Oil/Brine Pc (psia)	Ht. Above Free Water (ft.)	
								Gas/Brine	Oil/Brine
5.19	41.12	0.0	100.0	0.00	0.71	0.34	0.43	1.8	3.8
5.49	38.86	0.0	100.0	0.00	0.75	0.36	0.45	1.9	4.0
5.84	36.54	0.0	100.0	0.00	0.79	0.38	0.48	2.0	4.3
6.24	34.20	0.0	100.0	0.00	0.85	0.41	0.51	2.2	4.5
6.49	32.87	0.0	100.0	0.00	0.88	0.42	0.53	2.2	4.7
6.74	31.66	0.0	100.0	0.00	0.92	0.44	0.55	2.3	4.9
7.04	30.31	0.0	100.0	0.00	0.96	0.46	0.58	2.4	5.1
7.34	29.08	0.0	100.0	0.00	1.00	0.48	0.60	2.5	5.3
7.59	28.11	0.0	100.0	0.00	1.03	0.49	0.62	2.6	5.5
7.84	27.22	0.0	100.0	0.00	1.07	0.51	0.64	2.7	5.7
8.19	26.06	0.0	100.0	0.00	1.11	0.53	0.67	2.8	6.0
8.54	24.99	0.0	100.0	0.00	1.16	0.56	0.70	2.9	6.2
9.08	23.50	0.0	100.0	0.00	1.23	0.59	0.74	3.1	6.6
9.61	22.21	0.0	100.0	0.00	1.31	0.62	0.79	3.3	7.0
10.44	20.44	0.0	100.0	0.00	1.42	0.68	0.86	3.6	7.6
11.35	18.80	0.0	100.0	0.00	1.54	0.74	0.93	3.9	8.3
12.33	17.30	0.0	100.0	0.00	1.68	0.80	1.01	4.3	9.0
13.40	15.92	0.0	100.0	0.00	1.82	0.87	1.10	4.6	9.8
14.57	14.64	0.0	100.0	0.00	1.98	0.95	1.19	5.0	10.6
15.83	13.47	0.0	100.0	0.00	2.15	1.03	1.30	5.5	11.5
17.21	12.40	0.0	100.0	0.00	2.34	1.12	1.41	5.9	12.5
18.70	11.41	0.0	100.0	0.00	2.54	1.22	1.53	6.5	13.6
20.32	10.50	0.0	100.0	0.00	2.76	1.32	1.67	7.0	14.8
22.09	9.66	0.0	100.0	0.00	3.00	1.44	1.81	7.6	16.1
24.01	8.89	0.0	100.0	0.00	3.27	1.56	1.97	8.3	17.5
26.09	8.18	0.0	100.0	0.00	3.55	1.70	2.14	9.0	19.0
28.96	7.37	0.0	100.0	0.00	3.94	1.88	2.37	10.0	21.1
31.74	6.72	0.0	100.0	0.00	4.32	2.06	2.60	11.0	23.1
34.76	6.137	0.0	100.0	0.00	4.73	2.26	2.85	12.0	25.3
38.06	5.605	0.0	100.0	0.00	5.18	2.47	3.12	13.1	27.7
41.56	5.133	0.0	100.0	0.00	5.65	2.70	3.41	14.3	30.3
45.89	4.648	0.0	100.0	0.00	6.24	2.98	3.76	15.8	33.4
48.61	4.389	0.0	100.0	0.00	6.61	3.16	3.99	16.8	35.4
55.22	3.863	0.0	100.0	0.00	7.51	3.59	4.53	19.1	40.2
59.56	3.581	0.0	100.0	0.00	8.10	3.87	4.88	20.5	43.4
64.90	3.287	0.0	100.0	0.00	8.83	4.22	5.32	22.4	47.2

AIR|MERCURY CAPILLARY PRESSURE DATA : BY PoroTechnology

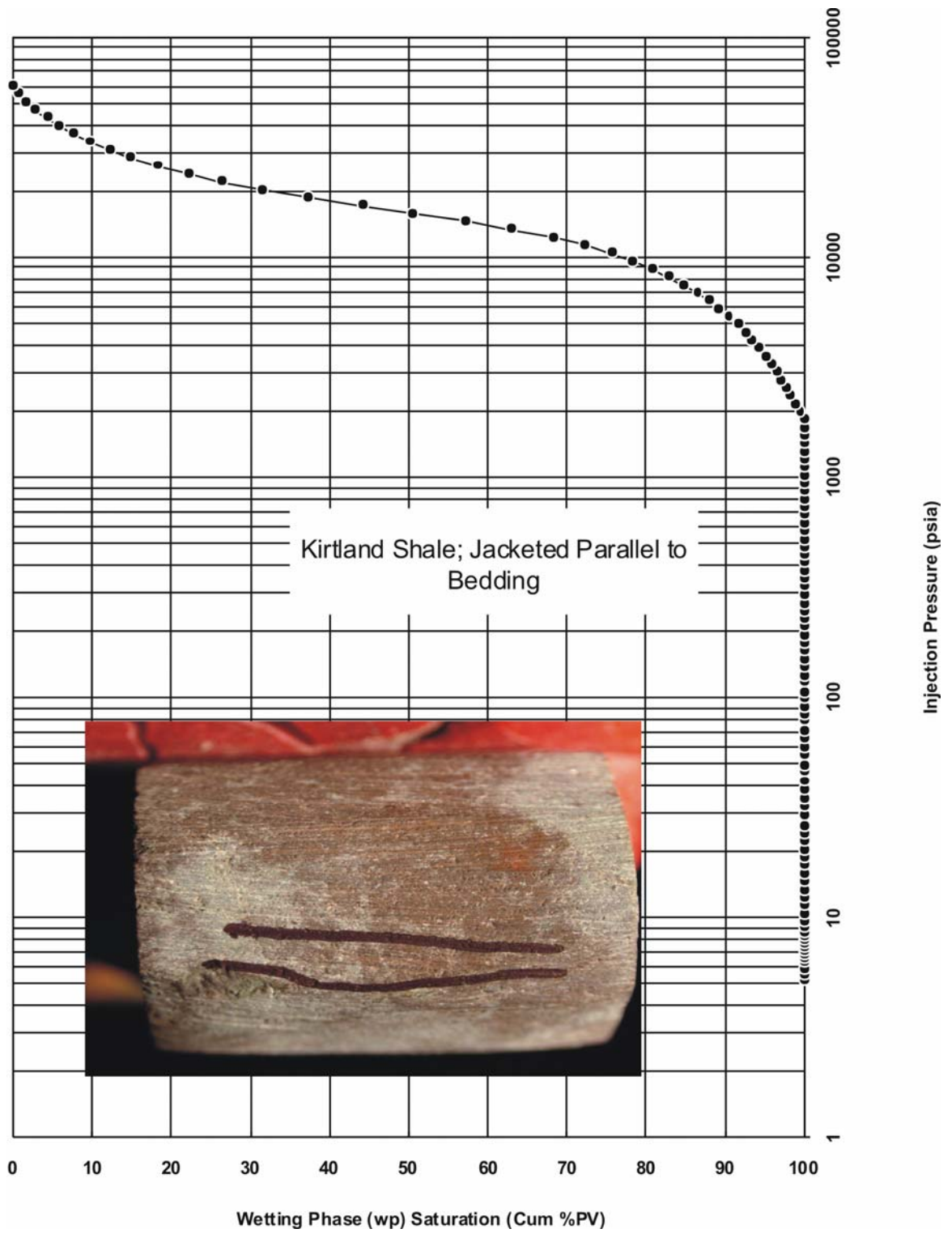
Jacketed Plug Parallel to Bedding

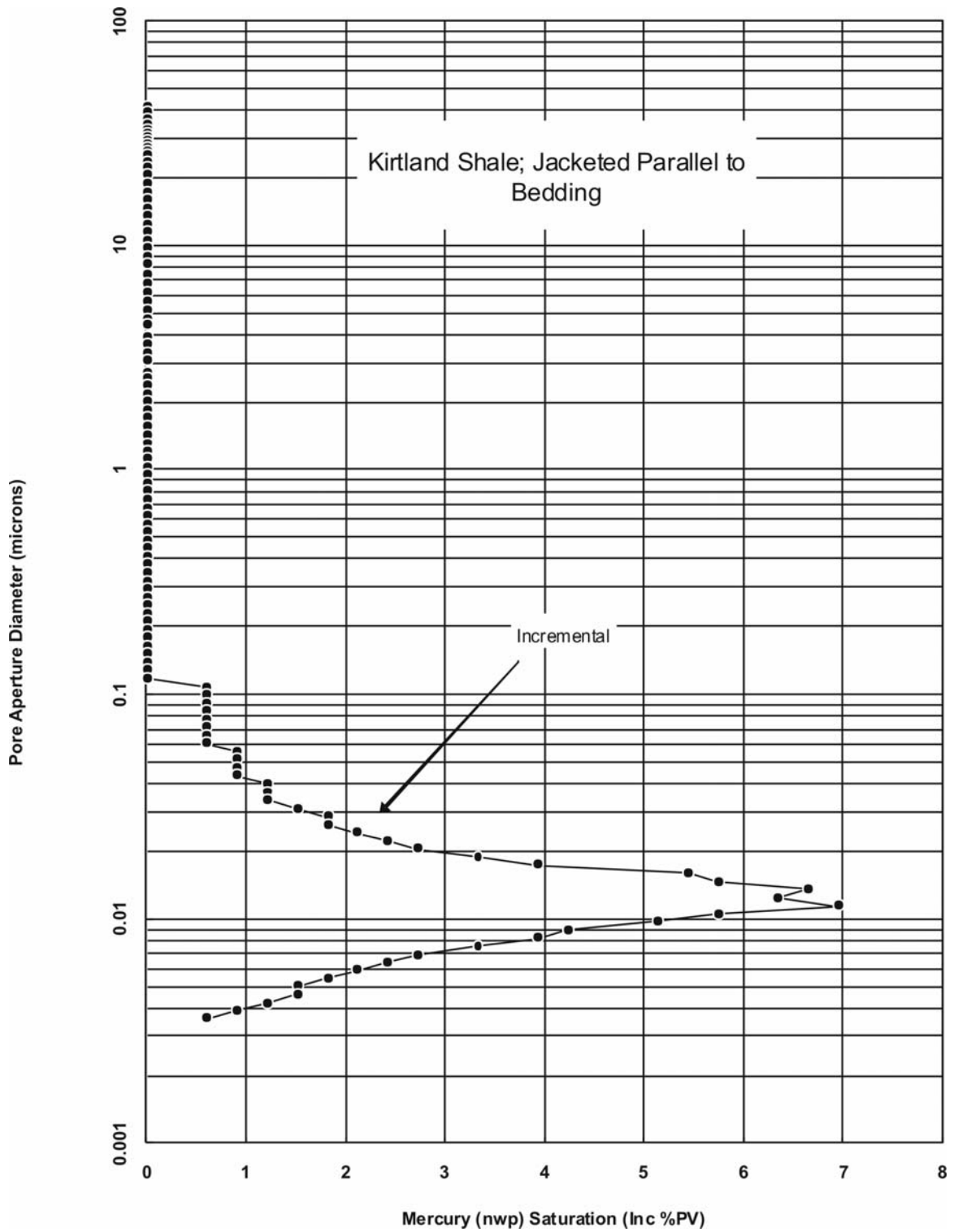
Injection Pressure (psia)	Pore Diameter (microns)	Hg (nwp) Saturation cum%PV	100-Hg(wp) Saturation cum%PV	Leverett "J" Function	Gas/Brine Pc (psia)	Gas/Oil Pc (psia)	Oil/Brine Pc (psia)	Ht. Above	Ht. Above
								Free Water (ft.)	Free Water (ft.)
								Gas/Brine	Oil/Brine
69.90	3.052	0.0	100.0	0.00	9.51	4.54	5.73	24.1	50.9
78.74	2.709	0.0	100.0	0.00	10.71	5.12	6.46	27.2	57.3
83.75	2.547	0.0	100.0	0.00	11.39	5.44	6.87	28.9	61.0
90.66	2.353	0.0	100.0	0.00	12.33	5.89	7.43	31.3	66.0
98.76	2.160	0.0	100.0	0.00	13.43	6.42	8.10	34.1	71.9
106.05	2.012	0.0	100.0	0.00	14.4	6.89	8.70	36.6	77.2
117.17	1.821	0.0	100.0	0.00	15.9	7.62	9.61	40.4	85.3
125.48	1.700	0.0	100.0	0.00	17.1	8.16	10.29	43.3	91.3
137.84	1.548	0.0	100.0	0.00	18.7	8.96	11.30	47.6	100.3
149.41	1.428	0.0	100.0	0.00	20.3	9.71	12.25	51.5	108.8
163.47	1.305	0.0	100.0	0.01	22.2	10.63	13.40	56.4	119.0
178.08	1.198	0.0	100.0	0.01	24.2	11.58	14.60	61.4	129.6
190.89	1.118	0.0	100.0	0.01	26.0	12.41	15.65	65.9	139.0
208.12	1.025	0.0	100.0	0.01	28.3	13.53	17.07	71.8	151.5
226.59	0.942	0.0	100.0	0.01	30.8	14.73	18.6	78.2	165.0
246.64	0.865	0.0	100.0	0.01	33.5	16.03	20.2	85.1	180
266.74	0.800	0.0	100.0	0.01	36.3	17.34	21.9	92.0	194
289.44	0.737	0.0	100.0	0.01	39.4	18.8	23.7	99.9	211
316.70	0.674	0.0	100.0	0.01	43.1	20.6	26.0	109.3	231
343.46	0.621	0.0	100.0	0.01	46.7	22.3	28.2	118.5	250
373.40	0.571	0.0	100.0	0.01	50.8	24.3	30.6	129	272
408.03	0.523	0.0	100.0	0.01	55.5	26.5	33.5	141	297
441.22	0.484	0.0	100.0	0.01	60.0	28.7	36.2	152	321
479.59	0.445	0.0	100.0	0.02	65.2	31.2	39.3	165	349
520.31	0.410	0.0	100.0	0.02	70.8	33.8	42.7	180	379
566.70	0.376	0.0	100.0	0.02	77.1	36.8	46.5	196	413
615.34	0.347	0.0	100.0	0.02	83.7	40.0	50.5	212	448
670.82	0.318	0.0	100.0	0.02	91.2	43.6	55.0	231	488
729.10	0.293	0.0	100.0	0.02	99.2	47.4	59.8	252	531
791.27	0.270	0.0	100.0	0.02	107.6	51.4	64.9	273	576
859.45	0.248	0.0	100.0	0.03	116.9	55.9	70.5	297	626
933.65	0.229	0.0	100.0	0.03	127.0	60.7	76.6	322	680
1014.20	0.210	0.0	100.0	0.03	137.9	65.9	83.2	350	738
1102.76	0.193	0.0	100.0	0.03	150.0	71.7	90.4	380	803
1201.67	0.178	0.0	100.0	0.04	163.4	78.1	98.5	415	875
1303.10	0.164	0.0	100.0	0.04	177.2	84.7	106.9	450	949
1416.12	0.151	0.0	100.0	0.04	192.6	92.0	116.1	489	1031
1542.27	0.138	0.0	100.0	0.05	209.7	100.2	126.5	532	1123
1672.23	0.128	0.0	100.0	0.05	227.4	108.7	137.1	577	1217
1819.52	0.117	0.0	100.0	0.06	247.5	118.3	149.2	628	1325
1977.77	0.108	0.6	99.4	0.06	269.0	128.6	162.2	682	1440
2149.68	0.099	1.2	98.8	0.07	292.4	139.7	176.3	742	1565
2336.09	0.091	1.8	98.2	0.07	317.7	151.8	191.6	806	1701
2537.54	0.0841	2.4	97.6	0.08	345.1	164.9	208.1	875	1847

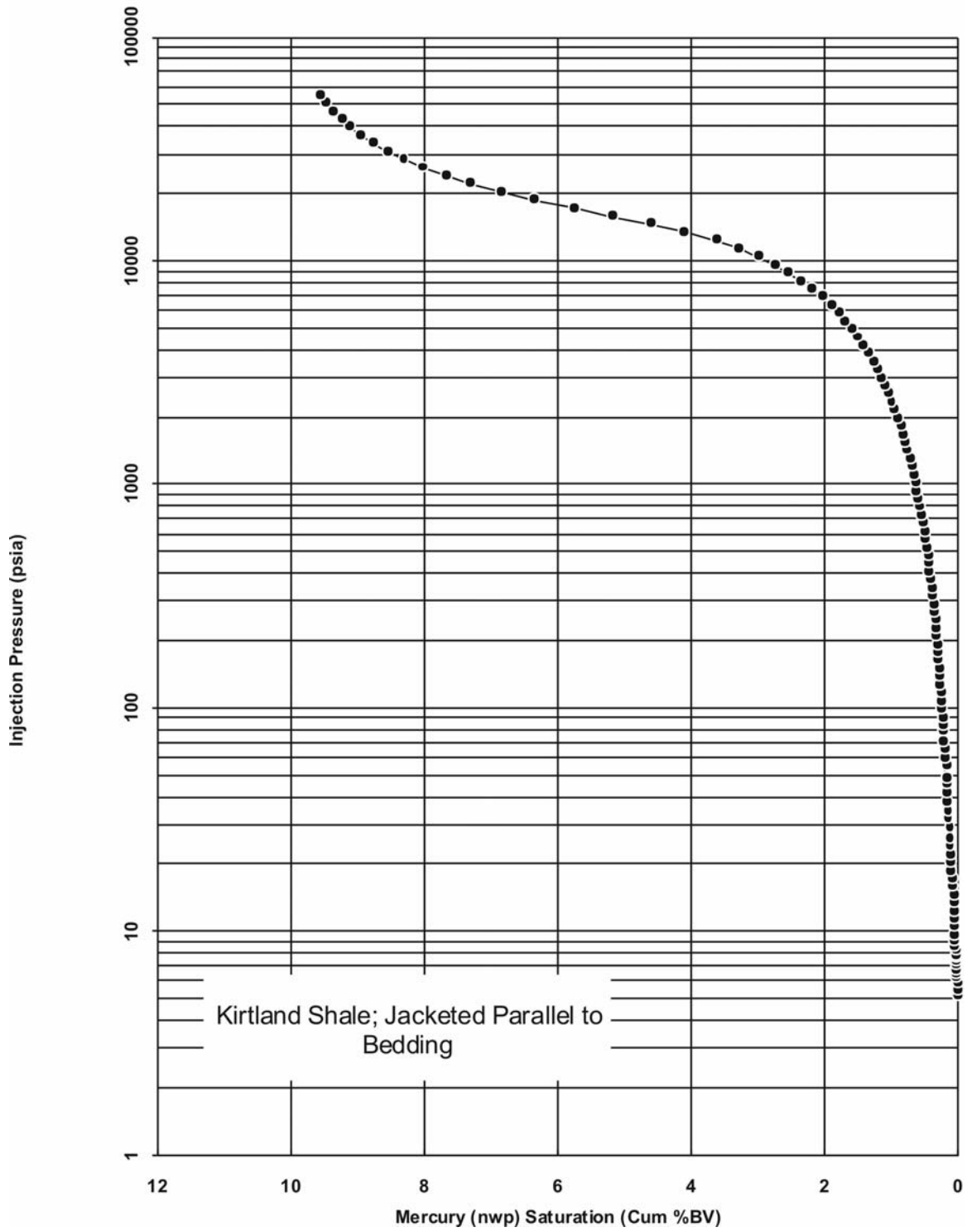
AIR/MERCURY CAPILLARY PRESSURE DATA : BY PoroTechnology

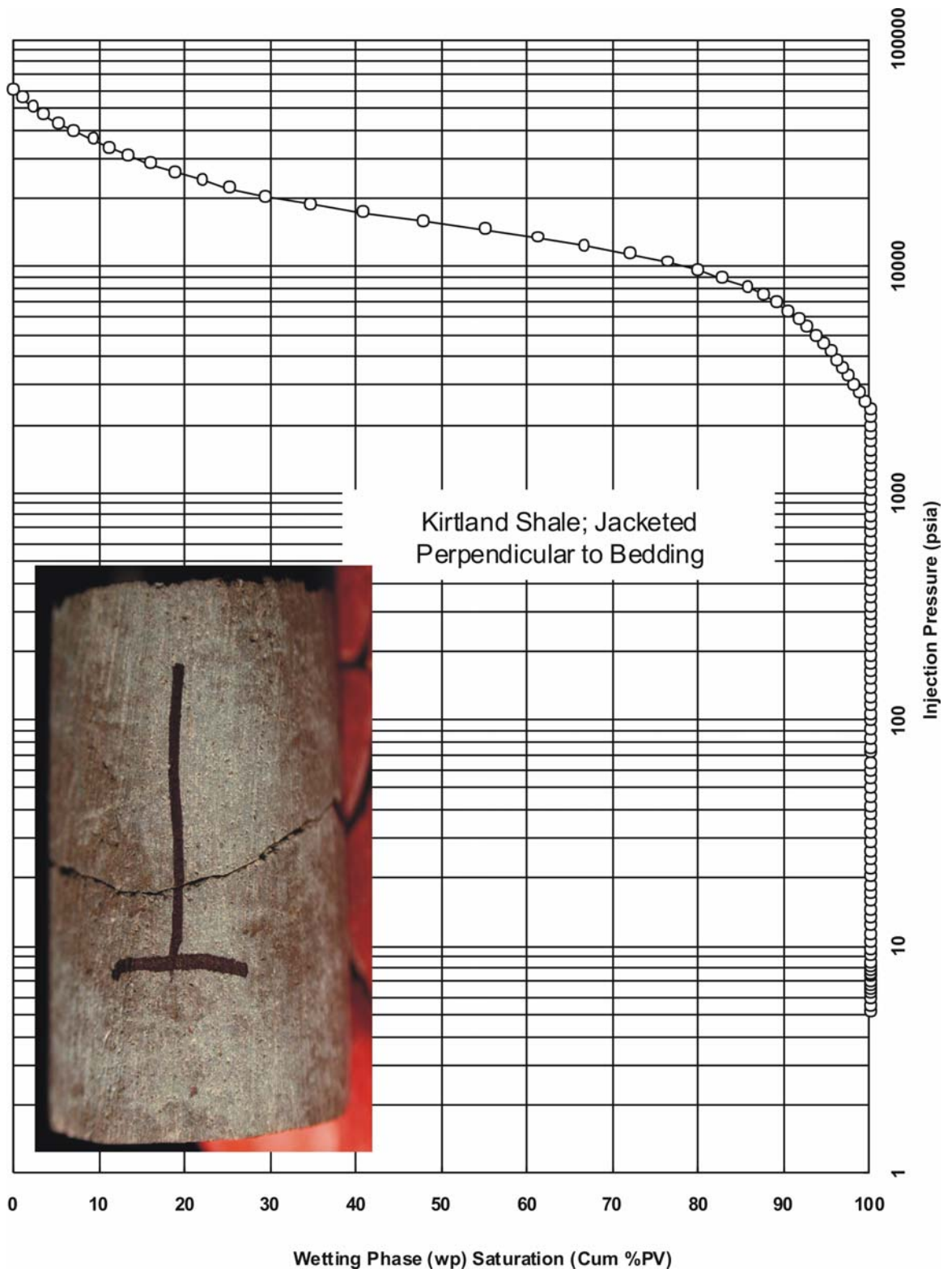
Jacketed Plug Parallel to Bedding

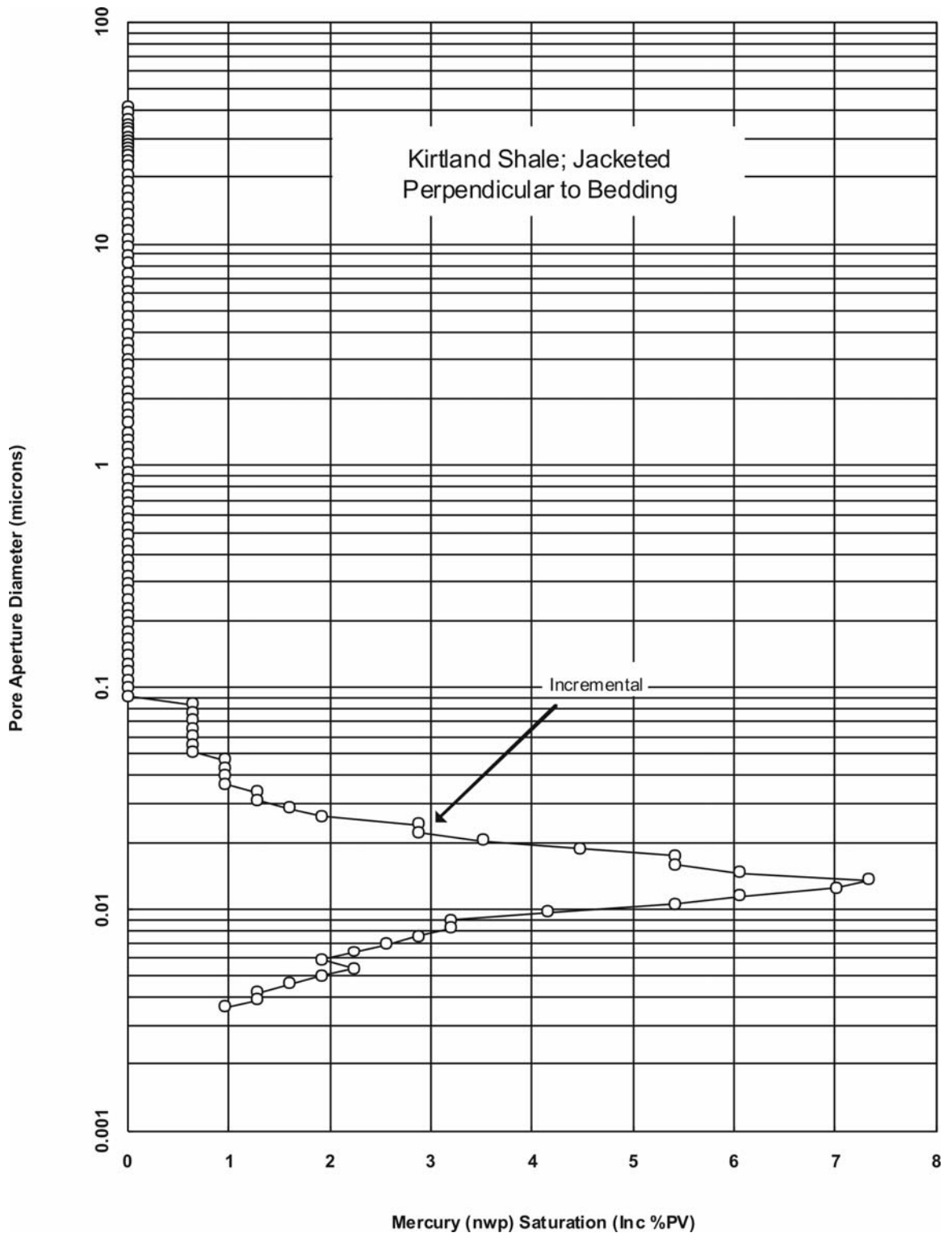
Injection Pressure (psia)	Pore Diameter (microns)	Hg (nwp) Saturation cum%PV	100-Hg(wp) Saturation cum%PV	Leverett "J" Function	Gas/Brine Pc (psia)	Gas/Oil Pc (psia)	Oil/Brine Pc (psia)	Ht. Above Free Water	Ht. Above Free Water
								(ft.) Gas/Brine	(ft.) Oil/Brine
2760.55	0.0773	3.0	97.0	0.09	375.4	179.4	226.4	952	2010
2996.28	0.0712	3.6	96.4	0.09	407.5	194.8	245.7	1034	2181
3256.51	0.0655	4.2	95.8	0.10	442.9	211.7	267.0	1123	2371
3537.98	0.0603	4.8	95.2	0.11	481.2	230.0	290.1	1221	2576
3851.07	0.0554	5.7	94.3	0.12	523.7	250.3	315.8	1329	2804
4179.97	0.0510	6.6	93.4	0.13	568.5	271.7	342.8	1442	3043
4544.44	0.0469	7.6	92.4	0.14	618.0	295.4	372.6	1568	3308
4939.21	0.0432	8.5	91.5	0.16	671.7	321.0	405.0	1704	3596
5368.60	0.0397	9.7	90.3	0.17	730.1	349.0	440.2	1852	3908
5834.39	0.0366	10.9	89.1	0.18	793.5	379.2	478.4	2013	4247
6338.73	0.0337	12.1	87.9	0.20	862.1	412.0	519.8	2187	4615
6888.21	0.0310	13.6	86.4	0.22	936.8	447.7	564.8	2376	5015
7487.09	0.0285	15.4	84.6	0.24	1018	486.7	613.9	2583	5451
8138.55	0.0262	17.2	82.8	0.26	1107	529.0	667.4	2808	5925
8845.11	0.0241	19.3	80.7	0.28	1203	574.9	725.3	3052	6439
9612.22	0.0222	21.8	78.2	0.30	1307	624.8	788.2	3316	6998
10447.48	0.0204	24.5	75.5	0.33	1421	679.1	856.7	3604	7606
11353.03	0.0188	27.8	72.2	0.36	1544	737.9	930.9	3917	8265
12339.43	0.0173	31.7	68.3	0.39	1678	802.1	1011.8	4257	8983
13411.54	0.0159	37.2	62.8	0.42	1824	871.8	1099.7	4627	9764
14575.33	0.0146	42.9	57.1	0.46	1982	947.4	1195.2	5028	10611
15839.78	0.0135	49.5	50.5	0.50	2154	1029.6	1299	5465	11531
17215.75	0.0124	55.9	44.1	0.54	2341	1119.0	1412	5939	12533
18710.59	0.0114	62.8	37.2	0.59	2545	1216.2	1534	6455	13621
20333.80	0.0105	68.6	31.4	0.64	2765	1322	1667	7015	14803
22098.41	0.0097	73.7	26.3	0.70	3005	1436	1812	7624	16088
24017.81	0.0089	77.9	22.1	0.76	3266	1561	1969	8286	17485
26101.46	0.0082	81.9	18.1	0.82	3550	1697	2140	9005	19002
28368.62	0.0075	85.2	14.8	0.90	3858	1844	2326	9787	20652
30830.17	0.0069	87.9	12.1	0.97	4193	2004	2528	10636	22444
33504.97	0.0064	90.3	9.7	1.06	4557	2178	2747	11559	24392
36415.91	0.0059	92.4	7.6	1.15	4953	2367	2986	12563	26511
39573.81	0.0054	94.3	5.7	1.25	5382	2572	3245	13653	28810
43008.77	0.0050	95.8	4.2	1.36	5849	2796	3527	14838	31310
46741.96	0.0046	97.3	2.7	1.48	6357	3038	3833	16126	34028
50798.15	0.0042	98.5	1.5	1.60	6909	3302	4165	17525	36981
55206.60	0.0039	99.4	0.6	1.74	7508	3588	4527	19046	40190
59990.63	0.0036	100.0	0.0	1.89	8159	3899	4919	20697	43673

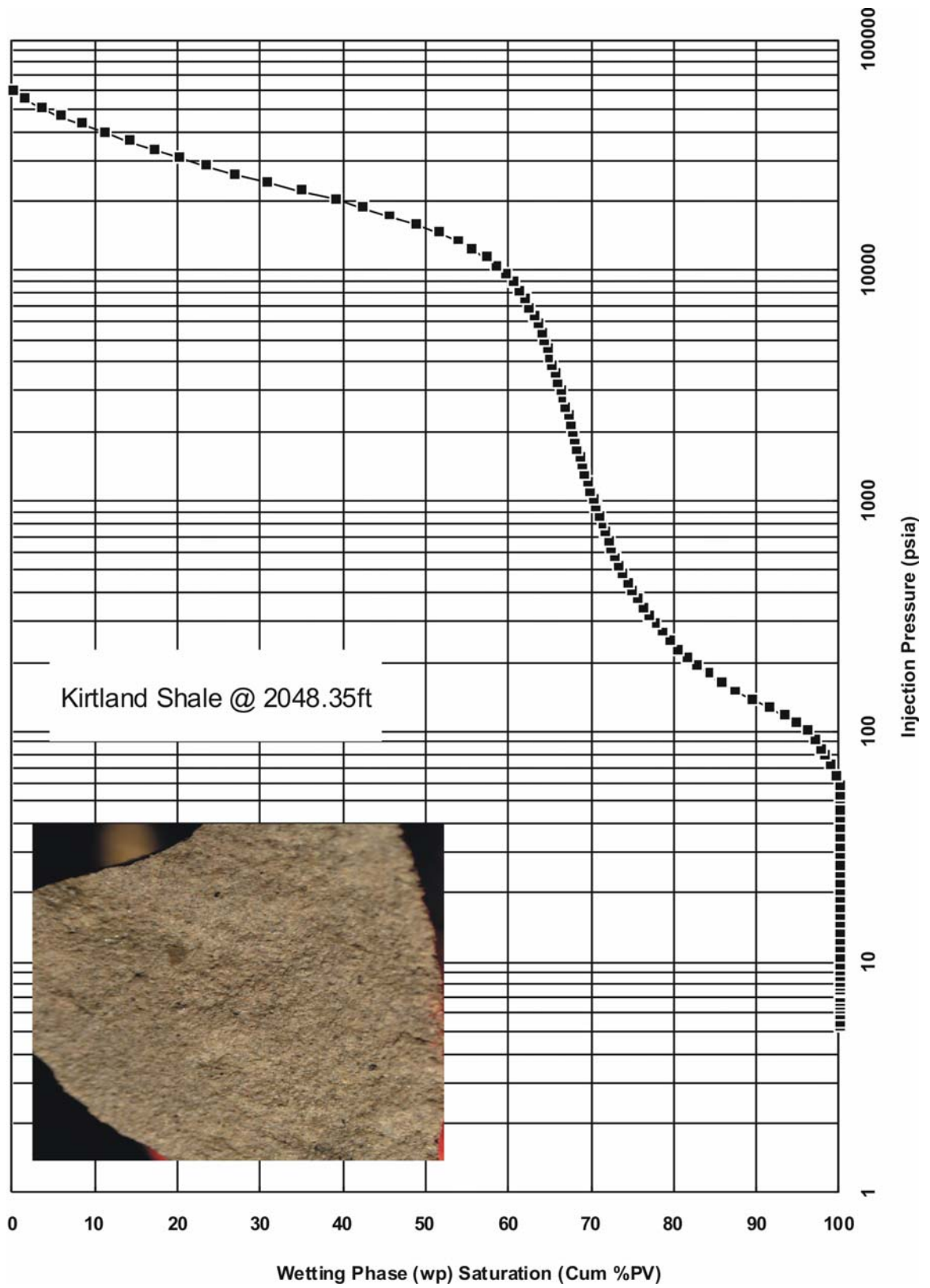


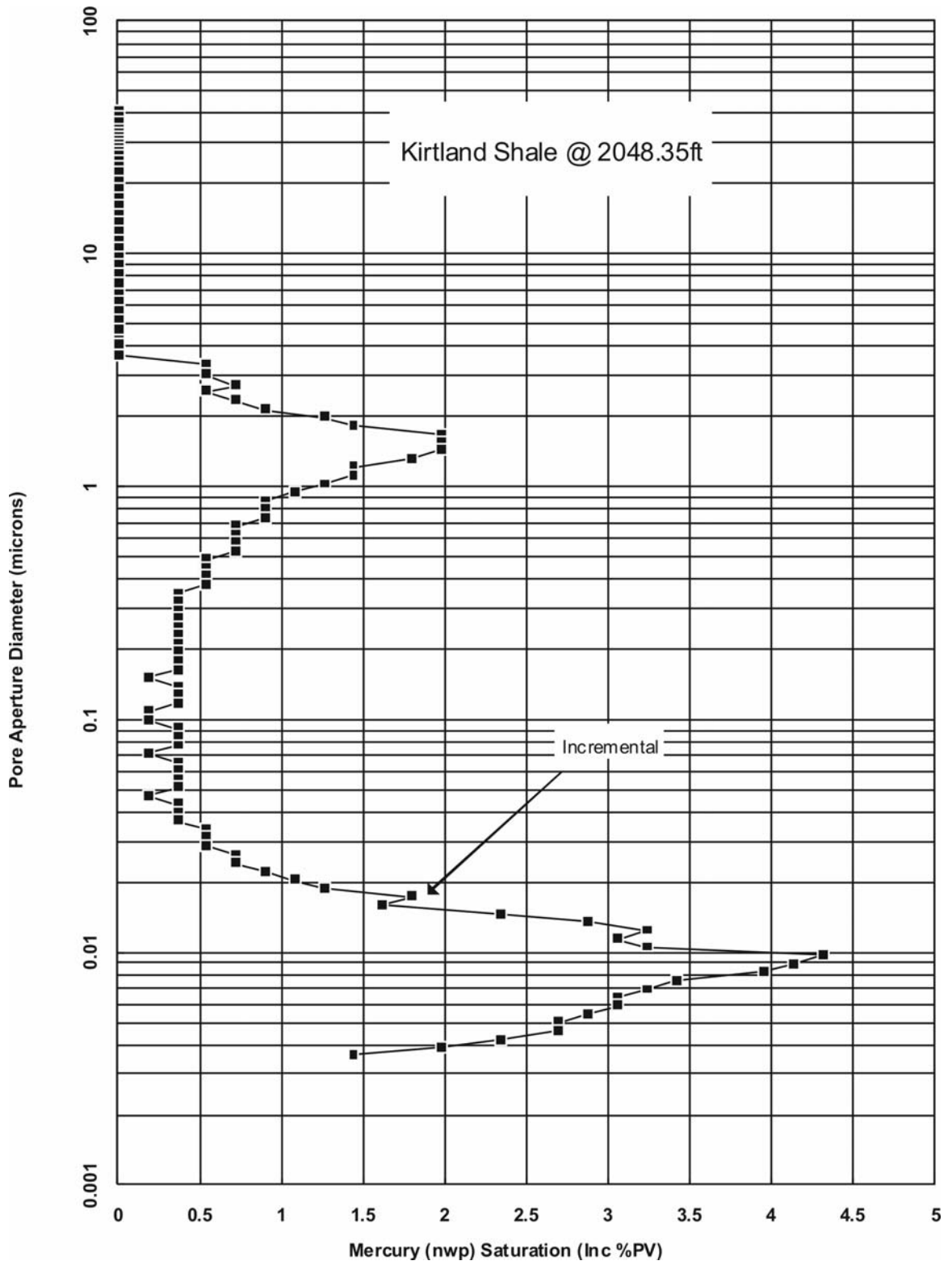


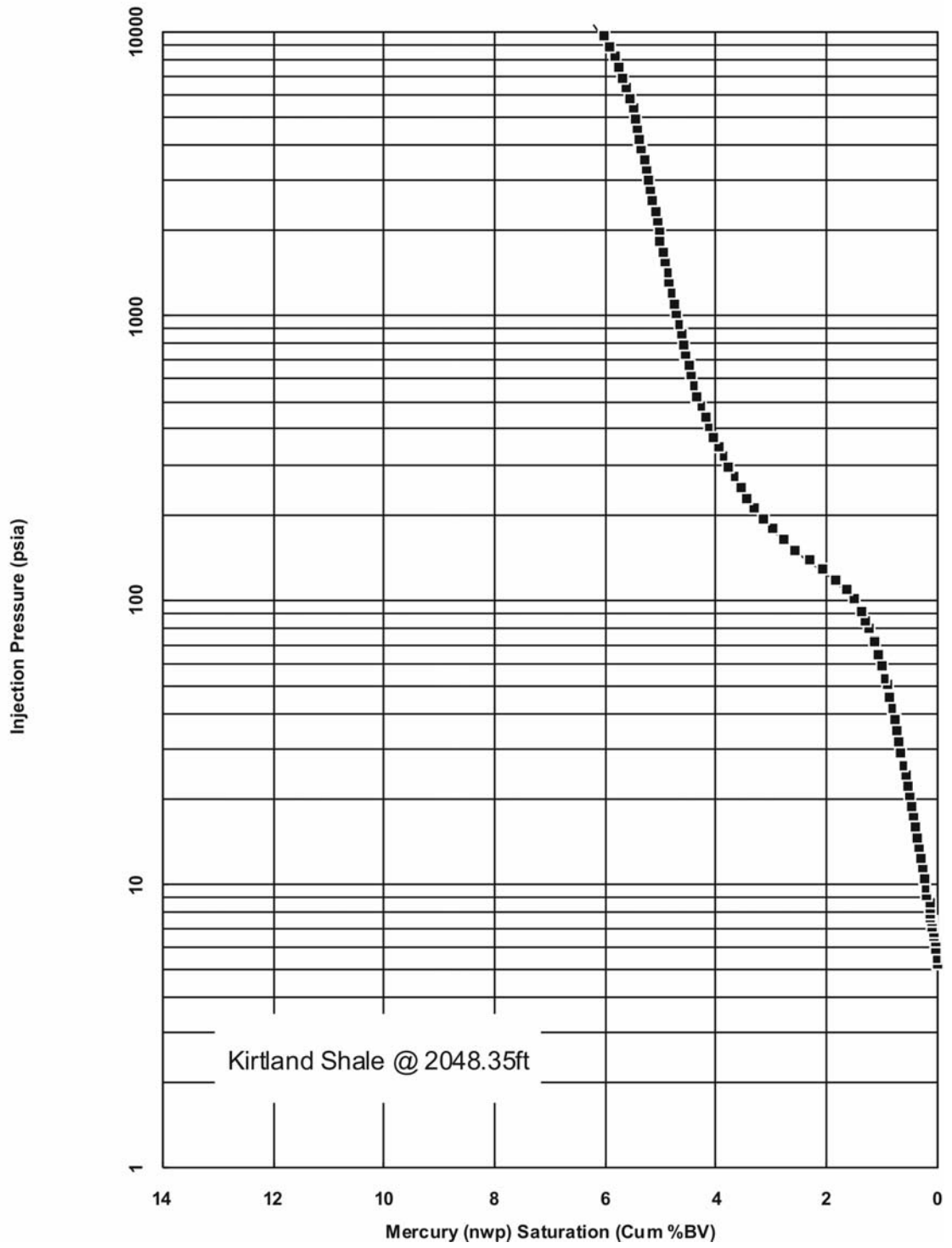


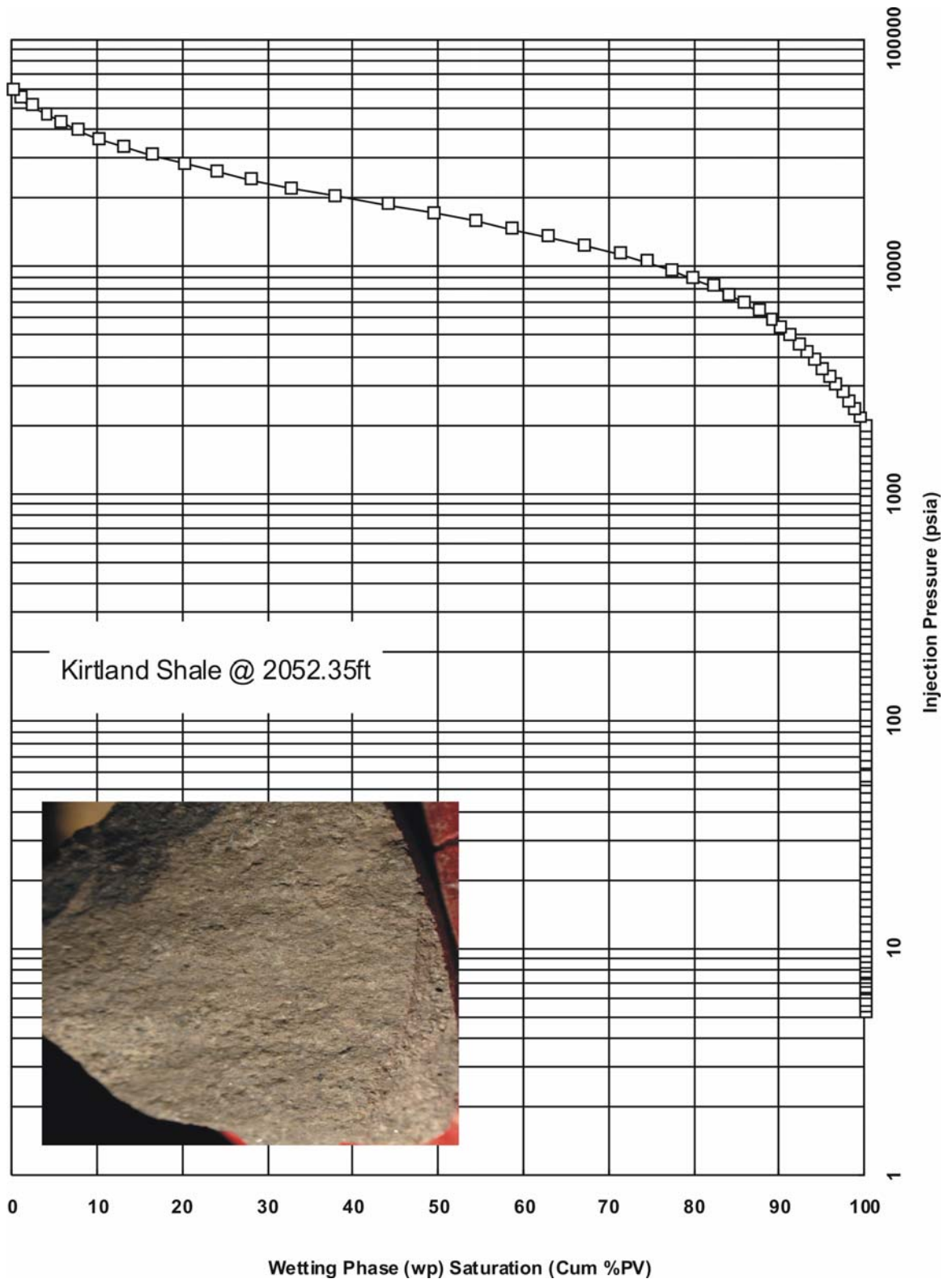


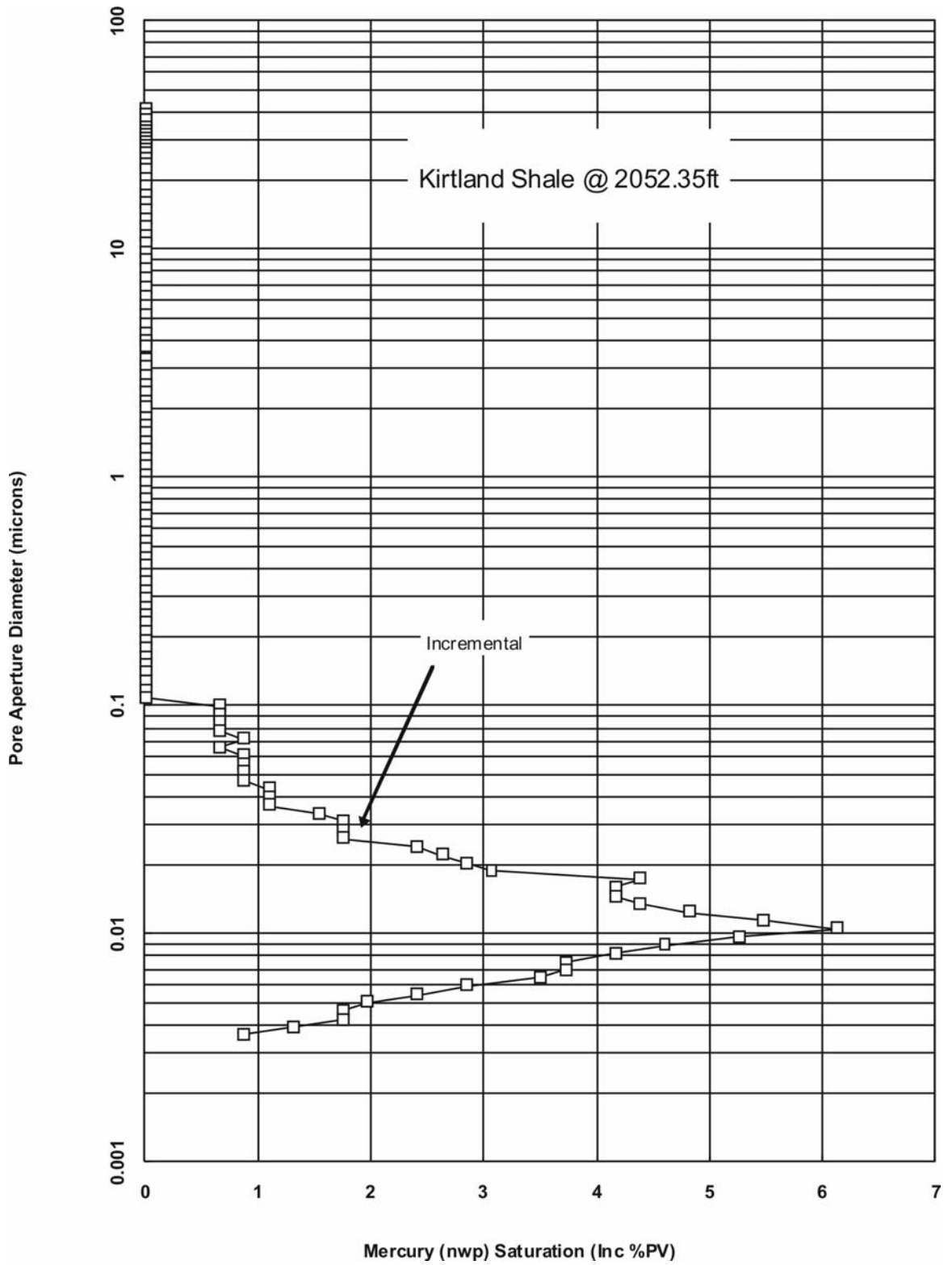


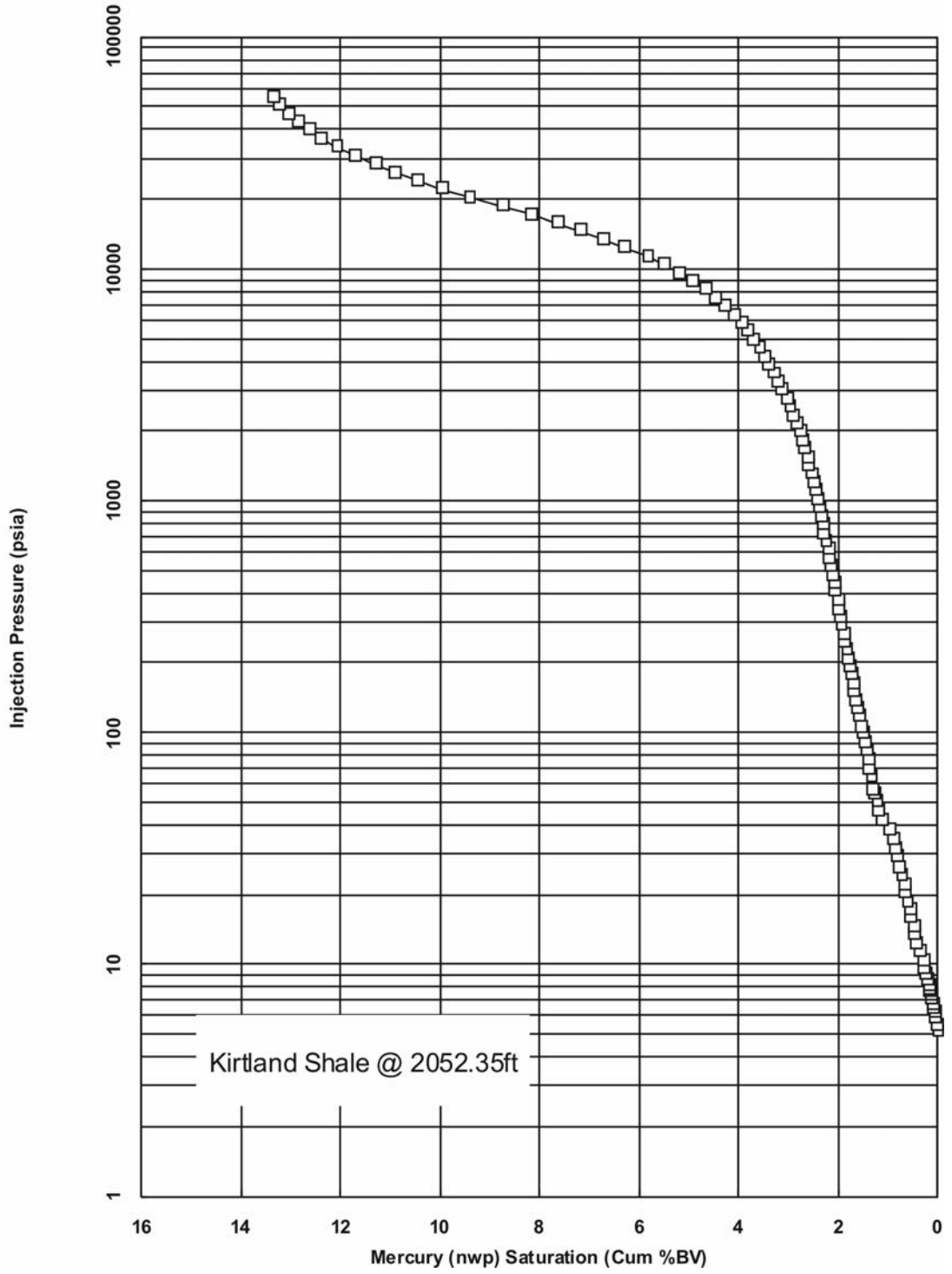


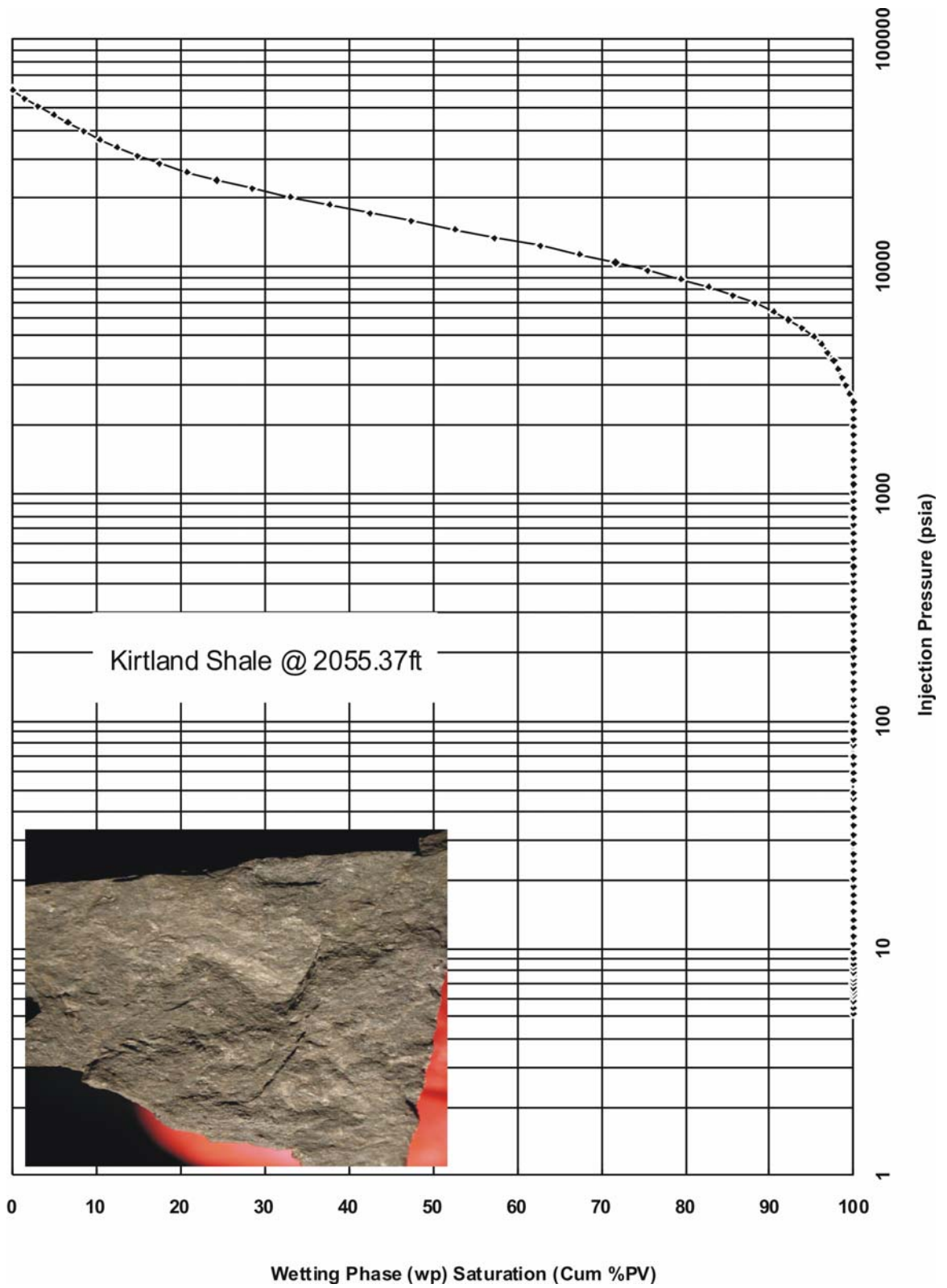


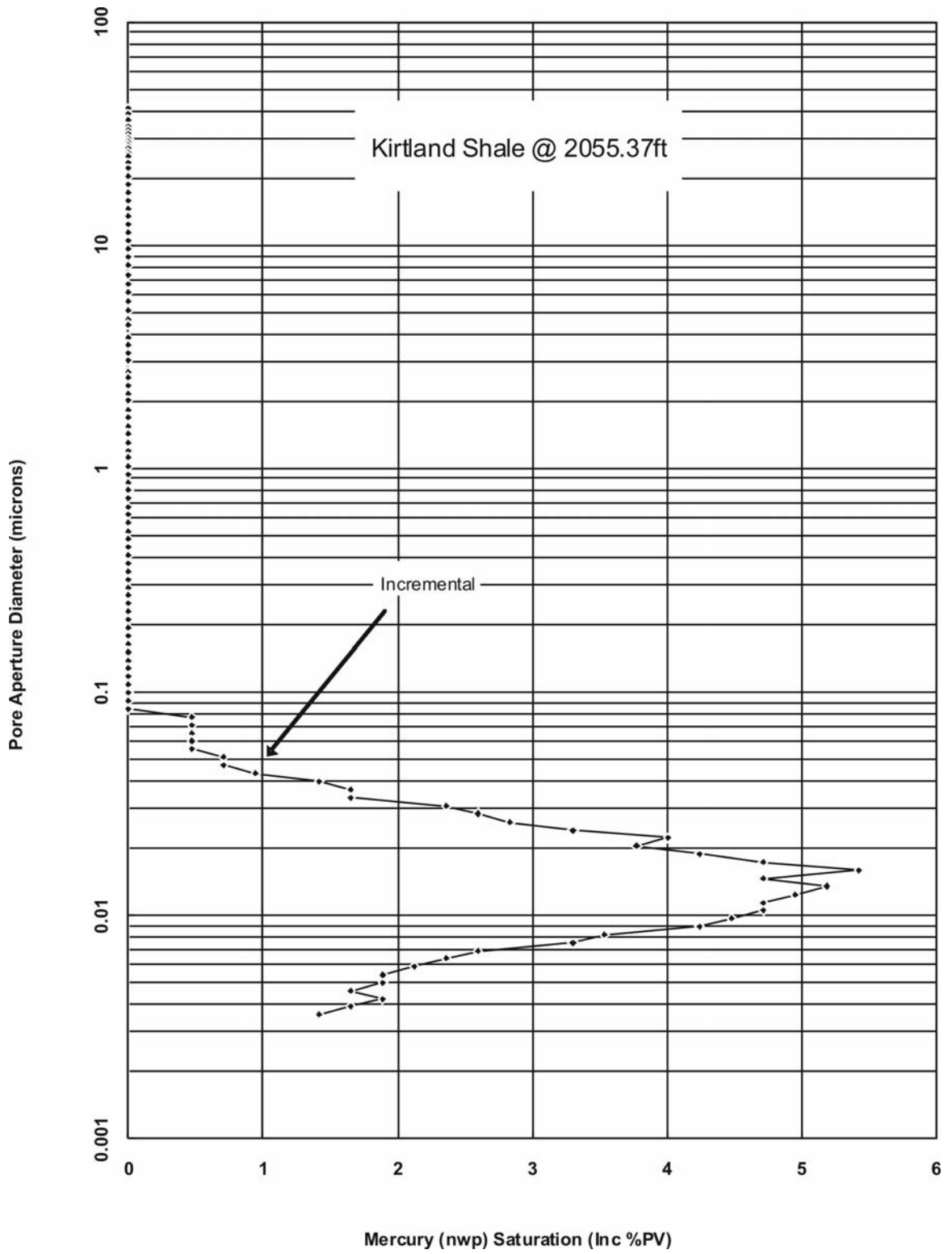


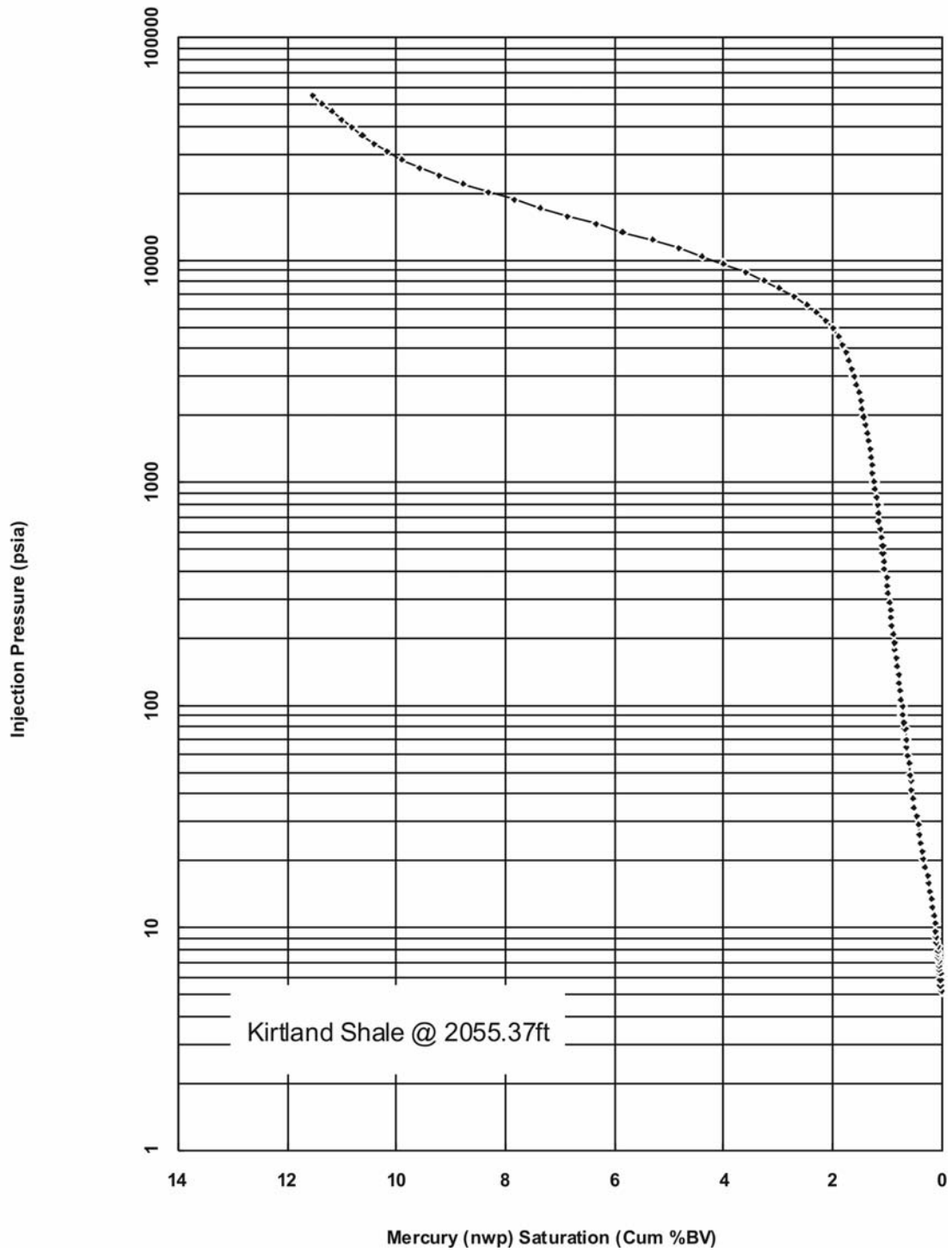


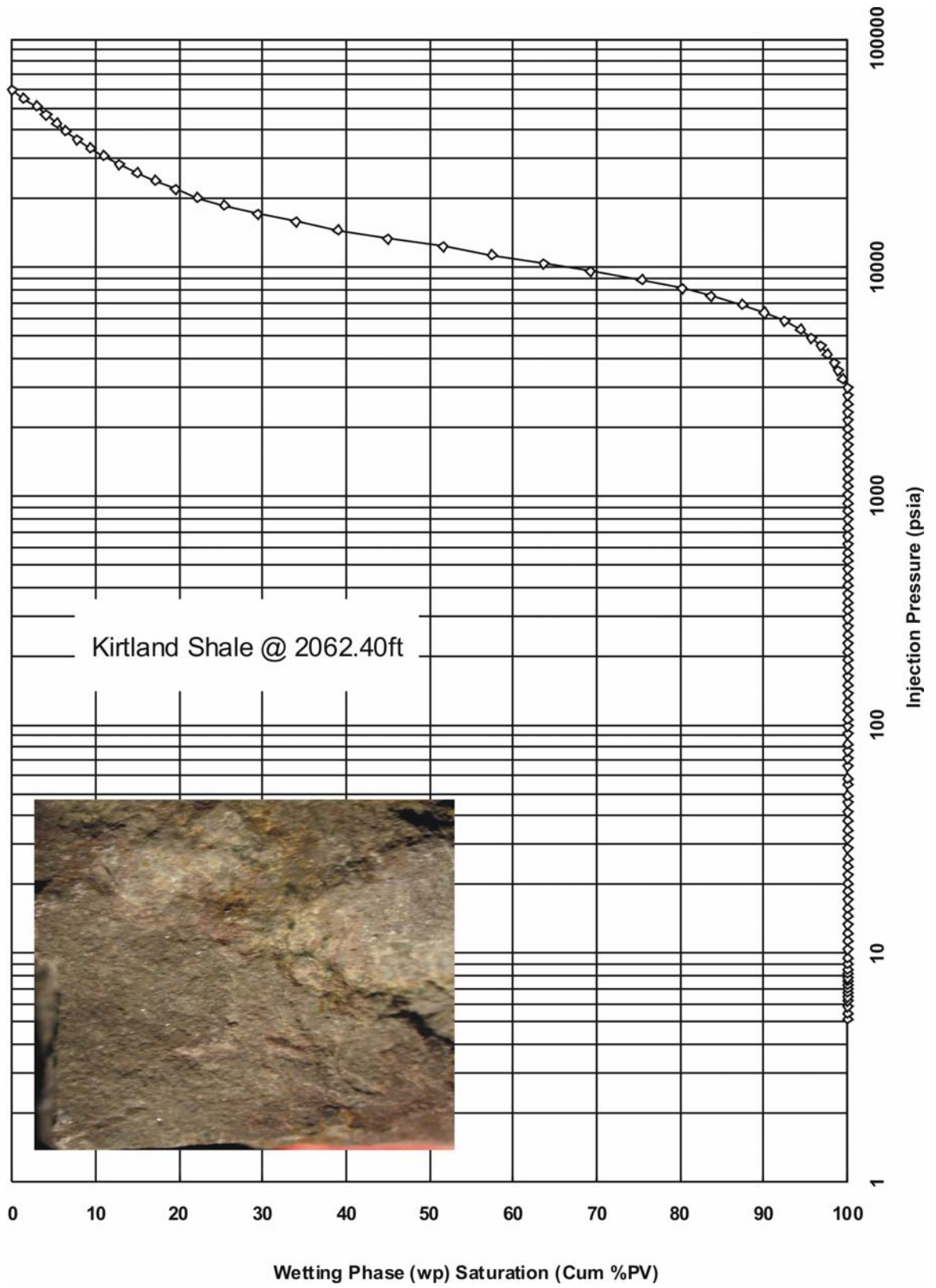


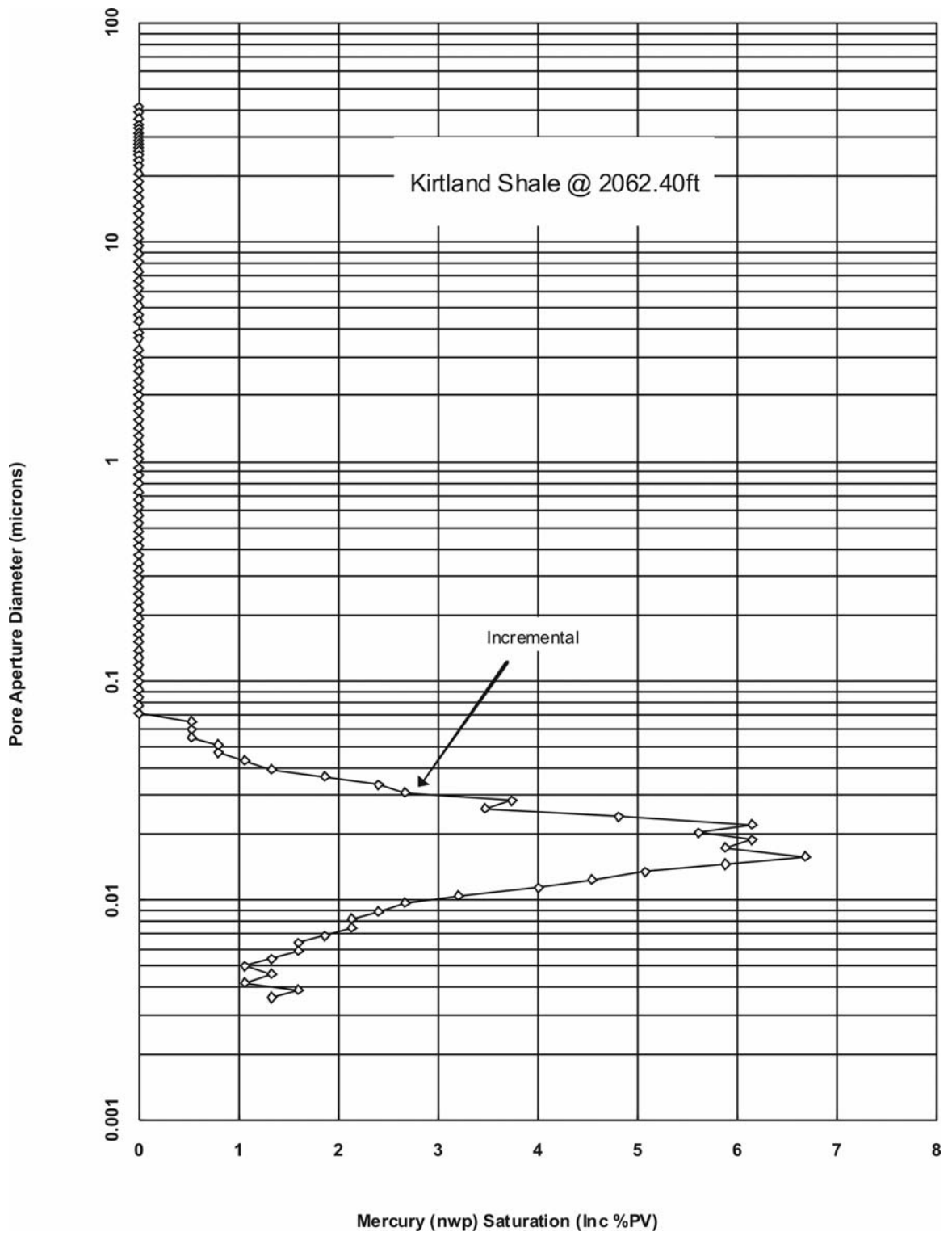


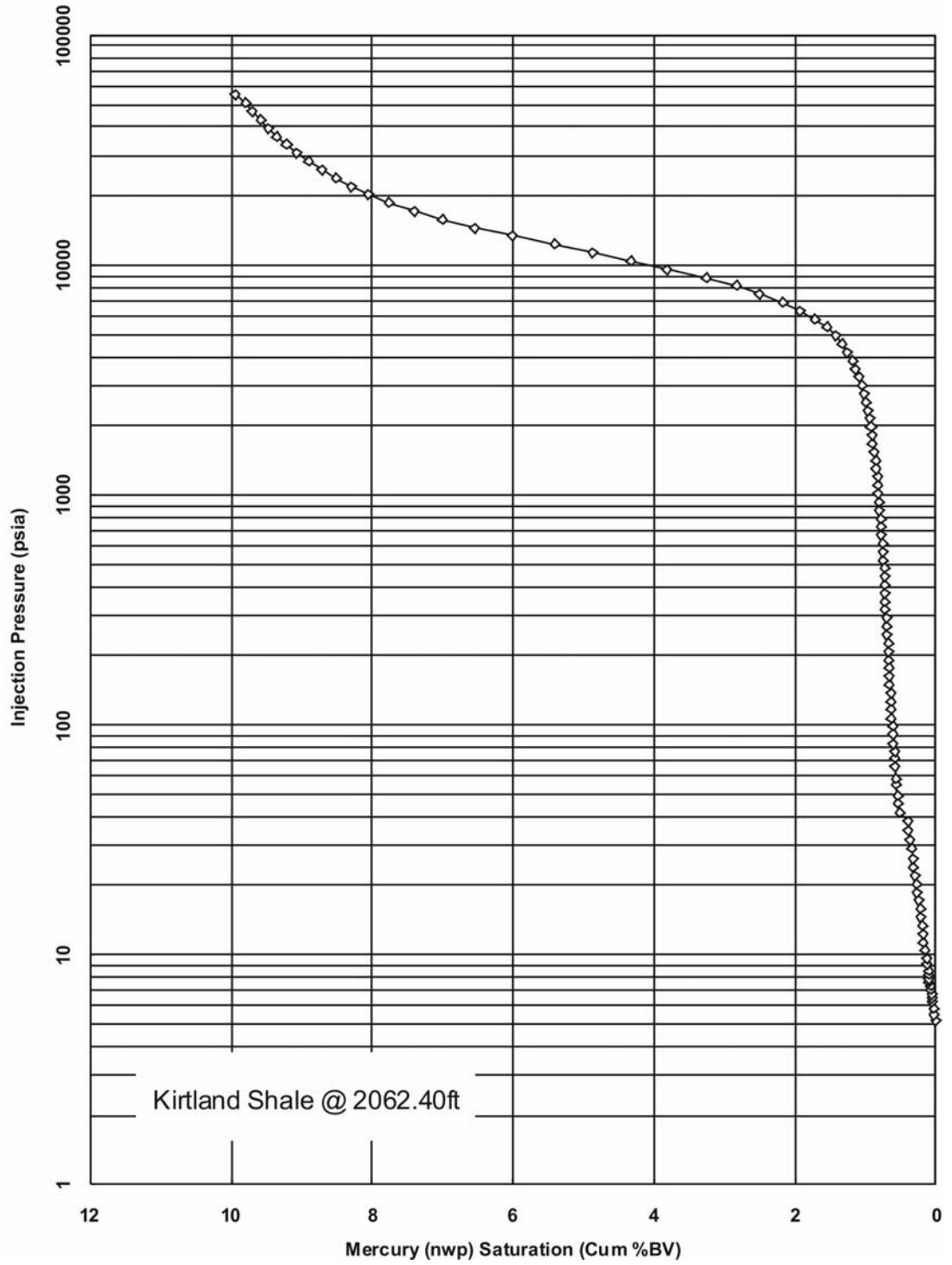


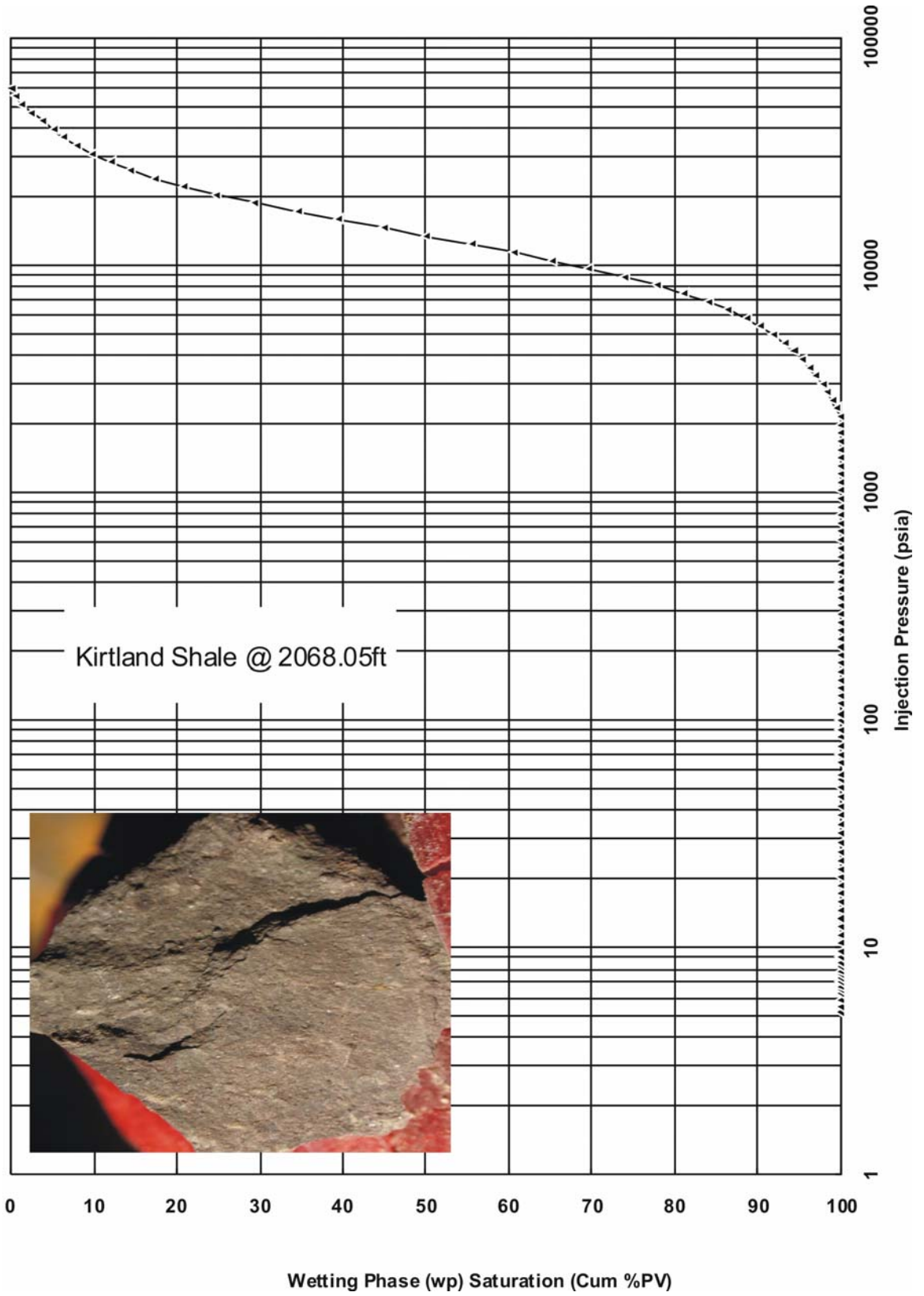


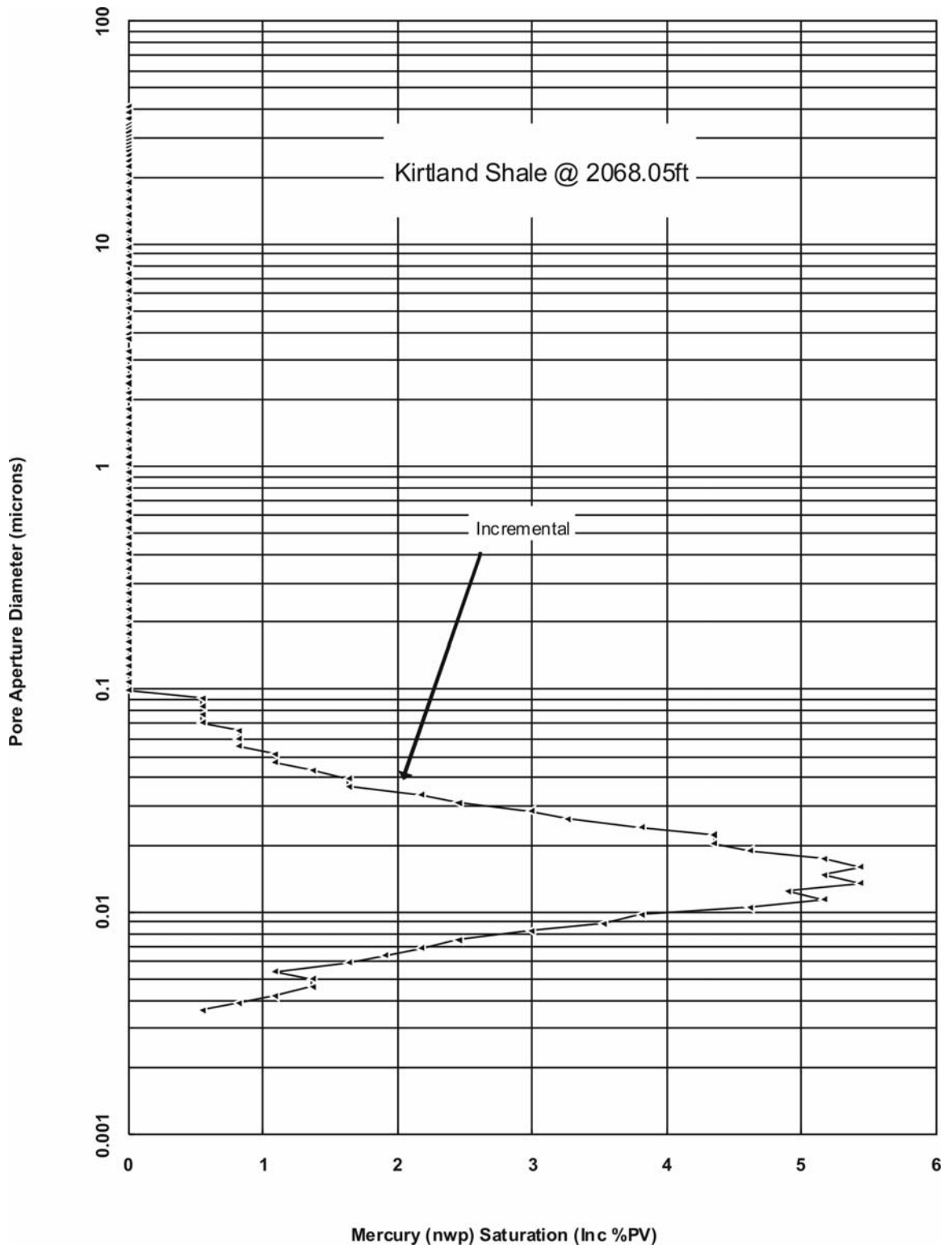


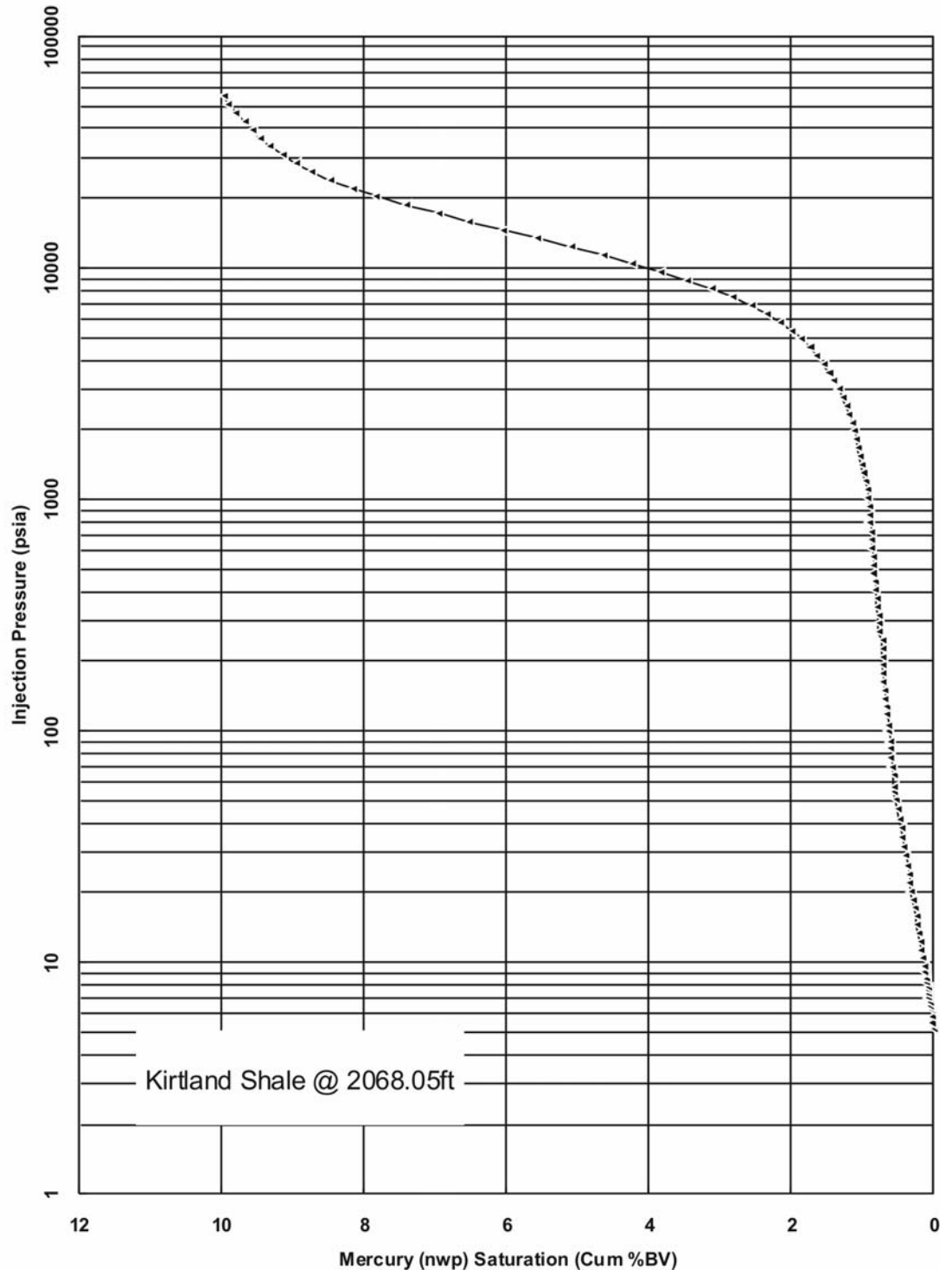


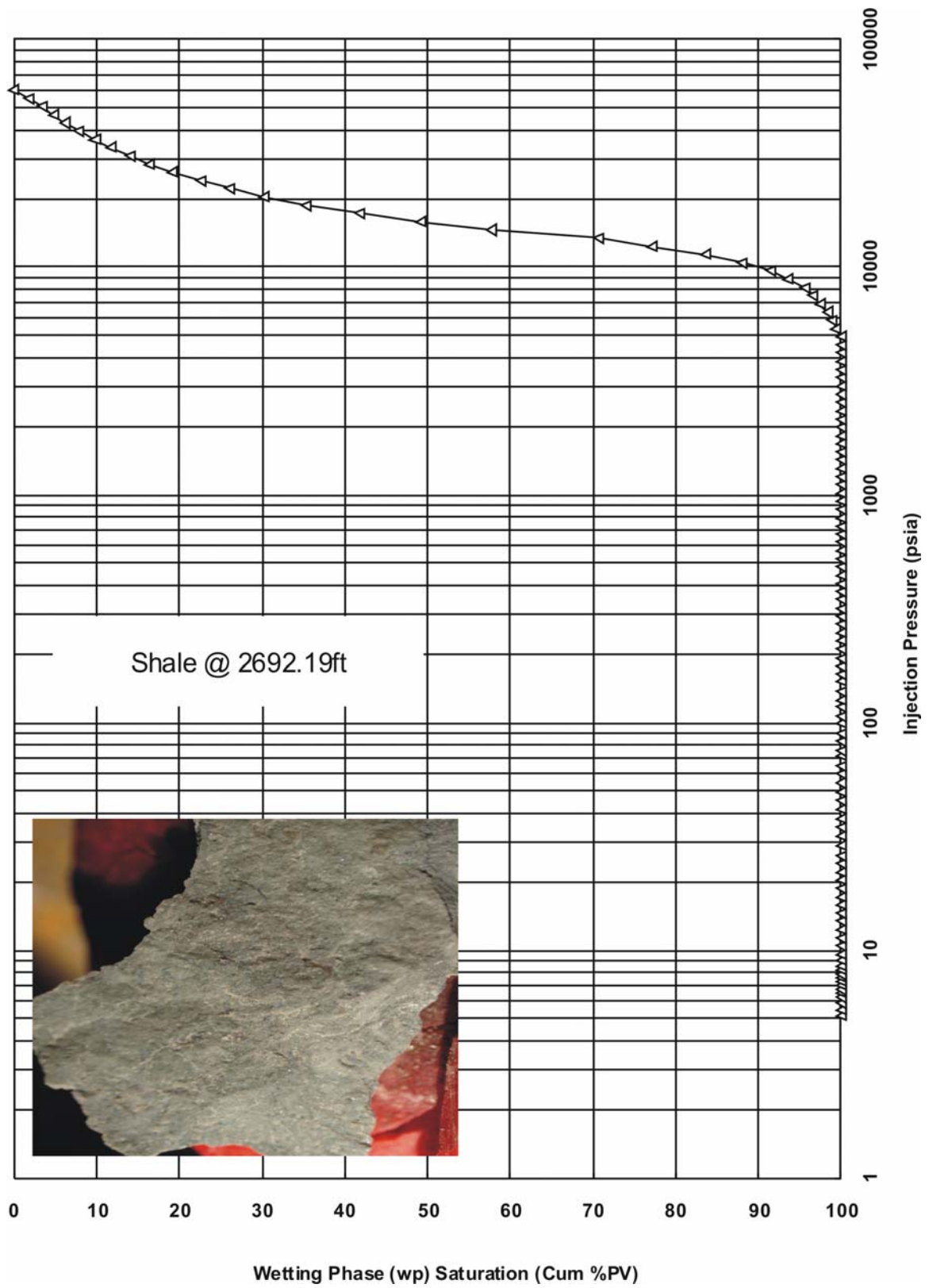


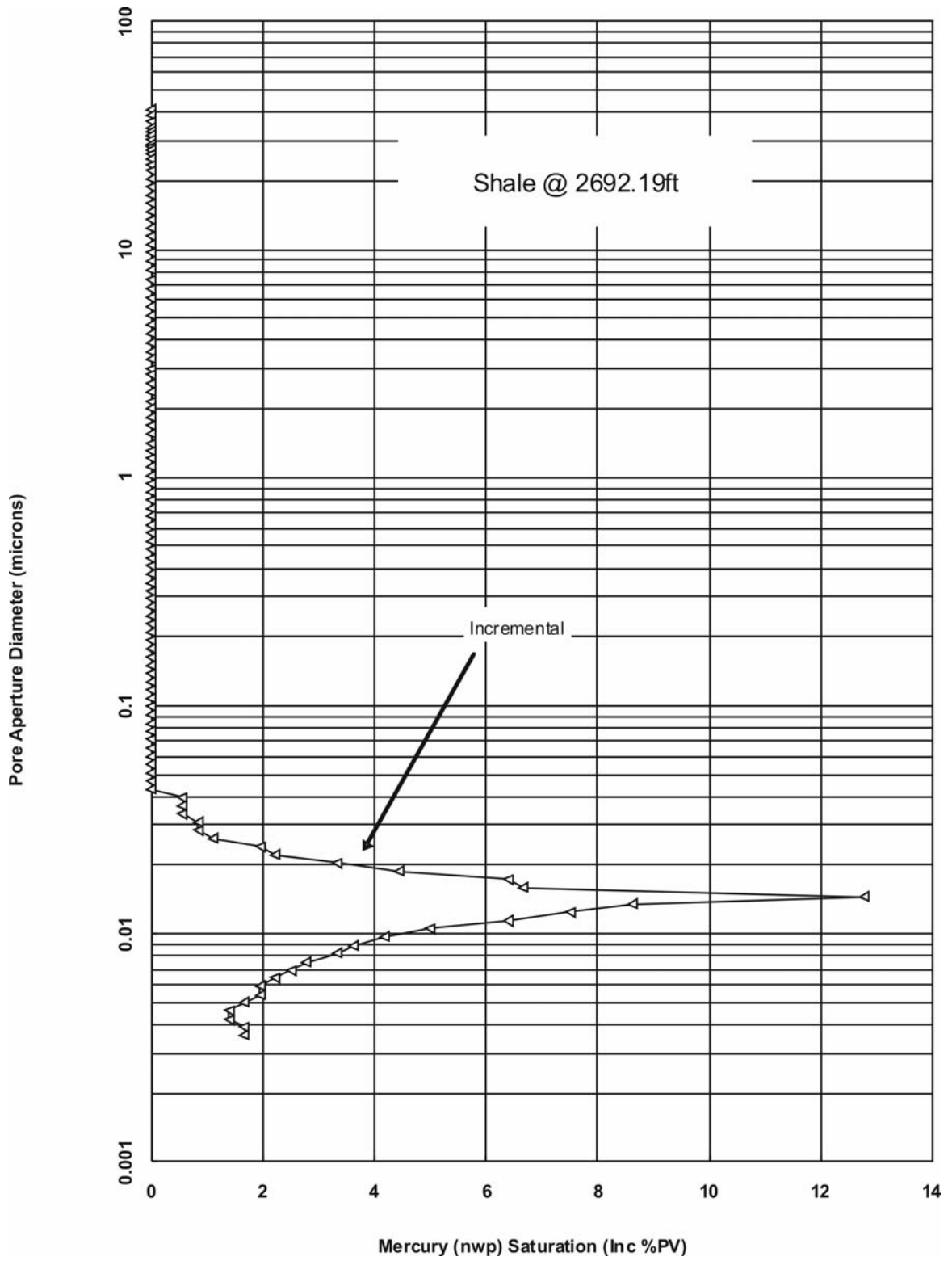


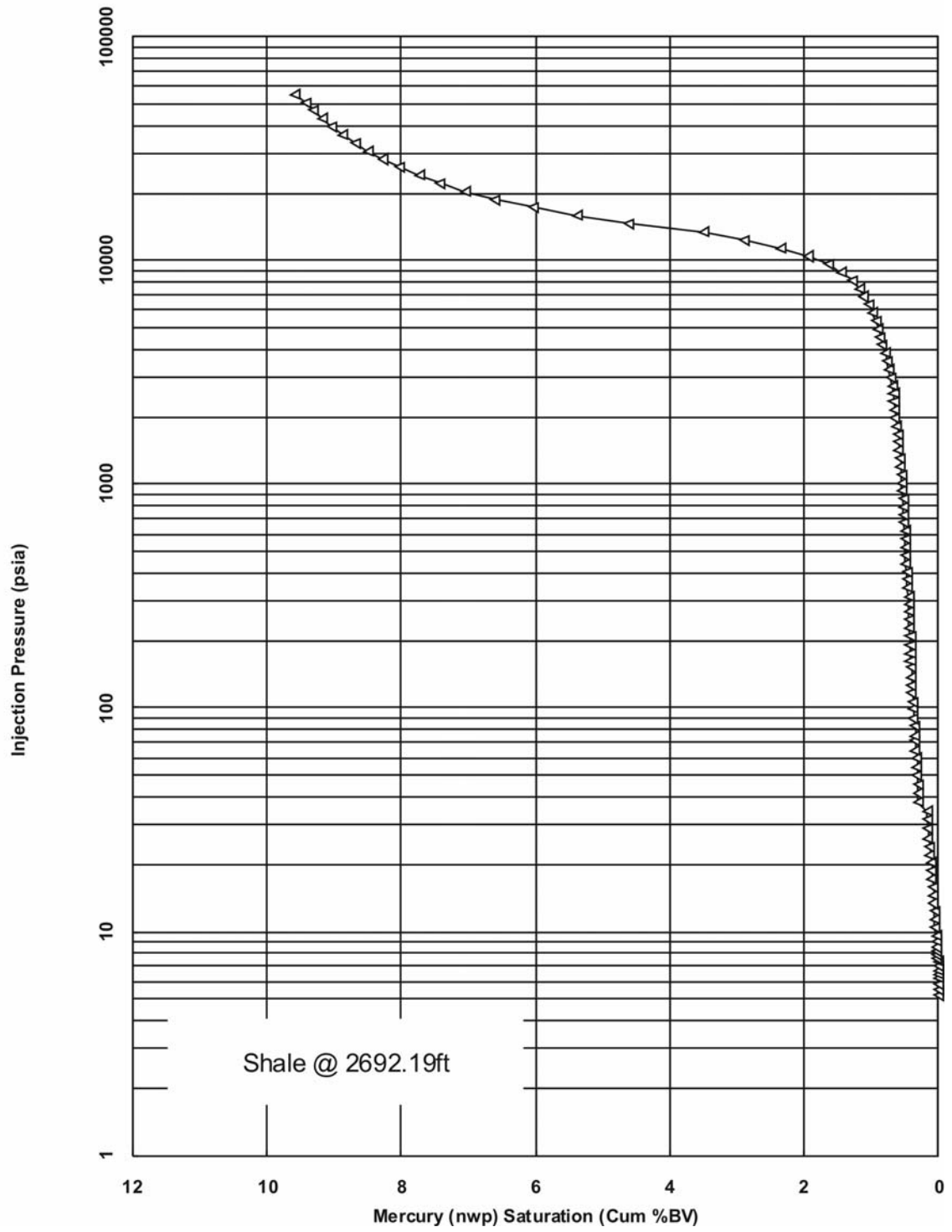












B.4 Inventory of Thin Sections and Billets

In addition to thin sections made by TerraTek, 21 additional thin sections and 21 billets (i.e., “thick” sections) were made by Wagner Petrographic, Lindon, UT, to support: 1) lithologic characterization of core at additional depths; 2) investigation of natural, mineralization fractures found in the core; and 3) laser scanning confocal microscopy at scanning penetration depths greater than the typical 30 μm of a standard thin section.

Each billet corresponds to a thin section—a cut was made in the rock samples such that the two adjacent surfaces made from the cut would be polished surfaces of a thin section and billet. Thus, the surfaces of the thin sections and billets were essentially mirror images of each other except for the loss of rock material for the cut and polishing. Many of the thin sections and billets were studied with electron microscopy, standard petrographic techniques, and laser scanning confocal microscopy, the results of which are given in Chapter 5.

Preparation of thin sections commissioned by TerraTek followed methods given in Appendix B.2.1. Preparation of additional thin sections and billets followed similar methods except that they were not stained, and they were polished in oil. All samples were impregnated with a low-viscosity fluorescent red-dye epoxy resin under high vacuum. The billet size corresponded approximately with the 24 mm \times 46 mm of the standard thin sections, and the thickness was between ~ 0.010 to < 0.018 m.

Figures in this appendix only show thin sections and not the corresponding billet. Billets were made for all thin section except those obtained by TerraTek. All thin sections were color scanned at 1200 dpi as “TIFF” files for use in documentation of locations of

microscopic investigation (Figures B.4.1 through B.4.4). The first line of the annotation under the thin section images gives the code used by Wagner Petrographic to identify the thin sections. The second line denotes the formation and depth ranges in ft with the following abbreviations:

OA = Ojo Alamo Sandstone

UK = upper shale member of the Kirtland Formation

LK = lower shale member of the Kirtland Formation

The remaining annotation lines, when given, provide additional information on the thin sections, such as the younging (or up) direction of the sample, where “Y.D.” represents “younging direction”. Typically, the notch made in many of the samples indicates the general younging direction—the notch is at the “youngest” or stratigraphic highest portion of the thin sections.

Table B.4.1. Inventory of thin sections

Wagner Petrographic Code	Formation and Depth Range	Polished	Stained
B1; CP-1	UK-2048.25		x
B2; CP-2	UK-2052.06		x
B3; CP-3	UK-2055.2		x
B4; CP-4	UK-2062.3		x
B5; CP-5	UK-2067.98		x
B6; CP-6	LK-2692.25		x
B7; CP-7	LK-2697.15		x
L1A	QA-2030.13-2030.71	x	
L2A	QA-2033.73-2034.44	x	
L3A	QA-2046.30-2046.67	x	
L4A	UK-2052.06-2052.58	x	
L5A	UK-2055.26-2055.74	x	
L6A	UK-2056.97-2057.46	x	
L7A	UK-2062.46-2063.01	x	
L8A	LK-2693.77-2694.25	x	
L9A	LK-2697.28-2697.50	x	
M1	UK-2056.16	x	
M2	UK-2056.30-2057.45 A	x	
M3	UK-2056.30-2057.45 B	x	
W1	LK-2698.22 A	x	
W2	LK-2698.22 B	x	
W3	LK-2698.22 C	x	
W4	UK-2056.92 A	x	
W5	UK-2056.92 B	x	
W6	UK-2056.42	x	
W7	UK-2056.60-1	x	
W8	UK-2056.60-2	x	
W9	UK-2056.40	x	



B1; CP-1
UK-2048.25



B4; CP-4
UK-2062.30



B7; CP-7
LK-2697.15



B2; CP-2
UK-2052.06



B5; CP-5
UK-2067.98



B3; CP-3
UK-2055.20



B6; CP-6
LK-2692.25

Figure B.4.1. Inventory of “B” set, which were obtained by TerraTek (see Appendix B.2.1).



L1A
QA-2030.13-2030.71
Y.D.: Unknown; either
upward or downward



L4A
UK-2052.06-2052.58
Y.D: downward



L7A
UK-2062.46-2063.01



L2A
QA-2033.73-2034.44
Y.D.: Unknown



L5A
UK-2055.26-2055.74



L8A
LK-2693.77-2694.25



L3A
QA-2046.30-2046.67
Y.D.: Unknown; to the
right or left



L6A
UK-2056.97-2057.45
Y.D.: To the left



L9A
LK-2697.28-2697.50
Y.D.: Unknown; probably
upward or downward

Figure B.4.2. Inventory of thin sections for the “L” set, which were obtained to further study of lithology at additional depths.



W1
LK-2698.22 A



W4
UK-2056.92 A



W7
UK-2056.70-1



W2
LK-2698.22 B



W5
UK-2056.92 B



W8
UK-2056.60-2



W3
LK-2698.22 C



W6
UK-2056.42



W9
UK-2056.40

Figure B.4.3. Inventory of thin sections for the “W” set, which were obtained to examine mineralized fractures observed in core.



M1
UK-2056.16
Notch indicates natural
fracture with dip of ~11-
15°



M2
UK-2056.30-2657.45A
Y.D.: Not definitely
known; notch marks
fracture that may dip ~10-
15°



M3
UK-2056.30-2057.45B
Y.D.: Not definitely
known; notch marks
fracture that may dip ~10-
15°

Figure B.4.4. Inventory of thin sections for the “M” set, which were obtained to examine mineralized fractures observed in core. Due to the friability of the core, the younging or up direction was lost during handle of the core. It is probably that the notch marks shallowly dipping fractures like that of M1.

B.5 Mud Log of Well EPNG Com A Inj #1

A mud log was taken during drilling and coring of well EPNG Com A Inj. #1, which follows below.

SOFTROCK GEOLOGICAL SERVICES, INC.



San Juan Basin's Premier Mudlogging Business

591 Co. Rd. 233 Durango, CO 81301
970.247.8868 fax 970.247.5108



- HORIZONTAL LOGGING
- WELLSITE CONSULTING
- PRECISION CHROMATOGRAPHY
- PHOTO MICROSCOPY
- COAL DESCRIPTION

Scale 1:240 (5"=100') Imperial
Measured Depth Log

Well Name: EPNG COM A INJ #1
Location: SENW Sec. 32 T31N R08W San Juan Co., NM
License Number: API # 30-045-34305 Region: Basin Fruitland
Spud Date: Spud on May 5, 2008 Drilling Completed: June 14, 2008
Surface Coordinates: 2500' FNL Lat. 36° 51.2891' North
2665' FWL Lon. 107° 41.8797' West
Bottom Hole Coordinates:

Ground Elevation (ft): 6321' K.B. Elevation (ft): 6332'
Logged Interval (ft): 1500' To: 2943' Total Depth (ft): 3156'
Formation: Cretaceous Nacimiento, Ojo Alamo, Kirtland, Fruitland
Type of Drilling Fluid: LSND FW Mud, Air/Mist

Printed by WellSight Log Viewer from WellSight Systems 1-800-447-1534 www.WellSight.co

CORE

Contractor: Coring Services (Midland, TX - 432.563.6280)
Core #: 1 & 2
Formation: Ojo Alamo/Kirtland, Lower Kirtland Shale
Core Interval: From: 2018' / 2690' Cut: 52' / 18'
To: 2070' / 2708' Recovered: 51' / 09'
Bit type: Ultrerra CPM-1208P / Gearhart MO812CB
Size: 8 (23/32)"
Coring Time: 3 hrs / 7 hrs

OPERATOR

Company: Burlington Resources Oil and Gas Company
Address: San Juan Dvission---COAL Team ATTN: Mr. Eddie Pippin
3401 E. 30th Street
Farmington, NM 87401

GEOLOGIST

Name: Dan McGinn, Bob Bradley, Mason Auger
Company: Softrock Geological Services, Inc.
Address: 591 County Rd. 233
Durango, CO 81301
(970) 247-8868 fax (970) 247-5108

Contractors

Aztec Well Services Rig #580 / #266
 Burlington Co. Rep. : Mr. Mike Frankinburger / Mr. Keith Jackson / Mr. Ron Coffee
 New Mexico Tech Univ.: Mr. Jason Heath, PhD Candidate / Dr. Reid Grigg, PhD
 Sandia National Labs: Mr. Scott Cooper
 US D.O.E. / NETL: Dr. Dustin McIntyre / Mr. Brian Tennant
 Schlumberger Wireline Logging

Instrument

i4 FID Chromatograph (Hydrogen fuel & carrier gas)
 Scotty Analyzed Gases Calibration Gas
 -->(1% each C1, C2, C3, iC4, nC4 / balance Nitrogen)
ACCOUNTING:
 FC AFE #: WAN.CDR.7085
 FC NW #: 10197739 / 10198155
 PO #: BCURLEY
 Activity Code: K200 Mudlogging

Hole / Casing Data

Hole Data: 12 ¼" to 230'
 8 ¾" to 2943'
 6 ¼" to 3156'
 Casing Data: 9 5/8" to 224' 32.3# H-40 ST+C
 7" to 2939' 20# J-55 ST+C
 5 1/2" perf'd liner and 2 3/8" tubing

ROCK TYPES

LITHOLOGY	Shale	Cement	Sand lens
Bentonite	Siltstone		Clay lens
Chert band	Clay	STRINGER	Carb shale
Coal	Fracture	Argillaceous	Coal streak
Conglom.	Marl	Bentonite	
Limestone	Carb shale	Coal lam.	
Sandstone	Mudstone	Lime	

ACCESSORIES

FOSSIL	MINERAL	Glaucanite	Orange inclusions
Shell hash	Argillaceous	Heavy min.	Water
Crinoid	Bentonite	Kaolinite	Fracfill
Fish	Calcareous	Marly	Smkyqtz
Fossil	Carby	Mica	Rose quartz
Oolite	Dark chert	Min. xl	Chlorite
Plant	Light chert	Pyrite	Jasper
Inoceramus	Dolomite	Sandy	Amber
	Feldspar	Silty	Inter. clay
	Ferromag	Silica/qtz	

OTHER SYMBOLS

INTERVALS	Sliding	Fracture	Tite conn
Core #1		Survey	Pitot
Core #2	EVENTS	Comp. samp.	Sea level
Core #3	Casing shoe	Dz canister	Fm. member
Core #4	Midnight	Gas show	Fm. tops
Wet cuts	Bit trip	Td	Interp. show

